Preparation and Analysis of RNA Crystals

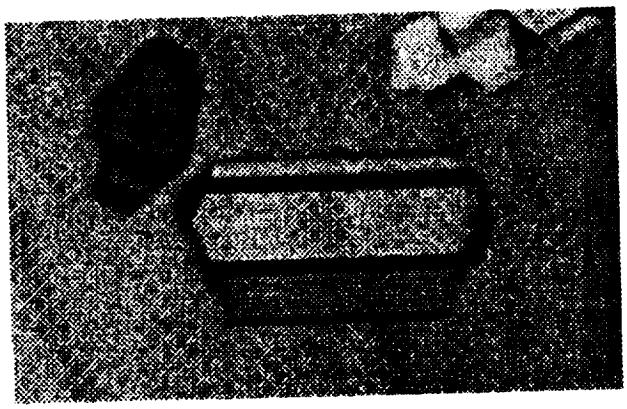

National Aeronautics and Space Administration

NAG8-1165

Final Report, May 2000
University of Colorado

PREPARATION AND ANALYSIS OF RNA CRYSTALS

TABLE OF CONTENTS

PART IV. TASK 3: MECHANISMS OF ACTION OF INERTIAL ACCELERATION

Chapter 1

Preamble

Introduction

This Final Report covers the period 1 July 1995 through 29 February 2000. The research was dedicated to the pursuit of three tasks in RNA crystallization

Changes in Scope

The final workplan identified three tasks: 1. Preparation of high-quality crystals, 2. Pathway to high-quality crystals, and 3. Mechanisms of action of inertial acceleration (gravity) on crystal nucleation and growth. The project adhered to the execution of these tasks with minor but significant modifications in scope as follows.

The revised work plan (Chapter 2) mainly had two effects on the originally proposed research: a reduced direct low-gravity research effort (Task 3) and reduced collaboration of crystallographers interested in high-quality crystals of specific oligonucleotides (Task 1). This modified scope is reflected in the relative volumes of the chapter sections that follow.

RNA was not the only substance studied. Certain space experiments could not be performed at the crystallization temperature of the model oligonucleotide selected, so protein crystallization studies were considered a valid alternative in view of the physical questions being asked (Task 3). Likewise, the pursuit of a generic hypothesis of oligonucleotide crystallization (Task 2) mandated the study of at least one DNA oligonucleotide.

As with many research efforts in the academic world, several personnel changes impacted the scope of the project, especially in the area of crystallography. Prof. Kundrot, the main co-investigator and project crystallographer, left the University to accept a leadership position at Marshall Space Flight Center (a well-defined contribution of this project to NASA's crystallization research effort). Prof. Schultz, in a similar role, underwent a period of reconsideration of his position at the University and was unavailable for over a year. Dr. Lehrman, who was providing oligonucleotides and guidance from a local oligonucleotide firm accepted a position in California. Dr. Z. R. Korzun, who voluntarily performed crystallography at the Brookhaven National Laboratory National Synchrotron Light Source died suddenly during the project. And Dr. Allen Edmundson, serving in a similar role, moved to a position in which his activities became severely constrained. Tasks 1 and 3 were therefore also limited by these events; however, an adequate amount of crystallography was nonetheless performed to support the objectives of Task 2.

Organization of the Final Report

The Report is divided into four parts. Part I (which includes this preamble) consists of the revised statement of work (Chapter 2), which was requested at the time of the original approval of the project for funding. It is the purpose of this chapter to clarify the subject matter to which the scope of the research was reduced from that proposed in the original grant application. Chapter 3 alludes to the individual accomplishments and summarizes the results and significance of Chapters 9-31. Chapters 3 and 4 are re-submissions of the annual task reports and cumulative bibliography, respectively.

Part II contains individual chapters related to Task 1, the *preparation of high-quality crystals and their complexes.* Chapters 7 and 8 are published articles from the work of co-investigator Craig E. Kundrot and associated workers.

Part III contains chapters and published papers describing the bulk of the work and the main emphasis of this project, namely *the pathway to high-quality oligonucleotide crystals (Task 2),* and is a reflection of what engineering research has to offer to the crystallization field. Chapters 9-11 are introductory and deal with the thermodynamic concepts and purity issues in controlled crystal growth. Chapters 12-14 emphasize the most significant discoveries of the project; namely, oligonucleotides in solution behave as electrokinetically stabilized colloids, and the rules of such colloids apply to the thermodynamics of oligonucleotide solutions and crystal growth. While Chapters 9-14 deal mainly with equilibria, Chapters 15-25 deal with kinetics, ranging from detailed analyses of crystal growth in osmotic dewatering (15-17) through vapor-transport issues (18,19) to transport studies on membranes used in crystal growth methods being popularized by the project laboratory (20-25). Finally the thermodynamic results are brought together with the kinetic results in Chapter 26 to demonstrate that *the proper delivery rate of multivalent cations to an oligonucleotide solution is all that is required for the growth of diffraction-quality crystals.* The significance of this lesson cannot be overemphasized and is, perhaps, alone worth the entire monetary expenditure associated with the project.

Part IV is a presentation of five chapters associated with low-gravity research performed on the project with the intention of exploring *mechanisms of action of inertial acceleration (Task 3).* This aspect of the work was substantially reduced in scope in the revised statement of work (Chapter 2). Considerable external collaboration was utilized in this work, resulting in correspondingly multiple organizations and co-investigators participating with and without support from the project budget.

The origins of the chapters are varied. Some of them are reprints of published papers, in which case the pages and page numbers do not indicate their serial position in the report, but each chapter has a colored separator page by which it can be located. Some chapters are derived from thesis chapters, in which case some of them will have section numbers corresponding to their position in this report. Yet other chapters are manuscripts in

various forms of maturation, many of which have been submitted for publication. Finally, proceedings papers are also included in this report, and these may tend toward redundancy with other chapters while containing important increments of information.

Leverage

Owing to the high level of interest in both oligonucleotide technology and low-gravity research in Boulder, Colorado, the augmentation of the financial and labor resources dedicated to this project was phenomenal. External guidance was provided by some of the best minds in both fields without cost. Such individuals, too numerous to be listed unless by request, were provided by the CU departments of Chemistry and Biochemistry, Molecular, Cellular and Developmental Biology, Aerospace Engineering Sciences, Mechanical Engineering and Chemical Engineering. Within this context research centers played a key role, both intellectually and financially: The Center for Low-Gravity Fluid Mechanics and Transport Phenomena, Center for Separations Using Thin Films, BioServe Space Technologies Center, Colorado RNA Center and Colorado Institute for Research In Biotechnology. The last three provided assistantships and fellowships to key graduate students on the project, which facilitated an 8-month no-cast extension to the performance period of the project. Of particular note is the considerable cost savings associated with successful labor barters with two firms providing space flight services, Instrumentation Technology Associates and Space Hardware Optimization Technology, Inc. In an excellent model of university-industry cooperation it was possible to bring excited students to the realm of hands-on space flight research while significantly reducing the cost of access to space for a peer-reviewed and approved scientific low-gravity project. These firms also provided access to unique flight hardware that perfectly matched the project objectives including, to our knowledge, the only opportunities to provide impeller mixing and osmotic dewatering methods so critical to Task 3.

Conclusion

The purpose of this Preamble has been to orient the reader to the field of the research, the specific tasks undertaken, the scope of the research, and the material and labor leverage achieved on behalf of the project. The technical executive summary is reserved for Chapter 3, below.

Chapter 2

Preparation and Analysis of RNA Crystals
Revised Statement of Work
1995

Paul Todd

Paul Todd

CHAPTER 2

Revised Statement of Work

"Preparation and Analysis of RNA Crystals"

(1) Applicant Organization: Regents of the University of Colorado
Boulder, Colorado 80309

(2) Brief Project Title: Preparation and Analysis of
RNA Crystals

(3) Type of Organization: Non-profit, educational

(4a) Principal Investigator: Prof. Paul Todd
Telephone 303-492-5936
Telefax 303-492-4341
E-mail TODD_PW@cubldr.colorado.edu

(4b) Business Personnel: Mr. Laurence D. Nelson
Telephone 303-492-2695

(5) Other Organization Evaluating This Proposal: None

(6) Specific NRA: NRA 94-OLMSA-02, "Microgravity Biotechnology:
Research and Flight Experiment Opportunities"

(7a) Dollar Amount Requested:

(7b) Proposed Starting Date: 1 July, 1995

(7c) Duration of Project: Four years.

(8) Date of Submission: 8 June, 1994

(9) Signature of Authorized Representative: Carol B. Lynch

Carol B. Lynch, Associate
Vice Chancellor for
Research

(10) Signature of Principal Investigator: Paul Todd

Steve Schultz

Craig Kundrot

University of Colorado at Boulder

Department of Chemical Engineering

Engineering Center, ECCH 1-43
Campus Box 424
Boulder, Colorado 80309-0424
(303) 492-7471
FAX: (303) 492-4341

5 June, 1995

Joyce Mallory, Contracting Officer
National Aeronautics and Space Administration
George C. Marshall Space flight Center
Marshall Space Flight Center, AL 35812

Dear Joyce Mallory:

Enclosed please find our response to your letter of 24 May, 1995, concerning our response to 94-NRA OLMSA-02, "Microgravity Biotechnology: Research and Flight Experiment Opportunities". A revised statement of work, as requested, for the proposal titled "Preparation and Analysis of RNA Crystals" is enclosed.

The total effort has been reduced to less than half of the proposed project, consistent with the recommended reduction in budget. Consistent with the reviewers' comments, the investigation of a variety of methods has been retained, but the number of ground- and space-based experiments will be about half that proposed, while certain pursuits, such as atomic-force microscopy, have been eliminated. We will also be unable to synthesize as much material for crystallization as originally planned. There will be no attendance at national or international meetings. Theoretical work is retained, as it is relatively inexpensive and intrinsic to Ph.D. thesis research.

Please notify me if you have any questions concerning the revised statement of work.

Sincerely yours,

Paul Todd

Paul Todd
Research Professor

Paul Todd

PREPARATION AND ANALYSIS OF RNA CRYSTALS

Executive summary

What is planned: The over-riding objective of this project is the routine growth of crystals of oligonucleotides (RNAs, ribonucleic acids) that diffract x-rays to high resolution. First, high-quality crystals of RNAs currently under study will be grown. Second, rules for the successful crystallization of RNAs will be sought. Third, the microphysics of gravitational effects on RNA crystal nucleation and growth will be examined in terms of the full range of transport processes involved: sedimentation, convection, diffusion, capillary flow and their associated driving forces.

How it is to be done: These objectives will be pursued by the application of a sparse matrix of trial conditions, including standard and novel crystallization techniques ranging from the traditional hanging-drop, vapor diffusion method through osmotic dewatering to the newly invented step-dialysis technique. Promising methods will be practiced in the low-gravity environment of orbital space flight to further refine the resolution of those crystals that are grown successfully. All of the tested methods will be performed on the ground and in space flight. By performing crystallization studies in solutions of various densities, levels of inertial acceleration ("gravity"), and concentration rates using RNAs and surrogate molecules (proteins), the microphysics of optimized nucleation and growth will be studied. A team of nationally-prominent investigators has been assembled at the University of Colorado and associated biotechnology companies to address these problems; they include oligonucleotide chemists, x-ray crystallographers, molecular biologists, low-gravity researchers and hydrodynamicists.

Importance of the proposed research: Oligonucleotides as therapeutic and diagnostic agents have captured the imagination of our nation's most outstanding biochemists, and nearly a dozen biotechnology, chemical and pharmaceutical firms have collectively invested a few hundred million dollars in the promise of oligonucleotides as commercial products. Oligonucleotides are rich in three-dimensional tertiary structure, carefully chosen RNAs can be designed to have hydrolytic activity against specific genes such as those of infectious agents, they can be designed to foul the genes of infectious agents, and they can be designed to selectively inhibit the products of infectious agents such as HIV reverse transcriptase. All of these issues are under vigorous pursuit at the University of Colorado and in the community of Boulder biotechnology companies. Although rules for predicting the tertiary structure of oligonucleotides are evolving, the industry craves three-dimensional structural data at high resolution. For example, pseudoknot structures are difficult to predict, but they are very important in advanced biopharmaceutical research. The effect on tertiary structure of primary chemical modification of nucleosides, which enhances stability, cannot presently be predicted.

Microgravity relevance: There are several reasons to believe that superior RNA crystals can be prepared in low gravity by novel methods. At the current state of affairs, a few interesting ribozyme fragments and some small synthetic oligonucleotides have been

crystallized and shown to diffract x-rays. Diffraction resolutions to about 2.5Å, 3.4Å, and 8 Å have been achieved in three exemplary cases. This state of affairs is rather similar to that of human recombinant γ-interferon, canavalin and porcine elastase about 5 years ago, before these proteins had been crystallized in low gravity. In these cases, low-gravity crystallization solved problems of adequate resolution for unambiguous assignments of functional groups, excessively twinned crystals due to sedimentation, and excessively branched crystals due to unstable dendritic growth, respectively. We are able to bring a combination of laboratory and spaceflight equipment to bear on these problems that no other applicant can claim. These same three problems have been identified in RNA crystallization experiments, and it is proposed that they can be solved by crystal *growth* in low gravity and/or crystal-growth *studies* in low gravity. The former will yield crystals immediately useful for diffraction studies, and the latter will reveal the changes in procedure required for successful crystal growth in the laboratory. We are confident that both approaches will yield a bright future for RNA science.

RESEARCH PROJECT DESCRIPTION

A. Statement of Hypothesis, Objectives and Value of the Research

1. Hypothesis and objectives

The hypothesis under test is that RNA crystallization, like the growth of other crystals, is affected by inertial acceleration and that the effect(s) of inertial acceleration can be overcome by reducing inertial acceleration in space flight and by reducing its effects in the laboratory once the causative factors are understood. Therefore, research is proposed with the following specific objectives:

Specific Objective 1. Grow crystals of specific RNAs and RNA-peptide complexes that diffract x-rays to high resolution (d_{min} < 3Å).

Specific Objective 2. Identify pathways that lead to highest-quality crystals of RNAs and their complexes.

Specific Objective 3. Detail the mechanism of the role of inertial acceleration (gravity) in high-resolution RNA crystal growth.

B. Description of Tasks and Experimental Methods that Will be Used

1. Preparation of high-quality crystals of RNAs and their complexes

A phased, focused program initially involving two single molecules and two complexes is planned. The acquisition of high-quality crystallographic data will take place in three steps: (1) discovery of chemical conditions that allow crystals to grow, whether or not the crystals produce an x-ray diffraction pattern; (2) determination of chemical conditions that produce RNA crystals that produce a low-resolution x-ray diffraction pattern, one that can be used to determine space groups, unit cell dimensions, and occasionally domain maps at about the 5-8Å level; and (3) the production of high-resolution crystals from which atomic positions can be calculated. In some cases, the early steps have been achieved.

The specific first-year research objective is to produce high-quality (diffraction to at least 2.5Å resolution) crystals of two significant polyribonucleotides, one that is easy to prepare and apparently easy to crystallize and one that is of high commercial value but difficult to prepare. One example of each has been selected, and the first (easy) is a dodecamer with a putative U-U base pair in its secondary structure ("UU-dodecamer"); the second is the "pseudoknot" 26-mer or 28-mer that binds and inhibits HIV reverse transcriptase ("PK").

The crystallization methods to be applied in a logical sequence of trials have been used previously: "sparse-matrix" testing of chemical conditions, "osmotic dewatering" to produce and maintain saturation, "double diffusion" using a stabilized free interface, "single diffusion" using dialysis, and "step diffusion" using early nucleation. Two principal products of this research are expected: high-quality crystallographic data for the two proposed example molecules of each type, and the beginnings of a paradigm for a rapid path to the

production of diffraction-quality crystals of RNAs in general (Specific Objective 2).

Sparse matrix studies can be performed with any method, but, to date, only the vapor diffusion ("hanging drop") method has been used. A multi-chamber device for performing sparse matrix experiments using the osmotic dewatering method has been designed and successfully tested by growing protein crystals. This device is applicable to two other methods. Low-gravity methods are also practiced in multichamber devices, but it is not economically rational to test 44 conditions for crystallizing a single substance.

To reiterate the project goals, two different RNAs have been selected for initial crystallization study, and the first (easy) is "UU-dodecamer" (aka UU); the second is the "pseudoknot" ("PK") 26-mer or 28-mer that binds and inhibits HIV reverse transcriptase. We consider as the starting point for the planned research the assumptions that step (1) has been achieved for UU dodecamer, PK 28-mer, and the two complexes that will by studied, while step (2) has been accomplished only for PK 26-mer and one complex. And the principles underlying step (3) have been established using a surrogate protein, lysozyme from hen egg white.

At each step, RNA crystals will be studied by x-ray diffraction, and cryocooling technique will be applied in most cases. In recent experience this has been accomplished by soaking crystals in a cryostabilizer (solutions of glycols) then freezing in liquid propane just above its freezing point.

The steps to be performed consist of moving beyond this point through the following, generally chronological steps:

1. Synthesis and purification of UU dodecamer.
2. Osmotic dewatering studies with UU dodecamer (utilizing results of sparse matrix experiments using the hanging drop method).
3. Double diffusion studies with UU dodecamer utilizing the method developed for stabilizing lysozyme solutions in the presence of buoyancy forces ("g").
4. Single diffusion studies with UU dodecamer utilizing 1,000 MWCO membrane.
5. Further sparse matrix studies with PK 26-mer.
6. Detailed matrix (limited concentration ranges) with both PK molecules, especially to establish highest salt and lowest PK concentrations so that double diffusion and fast nucleation methods can be applied in the laboratory.
7. Osmotic dewatering studies with PK.
8. Double and single diffusion studies with PK.
9. Osmotic dewatering, double diffusion and step diffusion studies with PK and UU dodecamer in low gravity utilizing facilities offered by Instrumentation Technology Associates.
10. Osmotic dewatering, single diffusion and step diffusion (dialysis) studies with PK's and UU dodecamer in low gravity utilizing facilities offered by BioServe Space Technologies, the only hardware in which these processes can be performed simultaneously with the opportunity of including lysozyme positive controls.

The concentrated solutions of pure RNAs required for the completion of the above steps will be synthesized by in vitro transcription, with RNA polymerase transcribing immobilized synthetic DNA templates. We intend to make use of recent progress in immobilizing template DNA, which improves transcription efficiency in the case of PK 28-

mer and conserves template DNA or to make use of recent progress in immobilizing the polymerase, which allows recycle of the enzyme and extends the period of maximum transcription rate.

Steps 9 and 10 will be executed after achieving the preceding steps and will be partially supported by the respective spaceflight facility providers, ITA and BioServe Space Technologies and, if possible, available NASA facilities. Low-gravity experiments will be performed during the 3rd quarter of 1995 using ITA middeck facilities and, as currently planned, on space shuttle flights STS-69, STS-73 (USML-2), STS 74 (SpaceHab 4) and possibly a 90-day Mir space station mission in the BioServe Space Technologies program, as currently scheduled. The three shuttle flights occur during the first fiscal year of the project, namely, July 1995, September, 1995, and April, 1996, respectively.

Small amounts of potentially hazardous chemicals are used in RNA crystallization, such as acetic acid, cacodylic acid and methylpentanediol. They are dissolved in water at fractional molar concentrations in volumes up to 100 μl per sample. These solutions in these quantities have been approved for space flight on the U.S. space shuttle by the toxicology committee and the office of the flight surgeon in both ITA and BioServe containers, which provide three levels of containment of all samples. The feasibility of performing the planned experiments on the space shuttle is therefore not in question, and it is assumed that the same approval procedures that we normally follow will also apply to NASA-supplied crystallization facilities, such as MCAM, which we have also already used.

2. Pathway to high-quality RNA crystals

The four RNAs/complexes to be studied during the first year have been crystallized by the hanging-drop method, and they diffract x-rays to various resolutions (see section C). Therefore a pathway to the preparation of higher-resolution crystals remains to be determined. Adequate amounts of all four RNAs will be prepared by transcription. Each will be crystallized under 20 conditions by osmotic dewatering, starting with the same crystallizing solution as used for each in the hanging-drop method and a higher concentration of reservoir solution than used in the hanging-drop method. The resulting crystals will be evaluated by microscopy and the best ones mounted for x-ray diffraction. The potential results are: the quality of crystals grown by osmotic dewatering are the same, better, or poorer than those grown by hanging drop.

This procedure will be repeated using the dialysis and step dialysis methods. In the case of each RNA, the method that resulted in the greatest improvement will be identified, and its counterpart will be applied in low gravity. For example, if step dialysis produces the best crystals in the laboratory, then that RNA will be crystallized using step diffusion or step dialysis in low gravity.

In some low-gravity experiments we intend to bridge gap to protein crystal growth using hen-egg lysozyme, which is heavily tested, both to monitor space flight conditions and to continue the comparison of the idealized pathway for proteins to that of RNA. These experiments will be performed on a space-available basis when lysozyme crystallization does not significantly displace experiments with other valuable substances.

Finally, by using the results of part 3 (next, below), the optimized pathway will be

rationalized. This aspect of the research is a blend of objectives 1 and 3 and will be carried out at minimal cost.

3. Mechanisms of action of inertial acceleration (gravity) on crystal growth.

Our research group is actively involved in microhydrodynimics research and has worked out detailed theories of small (10-100 μm) particle motion caused by diffusion, convection, sedimentation, thermocapillary convection, solutocapillary convection, electrokinetic migration and transmembrane advection or flow. Most of the tools are now in place for the calculation of collision efficiencies affected by these processes.

By making use of our unique access to multiple crystallizer types, a versatility no other applicant can claim, we will perform experiments and computations to distinguish among the following hypotheses (a-g) described in detail as follows:

Studies undertaken in the laboratories of F. Rosenberger [32], G. Feher [17] and R. Feigelson [33] have been aimed at elucidating gravity-dependent mechanisms of macromolecular crystal growth. Their findings to date imply that growth rates vary among crystal faces and that the addition of new molecules to the surface of the growing crystal plays a critical role in final crystal size.

Purely theoretical studies have been undertaken, such as that of Saville, in which the transport processes associated with crystal growth are summarized, some of which can be characterized as gravity-dependent [34]. These studies were based mainly on approximations using engineering correlations and provided a sense of the potential importance of convective currents around the growing crystal, the shear forces they produce, mass transport of solute to the crystal and its incorporation, the rejection of precipitant and other qualitatively considered forces. Most of the calculations of this study led to the view that these forces are too small to have an appreciable effect, with the possible exception of forces associated with precipitant rejection.

The convective currents around a growing triglycine sulfate crystal were simulated by Lockheed workers in the 1980's and reported by Dressler [35], who recommended the use of a Rayleigh number of the following form

$$Ra = 2g\Delta\rho D^3/\rho\nu\kappa \qquad (1)$$

where ν = kinematic viscosity, and the other symbols have their usual meanings. The two-dimensional transient velocity is directly proportional to Ra, so the cubic dependence on D means that, especially for high-molecular-mass solutes, Ra could be so low that such motion can be ignored. However, experimental results must also be considered [31]. Computer codes are available for calculating two-dimensional velocity profiles [36], and the adjustment of these to accomodate realistic parameters and realistic geometries for oligonucleotide crystal growth should have merit.

Taking another approach, Sibille and Baird and [37] analyzed the transport of vapor in space flight and on the ground and found quite discrepant transport rates. Since nearly all quality low-gravity experiments have been performed using the vapor diffusion method in almost identical equipment, then two variables have been imposed on the experiments

to date: inertial acceleration and evaporation rate. By using the osmotic deqatering method, we plan to control the solvent transport rate on the ground and in space, so that the role of this variable can be determined. As will be seen below, our studies have already included varying solvent evaporation rate in the laboratory and in low g.

Experiments and calculations will be performed to distinguish among the following hypotheses:

Hypothesis a: Inertial acceleration affects the balance between solute consumption rate and solute diffusion rate. In the context of purification, chemical engineers have always addressed the question of reaction-rate-limited vs. diffusion-rate-limited crystal nucleation and growth. The modeling framework in which this is done involves the kinetic equations for nucleation and growth. The rate of increase in crystal (nuclei) number, N, depends on degree of supersaturation in a reaction of order m:

$$dN/dt = k_1(c - c^*)^m \qquad (2)$$

where k_1 is the empiricial rate constant of appropriate dimensions, c is instantaneous solute concentration, c^* is concentration at saturation, and m is usually empirically determined. dN/dt must be kept small, but not so small that no nucleation occurs.

The rate of crystal mass, M, increase is usually first-order:

$$dM/dt = k_2A(c - c^*) \qquad (3)$$

where k_2 = mass transfer coefficient that depends solely on diffusion in the absence of mixing. There are various ways of controlling k_2, such as by mixing or flow [29], active stirring, concentration gradients, viscosity control, and temperature changes [1]. Depending on conditions, such as mixing, the rate of growth may not be diffusion controlled, and the surface reaction rate constant k_3 will play a role, so that eq. (3) becomes

$$dM/dt = [1/k_2 + 1/k_3]^{-1}A(c - c^*). \quad (4)$$

It has been customary in protein crystal growth to attempt to hold $(c - c^*)$ nearly constant by removing water to maintain c while solute is consumed or by adding precipitant via dialysis to decrease c^*. There is no clear agreement concerning which approach is more effective, either in the laboratory or in low gravity.

Grant and Saville [34] used the Ranz-Marshall correlation, in which the Schmidt number is used to evaluate mass-transfer limitations. Another approach is to attempt to calculate the Damkohler number, which is the ratio of rate of consumption to diffusion rate, in this case

$$Da = k_1/k_2 \text{ for crystal nucleation} \qquad (4)$$

and

$$Da = k_3/k_2 \text{ for crystal growth} \qquad (5)$$

where k_2 in low gravity is derived from the diffusion coefficient, but the ratio may depend on the determination of a length scale. Gravity-dependent variation in k_2 would imply a role of convective transport in bringing solute molecules to the crystal surface.

Hypothesis b: Inertial acceleration induces Rayleigh convection (buoyancy-driven flow) near the unstirred layer of growing crystals. This is a variant of hypothesis a, and evidence for its existence has been reported during crystallization of triglycine sulfate [30] and of lysozyme [31] using schlieren optics, as mentioned above. A critical Rayleigh number for this process has not been reported, and detailed modeling studies are needed before further understanding of the role of this process can be achieved.
A critical Rayleigh number could be used to estimate conditions leading to convective overturn and hence predicted modification of k_2 in eq. (2). The computational work of Dressler [35] and of Spradley [36] will form the foundation for this portion of the study. This treatment does not address any effects of low gravity on the nucleation process.

Hypothesis c: Inertial acceleration induces Rayleigh convection over the height of the drop or vessel. Internal circulation of liquid during evaporation from the surface of a hanging drop has been predicted. Some of this could be due to thermocapillary or solutocapillary (Maringoni) flow, which has been modeled in considerable detail in recent work in our group. Rayleigh convection depends on gravity but capillary flow does not. Our current research includes the comparison of crystal growth in hanging drops and in fully enclosed containment. Thus, a combination of suitable modeling and experiments with open and closed solutions in the presence and absence of gravity should distinguish among these possibilities. The computational approach of Sibille and Baird [37] will serve as basis for this study.

Hypothesis d: The molecular self-assembly process is gravity-dependent. If dissipative structures (geometrically ordered solute concentrations) play a role in the growth of macromolecular crystals, as they seem to do in certain biological self-assembly processes [38], then the early post-nucleation growth of crystals should be sensitive to changes in orientation of inertial acceleration. By judicious use of our fully-enclosed crystallizers, reorientation and/or brief centrifugation can be performed to test this (relatively unlikely) hypothesis. The theory of symmetry breaking, a subset of bifurcation theory [38,39] will serve as starting point of this study.

Hypothesis e: Inertial acceleration causes simple sedimentation of growing crystals, setting up undesired convective currents at the shear plane, causing crystal-crystal collisions (hence twinning), or forced crystal growth on the "floor" of drops or containers. This hypothesis, with its three subsets, is a favorite among low-gravity crystal growers [1,7,8]. Analysis of photographs from previously-performed experiments [21] as well as our own [27], is consistent with, but has not proven, a reduced twinning rate. The growth (and presumably nucleation) of canavalin crystals in suspension, out of contact with containment boundaries resulted in spectacular improvement of crystal quality. That this is the primary effect of gravity on crystal growth is a popular belief [28]. If a brief period of centrifugation shortly after nucleation increases the rate of twinning, then evidence favoring this explanation will have been obtained.

This is the simplest hypothesis. If it is correct, it points the way toward the serious development of methods that avoid simple sedimentation, such as the growth of biological crystals in high-density, high-viscosity media including gels [40]. Published data on gel crystallization [41] of proteins will be used, along with buoyant transport theory [42,43].

Growth of crystals in gels [1] results in crystal quality intermediate between that of low g and ground-grown crystals. Gels have two effects, suppression of convective flows [31]

and prevention of sedimentation. Therefore gel-growth experiments do not distinguish between these two hypothesis (b) and (d), respectively.

Hypothesis f. Reduced inertial acceleration allows nucleated crystals to remain suspended and not grow on a surface of the crystallizer. Free nucleation, vs. heterogeneous nucleation on a surface was shown to lead to superior crystals of Canavalin, for example [8], while crystals grown after nucleation on a solid surface were unrecoverable and undiffractable. Crystals grown surface-free and in contact with a surface should exhibit the submicron mosaicity that seems to cause the lower quality of earth-grown crystals. Atomic force microscopy is now an excellent means to detect submicron mosaicity in fully-hydrated crystals. If the hypothesis that submicron level mosaicity is the problem is correct, it needs to be explored at the submicron level. We have evidence favoring the submicron mosaicity hypothesis, whatever its cause, via rocking curve and relative Wilson plots.

Hypothesis g: Evaporation rate is affected by space flight conditions in hanging-drop experiments. Sibille & Baird [37] have reported on the calculated and measured evaporation rates in spaceflight and in the laboratory. The two are significantly different. We have developed the capability to routinely determine an adequate variety of transport rates, with the availability of fluid transport codes such as FIDAP and to factor in surface effects on evaporation rates. We have chosen not to develop an extensive monitoring capability in space for this purpose--high-quality monitoring has not proven itself as a means of elucidating mechanism. We consider being able to perform crystallographic analysis and microscopy very soon after recovery a more important probe of crystal-growth quality.

4. Data Analysis

All crystals will be examined by light microscopy and measured and assessed by polarized light. Records will be made of size, habit, and birefringence. Potentially valuable crystals or crystals providing important data will be photographed. When appropriate, photographs will be analyzed quantitatively by image analysis (for permanent recording of dimensions and size distributions) using "Global Image" commercial software.

Diffraction studies will be performed on mountable crystals of 50 μm and larger. Specifically, mosaicity will be evaluate by Wilson statistics and rocking curves, and the diffraction limit will be determined. The detailed structure analysis of the RNAs is a goal of the projects for which this one will provide crystals and is not included in the analysis to be supported by NASA for this project.

5. Timetable

Year 1: Finish construction and testing of ground-based crystallizers (already underway), optimize crystallization conditions for UU, PK, 3APp36 complex and X1rbpal-2, perform low-gravity crystallizations of each of these using novel methods chosen on the basis of laboratory studies, set up theoretical framework for microphysics analysis. Perform crystallizations of UU by liquid-liquid diffusion, dialysis diffusion and osmotic dewatering in low gravity, first two quarters (Jul-Dec 1995). Repeat these experiments in 3rd and 4th-quarter flights (Jan-Jun 1996). Retrieve crystals for x-ray analysis. Establish availability of NASA crystallization facilities.

Year 2: Continue work on year-one goals. Synthesize PK in large quantities and follow crystallization procedures, including spaceflight experiments as was done for UU in year one. Complete study of one protein-RNA complex by novel methods on the ground, including comparison of methods using diffraction statistics. Include complex(es) in 3rd and 4th-quarter flight experiments (Jan-Jun 1997). Dedicate some flight experiments tostep-diffusion and step dialysis experiments with RNAs and complexes.

Years 3 and 4: Anticipated research includes arriving at conclusions concerning the role of gravity in crystal submicron mosaicity, reporting of consistent trends on the basis of AFM and diffraction statistics, conducting crystallization experiments in gels and other media to approach low-gravity conditions in the laboratory, and crystallizing all of the remaining target molecules in the proposal, for good diffraction results, in the laboratory, in spaceflight, or, preferably, both, using lessons learned from low-gravity crystallization by several methods. At the end of this period the most appropriate crystallization method for oligonucleotides and complexes in the laboratory and in low gravity should have been established.

C. Justification of the Budget Request

1. *Personnel.* Graduate students will be degree candidates in the Departments of Chemical Engineering and Chemistry and will develop procedures in Dr. Todd's laboratory in the Chemical Engineering Department, then move the procedures to the Dr. Kundrot's laboratory in the Department of Chemistry and Biochemistry, where the procedures will be practiced jointly with the undergraduate (Independent Study) students and post-doctoral worker(s) under laboratory conditions more favorable for crystallographic goals.

2. *Equipment.* Crystallization devices to be constructed are mainly multichambered membrane units that can be used in sparse matrix experiments in the osmotic dewatering, single diffusion and step diffusion methods. Preparative HPLC columns are required for purifying the milligram quantities of oligoucleotides required for this research.

3. *Supplies:* The most expensive item in oligonucleotide research is RNA polymerase. It is normal to purify this enzyme from recombinant bacteria or to purchase it from US Biochemicals. Either way, it is necessary for the project to bear the cost.

4. *Travel:* Three trips per year by one individual (not necessarily the same one) to launch and recovery sites is necessary. This conclusion is derived from the advice of other protein crystal growers and our own experience with 8 space shuttle flight experiments and three sounding-rocket experiments. It is very important to be there.

Specific travel during the first fiscal year consists of:

One investigator to Kennedy Space Center in July, 1995, to launch samples on STS-69.
One investigator to Kennedy Space Center in August, 1995, to recover samples from STS-69.
One investigator to Kennedy Space Center in September, 1995, to launch samples on STS-73.
One investigator to Kennedy Space Center in September, 1995, to recover samples from STS-73.

One investigator to Kennedy Space Center in April, 1996, to launch samples on STS-74.
One investigator to Kennedy Space Center in April, 1996, to recover samples from STS-74.
It has been our experience that an investigator remaining in Florida throughout an entire space flight consumes more travel funds and is a wasteful use of personnel time. We intend to make use of any evidence to the contrary.

5. *Other expenses.* By policy, the tuition of graduate students working on research projects is paid from the project's research budget. Less than about 10% of the budget will be spent accessing the low-gravity environment of space flight. Based on the last 2 years' experience, if this access is used wisely, there will be a high economic return.
Other expenses: These cover normal, day-to-day costs of operating a crystallization research program. The utilization of BioServe and ITA facilities for only a portion of their actual costs (none, in the case of BioServe) represents highl leverage to NASA, since there will be no requirement for expensive participation of NASA personnel, hardware, or flight programs. It is assumed that NASA low-gravity crystallization facilities, which are limited to one or two crystallization methods per flight, will be available at no charge to the project. Computationa services are very inexpensive at the University of Colorado, and even the computationally intense calculations of molecular structure are performed using workstations that have been paid for. The machine shop in the Department of Chemical Engineering has been manufacturing crystallizers for the implementation of the new techiques under study. It is heavily subsidized by the Department and makes efficient use of investigator and student labor, so costs are held to $10-20/hr.

The revised budget pages follow.

D. Signed Certifications

These follow on the attached forms following a the revised budget pages.

Chapter 3

Executive summary

CHAPTER 3

Preparation and Analysis of RNA Crystals
Executive Summary

NAG8-1165
Final Report
Period Covered: 1 July 1995 - 29 February 2000

This report follows Part B of the outline of the revised statement of work, 8 June, 1995. The relevant pages of the Statement of Work are found in Chapter 2. Subsections that were not addressed during this reporting period are not mentioned in the report below.

3.1 TASK 1. Preparation of high-quality crystals of RNAs and their complexes.

3.1.1 Synthesis and purification of UU dodecamer.

The synthesis of the UU dodecamer was optimized using the method of Marble and Davis, developed in our department, as basis. In brief, the DNA template is immobilized in a reaction mix containing recombinant RNA polymerase from bacteriophage T7 and stoichiometric ratios of nucleoside triphosphates. This procedure has been described in detail in Dr. C. Y. Lee's and Mr. Stephen Cape's theses (see bibliography, Chapter 5 below). More significantly, several details of the purification of the two dodecamer species, phosphorylated vs. hydroxylated, from each other are given in Chapter 10. In brief, a chromatographic method for purifying these extremely closely related species was devised and compared with gel electrophoresis. The latter is the usual method used by molecular biologists but does not scale up. The quantitative advantages of ion-exchange chromatography are clearly described in Chapter 10. These closely-related species are able to co-crystallize, as shown in detail in Chapter 11, which is chapter 3 from Mr. Cape's M. S. thesis. In summary of this work, it was found that increasing the ratio of 5'-phosphorylated to 5'-hydroxyl dodecamer (1) increased the mass crystallized, (2) decreased crystal quality and (3) increased the number of crystals. This entire study utilized the hanging-drop method.

3.1.2 Osmotic dewatering studies with U-U dodecamer.

This oligonucleotide model was used to further characterize the osmotic dewatering method as a means of producing quality crystals routinely. A sparse-matrix dewatering crystallizer ("MODC") was developed, and it underwent preliminary characterization and modeling studies described in Chapter 15, a symposium paper presented by Dr. Lee. In a more detailed published article, Chapter 16, the complete model and the governing equation ("TEFOD") of osmotic dewatering are presented, and results of crystal growth experiments in the laboratory and in low gravity are detailed. The TEFOD equation is solved in closed analytical form and requires no fitted parameters, although the membrane resistance, R_m, is usually determined from an experimental data point. Further studies on the membrane resistance and membrane performance issue have been performed as

described in Sectionn 3.2 below. This task represented the largest effort of the project year and resulted in the completion of Dr. Lee's Ph.D. thesis and two major peer-reviewed publications (Chapters 16 & 17) in addition to numerous presentations and increased visibility for the osmotic dewatering method.

3.1.3 Double diffusion studies with U-U dodecamer.

Interestingly, these experiments may be impossible in 1-g. Success was achieved in stabilizing crystal-growth systems for lysozyme, in which case a high salt concentration in the precipitant phase prevents immediate sedimentation of crystal nuclei. In the case of oligonucleotides, which have a higher density than proteins, the crystal density causes sedimentation of microcrystals when they reach the apparent critical size of 5 μm. The precipitant, methylpentanediol, has the effect of decreasing the density of the mother liquor. This concept was tested by performing osmotic dewatering experiments in an inverted MODC; the microcrystals never grew beyond 5 μm before they sedimented out of the saturation zone adjacent to the membrane at the top of the chamber. In contrast, crystals nucleated at the bottom of the chamber stayed in place and grew to over 200 μm. There is a continuing effort to perform these experiments in low gravity; however, this product crystallizes at 37°C, and very few opportunities to perform flight experiments at this temperature arose. Therefore this concept was verified by the growth of protein crystals on the space shuttle during video monitoring as described in Chapters 27 and 28 and in Section 3.3 below.

3.1.5 Further sparse matrix studies with "pseudoknot" (PK).

The structure of PK was solved by Dr. Kundrot's group shortly after the beginning of the project. Rather than deal with two "model" oligonucleotides, a new oligonucleotide, 225t3 which is a 35-base aptamer for a different protein (a human peptide growth factor), was chosen as the "difficult" crystallization problem. It has been subjected to several "screens", each having about 80 conditions, using mother-liquor compositions considered appropriate for oligonucleotides. Our experience and results from the literature indicate that high concentrations of ammonium ion enhance the solubility of the oligomer and maintain a high concentration of oligomer during crystal growth. In early stages of the project it appeared that low-molecular-mass polyethylene glycol and other glycols were emerging as the precipitants of choice for short oligomers. These two rules were applied to "225t3" , an interresting 35mer, but no diffractable crystals were grown. Thus the project diverged from a focus on PK crystallization to the study of other oligomers.

3.1.6-3.1.8 Refined studies with PK using osmotic dewatering and single diffusion

As just mentioned, several oligonucleotides were studied after PK had been successfully crystallized. Owing to a shift of emphasis toward Task 2, the pathway to high-quality RNA crystals, the growth of high-quality crystals of specific oligonucleotides became a less important goal than mechanistic studies with oligonucleotides that had been crystallized. Indeed, even the new 35mer 225t3, was abandoned in favor of other dodecamers that served as models. One interesting exception is the 3' terminal 71mer of poliovirus RNA,

which is thought to possess a closely aligned pair of loops with regions complementary to each other, a geometry referred to as "kissing hairpins". Considerable effort was expended identifying proper configurations for crystallization by the manipulations of magnesium ion concentration. Gel electrophoresis was used as a tool, and, under some conditions an extremely large number of stereoisomers was found to exist. This molecule has yet to be crystallized. A list of study molecules is given in Chapter 6.

3.1.9 Osmotic dewatering, double diffusion and step diffusion studies in low gravity.

To the extent possible, these experiments were performed on space shuttle flight STS-80. On a previous flight dodecamer crystals were grown at ambient temperature, which was surprising, but on STS-80 no dodecamer crystals could be seen to grow at ambient temperature. Further, water transport in some samples was not as expected, so a program of membrane quality control was undertaken (Chapters 20-25). Briefly, it was found that the sealing of membranes into their wells must be performed to meet rigid requirements, that the resistance of membranes varies from small area to small area (each dewatering chamber covers about 0.1 cm^2), that there is an initial rapid and late slow flux decline in membranes and that pre-compressed membranes are more uniform. A byproduct of this study was the observation that RO membranes are severely compacted when subjected to reverse osmosis under high pressure but mechanically unaffected when used in osmotic dewatering mode under high osmotic pressure. An article on membrane quality control and analysis was written for the crystallography community (Chapter 21).

3.2. Pathway to High-Quality Crystals

A paradigm for oligonucleotide crystal growth appears to be emerging. This is the result of seeking optimized combinations of solution equilibrium thermodynamics and kinetics of nucleation and crystal growth. However, it will become clear in this section that this paradigm is significant, new and fundamental.

3.2.1 Solution thermodynamics

Purity was found to be important; this is not a new finding, but the combination of very similar molecules showed that a 5'OH dodecamer cocrystallizes with its 5' phosphoryl counterpart with no selective partitioning of either species into the crystalline phase. The contaminant, even when so closely related, is detrimental to the quality of the crystals, as shown in Chapters 10 and 11. This finding was further modeled with proteins in Chapters 29 and 30 to investigate the role of gravity in the partitioning of impurities. This role was not found to be great relative to the apparent roles of sedimentation and convection.

Solubility was found to be important, and, in most cases this has been manipulated by modifying the monovalent salt concentration.

Based on our research to date, the following kinetic approach would be recommended:

(1) Be sure the starting mother liquor is in the one-phase region, using ammonium ion to enhance solubility, but a glycol is not necessary as precipitant.
(2) Dewater rapidly to transform the mother liquor conditions to high supersaturation (penetrate the 2-phase region deeply).
(3) Nucleate in suspension, preferably homogeneously.
(4) As soon as nucleations (as few as possible) have occurred, move conditions very close to the equilibrium line and into conditions of optimized second osmotic virial coefficient.
(4) Before cessation of growth occurs increase the dewatering rate, which maintains conditions of optimum second virial coefficient.

In addition to revealing a recommended kinetic approach to oligonucleotide crystal growth, the more significant paradigm is thermodynaimic (related to solution equilibria). These lead to the following recommendations, which replace the traditional "screen" with the desired scientific approach to crystallization trials:

(1) Prepare electrokinetically stabilized solutions of oligomer in NaCl and cacodylate buffer and a minimum concentration (1 - 5 mM) of $MgCl_2$ at various concentrations of oligomer near saturation, in crystal-growth chambers with a membrane **(Chapters 22 and 28)**.
(2) $MgCl_2$ at various concentrations is placed outside the mambrane at about around 10 mM **(Chapter 13)** is placed on the opposite side of the membrane **(Chapter 28, p. 28-5)**.
(3) The chambers containing oligomer solutions are separated from the external ("precipitant") solution using a 1000 molecular-weight cutoff dialysis membrane.
(4) Hold this assembly at ambient temperature for 4 to 20 days, and crystals can be harvested for microphotography and x-ray diffraction studies.

Chapters 12 through 14 present in great detail the rationale behind the above paradigm. In this case, studies of osmotic and molecular-weight parameters using static and dynamic light scattering, respectively, led to the finding that glycols are not precipitants for nucleic acids, but multivalent cations such as magnesium and spermine serve this purpose. The membrane technologies that make the kinetic approach possible are found in **Chapters 15 throuigh 22 and 28.**

3.3. Mechanism of action of inertial acceleration on crystal growth

Principles are emerging from our work. It is clear from controlled osmotic dewatering studies that rapid movement deep into the two-phase zone of the phase diagram results in the formation of a small number of nuclei. A rapid return to the metastable region causes these nuclei to grow into large, high-quality crystals. This finding was confirmed in another way. Batch crystallization in low gravity results in the rapid formation of nuclei after vigorous mixing. These nuclei deplete their immediate environment of feed molecules, and nucleation stops. As new molecules diffuse through this depletion zone,

this zone re-enters the two-phase envelope of the phase diagram and gradual growth of crystal resumes. This hypothesis was tested on the Mir space station. Since 37°C was not available, the experiment was performed with lysozyme. The results were astonishing: batch-grown lysozyme crystals in low gravity had the lowest mosaicity of any samples, as shown in Chapters 29 and 30. See also 3. 3f, below.
Several of the proposed hypotheses (Part 3 , Chapter 2, page 5) have been examined, and the results of those that have been studied sufficiently to reveal trends are given below:

3c. Inverse solute gradients (denser at the top) would be expected to convect, and a critical solutal Rayleigh number is normally used as a prognosticator of the onset of such natural convection. A series of experiments was performed to evaluate convective turn-over in osmotic dewatering chambers (MODC in Chapter 16). The dewatering rate was measured as a function of time with the membrane at the top of the chamber and with the membrane at the bottom of the chamber. If convective mixing occurred the dewatering rate was predicted to be faster with the membrane at the top of the chamber. It was not. Further experiments and calculations are underway to confirm that the diffusive removal of solute from the immediate vicinity of the membrane (polarization layer) is more rapid than the removal of water through the membrane under typical driving forces used in osmotic dewatering crystallizations.

3e. The effect of movement of crystals due to body forces (inertial) was investigated using dodecamer as model in the laboratory and hen egg lysozyme as model in low gravity. It was shown (above) that movement of dodecamer microcrystals out of the saturation zone results in premature cessation of crystal growth. In low gravity, video recording and modeling of orbital mechanics (Chapters 27 and 28) showed that a grown crystal (of lysozyme) can move around under very low (0.3 μg) inertial acceleration without changing its size. Furthermore, diffraction studies were performed on lysozyme crystals from the same low-gravity experiment (using the National Synchrotron Light Source at Brookhaven National Laboratory), and resolution of diffraction was less than 1.5 Å.

3f. Batch crystallization of biological macromolecules is seldom seriously considered for crystallography. The vapor-diffusion paradigm grew out of the 1-g world, and it is not obvious that slow crystal growth is a virtue. Batch crystallization in space offers crystals that can grow at the same location as that at which they nucleated. Hen egg lysozyme was crystallized in batch experiments on earlier shuttle flights on the USA-3 mission to the Mir Space Station. The result was astonishing: thousands of brilliant, uniform 400-μm equiaxed crystals that obviously nucleated in free suspension, possibly homogeneously (the mother liquors had been filtered through 0.22 μm membranes). These crystals have been maintained in natural mother liquor for up to 3 years without evidence of visual modification. Identical conditions on the ground led to inhomogeneous, cracked crystals attached to the wall of the vessel. Attachment patterns are consistent with sedimentation to the vessel wall during crystal growth, as opposed to heterogeneous nucleation on the walls. The main experiment in Appendix 9, 5 methods of crystallization of lysozyme on the Mir Space Station (no 37°C facilities were available, so the experiment could not be performed with RNA dodecamer), included batch crystallization, which resulted in the lowest relative mosaicity of all methods tested, although this measurement has not yet been proven to be

statistically significant. In any case, batch crystallization in low gravity should be given a more substantial trial, as it offers a more gradient-free environment and a guarantee of nucleation and growth in suspension.

3g. Evaporation rates of hanging drops were measured in **Chapters 18 & 19** using a microvolumetric method and matching data to the model of Fowlis et al. and to the TEFOD equation in **Chapter 16.** The resulting insights, prompted by the observed and predicted modified dewatering rate in space by DeLucas and others, point toward rapid movement into supersaturation conditions to assure good nuclei that will grow into diffractable crystals. A real-time image-capture system for monitoring the dimensions of pendant drops has been adapted for the study of crystallization. This will save considerable labor.

Finally studies of the role of purity were performed for both oligonucleotides and for proteins, which were easier to crystallize in low gravity. The findings appear in **Chapters 29 - 31** and are as follows: When Lysozyme from two sources having different purities was studied the lower purity resulted in lower-quality crystals based on two methods in space as well as on the ground. Deliberately adding lysozyme dimer resulted in the addition of dimer molecules to the crystal structure. This resulted in lower quality crystals both on the ground and in low gravity, although low-gravity grown crystals were generally of higher quality. The effects of dimer contaminant on crystal size, crystal mosaic spread and per cent dimer in crystals did not seem to be modified by crystal growth in low gravity using the liquid-liquid diffusion method on Mir space station **(Chapter 30).** This field of study is still controversial, as pointed out in **Chapter 30**. The emerging trend, however, is leading to a weak dependence upon gravity of the incorporation of impurities into growing crystals and an interpretation that impurity partitioning may not be greatly modified but may depend on the identity of the contaminant in low gravity experiments.

4. Data Analysis

The project has routine access to three different image analysis packages in the Department of Chemical Engineering. Currently two are being utilized in drop-size analysis in support of fine-tuning drop evaporation (dewatering) rate.

A Brookhaven Instruments static and dynamic light scattering apparatus has been acquired at no expense to the project. However, the measurement of refractive index slope, dn/dc, necessary for the measurement of osmotic virial coefficients, will require the acquisition of a high-quality refractometer.

The project has been suported by excellent crystallography (see **Chapters 7, 8, 26, 28 and 30**) via Prof. Craig Kundrot, co-principal investigator, and the late Dr. Z. Richard Korszun, brought to us via our subcontractor Instrumentation Technology Associates (ITA), who provided access to the National Synchrotron Light Source. There will be a delay in the completion of the analysis of the data that Dr. Korszun helped us obtain, as this was a partially completed task at the time of his passing. In any case, a wealth of high-quality x-ray data has been collected on crystals grown in low gravity.

Chapter 4

Task Reports and Bibliographies by Year, as Submitted

Prof. Paul Todd MSFC T Biotechnology

FY95 Task Progress

The following progress has been made in addressing the tasks listed above:

1. Preparation of high-quality crystals of RNAs and their complexes: Oligonucleotide "UU-dodecamer" and nucleic acid-protein complex crystals were grown in Fluid Processing Apparatus (FPA) and Materials Dispersion Apparatus (MDA") on space shuttle mission STS-69. At the time of this writing additional samples are awaiting the launches of space shuttle STS-73 and METEOR commercial experiment carrier (unmanned orbiter). The methods of double diffusion, step diffusion, and osmotic dewatering were employed on all three flights, and crystals were formed by these methods on STS-69, including one diffraction-quality crystal of the UU-dodecamer and a few diffraction-quality crystals of nucleic acid-protein complexes.

2. Pathway to high-quality RNA crystals: An osmotic crystallizer with 24 reaction chambers has been built and tested. A successful transport model has been applied to the control of solute concentration rate. A transport rate measuring device has been built and tested. A 12-base RNA "UU-dodecamer" has been synthesized by in vitro transcription; its phase diagram in methylpentane diol and ammonium acetate at 37° C has been determined, and crystals of this material have been grown by osmotic dewatering in the laboratory.

3. Mechanisms of action of inertial acceleration (gravity) on crystal growth: Crystal/nucleus sedimentations as a factor has been studied by growing crystals with the above crystallizer upside-down in the laboratory. Under this condition, crystallization seldom proceeds beyond the nucleation stage, and the concentration of solutes at the "top" of the chamber leads to a high frequency of continuous nucleation. Low-gravity experiments have been performed as mentioned above.

FY95 Bibliographic Citations by NASA MSAD Task PI's

Proceedings
Lee, C. Y., Sportiello, M. G., Cape, S., Ferree, S., Todd, P., Kundrot, C. E. and Barnes C. "Application of osmotic dewatering to the crystallization of oligonucleotides for crystallography." Proceedings of 25th Annual Biochemical Engineering Symposium, Ed. R. Bajpai, University of Missouri, Columbia, Missouri (In press) 1995.

Presentation
Lee, C. Y., Sportiello, M. G. Cape, S., Ferree, S., Todd, P., Kundrot, C. E. and Barnes C. "Application of osmotic presented at 6th Annual Colorado Biotechnology Symposium, Boulder, CO, September, 1995.

Presentation
Lee, C. Y., Sportiello, M. G. Cape, S., Ferree, S., Todd, P., Kundrot, C. E. and Barnes C. "Application of osmotic dewatering to the crystallization of oligonucleotides for crystallography." presented at 25th Annual Biochemical Engineering Symposium, University of Missouri, Columbia, Missouri, September 1995.

Dr. Paul Todd | 962-23-08-42 | MSFC | Ground | Biotechnology

Preparation and Analysis of RNA Crystals

TASK PROGRESS (FOR FY96 ONLY)

1. Preparation of high-quality crystals of RNA's and their complexes: Using hanging-drop, sitting-drop and osmotic dewatering methods, diffraction-quality crystals of the oligonucleotide "UU-dodecamer" were grown to 0.3 mm or more in length. Two growth habits were noted for crystals having the same space group. Average resolution was better than 3.0 Å and maximum resolution was 2.46 Å by all crystallization methods. The structure of this molecule was solved and published. A second oligonucleotide, a 35-base Nexamer molecule "225T3", which reacts with insulin-like growth factor has been chosen as the next example to crystallize. Initial screens have been completed, and refinements are underway using hanging-drop, osmotic dewatering and low-gravity techniques. Samples are being prepared for space shuttle mission STS-80 using "C-MIX" payload hardware.

2. Pathway to high-quality RNA crystals: A controlled dewatering device has been tested and modeled. The rate of water removal through a reverse osmosis membrane has been analyzed in complete detail by a model equation in closed form that requires only one fitted parameter, the Darcy's-law membrane resistance, R_m. The theory has been successfully tested on a multichamber osmotic dewatering device capable of crystallizing 24 samples simultaneously, enough for a sparse-matrix screen using this method. Furthermore, by controlling the osmolarity drop across the membrane, a dewatering profile identical to that achieved by vapor diffusion (hanging drop) has been achieved, and UU-dodecamer crystals grown by both methods at the same rate are of comparable quality. The role of the control achieved by the osmotic dewatering method was further confirmed by dynamically adjusting the dewatering rate to allow (1) early nucleation at high saturation rate followed by (2) a period of quiescent growth at lower saturation and finally (3) continued growth by return to higher saturation after initial equilibrium was achieved. The resulting crystals were the product of more highly controlled nucleation and growth to larger final size. The effect of purity has also been tested in three ways: (1) crystal growth in samples of 89% vs. 95% purity have been compared with a small increment in crystal size and quality at the higher purity, (2) the growth of crystals in deliberate mixtures of UU-dodecamer and a closely-related derivative of the same size with smaller and lower-quality crystals appearing in the presence of increasing concentrations of the derivative, and (3) ion-exchange chromatography has been found to rival gel electrophoresis for oligonucleotide purification.

3. Mechanisms of action of inertial acceleration (gravity) on crystal growth: the highest-quality crystal grown by osmotic dewatering was produced in a space-hardware version of the crystallizer; however, this crystallizer, "Fluid Processing Apparatus (FPA) Insert" is subject to erratic behavior that appears to be due to a combination of membrane variability and method of assembly. This device has been further characterized in preparation for continued low-gravity crystallization experiments. The UU-dodecamer normally crystallizes at 37°C and has not been observed to form crystals at lower temperatures; however, in one low-gravity experiment performed at 23°C a small crystal was seen to form. Using hen-egg lysozyme as surrogate in ambient-temperature studies in low gravity, the concepts developed in part 2, above, were tested by changing osmotic gradients during flight and during crystal growth. The expected outcomes were observed; namely, larger, more regular, protein crystals. This concept is now ready for testing in forthcoming low-gravity experiments with oligonucleotides.

FY96 BIBLIOGRAPHIC CITATIONS BY NASA MSAD TASK PI'S

(OCT. 1, 1995 - SEPT. 30, 1996 ONLY)

Journal

Lietzke, S. E., Barnes, C. L., Berglund, J. A. and Kundrot, C. E. The structure of an RNA dodecamer shows how tandem U-U base pairs increase the range of stable RNA structures and he diversity of recognition sites. Structure 4, 917-930, 1996.

Journal

Sygusch, J., Coulomb, R., Cassanto, J. M., Sportiello, M. G. and Todd, P. Protein crystallization in low gravity using a novel liquid-liquid diffusion method. J. Crystal Growth 162, 167-172, 1996.

Proceedings

Lee, C. Y., Sportiello, M. G., Cape, S., Ferree, S., Todd, P., Kundrot, C. E. and Barnes, C. Application of osmotic dewatering to the crystallization of oligonucleotides for crystallography. Proceedings of 25th Biochemical Engineering Symposium, Ed. R. Bajpai, University of Missouri, Columbia Missouri, pp. - , 1995.

Proceedings

Cassanto, J. M., Morrison, D. R., Hymer, W., Todd, P., Korszun, Z. R., Mosier, B., Edmundson, A., Sygusch, J., Bower, D., Kearney, G. P., Dunfee, W., Alvarado, U., Guintini, R., and Bem, M. Concept of a commercial automated biotechnology space processing payload onboard the space shuttle and space station. Space and . . Proceedings of the Space Technology & Applications International Forum. Albuquerque, NM, Institute for Space Power, University of New Mexico, 2-3 June, 1996.

Proceedings

Johnson, T., Todd, P., and Stodieck, L. Microgravity: New opportunities to facilitated biotechnology development. Proceedings of the Space Technology & Applications International Forum. Albuquerque, NM, Institute for Space Power, University of New Mexico, paper #275, 1996.

Proceedings

Sportiello, M. G., Todd, P., Lee, C.-Y., Kundrot, C. E., Schultz, S., Stodieck, L. S. and Cassanto, J. M. High frequency access to low gravity experimentation in organic crystal growth from solutions. Proc. Space 96, 5th International Conference on Engineering, Construction and Operations in Space, Albuquerque, NM, 2-6 June, 1996.

Presentation

Lee, C.-Y., and Todd, P. Characterization and application of osmotic dewatering to the crystallization of biomolecules." American Chemical Society Annual National Meeting, New Orleans, LA, 24-28 March, 1966.

Presentation

Todd, P. Analysis of crystallization by osmotic dewatering and its application to oligonucleotides. Protein Crystal Growth Conference, Panama City Beach, FL, 28-30 April, 1966.

Presentation

Lee, C.-Y., Sportiello, M. G., Cape, S. P., Ferree, S., Todd, P., Kundrot, C. E., Lietzke, S. and Barnes, C. Characterization and application of osmotic dewatering to the crystallization of oligonucleotides. Colorado Biotechnology Symposium, Ft. Collins Colorado, 1996. Also Biochemical Engineering Symposium, Manhattan, KS, 1996.

Presentation

Cape, S. P., Lee, C.-Y., Petrini, K., Ferree, S., Sportiello, M. G. and Todd, P. Chromatographic purification of oligonucleotides: comparison with electrophoresis. Colorado Biotechnology Symposium, Ft. Collins Colorado, 1996. Also Biochemical Engineering Symposium, Manhattan, KS, 1996.

FY97 Task Progress

1. Preparation of high-quality crystals of RNA's and their complexes: **1.1 U-U dodecamer:** Studies on an RNA dodecamer, "U-U Dodecamer" have been completed; high-quality crystals have been grown and its structure, which contains interesting non-canonical base pairs, has been published. This molecule has been adopted, in our research, as the "lysozyme" of the RNA oligonucleotide world. **1.2 225t3 35-mer:** This oligonucleotide, which interacts with insulin-like growth factor (IGF), is expected to be difficult to crystallize, because it forms at least three native isomers and has very little secondary structure. Nevertheless three lead conditions have been identified that result in 20-50 μm crystals of pure oligomer in several weeks at room temperature, and a few lead conditions have been identified for crystallizing its complex with IGF. The lead conditions for pure oligomer crystallization are currently being exercised aboard the Mir space station.

2. Pathway to high-quality RNA crystals: **2.1 Osmotic second virial coefficient:** It is widely held that solute-solute interactions determine crystal quality and that the osmotic second virial coefficient "B_{22}" is an accurate representation of these interactions. This principle leads to the identification of optimum conditions for crystal *growth* (as opposed to nucleation), so light-scattering experiments have been performed that confirm the optimum value of B_{22} for hen-egg lysozyme, and the experimental capability to determine optimum B_{22} for oligonucleotides has been established. Rapid nucleation at high supersaturation leads to small numbers of nuclei that can subsequently grow to high-quality crystals. **2.2 Kinetic control:** The osmotic dewatering method was shown to permit rapid nucleation and subsequent crystal growth at lower supersaturation avoiding further nucleation. Furthermore, late increases in solute and precipitant concentration lead to further crystal growth. These findings have been accepted for publication, and current research is directed at obtaining a similar level of nucleation and growth control using hanging-drop, vapor-diffusion methods via video-based drop-size monitoring. **2.3 Osmotic dewatering method:** Up to the present we have assumed constant membrane permeability when water is removed from mother liquor through a reverse osmosis membrane by osmitc pressure. This assumption has been investigated in detail, and it was found that flux decline does occur during osmotic dewatering and that membrane pretreatments improve the consistency of water flux and presumably the consistency of crystal growth. **2.4 Purity and crystal quality:** Two dodecamers with identical sequence but different 5' termini (phosphorylated vs. OH) were shown to co-crystallize at any molar ratio with crystal composition always the same as mother-liquor composition. This result leads to several conclusions: (1) high purity is required for crystals that can be used for structure determination, (2) crystallization cannot be used as a purification method for separating oligonucleotides with differing 5' termini, and (3) the 5' terminus plays little or no role in lattice-forming bonds between asymmetric units. **2.5 Lattice-forming motifs:** A search for lattice-forming motifs using crystallographic databases and "Rasmol" molecular graphic software is underway. The sparse database has, to date, not yielded obvious trends in oligonucleotide inter-unit-cell bonds.

3. Mechanisms of action of inertial acceleration (gravity) on crystal growth: **3.1 On-orbit accelerations:** Inertial acceleration, the independent variable in low-gravity experiments, has been subjected to inadequate quantitation in the past. During the current project year the spectrum of accelerations to which crystallization experiments are subjected on space shuttle and Mir space station flights have been analyzed, and these were divided into three categories for convenience: steady accelerations due to orbital mechanics, brief accelerations due to orbital maneuvers, and g-jitter due to spacecraft vibrations resulting from crew or machine operations. Very low g-levels, such as 10^{-7} g, can cause significant movement of large crystals over long periods of time, and calculations of these movements were verified in video records of grown lysozyme crystals in a space-shuttle mid-deck locker. **3.2 Test of five methods on Mir space station:** The Mir space station often has a very low level ($<10^{-4}$ g) of low frequency (< 0.1 Hz) accelerations (g-jitter), and this quiescent environment allowed the growth of lysozyme crystals with about 1/2 the mosaic spread of their earth-grown counterparts, as determined using rocking curves derived from data taken at the National Synchrotron Light Source, Brookhaven National Laboratory. Five different methods were used to grow lysozyme crystals on the Mir space station while the inertial environment was monitored, and even the most rapidly grown crystals (batch method) were as good as those grown by any other method, on the basis of mosaic spread and maximum resolution. (Lysozyme was used for long-term space experiments owing to the lack of the proper temperature (37°C) for growth of our oligonucleotide crystals.)

FY97 Bibliographic Citations by NASA MSAD Task PI's (Oct. 1, 1996 - Sept. 30, 1997 ONLY)

Journal
Lee, C.-Y., Sportiello, M. G., Cape, S. P., Ferree, S., Todd, P., Kundrot, C. E., Lietzke S. and Barnes, C. Characterization and application of osmotic dewatering to the crystallization of oligonucleotides. Biotech. Progress 13, 77-81 (1997).

Journal
Lietzke, S. E., Barnes, C. L., Berglund, J. A. and Kundrot, C. E. The structure of an RNA dodecamer shows how tandem U-U base pairs increase the range of stable RNA structures and the diversity of recognition sites. Structure 4, 917-930 (1996).

Journal
Lietzke, S. E., Carperos, V. E. and Kundrot, C. E. Data reduction from twinned RNA crystals. Acta Crystallographica D 52, 687-692 (1996).

Proceedings
Sportiello, M. G., Todd, P., Lee, C.-Y., Kundrot, C. E., Schultz, S. C., Stodieck, L. S. and Cassanto, J. M. High-frequency access to low-gravity experimentation in organic crystal growth from solutions. Space '96. 5th International Conference on Engineering, Construction and Operations in Space, Albuquerque, 2-6 June. Amer. Soc. of Civil Engineers, 1996.

Proceedings
Cape, S. P., Lee, C.-Y., Petrini, K., Ferree, S., Sportiello, M. G. and Todd, P. Chromatographic purification of oligonucleotides: Comparison with electrophoresis. Proc. 26th Ann. Biochem. Engin. Symp., Ed. L. E. Erickson, Kansas State University, Manhattan, KS, (1997).

Presentation
Todd, P., Lee, C.-Y. and Sygusch, J. Effects of orbital maneuvers on biomolecule crystal growth from solution: modeling studies. Spacebound 97 Proceedings (1997).

Presentation
Sportiello, M. G., Todd, P., Korszun, Z. R., Tran, P. H. and Cassanto, J. M. Lysozyme crystallization in low gravity: Crystal quality, g-forces and video analysis. Spacebound 97 Proceedings (1997).

Presentation
Cape, S. P., Lee, C.-Y. and Todd, P. Electrophoretic and chromatographic separation of closely related oligonucleotides. Abstract P-28, Programs and Abstracts, International Council of Electrophoresis Societies, Seattle, 23-27 Mar 1997.

Presentation
Cape, S., McEntyre, S., Ferree, S., Kundrot C. E., Todd, P. and Lehrman, S. R. Effect of closely related oligonucleotides on oligonucleotide crystallization. Spacebound 97 Conference, Montreal, CN, 11-14 May, 1997.

Presentation
Todd, P., Sygusch, J., Sportiello, M. G., Edmundson, A., Cassanto, J. M., and Korszun, Z. R. Video monitoring of protein crystal motion in low gravity. Spacebound 97 Conference, Montreal, CN, 11-14 May, 1997.

Presentation
Cape, S. P. and Todd, P. Effect of a closely related contaminant on the crystallization of an oligonucleotide. Paper #11, 27th Annual Biochemical Engineering Symposium, Colorado State University, !4 Sept. 1997.

Presentation
Cape, S. P., Sportiello, M. G., Wang, Y., Lee, C.-Y., Shah, M., Todd, P., Korszun, Z. R., and Tran, P. Trends in oligonucleotide and protein crystallization. Paper P11, Tenth Annual Colorado Biotechnology Symposium, Boulder, CO, 23 Sept. 1997.

Presentation
Cannone, J. J., Lietzke, S. E., Barnes, C. L. and Kundrot, C. E. Co-crystallization of an aptamer-target complex. Paper P8, Tenth Annual Colorado Biotechnology Symposium, Boulder, CO, 23 Sept. 1997.

Thesis
Lee, C.-Y.. Crystallization of oligonucleotides by osmotic dewatering and cell separation by inclined sedimentation. Ph.D. Chemical Engineering, University of Colorado (1996).

Thesis
Cape, S. P. Chromatography and crystallization as steps in oligonucleotide purification.
M.S., Chemical Engineering, University of Colorado (1997).

FY98 PI DATA UPDATE FORM
MICROGRAVITY RESEARCH DIVISION
TASK DESCRIPTION/BIBLIOGRAPHY
DATABASE

Dr. Paul W. Todd: University of Colorado, Boulder
Preparation and Analysis of RNA Crystals

FY98 TASK PROGRESS **PI MUST PROVIDE ALL-NEW TEXT TO REFLECT WORK PERFORMED ONLY IN THE TIME PERIOD OCTOBER 1, 1997-SEPTEMBER 30, 1998**

Task 1: Preparation of high-quality crystals and their complexes. Samples of an RNA dodecamer, "UU-dodecamer" crystals were diffracted using synchrotron x-rays at the National Synchrotron Light Source at Brookhaven National Laboratory. Diffraction data await further analysis, the objective being to relate crystal quality to method of crystallization. Studies on the effects of closely-related impurities were completed and written for publication.

Task 2: Pathway to high-quality RNA crystals. A careful study of water transport phenomena in crystallization methods was performed during this fiscal year. Four methods were studied: osmotic dewatering, hanging-drop vapor transport, osmotic dewatering with vapor-phase transport and intracapillary vapor diffusion. All of these methods have been or will be practiced in low gravity. Osmotic dewatering involves the removal of water from mother liquor by diffusion down a water gradient through a reverse osmosis (RO) polymer membrane. We found that the rate of dewatering was profoundly influenced by a little-known process known as internal concentration polarization. This process was characterized quantitatively, and we made membranes that do not have this characteristic. Two papers about this subject have been written for publication. Osmotic dewatering with a vapor gap is practiced frequently in space (Canadian Space Agency's CAPE mission is a good example.) We characterized this process quantitatively and with a transport model. Three factors that could be overlooked were found: the effect of method of membrane saturation ("priming"), hydraulic pressure that was originally considered negligible, and the rate-limiting character of the transport of water through the vapor phase. The dewatering rate of hanging drops was studied, and evidence was found that truly quiescent drops may experience less internal mixing and less dependence on the rate of water transport in the vapor phase. Methylpentane diol (MPD), poly(ethylene glycol) 400 (PEG) and other polyols are popular precipitants for oligonucleotides. Following a lead from the literature, the regular use of PEG was examined using crystallization screens and static light scattering, the latter being used to determine osmotic second virial coefficients as a means of predicting optimum crystal growth conditions.

Task 3: Mechanism of action of inertial acceleration (gravity) on crystal growth. Using protein surrogates crystal motions were recorded by video during space shuttle flight STS-80 and subjected to quantitative analysis and correlated with steady accelerations such as atmospheric drag and gravity gradient, orbital maneuvers such as satellite pusuit, and g-jitters due to crew activity. Rocking curves were performed on crystals grown by 5 space-based methods on Mir space station, and in all cases mosaic spread was ½ that found in earth-grown crystals. Surprisingly, batch-crystallized protein exhibited the lowest mosaic spread. A relationship between mosaic spread and maximum resolution is being sought using these data.
Membrane-based methods of crystallization in low gravity have shown unsatisfactory reliability in the past. Apparatus-related studies were performed, and the standard deviation of dewatering rates in space-rated equipment was reduced by a factor of 4. Data were collected on the rate of vapor transport in a new space-based method to be tested on space shuttle flight STS-95.

FY98 BIBLIOGRAPHIC CITATIONS
BY NASA MSAD TASK PI'S
(OCT. 1, 1997 - SEPT. 30, 1998 ONLY)

Journal
Lee, C.-Y., McEntyre, S. R., Todd, P., Schaefer, K. and Kundrot, C. E. Control of nucleation in olignucleotide crystallization by the osmotic dewatering method with kinetic water removal rate control. J. Crystal Growth, 187, 490-498 (1998).

Proceedings
Todd, P., Lee, C.-Y. and Sygusch , J. Effects of orbital maneuvers on biomolecule crystal growth from solution: modeling studies. Spacebound '97, J. Sygusch, ed., University of Montreal, 242-244 (1998).

Presentation
Cape, S.P., McEntyre, S., Ferree, S., Kundrot, C. E. and Todd P. Crystallization of an oligonucleotide in the presence of a closely related contaminant. AIChE Annual Meeting, Los Angeles, CA, 16-21 November, 1997. Paper 15L

Presentation
Lee, C.-Y. Wang, S., Cape, S. P., Krantz, W. B. and Todd, P. Effect of nucleation rate on growth of olignucleotide crystals. AIChE Annual Meeting, Los Angeles, CA, 16-21 November, 1997. Paper 16f

Presentation
Sportiello, M.G., Korszun, Z. R., Tran, A. and Todd P. Mosaicity of tetragonal lysozyme crystals grown by five different methods in long duration low-gravity space flight. AIChE Annual Meeting, Los Angeles, CA, 16-21 November, 1997. Paper 38e

Presentation
Wang, Y. and Todd, P. Transport phenomena in the hanging drop crystallization method. Eleventh Annual Colorado Biotechnology Symposium, Fort Collins, CO, September 22, 1998, Poster IIA.13

Presentation
Sportiello, M.G., Todd, P., Cassanto, J. M., Dunfee, W., Lewis, R., Britz, W. and Reynolds, F. A quantitative assessment of quiescence in low gravity crystallization experiments on the U.S. space shuttle. Eleventh Annual Colorado Biotechnology Symposium, Fort Collins, CO, September 22, 1998, Poster IIA.14

Presentation
Cape, S. P., Lee, C.-Y. and Todd, P. Preparative scale high performance liquid chromatography for separation of closely related oligonucleotides. Eleventh Annual Colorado Biotechnology Symposium, Fort Collins, CO, September 22, 1998, Poster IIA.17

FY99 DATA UPDATE FORM
MICROGRAVITY RESEARCH DIVISION
PROGRESS REPORT

(In addition to your progress report, please remember to attach your FY99 bibliography)

[redacted]

Preparation and Analysis of RNA Crystals

Task 1: Preparation of high-quality crystals and their complexes. In addtion to samples of the RNA dodecamer, "UU-dodecamer" crystals were grown of one more RNA dodecamer and two DNA dodecamers ("Drew-Dickerson DNA") whose crystal structures have been solved in the literature. It was found that almost any oligonucleotide can be crystallized by appropriate adjustment of divalent magnesium concentration. Phase diagrams for the oligonucleotide-magnesium system have been determined. Crystals grown using this principle are currently being prepared for diffraction studies. In an attempt to demonstrate the extension of this principle to general cases, intensive study was initiated on a 72-base RNA that occurs at the 3' end of the poliovirus RNA genome. A secondary, but not tertiary, structure has been predicted ("kissing hairpins") for this important RNA, but it has never been crystallized or diffracted. Obtaining diffraction data as planned will fulfill the final objective, to relate crystal quality to method of crystallization.

Task 2: Pathway to high-quality RNA crystals. Investigations of equilibrium and transport in oligonucleotide crystallization were continued. Concerning equilibrium, phase diagrams of oligonucleotide-magnesium aqueous systems have been compiled. These are based on microscopic observations of precipitation and on dynamic light-scattering measurements. If a "precipitant" is defined as that solute which has the maximum effect on oligonucleotide solubility, then in most cases to date divalent magnesium is the precipitant. Dynamic light scattering data have provided precise information about the sizes of molecular aggregates and about conditions that do and do not allow hydrogen-bonded duplexes to exist. These data also serve as a guide for static light-scattering experiments, the goal of which is the determination of osmotic virial coefficients, especially the second virial coefficient, B_{22} . To date, a "crystallization slot" (narrow range of values of second virial coefficient) has not been identified for oligonucleotides as has been done for proteins. If a "slot" exists, it occurs at about 50 times the B_{22} value published for proteins. The consistency of this finding across oligonucleotides is the subject of current investigation. Concerning kinetics, the careful study of water transport phenomena in crystallization methods was continued during this fiscal year. Osmotic dewatering statistics have been compiled for over 100 laboratory and space experiments, and the transport of water through various components of composite reverse-osmosis (RO) membranes has been subjected to modeling and measurement. It was found that care is required to obtain consistent results with RO membranes in spaceflight hardware, and a pressurized pretreatment or wetting only the RO surface is desirable. In further research, dewatering via a phase change, as in hanging and sessile drop methods but through a membrane, was found to allow some control over mass transfer rates. Additional kinetic studies have revealed a pattern whereby, in traditional hanging-drop configuration, an initial granular precipitate forms during dewatering, and crystals grow after osmotic equilibrium has been achieved. The study of equilibrium and kinetics has as its goal the quantification and the simplification of the paradigm for successful oligonucleotide crystallization.

Task 3: Mechanism of action of inertial acceleration (gravity) on crystal growth. Using protein surrogates rocking curves were performed on crystals grown by space-based methods on recent Mir space station and space shuttle flights. In low-gravity experiments mosaic spread was ½ that found in earth-grown crystals, and this appeared to be the case even when the mother liquor was deliberately spiked with an impurity. In these cases hen egg lysozyme having two different intrinsic purities or having added amounts of lysozyme dimer were studied. While the presence of dimer increased mosaic spread it does not prevent low-gravity crystallization from reducing mosaic spread. These crystals also afford an opportunity to directly measure the effect of mosaic

spread on resolution, as new data-collection methods permit the determination of rocking curves of numerous reflections that have known resolution and known statistics. The work associated with this task has been presented at meetings, and manuscripts are in preparation.

FY99 BIBLIOGRAPHIC CITATIONS
NASA MSAD TASK PI'S

(OCT. 1, 1998 - SEPT. 30, 1999 ONLY)

PLEASE DO NOT INCLUDE "SUBMITTED" PUBLICATIONS -- INCLUDE ONLY THOSE PUBLICATIONS THAT ACTUALLY APPEARED IN FY99. IF YOU HAVE MORE THAN ONE TASK BEING FUNDED BY NASA MARSHALL SPACE FLIGHT CENTER, DO NOT COMBINE ALL OF YOUR BIBLIOGRAPHIC CITATIONS INTO ONE LONG LIST (DIVIDE THE CITATIONS INTO SEPARATE LISTS AND KEEP THEM WITH THE ASSOCIATED TASK). IF YOU INCLUDE A CITATION THAT DOESN'T CITE THE PI AS AN AUTHOR, MAKE SURE THAT THE CO-I IS LISTED ON THE TASK INFORMATION SHEET.

Journal
P. Todd, J. F. Doyle, P. Carter, H. Wachtel, M. S. Deuser, J. C. Vellinger, J. M. Cassanto, U. Alvarado, J. Sygusch and T. B. Kent. Magnetic space shuttle experiments. J. Magnetism Magnetic Mat. 194, 96-101 (1999).

Journal
C.-Y. Lee, S. R. McEntyre, P. Todd, K. Schaefer and C. E. Kundrot. Control of nucleation in oligonucleotide crystallization by the osmotic dewatering method with kinetic water removal rate control. J. Crystal Growth 187, 490-498 (1998).

Proceedings
Cape, S. P., Shah, M., and Todd, P. "Divalent magnesium cation as a critical player in the crystallization of an oligonucleotide." Preprints, American Institute of Chemical Engineers, Annual Meeting, 1999.

Proceedings
P. Todd, C.-Y. Lee and J. Sygusch. Effects of orbital maneuvers on biomolecule crystal growth from solution: modeling studies. Spacebound 1997 Proceedings pp. 242-244, Canadian Space Agency (1998).

Presentation
C.-Y. Lee, P. Scovazzo and P. Todd. Dynamics of composite reverse-osmosis membranes in dewatering mode with applications in crystal growth by osmotic dewatering. Paper 145c, 137h. Annual Meeting, American Institute of Chemical Engineers, Miami Beach, FL, 15-20 November, 1998.

Presentation
Todd, P. "Oligonucleotide Crystallization: Membrane-based and Low-gravity Methods" Department of Chemical Engineering (seminar), Colorado State University, Ft. Collins, 6 November, 1998.

Presentation
Todd, P. Bioprocessing in Microgravity. 21st Symposium on Biotechnology for Fuels and Chemicals, Ft. Collins, CO 2-6 May, 1999.

Presentation
Cape, S. P., Shah, M. and Todd, P. The role of Mg^{++} ions in the crystallization of an oligonucleotide International Union of Crystallography Congress, Glasgow, Scotland, 4-10 August, 1999.

Presentation
Sportiello, M.G., Todd, P., Snell, E., Judge, R., Pusey, M. and Cassanto, J. M. Effect of dimer contaminants and low gravity on lysozyme cyrstal mosaicity. 12th Annual Colorado Biotechnology Symposium, Boulder, CO 14 Sep 1999

Presentation
Cape, S. P., Shah, M. and Todd P. The role of Mg^{++} ions in the crystallization of an oligonucleotide. 12th Annual Colorado Biotechnology Symposium, Boulder, CO 14 Sep 1999

Chapter 5

Cumulative bibliography

CHAPTER 5

Cumulative Bibliography

5.1 Articles:

J. Sygusch, R. Coulomb, J. M. Cassanto, M. G. Sportiello and P. Todd. Protein crystalliztion in low gravity using a novel liquid-liquid diffusion method. J. Crystal Growth 162, 176-172 (1996).

S. E. Lietzke, C. L. Barnes, J. A. Berglund and C. E. Kundrot. The structure of an RNA dodecamer shows how tandem U-U base pairs increase the range of stable RNA structures and the diversity of recognition sites. Structure 4, 917-930 (1996).

M. G. Sportiello, P. Todd, C-Y. Lee, C. E. Kundrot, S. C. Schultz, L. S. Stodieck, and J. M. Cassanto, High-frequency access to low-gravity experimentation in organic crystal growth from solutions. Space '96. 5th International Conference on Engineering, Construction and Operations in Space, Albuquerque, 2-6 June. Amer. Soc. of Civil Engineers, 1996.

C.-Y. Lee, M. G. Sportiello, S. P. Cape, S. Ferree, P. Todd, C. E. Kundrot, S. Lietzke and C. Barnes. Characterization and application of osmotic dewatering to the crystallization of oligonucleotides. Biotech. Progress 13, 77-81 (1997).

S.P. Cape, C.-Y. Lee, K. Petrini, S. Ferree, M. G. Sportiello and P. Todd. Chromatographic purification of oligonucleotides: Comparison with electrophoresis. Proc. 26th Ann. Biochem. Engin. Symp., Ed. L. E. Erickson, Kansas State University, Manhattan, KS, (1997).

S.P. Cape, M. G. Sportiello and P. Todd. Crystallization of an oligonuceotide in the presence of a closely related contaminant. AIChE Preprint 15I (3337). Written for journal submission.

C.-Y. Lee, S. R. McEntyre, P. Todd, K. Schaefer and C. E. Kundrot. Control of nucleation in oligonucleotide crystallization by the osmotic dewatering method with kinetic water removal rate control. J. Crystal Growth 187, 490-498 (1998).

S. P. Cape, C.-Y. Lee, K. Petrini, S. Ferree, M. G. Sportiello and P. Todd. Chromatographic purification of oligonucleotides: Comparison with electrophoresis. Proc. 26th Ann. Biochem. Engin. Symp., Ed. L. E. Erickson, Kansas State University, Manhattan, KS, (1997).

P. Todd, C.-Y. Lee and J. Sygusch. Effects of orbital maneuvers on biomolecule crystal growth from solution: modeling studies. Spacebound 1997 Proceedings pp. 242-244, Canadian Space Agency (1998).

S. P. Cape, M. Shah and P. Todd. Role of divalent magnesium cations as a critical player in the crystallization of an oligoribonucleotide. 4th Topical Conference on Separations Science and Technology, November 1999, Session T1010, AIChE Preprint. Written for journal submission.

P. Todd, J. F. Doyle, P. Carter, H. Wachtel, M. S. Deuser, J. C. Vellinger, J. M. Cassanto, U. Alvarado, J. Sygusch and T. B. Kent. Magnetic space shuttle experiments. J. Magnetism Magnetic Mat. 194, 96-101 (1999).

5.2 Theses and Dissertations:

Ching-Yuan Lee. Crystallization of oligonucleotides by osmotic dewatering and cell separation by inclined sedimentation. Ph.D. Dissertation. Chemical Engineering, University of Colorado (1996).

Stephen P. Cape. Chromatography and crystallization as steps in oligonucleotide purification. M.S.Thesis, Chemical Engineering, University of Colorado (1997).

Paul Scovazzo. Multiple phase transport in membranes and porous media in low-gravity experiments. Ph. D. Dissertation, Chemical Engineering, University of Colorado, 1998.

Stephen P. Cape. Mechanisms of oligonucleotide crystallization. Ph.D. Dissertation, Chemical Engineering, University of Colorado.(in progress)

Yanqiu Wang. Direct observation and modeling of vapor transport in protein crystal growth. M.S.Thesis, Chemical Engineering, University of Colorado, 1999.

Keith B. Neeves. Osmotic dewatering of biological macromolecule solutions with a phase change: A Novel Crystal Growth Technique. B.S. Thesis, Chemical Engineering, University of Colorado, 2000.

5.3 Manuscripts:

S. P. Cape, C.-Y. Lee and P. Todd. Chromatographic purification of closely-related oligonucleotides: Scalability and comparison with electrophoresis. Written for Submission.

S. P. Cape, M. G. Sportiello and P. Todd. Crystallization of an oligonuceotide in the presence of a closely related contaminant. AIChE Preprint 15I (3337). Written for journal submission.

P. Todd. Separations research in low gravity. Sep. Purif. Meth., in preparation. Completion 2000.

S. P. Cape, C.-Y. Lee and P. Todd. Chromatographic purification of closely-related oligonucleotides: Scalability and comparison with electrophoresis. To be Submitted (2000).

S. P. Cape, M. G. Sportiello and P. Todd. Crystallization of closely related oligonucleotides. To be submitted, 1999.

M. G. Sportiello, A. Tran, Z. R. Korszun, E. Brucker, M. E. Moskowitz and P. Todd. Lysozyme crystallization on space station Mir using five techniques: crystal qualilty and g-environment. Written for submission.

R. A. Judge, E. H. Snell, M. G. Spoprtiello, H. Bellamy, G. E. Borgstahl, M. Pokros, M. L. Pusey, J. M. Cassanto and P. Todd. Biochemical and X-ray mosaicity analysis of impurity doped microgravity and ground-grown lysozyme crystals. Submitted to Spacebound 2000 Proceedings, Canadian Space Agency, May 2000.

J. Vellinger, M. S. Deuser, P. Todd, J. F. Doyle, N. Thomas, K. Barton, W. Metz, M. G. Sportiello and R. P. Cooper. Biotechnology experiiments in the "ADSEP" Payload on space shuttle flight STS-95 (1998). Submitted to Spacebound 2000 Proceedings, Canadian Space Agency, May 2000.

5.4 Abstracts of Presentations:

C. Y. Lee, M. G. Sportiello, S. P. Cape, S. Ferree, P. Todd, C. E. Kundrot and C. Barnes. Applications of osmotic deswatering to the crytsallization of oligonucleotides for crystallography. 6th Annual Colorado Biotechnology Symposium, Boulder, CO, September, 1995.

C. Y. Lee, M. G. Sportiello, S. P. Cape, S. Ferree, P. Todd, C. E. Kundrot and C. Barnes. Applications of osmotic deswatering to the crytsallization of oligonucleotides for crystallography. 25th Annual Biochemical Engineering Symposium, University of Missouri, Columbia, MO, September, 1995.

M. G. Sportiello, P. Todd, C.-Y. Lee, C. E. Kundrot, S. C. Schultz, L. S. Stodieck and J. M. Cassanto. High frequency access to low gravity experimentation in organic crystal growth from solutions. Proc. Space 96, 5th International Conference on Engineering, Construction and Operations in Space, Albuquerque, NM, 2-6 June 1996.

C.-Y. Lee and P. Todd. Characterization and application of osmotic dewatering to the crystallization of biomelodules. American Chemical Society Annual National Meeting, New Orleans, LA, 24-248 March, 1996.

P. Todd. Analysis of crystallization by osmotic dewatering and its applilcation to oligonucleotides. Proten Crystal Growth Conference, Pnama City Beach, Fl, 28-30 April, 1996

J. J. Cannone, S. E. Lietzke, C. L. Barnes and C. E. Kundrot. Co-crystallization of an aptamer-target complex. Paper P8, 10th Colorado Biotechnology Symposium. Boulder, CO, Septamber, 1997.

S.P. Cape, C.-Y. Lee and P. Todd. Preparative scale high performance liquid chromatography for separation of closely related oligonucleotides. Poster IIA.17. 11th Ann. Colorado Biotechnol. Symp., Ft. Collins, 22 September, 1998.

S.P. Cape, C.-Y. Lee and P. Todd. Electrophoretic and Chromatographic seapration of closely-related oligonucleotides: International Council of Electrophoresis Societies, Seattle, WA, Mach 23-27, 1997, Program and Abstracts, P. 31.

S. P. Cape, S. McEntyre, S. Ferree, C. E. Kundrot and P. Todd. Effect of closely related oligonucletides on oligonucleotide crystallization. Spacebound '97 Conference, Montreal, Canada, May 11-15, 1997. Abstractes P. 69.

S. P. Cape, M. G. Sportiello, Y. Wang, C.-Y. Lee, M. Shah and P. Todd. Trends in oligonucleotide crystallization. 10th Ann. Colorado Biotechnology Symposium, Boulder, CO, September 23, 1997. Book of Abstracts, p 18, Abstract P11.

S. P.Cape S. McEntyre, S. Ferree, C. Kundrot and P. Todd. Crystallization of an oligonucleotide in the presence of a closely-related contaminant. AIChE Annual Meeting, Los Angeles, CA 16-21 November, 1997. Paper 15l

C. Y. Lee, Y. Wang, S. Cape, W. Krantz and P. Todd. Effect of nucleation rate on growth of oligonuceotide crystals. AIChE Annual Meeting, Los Angeles, CA 16-21 November, 1997. Paper 16f.

Y. Wang and P. Todd. Transport phenomena in the hanging drop crystallization method. Poster Iia.13. 11th Ann. Colorado Biotechnol. Symp., Ft. Collins, 22 September, 1998.

M. G. Sportiello, P. Todd, J. M. Cassanto, W. Dunfee, R. Lewis, W. Britz and F. Reynolds. A quantitative assessment of quiescence in low gravity crystallization experiments on the U.S. space shuttle. Poster IIA.14. 11th Ann. Colorado Biotechnol. Symp., Ft. Collins, 22 September, 1998.

S. P. Cape, C.-Y. Lee and P. Todd. Preparative scale high performance liquid chromatography for separation of closely related oligonucleotides. Poster IIA.17. 11th Ann. Colorado Biotechnol. Symp., Ft. Collins, 22 September, 1998.

C.-Y. Lee, P. Scovazzo and P. Todd. Dynamics of composite reverse-osmosis membranes in dewatering mode with applications in crystal growth by osmotic dewatering. Paper 145c, 137h. Annual Meeting, American Institute of Chemical Engineers, Miami Beach, FL, 15-20 November, 1998.

Cape, S. P., Shah, M., and Todd, P. "Divalent magnesium cation as a critical player in the crystallization of an oligonucleotide." Preprints, American Institute of Chemical Engineers, Annual Meeting, 1999.

P. Todd, C.-Y. Lee and J. Sygusch. Effects of orbital maneuvers on biomolecule crystal growth from solution: modeling studies. Spacebound 1997 Proceedings pp. 242-244, Canadian Space Agency (1998).

C.-Y. Lee, P. Scovazzo and P. Todd. Dynamics of composite reverse-osmosis membranes in dewatering mode with applications in crystal growth by osmotic dewatering. Paper 145c, 137h. Annual Meeting, American Institute of Chemical Engineers, Miami Beach, FL, 15-20 November, 1998.

Todd, P. "Oligonucleotide Crystallization: Membrane-based and Low-gravity Methods" Department of Chemical Engineering (seminar), Colorado State University, Ft. Collins, 6
November, 1998.

Todd, P. Bioprocessing in Microgravity. 21st Symposium on Biotechnology for Fuels and Chemicals, Ft. Collins, CO 2-6 May, 1999.

Cape, S. P., Shah, M. and Todd, P. The role of Mg^{++} ions in the crystallization of an oligonucleotide International Union of Crystallography Congress, Glasgow, Scotland, 4-10 August, 1999.

Sportiello, M.G., Todd, P., Snell, E., Judge, R., Pusey, M. and Cassanto, J. M. Effect of dimer contaminants and low gravity on lysozyme cyrstal mosaicity. 12th Annual Colorado Biotechnology Symposium, Boulder, CO 14 Sep 1999

Cape, S. P., Shah, M. and Todd P. The role of Mg^{++} ions in the crystallization of an oligonucleotide. 12th Annual Colorado Biotechnology Symposium, Boulder, CO 14 Sep 1999

P. Scovazzo, C.-Y. Lee, A. Frometa and P. Todd. Dynamics of reverse osmosis membranes in osmotic dewatering mode in crystal growth. Bioengineering Biotechol., submitted (1999).

R.A. Judge, E.H. Snell, M. G. Sportiello, H. Bellamy, G. E. Borgstahl, M. Pokros, M. L. Pusey, J. M. Cassanto and P. Todd. Biochemical and X-ray mosaicity analysis of impurity doped microgravity and ground-grown lysozyme crystals. J. Crystal Growth, submitted 1999.

R. A. Judge. The effect of impurities on protein crystal growth: case studies on earth and in microgravity. Poster PO9.OB.007. XVIIIth International Union of Crystallography Congress, 4-13 Aug 1999, Glasgow. Programme .\p, 83.

S. P. Cape. The role of Mg++ ionis in the crystallisation of an oligonucleotide. . XVIIIth International Union of Crystallography Congress, 4-13 Aug 1999, Glasgow. Programme . p.

R. A. Judge, E. H. Snell, M. G. Spoprtiello, H. Bellamy, G. E. Borgstahl, M. Pokros, M. L. Pusey, J. M. Cassanto and P. Todd. Biochemical and X-ray mosaicity analysis of impurity doped microgravity and ground-grown lysozyme crystals. Spacebound 2000 Conference, Vancouver, BC, Canada, 15-18 May, 2000.

J. Vellinger, M. S. Deuser, P. Todd, J. F. Doyle, N. Thomas, K. Barton, W. Metz, M. G. Sportiello and R. P. Cooper. Biotechnology experiiments in the "ADSEP" Payload on space shuttle flight STS-95 (1998). Spacebound 2000 Conference, Vancouver, BC, Canada, 15-18 May, 2000.

PART II. TASK 1: PREPARATION OF HIGH-QUALITY CRYSTALS AND THEIR COMPLEXES

Chapter 6

Synopsis of oligonucleotides studied

CHAPTER 6
SYNOPSIS OF OLIGONUCLEOTIDES STUDIED

6.1 Case Study Oligonucleotide: the "UU-dodecamer"

A twelve-nucleotide nearly self-complimentary RNA oligomer with the sequence 5'-GGCGCUUGCGUC-3' (the 5'-hydroxylated form) was the oligonucleotide chosen for this study, and will be referred to as the "UU-dodecamer" or simply "dodecamer" in this work. The primary reasons for choosing this particular molecule were the wealth of local expertise available regarding it and the production process and infrastructure that were already in place. But it is also interesting in its own right as an RNA sequence that contains the CUUG tetraloop motif. Most of the UU-dodecamer RNA used in this study was produced by *in vitro* transcription and enzymatically digested.

It has been the subject of NMR studies which showed that it forms a symmetrical duplex under high salt conditions and a hairpin under low salt conditions (Jucker, 1995; Jucker & Pardi, 1995). The crystallographic structure of the UU-dodecamer has been solved to 2.4Å resolution (Lietzke *et al.*, 1996b) and the coordinate file for the asymmetric unit are available at the Nucleic Acid Database (NDB ID# URL050; Berman *et al.*, 1992). This RNA dodecamer has been used as a model oligonucleotide for the development and testing of novel crystallization techniques (Lee, 1997; Lee *et al.*, 1998; Lee *et al.*, 1997) and for the investigation of crystallization and chromatography as techniques for purifying very closely related oligonucleotides (Cape, 1997; Cape *et al.*, manuscript in preparation). It has also been used as a model in studies seeking to optimize (and eventually scale up) the *in vitro* transcription of RNA oligonucleotides (Marble & Davis, 1995; Kern, 1997; Kern & Davis, 1997; Kern & Davis, 1999; Young *et al.*, 1997; Davis & Breckenridge, 1999).

6.3 Uncrystallized Aptamer: "225t3"

A 35-nucleotide DNA oligomer with a proprietary sequence binds to insulin-like growth factor (IGF). It is of significant pharmaceutical interest and is the property of NexStar (now Gilead Life Science) in Boulder, CO. Crystallization conditions were not found for this molecule.

6.4 HIV Reverse Transcriptase Aptamer: "Pseudoknot (PK)"

A 28-nucleotide RNA which is a potent inhibitor of HIV-1 reverse transcriptase. This molecule is the product of RNA ligand design using in vitro selection ("Selex") techniques. It is the first detailed look at a pseudoknot RNA structure. Knowing its structure will aid in guiding the design of a stable antiviral pharmaceutical.

6.5 Drew-Dickerson DNA

A 12-nucleotide DNA with the sequence 5'-CGCGAATTCGCG-3', this is the most studied DNA fragment. There are currently 72 structures with this 12 nucleotide sequence deposited in the Nucleic Acid Database (Berman *et al.*, 1992). Of these, 43 are

structures of the Dickerson DNA bound to drugs, 1 is a complex with an organic ligand, and 4 are complexes with endonucleases. In addition, 26 of the 72 structures contain base (19 structures) or sugar (7 structures) modifications. Only 9 of the 72 structures are of the non-complexed, unmodified Dickerson DNA crystallized and/or resolved under different conditions or to different resolution limits. In 5 of these 9 structures, multivalent cations (spermine, magnesium or calcium) have been identified (NDB entries BD0004, BD0005, BD0014, BD0029, and BDL084).

Two of the 9 structures are worthy of special mention in the context of the study here: BDL001 and BDL084. Richard Dickerson and his coworkers were the first to report a single-crystal structure analysis (resolved to 1.9Å) of a complete turn of right-handed B-DNA (Wing *et al.*, 1980). This original structure of this B-DNA, the Dickerson DNA as this sequence is referred to here, is given in the Nucleic Acid Database as NDB entry BDL001 (Drew *et al.*, 1981). This structure is the standard model in many biochemistry textbooks for the B-form of DNA (Voet & Voet, 1987). The other Dickerson DNA structure worthy of special note is NDB entry BDL084, which was resolved to 1.4Å (Shui *et al.*, 1998a). This structure provided refined details of the B-DNA conformation and was the first Dickerson DNA structure in which a hydrated magnesium ion and part of spermine molecule were unambiguously identified. Early on it was assumed that magnesium cations were involved in the structure but were designated as disordered and undiscernable, and Drew and Dickerson had limited success in fitting part of spermine molecule in the electron density map (Drew & Dickerson, 1981). The presence of the hydrated magnesium cation and the partial spermine molecule was unambiguously confirmed in a second structure of the Dickerson DNA that was solved to 1.5Å resolution (NDB entry BD0005; Shui *et al.*, 1998b). Dickerson DNA was purchased from Macromolecular Resources, Dept. of Biochemistry, Colorado State University, Fort Collins, CO.

6.6 Holbrook RNA

A 12-nucleotide nearly self-complimentary RNA oligomer with the sequence 5'-GGACUUCGGUCC-3' is referred to in this work as the "Holbrook RNA" after the first author of the paper describing its crystal structure. The structure of the Holbrook RNA has been solved to 2.0Å resolution and is known to crystallize as a duplex (NDB entry ARL037; Holbrook *et al.*, 1991) even though it forms an exceptionally stable hairpin in solution even under high salt conditions that approximate those used to grow the crystal (Kanyo *et al.*, 1996). Because of its exceptional stability in the hairpin conformation, the Holbrook RNA has been the subject of extensive research that includes NMR spectroscopy (Kanyo *et al.*, 1996; Varani *et al.*, 1991; Cheong *et al.*, 1990), melting profiles (Varani *et al.*, 1991; Antao *et al.*, 1991), time-resolved fluorescence depolarization (Kanyo *et al.*, 1996), and numerous theoretical studies using molecular dynamics simulations (Miller & Kollman, 1997a; Miller & Kollman, 1997b; Simmerling *et al.*, 1998; Srinivasan *et al.*, 1998). Holbrook RNA was purchased from Dharmacon Research, Inc. (Boulder, CO).

CHAPTER 6
SYNOPSIS OF OLIGONUCLEOTIDES STUDIED

6.1 Case Study Oligonucleotide: the "UU-dodecamer"

A twelve-nucleotide nearly self-complimentary RNA oligomer with the sequence 5'-GGCGCUUGCGUC-3' (the 5'-hydroxylated form) was the oligonucleotide chosen for this study, and will be referred to as the "UU-dodecamer" or simply "dodecamer" in this work. The primary reasons for choosing this particular molecule were the wealth of local expertise available regarding it and the production process and infrastructure that were already in place. But it is also interesting in its own right as an RNA sequence that contains the CUUG tetraloop motif. Most of the UU-dodecamer RNA used in this study was produced by *in vitro* transcription and enzymatically digested.

It has been the subject of NMR studies which showed that it forms a symmetrical duplex under high salt conditions and a hairpin under low salt conditions (Jucker, 1995; Jucker & Pardi, 1995). The crystallographic structure of the UU-dodecamer has been solved to 2.4Å resolution (Lietzke *et al.*, 1996b) and the coordinate file for the asymmetric unit are available at the Nucleic Acid Database (NDB ID# URL050; Berman *et al.*, 1992). This RNA dodecamer has been used as a model oligonucleotide for the development and testing of novel crystallization techniques (Lee, 1997; Lee *et al.*, 1998; Lee *et al.*, 1997) and for the investigation of crystallization and chromatography as techniques for purifying very closely related oligonucleotides (Cape, 1997; Cape *et al.*, manuscript in preparation). It has also been used as a model in studies seeking to optimize (and eventually scale up) the *in vitro* transcription of RNA oligonucleotides (Marble & Davis, 1995; Kern, 1997; Kern & Davis, 1997; Kern & Davis, 1999; Young *et al.*, 1997; Davis & Breckenridge, 1999).

6.3 Uncrystallized Aptamer: "225t3"

A 35-nucleotide DNA oligomer with a proprietary sequence binds to insulin-like growth factor (IGF). It is of significant pharmaceutical interest and is the property of NexStar (now Gilead Life Science) in Boulder, CO. Crystallization conditions were not found for this molecule.

6.4 HIV Reverse Transcriptase Aptamer: "Pseudoknot (PK)"

A 28-nucleotide RNA which is a potent inhibitor of HIV-1 reverse transcriptase. This molecule is the product of RNA ligand design using in vitro selection ("Selex") techniques. It is the first detailed look at a pseudoknot RNA structure. Knowing its structure will aid in guiding the design of a stable antiviral pharmaceutical.

6.5 Drew-Dickerson DNA

A 12-nucleotide DNA with the sequence 5'-CGCGAATTCGCG-3', this is the most studied DNA fragment. There are currently 72 structures with this 12 nucleotide

sequence deposited in the Nucleic Acid Database (Berman *et al.*, 1992). Of these, 43 are structures of the Dickerson DNA bound to drugs, 1 is a complex with an organic ligand, and 4 are complexes with endonucleases. In addition, 26 of the 72 structures contain base (19 structures) or sugar (7 structures) modifications. Only 9 of the 72 structures are of the non-complexed, unmodified Dickerson DNA crystallized and/or resolved under different conditions or to different resolution limits. In 5 of these 9 structures, multivalent cations (spermine, magnesium or calcium) have been identified (NDB entries BD0004, BD0005, BD0014, BD0029, and BDL084).

Two of the 9 structures are worthy of special mention in the context of the study here: BDL001 and BDL084. Richard Dickerson and his coworkers were the first to report a single-crystal structure analysis (resolved to 1.9Å) of a complete turn of right-handed B-DNA (Wing *et al.*, 1980). This original structure of this B-DNA, the Dickerson DNA as this sequence is referred to here, is given in the Nucleic Acid Database as NDB entry BDL001 (Drew *et al.*, 1981). This structure is the standard model in many biochemistry textbooks for the B-form of DNA (Voet & Voet, 1987). The other Dickerson DNA structure worthy of special note is NDB entry BDL084, which was resolved to 1.4Å (Shui *et al.*, 1998a). This structure provided refined details of the B-DNA conformation and was the first Dickerson DNA structure in which a hydrated magnesium ion and part of spermine molecule were unambiguously identified. Early on it was assumed that magnesium cations were involved in the structure but were designated as disordered and undiscernable, and Drew and Dickerson had limited success in fitting part of spermine molecule in the electron density map (Drew & Dickerson, 1981). The presence of the hydrated magnesium cation and the partial spermine molecule was unambiguously confirmed in a second structure of the Dickerson DNA that was solved to 1.5Å resolution (NDB entry BD0005; Shui *et al.*, 1998b). Dickerson DNA was purchased from Macromolecular Resources, Dept. of Biochemistry, Colorado State University, Fort Collins, CO.

6.6 Holbrook RNA

A 12-nucleotide nearly self-complimentary RNA oligomer with the sequence 5'-GGACUUCGGUCC-3' is referred to in this work as the "Holbrook RNA" after the first author of the paper describing its crystal structure. The structure of the Holbrook RNA has been solved to 2.0Å resolution and is known to crystallize as a duplex (NDB entry ARL037; Holbrook *et al.*, 1991) even though it forms an exceptionally stable hairpin in solution even under high salt conditions that approximate those used to grow the crystal (Kanyo *et al.*, 1996). Because of its exceptional stability in the hairpin conformation, the Holbrook RNA has been the subject of extensive research that includes NMR spectroscopy (Kanyo *et al.*, 1996; Varani *et al.*, 1991; Cheong *et al.*, 1990), melting profiles (Varani *et al.*, 1991; Antao *et al.*, 1991), time-resolved fluorescence depolarization (Kanyo *et al.*, 1996), and numerous theoretical studies using molecular dynamics simulations (Miller & Kollman, 1997a; Miller & Kollman, 1997b; Simmerling *et al.*, 1998; Srinivasan *et al.*, 1998). Holbrook RNA was purchased from Dharmacon Research, Inc. (Boulder, CO).

Chapter 7

Data Reduction from Twinned Crystals

Susan E. Lietzke, Vasili E. Carperos and Craig E. Kundrot

Acta Cryst. (1996). D52, 687–692

Data Reduction from Twinned RNA Crystals

SUSAN E. LIETZKE, VASILI E. CARPEROS AND CRAIG E. KUNDROT

Department of Chemistry and Biochemistry, University of Colorado, Boulder, CO 80309-0215, USA.
E-mail: kundrot@colorado.edu

(Received 18 October 1995; accepted 5 January 1996)

Abstract

Methods were developed to process diffraction data from epitaxially twinned crystals. Four programs for data reduction and two display programs were developed to augment the data-reduction program *XDS* [Kabsch (1988). *J. Appl. Cryst.* **21**, 916–924]. The programs can be generalized for use with other data-reduction software that provides the user with a list of the reflections used to determine lattice constants and crystal orientation. *LATTICE_VIEW* generates a PDB file containing 'water molecules' at the reciprocal-space coordinates of the strong spots found in the initial data frames. The PDB file is visualized to identify spots that belong to the same lattice, obtain unit-cell dimensions for a lattice, and assess data quality. *VECTOR_MATCH* is used to find additional spots belonging to a lattice. *ACCOUNT*4 determines which spots have been processed by *XDS*. *COMFORT* discards reflections that are too close to a reflection in another lattice. The display programs provide useful visual information on the quality of the crystal orientations used. Data with an R_{merge} of 7.1% at 2.4 Å resolution were obtained from epitaxially twinned crystals of an RNA dodecamer. The data were of sufficient quality to solve the structure with a combination of molecular replacement and single isomorphous replacement methods.

1. Introduction

Stronger X-ray sources now permit more users to collect diffraction data from crystals much smaller in size than was possible ten to 15 years ago. These hardware improvements have done little to allow users to collect and reduce data from twinned crystals. There has been some success at solving macromolecular structures from twinned data sets by some innovative software methods (Fisher & Sweet, 1980; Goldman, Ollis & Steitz, 1987; Redinbo & Yeates, 1993; Lu, Lindqvist & Schneider, 1995).

The RNA dodecamer GGCGCUUGCGUC forms twinned crystals whose diffraction patterns do not fully overlap (Doudna, Grosshans, Gooding & Kundrot, 1993) (Fig. 1). This type of twinning has been referred to as epitaxial twinning (Redinbo & Yeates, 1993). The twin domains are apparent when viewed between crossed polarized light, but attempts to physically separate the domains were unsuccessful.

Attempts to reduce and index the data with *XDS* (Kabsch, 1988) were not successful. Therefore, programs were developed for: (1) viewing the reciprocal-space coordinates listed in the SPOT.XDS file produced by *XDS*, (2) selecting spots that belong to one lattice, (3) identifying which spots correspond to a particular lattice and (4) merging data from different lattices. The programs used in this analysis allowed the dodecamer structure to be solved by molecular replacement and single isomorphous replacement methods using the data from epitaxially twinned crystals.

The programs developed are general in that they can treat more than two lattices and the lattices can have different cell dimensions. Furthermore, they can be generalized for any data-reduction software that provides the user with a file containing the reflections used to determine lattice constants and crystal orientation.

2. Methods

Four programs have been developed for use with *XDS* (Kabsch, 1988) to enable data reduction from epitaxially twinned crystals (Fig. 2). Following the terminology of *XDS*, 'spots' are putative, strong reflections

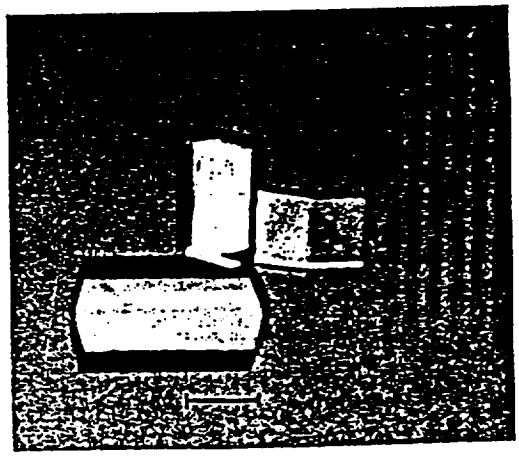

Fig. 1. Crystal of the RNA dodecamer GGCGCUUGCGUC. The bar is 100 μm.

identified from the first frames of a data set and 'reflections' are reflections that are reduced to (h, k, l, I, σ) later on in the data-reduction process.

The essence of the approach is to intervene in the data-reduction process between the stages of generating a list of spots and using the spots to determine unit-cell parameters and a crystal orientation. The approach can be used with any data-reduction software that provides the user with a file containing spot positions and the opportunity to intervene at the appropriate stage in the data-reduction process. Unless otherwise indicated, all programs are written in FORTRAN 77. A description of each program follows, along with general remarks about its use. The *Results* section contains more specific results concerning the dodecamer.

2.1. *LATTICE_VIEW*

2.1.1. *Description*. *XDS* reads a number of initial data frames (typically 30), identifies strong reflections and writes the (x, y, φ) coordinates to the file SPOT.XDS. x and y are the coordinates on the detector and φ is the value of the spindle axis.

LATTICE_VIEW reads the SPOT.XDS file and generates a coordinate file [in Protein Data Bank (PDB) format] that contains 'water molecules' at the reciprocal-space coordinates of the spots. Each residue in the file contains one water molecule in the form of an O atom only. The PDB file can be examined with any macromolecular graphics program to visually identify spots that belong to the same lattice (Fig. 3).

There are three chains in the PDB file: *A*, *B* and *C*. Water molecules in the *A* chain have coordinates (0,0,0), (20,0,0), (0,20,0), (0,0,20) in Å, and are useful for visualizing the laboratory coordinate system used by *XDS*.

The *B* chain contains waters at the reciprocal-space coordinates of the spots in the SPOT.XDS file (Fig. 3). The crystal-to-detector distance, direct-beam position and detector swing angle are read in from the XDS.DATA file. The (x, y, φ) coordinates and intensity of each spot are obtained from the SPOT.XDS file. The (x, y, φ) coordinates are transformed into orthogonal reciprocal-space coordinates using a coordinate system in which the origin is located where the direct beam intersects Ewald's sphere, the x axis is perpendicular to the direct beam and the crystal rotation axis, the y axis points from the crystal toward the detector along the direct beam and the z axis is parallel to the crystal rotation axis. For convenience in viewing, the reciprocal-space coordinates are multiplied by a conversion factor of 400 Å^2 prior to writing the PDB file. The coordinates of the spots are written out to the PDB file in the same order that they are read in from the SPOT.XDS file (*i.e.* in order of decreasing intensity).

```
While an unprocessed lattice exists
   Run LATTICE_VIEW (and XCL_VIEW) and identify spots belonging to an
        unprocessed lattice
   While less than 25 spots have been identified
        Pick two spots for reference vector
        Run VECTOR_MATCH to get more spots
   End while
   Run XDS with spots picked by VECTOR_MATCH
   Check quality of lattice orientation with PREDICT2POS
   Run ACCOUNT6 to identify spots not belonging to a lattice
End while
Run COMFORT to eliminate reflections that are too close in reciprocal
   space.
Scale data together with XSCALE.
```

Fig. 2. Pseudocode describing the data-reduction process.

The *C* chain contains coordinates of vectors between the spots (Fig. 4). The vectors between all pairs of spots are calculated and those with a magnitude less than 0.025 Å^{-1} are retained. The vectors are sorted by the product of the intensities of the two spots in decreasing order. For example, residue number one is generated from the two strongest spots. The top 6000 difference vectors are written to the PDB file.

2.1.2. *Use*. The *B* chain shows reciprocal-space coordinates of the spots used by *XDS* to index the reflections. Noise peaks at the perimeter of the detector are readily recognized as not belonging to a regular lattice. Since the residue number of the spots corresponds to their rank order intensity, one can easily determine a residue range that, when displayed, appears free of noise. The SPOT.XDS file can then be edited to retain only these spots. The reciprocal-lattice sampling revealed by the *B* chain is usually too sparse to allow one to measure all six reciprocal unit-cell constants, particularly in the direction perpendicular to the detector face. In preparation for *VECTOR_MATCH*, the residue numbers of spots that appear to belong to the same lattice are recorded.

The *C* chain is useful for obtaining unit-cell dimensions for the lattice(s). An untwinned crystal will produce a cluster of *C*-chain 'water molecules' at each reciprocal-lattice point. If there are many low-intensity noise spots, then many *C*-chain residues with high residue numbers will be scattered through reciprocal space. The *C*-chain residues with low residue numbers can still be used to identify the reciprocal unit-cell dimensions. However, if the crystal slipped during the data collection or if it is twinned, the waters may be too dispersed to obtain reciprocal unit-cell dimensions. If the crystal is twinned, but one twin diffracts much stronger than the other, it is often still possible to obtain reciprocal unit-cell dimensions from the low residue number spots. In our experience, a *C* chain with tight clustering about the reciprocal-lattice positions always indexes well in the *XDS* subroutine *IDXREF*.

2.2. *VECTOR_MATCH*

2.2.1. *Description.* *VECTOR_MATCH* identifies spots in the SPOT.XDS file that belong to the same lattice by identifying pairs of spots that define equivalent vectors. The magnitudes of two vectors are defined as equivalent if they differ by less than a user-specified fraction. The directions of two vectors are regarded as equivalent if the angle between them is less than a user-specified value.

VECTOR_MATCH reads the SPOT.XDS file and the PDB file created by *LATTICE_VIEW*. The user inputs the residue numbers of two spots from the *B* chain created by *LATTICE_VIEW* to define the reference vector, Δ. All possible vectors, $\mathbf{d}_{ij}$, between spots *i* and *j* in the SPOT.XDS file are calculated and compared to Δ. If the magnitudes and directions of $\mathbf{d}_{ij}$ and Δ are equivalent, then spots *i* and *j* are considered to be part of the same lattice and they are written to the output file. The output file is in SPOT.XDS format.

2.2.2. *Use.* One selects length and angular criteria to get at least 25 spots from *VECTOR_MATCH*. To check the quality of the spots chosen, *LATTICE_VIEW* is run using the new spots from the *VECTOR_MATCH* file as input. If the residues in the resulting file do not cluster tightly, more stringent length and/or angle criteria are needed.

If too few spots are chosen, the procedure can be repeated with a different pair of spots and the output from both runs of *VECTOR_MATCH* combined into one SPOT.XDS file. The spots file generated at this stage is used in *XDS* to process data from one lattice.

2.3. *ACCOUNT4*

2.3.1. *Description.* *ACCOUNT4* is used to determine which spots in the original SPOT.XDS file are accounted for by the lattice(s) processed by *XDS*. The program reads in the original SPOT.XDS file, an XDS.DATA file and an XDS.HKL file for each lattice. The reciprocal-space distance between each spot and the nearest reflection in the XDS.HKL files is determined. If the distance is less than a user-specified value, the spot is regarded as being the same as the reflection and is, therefore, accounted for by a particular orientation of a particular reciprocal lattice. The output is a set of files in SPOT.XDS format. For each XDS.HKL file, there is a file that contains the spots accounted for by the reflections in that file. One additional file contains the spots that were not accounted for by reflections in any of the XDS.HKL files.

2.3.2. *Use.* The objective is to account for all spots in the original SPOT.XDS file. Some spots are never accounted for because *XDS* does not process reflections that have incomplete peak profiles, that are near the spindle axis or that are outside the trusted region of the detector. Some spots may be noise rather than reflections. If a large number of spots remain, the *LATTICE_VIEW/VECTOR_MATCH/ACCOUNT4* sequence can be repeated to find additional lattices.

2.4. *COMFORT*

2.4.1. *Description.* *COMFORT* compares the reciprocal-space coordinates of reflections from two XDS.HKL files and discards those reflections that are 'too close for comfort'. The user specifies the distance criterion for designating two reflections as being too close. *COMFORT* writes the accepted reflections to two XDS.HKL formatted files, one for each of the input files.

2.4.2. *Use.* One uses *COMFORT* in conjunction with the merging program *XSCALE* (Kabsch, 1988) to decide what distance cut off should be used. One seeks to balance a low R_{merge} against a high completeness.

2.5. *PREDICT2POS*

2.5.1. *Description.* *PREDICT2POS* is a program that displays a data frame and shows where reflections are predicted by two different runs of *XDS*, *i.e.* one for each lattice (Fig. 5). *PREDICT2POS* is not necessary for the data reduction, but provides useful visual information on the quality of the crystal orientations used. *PREDICT2POS* is written in IDL (Research Systems, Inc., Boulder, CO). It reads a data frame and the following files from two different *XDS* runs: MODPIX.XDS, XDS.DATA, XPARM.XDS, XYCORR.TABEL. It then calls two FORTRAN subroutines. One subroutine reads a data frame and returns an INTEGER*2 array 512 by 512 pixels containing the intensity of each pixel. The other subroutine is based on the *XDS* subroutine *COLPROF*. Using the data from the *XDS*-generated files, it returns the values of an INTEGER*2 array with dimensions 512 by 512. The array elements are equal to one if the corresponding pixel borders the active region of a reflection and are zero otherwise. *PREDICT2POS* then displays the data frame and the outlines of the active areas.

2.5.2. *Use.* One uses *PREDICT2POS* to determine how well the crystal unit-cell dimensions and orientation are defined. Reflections should only appear in the center of the active region outlines. If the crystal is twinned, one can determine how well each lattice is oriented and how well separated the reflections are.

2.6. *HKL_VIEW*

2.6.1. *Description.* *HKL_VIEW* is a companion program to *LATTICE_VIEW* that helps one determine if unaccounted for spots actually belong to a lattice. The program reads an XDS.HKL file and its corresponding XDS.DATA file and produces a PDB file containing waters at the reciprocal-space coordinates of the

processed reflections. These spots are then viewed along with the spots from a *LATTICE_VIEW* run.

2.6.2. *Use*. Some reflections are not processed by *XDS* because they have incomplete peak profiles, are near the spindle axis or are outside the trusted region of the detector. It is easy to determine if an unaccounted for spot in SPOT.XDS belongs to a lattice if there are many neighboring spots available for comparison. *HKL_VIEW* provides such spots, *i.e.*, the processed reflections. By examining unaccounted for spots this way, one can determine if another lattice exists or not.

3. Results and discussion

The programs described above were used with *XDS* to process and merge data from twinned crystals of the RNA dodecamer GGCGCUUGCGUC. This molecule contains non-canonical U–U base pairs at the center of the duplex. Dodecamer crystals were grown at 311 K from 10% 2-methyl-2,4-pentanediol, 50 m*M* sodium cacodylate pH 7.0, 100–300 m*M* ammonium acetate, and 25 m*M* magnesium chloride. The crystals were twinned (Fig. 1) and broke into irregular fragments when physical manipulation was attempted. Diffraction data to 2.4 Å were collected with a Siemens area detector from crystals at 100 K. The dodecamer crystals contained two lattices; both belonged to space group P_1 and had the same unit-cell dimensions: $a = 29.4$, $b = 28.9$, $c = 46.5$ Å, $\alpha = 98.9$, $\beta = 72.9$ and $\gamma = 96.1°$. The two lattices were oriented in different directions, but shared the same a axis. Prior to implementation of the methods described here, data from the twinned dodecamer crystals were not successfully processed by *XDS*.

The general procedure used to process a dodecamer data set is summarized in Fig. 2. After a SPOT.XDS file was generated by running *XDS*, this original SPOT.XDS file was used as input to *LATTICE_VIEW*. The resulting coordinate file was examined with *InsightII* (Biosym Inc., 1994). For a typical twinned dodecamer data set, portions of the *B* chain appeared to belong to a single lattice while spots in other regions

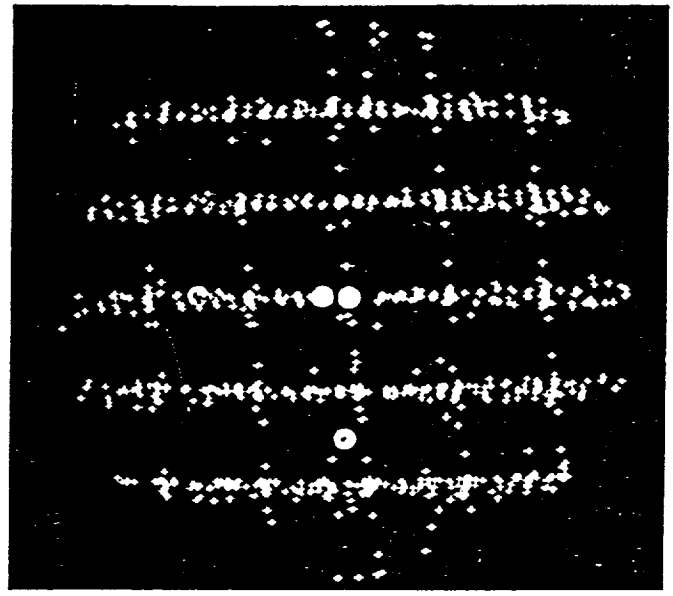

(*a*)

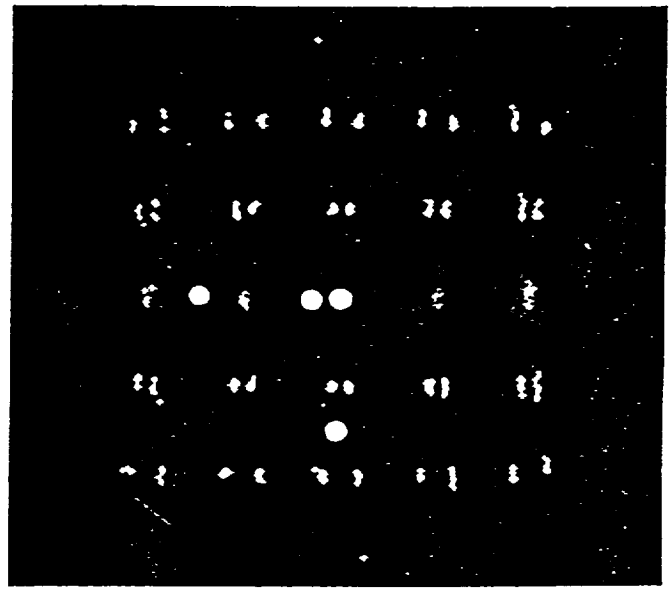

(*b*)

Fig. 4. The *C* chain from *LATTICE_VIEW*. (*a*) The difference vectors from the original spots file. (*b*) difference vectors belonging to lattice 1 (blue), lattice 2 (yellow-green) after spots have been assigned to one of the lattices. The *A* chain is shown in yellow (origin) and orange (*x*, *y* and *z* axes).

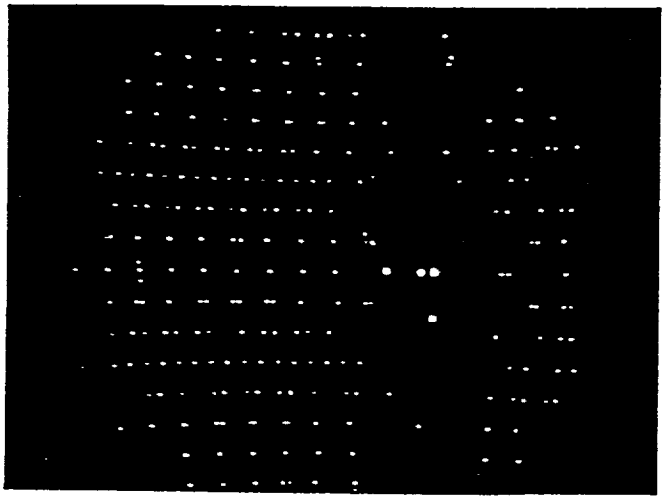

Fig. 3. The *B* chain from *LATTICE_VIEW*. The *B* chain contains spots belonging to lattice 1 (blue), lattice 2 (yellow-green), both lattices (cyan) and neither lattice (orange). The *A* chain is shown in yellow (origin) and orange (*x*, *y* and *z* axes).

Table 1. *Statistics on dodecamer native data set*

	Spots accounted for by lattice			Lattice 1				Lattice 2				Merged lattices		
Wedge	1	2	Neither	R_{sym}* (%)	No. of unique reflections	Total No. of observations	% Complete	R_{sym}* (%)	No. of unique reflections	Total. No. of observations	% Complete	R_{merge} (%)	No. of unique reflections	Total. No. of observations	% Complete
a	127	67	38	2.9	4395	5062	77	3.5	4437	5143	78	6.7	5408	10042	95
b	131	76	37	2.9	2366	2398	42	2.8	2369	2415	42	7.2	2893	4409	51
c	132	75	44	—†	442	442	8	—†	451	452	8	5.9	858	890	15
d	92	108	44	2.6	2219	2261	39	2.3	2239	2273	39	5.4	3633	4442	64

* Data from 47 to 2.4 Å. † Did not contain enough observations to calculate R_{sym}.

Table 2. *XSCALE merging statistics for one wedge of native data from 47 to 2.4 Å after running the program COMFORT*

COMFORT cut off (Å)	R_{merge} (%)	No. of unique reflections accepted	Total No. of observations accepted	Completeness (%)
0.000	6.7	5408	10042	95.1
0.003	6.4	5121	9428	90.0
0.005	6.4	5058	9358	88.9
0.008	6.2	4722	8241	83.0
0.011	6.2	3231	5439	56.8

indicated that there was more than one lattice. In the *C* chain, one dimension was fairly well resolved, however the spots in the other two dimensions were scattered.

In order to obtain a SPOT.XDS file that contained spots belonging to a single lattice orientation, the program *VECTOR_MATCH* was used. The fractional length and angular cutoffs used were generally 0.1–0.3 and 1–5°. In the dodecamer case, it was important to avoid choosing spots along the *a* axis, since the twinned domains have this axis in common. The SPOT.XDS file output by *VECTOR_MATCH* was input to *LATTICE_VIEW* and the PDB coordinate file visually examined. This procedure of choosing a pair of spots, running *VECTOR_MATCH*, and looking at the new SPOT.XDS file generally had to be repeated multiple times before a SPOT.XDS file suitable for processing a lattice orientation was obtained.

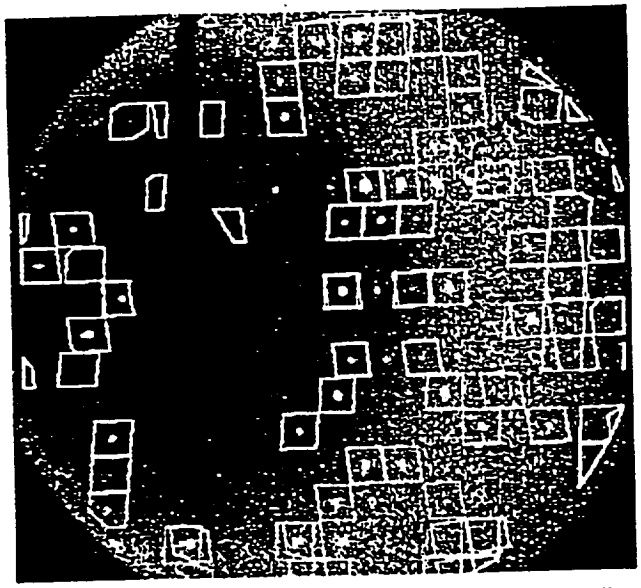

Fig. 5. *PREDICT2POS* output showing a data frame and the predicted positions of reflections from two lattices. The predicted positions are shown in white for one lattice and yellow for the other lattice.

The unit-cell dimensions of the dodecamer crystals were measured from the lattice(s) formed by the *C* chain vectors. Several trials were usually required to obtain a SPOT.XDS file that clearly defined a reciprocal lattice. If the lattices were hard to separate, it was frequently helpful to select a different wedge of data to identify the lattices. Unlike the method of Lu *et al.* (Lu *et al.*, 1995), identification of the two lattices did not require a zone to be aligned in a particular orientation.

Next, the SPOT.XDS file from *VECTOR_MATCH* was substituted for the original SPOT.XDS file and used for processing with *XDS*. After the first lattice orientation, 'lattice 1', was processed, the program *ACCOUNT4* was used to identify spots belonging to 'lattice 2'. *LATTICE_VIEW* and *VECTOR_MATCH* were used to generate a SPOT.XDS file for *XDS* for processing lattice 2. During processing, *PREDICT2-POS* was used to evaluate how well the two lattice orientations were being processed (Fig. 4).

ACCOUNT4 was used to verify that the crystals contained only two lattices. Out of 330 total spots in the SPOT.XDS file from one specimen, 136 belonged to lattice '1' and 105 to lattice '2'. Because the *a* axis of both lattices is the same, 67 spots were accounted for by both lattices. Only 22 spots were unaccounted for by either lattice. These spots were examined and all were not processed by *XDS* because they fell along the spindle axis, were not fully recorded, or were noise spots and not reflections. The partial reflections were readily identified by comparing the spot coordinate to the reflection coordinates produced by *HKL_VIEW*.

Data from a native crystal were collected in four wedges resulting in eight reduced data sets. The two

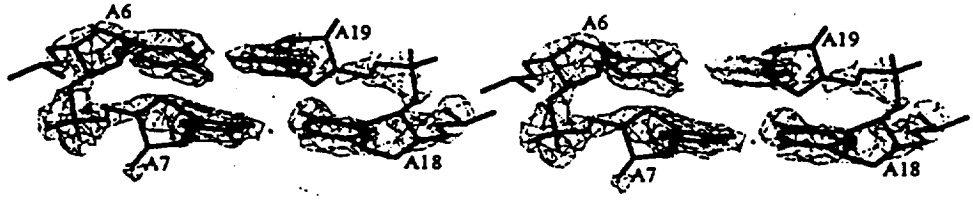

Fig. 6. The current model of the dodecamer. Base pairs U16–U19 and U7–U18 are shown along with $2F_o - F_c$ electron density contoured at 1.0σ.

lattice orientations in each wedge were processed individually, following the procedure above (Table 1). Typically, the two lattices have very comparable data-collection statistics. Data in the highest resolution shell of lattice 1, however, were often more complete than those of lattice 2 because of the stronger diffraction from lattice 1. The R_{merge} values from the two lattice orientations in the native crystal ranged from 5.4 to 7.2% for data between 47 and 2.4 Å.

Prior to merging the data with the program *XSCALE* (Kabsch, 1988), the program *COMFORT* was run in order to remove reflections that were close in reciprocal space. 'Comforting' the two data sets led to a decrease in the R_{merge} value. The first wedge of data was used to test the effect of varying the comfort cut-off level (Table 2). A *COMFORT* cut-off level of 0.003 Å was chosen to balance a low R_{merge} against high completeness. The data from each of the eight data sets, filtered through *COMFORT* with a 0.003 Å cut off, were then merged together. In addition, resolution cut offs were also applied to some of the data because of the weaker diffraction of lattice 2. The final merged native data set had an R_{merge} of 7.1% and was 91% complete. There were 5185 unique reflections and 16679 total observations. Data sets from six candidate heavy-atom derivatives and other native crystals were also successfully processed with the same techniques.

These methods should be applicable to crystals with larger unit cells. The unit cell of the dodecamer is relatively small for a macromolecule and the reciprocal-lattice points are far apart. *LATTICE_VIEW*, however, has provided initial unit-cell dimensions from crystals of other macromolecules with dimensions up to 180 Å. Extrapolating from our experience with the dodecamer suggests that lattice orientations differing by 5–10° can be isolated with *VECTOR_MATCH*. Our experience with *COMFORT* suggests that there is little problem with reflections from different lattices being too close together. It may, however, be useful to modify the background updating procedure in *XDS* for crystals with larger unit cells. The background counts for a pixel are updated when a pixel is far from the nearest predicted reflection. When more than one lattice is diffracting X-rays, a pixel may receive counts from a reflection in a lattice not being processed. One way to solve this problem would be to make sure that a pixel is not unusually strong before it is used to update background.

The data obtained using the methods described in this paper were of sufficient quality to determine the dodecamer structure. Isomorphous-replacement and molecular-replacement techniques were used. The current model includes two duplexes and 78 solvent molecules in the asymmetric unit. It has been refined to a crystallographic R value of 20.3% and R_{free} of 27.0% for data to 2.4 Å (Fig. 6).

4. Conclusions

A method was developed to allow currently available software to reduce data from epitaxially twinned crystals. Programs written to interface with the program *XDS* were created and tested on data from crystals of a RNA dodecamer. The programs developed are general in that they can treat more than two lattices and the lattices can have different cell dimensions. Furthermore, they can be generalized for any data-reduction software that provides the user with a file containing the reflections used to determine lattice constants and crystal orientation. The method is successful; the structure of the dodecamer has been determined and refinement is in progress. The current model has an R value of 20.3% and R_{free} of 27.0%. An analysis of the structure and details of the structure determination will be published elsewhere.

Requests for the programs can be made to CEK at kundrot@colorado.edu. This work was funded by the Colorado RNA Center, W.M. Keck Foundation, and the National Science Foundation (MCB-9221307).

References

Biosym Inc. (1994). *Insight*II. Biosym Inc., San Diego, CA, USA.

Doudna, J. A., Grosshans, C., Gooding, A. & Kundrot, C. E. (1993). *Proc. Natl Acad. Sci. USA*, 90, 7829–7833.

Fisher, R. G. & Sweet, R. M. (1980). *Acta Cryst.* A36, 755–760.

Goldman, A., Ollis, D. L. & Steitz, T. A. (1987). *J. Mol. Biol.* 194, 143–153.

Kabsch, W. (1988). *J. Appl. Cryst.* 21, 916–924.

Lu, G., Lindqvist, Y. & Schneider, G. (1995). *Acta Cryst.* D51, 13–20.

Redinbo, M. R. & Yeates, T. O. (1993). *Acta Cryst.* D49, 375–380.

Chapter 8

The structure of an RNA Dodecamer Shows How Tandem U-U base pairs Increase the Range of Stable RNA Structures and the Diversity of Recognition Sites

Susan E. Lietzke, Cindy J. Barnes, J. Andrew Berglund and Craig E. Kundrot

The structure of an RNA dodecamer shows how tandem U–U base pairs increase the range of stable RNA structures and the diversity of recognition sites

Susan E Lietzke, Cindy L Barnes, J Andrew Berglund and Craig E Kundrot*

Background: Non-canonical base pairs are fundamental building blocks of RNA structures. They can adopt geometries quite different from those of canonical base pairs and are common in RNA molecules that do not transfer sequence information. Tandem U–U base pairs occur frequently, and can stabilize duplex formation despite the fact that a single U–U base pair is destabilizing.

Results: We determined the crystal structure of the RNA dodecamer GGCGCUUGCGUC at 2.4 Å resolution. The molecule forms a duplex containing tandem U–U base pairs, which introduce an overall bend of 11–12° in the duplex resulting from conformational changes at each interface between the tandem U–U base pairs and a flanking duplex sequence. The formation of the U–U base pairs cause small changes in several backbone torsion angles; base stacking is preserved and two hydrogen bonds are formed per base pair, explaining the stability of the structure.

Conclusions: Tandem U–U base pairs can produce stable structures not accessible to normal A-form RNA, which may allow the formation of specific interfaces for RNA–RNA or RNA–protein recognition. These base-pairs show an unusual pattern of hydrogen-bond donors and acceptors in the major and minor grooves, which could also act as a recognition site.

Address: Department of Chemistry and Biochemistry, University of Colorado Boulder, CO 80309-0215, USA.

*Corresponding author.
E-mail: kundrot@colorado.edu

Key words: difference distance matrix, RNA structure, solvent accessible surface, U–U base pair, X-ray crystallography

Received: **22 April 1996**
Revisions requested: **16 May 1996**
Revisions received: **30 May 1996**
Accepted: **6 June 1996**

Structure 15 August 1996, 4:917–930

Introduction

Non-canonical base pairs occur frequently in naturally occurring RNAs as conserved structural building blocks. The canonical base pairs G–C, A–U and G–U convey primary structure information in transcription and translation, and adopt similar geometries. In contrast, RNA sequences that do not bear sequence information can exploit the full range of possible base pairing interactions to produce functional structures. Twenty-five potential non-canonical base pairs containing two hydrogen bonds have been hypothesized [1]. Still more possibilities arise if one includes the possibility of water molecules that bridge two bases as seen in C–U base pairs [2]. Non-canonical base pairs adopt geometries quite different from those of canonical base pairs and are very common in RNA molecules whose primary purpose is not the transfer of information through primary and secondary structure. For example, 3% of the base pairs in 16S and 23S rRNA are G–A and 1% are U–U [3]. When other non-canonical base pairs such as C–C, A–A, and G–G are included, the total percentage of non-canonical base pairs in rRNA is 6%. Comparative sequence analysis shows that non-canonical base pairs often interconvert exclusively with other non-canonical base pairs, for example, A–A interconverting with G–G [3]. Non-canonical base pairs are, therefore, essential structural building blocks rather than errors in less critical parts of the structure.

Non-canonical base pairs can be functionally important in at least two ways: adopting unusual structures and altering the stability of base paired regions. The structure of non-canonical base pairs deviates from the familiar A-form geometry of RNA and can therefore affect interactions with proteins or other RNA molecules. Such non-canonical structures may interact directly with other molecules or they may position other parts of the RNA molecule in the correct orientation for interactions to take place. Non-canonical base pairs could also be used to tune the stability of a duplex, allow the formation of alternate secondary structures [4] or refine the turnover rate of the molecule in the cell. Non-canonical base pairs can stabilize or destabilize double-stranded helices [5–8]. A thorough study of the stability of tandem mismatches as a function of the flanking sequences [5] showed that GA, AG and UU sequences can stabilize duplexes. The stability, however, depends heavily on the base pairs flanking the 5′ and 3′ ends of the non-canonical base pairs.

U–U base pairs occur in several RNAs [9–11]. The dodecamer examined in this study, GGCGCUUGCGUC ('CUUG'), provides an example of a tandem U–U base pair, that is, two consecutive U–U base pairs. Single U–U base pairs destabilize a helix [7,12], but with the right combination of flanking base pairs, tandem U–U base pairs can stabilize a duplex [5]. Consistent with the thermodynamic

stabilization, NMR data show evidence that the CUUG duplex forms U–U base pairs [13]. The crystal structure of tandem U–U base pairs flanked by G–U base pairs, instead of C–G base pairs (the 'UUUG' dodecamer), shows one U–U base pair making two hydrogen bonds and the other base pair making only one hydrogen bond [14].

This paper describes the structure of tandem U–U base pairs flanked by C–G base pairs in the molecule CUUG. This sequence stabilizes duplex formation from single-stranded RNA [5]. The structure of the U–U base pairs in the stable CUUG sequence is different from that of the U–U base pairs in the UUUG sequence and shows how tandem mismatches can redirect the path of duplex RNA in different ways. The structural differences also help explain why the stability of the sequences varies.

Results and discussion

Structure solution and refinement

This paper describes the crystal structure of the RNA dodecamer duplex CUUG (Fig. 1a). The oligonucleotide contains the tetraloop sequence CUUG [15]. At low salt concentrations, the dodecamer forms a hairpin loop, but at the salt concentrations used for crystallization, the dodecamer forms a duplex [16]. The structure of the CUUG dodecamer was solved by a combination of molecular replacement and single isomorphous replacement techniques (as described in the Materials and methods). The structure of the dodecamer was refined with X-PLOR [17] to a crystallographic R value of 19.1% and R free of 24.0%, for 5142 reflections greater than 2σ in the 8.0–2.4 Å resolution shell. The geometry is reasonable; root mean square deviations (rmsd) from ideality are 0.01 Å in bond length, 1.26° for bond angles, 8.0° for dihedral angles, and 1.50° for improper angles. The final model contains two independent copies of the dodecamer duplex, helix I and helix II, and 158 solvent sites in the asymmetric unit. Helix I and helix II are both numbered from G1 to C24 (Fig. 1a).

Global structure and backbone geometry

The two CUUG dodecamer duplexes in the asymmetric unit form very similar antiparallel double-stranded helices. The rmsd for all atoms between helix I and helix II is 0.4 Å, when G1 of helix I is aligned with G1 of helix II, and 0.6 Å, when G1 of helix I is aligned with G13 of helix II (Fig. 1b,c). Each CUUG dodecamer has approximately twofold symmetry (rmsd=0.5–0.6 Å) and can be thought of as comprising two copies of a hexamer duplex; for example, one copy would be G1–U6:U19–C24. These four hexamers in the asymmetric unit are very similar (rmsd=0.4–0.5 Å), indicating that the structure of the hexamer is independent of its microenvironment in this crystal form. The similarity of the hexamer structures, despite the differences in the packing environments, suggests that the structure adopted in the crystal reflects the real average structure in solution.

The backbone torsion angles do not, in general, deviate much from values observed for A-form RNA. The average pseudo-rotation angle (and standard deviation) for the ribose rings in the two helices is 14.2° (6.9°), normal for the A-form North or C3′-endo conformations. The backbone torsion angles are within the range typically observed in A-form RNA [18,19], with the exception of two residues. The average values of the torsion angles (and standard deviations) are: α=278.9° (47.5°), β=177.4° (12.8°), γ=59.1° (43.0°), δ=82.6° (3.8°), ϵ=206.4° (7.8°), ζ=287.5° (9.5°) and ψ=200.1° (8.3°). When the two outliers in α and γ are excluded, the average values of α and γ are 294.6° (10.0°) and 50.8° (8.6°), respectively. The two exceptions are a 'crankshaft rotation' of α and γ that occurs at one nucleotide in each helix: C17 in helix I and U7 in helix II. The crankshaft rotation changes the value of α from ≈290° to 111.0° and 42.8°, for C17 and U7 respectively, and changes γ from ≈50° to 190.5° and 310.4°, for C17 and U7 respectively. The pseudo-rotation angles of residues U7 and C17 must change along with the crankshaft motion [20]; they are the only two residues in the structure that adopt pseudo-rotation values for the C2′-endo conformation: –11.3° and –3.6°, respectively. One of the residues is involved in a crystal contact (C17 2′OH in helix I hydrogen bonds with the U23 O2P of helix II), but none of the atoms defining the torsion angles are involved in the contacts. When the four hexamers are superimposed, the crankshaft motion produces a shift of the base of ≤ 0.8 Å and a shift of the non-bridging oxygens of ≤ 1.7 Å. Thus, this type of crankshaft motion can modulate the detailed structure of a local region by a significant amount.

The phosphate–phosphate distances fall within the 'normal' range for A-form RNA helices, but both the major and minor grooves are narrower than in an A-form RNA helix (Fig. 1d). Helices I and II have an average phosphate–phosphate distance of 5.7 Å (standard deviation 0.3 Å), which is close to the A-form value of 5.65 Å. In A-form RNA, as determined by fiber diffraction, the major groove is 4.1 Å wide and the minor groove 11.3 Å wide [21]. The major groove width of the CUUG helices is 3.1 Å (standard deviation 0.8 Å). The major groove contracts sharply in the region around the U–U base pairs (Fig. 1d). The minor groove width is 9.8 Å (standard deviation 1.1 Å), also less than in A-form.

Despite having only small deviations in backbone parameters from A-form RNA, neither CUUG helix superimposes well onto A-form RNA. The CUUG structures superimpose on an A-form helix with an rmsd of 1.8 Å for all atoms and 1.6 Å for backbone atoms. When the first five base pairs of either CUUG helix are superimposed on the first five base pairs of an A-form helix, the terminal base pair of the CUUG dodecamer superimposes closely to the penultimate base pair of the A-form dodecamer. In other words, the CUUG dodecamer is shorter than A-form by one base

Figure 1

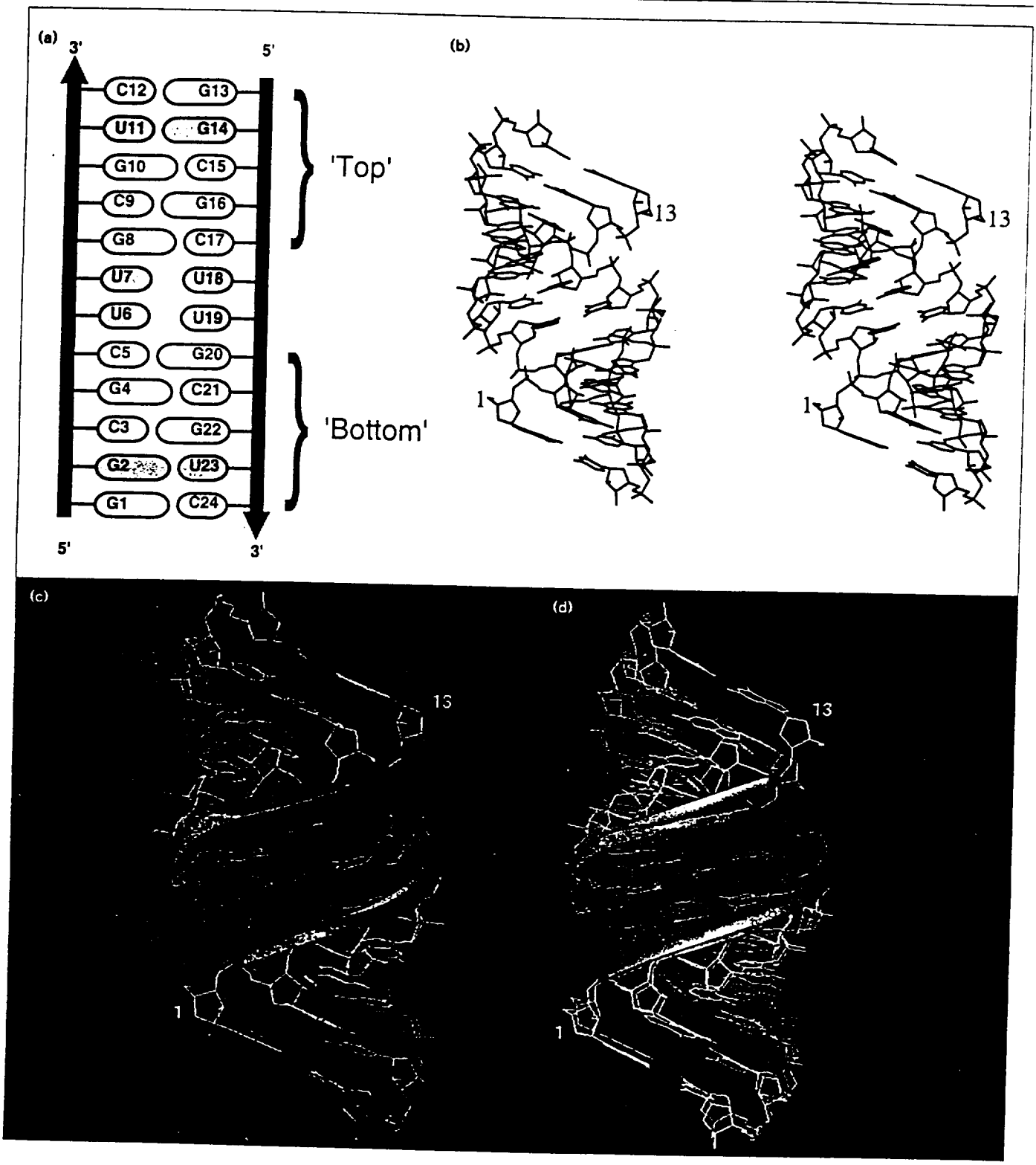

The CUUG duplex. (a) Schematic diagram of the CUUG duplex, non-canonical base pairs are shaded gray and canonical base pairs are white. **(b)** Stereo view of helix I, the positions of the nucleotides 1 and 13 are marked. (Figure prepared with the program MOLSCRIPT [38]). **(c)** Helix I (turquoise) superimposed on helix II (purple). All atoms were used for the superposition (rmsd=0.4 Å). **(d)** Helix I (turquoise) superimposed onto an A-form helix (yellow). All atoms were used for the superposition (rmsd=1.8 Å).

pair. The long axis of the last base pair, however, is oriented between the axes of the eleventh and twelfth base pairs of the A-form RNA. So, in terms of the position of the terminal base pairs, the CUUG dodecamer is a close, but not exact, replacement for an A-form undecamer (11 base pair duplex).

Distance matrix analysis

The structures of the CUUG helices were also compared to A-form RNA using difference distance matrices (DDM) [22,23]. The distance matrix of a molecule contains elements d_{ij} that equal the distance between atoms i and j. The difference distance matrix for a structure that undergoes a change is the difference between two distance matrices: $\Delta_{ij}=d_{ij}(\text{final})-d_{ij}(\text{initial})$. Invariant, or 'rigid', regions will have difference distance elements equal to or close to zero. The major advantage of this method is that it is independent of both superposition (unlike rmsd calculations) and local frames of reference (unlike helical parameter calculations). We compared helices I and II of CUUG to the same sequence in the ideal A-form conformation to determine which parts of the structure deviate the most from A-form. For simplicity, we will describe these changes as 'motions'.

We calculated the standard DDM between all 504 atoms in the structure as well as an rms residue average DDM (ADDM). The elements in the ADDM, D_{lm}, are equal to the average value of DDM elements Δ_{ij} squared, where the average is calculated over all atoms i in residue l and all atoms j in residue m, ($D_{lm}=\langle\Delta_{ij}^2\rangle^{1/2}$). The DDM and ADDM show the same trends, but the ADDM is easier to analyze (Fig. 2a).

The ADDM shows which regions of the structure are most like A-form RNA. Square submatrices centered on the dashed diagonal contain distances between base paired residues. An absence of elements above a specified cut-off in these submatrices indicates which duplex regions are most like A-form RNA. Square submatrices centered on the solid diagonal contain distances between contiguous residues of one strand. There is a tendency for these elements to have lower values than the rest of the ADDM because bases tend to move in the plane of a base pair, that is, approximately perpendicular to vectors between atoms in different residues. Movements perpendicular to interatomic vectors will produce a small change in the interatomic distance. At the 1.0 Å cut-off level, the ADDM for CUUG only shows large blocks of rigid nucleotides near the solid diagonal as a result of this tendency of nucleotides to move in the plane of the base pair.

The 1.5 Å cut-off level shows that the regions that are most like A-form RNA occur in blocks. Along the dashed diagonal residues 1–5, 20–24 and 8–17 are most like A-form RNA. These duplex regions are at the ends of the duplex and are separated by the U–U base pairs. Superposition of A-form and CUUG molecules using the terminal duplex regions (e.g. residues 1–5 and 20–24), results in an apparently complex structural change that is not easily described in a qualitative manner. A clearer impression of this structural change is obtained by superimposing consecutive residues from one of the two strands. Along the solid diagonal residues 1–4, 4–9, 9–16, 16–22 and 20–24 are most like A-form. Superposition using residues 4–9 shows that the two duplex regions that flank the tandem U–U base pairs undergo different motions (Fig. 2b). The bottom region, (residues 1–5 and 20–24), shows a striking swinging motion while the top region, (8–17), shows much less of a swinging motion. Both top and bottom stem regions are compressed relative to A-form RNA; they have an average helical rise of 2.4 Å, while the A-form has an average helical rise of 2.8 Å.

The relative motions of the top, middle and bottom sections of the helix can be quantitated by determining the helical axes for the top and bottom sections and comparing them to the helical axis for the middle region. The CUUG helix was superimposed on A-form RNA using residues 4–9. The helical axis was then calculated for the top (residues 8–17), and bottom (residues 1–5 and 20–24) regions of CUUG and compared to the helical axis of the A-form duplex. The bottom helical axis makes an angle of 14–16° with the A-form axis, demonstrating the swinging motion. The top helical axis makes an angle of only 7–10° with the A-form axis, illustrating the smaller swinging motion that is observed. The angle between the top and bottom helical axes is 11–12°, therefore the insertion of this structure into a longer helical section would introduce an overall bend of 11-12°. Thus, superimposing the structures using the most invariant region in the middle of the molecule allows one to differentiate the effect on the two different flanking regions.

For both the top and bottom stems, the rotations result from changes in several backbone torsion angles. The rotation of the bottom stem is most localized. The largest contribution to the rotation of the bottom stem is a 9° rotation about the γ torsion angle of U6. This is not a large change in γ compared to the standard deviation in helices I and II (8.6°). The rotation of the top stem is even less localized.

Base pairs

The U–U base pairs are the most unusual base pairs in the structure. Each U–U base pair makes two direct hydrogen bonds (Fig. 3). No well-defined solvent sites mediate hydrogen bonds between the uridines, nor are there any conserved solvent sites in the major or minor grooves that stabilize the U–U base pairs or the base step between them. Rather, the O2 and N3 of one uridine hydrogen bond directly to the N3 and O4 of the other uridine. The hydrogen bond lengths between the bases are between 2.6–3.0 Å. To make these hydrogen bonds between two pyrimidines, the distance between the C1′ atoms in the

Figure 2

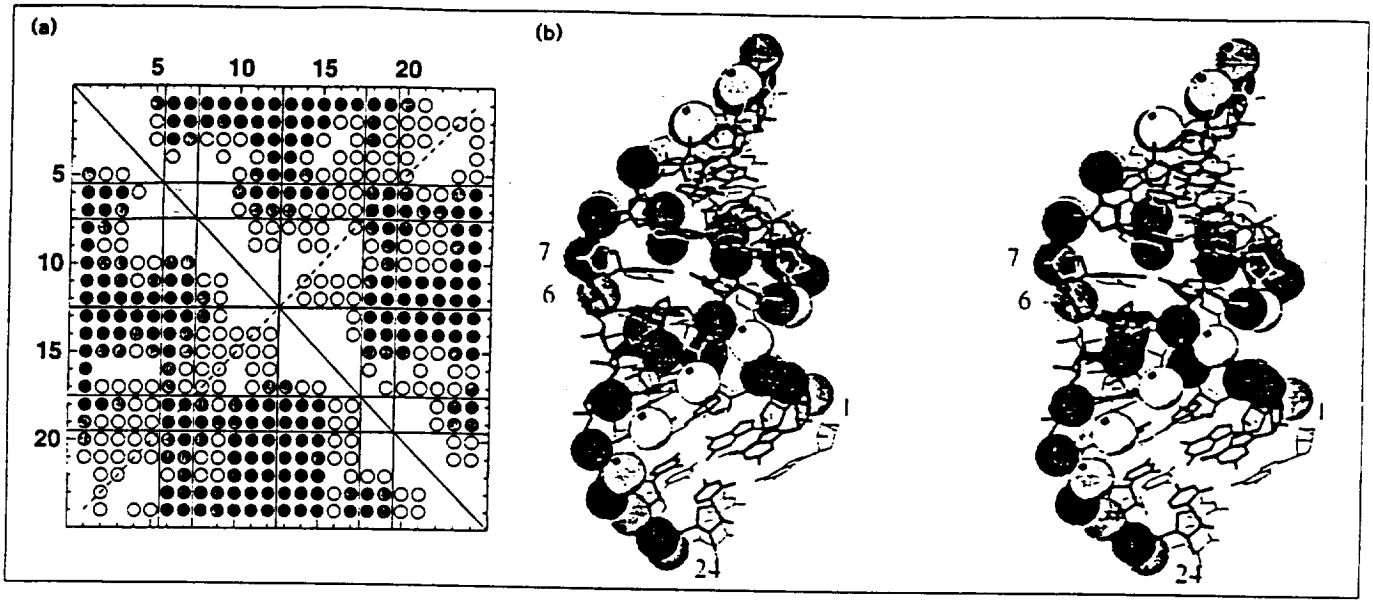

Average difference distance matrix (ADDM). **(a)** The matrix contains elements D_{im} (see text) with values 1.0 Å < D ≤ 1.5 Å, 1.5 Å < D ≤ 2.0 Å and 2.0 Å < D indicated by open circles, gray circles and black circles, respectively. The upper and lower matrices compare helix I and helix II, respectively, to A-form RNA. The bold line between residues 12 and 13 delineates the two strands and the lines flanking residues 6–7 and 18–19 delineate the tandem U–U region. The dashed line indicates elements between base-pairing residues. **(b)** Stereo view of helix I superimposed onto an A-form helix using residues 4–9 (rmsd=1.1 Å). The A-form model is shown in light gray and the CUUG helix in dark gray. The phosphorous atoms are shown as spheres. (Figure generated with MOLSCRIPT [38].)

base pair must narrow from a value of 10.5 Å observed for canonical base pairs to 8.1–8.7 Å (Table 1). Both C1′ atoms move towards each other and towards the helical axis (thus reducing the X-displacement, Table 1) to close the gap. To orient the hydrogen bond donors and acceptors correctly, the bases must also be rotated with respect to one another. The λ angle (defined as the N1–C1′–C1′ angle) provides a measure of this rotation. The value of the λ angle ranges from 51°–60° in Watson–Crick base pairs and from 44°–69° in the G–U 'wobble' base pairs in CUUG (Table 1). The uridine that contributes an O4 to the base pair has a regular λ value of 47–50°. The other uridine, which contributes the O2 to the U–U base pair, has an unusually high value of 78–80°, which makes this base 'open' towards the major groove. We refer to the base with a high λ angle as adopting an open conformation, while the base with the lower (normal) λ angle adopts a closed conformation. The electron density around the U–U base pairs is very clear and there is no indication that any of the uridines alternate between open the and closed conformation. In summary, the combination of the translation along the C1′–C1′ direction and rotation about the λ angle moves the uridine bases closer together and towards the helical axis, rotating one base towards the major groove.

The base pairing pattern of the U–U base pairs drives the different motions of the top and bottom stems described in the previous section. U6 forms a hydrogen bond with U19(N3) through its O2 atom while U19 forms a hydrogen bond with U6(N3) through its O4 atom (Fig. 3). Similarly, the U7–U18 base pair has interactions U18(O2)–U7(N3) and U7(O4)–U18(N3). The open conformation of U6 requires its base pair partner, U19, to move towards the minor groove side of U6, this requires a large movement, especially for the backbone. To quantitate these movements, residues 4–9 of CUUG were superimposed on A-form RNA with the same sequence. Compared to the A-form conformation, U19(N3) must move 2.3–2.5 Å and U19(P) must move 3.6–4.3 Å. This motion produces the 14–16° rotation of the bottom part of the duplex stem. In contrast, U18 moves towards the major groove side of U7 and requires smaller displacements. Compared to the A-form conformation, U18(N3) must move 1.3–1.8 Å and U18(P) must move 2.0–2.5 Å. This movement only produces a 7–10° rotation of the top part of the duplex stem (Fig. 2b).

Unlike canonical base pairs, each U–U base pair presents two hydrogen bond acceptors in the major groove, two hydrogen bond acceptors in the minor groove and no hydrogen bond donors in either groove. Although the two acceptors are close to each other (3.4–3.9 Å), because one uridine is in an open conformation and the other in a closed conformation, only one of the oxygens is very solvent accessible. For example, in the very accessible minor groove, the O2 of U19 (in the closed conformation)

Figure 3

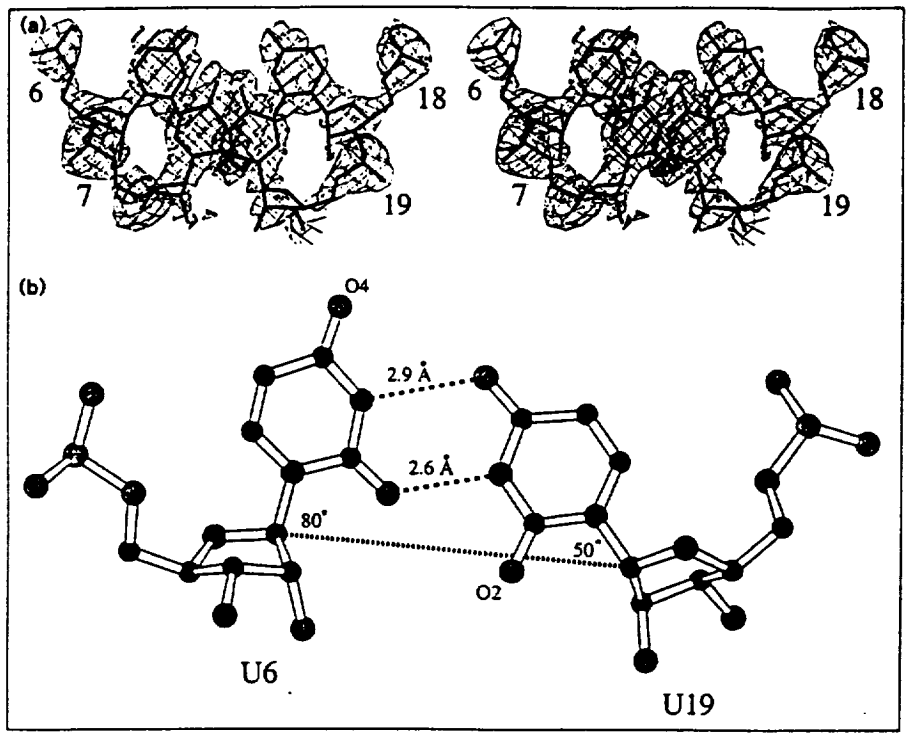

The U–U base pairs. (a) Representative section of the final $2F_o-F_c$ electron-density map. Stereo view of the U6–U19, and U7–U18 base pairs in helix I with the $2F_o-F_c$ map contoured at 1σ. (b) Ball-and-stick diagram showing the base pairing between U6 and U19. Two hydrogen bonds are formed: between U6(O2)–U19(N3) and between U6(N3)–U19(O4). The hydrogen bonds are indicated by the dashed lines. The λ angle (N1/N9–C1′–C1′) values are shown; the dotted line indicates the C1′–C1′ line segment used to define the angle λ. U6 is in the open conformation, and U19 is in the closed conformation (see text). Oxygen atoms are shown in red, nitrogen atoms in blue, phosphorous in magenta, and carbon in green. (Figure generated with MOLSCRIPT [38].)

is mostly inaccessible and the atoms available for hydrogen bond formation are U6(O2′), U6(O2) and U19(O2′). In the major groove, however, U19(O4) is more solvent accessible than the U6(O4).

The non-Watson–Crick G–U base pairs in CUUG are similar to G–U base pairs seen previously [2,14,24]. Two of the G–U base pairs are involved in crystal packing interactions through their 2′OH or minor groove atoms. At one of the remaining G–U base pairs, a solvent site, presumably water, mediates a hydrogen bond between the 2′OH and the G(N2) as observed in previous structures [2,24]. Unlike the environment around the U–U base pairs, there are solvent sites in the major and minor groove around all of the G–U base pairs. The remaining base pairs in the helix are all canonical base pairs and exhibit typical Watson–Crick geometry (Table 1).

Base steps

The base step between the U–U base pairs in each CUUG helix is also very different from that observed in A-form RNA (Table 1, Fig. 4a). These base steps have a large negative slide (–2.2 and –2.5 Å) and high twist (55–57°). The average base-step slide in the CUUG helices is –1.4 Å (–1.5 Å for A-form) and the average twist is 34.3° (32.7° for A-form). The rise of the base step between the U–U base pairs is very small: only 1.5–1.6 Å compared to the average value within the dodecamer of 2.3 Å (2.8 Å for A-form). The base steps on either side of the U–U base pairs also have unusually short rises.

The base step between the two U–U base pairs is flexible. When the first five base pairs of each of the four hexamer copies are superimposed, the rmsd for superimposed atoms is 0.3–0.5 Å. The rmsd for the U6–U19 base pair is 0.4–0.7 Å, and the rmsd of the next base pair, U7–U18, is 0.5–1.0 Å (Fig. 4b). So, while the U–U base step is symmetric in terms of hydrogen bonding arrangements and λ values, it is asymmetric in terms of the precise positions of the atoms.

The base steps flanking the tandem U–U base pairs dictate which uridine will be in the open conformation. These base steps are between a U–U base pair and a C–G base pair. The U–U base pair slides towards the helix axis by ≈1 Å (X-displacement) and maintains a twist of nearly 30° with the adjacent C–G base pair (Fig. 4c). The rise of these base steps is shorter, 1.8–2.1 Å, than the helical average of 2.3 Å (Table 1). The stacking of this base step seems to determine which uridine is in the open conformation (λ≈80°). For example, U6 is open because it can still stack well upon the C5–G20 base pair (Fig. 4c). U19 does not stack particularly well upon the C–G base pair in the closed conformation, but it would not stack at all in the open conformation. U6, therefore, adopts the open conformation rather than U19.

Table 1

Helical parameters for helix I and helix II.*

Base pair	Base pair				Base step		
	X-displacement (Å)	C1′–C1′ (Å)	λ1 (°)	λ2 (°)	Rise (Å)	Twist (°)	Slide (Å)
G1–C24	−3.7, −3.8	10.6, 10.7	55.8, 55.6	57.3, 54.5			
					2.2, 2.3	41.4, 41.2	−1.7, −1.6
G2–U23	−3.9, −3.8	10.2, 10.5	45.8, 43.7	67.7, 65.1			
					2.6, 2.2	28.0, 27.6	−0.7, −1.1
C3–G22	−4.1, −4.1	10.4, 10.6	55.1, 54.8	56.1, 52.9			
					2.6, 2.5	34.7, 34.5	−1.6, −1.5
G4–C21	−4.3, −4.4	10.3, 10.5	53.2, 55.7	59.8, 57.3			
					2.3, 2.5	31.5, 30.2	−1.3, −1.2
C5–G20	−4.1, −4.1	10.1, 10.2	59.5, 58.7	56.5, 54.4			
					2.1, 1.8	25.1, 29.6	−1.2, −1.2
U6–U19	−3.8, −3.7	8.1, 8.4	80.2, 78.3	50.2, 50.2			
					1.6, 1.5	57.4, 54.7	−2.2, −2.5
U7–U18	−3.2, −3.6	8.2, 8.7	47.3, 46.8	79.5, 77.8			
					2.1, 2.1	28.5, 25.8	−1.2, −1.5
G8–C17	−3.9, −4.3	10.5, 10.3	51.2, 53.4	56.1, 59.1			
					2.6, 2.4	28.8, 31.7*	−0.5, −1.2
C9–G16	−4.4, −4.7	10.4, 10.8	54.8, 53.1	51.9, 53.6			
					2.5, 2.7	34.1, 31.7	−1.9, −1.6
G10–C15	−3.9, −4.4	10.4, 10.4	53.9, 56.2	57.9, 56.4			
					2.2, 2.1	28.5, 30.1	−1.1, −1.3
U11–G14	−4.0, −4.1	10.5, 10.3	68.7, 64.4	47.5, 46.2			
					2.3, 2.3	41.4, 39.1	−1.7, −1.9
C12–G13	−4.0, −4.3	10.4, 10.7	55.5, 55.6	51.8, 52.1			

*Parameters were calculated using NEWHEL93 by RE Dickerson, available from the Brookhaven Protein Data Bank. The helical axis was defined by the C1′ and N1 or N9 atoms for two stems: residues (1–5, 20–24) for the first six base pairs; and residues (8–17) for the second six base pairs. The base step parameters reported for the base step between U6–U19 and U7–U18 were averaged from the results for the two stems.

Solvent

The O1P and 2′OH groups have the largest number of neighboring solvent sites in the structure. Of 158 solvent sites in the asymmetric unit, 126 make direct contacts with RNA. Of those making direct contacts to RNA, 70% contact the backbone, 14% contact the major groove, 6% contact the minor groove, and 10% contact both the backbone and the major or minor groove. The O1P atoms which face the major groove are the most solvated; 73% have a solvent site nearby whereas only 46% of the O2P atoms have a solvent site nearby. The 2′OH groups are also highly solvated. Of the 2′OH groups, 56% have a solvent site nearby; 17% of the 2′OH interact with a solvent site that also contacts a pyrimidine O2 or guanosine N3. There are no cases where a solvent site bridges O1P and O2P of the same nucleotide. The bridging oxygen atoms have many fewer solvent sites nearby; only 19% of the 3′O and 6% of the 5′O have nearby solvent sites. Eight percent of the 4′O are solvated and another 15% could form a hydrogen bond with a neighboring 2′OH. Ten solvent sites directly bridge atoms in strands from helix I and helix II. The solvation trends observed in the CUUG structure are similar to those reported for other RNA duplexes [19,25].

No distinct patterns of hydration were observed in either the major or minor groove. In both grooves, the guanosines have the most ordered solvent sites nearby. Solvent sites are located within 3.5 Å of ten of the twenty G(N7), but only three of the twelve U(O4) and two of the twelve C(N4) are solvated. In the minor groove, nine of the twenty G(N3) have a solvent site nearby while only one of twelve U(O2) and three of twelve C(O2) are solvated.

Intermolecular contacts

Helices I and II stack with symmetry related helices to form quasi-continuous helices in the crystal that are 90° to each other (Fig. 5a). Helix I runs in the direction of (but at a slight angle to) the unit cell a axis and helix II runs parallel to the b axis. In both cases, the backbone of one helix fits into the minor groove of the other helix (Fig. 5b,c). Water molecules, but no identifiable ions, mediate the interaction. Two contacts occur between the helices. Contact one involves 13 direct hydrogen bonds between the two helices, eight of which involve 2′ OH (Table 2, Fig. 5b). Contact two involves eight direct hydrogen bonds, of which five involve 2′ OH (Table 2, Fig. 5c). Solvent molecules make an additional 11 interactions in the first contact and nine in the second. While 2′ OH are

Figure 4

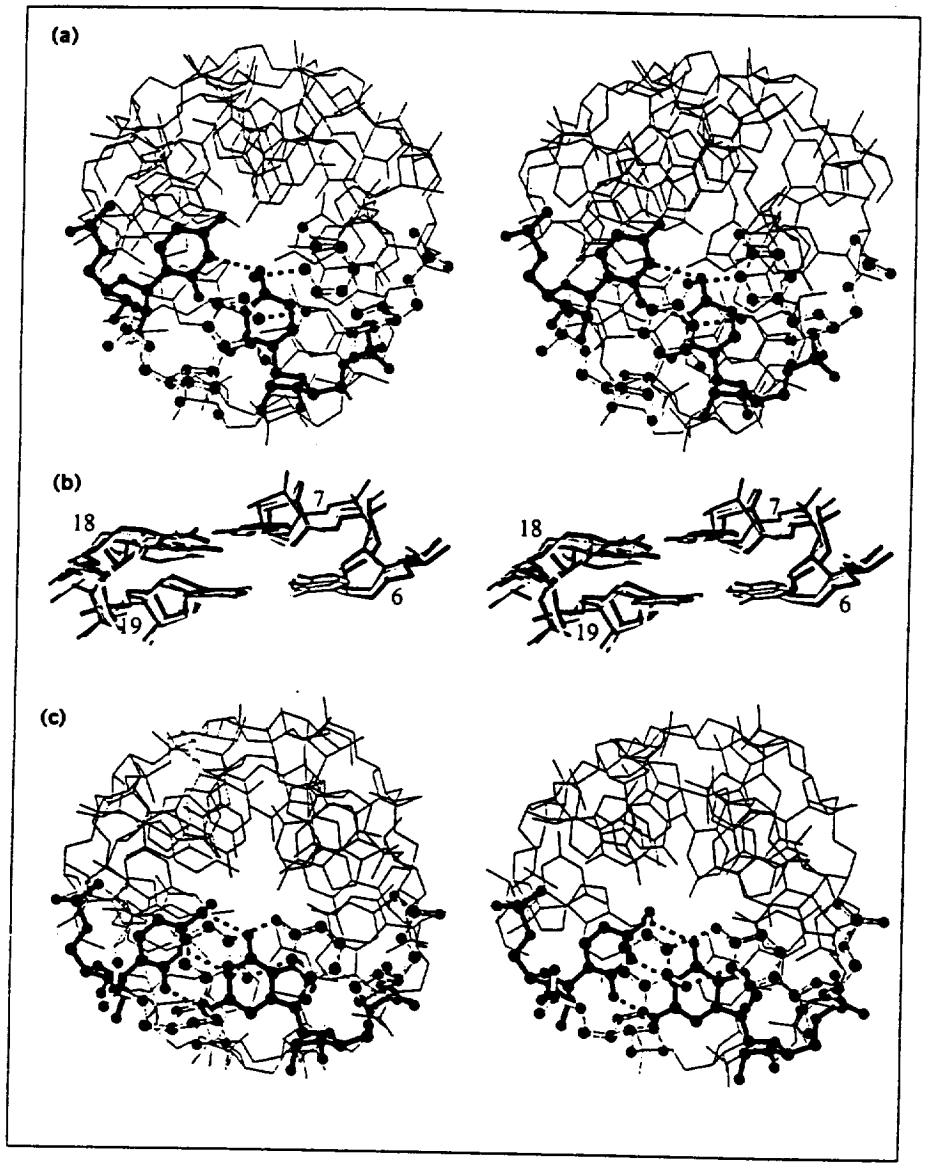

The base step between U–U base pairs. **(a)** Stereo view down the helical axis of helix I showing the stacking at the base step between U–U base pairs. The U–U base pairs are shown in ball-and-stick form and the other atoms in wire frame form. U6–U19 is shaded in dark gray; U7–U18 is in light gray. Carbon atoms are shown in green, nitrogen in purple, oxygen in red, and phosphorous in magenta. Hydrogen bonds formed between the bases are indicated by dashed lines. **(b)** Stereo view of the U–U base pairs in the four CUUG hexamers. The hexamers were superimposed on each other using their first five base pairs (e.g. residues 1–5 and 20–24). **(c)** Stereo view down the helical axis of helix I illustrating the stacking at the base step between C5–G20 and U6–U19. The C5–G20 base pair is in dark gray ball-and-stick form, and U6–U19 is in light gray. The helix is shown in wire frame representation. The coloring scheme for the atoms is the same as in (a). Dashed lines indicate the hydrogen bonds formed between the bases. The stacking of U–U base pairs on C–G base pairs is similar in all four instances in the asymmetric unit; the rmsd of the bases is 0.20–0.27 Å. (Figure generated using MOLSCRIPT [38].)

used most extensively in these two contacts, phosphate oxygens, and minor groove atoms are also used as has been seen in other RNA structures [14,19,25–27].

The quasi-continuous helices are not in a position to form truly continuous helices; each helix is shifted relative to its symmetry mate (Fig. 5d). The base step parameters for the 'step' between symmetry mates have a large negative slide (–4.1 and –3.7 Å), low twist (13.4° and 8.9°), and a low rise (1.7 Å). Phosphate linkages between helices could not be modeled across the junction between symmetry mates. The stacking between the base pairs at both junctions is unusual in that the guanosines from the two duplexes stack to overlay their six-membered rings (Fig. 5d).

Stacking analysis

Another unusual aspect of the U–U base pairs is the amount of stacking between the bases. The stacking interactions were examined by calculating the amount of solvent accessible surface area buried when two base pairs were brought together to form a base step (Fig. 6). The U–U base pairs are smaller than the purine-pyrimidine base pairs and so have less surface area to bury. Nonetheless, the amount of non-polar area buried is comparable to purine-pyrimidine base pairs. The U–U base pairs do bury less polar surface area than other base pairs because of the high accessibility of the O4 atoms of uridines in the open conformation. The surface area buried between two quasi-continuously stacked dodecamers is also smaller than between canonical base steps, but like the U–U base pairs, the amount of

Figure 5

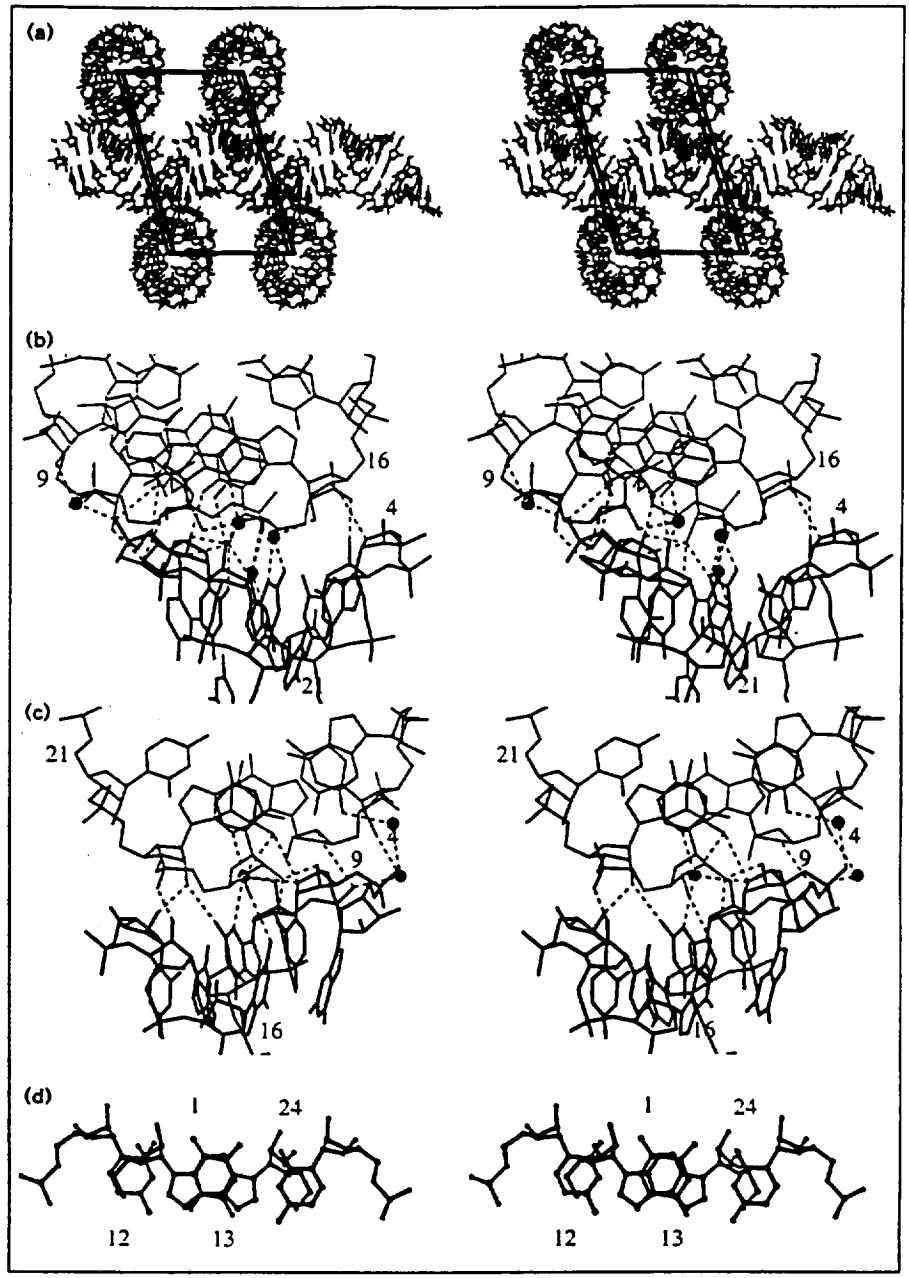

Interactions between symmetry related molecules. **(a)** Stereo view of the unit cell with the helical axis of helix I parallel to the plane of the paper and helix II oriented perpendicularly to the plane of the paper. The view is looking down the b axis of the crystal towards the origin. One molecule of helix I is drawn with thick lines. **(b)** Stereo view of one contact between helix I (residues 1–4 and 21–24, shown in black) and helix II (residues 7–10, 12 and 15–18, shown in gray) including four water molecules that make contacts to both helices (shown as gray spheres). The orientation of the helices is as in (a). **(c)** Stereo view of one contact between helix I (residues 7–10 and 15–18, shown in black) and helix II (residues 2–4 and 21–23, shown in gray) including three water molecules that make contacts to both helices (shown as gray spheres). The orientation of the helices is as in (a). **(d)** Stereo view of the stacking interactions between helix I molecules. The terminal base pair, between residues 12 and 13 of one helix, is shown in dark gray and the first base pair, between residues 1 and 24 of the next helix, is shown in light gray.

non-polar surface area buried is comparable to canonical base pairs. At the interface between the two helices, the ribose backbone stacks over the ring of the pyrimidine in the adjacent helix (Fig. 5b). Thus, base steps involving U–U base pairs, or junctions between quasi-continuous helices, bury less surface area than canonical base steps because of a reduction in the amount of polar area buried.

Comparison to the UUUG structure

The symmetry of the U–U base pairs in the CUUG duplexes contrasts with the asymmetry seen in the UUUG structure [14]. The base step between U–U base pairs is similar in both structures in that it has a short rise and a large twist angle (Fig. 7). However, the U–U base pairs in CUUG and UUUG are very different. One U–U base pair in the UUUG structure makes the same hydrogen-bonding pattern as the U–U base pairs in the CUUG structure (Fig. 7c). But the other U–U base pair in the UUUG structure makes only one hydrogen bond; a very large propeller twist breaks the N3–O2 interaction (Fig. 7a,b). The U–U base pairs also differ in their values of λ. While one uridine in each UUUG U–U base pair is in

Table 2

Intermolecular contacts.

Contact		Distance (Å)
Contact 1		
G2 N2	C17 O2′	2.76
G2 N2	C17 O3′	3.00
C3 O2′	C17 O2P	2.65
G4 O4′	G16 O3′	2.91
G22 O2′	G16 N2	3.13
U23 O2P	G10 O4′	3.03
U23 O2P	C9 O2′	2.68
U23 O2	C17 O2′	2.83
U23 O2′	C17 O2′	2.58
U23 O2′	C17 O2	2.70
U23 O3′	G8 N2	3.11
C24 O2P	G8 N2	3.16
C24 O4′	C17 O2′	3.16
W1 O	G16 O2′*	2.78
W1 O	G22 N2	3.11
W1 O	G22 N3	2.61
W2 O	U18 O2P*	2.64
W2 O	G2 N3	3.09
W3 O	G10 N3*	2.86
W3 O	G10 O2′*	2.67
W3 O	G22 O2′	2.62
W4 O	G8 O2′*	2.58
W4 O	C9 O4′*	2.95
W4 O	C24 O2P	2.49
Contact 2		
G8 N2	G22 O2′	2.83
C9 O2P	G4 O4′	3.20
C9 O4′	G22 N2	3.11
C9 O2	U23 O2′	2.67
C9 O2′	U23 O2′	2.63
G16 N2	U23 O3′	2.99
C17 O2′	U23 O2P	2.46
U18 O2′	G22 O2′	2.67
W5 O	G2 N2*	2.93
W5 O	G10 O2P	2.80
W6 O	C3 O2′*	3.09
W6 O	C9 O2P	2.78
W7 O	G22 N2*	2.95
W7 O	G22 N3*	2.61
W7 O	G8 O2′	2.77
W7 O	C9 O4′	3.16
W7 O	G8 N3	3.04

Water–RNA contacts are to helix II when labeled with an asterisk and otherwise to helix I.

a more open conformation than the other, the change in λ is significantly less than observed in the CUUG dodecamer. The uridine in the open conformation of UUUG has λ = 62–64°; the uridine in the closed conformation has λ = 41–48°. In contrast, the open and closed λ angles of the U–U base pairs in CUUG are 78–80° and 47–50°, respectively. The differences between these structures suggest that the structure of U–U base pairs are sensitive to the flanking sequence or environment or both. In either structure, U–U base pairs are flexible.

Figure 6

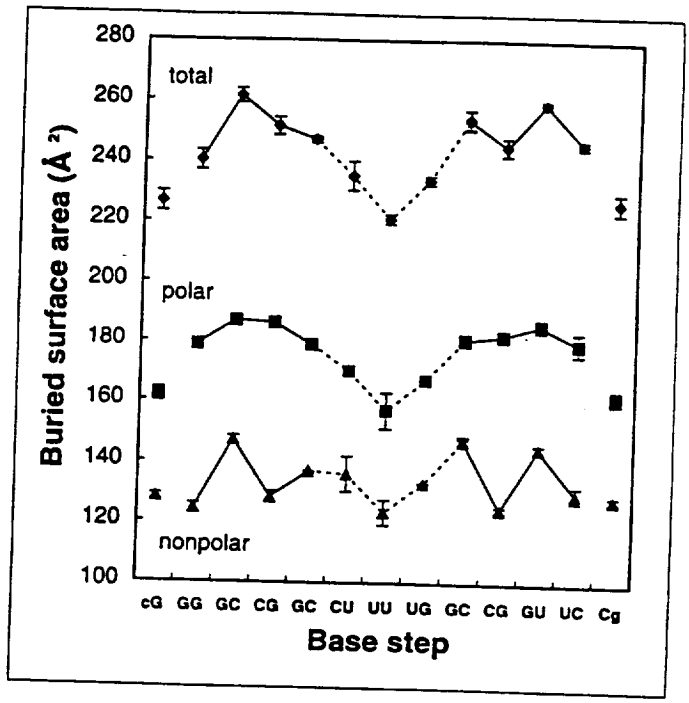

Buried surface area of base steps. The average value of the buried area for helices I and II are plotted with bars extending to the individual values for helix I and helix II. Solid lines connect base steps that do not contain U–U base pairs, dashed lines connect base steps containing U–U base pairs. The lone cG and Cg end points indicate the stacking between the two co-axially stacked duplexes in the crystal. The buried surface area was calculated as $(A_1+A_2-A_{12})/2$, where A_1, A_2 and A_{12} are the solvent accessible areas of base pair 1, base pair 2 and the base step formed by base pairs 1 and 2, respectively. The areas were calculated for the non-hydrogen atoms comprising the bases using a probe radius of 1.4 Å in X-PLOR [17].

The difference between the two structures can explain their different stabilities. U–U base pairs flanked by U–G base pairs (as in UUUG) disfavor duplex formation by 2.5 kcal mol^{-1}, whereas U–U base pairs flanked by C–G base pairs (as in CUUG) favor duplex formation by 0.5 kcal mol^{-1} [28]. The loss of one direct hydrogen bond between uridines in the UUUG structure is sufficient to account for this difference. The cause of the different geometries adopted by the U–U base pairs, however, remains unclear.

Comparison to *trans* U–U base pairs

Tandem U–U base pairs have also been observed between RNA duplexes with UU overhangs [29]. The overhanging UU nucleotides in the hexameric sequence UUCGCG form base pairs with the UU nucleotides of another molecule in the crystal to form quasi-continuous helices, i.e. molecules A and C form base pairs $U1^a$–$U2^c$ and $U2^a$–$U1^c$ (Fig. 7d). The two base pairs have the same structure because they are related to each other by a crystallographic twofold axis. The base pairs form hydrogen bonds between $U1^a$ O4 and $U2^c$ N3(H) and between $U1^a$ C5(H)

Figure 7

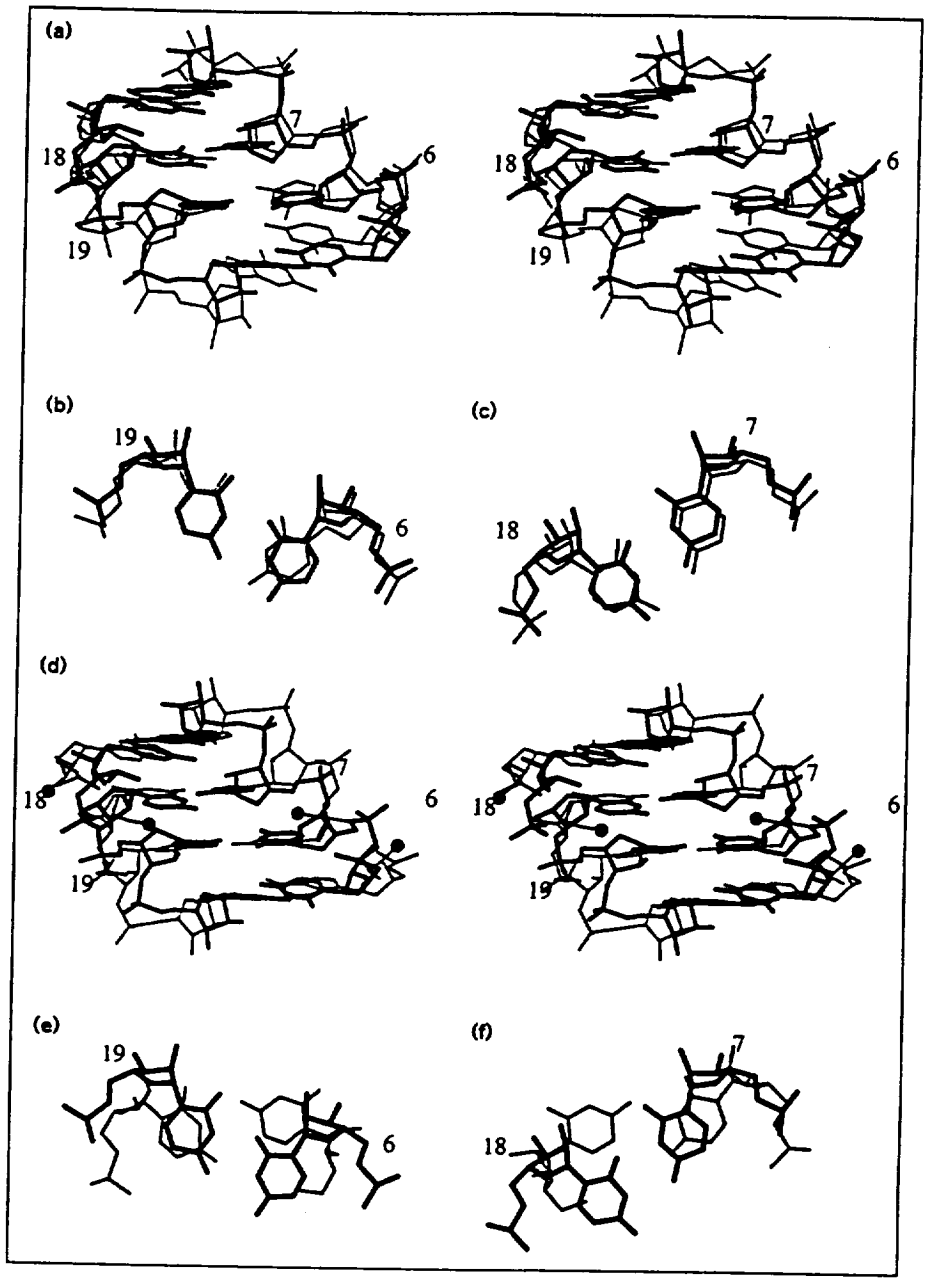

Comparisons to other tandem U–U base pairs. **(a)** Stereo view of residues 5–8 and 17–20 of the GUUU structure (gray) superimposed upon CUUG (black). The bases of residues 6,7,18 and 19 were used for the superposition (rmsd = 0.63 Å). **(b)** The base pair between residues 6–19 in GUUU (gray) and CUUG (black) superimposed as in (a). The view is down the helical axis. **(c)** The base pair between residues 7–18 in GUUU (gray) and CUUG (black) from the same viewpoint as (b). **(d)** Stereo view of residues from the UUCGCG hexamer structure (gray) superimposed upon CUUG (black). Four symmetry related strands from the hexamer structure are shown. The correspondence between hexamer residues (strands A, B, C and D) and CUUG residues is: A1–A3=6–8; B6=5; C1–C3=18–20; D6=17. The backbone of the hexamer structure corresponding to CUUG residues 5–8 and 17–20 were used for the superposition (rmsd = 2.80 Å). The O5′ and O3′ termini of the hexamer strands are shown as gray spheres. **(e)** The base pair corresponding to residues 6–19 in the UUCGCG hexamer (gray) and CUUG (black) superimposed as in (d). The view is down the helical axis. **(f)** The base pair corresponding to residues 7–18 in the UUCGCG hexamer (gray) and CUUG (black) from the same viewpoint as (e).

and $U2^c$ O4 (Fig. 7e,f) by retaining the anticonformation and using the Watson–Crick face of $U2^c$ and the Hoogsteen face of $U1^a$. The Hoogsteen face of $U1^a$ is presented by changes in the backbone torsion angles β, ϵ, and ζ that rotate the base about 55 Å towards the minor groove. This rotation, along with a ≈1 Å translation, would not be compatible with a continuous duplex (note positions of O5′ and O3′ termini in Fig. 7d). Thus, this *trans* U–U base pair is apparently stable when located at the terminus of a duplex but would require large deformations if it were located within a continuous duplex.

Biological implications

The diversity of functions executed by RNA and the complexity of its secondary structure indicate that we are only just beginning to understand the principles of RNA structure and how they relate to biological functions. Much work lies ahead as we determine the three dimensional structure of RNAs from diverse systems and connect their functional properties to the underlying structure. One task is to understand how RNA molecules utilize non-canonical base pairing to modify the structure and stability of duplex regions. The structure of

the dodecamer GGCGCUUGCGUC (CUUG) shows how a duplex region of RNA can adopt a structure that is significantly different than A-form RNA and how tandem U–U base pairs can be stable.

There are two types of deviation from A-form RNA in CUUG. The first type is caused by the presence of tandem U–U base pairs. Each U–U base pair makes two direct hydrogen bonds and the helix structure must be perturbed in order to form these base pairs. The major and minor groove widths decrease because of the U–U base pairs. Part of the deformation is localized to the base step between the U–U base pairs and part requires a 7–16° rotation of one of the adjacent helical stems. The second type of deviation seen is a smaller rise per base pair. This does not seem, however, to be caused by the tandem U–U base pairs. In CUUG, the overall effect of the smaller rise and the deformations caused by the tandem U–U base pairs is to create a helix which is as long as 11 nucleotide A-form RNA with a helical pitch corresponding to approximately 11.5 base pairs of A-form RNA. Comparison of the CUUG structure to the previously determined structure of UUUG shows that the structure of the tandem U–U base pairs depends on the flanking sequence, environment, or both. However, in both cases the tandem U–U base pairs deviate significantly from A-form RNA.

Thus, tandem U–U base pairs may be used in large RNA structures to form structures that would not be possible with A-form RNA. In contrast to canonical base pairs, U–U base pairs present only hydrogen bond acceptors, O4 and O2 atoms, in the major and minor grooves, respectively. Tandem U–U base pairs, therefore, exhibit a unique pattern of hydrogen-bond donors and acceptors in the major and minor grooves that could act as a recognition site. Tandem U–U base pairs could also be recognized by the decrease in the width of the major and minor grooves. Finally, tandem U–U base pairs may be used to tune the structure of large RNAs as they can alter the course of the helix axis by 11–12°.

Materials and methods

RNA synthesis and purification

Dodecamer RNA was prepared by transcription with T7 RNA polymerase from a single-stranded DNA template containing a 17 base pair double stranded promoter region for the polymerase [30]. Optimum transcription yields from a 10 ml reaction were obtained with 40 mM Tris-HCl pH 8.0, 50 mM magnesium acetate, 1 mM spermidine, 10 mM dithiothreitol, 6.4 mM CTP, 4.8 mM UTP, 8.0 mM GTP, 5.0 mM GMP, 0.05% Tween-20, 1 μM template DNA, and 0.04 mg ml^{-1} T7 RNA polymerase. All components except the polymerase were preincubated at 37°C for 15 min. The polymerase was added and the transcription reaction was incubated at 37°C for 4h at which time the polymerase concentration was doubled to 0.08 mg ml^{-1}. Transcription was allowed to continue at 37°C for a further 4h and was then quenched by adding 1 ml of 0.5 M EDTA pH 8.0, followed by 1 ml 3.0 M NaOAc pH 5.5 and 25 ml ethanol. The transcription product was precipitated overnight at −20°C. The mixture was centrifuged at 17,000 g for 1h and the pellet dissolved in a minimal amount of deionized distilled H_2O, typically 2–3 ml.

Purification of the dodecamer RNA proceeded through a four step process: size exclusion chromatography, phosphatase digestion, denaturing polyacrylamide gel electrophoresis (PAGE), and anion exchange high pressure liquid chromatography (HPLC). The RNA sample was applied to a 22 ml P-4 Biogel size exclusion column equilibrated with 50 mM Tris-HCl pH 8.5, 0.1 mM EDTA; 2.5 ml fractions were collected and the RNA concentration determined from the absorbance at 260 nm. Two peaks eluted from the column; the first contained the desired product and long transcription 'aborts'. The second peak contained short RNA aborts, nucleotides and salts.

The RNA was treated with calf intestinal alkaline phosphatase (CIAP) to generate molecules with 5′ hydroxyl termini. The transcription reaction produced molecules with 5′ triphosphate or 5′ monophosphate termini depending on whether GTP or GMP was incorporated as the first nucleotide. Fractions from the size exclusion column were pooled and 1 μl CIAP (1 unit μl^{-1}) was added per 50 nanomoles of RNA 5′ termini. The reaction was incubated at 37°C for 1h and stopped by the addition of 1/10th volume 0.5 M EDTA pH 8.0 and heating at 65°C for 10 min.

The RNA was then purified by 20% denaturing PAGE. Plates with dimensions of 42 cm×37 cm and 45 cm×37 cm were used with 0.3 cm spacers; these dimensions make a gel with a volume of about 500 ml. The gels were pre-electrophoresed at 45 W for 6h. The RNA was then electrophoresed at 45–50 W for 8–10 h at 45°C as measured with a liquid crystal strip thermometer attached to the glass plate (Bio-Rad Laboratories). Four separate gels were run for a typical 10 ml transcription reaction. The full length transcription product was visualized by UV shadowing and the product band (approximately 15 ml) was excised with a sterile razor blade. The gel pieces were frozen at −20°C for 1h, then crushed with an autoclaved mortar and pestle. The RNA was eluted from the gel with 30 ml of 10 mM Tris-HCl pH 7.5, 1 mM EDTA, and 500 mM NaCl, per 15 ml crushed gel, and shaking overnight (6–12h) at 4°C. The eluted RNA was recovered by removing particulate acrylamide with a sterile Nalgene disposable 0.2 μm filter unit, and then precipitating with sodium acetate and ethanol as described above. The pellet was redissolved in a minimal amount of water, typically 1 ml.

The final purification step used anion exchange HPLC with a Dionex column (Nucleopac TM PA-100, 22×250 mm). The column heater was set at 90°C to denature secondary structure. The gradient ranged from 160–800 mM NH_4Cl in 25 mM Tris-HCl pH 8.0 and 0.5% acetonitrile with a flow rate of 1.5 ml min^{-1}. This protocol has been optimized for 400 μg dodecamer RNA per run. Dodecamer RNA eluted at about 450 mM NH_4Cl. The RNA was then desalted and concentrated with successive sterile water washes in Centricon-3™ units (Amicon). One 10 ml transcription reaction typically yielded 1.2 mg of 96–99% pure dodecamer.

CUUG with a bromo-uridine at position 11 was synthesized on an Applied Biosystems Model 394 DNA synthesizer using phosphoramidite chemistry [31] and commercially available phosphoramidites (Glen Research). The PAGE and HPLC procedures used for purifying unmodified CUUG were used to purify the derivative. The derivative was kept in the dark during deprotection, gel electrophoresis, and storage to minimize light induced debromination.

Crystallization

The RNA was re-annealed prior to crystallization. A solution of 1.25 mg ml^{-1} RNA and 10 mM $MgCl_2$ was heated at 65°C for 5 min in a dri-block. The dri-block was removed from the heating element and allowed to cool to room temperature over ≈30 minutes.

The dodecamer RNA was crystallized by vapor diffusion with either hanging drop (Linbro™ plates and silanized glass cover slips) or sitting drop (Cryschem) set-ups. The initial drop contained 0.63 mg ml^{-1} RNA, 12.5 mM $MgCl_2$, 25 mM sodium cacodylate (Sigma) pH 7.0, 2.5% or

5% 2-methyl-2,4-pentanediol (MPD) (Aldrich), and 100–300 mM ammonium acetate (Mallinkrodt). The reservoir solution consisted of 5 or 10% MPD, 50 mM sodium cacodylate pH 7.0 and 15 mM $MgCl_2$. The trays were set-up at room temperature and then incubated at 37°C. Crystals grew in three to seven days and were typically 250×150×100 μm in size.

Crystals of the derivative dodecamer were set-up using the same conditions as the native dodecamer. When crystals were not observed after two weeks, additional RNA (1.9 μg) was added to the drops to obtain crystals. Crystals with the same morphology as the native then grew within one week. Both native and derivative crystals belonged to space group P1 with unit cell dimensions a=29.4 Å, b=28.9 A, c=46.5 Å, α=98.9°, β=72.9°, and γ=96.1°.

Cryocooling

Crystals used for the structure determination were stabilized in three steps. The first step was to equilibrate the crystals to room temperature by placing the 37°C crystallization trays in a Styrofoam box and transferring the box to room temperature. After an overnight equilibration to room temperature, the crystals were soaked in 20% glycerol stabilizer for 15 min to 1 h. In the final step, the crystals were soaked in 30% glycerol stabilizer for 5–30 min. All stabilizer solutions also contained 10% MPD, 50 mM sodium cacodylate pH 7.0, and 25 mM $MgCl_2$. The crystals were mounted directly from the 30% glycerol stabilizer with an ethilon™ loop attached to a magnetic base [32]. The crystal was immediately plunged into freshly thawed liquid propane.

Data collection

X-ray data were collected with a Siemens X100 area detector and a Rigaku RU-200BH rotating-anode X-ray generator with a Huber graphite monochromator operated at 50 kV and 50 mA. During data collection the crystals were maintained at 100K in a stream of liquid nitrogen from an Oxford Cryostream Cooler. Both native and derivative crystals were twinned. The X-ray data were reduced with a set of programs developed in the lab for processing data from twinned crystals [33] and XDS [34]. X-ray data from each of the two lattices in the twinned crystals were processed individually and then merged with XSCALE [34]. Data collection statistics for the native and derivative data sets are summarized in Table 3.

Structure determination

Molecular replacement calculations were carried out with the AMoRe program [35]. The unit cell volume suggested that there were two copies of the dodecamer duplex in the unit cell. Two search models were used: a canonical A-form model with a similar sequence to the dodecamer, generated with InsightII (Biosym Inc., San Diego, CA); and later a dodecamer containing the *Escherichia coli* Shine-Dalgarno sequence [27] with the sequence changed to that of the dodecamer. A molecular replacement solution was found only with the second search model. The second search model was chosen because it had a lower rise (2.64 Å /residue) than the A-form model and the unit cell edges suggested that the CUUG dodecamer helix would have a lower rise than canonical A-form.

Six molecular replacement trials with the second search model were run at different resolution ranges: 15–6, 10–4, 10–6, 15–10, 15–4, and 15–5 Å. Once a rotation search was run, all combinations of the top 50 solutions were input pairwise into a translation search. One rotation solution was fixed and a translation search was run on the second rotation solution. Finally, the top 50 translation search solutions in each resolution trial were subjected to a round of rigid-body minimization. Even after rigid-body minimization, the top solution in each trial did not stand out distinctly from the other solutions. The top solution from each resolution trial was examined with InsightII and its packing examined. In all but one of the molecular replacement solutions (the 15–10 Å solution), the two copies of the dodecamer duplex were oriented at approximately a 90° angle to each other. Because the crystals belonged to space group P_1, the origin of the first helix in each solution had been determined arbitrarily and none of the solutions superimposed upon each other. Five solutions had reasonable packing and coaxial stacking of the helices; only the 15–10 Å solution had unreasonable packing. $2F_o-F_c$ electron-density maps of the two solutions with the best R factors were calculated and examined with O [36]. The 15–4 Å solution model was selected for further refinement.

After one round of simulated annealing refinement in X-PLOR [17], the molecular replacement solution had an R factor of 30.3% and R free of 45.2%. In addition to the high R factors, examination of the $2F_o-F_c$ electron-density map also suggested that something was wrong with the model. The dodecamer has 5′ hydroxyl termini, but density for 13 consecutive phosphates was observed in the map, and one of the helices looked out of density at the junction between symmetry mates. This indicated that one or both of the helices was out of register. In an attempt to find the correct register, each helix was individually advanced one base pair at a time, and refined with simulated annealing. No significant improvements in R factor were observed for any of the shifted models.

In order to determine the correct register of the two helices, data from a dodecamer with 5-bromo-uridine at position 11 was collected. R_{cross} between the bromine derivative and the native data set was 8.2%. A difference Fourier (F_{Br}-F_{nat} coefficients and model phases) was calculated and the difference map was examined. The position of the top four difference peaks, at 4–7σ, clearly indicated the positions of the bromines and the correct position of the duplexes. Helix I was out of register by one base pair and helix II by two base pairs. After refinement of the corrected model, the difference Fourier was recalculated and the top difference peaks were at 11–14σ.

Structure refinement

The corrected model was refined with X-PLOR by rigid-body minimization, conjugate gradient minimization, simulated annealing, and individual isotropic temperature factor refinement. The RNA-DNA topology and parameter set (from H Berman's group) was used during refinement [37]. After one cycle of refinement, the R factor had dropped to 23.6% and R_{free} to 33.3%. New electron-density maps were calculated and examined; no rebuilding of the corrected model was required. Additional rounds of refinement consisted of the addition of solvent sites, followed by conjugate gradient minimization and B factor refinement. Solvent molecules were assigned to sites with F_o-F_c difference peaks greater than 3σ and which formed a potential hydrogen bond with the RNA or solvent. During refinement, solvent sites were treated as oxygen atoms with an occupancy of one. A bulk solvent correction was applied after the first cycle of solvent addition. The final model contains two copies of the dodecamer duplex and 158 solvent sites in the unit cell. The R factor is 19.1% and R_{free} is 24.0% for data greater than 2σ in the 8.0–2.4 Å resolution shell (Table 4).

Table 3

Data collection statistics.

	Crystal 1	Crystal 2	Merged native	Br-derivative
No. of reflections	17370	9227	26632	3687
No. of unique observations	5187	4811	5429	3192
R_{merge}* (%)	7.1	5.0	7.6	–
R_{sym}† (%)	–	–	–	2.7
R_{cross}‡ (%)	–	–	–	8.2
Completeness (%)	91.2	84.6	95.4	85.5
$\langle I/\sigma \rangle$	38.5	22.4	44.6	9.3
Resolution (Å)	2.4	2.4	2.4	2.8

$R=[\Sigma_h\Sigma_i|(I_{hi}-\langle I_h\rangle)|/\Sigma_h\Sigma_i I_{hi}]$. * Data from two lattices; †data from one lattice; ‡a comparison between the derivative and the native data.

Table 4

Refinement statistics.

Resolution (Å)	8.0–2.4
No. of reflections $> 2\sigma$	5142
No. of non-hydrogen RNA atoms	1008
No. of solvent molecules	158
R factor (%)	19.1
R_{free} (%)	24.0
Rms deviations from ideality	
bond length (Å)	0.01
bond angle (°)	1.26
dihedral angle (°)	8.0
improper angle (°)	1.50

Accession number

The atomic coordinates have been deposited in the Nucleic Acid Database (http://ndbserver.rutgers.edu:80/).

Acknowledgements

This work was funded by the Colorado RNA Center, WM Keck Foundation, National Science Foundation (MCB-9221307) and the Whitaker Foundation. Thanks to Jennifer Doudna for transcription and purification advice, Steve Schultz and Jodi Ryter for CIAP and HPLC advice, to Jamie Cate and Andreas Löw for T7 RNA polymerase and Vasili Carperos for help in data collection. Thanks also to Art Pardi for encouragement and helpful discussions.

References

1. Saenger W. (1984). Principles of Nucleic Acid Structure. Springer Advanced Texts in Chemistry, ed. C.R. Cantor. Chapter 6- Forces Stabilizing associations between bases: Hydrogen bonding and base stacking, pp. 116–158. Springer-Verlag, NY, USA.
2. Holbrook S.R., Cheong, C., Tinoco, I.J. & Kim, S.H. (1991). Crystal structure of an RNA double helix incorporating a track of non-Watson–Crick base pairs. *Nature* **353**, 579–581.
3. Gutell, R.R. (1996). Comparative sequence analysis and the structure of 16S and 23S rRNA. In *Ribosomal RNA: Structure, Evolution, Processing, and Function in Protein Biosynthesis*. (Zimmerman, R.A. and Dahlberg, A.E., eds), pp. 109–128, CRC Press, NY, USA.
4. LeCuyer, K.A. & Crothers, D.M. (1994) Kinetics of an RNA conformational switch. *Proc. Natl. Acad. Sci. USA* **91**, 3373–3377.
5. Wu, M., McDowell, J.A. & Turner, D.H. (1995). A periodic table of symmetric tandem mismatches in RNA. *Biochemistry* **34**, 3204–3211.
6. Peritz, A.E., Kierzek, R., Sugimoto, N. & Turner, D.H. (1991). Thermodynamic study of internal loops in oligoribonucleotides: symmetric loops are more stable than asymmetric loops. *Biochemistry* **30**, 6428–6436.
7. SantaLucia, J.J., Kierzek, R. & Turner, D.H. (1991). Stabilities of consecutive A·C, C·C, G·G, U·C, and U·U mismatches in RNA internal loops: evidence for stable hydrogen-bonded U·U and C·C+ pairs. *Biochemistry* **30**, 8242–8251.
8. He, L., Kierzek, R., SantaLucia, J.J., Walter, A.E. & Turner, D.H. (1991). Nearest-neighbor parameters for G.U mismatches: 5'GU3'/5'GU3' is destabilizing in the contexts 5'CGUG3'/5'CGUG3', 5'UGUA3'/5'UGUA3', and 5'AGUU3'/5'AGUU3' but stabilizing in 5'GGUC3'/5'GGUC3'. *Biochemistry* **30**, 11124–11132.
9. Gutell, R.R., Gray, M.W. & Schnare, M.N. (1993). A compilation of large subunit (23S and 23S-like) ribosomal RNA structures. *Nucleic Acids Res.* **21**, 3055–3074.
10. Gutell, R.R. (1994). Collection of small subunit (16S- and 16S-like) ribosomal RNA structures. *Nucleic Acids Res.* **22**, 3502–3507.
11. Cech, T.R., Damberger, S.H. & Gutell, R.R. (1994). Representation of the secondary and tertiary structure of group I introns. *Nat. Struct. Biol.* **1**, 273–280.
12. Alkema, D., Hader, P.A., Bell, R.A. & Neilson, T. (1982). Effects of flanking G·C base pairs on internal Watson-Crick, G·U, and nonbonded base pairs within a short ribonucleic acid duplex. *Biochemistry* **21**, 2109–2117.
13. Nikonowicz, E.P. & Pardi, A. (1992). Three-dimensional heteronuclear NMR studies of RNA. *Nature* **355**, 184–186.
14. Baeyens, K.J., De Bondt, H.L. & Holbrook, S.R. (1995). Structure of an RNA double helix including uracil–uracil base pairs in an internal loop. *Nat. Struct. Biol.* **2**, 56–62.
15. Woese, C.R., Winker, S. & Gutell, R.R. (1990). Architecture of ribosomal RNA: constraints on the sequence of 'tetra- loops'. *Proc. Natl. Acad. Sci. USA* **87**, 8467–8471.
16. Jucker, F.M. & Pardi, A. (1995). Solution structure of the CUUG hairpin loop: a novel RNA tetraloop motif. *Biochemistry* **34**, 14416–14427.
17. Brünger, A.T. (1993). X-PLOR Manual, Version 3.1. Yale University, New Haven, CT.
18. Dock-Bregeon, A.C., *et al.*, & Johnson, J.E. (1988). High resolution structure of the RNA duplex [U(U-A)6A]2. *Nature* **335** 375–378.
19. Leonard, G.A., McAuley, H.K., Ebel, S., Lough, D.M., Brown, T. & Hunter, W.N. (1994). Crystal and molecular structure of r(CGCGAAUUAGCG): an RNA duplex containing two G(anti).A(anti) base pairs. *Structure* **2**, 483–494.
20. Jack, A., Klug, A. & Ladner, J.E. (1976). 'Non-rigid' nucleotides in tRNA: a new correlation in the conformation of a ribose. *Nature* **261**, 250–251.
21. Arnott, S., Hukins, D.W.L., Dover, S.D., Fuller, W. & Hodgson, A.R. (1973). Structures of synthetic polynucleotides in the A-RNA and A'-RNA conformations: X-ray diffraction studies of the molecular conformations of polyadenylic acid polyuridylic acid and polyinosinic acid polycytilylic acid. *J. Mol. Biol.* **184**, 119–145.
22. Nishikawa, K. & Ooi, T. (1974). Comparison of homologous tertiary structures of proteins. *J. Theor. Biol.* **43**, 351–374.
23. Richards, F.M. & Kundrot, C.E. (1988). Identification of structural Motifs from protein coordinate data: secondary structure and first-level supersecondary structure. *Proteins* **3**, 71–84.
24. Cruse, W.B., Saludjian, P., Biala, E., Strazewski, P., Prange, T. & Kennard, O. (1994). Structure of a mispaired RNA double helix at 1.6-Å resolution and implications for the prediction of RNA secondary structure. *Proc. Natl. Acad. Sci. USA* **91**, 4160–4164.
25. Dock-Bregeon, A.C., *et al.*, & Moras, D.(1989). Crystallographic structure of an RNA helix: $[U(UA)_6A]_2$. *J. Mol. Biol.* **209**, 459–474.
26. Betzel, C., *et al.*, & Erdmann, V.A. (1994). Crystal structure of domain A of *Thermus flavus* 5S rRNA and the contribution of water molecules to its structure. *FEBS Lett.* **351**, 159–164.
27. Schindelin, H., Zhang, M., Bald, R., Fürste, J.-P., Erdmann, V.A. & Heinemann, U. (1995). Crystal structure of an RNA dodecamer containing the *Escherichia coli* Shine-Dalgarno sequence. *J. Mol. Biol.* **249**, 595–603.
28. Draper, D.E. (1990). Pseudoknots and the control of protein synthesis. *Curr. Opin. Cell Biol.* **2**, 1099–1103.
29. Wahl, M.C., Rao, S.T. & Sundaralingam, M. (1996). The structure of r(UUCGCG) has a 5'-UU-overhang exhibiting Hoogsteen-like *trans* U·U base pairs. *Nat. Struct. Biol.* **3**, 24–31.
30. Milligan, J.F., Groebe, D.R., Witherell, G.W. & Uhlenbeck, O.C. (1987). Oligoribonucleotide synthesis using T7 RNA polymerase and synthetic DNA templates. *Nucleic Acids Res.* **15**, 8783–8798.
31. Ogilvie, K.K., Usman, N., Nicoghosian, K. & Cedergren, R.J. (1988). Total chemical synthesis of a 77-nucleotide-long RNA sequence having methionine-acceptance activity. *Proc. Natl. Acad. Sci. USA* **85**, 5764–5768.
32. Rodgers, D.W. (1994). Cryocrystallography. *Structure* **2**, 1135–1140.
33. Lietzke, S.E., Carperos, V.E. & Kundrot, C.E. (1996). Data reduction from twinned RNA crystals. *Acta. Cryst. D* **52**, in press.
34. Kabsch, W. (1988). Evaluation of single-crystal X-Ray diffraction data from a position-sensitive detector. *J. Appl. Cryst.* **21**, 916–924.
35. Navaza, J. (1994). AMoRe: an automated package for molecular replacement. *Acta. Cryst. A* **50**, 157–163.
36. Jones, T.A. & Kjeldgaard, M. (1993). O- the manual. Uppsala University, Sweden.
37. Parkinson, G., Vojtechovsky, J., Clowney, L., Brünger, A.T. & Berman, H.M. (1996). New parameters for the refinement of nucleic acid-containing structures. *Acta. Cryst. D* **52**, 57–64.
38. Kraulis, P.J. (1991). MOLSCRIPT: a program to produce both detailed and schematic plots of protein structures. *J. Appl. Cryst.* **24**, 946–950.

Chapter 9

Introduction to the Interplay between Solution Thermodynamics and Crystal Nucleation and Growth Kinetics

Stephen P. Cape and Paul Todd

Chapter 10

Chromatographic Purification of Closely Related Oligonucleotides: Comparison with Electrophoresis

Stephen P. Cape, C.-Y. Lee and Paul Todd

1997

CHROMATOGRAPHIC PURIFICATION OF CLOSELY RELATED OLIGONUCLEOTIDES: COMPARISON WITH ELECTROPHORESIS

Stephen P. Cape, Ching-Yuan Lee, and Paul Todd

Department of Chemical Engineering
University of Colorado, Boulder
Boulder, CO 80309-0424

ABSTRACT

The purification of nucleic acids on the basis of molecular weight is usually accomplished by gel electrophoresis, which is not readily scaled to industrial production levels or to levels required for structural and clinical studies. A higher loading capacity is possible in chromatography than in gel electrophoresis. Therefore, a direct comparison was made between chromatography and gel electrophoresis for the separation of closely related oligonucleotide species, in this case a 5'-hydroxylated and a 5'-phosphorylated RNA dodecamer synthesized by transcription and modified (or not) by 5'-dephosphorylation using calf intestine alkaline phosphatase. The two methods were compared on the basis of resolution (calculated in the standard way), speed (time required to collect pure material from a starting reaction mixture), and capacity (mass that can be processed in a scaled unit operation). Under conditions studied to date, the two species can be separated with higher resolution and higher speed by chromatography. Under native conditions (low column temperatures, e.g. $\leq$ 30°C), mixtures of the two forms of dodecamer give chromatographic peaks which are not fully resolved and which may contain heterogeneity. Under denaturing conditions (high column temperatures, e.g. 80°C), unphosphorylated and phosphorylated dodecamer can be separated from each other with good peak resolution.

INTRODUCTION

Gel electrophoresis is often the method of choice for laboratory-scale purifications of oligonucleotides. However, with the development of oligonucleotides for therapeutic use, the need for a robust, high-resolution, large-scale purification technique becomes obvious, since gel electrophoresis does not lend itself to scale-up. Chromatography has become established as the purification workhorse in therapeutic protein production and appears to also hold promise for oligonucleotide purification. Warren and Vella (1994) described the analysis and purification of synthetic oligonucleotides by HPLC and showed that *n* versus *n*-1 resolution can be achieved with anion-exchange chromatography.

A preparative-scale gel electrophoresis technique capable of purifying milligram quantities of RNA produced by *in vitro* transcription (Cunningham et al., 1996) has been developed by BioRad (Model 491 Prep Cell, CA). This method separates the oligonucleotide mixture (up to about 6 mg in a single run) on a cylindrical gel and elutes the product bands, which are detected by a UV-vis detector, using a peristaltic pump. A single gel preparation was used consecutively up to three times. While this technique appears to be somewhat promising for milligram-scale purifications it does not lend itself to gram-scale purifications and resolution between *n* versus *n*-1 or *n*+1 transcripts was not achieved.

The usefulness of chromatography for separating closely related oligonucleotide species that have very subtle sequence or conformational differences has not been extensively studied. Delort et al. (1984) used reversed-phase HPLC to separate oligonucleotides up to 19 nucleotides in length that differed only in the type of end-group at the 5' terminus, that is, they were 5'-hydroxylated or 5'-phosphorylated, but otherwise the same in nucleotide sequence. Reversed-phase HPLC has also recently been used to detect secondary structure differences (B- versus B'-conformation of double strands) in sequence isomeric self-complementary oligonucleotides (Potaman et al., 1993).

Several reasons can be cited for preferring ion-exchange chromatography to reversed-phase chromatography (RPC). RPC typically requires large quantities of hazardous solvents such as methanol and acetonitrile. Larger oligonucleotides often require chromatography to be carried out under strong denaturing conditions, such as occur in heated columns. High temperature chromatography is commonly used with ion-exchange columns, but not with reversed-phase columns where the solvents used are often volatile. In addition, traces of the organic solvents used in RPC can hamper the crystallization of the purified molecule (Giegé et al., 1986) and approval for pharmaceutical application. The focus of this research was therefore to apply strong anion-exchange chromatography to the separation of very closely related RNA oligonucleotide species.

Yamamoto et al. (1987) derived a useful equation for the constant-resolution scale-up of protein chromatography in linear gradient elution ion-exchange and hydrophobic interaction chromatography. This resolution relationship was tested experimentally and found to be "valid except for very short columns with a shallow slope of the gradient and for low flow-rates" (Yamamoto et al., 1987). Yamamoto et al. (1990) also reported a method for determining stepwise elution conditions from data obtained from linear gradient elution experiments. A method for predicting the zone-sharpening effect in linear gradient and stepwise elution chromatography of proteins was also reported (Yamamoto et al., 1993). These strategies were applied to the separation of a 5'-phosphorylated RNA dodecamer from its 5'-hydroxylated counterpart with resolution equal to or better than that provided by gel electrophoresis.

MATERIALS AND METHODS

UU-dodecamer (12mer) RNA

A 12mer RNA ("UU-dodecamer") with the following primary sequence was used as the model oligonucleotide:

5'-GGCGCUUGCGUC-3'

It was synthesized by *in vitro* transcription using the immobilized DNA template method developed by Marble and Davis (1995) and purified by gel electrophoresis. Final UU-dodecamer purity was typically about 90%. The 5'-phosphorylated transcription product was converted, if desired, to the 5'-hydroxylated form by CIP (calf-intestine alkaline phosphatase, Boehringer Mannheim, Indianapolis, IN, Cat. # 713 023) digestion prior to gel electrophoresis. Throughout this paper, the terms "CIP 12mer" and "unCIP 12mer" will be used, respectively, for UU-dodecamer transcription samples that were CIP digested, and therefore primarily 5'-hydroxylated, and those that were <u>not</u>, and therefore primarily 5'-phosphorylated. Depending on the ionic strength of the surrounding solution, the UU-

dodecamer, which is self-complementary, can occur either in a hairpin (low salt) or a duplex (high salt) structure at temperatures below its melting point (Jucker, 1995).

Gel electrophoresis of UU-dodecamer

Denaturing polyacrylamide (T = 20%, C = ??%) gel electrophoresis separations were conducted using Sigma (St. Louis, MO) Techware equipment and BIO-RAD power supplies (3000Xi or PowerPac 3000). Gels were electrophoresed at constant current between 10 and 15 mAmps. Analytical gel dimensions were 26 × 14 × 0.8 cm and preparative gels were 26 × 14 × 1.5 cm. RNA bands were visualized using Stains-All (Sigma), and permanent records of the gels were made using a Personal Densitometer™ and ImageQuant™ software (Molecular Dynamics, Inc., Sunnyvale, CA) to scan the gels and process the image data.

Resolution between bands in a gel was calculated from the line graph of the area integration of a given gel lane. The following classical definition of resolution was used for both gel electrophoresis and chromatographic separations:

$$R = \frac{Separation\ between\ adjacent\ peaks}{\frac{1}{2}\cdot(Sum\ of\ \ peak\ widths)} = \frac{P_2 - P_1}{\frac{1}{2}\cdot(W_1 + W_2)}$$

FPLC of UU-dodecamer

FPLC (Fast Protein Liquid Chromatography) experiments were conducted using a Pharmacia FPLC system, consisting of a GP-250 Plus Programmer module, a UV-MII monitor and detector module, two P-500 pump modules, a solvent mixer, a V-7 valve, a Frac-200 fraction collector, and an XK 26/40 (26 mm × variable length up to 400 mm) column. The column was packed with 50 mL of Pharmacia SOURCE™ 15Q, a strong anion-exchange media. The voltage signal output from the UV-MII monitor was collected using a Houston Instrument OmniScribe Series D5000 Recorder or a Nova computer with a data acquisition board. Column heating was achieved by flowing heated water from a recirculating water bath through the thermostatic jacket of the XK 26/40 column, which was insulated using glass fiber pipe insulation. The FPLC system, including the column but not the recirculating water bath or data collection units, was located in a sliding-glass door refrigerator. Specific operating conditions are given with the related results discussed below.

HPLC of UU-dodecamer

HPLC (High Performance Liquid Chromatography) experiments were conducted using a Waters Chromatography HPLC system. A NucleoPac™ PA-100 column (4 × 250 mm) was used with the Waters system, consisting of a 600S Controller, 486 Tunable Absorbance Detector, 626 Pump, and 717plus Autosampler, all controlled by Waters software using an NEC computer. Column heating with the Waters system was achieved using the column heater built into the 626 Pump unit. Specific operating conditions are given with each set of experimental results discussed below.

RESULTS AND DISCUSSION

Gel electrophoresis of CIP 12mer and unCIP 12mer mixtures

Figure 1 shows the line graph of the area integration of the boxed gel lane shown in the insert. The insert shows the portion of an analytical gel slab containing UU-dodecamer bands. The first six lanes from the left are of various time points during an enzymatic digestion using CIP to convert gel-purified 5'-phosphorylated UU-dodecamer to its 5'-hydroxylated form. The last lane on the right is of a mixture of gel-purified CIP and unCIP 12mer samples. Good separation between the two UU-dodecamer species was achieved as can be observed qualitatively, as well as quantitatively by the resolution value of 1.2. This value for resolution was used as the standard of comparison for other purification techniques (see below).

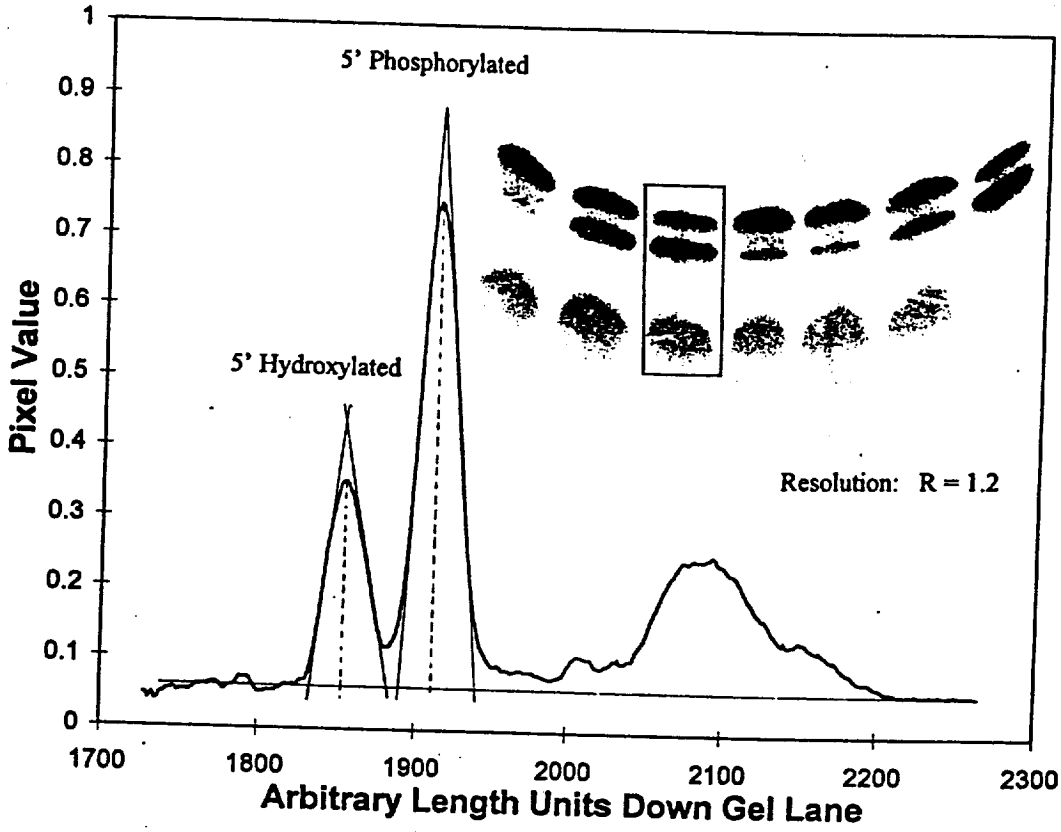

Figure 1: Line graph of the area integration of the of the boxed gel lane shown in the insert. The gel scan is of mixtures of 5'-hydroxylated UU-dodecamer and 5'-phosphorylated UU-dodecamer separated on an analytical denaturing 20% polyacrylamide gel. Tangent lines and vertical lines at the peak maxima were drawn in for determination of peak widths and distance between peak maxima (used in the resolution calculations).

FPLC of CIP 12mer and unCIP 12mer mixtures

Figures 2 and 3 show the results of low (~15°C) and high (70°C) temperature FPLC separations of equal-mass mixtures of gel-purified samples of CIP 12mer and unCIP 12mer using the operating conditions described above and given in the figure captions. At low temperature, it appears that the four labeled peaks correspond to the different UU-dodecamer species (5'-hydroxylated and 5'-phosphorylated) since at high temperature these collapse into a single, sharp peak. Peak 1 in Figure 2 appears to correspond to UU-dodecamer species in a hairpin structure, and peaks 2 through 4, to homogeneous and heterogeneous dimers of the two species.

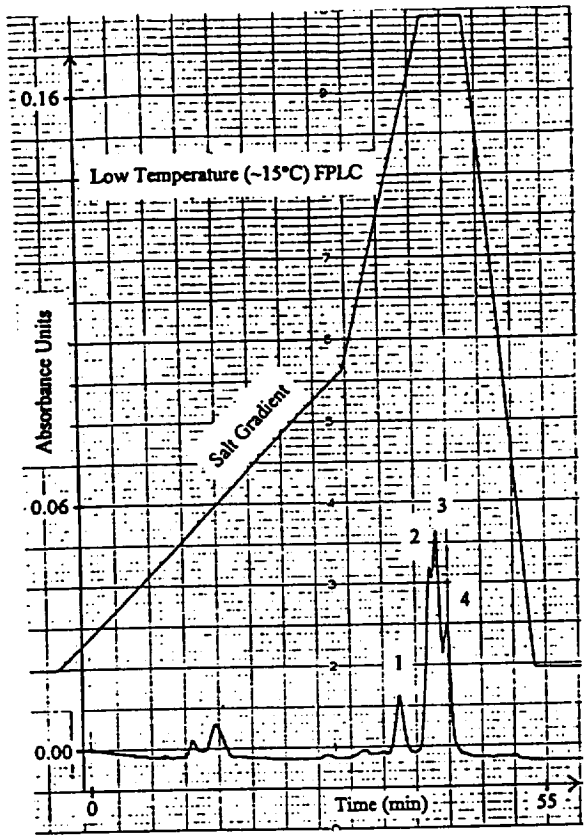

Figure 2: Low temperature (~15°C) FPLC chromatogram of an equal-mass mixture of CIP 12mer and unCIP 12mer. Flow rate = 4.7 mL/min. Buffers: A = 25 mM Tris, pH 8.0; B = A + 0.8 M ammonium chloride, pH 8.0

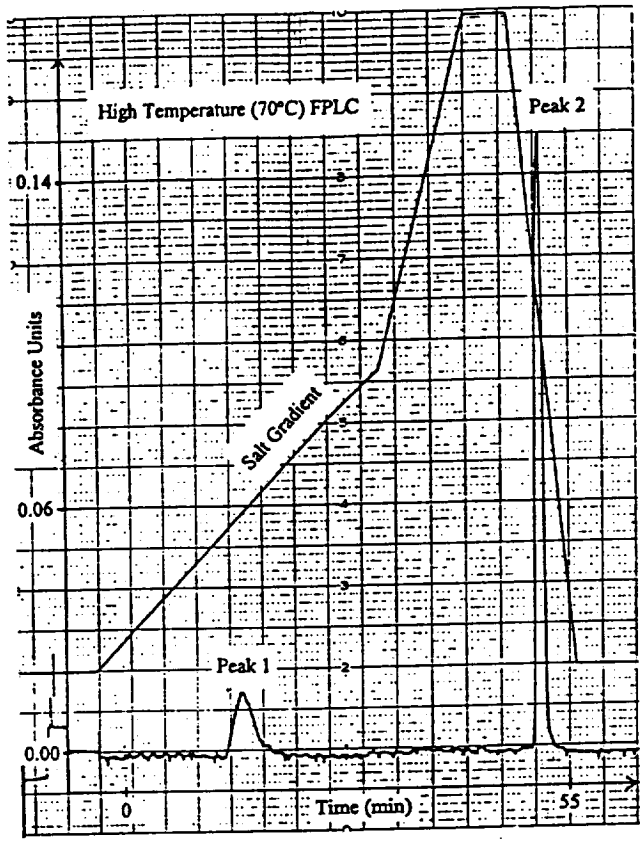

Figure 3: High temperature (70°C) FPLC chromatogram of an equal-mass mixture of CIP 12mer and unCIP 12mer. Same flow rate and buffers as in Figure 2.

Attempts were made to resolve the various peaks at low temperature, in order to collect and analyze them. This proved to be very challenging. Many separations were conducted at various gradient slopes. Based on tests of several simple linear elution gradients, more complex elution schemes were developed which combined intervals of isocratic and gradient elution. The best resolution achieved is represented in Figure 4. The combination of gradients used is represented on the chart. The computed resolutions between adjacent peaks are also given on the chart. Room-temperature FPLC did not yield resolution comparable to denaturing gel electrophoresis and may have resulted in losses due to heterodimer formation.

HPLC of CIP 12mer and unCIP 12mer mixtures

The investigation into separating the closely related UU-dodecamer species, especially under denaturing conditions, was continued using a Waters Chromatography HPLC system and a NucleoPac™ PA-100 (4 × 250 mm) column. A preliminary elution scheme suggested by Christina Hall (personal communication, 1996) at NeXstar had given very similar results to those seen in figures 2 and 3, namely, several poorly resolved peaks at low temperature and a single, sharp main peak at high temperature. It was expected that considerable effort would be required to achieve the desired separation. However, simply decreasing the gradient slope

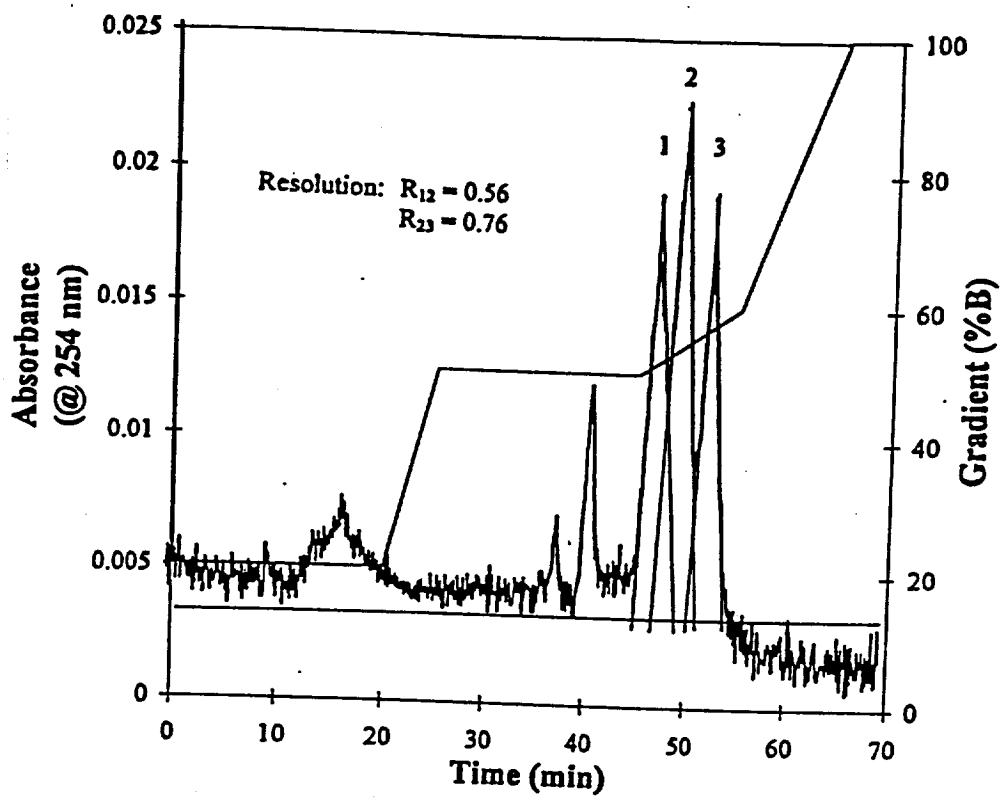

Figure 4: Improved low temperature (~27°C) FPLC chromatogram of an equal-mass mixture of CIP 12mer and unCIP 12mer. Tangent lines were drawn in for determination of peak widths (used in the resolution calculations). Flow rate = 4.7 mL/min. Elution buffers: A = 25 mM Tris, pH 8.0; B = A + 0.8 M ammonium chloride, pH 8.0.

considerably resulted in very good separation at high temperature (80°C) and somewhat improved separation at room temperature. Table 1 below gives these optimized operating conditions.

Figure 5 summarizes the results at both temperatures. Chromatograms a) and c), respectively, show the high-temperature separations of the individual CIP 12mer and unCIP 12mer samples. The CIP 12mer sample appears to have been quite pure, while the unCIP 12mer sample obviously contained at least three different species. In increasing order of retention times, the peaks apparently correspond to the 5'-hydroxylated and two 5'-phosphorylated UU-dodecamer species, probably mono- and di-phosphorylated based on previous HPLC results (data not shown) in which three closely eluting main peaks were observed. Chromatogram e) in Figure 5 shows the high-temperature analysis of the equal mass CIP/unCIP 12mer mixture and confirms the 5'-hydroxylated species peak assignment. Chromatograms b) and d) show the low-temperature results for the individual samples, in which it is seen that the 5'-hydroxylated species elutes later than the 5'-phosphorylated species. Since this elution order is the reverse of that at high temperature (in which charge and size should be the basis for separation), secondary structure differences apparently have a significant effect at low temperature. In addition, Chromatogram f) shows that a third intermediate peak appears at low temperature when a mixture of the two samples is injected.

Since the new peak cannot be explained away by simply numerically summing the absorbance data in chromatograms b) and d), it must represent a real component, probably a heterogeneous dimer. The flanking peaks probably represent the homogeneous dimers.

Table 1: HPLC operating conditions and gradient elution scheme for the optimized separation of 5'-hydroxylated and 5'-phosphorylated UU-dodecamer (see Figure 4). Elution conditions at specified time points change linearly between time points.

System: Waters HPLC			
Column: Dionex NucleoPac™ PA-100 (4 × 250 mm)			
Column Temperature: room temp. (~25°C) and 80°C			
Elution Buffers: A = 25 mM Tris, 1% acetonitrile, pH 8.0 B = A + 1.0 M ammonium chloride, pH 8.0			
Gradient Elution Scheme			
Time (min)	Flow Rate (mL / min)	% A	% B
0.00	1.50	90.0	10.0
2.00	1.50	90.0	10.0
52.00	1.50	30.0	70.0
55.00	1.50	30.0	70.0
56.00	1.50	0.0	100.0
60.00	1.50	0.0	100.0
61.00	1.50	90.0	10.0
70.00	1.50	90.0	10.0

Comparison with gel electrophoresis

The best resolutions obtained using low-temperature FPLC and high-temperature HPLC were compared to that achieved using analytical gel electrophoresis. Resolutions were calculated using the chromatogram in Figure 4 and a magnified version of chromatogram e) in Figure 5, and these were compared to the resolution calculated using the line graph of the area integration of the boxed gel lane shown in Figure 1 (see above). For low-temperature FPLC, the best resolutions were 0.56 and 0.76; for high-temperature HPLC, 3.5 (between the peaks corresponding to the 5'-hydroxylated and 5'-mono-phosphorylated species); and for gel electrophoresis, 1.2. High temperature HPLC clearly provided the best separation between the UU-dodecamer species.

Table 2 compares estimated production times for the UU-dodecamer if chromatography (proposed for the FPLC system) were used as the primary purification step rather than gel electrophoresis (as currently done). The decrease in production time from 49 hours to 32 hours if chromatography were employed strongly encourages the expenditure of effort in scaling up the high-resolution analytical chromatographic separation discussed above.

CONCLUSIONS

High temperature anion-exchange chromatography appears to be a promising technique for purifying UU-dodecamer RNA (and probably any oligonucleotide of up to at least 20 or 30 nucleotides) from very closely related contaminants. For example, analytical high temperature anion-exchange HPLC was able to separate 5'-hydroxylated UU-dodecamer from its 5'-phosphorylated analogs with a resolution that was much better than that of analytical gel electrophoresis (a resolution of 3.5 as compared to 1.2), which is encouraging

since chromatography is much more scaleable than gel electrophoresis. The successful scale-up from analytical HPLC columns still must be accomplished, but it would be a very worthwhile endeavor, even for the UU-dodecamer production scale required for laboratory research, given the relative labor intensiveness of gel electrophoresis. Low temperature anion-exchange chromatography appears to hold promise as an analytical tool for investigating secondary structural differences of oligonucleotides, both of a single oligonucleotide and of very closely related ones.

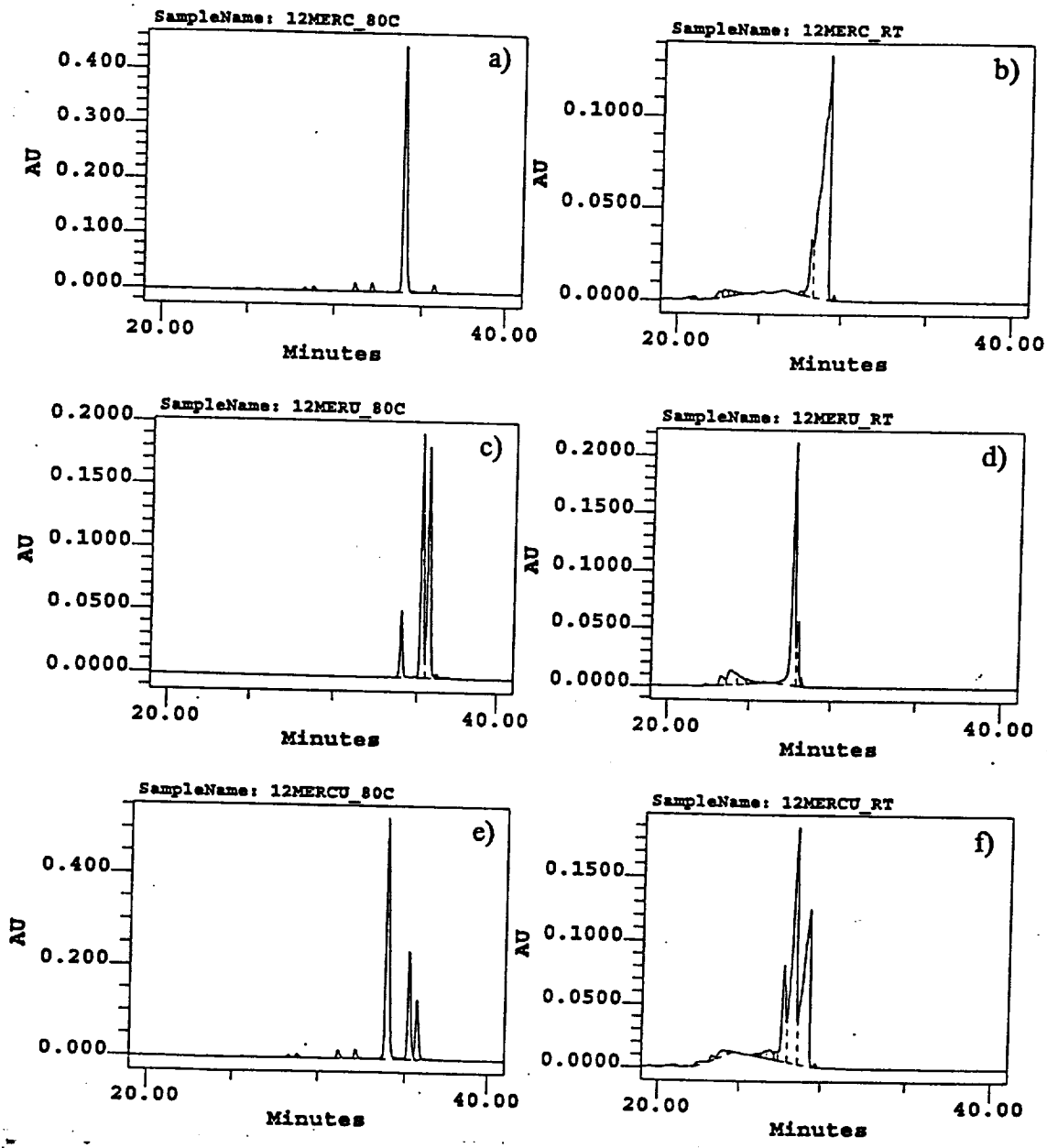

Figure 5: HPLC chromatograms of individual samples and equal-mass mixtures of CIP 12mer and unCIP 12mer using a Dionex NucleoPac™ PA-100 (4 × 250 mm) column at both high (80°C) and room temperature (RT). Chromatograms: a) CIP 12mer, 80°C; b) CIP 12mer, RT; c) unCIP 12mer, 80°C; d) unCIP 12mer, RT; e) equal-mass mixture, 80°C; and f) equal-mass mixture, RT. See Table 1 for the complete operating conditions and gradient elution scheme.

Table 2: Comparison of UU-dodecamer production times using chromatography versus gel electrophoresis as the purification step.

Chromatography (Proposed for the FPLC System) Capacity: >>> Six 1mL Transc. Rxns per 50mL Column		Gel Electrophoresis (Method Currently Used) Capacity: Six 1mL Transc. Rxns per 8 prep gels. About 1.5 mg of UU-dodecamer Recovered	
Step	Time (hours)	Step	Time (hours)
Transcription	5.0	Transcription	5.0
EtOH Precipitation	4.0	EtOH Precipitation	4.0
Desalt Sample	8.0	Desalt Sample	8.0
CIP Rxn	2.0	CIP Rxn	2.0
High Temp FPLC	3.0	Gel Electrophoresis	15.0
Desalt Product Fraction	6.0	Band Elution	5.0
Concentrate Sample	4.0	Desalt Sample	6.0
		Concentrate Sample	4.0
Total Time	32.0	Total Time	49.0

ACKNOWLEDGMENTS

This research was supported by the Colorado RNA Center, Colorado Institute for Research in Biotechnology, National Institutes of Health (Integrated Training Grant for Leadership in Biotechnology), NeXstar Pharmaceuticals, Inc. both financially and by providing HPLC capabilities, and the National Aeronautics and Space Administration through grant NAG8-1167. Christina Hall and Stephanie Nieuwlandt at NeXstar deserve special recognition for all their help with the HPLC part of this research. Sean Ferree and Scott McEntyre worked tirelessly in transcribing the UU-dodecamer, and Mike Sportiello was always helpful with general lab techniques. Prof. Ted Randolph must also be thanked for graciously allowing the use of his laboratory for the FPLC experiments.

REFERENCES

Cunningham, L., Kittikamron, K., and Y. Lu, *Nucleic Acids Res.* 24: 3647 (1996).

Delort, A. M., Derbyshire, R., Duplaa, A. M., Guy, A., Molko, D., and R. Teoule, *J. Chromatogr.* 283: 462 (1984).

Giegé, R., Dock, A. C., Kern, D., Lorber, B., Thierry, J. C., and D. Moras, *J. Crystal Growth* 76: 554 (1986).

Jucker, F. M., RNA tetraloop: a study by multi-dimensional heteronuclear NMR spectroscopy, Ph.D. Thesis, Department of Chemistry and Biochemistry, University of Colorado (1995).

Marble, H. A., and R. H. Davis, *Biotechnol. Prog.* 11: 393 (1995).

Potaman, V. N., Chernov, I. P., and V. V. Demidov, *J. Chromatogr.* 648: 151 (1993).

Warren, J. W. and G. Vella, Analysis and Purification of Synthetic Oligonucleotides by High-Performance Liquid Chromatography, in *Methods in Molecular Biology, Vol. 26: Protocols for Oligomucleotide Conjugates*, Ed.: S. Agrawal (1994), Humana Press Inc., Totowa, NJ, pp. 233 - 264.

Yamamoto, S., Nomura, M., and Y. Sano, *J. Chromatogr.* 409: 101 (1987).

Yamamoto, S., Nomura, M., and Y. Sano, *J. Chromatogr.* 512: 89 (1990).

Yamamoto, S., Suehisa, T., and Y. Sano, *Chem. Eng. Comm.* 119: 221 (1993).

PART III. TASK 2: PATHWAY TO HIGH-QUALITY RNA CRYSTALS

Chapter 11

Crystallization of an Oligonucleotide in the Presence of a Closely Related Contaminant

Stephen. P. Cape, Scott R. McEntyre, Sean M. Ferree, Craig E. Kundrot and Paul Todd

Chapter 11

Paper Number: 15i (3337)

Crystallization of an Oligonucleotide in the Presence of a Closely Related Contaminant

Stephen P. Cape, Scott R. McEntyre, Sean M. Ferree, Craig E. Kundrot and Paul W. Todd.

Prepared for presentation at the AIChE 1997 Annual Meeting on Friday, November 21 in Session 15 (02b02), Crystallization of Pharmaceutical and Biological Molecules.

Date: July 1997

UNPUBLISHED

ABSTRACT

Whether crystals of biological macromolecules are grown for product purification or crystallography, these should contain only one chemical species. To date there is no information available concerning the effects of closely related species on the crystallization of oligonucleotides, and it is not known whether closely related species will co-crystallize, inhibit each other's crystallization or enhance each other's crystallization. Experiments were performed in which two identical RNA dodecamer sequences, one 5'-hydroxylated and the other 5'-phosphorylated, were crystallized in mixtures in which approximately 100, 95, 75, 50, 25 and 0% of the initial material was present as 5'-hydroxylated dodecamer. It was observed that the number of crystals and the mass of RNA found in crystals increased, and the quality of crystals declined with increasing "contamination" of the 5'-hydroxylated dodecamer by the 5'-phosphorylated dodecamer. In addition, the presence of ammonium acetate promoted the formation of large, single crystals. Chromatography of the crystals showed that they contained both versions of the dodecamer when both were present in the starting mixture. The ratios of 5'-hydroxylated to 5'-phosphorylated molecules in the crystals were nearly the same as those in the initial crystallization solutions; in other words, purification factors due to crystallization were very close to 1.0. This observation was taken as evidence that these two molecules co-crystallize, and this finding was confirmed in experiments that demonstrated the presence of both molecules in a single crystal. It is concluded that such closely related oligonucleotides will co-crystallize, and the level of contamination of one with the other will be reflected in crystals, so that heavily contaminated co-crystals may not be suitable for crystallography or purification.

INTRODUCTION

Protein crystallization has a long history [1], but despite being a nearly perfected art, the science behind it is somewhat poorly understood. Likewise, oligonucleotide crystallization is establishing itself as a successful art (but still poorly understood science), although its history is not as extensive. The crystallization of RNA has lagged considerably behind that of DNA because of higher cost and lower efficiency in the production of RNA [2], but in recent years the number of reports of successful RNA crystallizations and structure determinations have increased significantly due to newer, more efficient technologies. A recent search of the Nucleic Acids Database on the Internet (http://ndbserver.rutgers.edu/) returned 46 pure RNA and 350 pure DNA structures.

Using lysozyme as a model protein, Feher's laboratory categorized the crystallization process into three temporal phases: 1) nucleation, 2) postnucleation growth, and 3) cessation of growth [3]. Cessation of growth is not well understood, but a possible explanation for its occurrence is that contaminating molecules might poison favorable growth sites on the crystal surface. Giegé *et al.* [4], using aminoacyl-tRNA synthetases and transfer ribonucleic acids (tRNA) as examples, showed that, for successful crystallization, these biomacromolecules must be pure, not only in terms of (unrelated) contaminating molecules, but also in terms of sequence integrity and conformational homogeneity. Anderson *et al.* [5] examined the effects of sample purity on crystallization using immunoglobulin F_{ab} fragments. Microheterogeneities, introduced by the protease treatment used to produce the F_{ab} fragments, were detrimental to crystal growth, and it was

determined that the incorporation or segregation of impurities that are not totally excluded from the crystal depends on the growth rate. Abergel *et al.* [6] performed a series of studies on the controlled contamination of crystallizing solutions of turkey egg-white lysozyme (TEWL) with three related contaminants: hen (HEWL), quail (QEWL), and pheasant (PEWL) egg-white lysozymes. Contaminations by the related proteins affected both nucleation and growth, although not all in the same manner. Low and medium levels of contamination by HEWL and QEWL resulted in partial inhibition of nucleation (measured by the total number of crystals after three weeks of growth) and shortening of the c-axis of the crystals. Higher levels of these same contaminants led to co-crystallization. Contamination by PEWL did not cause a shortening of the c-axis, but crystals seemed to grow in bundles. An unrelated contaminant, ribonuclease A, had an effect on nucleation similar to that of the related contaminants, but no changes in crystal morphology were observed.

Crystallization has often been used in the traditional chemical industry as a purification (or more often as a polishing) step in the production of industrial chemicals and pharmaceutical products. However, its usefulness as a step in oligonucleotide purification has not been investigated. As seen above with proteins (and tRNA), a certain level of purity is required *a priori* to obtain good crystals, at least under the conditions studied. Under which conditions this holds true in oligonucleotide crystallization and under which crystallization itself is useful for purification remains to be investigated. The goals of this research were to examine the effects of a closely related contaminant on the crystallization of an RNA oligonucleotide.

MATERIALS AND METHODS

A 12mer RNA ("UU-dodecamer" or simply "dodecamer") with the primary sequence 5'-GGCGCUUGCGUC-3', was synthesized by *in vitro* transcription using the immobilized DNA template technique of Marble and Davis [7]. It was purified by denaturing polyacrylamide gel electrophoresis (T = 20%, C = 5%, 8 M urea, 26 × 14 × 1.5 cm). Final UU-dodecamer purity was typically about 90%. The 5'-hydroxylated form was derived from the 5'-phosphorylated transcription product by CIP (calf-intestine alkaline phosphatase, Boehringer Mannheim, Indianapolis) digestion prior to gel electrophoresis. The terms "CIP 12mer" and "unCIP 12mer" refer, respectively, to UU-dodecamer transcription samples that were CIP digested, and therefore primarily 5'-hydroxylated, and to those that were not, and therefore primarily 5'-phosphorylated. The 5'-hydroxylated dodecamer was considered the target molecule for crystallization, and the 5'-phosphorylated dodecamer was considered the closely related contaminating species.

Controlled contamination experiments were conducted using two crystallization recipes and six mass ratios of CIP 12mer to unCIP 12mer: 100:0, 95:5, 75:25, 50:50, 25:75, and 0:100. Vapor diffusion from a hanging drop was the crystallization technique used. Each crystallization condition was set up in triplicate. The initial drop conditions for both crystallization recipes were the same, namely, 0.625 mg/mL total RNA, 2.5% 2-methyl-2,4-pentanediol (MPD), 100 mM ammonium acetate, 6.25 mM magnesium chloride, and 12.5 mM sodium cacodylate at pH 7.0. The initial reservoir conditions were nearly the same for both recipes, namely, 10% MPD, 25 mM magnesium chloride, and 50 mM sodium cacodylate, pH 7.0 in both cases. However, in one case (hereafter Experiment 1) ammonium acetate was not present initially in the reservoir, while in the other case (hereafter Experiment 2) ammonium acetate was present initially at 400 mM in the reservoir. Crystallization was allowed to proceed at 37°C for 12 days, after which the drops were observed for crystals and photographed (or digitally recorded) using a Nikon SMZ-U stereomicroscope with a Nikon AFX-II photomicrographic system and a Nikon 35mm SLR camera (or a CCD camera, Microvision, Kodak).

After observation, the RNA crystals were recovered and redissolved in pure water in order to be analyzed. The amount of crystallized mass and its composition were determined by UV spectrophotometry at 260 nm and HPLC, respectively. HPLC analysis was conducted at 80°C using a Waters Chromatography system with UV detection at 260 nm and a NucleoPac™ PA-100 (4 × 250 mm; DIONEX Corporation, Sunnyvale, CA) strong anion-exchange column. Buffer A consisted of 25 mM Tris and 1% acetonitrile at pH 8.0. Buffer B consisted of A plus 1.0 M ammonium chloride. The RNA peaks were eluted at 1.5 mL/min with a gradient of 10 to 56% Buffer B over 38 minutes.

RESULTS AND DISCUSSION

In Experiment 1, where there was no ammonium acetate in the reservoir solution initially, several effects on the crystallization of the UU-dodecamer were observed with increasing contamination by the closely related contaminant, 5'-phosphorylated dodecamer. First, the number of crystals generally increased, indicating that more nucleation occurred as contamination with the closely related species increased. Second, the visual quality of the crystals formed decreased with decreasing purity. As contamination increased, visual imperfections, such as cracks within the crystals and wavy or curved

surfaces and loss of symmetry, increased. The straight, sharp edges seen at the highest purities became rougher, or at least, less straight as purity decreased. Third, the total amount of crystallized RNA mass increased with increasing contamination, indicating a decrease in overall dodecamer solubility or promotion of crystal growth. And, fourth, the HPLC results indicate that the two closely related oligoribonucleotide species, 5'-hydroxylated dodecamer and 5'-phosphorylated dodecamer, co-crystallized in ratios almost identical to those initially present in the crystallization drop.

Polarized micrographs of representative crystals from Experiment 2 are shown in Figure 1. Again, in this experiment, ammonium acetate was present initially in both the crystallization drop and the reservoir solution. In this case, the decrease in visual quality with decreasing purity (also observed in Experiment 1) is clearly seen. Internally reflecting planes, seen as lines (crossing each other in an X pattern or somewhat parallel curved lines) through the middle of the better formed crystals, proceed from being very straight at the highest purity (Micrograph a)) to more wavy and curvy as the purity decreases (micrographs b) through d)). The obvious effect of purity on the number of crystals formed seen in Experiment 1 was not as clearly seen in Experiment 2. Large, single crystals were grown in Experiment 2 even at the higher levels of contamination, although with a clear and drastic decrease in crystal quality as seen in micrographs e) and f). However, in all five conditions where unCIP 12mer was added in controlled ratios (represented by micrographs b) through f)), at least one of the three drops of replicated conditions contained multiple crystals (up to about six in one drop), with the general trend towards more crystals at lower purities. In fact, the individual crystals of very poor visual quality shown in micrographs e) and f) could be interpreted as highly twinned crystals, that is, multiple smaller crystals that grew together. As in Experiment 1, the total amount of crystallized RNA mass was observed to increase with increasing contamination.

Figure 2 shows the results of HPLC analysis for Experiment 2, which are essentially identical to those of Experiment 1 (not shown). The chromatograms shown are of the redissolved crystals, and they clearly show that the two dodecamer species co-crystallized. In fact, ratios of the peak areas (obtained by peak integration) which are proportional to the mass of RNA show that the levels of co-crystallization were nearly identical to the levels of contamination in the initial drops. As a result, purification factors were close to 1.0 in all cases, that is, essentially no purification was accomplished by the crystallization process. The HPLC chromatograms also indicate that the phosphorylation of the unCIP 12mer sample was heterogeneous. HPLC chromatograms (not shown) of the original stock samples of CIP 12mer and unCIP 12mer reveal that the two closely eluting peaks on the right (clearly seen in chromatograms d) through f) of Figure 2) correspond to the 5'-phosphorylated species. In addition, they revealed that the unCIP 12mer stock also contained some of the 5'-hydroxylated species. The original CIP 12mer stock had a purity in terms of 5'-hydroxylated dodecamer of 90% or greater.

The observation in Experiment 1 of increased nucleation (more crystals) with increasing contamination by a closely related species stands in direct opposition to the results obtained by Abergel *et al.* [6] in their controlled-contamination crystallization studies of turkey egg-white lysozyme with other avian lysozymes. They observed partial inhibition of nucleation, as measured by the total number of crystals after three weeks of growth. However, direct comparison of these results is probably not warranted since 5'-hydroxylated UU-dodecamer and 5'-phosphorylated UU-dodecamer are much more closely related species than are the various avian lysozymes used by Abergel et al, and since in this case the crystallizing species are oligonucleotides, not proteins. However, these diametrically opposed results provide interesting opportunities for speculation (not engaged in here) and future research regarding the precise role that closely related contaminants play in the crystallization, or more likely, the nucleation process.

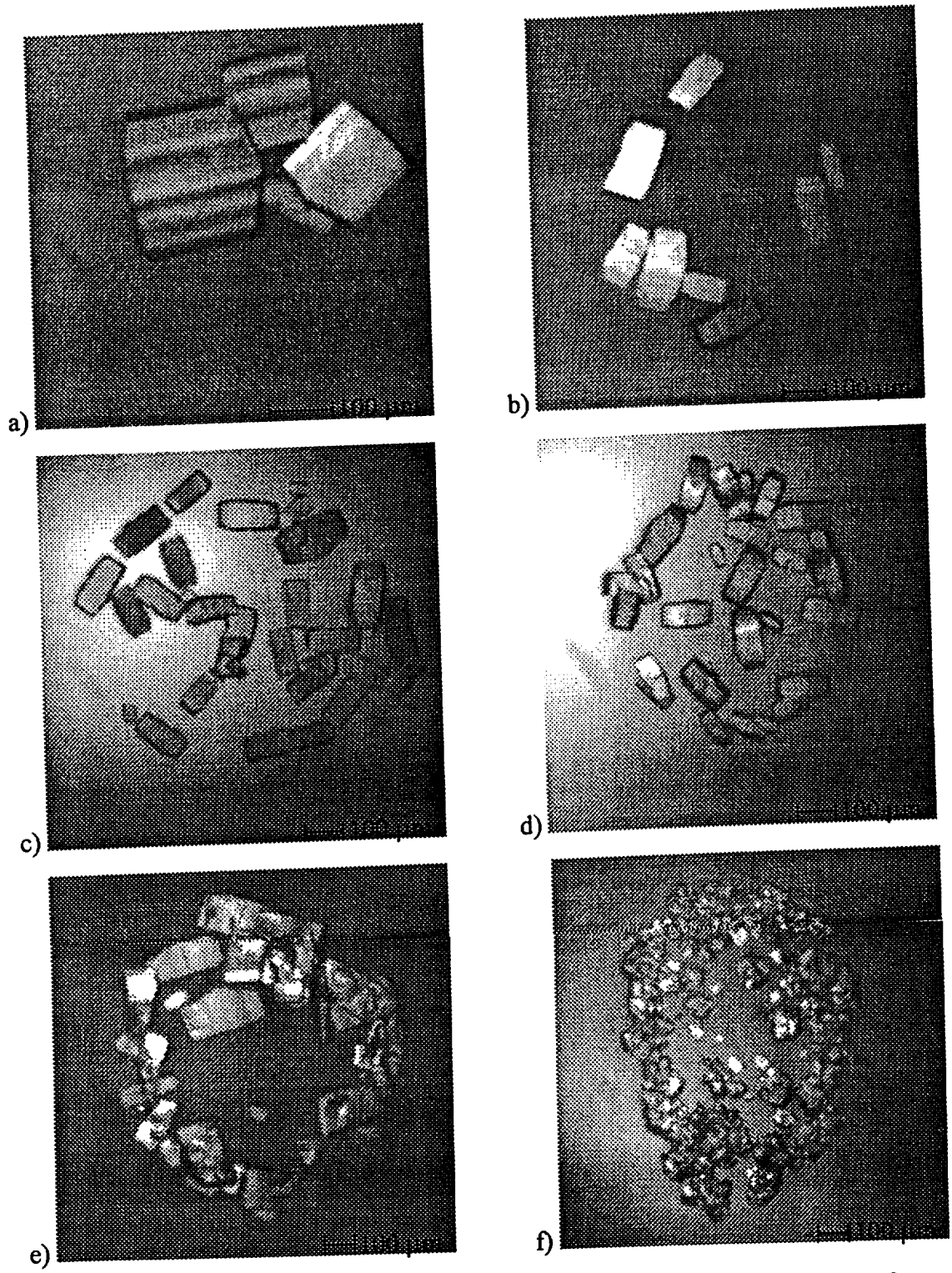

Figure 1: Polarized-light micrographs from Experiment 1 showing the effects of controlled mass ratios of CIP 12mer to unCIP 12mer on crystallization. Mass ratios (CIP : unCIP): a) 100:0, b) 95:5, c) 75:25, d) 50:50, e) 25:75, and f) 0:100. Ammonium acetate was initially present in the drops but not in the reservoir solutions.

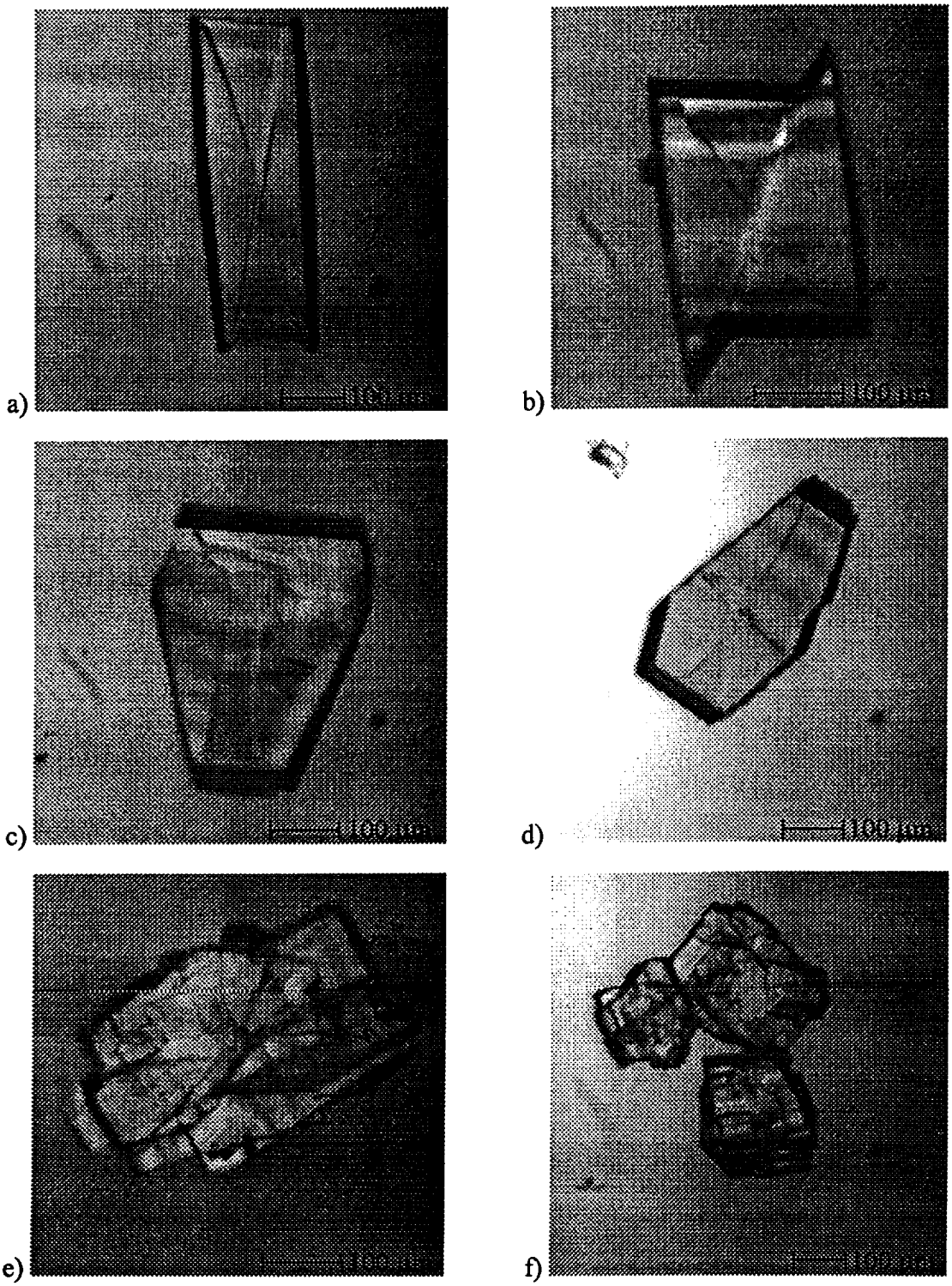

Figure 2: Polarized-light micrographs from Experiment 2 showing the effects of controlled mass ratios of CIP 12mer to unCIP 12mer on crystallization. Mass ratios (CIP : unCIP): a) 100:0, b) 95:5, c) 75:25, d) 50:50, e) 25:75, and f) 0:100. Ammonium acetate was initially present both in the drops and the reservoir solutions.

The decrease in crystal quality with increasing contamination that was observed in both experiments 1 and 2 was not wholly unexpected. If these closely related, but still somewhat dissimilar, oligonucleotide molecules co-crystallize (as the HPLC results clearly show they indeed do), the individual molecules probably cannot self-assemble as efficiently and in as orderly a crystal lattice structure as can identical molecules. The crystallographic structure of the UU-dodecamer has been solved [8], and the 5' end of the molecule does not appear to be directly involved in any intermolecular contacts in the crystal lattice. However, the difference at the 5' terminus between these two dodecamer species appears to be sufficiently great to cause stresses within the crystal lattice structure during assembly that are observable qualitatively on a macroscopic scale as visual imperfections.

The increase in crystallized RNA mass with increasing contamination was observed in both experiments 1 and 2. What may be occurring on a molecular level is that the solubility of a heterogeneous (5'-hydroxylated and

5'-phosphorylated) dodecamer sample is lower than that of a more homogeneous sample. If this is the case, the dodecamer will more readily come out of solution with increasing heterogeneity, forming nucleation sites and promoting crystal growth.

The fact that large, single crystals grew even at very low mass purity ratios in Experiment 2 (e.g. 25:75, Micrograph e) in Figure 1)), may possibly be explained by the presence of ammonium acetate in both the drop and reservoir solutions. The drops in Experiment 1 also contained ammonium acetate, at least initially (100 mM), but the reservoir solution did not. Ammonium acetate is a volatile component, so it probably moved by vapor diffusion from a given drop into the reservoir chamber and solution because of the large relative volume of the reservoir solution, establishing a new equilibrium, with its concentration in the given drop much lower than it was initially. In the case of Experiment 2, ammonium acetate was initially at a higher concentration in the reservoir solution (400 mM) than it was in any given drop (100 mM), which should have led to a new equilibrium with a higher ammonium acetate concentration than in the given drop initially. The presence of ammonium acetate increases the solubility of the dodecamer, so in the case of Experiment 2, the increased solubility probably counteracted the increase in dodecamer concentration due to dewatering of the drop by vapor diffusion, thereby decreasing the rate of nucleation and leading to single crystals or few of them. In Experiment 1, the loss of both ammonium acetate and water by vapor diffusion probably led to a relatively rapid decrease in the solubility of dodecamer, resulting in relatively more nucleations, and therefore more crystals, than in Experiment 2. This pair of experiments also reveals the interesting relationship between solubility and dewatering rate in controlling the onset of nucleation.

CONCLUSIONS

The controlled addition of a closely related contaminant (5'-phosphorylated dodecamer) in the crystallization of the 5'-hydroxylated dodecamer has several effects. Crystal quality (visually determined) decreases, while the number of crystals generally increases, with decreasing initial purity. Ammonium acetate clearly plays a role in the crystallization process, with its presence increasing dodecamer solubility and promoting the formation of large, single crystals by apparently allowing fewer nucleations to occur. Solubility, in this case, is also affected by the amount of closely related contaminant, with increasing contamination leading to increasing crystallized mass. Co-crystallization of the two dodecamer species clearly occurs under certain conditions, with the level of co-crystallization mirroring the level of contamination. The consistent determination of a purification factor close to 1.0 indicates that crystallization is not a promising purification technique for separating these very closely related UU-dodecamer species, at least under the conditions investigated here.

ACKNOWLEDGMENT

This research was supported by the National Aeronautics and Space Administration (grant no. NAG8-1165), the National Institutes of Health (Integrated Training Grant for Leadership in Biotechnology), the Colorado Institute for Research in Biotechnology and the Colorado RNA Center, both of the Colorado Advanced Technology Institute, and NeXstar Pharmaceuticals. Russ Lehrman, Christina Hall, Mike Vrkljan and Stephanie Nieuwlandt at NeXstar deserve special recognition for their help with the HPLC analysis.

LITERATURE CITED

1. McPherson, A., *J. Crystal Growth*, **110**, 1 (1991).

2. Wahl, M.C., B. Ramakrishnan, C. Ban, X. Chen and M. Sundaralingam, *Acta Cryst.*, **D52**, 668 (1996).

3. Feher, G., *J. Crystal Growth*, **76**, 545 (1986).

4. Giegé, R., A.C. Dock, D. Kern, B. Lorber, J.C. Thierry and D. Moras, *J. Crystal Growth*, **76**, 554 (1986).

5. Anderson, W.F., A. Boodhoo and C.D. Mol, *J. Crystal Growth*, **90**, 153 (1988).

6. Abergel, C., M.P. Nesa and J.C. Fontecilla-Camps, *J. Crystal Growth*, **110**, 11 (1991).

7. Marble, H.A. and R.H. Davis, *Biotechnol. Prog.*, **11**, 393 (1995).

8. Lietzke, S.E., V.E. Carperos and C.E. Kundrot, *Acta Cryst.*, **D52**, 687 (1996).

Chapter 12

Role of Divalent Magnesium Cation in the Crystallization of an Oligoribonucleotide

Stephen P. Cape, Moha Shah and Paul Todd

Chapter 12

Role of Divalent Magnesium Cation in the Crystallization of an Oligoribonucleotide

Stephen P. Cape, Moha Shah and Paul Todd.

University of Colorado, Department of Chemical Engineering, Campus Box 424, Boulder, CO 80309-0424.
(303) 492-8541
cape@rastro.colorado.edu

Prepared for Presentation at 4th Topical Conference on Separations Science & Technology, November 1999 in Session T1010, Crystallization of Pharmaceutical and Biological Molecules.

UNPUBLISHED

ABSTRACT

Methylpentanediol (MPD) and polyethylene glycol (PEG) are popular precipitants in RNA and DNA crystallization. While investigating the possibility of replacing MPD with PEG we found that a critical equilibrium exists that depends on Mg^{++} concentration. Nearly all solutions made for the study of nucleotides and nucleic acids contain divalent magnesium cations. It is thought that a stable cation-anion complex is formed, and that this complex is the physiological and chemical reacting unit in aqueous solutions. Additionally, Mg^{++} is one of the solutes that are manipulated in the crystallization of oligonucleotides, and most published mother liquors specify a Mg^{++} concentration. Furthermore, divalent magnesium cations have been located in the crystal structures of many oligonucleotides. Therefore, the solubility, crystallization and aggregation of a specific RNA dodecamer ("UU-dodecamer") were investigated. This oligomer exists as a duplex with Watson-Crick hydrogen bonds except in the case of 2 U's complementing 2 U's. Using MPD and PEG as precipitants, and manipulating ionic strength with monovalent ions, molecular interaction studies were performed as a systematic function of Mg^{++} concentration. These consisted of crystallization, solubility equilibria, determination of osmotic second virial coefficient by static light scattering, and aggregate growth measured by dynamic light scattering. The coordinates of solvent ions in the crystal structure were also assessed. The manipulation of Mg^{++} concentration is at least as important as controlling the concentration of the traditional precipitants MPD and PEG, leading to the notion that, at suitable concentrations Mg^{++} serves as "precipitant", and its control plays a significant role in the growth of high-quality crystals for diffraction study.

Oligonucleotide crystallization remains more of an art than a science. Although many hundreds of oligonucleotides have been successfully crystallized and their structures solved, arriving at solution conditions that give rise to high-quality crystals is currently most effectively accomplished through educated guessing and systematic screening approaches (sparse matrices of conditions based on past experience, etc.). The theoretical understanding of the crystallization process is still substantially incomplete.

BACKGROUND

Researchers have used a variety of approaches to further the elucidation of biomacromolecule crystallization. One approach has been to employ the techniques of static light scattering (SLS) and dynamic light scattering to investigate thermodynamic and transport properties of crystallizing solutions of proteins (George and Wilson, 1994; Rosenbaum and Zukoski, 1996; Muschol and Rosenberger, 1995). Using the SLS analytical technique described below, George and Wilson (1994) measured the osmotic second virial coefficient, B_{22}, for a number of proteins in both crystallizing and non-crystallizing solutions. They observed that solution conditions that favored the growth of protein crystals had small, negative values of B_{22} that fell in a narrow range. This narrow range, with values between -1×10^{-4} and -8×10^{-4} mol mL g^{-2}, they termed the "crystallization slot". Solutions with large negative values of B_{22} led to the formation of amorphous

precipitates, while those with positive values of B_{22} resulted in neither crystals nor precipitates. The empirical validity of the crystallization slot has been confirmed for some 20 different proteins (George *et al.*, 1997).

Zukoski and coworkers have provided a more theoretically rigorous explanation of Wilson's crystallization slot (Rosenbaum and Zukoski, 1996). Using simple fluid theory, they successfully predicted the phase boundary of lysozyme. They modeled the protein interactions using the adhesive hard sphere potential, a model successfully used in colloid science. Although this model provides an over-simplified description of the complex interactions that can occur in macromolecule crystallization, it nonetheless is a robust correlation that is applicable to a wide variety of macromolecules ranging from inorganic to biological (Rosenbaum *et al.*, 1996).

The osmotic second virial coefficient, B_{22}, is a dilute solution parameter, which empirically accounts for non-ideality in solutions and qualitatively provides a measure of two-body (for example, protein-protein) interactions. Positive values of B_{22} indicate that repulsive forces between the solute molecules under consideration dominate in a particular solvent, which can then be characterized as a "good solvent". The solute-solvent interactions are favored over the solute-solute interactions in this case. Negative values of B_{22} indicate that attractive forces are dominant between the same solute molecules, and the solvent can then be described as a "poor solvent".

Solutes which have molecular dimensions smaller than $\lambda/20$, where λ is the wavelength of the incident light, scatter light isotropically. In this case, the simplified Rayleigh equation given by Kratochvil (1987) can be used to interpret the SLS data.

$$\frac{Kc}{R_\theta} = \frac{1}{M_W} + 2B_{22}c \qquad [1]$$

where K is an optical constant, c is the solute concentrate, R_θ is the excess Rayleigh ratio measured at angle θ, M_W is the molecular weight of the solute, and N_A is Avogadro's number. The optical constant, K, is given by

$$K = \frac{4\pi^2 n_o^2 (dn/dc)^2}{N_A \lambda^4} \qquad [2]$$

where n_o is the solvent refractive index, and dn/dc is the refractive index increment. Plots of Kc/R_θ vs c (known as Debye plots) at a given detection angle (usually 90°) yield the molecular weight, M_W, from the intercept and the osmotic second virial coefficient, B_{22}, from the slope of the resulting linear SLS data.

A review of the literature quickly shows that 2-methyl-2,4-pentanediol (MPD) is the overwhelming precipitant of choice in oligonucleotide crystallization. However, Baeyens *et al.* (1994) have proposed that polyethylene glycol with a low molecular weight distribution (PEG-400) may be a good alternative to MPD, especially for crystallizing RNA oligomers. This begs the question of what the precise role is that polyols play in nucleic acid oligomer crystallization. The role that divalent cations play in oligonucleotide crystallization has been further clarified recently. McFail-Isom *et al.* (1998) showed that divalent cations interact favorably with the π-systems of nucleic acid bases. Such cation-π interactions have been known to contribute to the stability of protein native states and to the stability of protein-ligand complexes, but this is the first identification of such interactions in oligonucleotide structures. Among noncovalent interactions, cation-π bonds are thought to be among the strongest.

MATERIALS AND METHODS

A 12mer RNA ("UU-dodecamer" or simply "dodecamer") with the primary sequence 5'-GGCGCUUGCGUC-3', was synthesized by *in vitro* transcription. It was purified by anion-exchange (NucleoPac PA-100, Dionex Inc.) HPLC. Final UU-dodecamer purity was typically ≥95%. The 5'-hydroxylated form was derived from the 5'-phosphorylated transcription product by CIP (calf-intestine alkaline phosphatase, Boehringer Mannheim, Indianapolis) digestion prior to the final HPLC purification step. The crystal structure of this molecule was solved by Lietzke *et al.* (1996) from crystals grown at 37° in solutions containing MPD, magnesium chloride, ammonium acetate, and sodium cacodylate, pH 7.

Solubility experiments were carried out using a pseudo-batch hanging drop technique in multi-well crystallization plates. The technique used for the crystallization experiments was hanging drop vapor diffusion. Light scattering experiments (both static and dynamic) were conducted using a Brookhaven Instruments Corp. system (BI-200SM goniometer and BI-9000AT digital correlator with a 532nm solid state laser). The details of the precise solution conditions and compositions used in these experiments are given (when necessary and relevant) in the next section.

RESULTS AND DISCUSSION

Static light scattering experiments were conducted using the dodecamer crystallization conditions given above (see Materials and Methods section). Because directly measured *dn/dc* values under those solution conditions were not available, the *dn/dc* was varied in the SLS calculations to give the expected molecular weight of the dodecamer in solution. The resulting B_{22} values were on the order of -5×10^{-2} mol mL g^{-2}. These values are about two orders of magnitude more negative than the lower limit of Wilson's crystallization slot, indicating that oligonucleotides do not obey those criteria for crystallization. However, some difficulties in carrying out these SLS experiments cast some doubt on the validity of these very negative B_{22} values. One difficulty was the lack of directly measured *dn/dc* values. Attempts were made to measure these values, but could not be done with sufficient accuracy. Another difficulty was the very low solubility of the RNA in the crystallization solutions, which led to significant uncertainty in the actual concentrations of the RNA in solution. The low solubility also led to very low scattering intensity differences (above the solvent background and between samples) which could not be corrected by increasing the dodecamer concentration in solution. In spite of these difficulties, the order of magnitude of the B_{22} values was consistently reproducible.

Alternative crystallization conditions that might be more conducive to light scattering experiments were pursued by setting up a number of hanging drop vapor diffusion crystallization screens of a wide variety of solution compositions. Crystals were obtained at room temperature from solutions containing 5-10% PEG-400, 10-20 mM NaCl, 25 mM $MgCl_2$, and 50 mM Na Cacodylate, pH 7. It appeared that the UU-dodecamer RNA solubility was higher than in the original , published crystallization conditions. However, pseudo batch, hanging drop solubility experiments showed otherwise. In these partial factorial experiments the concentration of the solutions components were varied as follows: 1 to 3 mg/mL RNA; 0 to 25 mM $MgCl_2$; 0, 10 and 20 mM NaCl; 0, 25 and 400 mM ammonium acetate; and 0 to 10% PEG-400. In each case, the experiments were conducted at room temperature and the solutions were buffered with 50 mM Na Cacodylate, pH 7. In most of the solubility conditions tested, showers of small crystals (largest dimensions on the order of ≤10 μm) were obtained even if in many cases amorphous and/or crystalline precipitate occurred alongside the crystals. The experiments showed that the solubility of UU-dodecamer RNA was critically dependent on the $MgCl_2$ concentration but not as strongly dependent on the other solution components. In addition, a previous observation that ammonium acetate appeared to make the RNA more soluble was confirmed.

More evidence for the critical role of Mg^{++} was pursued by using dynamic light scattering to monitor the aggregation state of the UU-dodecamer RNA as a function of $MgCl_2$ concentration. DLS experiments at 0, 2.5 and 7.5% PEG-400 were carried out as a function of $MgCl_2$ concentration. The experiments were conducted at room temperature with the other solution conditions as follows: ~2 mg/mL RNA, 20 mM NaCl, and 50 mM Na Cacodylate, pH 7. Figure 1 below is representative of the resulting effective molecular diameters versus Mg^{++} concentration for all three experiments. The

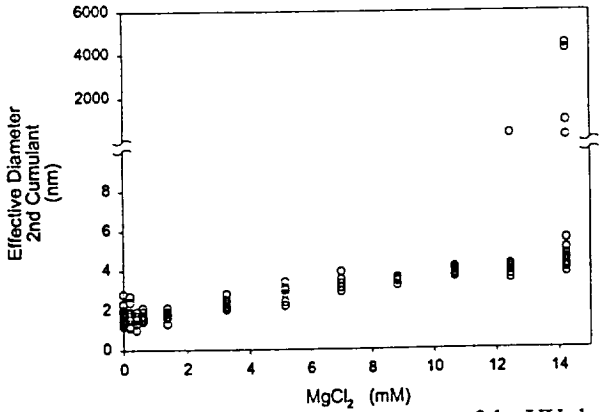

Figure 1: DLS results giving effective diameter of the UU-dodecamer as a function of $MgCl_2$concentration in a solution containing ~2 mg/mL RNA, 2.5% PEG-400, 20 mM NaCl, and 50 mM Na Cacodylate, pH 7.0.

effective diameter of the RNA in solution increases only slightly with $MgCl_2$ concentration until a critical point is reached where large aggregates begin to form. This critical point is essentially insensitive to PEG-400 concentration: in all three

experiments large aggregates began to form at $MgCl_2$ concentrations in the narrow range of 12 to 15 mM. The slight increase in effective diameter before the critical $MgCl_2$ concentration is reached may be due to the formation of embryos below the critical nucleus size (such as dimers, etc.). The DLS experiments confirm the observations from the solubility experiments. In addition, DLS experiments were performed in which $MgCl_2$ was titrated into an RNA solution (~2 mg/mL) in pure water. In this case, the effective diameter increases more strongly with $MgCl_2$ concentration, but above 10 mM the formation of very large aggregates is quite pronounced indicating a critical concentration value which is consistent with the other DLS experiments mentioned above.

With these DLS experiments as guidelines, SLS experiments were designed and conducted in which the problems of very low solubility and low scattering intensity were not significant. In all the crystallizing conditions identified for the UU-dodecamer, the $MgCl_2$ concentrations were higher than the critical concentration identified in the DLS experiments. Since SLS experiments cannot be carried out with $MgCl_2$ concentrations above the critical concentration of 12 to 15 mM, the SLS results unfortunately do not represent actual crystallization conditions. Instead they represent gradual steps in the solution conditions toward the limit of a crystallization solution; such solutions might be called "pre-crystallization" solutions. In these experiments, the osmotic second virial coefficient, B_{22} was determined as a function of two PEG-400 concentrations (0% and 7.5%) and three $MgCl_2$ concentrations (0 mM, 5 mM and 10 mM). Before and after each SLS experiment, the aggregation state of the RNA was monitored by DLS in order to justify the assumptions made regarding the molecular weight of the RNA in solution.

Figure 2 shows a typical Debye plot calculated from SLS data at 90° from which the B_{22} was calculated. Table 1 summarizes the results of the 90° Debye plots from all of the SLS experiments. The results clearly show that B_{22} is a strong function of Mg^{++} concentration, while it is a very weak function, if at all, of PEG-400 concentration. In fact, the differences in B_{22} are not statistically significant for the corresponding PEG-400 concentration at each $MgCl_2$ concentration. These results confirm those obtained in the crystallization, solubility and DLS experiments.

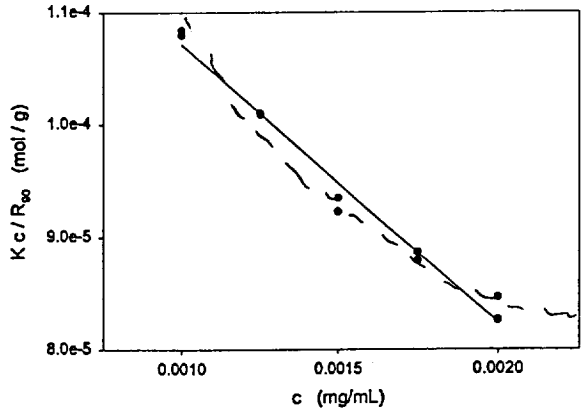

Figure 2: Debye plot at 90° of the UU-dodecamer RNA in 7.5% PEG-400, 10 mM $MgCl_2$, 20 mM NaCl, and 50 mM Na Cacodylate, pH 7.0.

Table 1: Summary of B_{22} (mol mL g^{-2}) results for UU-dodecamer in varied $MgCl_2$ and PEG-400 concentrations, determined from 90° Debye plots as in Figure 2. Other solution conditions: 20 mM NaCl, and 50 mM Na Cacodylate, pH 7.0.

$MgCl_2$	0% PEG-400		7.5% PEG-400	
(mM)	B_{22} (x10^3)	S.E. (x10^3)	B_{22} (x10^3)	S.E. (x10^3)
0	-2.32	0.39	-1.45	0.33
5	-8.23	0.44	-8.50	0.43

Figure 3 is a histogram showing the tabulated B_{22} results above in relation to Wilson's protein crystallization slot. It is clear that the second virial coefficients for UU-dodecamer oligonucleotide crystallization solutions (even for "pre-crystallization" solutions) do not fall anywhere near within the crystallization slot. It is not clear why this is the case, but the relatively smaller sizes and much lower solubilities and the strong polyelectrolyte nature of oligonucleotides in their crystallizing solutions may be starting points for explaining the drastic divergence from Wilson's robust (at least for proteins) observations. While oligonucleotide crystal growth may not occur in the protein crystallization slot, it is likely that they still follow Zukoski's correlation (Rosenbaum *et al.*, 1996), which is of a more general nature.

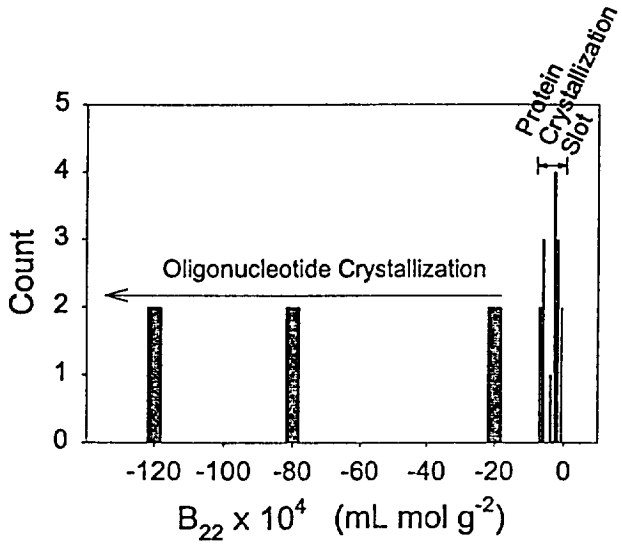

Figure 3: Histogram of B_{22} values for oligonucleotide "pre-crystallization" solutions in relation to the protein crystallization slot

The coordinates of solvent atoms in the UU-dodecamer crystal structure were assessed in order to determine whether any might be Mg^{++} ions interacting with the oligonucleotide molecules. Solvent atoms in the coordinate file are labeled as heteroatoms and identified as the oxygen atom of a water molecule. However, since water molecules and Mg^{++} ions have similar electron densities in the electron density maps generated by X-ray diffraction, it is difficult to distinguish between them in low-resolution structures. The UU-dodecamer structure was solved to 2.4Å, which is relatively low resolution. Several of the heteroatoms in the dodecamer structure meet the criteria, as put forth by McFail-Isom *et al.* (1998), for Mg^{++} ions interacting with nucleic acid bases in a cation-π bond, and may, therefore, indeed be Mg^{++} ions instead of water molecules. Such cation-π bonds, which, as mentioned before, are thought to be among the strongest noncovalent interactions, may explain the critical Mg^{++} dependence observed with the UU-dodecamer. However, without a structure of sufficiently high resolution, the Mg^{++} ions cannot be unambiguously identified and this explanation remains a speculative one.

The experiments reported here unambiguously show that Mg^{++} ions play a critical role in the crystallization and the structure of the UU-dodecamer RNA, even though a precise picture of this role has not yet been fully drawn. Mg^{++} appears to serve as the precipitant (or at least the primary one) in UU-dodecamer crystallization. This complicates somewhat the traditional definition and role of "precipitant" given to chemicals such as MPD or PEG-400, which occur in relatively high concentrations in almost all oligonucleotide crystallization solutions. Since this research suggests that, with proper control of the crystallization process, it should be possible to grow large, high quality crystals of the UU-dodecamer without the presence of a traditional precipitant (MPD or PEG-400), the question as to what role these polyols actually have must be asked. They are ubiquitous in oligonucleotide crystal growth solutions and have commonly been accepted as essential components.

This research with the UU-dodecamer RNA begs the question as to whether the results observed here are unique to this molecule or whether they are general characteristics of oligonucleotides (RNA and/or DNA) and their crystallization solutions. To answer this question, similar studies with other oligonucleotide molecules must be conducted.

CONCLUSIONS

Mg^{++} ions play a critical role in the structure of the UU-dodecamer RNA as demonstrated by the very strong dependence of the following on Mg^{++} concentration: osmotic second virial coefficient, solubility, nucleation and aggregate growth, and crystallization. In this case, Mg^{++} serves the role of "precipitant", and controlling its concentration is at least as important as (and probably more so than) controlling the concentration of the traditional precipitants MPD and PEG.

In light of the research presented here (especially the osmotic second virial coefficient results), the nature of molecular interactions in oligonucleotide crystallization may be significantly different from that in protein crystallization.

ACKNOWLEDGMENT

This research was supported by the National Aeronautics and Space Administration (grant no. NAG8-1165), the National Institutes of Health (Integrated Training Grant for Leadership in Biotechnology), the Colorado Institute for Research in Biotechnology and the Colorado RNA Center, both of which are agencies of the Colorado Advanced Technology Institute. A number of people deserve recognition for their helpful discussions and expertise: Mike Sportiello, Steve Schultz and Ted Randolph (University of Colorado at Boulder); Craig Kundrot (Marshall Space Flight Center); Bill Wilson (Mississippi State University); and Chip Zukoski (University of Illinois, Champaign-Urbana).

LITERATURE CITED

1. George, A. and W.W. Wilson, "Predicting protein crystallization from a dilute solution property" *Acta Crystallographica* D50: 361 - 365 (1994).

2. Rosenbaum, D.F. and C.F. Zukoski, "Protein interactions and crystallization" *Journal of Crystal Growth* 169: 752 - 758 (1996).

3. Muschol, M. and F. Rosenberger, "Interactions in undersaturated and supersaturated lysozyme solutions: static and dynamic light scattering results" *Journal of Chemical Physics* 103: 10424 - 10432 (1995).

4. George, A., Chiang, Y., Guo, B., Arabshahi, A., Cai, Z., and W.W. Wilson, "Second virial coefficient as predictor in protein crystal growth" *Methods in Enzymology* 276: 100 - 110 (1997).

5. Rosenbaum, D., Zamora, P.C., and C.F. Zukoski, "Phase behavior of small attractive colloidal particles" *Physical Review Letters* 76: 150 - 153 (1996).

6. Kratochvil, *Classical Light Scattering from Polymer Solutions.* Elsevier, Amsterdam (1987).

7. Baeyens, K. J., Jancarik, J., and S. R. Holbrook, "Use of Low-Molecular-Weight Polyethylene Glycol in the Crystallization of RNA Oligomers" *Acta Crystallographica* D50: 764 - 767 (1994).

8. McFail-Isom, L., Shui, X., and L.D. Williams, "Divalent Cations Stabilize Unstacked Conformations of DNA and RNA by Interacting with Base Π Systems" *Biochemistry* 37: 17105 - 17111 (1998).

9. Lietzke, S.E., Barnes, C.L., Berglund, J.A., and C.E. Kundrot, "The structure of an RNA dodecamer shows how tandem U-U base pairs increase the range of stable RNA structures and the diversity of recognition sites" *Structure* 4: 917 - 930 (1996).

Chapter 13

Role of Magnesium Ions in the Solution Behavior and Crystallization of an Oligonucleotide

Stephen P. Cape

CHAPTER 13

ROLE OF MAGNESIUM IONS IN THE SOLUTION BEHAVIOR AND CRYSTALLIZATION OF AN OLIGONUCLEOTIDE

13.1 ABSTRACT

Methylpentanediol (MPD) and polyethylene glycol (PEG) are popular precipitants in RNA and DNA crystallization. While investigating the possibility of replacing MPD with PEG we found that a critical equilibrium exists that depends on Mg^{++} concentration. Nearly all solutions made for the study of nucleotides and nucleic acids contain divalent magnesium cations. It is thought that a stable cation-anion complex is formed, and that this complex is the physiological and chemical reacting unit in aqueous solutions. Additionally, Mg^{++} is one of the solutes that are manipulated in the crystallization of oligonucleotides, and most published mother liquors specify a Mg^{++} concentration. Furthermore, divalent magnesium cations have been located in the crystal structures of many oligonucleotides. Therefore, the solubility, crystallization and aggregation of a specific RNA dodecamer ("UU-dodecamer") were investigated. This oligomer exists as a duplex with Watson-Crick hydrogen bonds except in the case of 2 U's complementing 2 U's. Using MPD and PEG as precipitants, and manipulating ionic strength with monovalent ions, molecular interaction studies were performed as a systematic function of Mg^{++} concentration. These consisted of crystallization, solubility equilibria, determination of osmotic second virial coefficient by static light scattering, and aggregate growth measured by dynamic light scattering. The coordinates of solvent ions in the crystal structure were also assessed. The manipulation of Mg^{++} concentration is at least as important as controlling the concentration of the traditional precipitants MPD and PEG, leading to the notion that, at suitable concentrations Mg^{++} serves as "precipitant", and its control plays a significant role in the growth of high-quality crystals for diffraction study.

13.2 INTRODUCTION

Oligonucleotide crystallization remains more of an art than a science. Although many hundreds of oligonucleotides have been successfully crystallized and their structures solved, arriving at solution conditions that give rise to high-quality crystals is currently most effectively accomplished through educated guessing and systematic screening approaches (sparse matrices of conditions based on past experience, etc.). The theoretical understanding of the crystallization process is still substantially incomplete. The goal of this study is to deepen the basic understanding of oligonucleotide crystallization using a particular RNA oligonucleotide as a case study.

13.2.1 Case Study Oligonucleotide: the "UU-dodecamer"

A twelve-nucleotide RNA oligomer with the sequence 5'-GGCGCUUGCGUC-3' (the 5'-hydroxylated form) was the oligonucleotide chosen for this study, and will be referred to as the "UU-dodecamer" or simply "dodecamer" in this chapter. The primary reasons for choosing this particular molecule were the wealth of local expertise available regarding it and the production process and infrastructure that were already in place. But it is also interesting in its own right as an RNA sequence that contains the CUUG tetraloop motif.

13.2.2 NMR Studies with the UU-dodecamer

Several C^{13} and/or N^{15} labelled UU-dodecamer RNA samples were used as the subject of NMR studies in the Pardi lab at the University of Colorado at Boulder (Jucker Franzusoff, 1995; Jucker & Pardi, 1995; Nikonowicz & Pardi, 1992; Nikonowicz *et al.*, 1992; Farmer *et al.*, 1994). These studies were designed to elucidate the solution structure of the UU-dodecamer. Under high salt conditions this dodecamer forms a symmetrical duplex with two non-canonical U-U base pairs, while under low salt conditions it forms a hairpin containing the CUUG loop (Jucker Franzusoff, 1995; Jucker & Pardi, 1995).

13.2.3 Crystallization Experience with the UU-dodecamer

The crystallographic structure of this dodecamer was solved in the Kundrot lab at the University of Colorado at Boulder to 2.4Å resolution (Lietzke *et al.*, 1996b). Epitaxially twinned crystals of space group P1 were grown at 37°C by vapor diffusion from solutions containing RNA, MPD (2-methyl-2,4-pentanediol), $MgCl_2$, $NH_4(OAc)$, and Na Cacodylate, pH7.0. Programs for data reduction and display were especially developed in order to solve the structure of the epitaxially twinned crystals (Lietzke *et al.*, 1996a). In the crystal structure, the RNA molecules form a duplex containing tandem U-U base pairs. Figure 3.1 shows a view of the asymmetric unit of the UU-dodecamer as well as a view containing symmetry-related molecules. The coordinates for the asymmetric unit of the crystal structure of this dodecamer are available at the Nucleic Acid Database (NDB ID# URL050; Berman *et al.*, 1992).

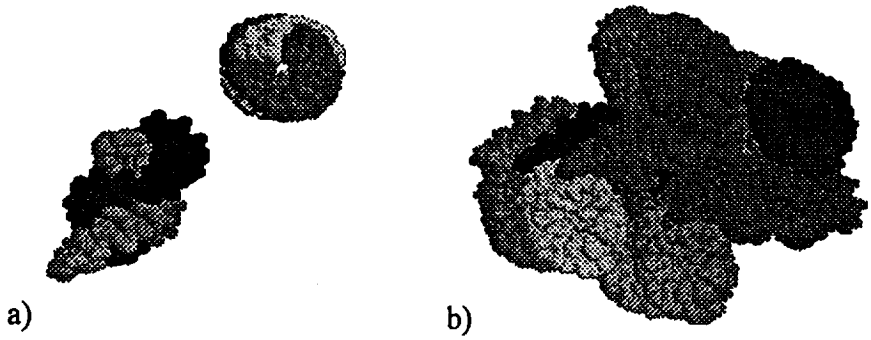

Figure 13.1: Molecular graphics rendering of the UU-dodecamer RNA (generated using Rasmol (v. 2.6) by Roger Sayle: a) asymmetric unit, and b) unit including symmetry-related molecules.

In the Todd lab at the University of Colorado at Boulder, the UU-dodecamer was used as a model oligonucleotide for the development and testing of novel crystallization techniques: osmotic dewatering and step osmotic dewatering (Lee, 1997; Lee *et al.*, 1998; Lee *et al.*, 1997). These techniques enable the experimentalist to kinetically control the dewatering rate from the crystallization solution by manipulating the concentration gradient across a reverse osmosis membrane. A transport model for the osmotic dewatering process was successfully developed (Lee *et al.*, 1997). By kinetically adjusting the dewatering rate, Lee and coworkers were able to reduce the number of crystals obtained while increasing crystal size. Diffraction quality of the crystals grown by osmotic dewatering was comparable to those grown by the more traditional hanging drop and sitting drop methods, which were used in solving the crystal structure of the UU-dodecamer (Lee *et al.*, 1998; Lietzke *et al.*, 1996b).

13.2.4 Purification and Crystallization Experience with the UU-dodecamer

The UU-dodecamer RNA was used as the model oligonucleotide in the present author's M.S. thesis work (Cape, 1997). It was shown that very closely related impurities (5'-phosphorylated RNA dodecamer) could be purified away from the target molecule (5'-hydroxylated RNA dodecamer) using high temperature anion-exchange HPLC (Cape *et al.*, manuscript in preparation). However, crystallization showed no promise as a step to separate the two closely related RNAs. They co-crystallized in proportions essentially identical to those originally in the crystallizing solution, although with a clear decrease in the quality of crystals formed as the fraction of impurity increased (Cape *et al.*, manuscript in preparation).

13.2.5 *In vitro* Transcription Experience with the UU-dodecamer

Optimisation of the *in vitro* transcription of RNA oligonucleotides using engineering approaches received substantial investigation in the Davis lab at the University of Colorado (Marble and Davis, 1995; Kern, 1997; Kern & Davis, 1997; Kern & Davis, 1999; Young *et al.*, 1997; Davis & Breckenridge, 1999). The UU-

Dodecamer was a key model oligonucleotide in these pursuits. Strategies investigated included engineering models of the transcription process, and the immobilization and recovery of the DNA template and the T7 RNA polymerase.

13.2.6 Literature Review and Theoretical Background

Researchers have used a variety of approaches to further the elucidation of biomacromolecule crystallization. One approach has been to employ the techniques of static light scattering (SLS) and dynamic light scattering to investigate thermodynamic and transport properties of crystallizing solutions of proteins (George and Wilson, 1994; Rosenbaum and Zukoski, 1996; Muschol and Rosenberger, 1995). Using the SLS analytical technique described below, George and Wilson (1994) measured the osmotic second virial coefficient, B_{22}, for a number of proteins in both crystallizing and non-crystallizing solutions. They observed that solution conditions that favored the growth of protein crystals had small, negative values of B_{22} that fell in a narrow range. This narrow range, with values between -1×10^{-4} and -8×10^{-4} mol mL g^{-2}, they termed the "crystallization slot". Solutions with large negative values of B_{22} led to the formation of amorphous precipitates, while those with positive values of B_{22} resulted in neither crystals nor precipitates. The empirical validity of the crystallization slot has been confirmed for some 20 different proteins (George *et al.*, 1997).

Zukoski and coworkers have provided a more theoretically rigorous explanation of Wilson's crystallization slot (Rosenbaum and Zukoski, 1996). Using simple fluid theory, they successfully predicted the phase boundary of lysozyme. They modeled the protein interactions using the adhesive hard sphere potential, a model successfully used in colloid science. Although this model provides an over-simplified description of the complex interactions that can occur in macromolecule crystallization, it nonetheless is a robust correlation that is applicable to a wide variety of macromolecules ranging from inorganic to biological (Rosenbaum *et al.*, 1996).

The osmotic second virial coefficient, B_{22}, is a dilute solution parameter, which empirically accounts for non-ideality in solutions and qualitatively provides a measure of two-body (for example, protein-protein) interactions. Positive values of B_{22} indicate that repulsive forces between the solute molecules under consideration dominate in a particular solvent, which can then be characterized as a "good solvent". The solute-solvent interactions are favored over the solute-solute interactions in this case. Negative values of B_{22} indicate that attractive forces are dominant between the same solute molecules, and the solvent can then be described as a "poor solvent".

Solutes which have molecular dimensions smaller than $\lambda/20$, where λ is the wavelength of the incident light, scatter light isotropically. In this case, the simplified Rayleigh equation given by Kratochvil (1987) can be used to interpret the SLS data.

$$\frac{Kc}{R_\theta} = \frac{1}{M_W} + 2B_{22}c$$

where K is an optical constant, c is the solute concentrate, R_θ is the excess Rayleigh ratio measured at angle θ, M_W is the molecular weight of the solute, and N_A is Avogadro's number. The optical constant, K, is given by

$$K = \frac{4\pi^2 n_o^2 (dn/dc)^2}{N_A \lambda^4}$$

where n_o is the solvent refractive index, and dn/dc is the refractive index increment. Plots of Kc/R_θ vs c (known as Debye plots) at a given detection angle (usually 90°) yield the molecular weight, M_W, from the intercept and the osmotic second virial coefficient, B_{22}, from the slope of the resulting linear SLS data.

A review of the literature quickly shows that 2-methyl-2,4-pentanediol (MPD) is the overwhelming precipitant of choice in oligonucleotide crystallization. However, Baeyens *et al.* (1994) have proposed that polyethylene glycol with a low molecular weight distribution (PEG-400) may be a good alternative to MPD, especially for crystallizing RNA oligomers. This begs the question of what the precise role is that polyols play in nucleic acid oligomer crystallization. The role that divalent cations play in oligonucleotide crystallization has been further clarified recently. McFail-Isom *et al.* (1998) showed that divalent cations interact favorably with the π-systems of nucleic acid bases. Such cation-π interactions have been known to contribute to the stability of protein native states and to the stability of protein-ligand complexes, but this is the first identification of such interactions in oligonucleotide structures. Among noncovalent interactions, cation-π bonds are thought to be among the strongest.

13.2.7 Experimental Approach

To better understand the solution behavior and crystallization mechanisms of the UU-dodecamer, the general approach outlined here was taken. Solubility and crystallization experiments were conducted to determine the effect of individual solution components on the solubility and crystallization of the dodecamer. Dynamic light scattering was used to measure the size of the dodecamer aggregates in solution under a range of conditions and to monitor the effect on dodecamer aggregate size and scattering intensity as the concentration of a given solution component (e.g. Mg^{2+}) was increased. Static light scattering was used to thermodynamically characterize solutions in terms of the osmotic second virial coefficent and to measure the effect on solution thermodynamics when given solution components were varied. Finally, the coordinates of solvent ions in the crystal structure of the UU-dodecamer were assessed.

13.3 MATERIALS AND METHODS

13.3.1 Solution Preparation and Handling

All the reagents used in carrying out the research described in this chapter were purchased from accepted suppliers (such as Sigma, Fisher, Mallinckrodt, etc.) except the T7 RNA polymerase which was generously provided by Art Pardi from an in-house production process. The high-quality water used in this research was produced using a Barnstead reverse osmosis and deionizing water purification system

(ROpure LP and NANOpure II). As a final step, the water was filtered through a 0.2 μm hollow fiber filter to give high-quality water designated as "DI H_2O" (deionized water) or through a 10,000 molecular weight cut-off ultrafilter in-line with another 0.2 μm hollow fiber filter to give "RDI H_2O" (ribonuclease-free water). RNA samples and any other solutions to be used in contact with RNA samples were prepared using RDI H_2O. Latex gloves were used whenever handling RNA samples or any solutions that would come in contact with RNA samples in order to avoid contamination with ribonucleases.

13.3.2 UU-dodecamer Production and Purification

The RNA dodecamer with primary sequence 5'-GGCGCUUGCGUC-3', was produced from a synthetic DNA template by the solution phase *in vitro* transcription technique using T7 RNA polymerase (Milligan *et al.*, 1987; Milligan and Uhlenbeck, 1989). It was purified and analyzed by high-temperature anion-exchange (NucleoPac PA-100, Dionex Inc.) HPLC. The 5'-hydroxylated form was derived from the 5'-phosphorylated transcription product by CIP (calf-intestine alkaline phosphatase, Boehringer Mannheim, Indianapolis) digestion prior to the final HPLC purification step. HPLC fractions containing the high purity RNA and a high salt content from the elution gradient were desalted by ultrafiltration using a stirred cell (Amicon, Model 8050) fitted with a 1000 molecular weight cut-off membrane (Amicon, YM1). Purified and desalted RNA samples were concentrated to dryness on a SpeedVac (Savant Instruments), then reconstituted to the desired volume with RDI H_2O, and as a final step, 0.22 μm filtered (Amicon, Micropure Separator) into the storage tube. Final UU-dodecamer purity was typically ≥95%. Details of the production and purification protocols are given in the appendix.

13.3.3 Solubility and Crystallization Experiments

Solubility and crystallization experiments were carried out in multi-well crystallization plates. A pseudo-batch hanging drop technique, in which the drop and reservoir solutions contained all the same components at the same concentrations except for the RNA in the drop, was used to determine solubility limits of the RNA under a range of solution conditions. Hanging drop vapor diffusion, in which a concentration gradient initially exists between the drop and reservoir solutions causing the drop to dewater to equilibrium with the reservoir and thereby concentrate the RNA in the drop, was used in attempts to crystallize the RNA under a range of solution conditions. Drop volumes were typically 8 μL for the solubility experiments and 12 μL for the crystallization experiments (in which a four-old dewatering of the drop was usually sought) with reservoir solution volumes of 1 mL in both cases. Drop volumes could range between 6 μL and 16 μL in some cases. Digital images of precipitate and crystals were obtained using a CCD camera (***Manufacturer, Model***) connected to a Macintosh G3 PowerPC. Detailed protocols for setting hanging drop experiments are available in the appendix.

13.3.4 Light Scattering Experiments

Light scattering (LS) experiments (both static and dynamic) were conducted using a Brookhaven Instruments Corp. (BIC) system (BI-200SM goniometer and BI-

9000AT digital correlator with a 532nm vertically polarized solid state laser). For dynamic light scattering (DLS) experiments, the viscosity of water was used as an adequate approximation for the viscosity of the aqueous solutions used as solvents for the oligonucleotide. In DLS experiments used to monitor the effect due to an increasing concentration of a given component (e.g. Mg^{2+}), small aliquots of solvent (typically microliters) containing a high concentration of the target component (typically 2 M to 4 M) were serially added to the oligonucleotide containing sample (typically 1 mL in initial volume) such that dilution of the oligo was minimal. In static light scattering (SLS) experiments, data as a function of oligonucleotide concentration was collected by serially diluting the sample from a high concentration to a low concentration with solvent. DLS measurements were performed on the highest and lowest SLS concentrations. Measurements of the oligonucleotide concentration by UV-Spec were also performed on the highest and lowest SLS concentrations in order to adjust the concentrations during analysis if necessary. The LS instrument was calibrated with toluene; the Rayleigh ratio for toluene of 2.78×10^{-5} cm^{-1} at 532 nm was interpolated using an inverse fourth order fit to published Rayleigh ratios of toluene at several different wavelengths (Coumou *et al.*, 1964; Kaye & McDaniel, 1974; BIC manual). Absolute Rayleigh ratios were determined from the excess scattering intensities relative to toluene. Analysis of the SLS data was conducted using the Microsoft Excel 97 spreadsheet program described in the appendix. Since empirically determined *dn/dc* values for the oligonucleotide solutions were not available and could not be accurately measured with the resources available to this researcher, the *dn/dc* values in the SLS calculations were adjusted to give the molecular weights expected from the DLS measurements of the effective diameter of the oligonucleotide in solution. All solutions used in light scattering experiments were filtered through 0.02 um syringe filters (Whatman, Anatop 10 and 25) to remove dust and particulates. Tubes, pipet tips and any other lab equipment that contacted LS solutions were subjected to rigorous cleaning protocols (see appendix). Unless otherwise noted, all light scattering experiments were conducted at room temperature and an angle of 90°. The details of the precise solution conditions and compositions used in these experiments are given (when necessary and relevant) with the results. Details of the DLS and SLS protocols are given in the appendix.

13.4 RESULTS

Prompted by the observation of a crystallization slot for proteins (George & Wilson, 1994), this researcher asked whether such a crystallization slot also existed for oligonucleotides and whether it would be characterized by the same numerical limits. In the pursuit of the answers to these questions, some interesting and unexpected observations were made regarding the solution behavior and crystallization mechanism of the UU-dodecamer. These observations will be discussed in this chapter and the crystallization slot topic will be left for Chapter 4.

13.4.1 Experiments with original crystallization conditions

Figure 3.2 shows several UU-dodecamer crystals obtained under solution conditions very similar to those used by the Kundrot group in solving the structure. The solubility of the dodecamer under these conditions (10% MPD, 25 mM $MgCl_2$,

400 mM $NH_4(OAc)$, 50 mM Na Cacodylate, pH 7.0, 37°C) is known to be just above 0.40 mg/mL (Lee, 1997; Lee *et al.*, 1997). Several light scattering experiments were attempted under these solution conditions with RNA concentrations between 0.2 and 0.4 mg/mL. Success was limited and the experiments not very

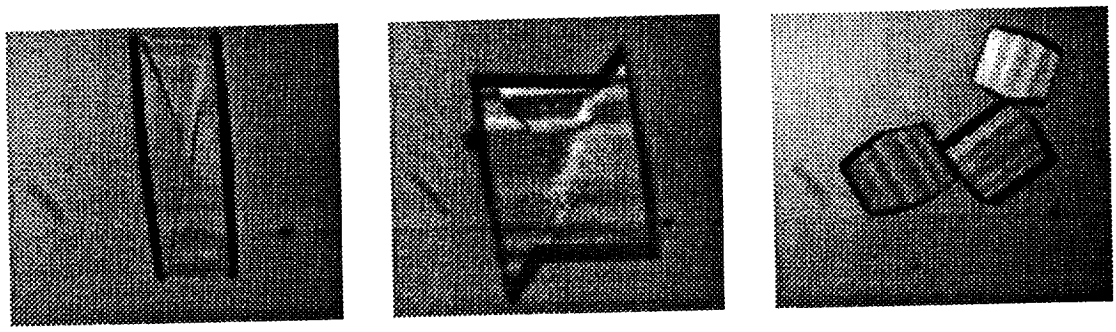

Figure 13-2: UU-dodecamer RNA crystals grown by hanging drop vapor diffusion at 37°C. Drops initially containing 0.33 mg/mL RNA, 2.5% MPD, 6.25 mM $MgCl_2$, 100 mM $NH_4(OAc)$, 12.5 mM Na Cacodylate, pH 7.0 were set against reservoir solutions four-fold concentrated in all components except RNA which was not present in the reservoir.

reproducible because of a number of difficulties encountered. Due to the very low RNA solubility, there was a significant amount of uncertainty in the actual RNA concentrations in solution; accurate values of concentration are necessary to correctly analyze the LS data. In addition, the very low RNA solubility resulted in very low scattering intensities, which in fact did not meet Wilson's criteria for statistically valid light scattering data: the intensity of light scattered from the lowest concentration sample should be at least twice that of the background solvent (W. W. Wilson, personal communication). At such small excess intensities and small differences in intensities between concentrations, the relative effects of dust and other particulates in solution and imperfections in the glass vials are magnified and lead to large scatter in the data. In spite of these difficulties, the order of magnitude of the measured B_{22} values was found to be consistently reproducible (about -5×10^{-2} mol mL g^{-2}). This large, negative osmotic second virial coefficient is about two orders of magnitude more negative than the lower limit of the protein crystallization slot.

13.4.2 Search for alternative crystallization conditions

Alternative crystallization conditions that might be more conducive to light scattering experiments were pursued by setting up a number of hanging drop vapor diffusion crystallization screens of a wide variety of solution compositions. Crystals were obtained at room temperature from solutions containing 4.0 mg/mL RNA, 5-10% PEG-400, 10-20 mM NaCl, 25 mM $MgCl_2$, and 50 mM Na Cacodylate, pH 7.0 at equilibrium. Figure 13-3 shows some representative crystals obtained under these conditions. It appeared that the UU-dodecamer RNA solubility was higher than in the original, published crystallization conditions. However, pseudo batch, hanging drop solubility experiments showed otherwise. In these partial factorial experiments, the concentrations of the solution components were varied as follows: 1 to 3 mg/mL

RNA; 0 to 25 mM $MgCl_2$; 0, 10 and 20 mM NaCl; 0, 25 and 400 mM ammonium acetate; and 0 to 10% PEG-400. In each case, the experiments were conducted at room temperature and the solutions were buffered with 50 mM Na Cacodylate, pH 7.0. Figure 3.screen shows the results for the first solubility screen, in which it

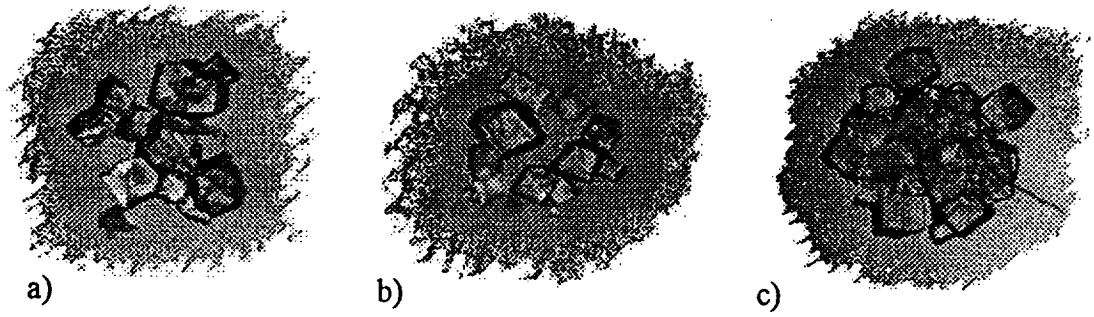

Figure 13-3: UU-dodecamer RNA crystals grown by hanging drop vapor diffusion at room temperature under alternative solution conditions. Equilibrium conditions (after two-fold dewatering of the drops): a) 5% PEG-400, 10 mM NaCl; b) 5% PEG-400, 20 mM NaCl; and c) 10% PEG-400, 20 mM NaCl. All drops also contained (at equilibrium) 4.0 mg/mL RNA, 25 mM $MgCl_2$, 50 mM Na Cacodylate, pH 7.0.

became apparent that PEG-400 was not primarily responsible for precipitating or crystallizing the RNA. This goes against the traditional designation of components like PEG and MPD as the "precipitant" in biological macromolecule crystallization solutions. When no PEG-400 was present, showers of tiny crystals still formed. However, PEG-400 does still play at least a secondary precipitating effect. As can be seen in Figure 3.screen, when PEG-400 is added and its concentration increased the precipitated mass in the drops increases, although it appears to be more amorphous. Since PEG-400 is not the primary precipitant, the question naturally was asked, "Which component is?" The divalent magnesium cation was quickly targeted as the culprit.

This first solubility screen turned out to be a defining experiment and significantly changed the focus of the research and the types of questions asked. Subsequent solubility and crystallization screens (as well as light scattering experiments) focused on the role of Mg^{2+}. In most of the solubility conditions tested, showers of small crystals (largest dimensions on the order of ≤ 10 μm) were obtained

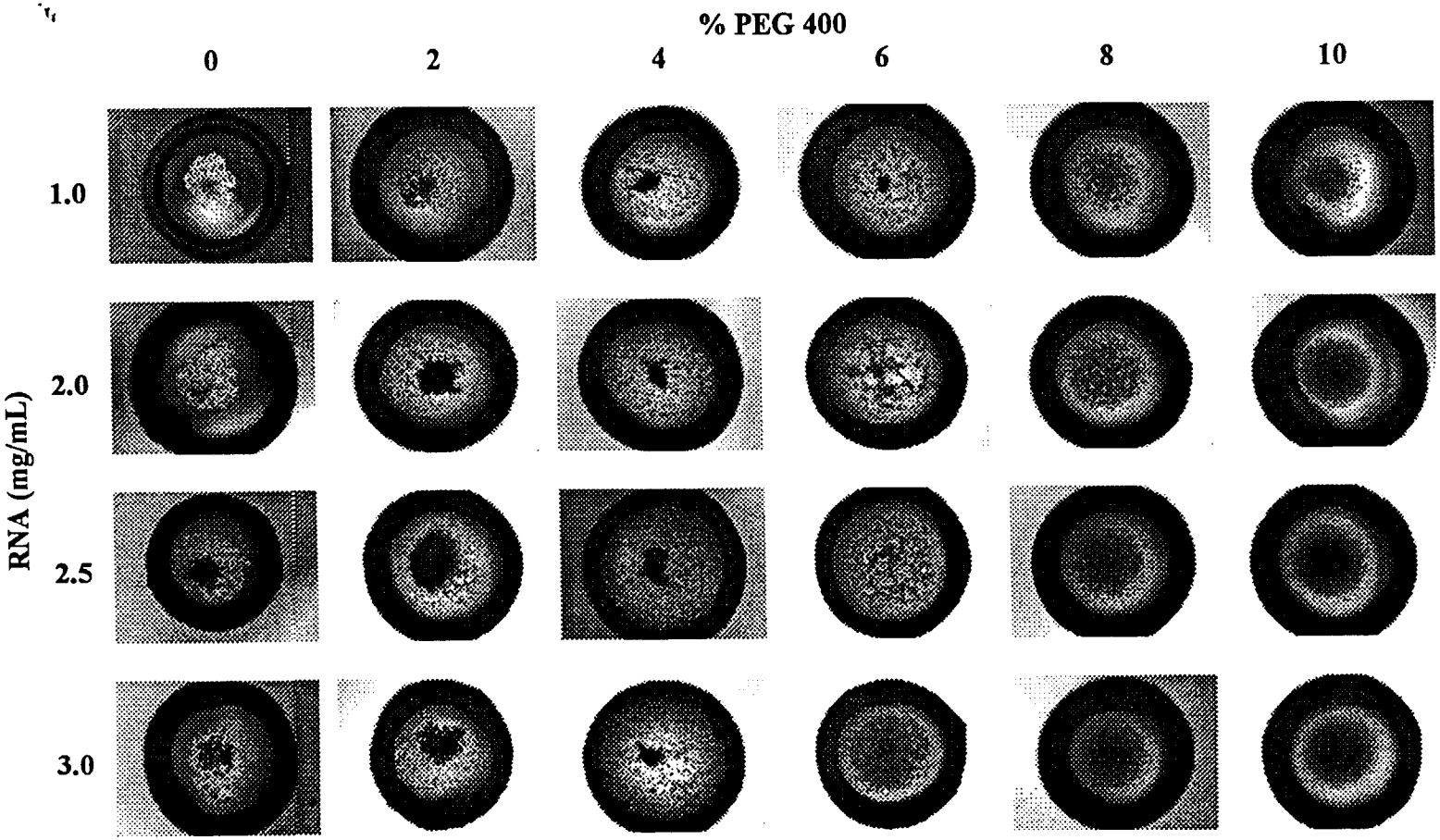

Figure 13-4: Pseudo-batch hanging drop solubility screen of the UU-dodecamer RNA at room temperature. All drops also contained 20 mM NaCl, 25 mM $MgCl_2$, 50 mM Na Cacodylate, pH 7.0.

even if in many cases amorphous and/or crystalline precipitate occurred alongside the crystals. The experiments showed that the solubility of UU-dodecamer RNA was critically dependent on the $MgCl_2$ concentration but not as strongly dependent on the other solution components. In addition, a previous observation that ammonium acetate appeared to make the RNA more soluble was confirmed.

13.4.3 Dynamic light scattering experiments

More evidence for the critical role of Mg^{++} was pursued by using dynamic light scattering to monitor the aggregation state of the UU-dodecamer RNA as a function of $MgCl_2$ concentration. DLS experiments at 0, 2.5 and 7.5% PEG-400 were carried out as a function of $MgCl_2$ concentration. The experiments were conducted at room temperature with the other solution conditions as follows: ~2 mg/mL RNA, 20 mM NaCl, and 50 mM Na Cacodylate, pH 7.0. Figure 13-5 below is representative of the resulting effective molecular diameters versus Mg^{++} concentration for all three experiments (the complete results for the three experiments can be found in the appendix). The effective diameter of the RNA in solution increases only slightly with $MgCl_2$ concentration until a critical point is reached where large aggregates begin to form. This critical point is essentially insensitive to PEG-400 concentration: in all three experiments large aggregates began to form at $MgCl_2$ concentrations in the narrow range of 12 to 15 mM. The slight increase in effective diameter before the critical $MgCl_2$ concentration is reached may be due to the formation of embryos below the critical nucleus size (such as dimer of duplexes, etc.). The DLS experiments confirm the observations from the solubility experiments. In addition, DLS experiments were performed in which $MgCl_2$ was titrated into an RNA solution (~2 mg/mL) in pure water (not shown). In this case, the effective diameter increases more strongly with $MgCl_2$ concentration, but above 10 mM the formation of very large aggregates is quite pronounced indicating a critical concentration value which is consistent with the other DLS experiments mentioned above.

13.4.4 Static Light Scattering Experiments

With these DLS experiments as guidelines, SLS experiments were designed and conducted in which the problems of very low solubility and low scattering intensity were not significant. In all the crystallizing conditions identified for the UU-dodecamer, the $MgCl_2$ concentrations were higher than the critical concentration identified in the DLS experiments. Since SLS experiments cannot be carried out with

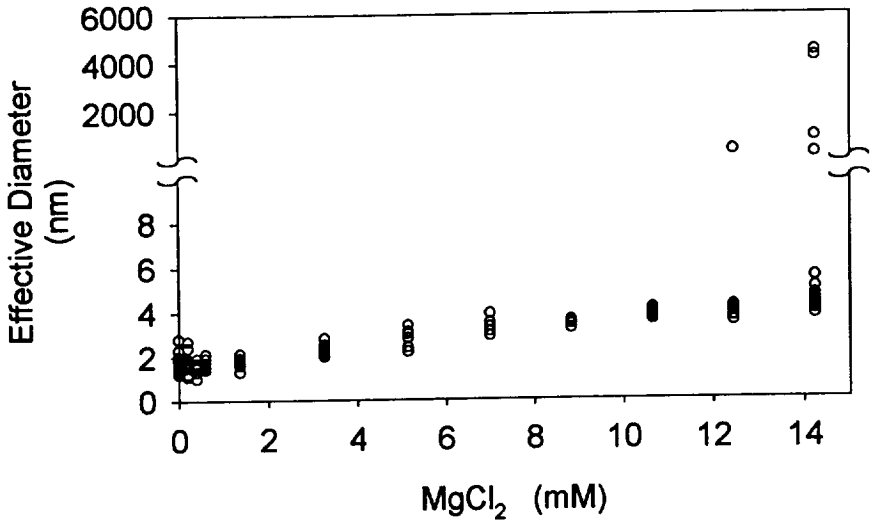

Figure 13-5: DLS results giving effective diameter of the UU-dodecamer as a function of $MgCl_2$ concentration in a solution containing ~2 mg/mL RNA, 2.5% PEG-400, 20 mM NaCl, and 50 mM Na Cacodylate, pH 7.0.

$MgCl_2$ concentrations above the critical concentration of 12 to 15 mM, the SLS results unfortunately do not represent actual crystallization conditions. Instead they represent gradual steps in the solution conditions toward the limit of a crystallization solution; such solutions might be called "pre-crystallization" solutions. In these experiments, the osmotic second virial coefficient, B_{22} was determined as a function of two PEG-400 concentrations (0% and 7.5%) and three $MgCl_2$ concentrations (0 mM, 5 mM and 10 mM). Before and after each SLS experiment, the aggregation state of the RNA was monitored by DLS in order to guide and justify the assumptions made regarding the molecular weight of the RNA in solution.

13.4.4.1 In the absence of PEG-400

Figure 13-6 is a summary of the Debye plots for different $MgCl_2$ concentrations, all in the absence of PEG-400. For these plots a *dn/dc* value of 0.19 mL/g was used in calculating the Debye data from the SLS data (the excess scattering intensities). This value of *dn/dc* was selected for a couple of reasons. In the published literature, directly measured values of *dn/dc* (at wavelengths of 514.5 nm and 546 nm) for large DNAs (with molecular weights on the order of 10^6 Da) vary between about 0.18 mL/g in water or solutions of a few millimolar NaCl and buffer components to about 0.17 mL/g in solutions of 0.2 M NaCl (Jolly & Eisenberg, 1976; Kam *et al.*, 1981). The *dn/dc* at 546 nm for native RNA of bacteriophage MS 2 has been reported to be a little less than 0.17 mL/g (Nieuwenhuysen *et al.*, 1981). Compared to these published values, 0.19 mL/g is not an unreasonable selection. In addition, as shown below, using this value of *dn/dc* in the analysis of the SLS data generates molecular weights at the different $MgCl_2$ concentrations that correlate well with the corresponding effective diameters measured by DLS.

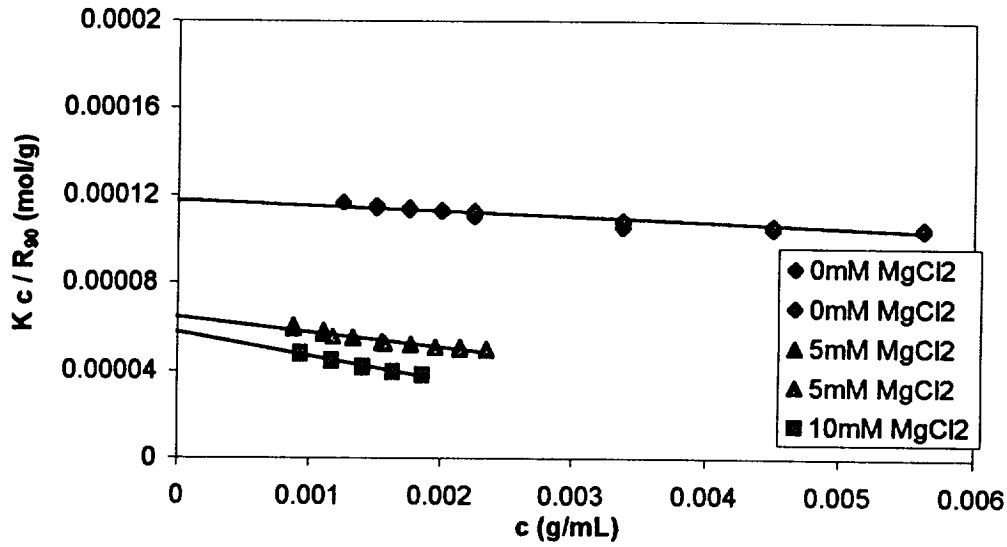

Figure 13-6: Debye plots for the UU-dodecamer at different $MgCl_2$ concentration in the absence of PEG-400. In all cases, the solutions contained 20 mM NaCl, and 50 mM Na Cacodylate, pH 7.0. A value of *dn/dc* = 0.19 mL/g was used in the SLS data analysis. The differently shaded data points at 0 mM and 5 mM $MgCl_2$ represent SLS data collected on separate occasions with different ranges of RNA concentration but otherwise under the same experimental conditions. In the SLS analysis, the data at each $MgCl_2$ concentration were pooled.

Several salient features of Figure 13-6 must be noted. One is the increasingly negative slope (i.e. increasingly negative B_{22}) of the Debye lines with increasing $MgCl_2$ concentration. Another is the decreasing intercept (i.e. increasing molecular weight). A large increase in molecular weight (M_W) occurs from 0 to 5 mM $MgCl_2$ while a smaller increase occurs between 5 and 10 mM $MgCl_2$. A final observation is that SLS data collected on separate occasions with different ranges of RNA concentration but otherwise under the same experimental conditions are internally consistent and demonstrate the reliability and reproducibility of the data itself and of the experimental techniques used in data collection.

Figure 13-7 shows B_{22} as a function of $MgCl_2$ concentration (determined from the slopes of the Debye lines in Figure 13-6). B_{22} decreases linearly with a slope of -4.1×10^{-4} mol mL g^{-2} mM^{-1}. At 0 mM $MgCl_2$ the data indicates that the UU-dodecamer exists as a duplex, but when $MgCl_2$ is present it aggregrates as a dimer of duplexes. It should be noted that fitting the data to a duplex versus a dimer doubles the absolute value of the B_{22}.

Figure13-8.dls_0-peg shows M_W as a function of $MgCl_2$ concentration (determined from the intercepts of the Debye lines in Figure 3.sls_0-peg). This representation of the data confirms that M_W increases from roughly that of a duplex (7584 Da) at 0 mM $MgCl_2$ to roughly that of a dimer of duplexes (15168 Da) and higher at 5 and 10 mM $MgCl_2$. The effective diameters of the UU-dodecamer RNA in solution were measured by DLS for the highest and lowest concentrations used in

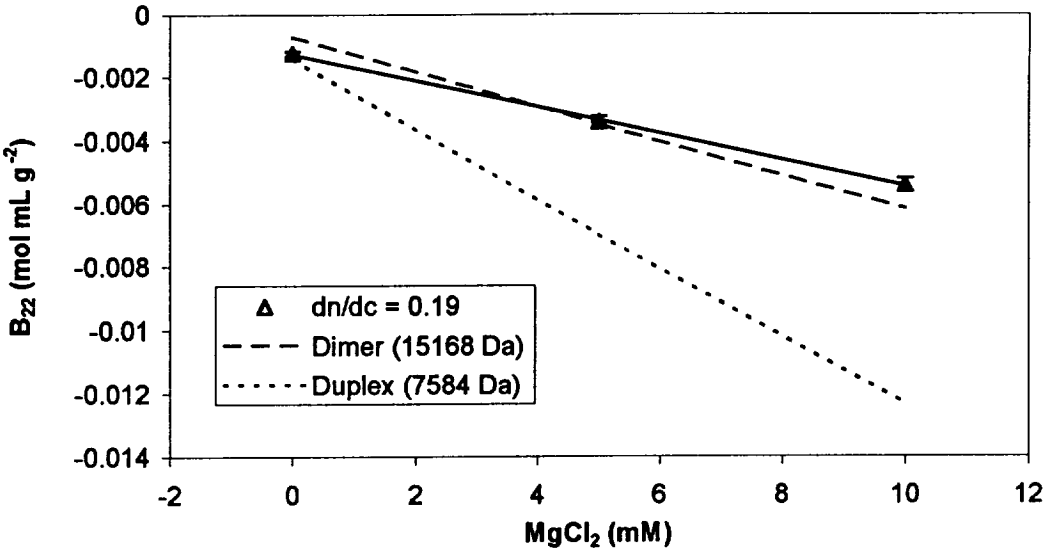

Figure 13-7: B_{22} as a function of $MgCl_2$ concentration for the UU-dodecamer in the absence of PEG-400. Determined from the Debye plots in Figure 3.sls_0-peg. The dashed lines indicate the values of B_{22} that would result if *dn/dc* were freely adjusted in each case to give the molecular weight of a duplex (lower limit) or a dimer of duplexes (upper limit). Error bars represent the standard error.

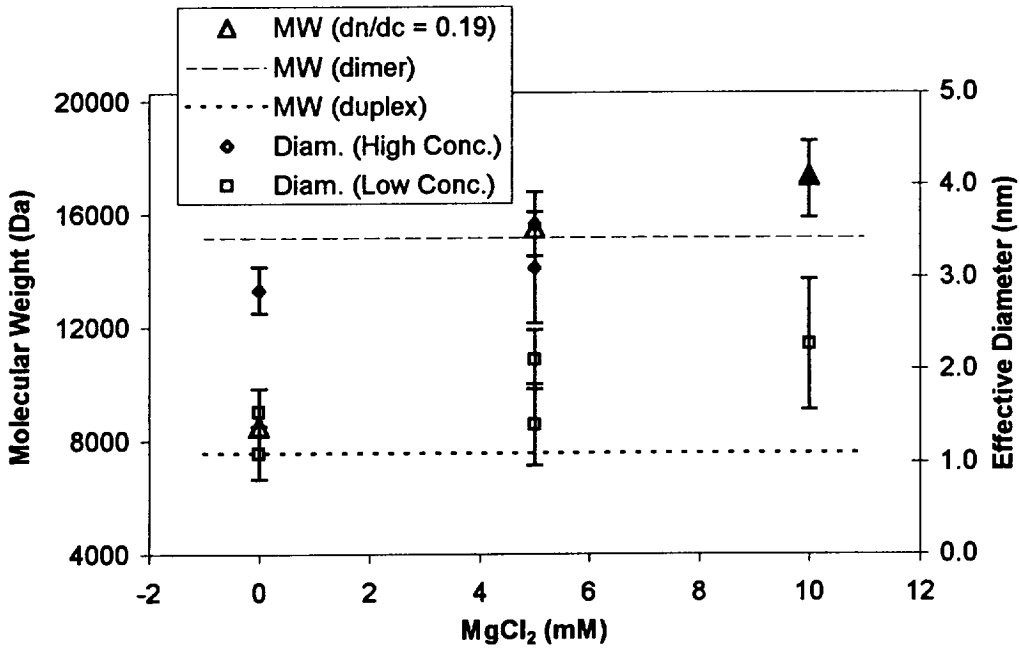

Figure 13-8: Primary axis: M_W as a function of $MgCl_2$ concentration for the UU-dodecamer in the absence of PEG-400. Determined from the Debye plots in Figure 13-6. The dashed lines indicate the molecular weight of a duplex (lower limit) or a dimer of duplexes (upper limit). Secondary axis: DLS measured effective diameters of the UU-dodecamer in the highest and lowest RNA concentration samples used in the SLS experiments. Error bars represent the standard deviation of the mean of multiple effective diameter measurements.

each SLS experiment. Figure 13-5 includes these diameters on a secondary axis and correlates them with the molecular weights obtained from the SLS experiments. Molecular weight and effective diameter track each other well as they both increase with increasing $MgCl_2$ concentration. For the purpose of making the correlation, it was assumed that the effective diameter measured at 0 mM $MgCl_2$ and the lowest RNA concentration represents that of the single duplex. This assumption is valid since it is known that the UU-dodecamer forms a duplex as the majority species in a buffered salt solution (Jucker Franzusoff, 1995; Jucker & Pardi, 1995). It is clear from Figure 3.dls_0-peg that in the course of most of the SLS experiments (particularly in the presence of $MgCl_2$ and/or at high RNA concentration) the aggregation state of the UU-dodecamer changed (probably from dimer of duplexes to duplexes) as the RNA samples were serially diluted.

13.4.4.2 In the presence of PEG-400

Figure 13-9 peg is a summary of the Debye plots for different $MgCl_2$ concentrations, all in the presence of 7.5% PEG-400. For these plots a *dn/dc* value of 0.17 mL/g was used in calculating the Debye data from the SLS data (the excess scattering intensities). This value of *dn/dc* was selected because it maintains the same good correlation between molecular weight and effective diamater (see Figure 13-9 below) as drawn when no PEG-400 was present in solution. And 0.17 mL/g is perfectly reasonable compared to the published values mentioned previously.

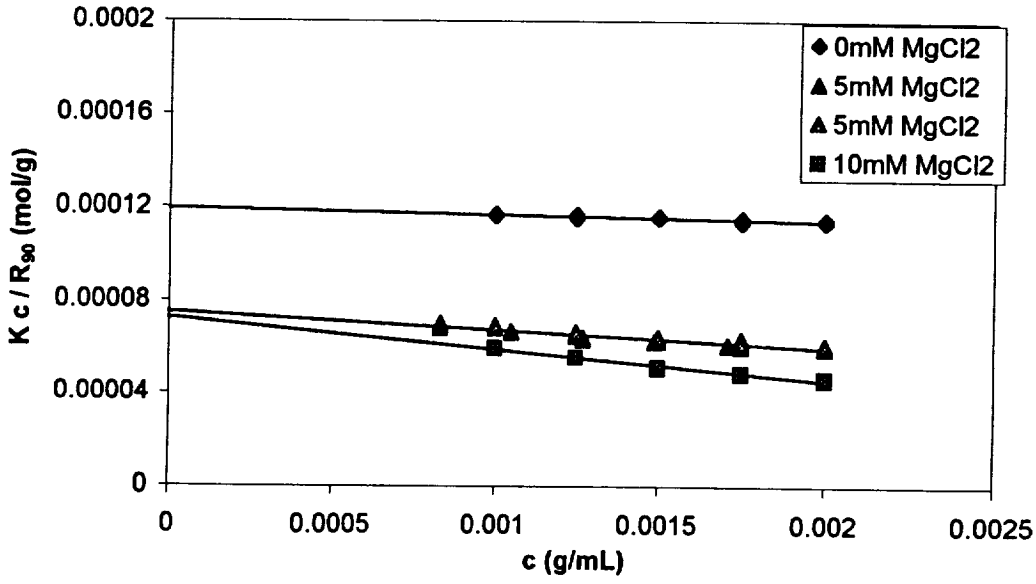

Figure 13-10: Debye plots for the UU-dodecamer at different $MgCl_2$ concentration in 7.5% PEG-400. In all cases, the solutions contained 20 mM NaCl, and 50 mM Na Cacodylate, pH 7.0. A value of *dn/dc* = 0.17 mL/g was used in the SLS data analysis. The differently shaded data points at 5 mM $MgCl_2$ represent SLS data collected on separate occasions with slightly different ranges of RNA concentration but otherwise under the same experimental conditions. In the SLS analysis, the data from these "repeated" experiments were pooled.

Again, salient features in Figure 13-10 include the increasingly negative slope (i.e. increasingly negative B_{22}) of the Debye lines and the decreasing intercept (i.e. increasing molecular weight) with increasing $MgCl_2$ concentration. Superficially, Figure 13-6 and Figure 13-10 appear very similar which suggests a minor or negligible effect due to PEG-400. However, some subtle differences do exist. These will be emphasized in the direct comparison below between results obtained in the absence versus in the presence of PEG-400. But to give a foretaste, a large increase in molecular weight (M_W) still occurs between 0 and 5 mM $MgCl_2$, but with a somewhat smaller magnitude than in the absence of PEG-400. Likewise, a small increase occurs between 5 and 10 mM $MgCl_2$, but with a difference small enough to possibly be negligible. Once again, the collection of SLS data on separate occasions with slightly different ranges of RNA concentration but otherwise under the same experimental conditions demonstrate the internal consistency, reliability and reproducibility of the data itself and of the experimental techniques used in data collection.

Figure 13-11 shows B_{22} as a function of $MgCl_2$ concentration (determined from the slopes of the Debye lines in Figure 13-10). B_{22} decreases linearly with a slope of -5.5×10^{-4} mol mL g^{-2} mM^{-1}. As observed in the absence of PEG-400, at 0 mM $MgCl_2$ the data indicates that the UU-dodecamer exists as a duplex, but when $MgCl_2$ is present it forms higher molecular weight aggregrates that approximate dimer of duplexes.

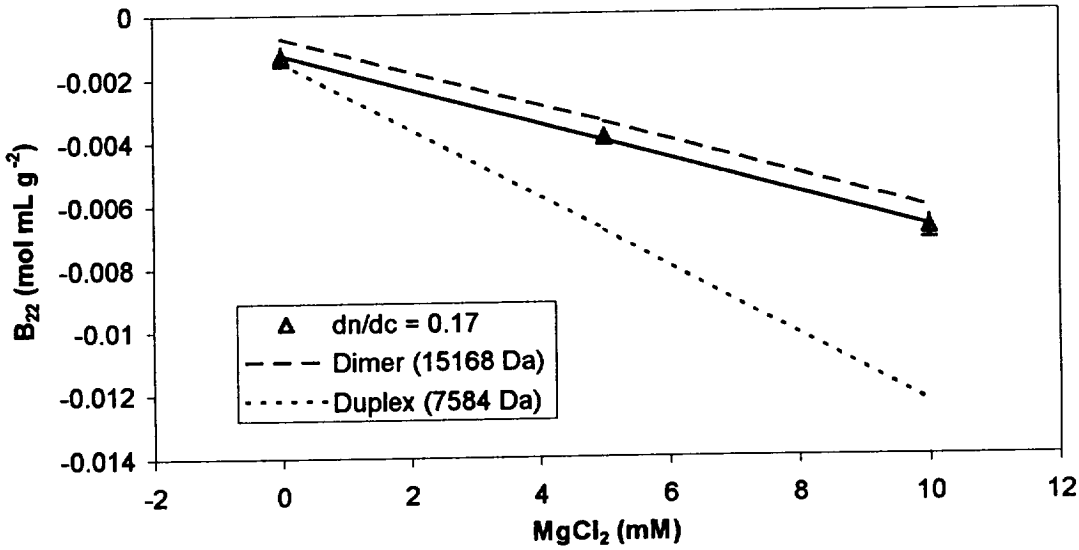

Figure 13-11: B_{22} as a function of $MgCl_2$ concentration for the UU-dodecamer in 7.5% PEG-400. Determined from the Debye plots in Figure 13-10. The dashed lines indicate the values of B_{22} that would result if *dn/dc* were freely adjusted in each case to give the molecular weight of a duplex (lower limit) or a dimer of duplexes (upper limit). Error bars represent the standard error.

Figure 13-12 shows M_W as a function of $MgCl_2$ concentration (determined from the intercepts of the Debye lines in Figure 13-10). This representation of the

data confirms that M_W increases from roughly that of a duplex (7584 Da) at 0 mM $MgCl_2$ to that approximating a dimer of duplexes (15168 Da) at 5 and 10 mM $MgCl_2$. As before, the effective diameters of the UU-dodecamer RNA in solution were measured by DLS for the highest and lowest concentrations used in each SLS experiment. Figure 13-10 includes these diameters on a secondary axis and correlates them with the molecular weights obtained from the SLS experiments using the same proportionality or scale as in the absence of PEG-400 (see Figure 13-6). In this case also, molecular weight and effective diameter track each other well as they both increase with increasing $MgCl_2$ concentration.

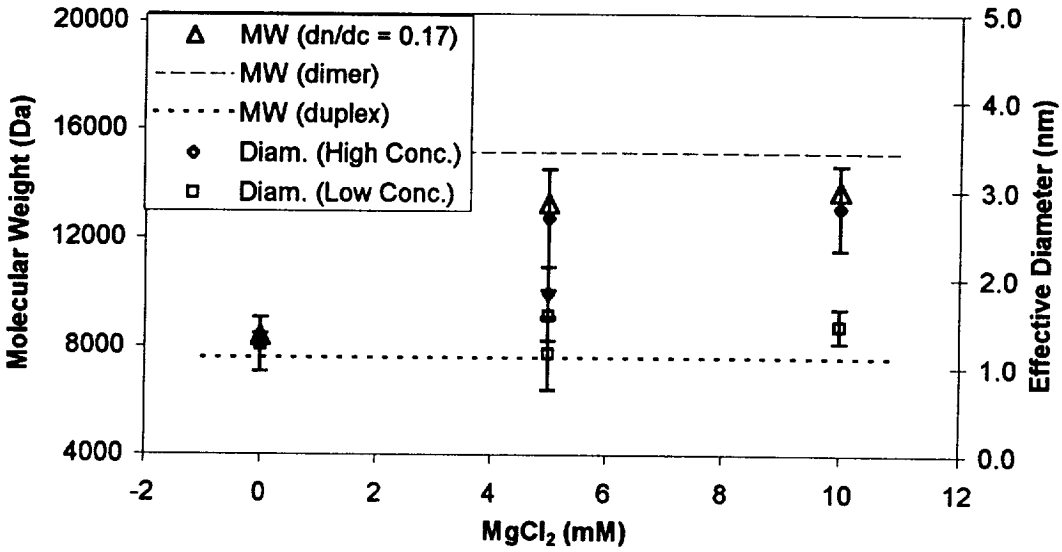

Figure 13-12: Primary axis: M_W as a function of $MgCl_2$ concentration for the UU-dodecamer in 7.5% PEG-400. Determined from the Debye plots in Figure 3.sls_75-peg. The dashed lines indicate the molecular weight of a duplex (lower limit) or a dimer of duplexes (upper limit). Secondary axis: DLS measured effective diameters of the UU-dodecamer in the highest and lowest RNA concentration samples used in the SLS experiments. Error bars represent the standard deviation of the mean of multiple effective diameter measurements.

Once again, it is clear that in the course of the SLS experiments in the presence of $MgCl_2$, the aggregation state of the UU-dodecamer changed somewhat (possibly from dimer of duplexes to duplexes) as the RNA samples were serially diluted. This effect is not as large in the presence of PEG-400 as in the absence of it.

13.4.4.3 Comparison of results with and without PEG-400

Table 3.summary summarizes the numerical results of the light scattering experiments with the UU-dodecamer as a function of $MgCl_2$ in the absence and presence of PEG-400. Both in the absence and presence of PEG-400, the osmotic second virial coefficient is a strong function of $MgCl_2$ concentration but a weak function of PEG-400 concentration. However, PEG-400 enhances the effect on B_{22} by $MgCl_2$ demonstrated by the larger absolute value of the slope of B_{22} versus $MgCl_2$

Table 13.1: Summary of light scattering results for UU-dodecamer in varied $MgCl_2$ and PEG-400 concentrations, determined from 90° Debye plots as in Figure 13-6 and Figure 13-10. Other solution conditions: 20 mM NaCl, and 50 mM Na Cacodylate, pH 7.0.

	0% PEG-400 (dn/dc=0.19 mL/g)				7.5% PEG-400 (dn/dc=0.17 mL/g)			
MgCl2 (mM)	M_W (g/mol)	B_{22} (x10^3) (mol mL g^{-2})	S.E. (x10^3)	d(B_{22})/d([Mg]) (mol mL g^{-2} mM^{-1})	M_W (g/mol)	B_{22} (x10^3) (mol mL g^{-2})	S.E. (x10^3)	d(B_{22})/d([Mg]) (mol mL g^{-2} mM^{-1})
0	8486	-1.26	0.09		8388	-1.31	0.30	
5	15486	-3.43	0.18	-4.1E-04	13284	-3.90	0.25	-5.5E-04
10	17329	-5.40	0.21		13763	-6.81	0.35	

when PEG-400 is present. With increasing $MgCl_2$, the UU-dodecamer RNA aggregrates in solution to some extent as seen by the increase in molecular weight both with and without PEG-400. However, PEG-400 appears to inhibit this aggregration some (at least under the concentration tested) as evidenced by the lower molecular weights measured by SLS and the smaller effective diameters measured by DLS (compare Figure 3-5 and Figure 13-9). PEG-400 also decreases the refractive index increment of the UU-dodecamer in solution.

The SLS results clearly demonstrate that magnesium plays a critically important role in the solution behavior and thermodynamics of the UU-dodecamer and fully confirm the results observed in the crystallization, solubility and DLS experiments.

13.4.5 Assessment of the UU-dodecamer RNA structure coordinate file

The coordinates of solvent atoms in the UU-dodecamer crystal structure were assessed in order to determine whether any might be Mg^{++} ions interacting with the oligonucleotide molecules. Solvent atoms in the coordinate file (NDB entry URL050) are labeled as heteroatoms and identified as the oxygen atom of a water molecule. However, since water molecules and Mg^{++} ions have similar electron densities in the electron density maps generated from X-ray diffraction data, it is difficult to distinguish between them in low-resolution structures (Craig Kundrot, personal communication; Feig & Uhlenbeck, 1999). The UU-dodecamer structure was solved to 2.4Å, which is relatively low resolution.

Conservative geometric criteria for cation-π interactions were defined by McFail-Isom *et al.* (1998). Figure 13-13 displays these criteria. In addition, to the criteria that the distance *d* between the cation and the centroid of the aromatic ring be less than or equal to 5.2 Å and that the angle defined by the positions of the cation, the ring centroid and the base normal be less than 52°, a criterion that is implicit in Figure 3.criteria is that the line between the cation and ring centroid not be obstructed by any other atoms.

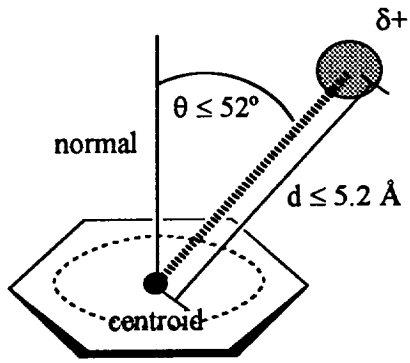

Figure 13-13: Geometric criteria for defining cation-π interactions.

A significant number of the heteroatoms in the UU-dodecamer structure coordinate file (NDB entry URL050) meet the criteria described above, and may, therefore, indeed be Mg^{++} ions instead of water molecules interacting with and stabilizing the tertiary structure of the dodecamer. Most of the heteroatoms identified that are potentially magnesium cations interacting with the nucleic acid bases do so within a given helix, some possibly stabilizing the U-U mismatch pairings and the G-U wobble. However, one heteroatom (labeled HOH69 in the coordinate file) appears to interact between two different helices at their contact point in the crystal lattice. HOH69 appears to interact in a cation-π configuration with the pyrimidine ring of G4 and with U23 in the first helix and with C17 in the second helix. These two helices contact each other at 90°, with the phosphate backbone of one nestled in the minor groove of the other. In addition, a number of traditional lone pair interactions between HOH69 (assuming it is a magnesium cation) and the two helices potentially occur. In fact, this heteroatom was designated by Kundrot and coworkers (Lietzke *et al.*, 1996b) to be one of seven water molecules participating in interhelical contacts. Because of the relatively low resolution (2.4Å) of the X-ray data set, this researcher suggests that HOH69 may instead be a magnesium cation participitating in the interhelical cation-π and lone pair interactions mentioned above.

If HOH69 is indeed a magnesium cation, then maybe it is the reason that $MgCl_2$ has such a strong precipitating effect on the UU-dodecamer. The analysis of the UU-dodecamer coordinate file described above was not exhaustive. Therefore, additional heteroatoms in the structure may fit the cation-π configuration and participate in interhelical contacts. Cation-π bonds, which, as mentioned before, are thought to be among the strongest noncovalent interactions, may explain the critical Mg^{++} dependence observed with the dodecamer. However, without a structure of sufficiently high resolution, Mg^{++} ions cannot be unambiguously identified and this explanation remains a speculative one.

13.5 DISCUSSION

The experiments reported here unambiguously show that Mg^{++} ions play a critical role in the crystallization and the structure of the UU-dodecamer RNA, even though a precise picture of this role has not yet been fully drawn. Metal ions,

particularly magnesium, are known to be critically important in the structural folding of many RNAs and in the catalytic activity of ribozymes (Hermann & Patel, 1999; Holbrook & Kim, 1997). In fact, it has been stated that "[a]ll RNAs require divalent cations for folding and catalysis" (Strobel & Doudna, 1997). The present research suggests that magnesium can also participate in structure formation (particularly tertiary or crystal structure) by providing the driving force for crystal nucleation and growth. Mg^{++} serves as the precipitant (or at least the primary one) in UU-dodecamer crystallization with MPD and PEG-400 playing a secondary role. This complicates somewhat the traditional definition and role of "precipitant" given to chemicals such as MPD or PEG-400, which occur in relatively high concentrations in almost all oligonucleotide crystallization solutions.

Speculation regarding the role of PEG-400 arises from results described above. In the presence of 7.5% PEG-400, the molecular weight and effective diameter diameter of the UU-dodecamer were smaller than in the absence of PEG-400, counteracting the increase in these parameters caused by the addition of $MgCl_2$. At the same time, the effect of $MgCl_2$ on the osmotic second virial coefficient was slightly enhanced by the addition of PEG-400. At the concentrations tested, is PEG-400 playing the role of stabilizer of the UU-dodecamer duplex? Is it competing with the RNA for the metal ion? Shui *et al.* (1998) report that MPD chelates divalent cations. PEG-400 might interact with divalent cations in a similar fashion. ***Metal ions, including magnesium, have been used to coordinate PEGs in the polymerization of pseudo-crown ethers from functionalized polymers*** (Check with Bowman about accuracy of this statement and for references). Therefore, PEG-400 may be chelating Mg^{++} and thereby inhibiting it from bringing UU-dodecamer duplexes together. Or PEG-400 may simply be providing kinetic stability to the RNA solution by providing a steric barrier to the aggregration of individual duplexes. A combination of the two is also a possibility. However, PEG-400 apparently still changes water activity (i.e. solution thermodynamics) and increases the attraction of duplexes for each other as reflected in the more negative second virial coefficients. In this latter effect, PEG-400 may be playing the more traditional role of precipitant, but at the concentrations tested, the other effects dominate.

PEG-400 lowers the refractive index increment, *dn/dc*, of the RNA in solution. Refractive index is a measure of the interaction of light with matter and since light is an electromagnetic wave, the refractive index is a function of the dieletric constants of the media through which light travels. The effect of PEG-400 on *dn/dc* may be due to an interaction between PEG and the RNA, which disrupts the surface charge distribution of the RNA, thereby changing the dielectric nature of the RNA. Glycerol has been observed to decrease the *dn/dc* of a protein, bovine pancreatic trypsin inhibitor (Farnum & Zukoski, 1999). The explanation given by Farnum and Zukoski for this effect appeals to the fact that glycerol increases the refractive index of the solvent, thus decreasing the difference in refractive index between the solvent and the protein. (***Is their explanation adequate?***)

Since this research suggests that, with proper control of the crystallization process, it should be possible to grow large, high quality (i.e. diffraction quality) crystals of the UU-dodecamer without the presence of a traditional precipitant (MPD or PEG-400), the question as to what role these polyols actually have must be asked.

They are ubiquitous in oligonucleotide crystal growth solutions and have commonly been accepted as essential components. But are they really essential components? Are they necessary in some cases but not in others?

DLS measurements on the highest and the lowest concentrations of RNA used in the SLS experiments revealed that the aggregration state of the UU-dodecamer changed during the course of the experiment. This fact suggests that interpreting the SLS results merely in terms of two body interactions may not be strictly accurate. More information or at least more precise information may be obtained by analyzing the SLS data using a quadratic fit. This higher order interpretation gives the third virial coefficient, which is a measure of the three body interaction. Such high order analysis will be presented in Chapter 4.

Assessment of the coordinate file for the UU-dodecamer provides some circumstantial evidence for this researcher's speculation that magnesium cations mediate interhelical interactions and actually drive the formation of interhelical contacts in the growing crystal lattice. However, positive proof of this hypothesis would require growing a diffraction size and quality crystal, preferably without the use of any traditional precipitant such as MPD or PEG-400, and solving the structure to a high enough resolution so that magnesium ions can be positively and unambiguously identified.

This research with the UU-dodecamer RNA begs the question as to whether the results observed here are unique to this molecule or whether they are general characteristics of oligonucleotides (RNA and/or DNA) and their crystallization solutions. To answer this question, similar studies with other oligonucleotide molecules must be conducted. In Chapter 4, such studies and their results are presented along with further analysis of the static light scattering data obtained with the UU-dodecamer.

13.6 CONCLUSIONS

Mg^{++} ions play a critical role in the structure of the UU-dodecamer RNA as demonstrated by the very strong dependence of the following on Mg^{++} concentration: osmotic second virial coefficient, solubility, nucleation and aggregate growth, and crystallization. In this case, Mg^{++} serves the role of "precipitant", and controlling its concentration is at least as important as (and probably more so than) controlling the concentration of the traditional precipitants MPD and PEG. In fact, MPD and PEG are not even necessary for nucleation and crystal growth, and may not be necessary for growing large, diffraction quality crystals of the UU-dodecamer RNA.

Chapter 14

Multivalent Cations and Oligonuceotide Solubility, Osmotic Virial Coefficients and Crystal Growth

Stephen P. Cape

CHAPTER 14

MULTIVALENT CATIONS AND OLIGONUCLEOTIDE SOLUBILITY, OSMOTIC VIRIAL COEFFICIENTS AND CRYSTAL GROWTH

14.1 ABSTRACT

By conventional wisdom oligonucleotides are crystallized for crystallography in solutions containing 2-methyl-2,4-pentanediol or polyethylene glycol, and these are considered "precipitants". It has been found possible to eliminate these solutes and grow crystals of certain oligonucleotides in solutions containing suitable concentrations of multivalent cations, namely magnesium and spermine. Magnesium has almost always been present in solutions of mono-, oligo- and polynucleotides in biochemical and structural studies, and this tradition is several decades old. Furthermore, magnesium ions have been located in the crystal structures of many oligonucleotides. Therefore, the solubility, crystallization and aggregation of three selected oligonucleotides were investigated as a function of magnesium or spermine concentration. It is now proposed that multivalent cations play two thermodynamic roles: on the one hand they destabilize the nucleic acid colloid by Debye screening and on the other hand they cause the formation of specific divalent-cation-bridge dependent bonds. It is further suggested that these cation-mediated lattice forming bonds may be of three types: direct ion pairing, hydrated-ion interaction, and cation-pi bonding. Crystallization and static and dynamic light-scattering experiments were performed as a function of Mg^{++} or spermine concentration on two nearly self-complimentary RNA dodecamers, one with tandem U-U pairs at its center ("UU-dodecamer"), the other with a GU wobble and tandem CU mismatches at its center ("Holbrook RNA"), and one DNA ("Dickerson DNA") dodecamer. Dynamic light scattering was used to estimate effective molecular diameter, and static light scattering was used to estimate second and third osmotic virial coefficients, B_{22} and C_{22}, respectively. Published structures were studied with molecular graphics viewers to seek evidence for a role of solvent ions in lattice-forming bonds. The following results were found: magnesium ions can both solubilize and aggregate oligomers depending on Mg^{++} concentration. The UU-dodecamer has a very large negative B_{22} and a significant positive C_{22} as crystallization conditions are approached by increasing Mg^{++} concentration from 0 through 5 to 10 mM. The Holbrook RNA has B_{22} indistinguishable from zero at 5 mM Mg^{++} but large negative B_{22} at 25 mM Mg^{++}. Published methods for crystallizing the Dickerson DNA include spermine, which was found to modify the DNA's B_{22} from a large positive to a large negative value in the presence Mg^{++} ions. Both Mg and spermine are found in the crystal structure of the Dickerson DNA. From these light-scattering observations we conclude that the suitable model for oligonucleotide solutions is an electrokinetically stabilized colloid. This is different from the empirical observations for proteins, which crystallize when B_{22} has a modest negative value and form amorphous

aggregates at larger negative B_{22} values (George & Wilson, 1994). In the case of proteins and inorganic colloids, an adhesive hard sphere model has been successful in describing crystallization phase boundaries (Rosenbaum *et al.*, 1996). A crystal growth screening strategy in which Mg^{++} or spermine is diffused into an oligonucleotide solution should therefore be tested.
****(Return to abstract and modify as necessary when this chapter is finished)****

4.2 INTRODUCTION

The crystallization of biological macromolecules has a history that spans 150 years, although for most of that history the approaches taken have been described in terms like "black art" or "alchemy" rather than "science" (McPherson, 1999, pp. vii - 1). In the past several decades more scientific approaches have been taken. However, biomacromolecular crystals are overwhelmingly desired for X-ray crystallography studies, and therefore the emphasis is placed primarily on obtaining a diffraction quality crystal and not so much on understanding the how or why of the crystallization process. As the demand for oligonucleotide crystals increases due to the pursuit of ever more detailed structural information and to the need for purification and formulation of therapeutic oligonucleotides, a systematic approach that is more rational and relies on a good understanding of oligonucleotide solution behavior and thermodynamics becomes increasingly important.

14.3 MATERIALS AND METHODS

14.3.1 Solution Preparation and Handling

text...

14.3.2 Production and Purification of Oligonucleotides

Most of the UU-dodecamer RNA used in this study was produced by *in vitro* transcription and enzymatically digested as described in Chapter 3 and the Appendix. Some of the UU-dodecamer and all of the Holbrook RNA were purchased from Dharmacon Research, Inc. (Boulder, CO). The Dickerson DNA was purchased from Macromolecular Resources (Dept. of Biochemistry, Colorado State University, Fort Collins, CO). RNA purchased from Dharmacon was deprotected using the recommended protocol. All oligonucleotide samples were purified and analyzed by high-temperature anion-exchange (NucleoPac PA-100, Dionex Inc.) HPLC and desalted by ultrafiltration, unless otherwise noted (See Chapter 3 and the Appendix). Final oligonucleotide purity was typically ≥95%.

14.3.3 Solubility and Crystallization Experiments

Solubility and crystallization experiments with the oligonucleotides in this study were carried out in multi-well crystallization plates using the pseudo-batch and vapor diffusion hanging drop techniques described in Chapter 13. Digital images of precipitate and crystals were obtained using a CCD camera connected to a Macintosh

G3 PowerPC. Detailed protocols for setting hanging drop experiments are available in the appendix.

14.3.4 Light Scattering Experiments

Light scattering (LS) experiments (both static and dynamic) and analysis in the present study involved the same instrument system, general protocols and techniques as described in Chapter 3. Again, unless otherwise noted, all light scattering experiments were conducted at room temperature and an angle of 90°. The details of the precise solution conditions and compositions used in these experiments are given (when necessary and relevant) with the results. Details of the DLS and SLS protocols are given in the appendix.

14.4 RESULTS

Following up on questions raised and/or left unanswered in the study of the UU-dodecamer presented in Chapter 3, this study revisits the light scattering data for the UU-dodecamer and expands to include a couple more oligonucleotides.

14.4.1 UU-dodecamer RNA: the data revisited

As observed in Chapter 3, the state of aggregration of the UU-dodecamer changed during the course of the SLS experiments as the samples were serially diluted (See Figure 13-5 and Figure 13-9. A close look at the SLS data presented in Chapter 13 reveals a systematic curvature to the data. These two facts strongly suggest that analyzing the data with a virial expansion that includes the third virial coefficient is a more accurate approach to handling the data. Table 14-1, indeed confirms that fitting the data with quadratic expressions as opposed to linear ones yield better results in all cases except one (7.5% PEG-400 and 0 mM $MgCl_2$), as measured by the coefficient of variance (R^2) and the F statistic. The F statistic is used to determine whether the observed relationship between the dependent and independent variables occurs by chance. The closer the F-observed value is to zero, the less the dependent variables are a function of the independent variables. Confidence levels for the model are determined by comparing the F-observed value to the F-critical value obtained from a statistical table using the degrees of freedom of the fit or model.

Table 14-1.: Statistical comparison of the linear and quadratic fits to the UU-dodecamer SLS data.

PEG-400	$MgCl_2$ (mM)	Coefficient of Variance (R^2)		F-statistic			
		Linear Fit	Quadratic Fit	Linear Fit	Quadratic Fit	F-critical	Confidence
0%	0	0.89	0.96	202.9	269.5	14.2	99.9%
	5	0.91	0.98	365.6	732.0	12.8	99.9%
	10	0.97	0.99	635.3	1161.3	15.7	99.9%
7.5%	0	0.71	0.71	19.4	8.5	16.2	99.5%
	5	0.87	0.90	250.2	156.3	12.9	99.9%
	10	0.98	0.99	389.1	540.2	29.3	99.9%

Although the F-observed value at 7.5% PEG-400 and 5 mM $MgCl_2$ for the quadratic fit (156.3) is lower than that for the linear fit (250.2), the former is

considered a better fit than the latter because R^2 for the quadratic fit is closer to unity and F-observed is still much larger than F-critical to a very high confidence level.

14.4.1.1 In the absence of PEG-400

Figure 14-1 summarizes the Debye plots for different $MgCl_2$ concentrations, all in the absence of PEG-400, fitted with a virial expansion that includes the quadratic term. As in the linear analysis, for these plots a *dn/dc* value of 0.19 mL/g was used in calculating the Debye data from the excess scattering intensities. Qualitatively this figure displays all the same general features as observed in Figure 13.6. However, the intercepts are shifted somewhat higher, indicating smaller measured molecular weights, and the initial slopes appear to be steeper, indicating more negative B_{22} values.

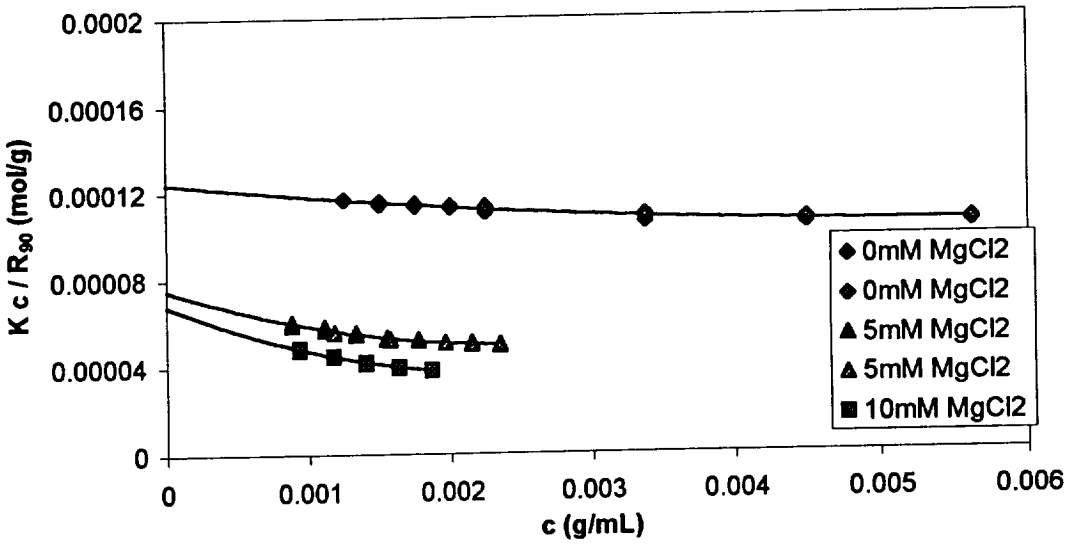

Figure 14-1: Debye plots for the UU-dodecamer at different $MgCl_2$ concentration in the absence of PEG-400. In all cases, the solutions contained 20 mM NaCl, and 50 mM Na Cacodylate, pH 7.0. A value of *dn/dc* = 0.19 mL/g was used in the SLS data analysis. The differently shaded data points at 0 mM and 5 mM $MgCl_2$ represent SLS data collected on separate occasions with different ranges of RNA concentration but otherwise under the same experimental conditions. In the SLS analysis, the data at each $MgCl_2$ concentration were pooled and fitted with a quadratic expression.

Figure 14-2 shows B_{22} as a function of $MgCl_2$ concentration (determined from the coefficient of the first order term of the Debye lines in

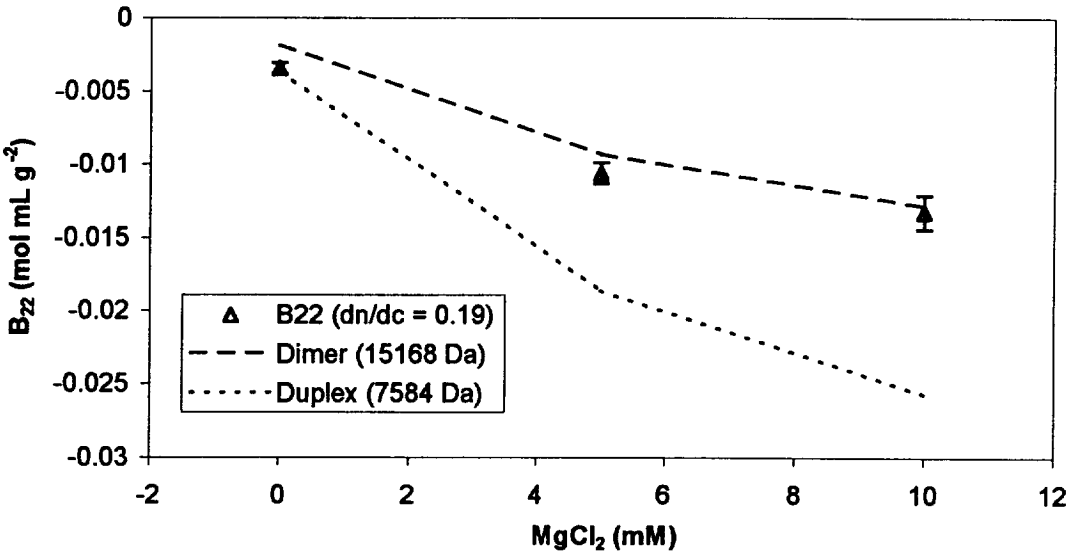

Figure 4-2: B_{22} as a function of $MgCl_2$ concentration for the UU-dodecamer in the absence of PEG-400. Determined from the Debye plots in Figure 4.sls_0-peg. The dashed lines indicate the values of B_{22} that would result if *dn/dc* were freely adjusted in each case to give the molecular weight of a duplex (lower limit) or a dimer of duplexes (upper limit). Error bars represent the standard error.

Figure 14-1). B_{22} decreases with an initial slope of -1.4×10^{-3} mol mL g^{-2} mM^{-1}. Quadratic analysis still indicates that at 0 mM $MgCl_2$ the UU-dodecamer exists as a duplex, but as $MgCl_2$ is added it aggregrates to a dimer of duplexes.

Figure 14-7 shows C_{22} as a function of $MgCl_2$ concentration (determined from the coefficient of the second order term of the Debye lines in Figure 14-1. C_{22} increases with $MgCl_2$ concentration. The values of the third virial coefficient at 5 and 10 mM $MgCl_2$ have standard errors that are large relative to the differences between them and may not be statistically different. However, C_{22} clearly has significant positive values at these $MgCl_2$ concentrations.

Molecular weights determined from the SLS experiments and effective diameters measured by DLS still correlate very well. Figure 4.dls_0-peg shows M_W

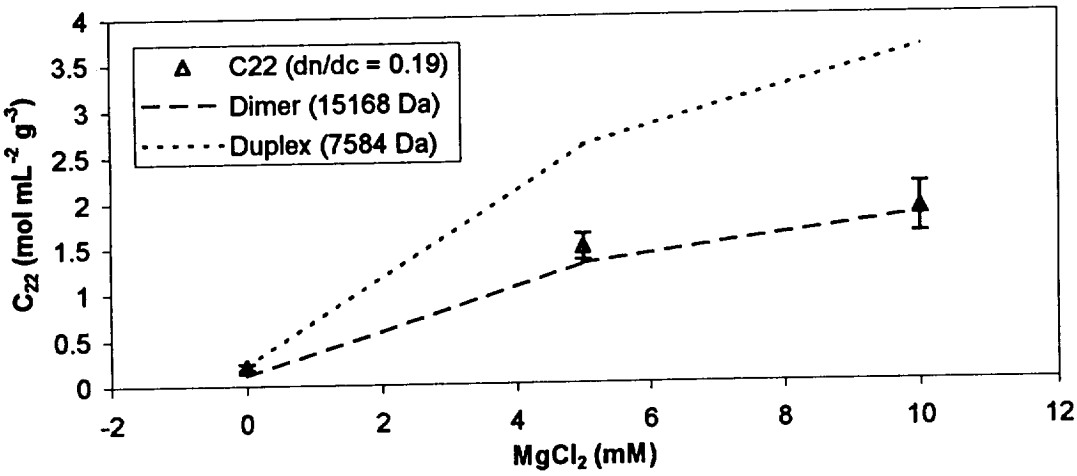

Figure 14-3: C_{22} as a function of $MgCl_2$ concentration for the UU-dodecamer in the absence of PEG-400. Determined from the Debye plots in Figure 4.sls_0-peg. The dashed lines indicate the values of B_{22} that would result if *dn/dc* were freely adjusted in each case to give the molecular weight of a duplex (lower limit) or a dimer of duplexes (upper limit). Error bars represent the standard error.

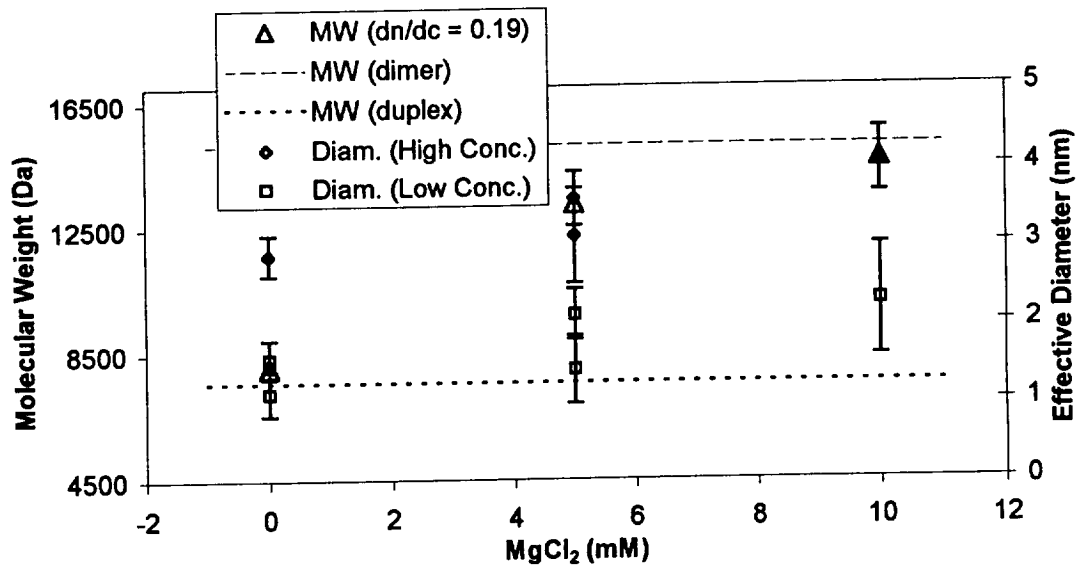

Figure 14-4: Primary axis: M_W as a function of $MgCl_2$ concentration for the UU-dodecamer in the absence of PEG-400. Determined from the Debye plots in Figure 14-1. The dashed lines indicate the molecular weight of a duplex (lower limit) or a dimer of duplexes (upper limit). Secondary axis: DLS measured effective diameters of the UU-dodecamer in the highest and lowest RNA concentration samples used in the SLS experiments. Error bars represent the standard deviation of the mean of multiple effective diameter measurements.

(determined from the intercepts of the Debye lines in Figure 14-1) as a function of $MgCl_2$ concentration. Although the molecular weights are somewhat smaller than in

the linear analysis, M_W is again seen to increase from roughly that of a duplex (7584 Da) at 0 mM $MgCl_2$ to roughly that of a dimer of duplexes (15168 Da) at 10 mM $MgCl_2$. On the secondary axis are shown the effective diameters as measured by DLS of the UU-dodecamer RNA in the highest and lowest concentration solutions used in each SLS experiment. As stated above, these correlate well with the molecular weights determined by SLS.

14.4.1.2 In the presence of PEG-400

Figure 14-5 is a summary of the Debye plots for different $MgCl_2$ concentrations, all in the presence of 7.5% PEG-400, fitted with a virial expansion that includes the quadratic term. A *dn/dc* of 0.17 mL/g was used, as in the linear analysis, in calculating the Debye data from the excess scattering intensities. As in the absence of PEG-400, the initial slope of the Debye lines, that is, the second virial coefficient decreases as $MgCl_2$ concentration increases. This is clearly seen in Figure 14-6, which shows B_{22} as a function of $MgCl_2$ concentration. B_{22} decreases with an initial slope of -1.5×10^{-3} mol mL g^{-2} mM^{-1}. The curvature in the Debye lines in the presence of $MgCl_2$ indicates a significant and experimentally accessible positive third virial coefficient. Figure 14-7 plots C_{22} as a function of $MgCl_2$ concentration.

In the presence of 7.5% PEG-400, both B_{22} and C_{22} have relatively large errors associated with them when compared to the corresponding data in the absence

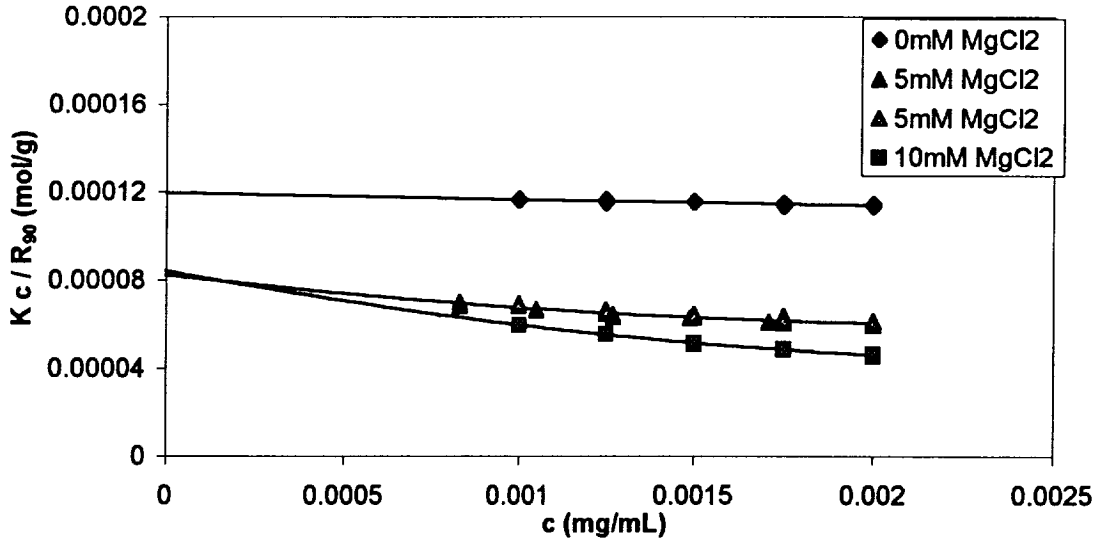

of PEG-400. This is due primarily to the fact that fewer data points over generally

Figure 14-5: Debye plots for the UU-dodecamer at different $MgCl_2$ concentration in 7.5% PEG-400. In all cases, the solutions contained 20 mM NaCl, and 50 mM Na Cacodylate, pH 7.0. A value of *dn/dc* = 0.17 mL/g was used in the SLS data analysis. The differently shaded data points at 5 mM $MgCl_2$ represent SLS data collected on separate occasions with slightly different ranges of RNA concentration but otherwise under the same experimental conditions. In the SLS analysis, the data from these "repeated" experiments were pooled and fitted with a quadratic expression.

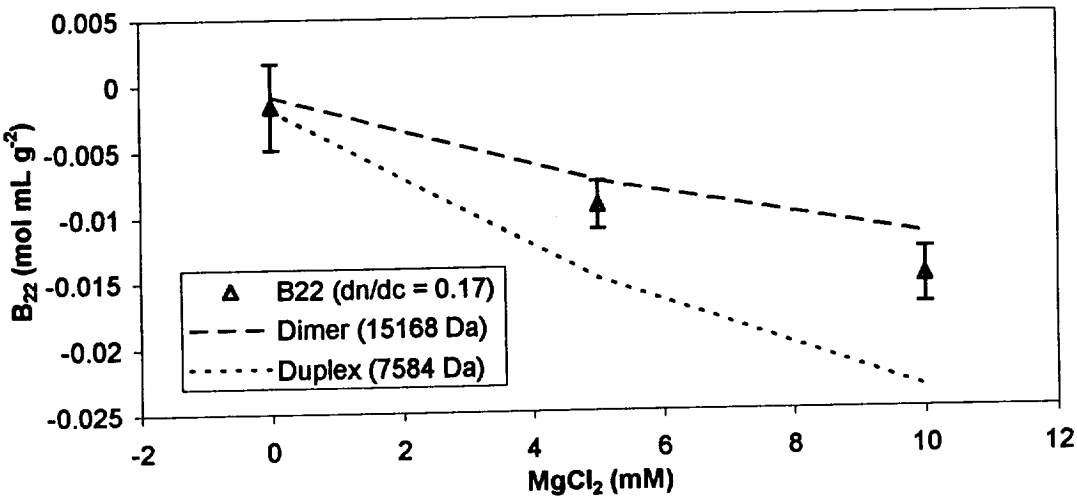

Figure 14-6: B_{22} as a function of $MgCl_2$ concentration for the UU-dodecamer in 7.5% PEG-400. Determined from the Debye plots in Figure 4.sls_75-peg. The dashed lines indicate the values of B_{22} that would result if *dn/dc* were freely adjusted in each case to give the molecular weight of a duplex (lower limit) or a dimer of duplexes (upper limit). Error bars represent the standard error.

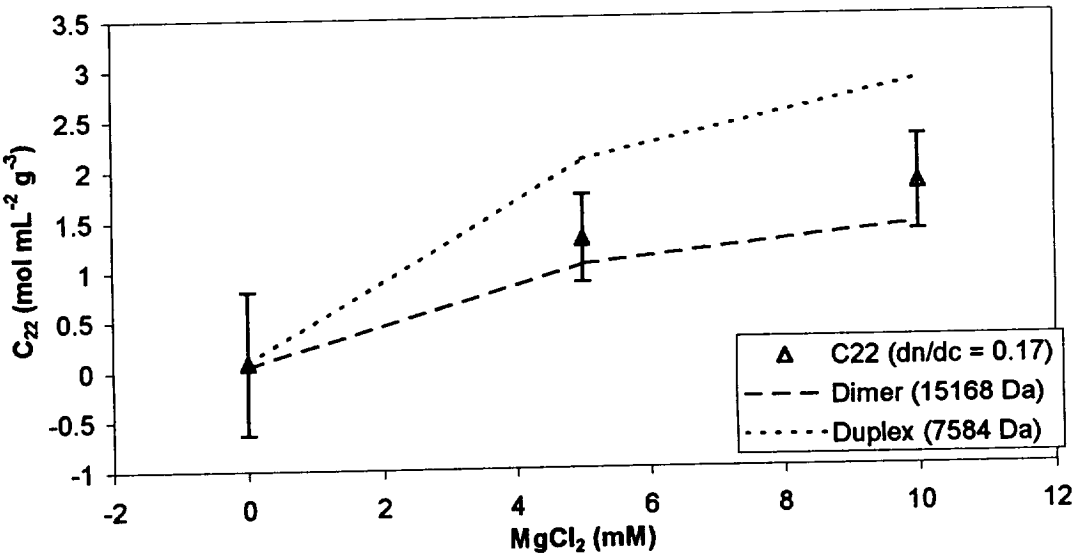

Figure 14-7: C_{22} as a function of $MgCl_2$ concentration for the UU-dodecamer in the 7.5% PEG-400. Determined from the Debye plots in Figure 14-5. The dashed lines indicate the values of C_{22} that would result if *dn/dc* were freely adjusted in each case to give the molecular weight of a duplex (lower limit) or a dimer of duplexes (upper limit). Error bars represent the standard error.

smaller ranges of RNA concentration were collected in the presence of PEG-400. However, the larger errors may suggest that PEG-400 complicates somewhat the solution behavior of oligonucleotides increasing the difficulty of light scattering and interpretation of the LS data. At 0 mM $MgCl_2$, the quadratic analysis which gives a

poorer statistical fit to the data than the linear analysis (see Table 4.F-test) contributes significantly to the unusually large errors.

In Figure 14-5, the intercepts of the Debye lines clearly indicate that a large increase in molecular weight occurs from 0 to 5 mM $MgCl_2$, while it remains essentially unchanged between 5 and 10 mM. This is more clearly seen in Figure 14-8, which shows the molecular weight determined by SLS as a function of $MgCl_2$ concentration on the primary axis. On the secondary axis are shown the effective diameters measured by DLS of the UU-dodecamer in the highest and lowest concentration samples used in the corresponding SLS experiments. Using the same primary to secondary axis scale (i.e. the same proportionality) as in the absence of PEG-400, the molecular weights and effective diameters again are observed to correlate well with each other.

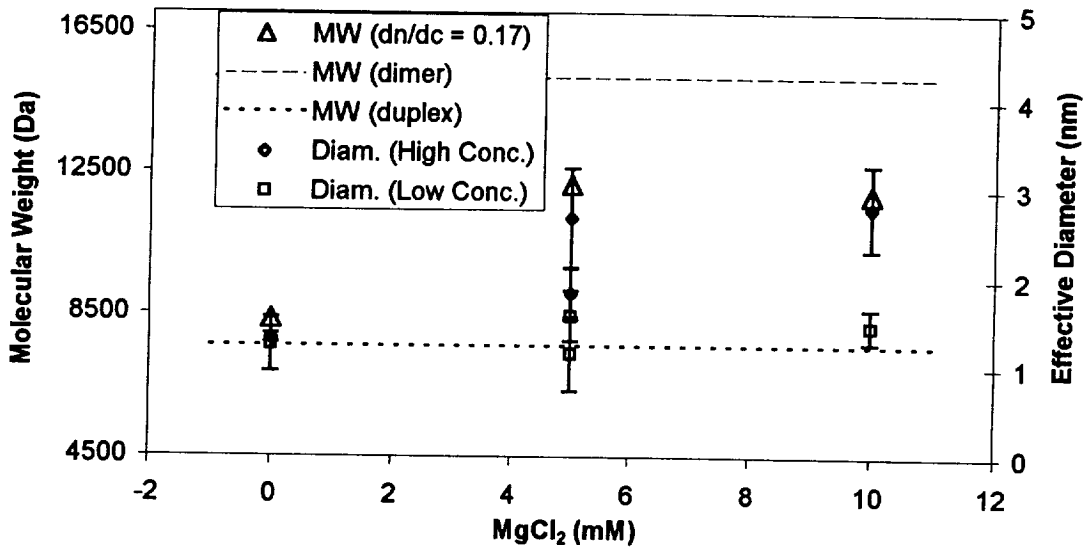

Figure 14-8: Primary axis: M_W as a function of $MgCl_2$ concentration for the UU-dodecamer in 7.5% PEG-400. Determined from the Debye plots in Figure 14-5. The dashed lines indicate the molecular weight of a duplex (lower limit) or a dimer of duplexes (upper limit). Secondary axis: DLS measured effective diameters of the UU-dodecamer in the highest and lowest RNA concentration samples used in the SLS experiments. Error bars represent the standard deviation of the mean of multiple effective diameter measurements.

4.4.1.3 Comparison of results

Table 14-2 summarizes the UU-dodecamer light scattering results when the data is analyzed using a quadratic fit. Molecular weight and the osmotic second and third virial coefficients are clearly strong functions of $MgCl_2$ concentration. Statistically, the virial coefficients are not affected by PEG-400 (at 80% confidence level of difference in all cases), at least for the concentrations of PEG-400 tested. At 0 mM $MgCl_2$ it may be argued that the effect of 7.5% PEG-400 is statistically significant. The results in Table 4.summary are all from the quadratic analysis of the data. However in Table 14-1, it was shown that the data at 0 mM $MgCl_2$ and 7.5% PEG-400 are more accurately analyzed using a linear fit. In this specific case,

regardless of whether one uses a linear or quadratic fit, the second virial coefficients are not statistically different, even down to the very low confidence level for difference of 60% (see Table 14-3). In the linear analysis, the standard error

Table 14-2: Summary and comparison of light scattering results for UU-dodecamer in varied $MgCl_2$ and PEG-400 concentrations, determined from the 90° Debye plots shown in Figure 4.sls_0-peg and Figure 4.sls_75-peg. Other solution conditions: 20 mM NaCl, and 50 mM Na Cacodylate, pH 7.0.

$MgCl_2$ (mM)	PEG-400	M_W (g/mol)	B_{22} (x10^3) (mol mL g^{-2})	S.E. (x10^3)	Statistically Different? (t-test, 80%)	C_{22} (mol mL^{-2} g^{-3})	S.E.	Statistically Different? (t-test, 80%)
0	0%	8067	-3.43	0.36	NO	0.21	0.03	NO
	7.5%	8352	-1.68	3.25		0.08	0.72	
5	0%	13272	-10.63	0.71	NO	1.48	0.15	NO
	7.5%	12145	-9.33	1.83		1.29	0.43	
10	0%	14688	-13.28	1.15	NO	1.88	0.27	NO
	7.5%	11872	-14.98	2.13		1.82	0.47	

Table 14-3: Statistical comparison of B_{22} obtained from linear analysis and quadratic analysis of the UU-dodecamer light scattering data. Other solution conditions: 20 mM NaCl, and 50 mM Na Cacodylate, pH 7.0.

		Linear Fit			Quadratic Fit			B_{22}
$MgCl_2$ (mM)	PEG-400	M_W (g/mol)	B_{22} (x10^3) (mol mL g^{-2})	S.E. (x10^3)	M_W (g/mol)	B_{22} (x10^3) (mol mL g^{-2})	S.E. (x10^3)	Statistically Different? (t-test, 99%)
0	0%	8486	-1.26	0.09	8067	-3.43	0.36	YES
	7.5%	8388	-1.31	0.30	8352	-1.68	3.25	NO
5	0%	15486	-3.43	0.18	13272	-10.63	0.71	YES
	7.5%	13284	-3.90	0.25	12145	-9.33	1.83	YES
10	0%	17329	-5.40	0.21	14688	-13.28	1.15	YES
	7.5%	13763	-6.81	0.35	11872	-14.98	2.13	YES

associated with B_{22} is an order of magnitude smaller than that in the quadratic analysis. With this smaller standard error, the values of B_{22} at 0 mM $MgCl_2$ in the absence and in the presence PEG-400 then become statistically different to a confidence level greater than 99%. What this indicates is that, while PEG-400 may have some effect on the solution thermodynamics of the UU-dodecamer, this effect is much smaller than that caused by $MgCl_2$.

14.4.2 Dickerson DNA Dodecamer

14.4.2.1 Crystallization and solubility screens

Figure 14-9 shows crystals grown under conditions very similar to those reported in the original crystallographic structure determinations of the Dickerson DNA (Wing *et al.*, 1980). Visually, the quality of the crystals grown under these conditions did not appear to be very high. The high MPD content did not promise to be very conducive to light scattering experiments based on past experience with the UU-dodecamer RNA.

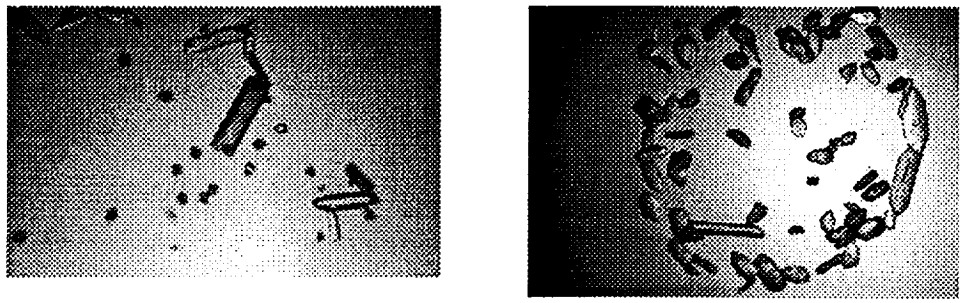

Figure 14-9: Dickerson DNA crystals grown by the vapor diffusion hanging drop technique at room temperature. Drops initially containing 4 mg/mL DNA, 13.5% MPD, 4.0 mM $Mg(Oac)_2$, and 0.75 mM Spermine (free base) were set against reservoir solutions two-fold concentrated in all components except DNA which was not present in the reservoir.

A large number of crystallization and solubility screens were conducted on the Dickerson DNA, in an attempt to determine the solubility limits of the DNA and to find conditions conducive to light scattering. These screens spanned the following ranges of solution components: 1 to 8 mg/mL DNA, 0 to 200 mM $MgCl_2$, 0 to 50 mM $Mg(OAc)_2$, 0 to 27% MPD, 0 and 1.5 mM spermine free base, 0 to 5 mM spermine tetrahydrochloride (spermine-4HCl). Generally speaking, the qualitative results from all these screens are summarized as follows. Dickerson DNA solubility depends critically on spermine-4HCl, but very weakly, if at all, on spermine free base. $MgCl_2$ and $Mg(OAc)_2$ counteract the precipitating effect of spermine-4HCl, with the acetate salt having a stronger effect than the chloride salt. Both MPD and $MgCl_2$ precipitate Dickerson DNA at sufficiently high concentrations (about 27% MPD or 100 to 200 mM $MgCl_2$), although the DNA precipitated under these conditions tended to be amorphous, while the DNA precipitated with spermine tended to be crystalline.

Figure 4.dna-xtals-2 shows crystals of the Dickerson DNA that were grown from a solution containing only DNA, $MgCl_2$, and spermine-4HCl in a pseudo-batch

Figure 14-10: Dickerson DNA crystals grown by the pseudo-batch hanging drop technique at room temperature. Drops containing 4 mg/mL DNA, 25 mM $MgCl_2$, and 1.5 mM spermine-4HCl were set against reservoir solutions with the same composition in all components except DNA which was not present in the reservoir.

hanging drop experiment. Although not immediately apparent because of the quality of the images in Figure 14-10, these crystals possessed a much better visual quality (as observed under a polarized-light stereo zoom microscope) than the crystals shown in Figure 14-9. An interesting feature of the experiment in which crystals were grown

in the presence of only $MgCl_2$ and spermine-4HCl is that a layer of precipitant apparently first formed at the surface of the hanging drop and then the well-formed rod-like crystals nucleated in the precipitate layer and grew into the drop.

It should be noted here that the Dickerson DNA sample used in virtually all the crystallization and solubility screens mentioned above, including those represented in Figure 14-9 and Figure 14-10, was purchased from Macromolecular Resources (MMR) as the reverse-phase purified product and was used without further purification. A second batch of the Dickerson DNA was likewise purchased from MMR as the reverse-phase purified product. It was observed that the second batch behaved somewhat differently than the first. Specifically, the second batch required much lower concentrations of spermine-4HCl to precipitate or crystallize the DNA (about 0.35 mM versus 1.5 mM, both in the presence of 25 mM $MgCl_2$). Apparently, the two batches of DNA were not identical even though they were supposedly subjected to identical production and processing steps. All subsequent batches of DNA purchased from MMR were subjected to the anion-exchange HPLC and desalting purification process described in the Materials and Methods section above. The anion-exchange HPLC purified DNA samples behaved more like the second unpurified batch above. It is this researcher's assumption that the first batch of DNA contained some impurities (possibly buffer components and/or salts left over from the reverse-phase purification procedure) which inhibited somewhat the effectiveness of the spermine-4HCl to precipitate the DNA.

In all the screens performed with the Dickerson DNA, the pH of the solutions was not controlled with a buffering component such as sodium cacodylate. Therefore, the pH can vary significantly depending on the types of solution components and their concentrations. Table 4-4 gives the pH of a number of these solutions.

Table 4-4: pH of some of the solutions used in the Dickerson DNA solubility and crystallization screens. The solutions did not contain any DNA which would also affect the pH of the solutions somewhat.

Spermine		Magnesium Cation		
Type	Conc. (mM)	Counter-ion	Conc. (mM)	pH
Free base	1.5	acetate	0	10.83
			5	9.91
			50	9.61
		chloride	0	10.86
			5	9.87
			50	9.47
Tetrachloride	1.5	acetate	0	5.47
			5	6.51
			50	7.09
		chloride	0	5.56
			5	5.45
			50	5.52

Solutions containing spermine free base were quite basic, with both $MgCl_2$ and $Mg(OAc)_2$ having a very similar effect: decreasing basicity with increasing magnesium salt concentration. In contrast, solutions containing the tetrachloride form of spermine were acidic, with the two magnesium salts affecting the solutions quite differently. The acetate salt decreases the acidity of the solution as its concentration increases, neutralizing the solution at the highest concentration tested (50 mM). However, the chloride salt has essentially no effect on the pH of spermine-4HCl solutions. These latter pH observations make sense when one recalls that acetate is the anion of a weak acid, while chloride is the anion of a strong acid.

14.4.2.2 Dynamic light scattering experiments

DLS experiments were performed in which the aggregation state of the Dickerson DNA as a function of $MgCl_2$, $Mg(OAc)_2$, and spermine-4HCl was monitored. These provided quantitative confirmation of the general, qualitative results observed in the crystallization and solubility screens mentioned above.

Figure 14-11 and Figure 14-12 show the results for two experiments, one in which $MgCl_2$ was added to a solution of DNA in pure water and

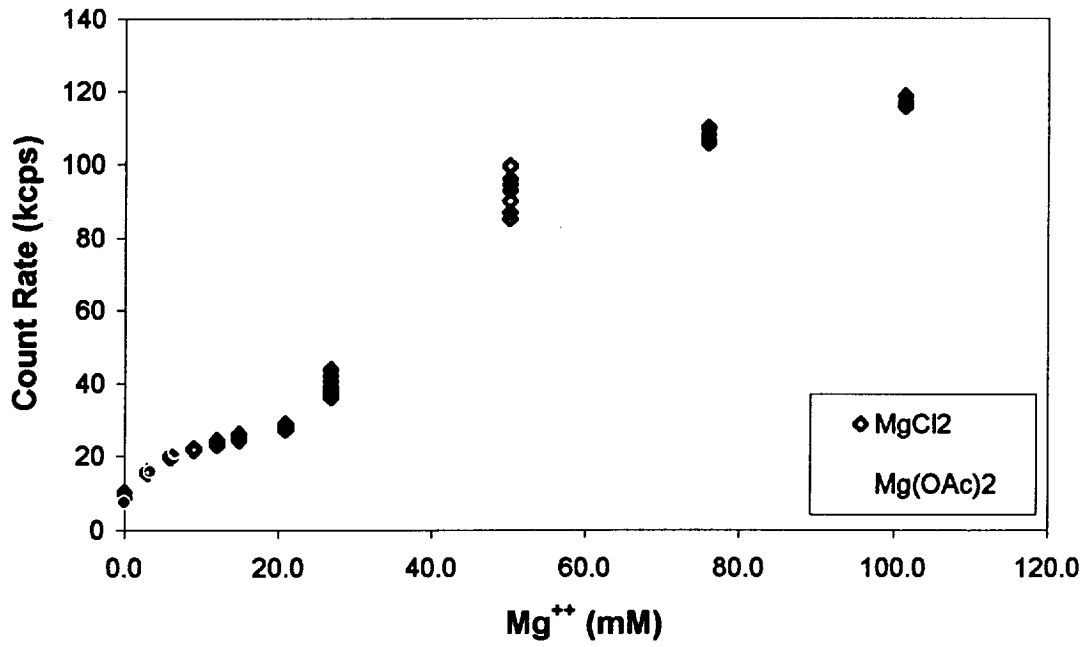

Figure 14-11: Intensity of light scattered from a 2.0 mg/mL Dickerson DNA sample in pure water as a function of magnesium salt concentration. The count rate was measured during the course of a DLS experiment (see Figure 14-12).

the other in which $Mg(OAc)_2$ was added. In both cases, the DNA concentration over the course of the entire experiment was diluted (due to the addition of concentrated magnesium salt solution) from 2.0 mg/mL by no more than 6.7%. DNA samples for both experiments were purchased from Macromolecular Resources as the reverse-phase purified product and used without further purification. The unpurified DNA batches mentioned above in the screening experiments were the same ones used in these DLS experiments.

In Figure 14-11 the intensity of light scattered from a solution of DNA in pure water is plotted as a function of magnesium salt concentration. The increase in intensity indicates that the DNA aggregates in solution with increasing magnesium cation concentration. Aggregation of the DNA in solution is positively shown in Figure 14-12, in which the effective diameter of the DNA is plotted as a function of Mg^{++} concentration. While the general features are similar, quantitatively, $MgCl_2$ and $Mg(OAc)_2$ affect DNA aggregation differently. Both figures show that

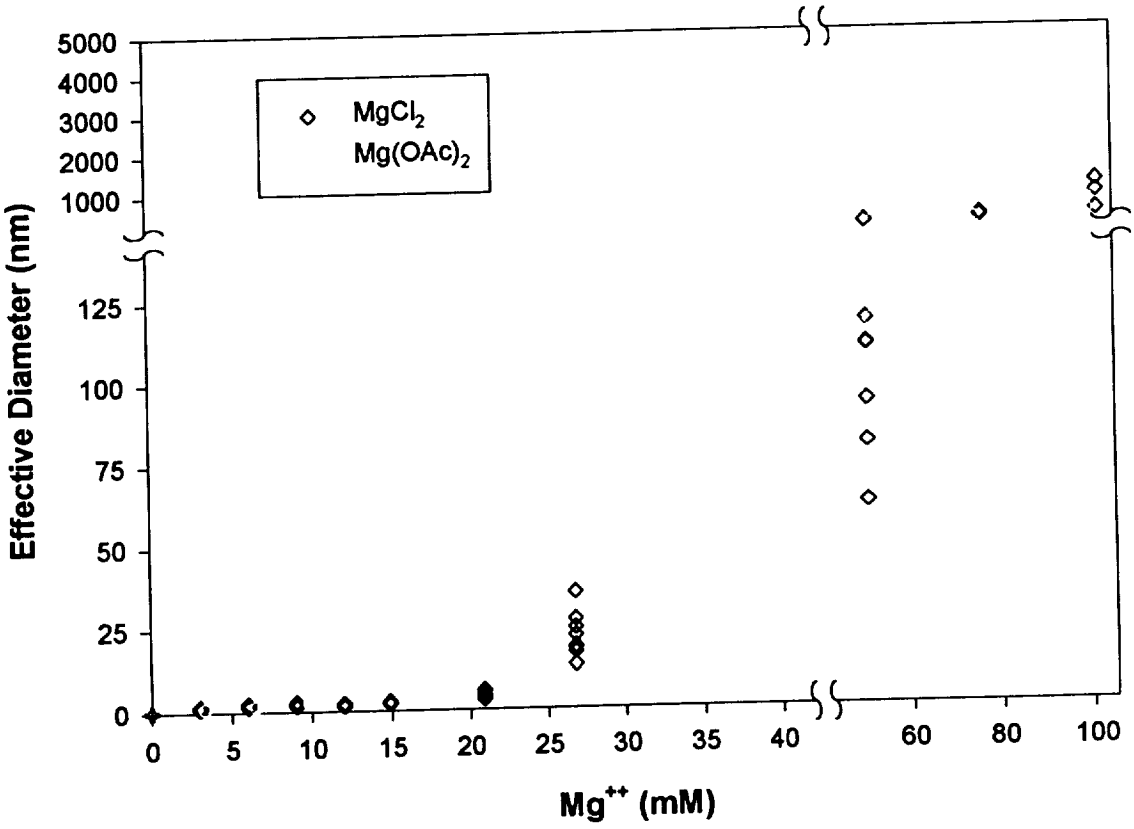

Figure 14-12: Effective diameter of a 2.0 mg/mL Dickerson DNA sample in pure water as a function of magnesium salt concentration. Diameters were measured by DLS. See also Figure 14-11.

$MgCl_2$ begins to strongly aggregate the DNA at about 25 mM and above, whereas $Mg(OAc)_2$ has this effect at about 10 mM and above. Figure 14-11 indicates that between about 10 mM and 30 mM the acetate salt has a stronger effect than the chloride salt. However, above about 30 mM the chloride salt has a much stronger effect: at 100 mM the intensity in the chloride salt case is almost twice that in the acetate salt case. Although the DLS experiments show a high level of aggregation in solution, in neither case was precipitate visible, even under a polarized light microscope.

Figure 14-13 and Figure 14-14 show the results for two experiments similar to the ones just described, except that in these cases, instead of DNA in pure water, the DNA was in the presence of 1.5 mM spermine-4HCl. Again, throughout the course of the titrations, the DNA was diluted from 2.0 mg/mL by no more than 6.7% due to the addition of concentrated magnesium salt solution, which also contained 1.5 mM spermine-4HCl. The same batches of DNA mentioned above were used in these experiments. In both experiments, initially (i.e. when no magnesium salt had yet been added) the DNA was very strongly precipitated by the spermine-4HCl. Both samples were far too turbid initially to permit any DLS measurements. As Mg^{++} was added, both samples visibly cleared up eventually making DLS measurements possible. However, as indicated in Figure 14-13 by the Mg^{++} concentrations at which intensity measurements were first recorded, it took 50 mM $MgCl_2$ to sufficiently clarify the solution, but only about 6 mM $Mg(OAc)_2$ (or less) to do the same. In addition, the intensity of scattered light was relatively low throughout the addition of the acetate salt, but was initially very high in the chloride salt case, asymptotically approaching the intensity of the acetate salt case as $MgCl_2$ was added. By the end of both experiments, the solutions were completely clarified. The precipitate visibly dissolved more quickly (i.e. at lower Mg^{++} concentrations) in the acetate salt case. These results clearly demonstrate the ability of Mg^{++} to solubilize DNA precipitated by spermine and unambiguously show that this effect strongly depends on the associated anion, providing quantitative confirmation of the results observed in the screens mentioned above.

Although the DNA solutions were clarified visibly (both to the naked eye and under a polarized-light microscope) to completion, Figure 14-14, which plots the effective diameter of the DNA in 1.5 mM spermine-4HCl solution as a function of magnesium salt concentration, shows that the DNA remained in a highly aggregated state. So Mg^{++} counteracts the precipitating effect of spermine, but because of its own precipitating effect at sufficiently high concentrations (observed in the screening experiments above), the DNA does not completely disaggregate. These data indicate that Mg^{++} can have both a "salting in" and a "salting out" effect depending on

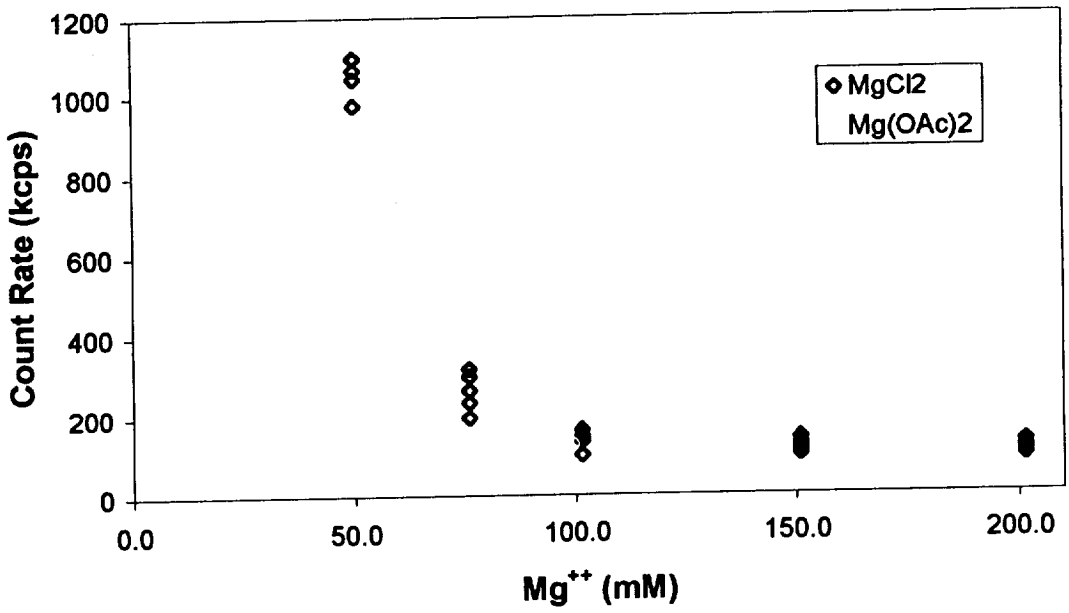

Figure 14-13: Intensity of light scattered from a 2.0 mg/mL Dickerson DNA sample in 1.5 mM spermine-4HCl as a function of magnesium salt concentration. The count rate was measured during the course of a DLS experiment (see Figure 14-14).

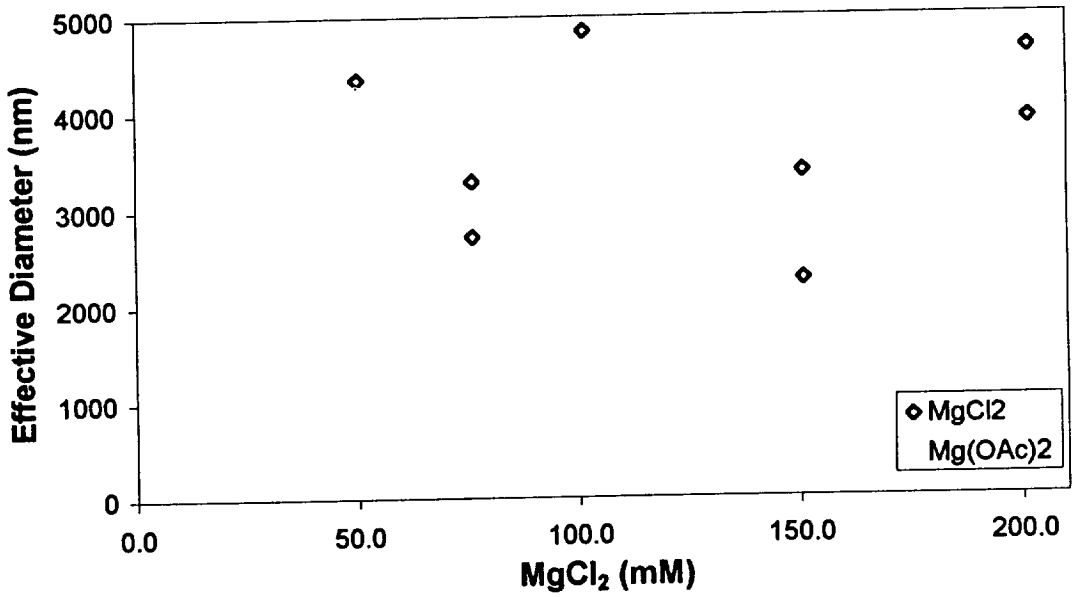

Figure 14-14: Effective diameter of a 2.0 mg/mL Dickerson DNA sample in 1.5 mM spermine-4HCl as a function of magnesium salt concentration. Diameters were measured by DLS. See also Figure14-13.

concentration. The data also suggests a competition between Mg^{++} and spermine for the same binding sites on the Dickerson DNA molecule.

The experiments with the Dickerson DNA described thus far suggest a pH dependence in the effectiveness of spermine to precipitate DNA. A final DLS-titration experiment was designed to further test the pH effect and to investigate solution conditions that more closely resemble those used with the UU-dodecamer, thus allowing some level of comparison between the two oligonucleotides. In this experiment, spermine-4HCl was added to a solution of 3.0 mg/mL Dickerson DNA that contained 5 mM $MgCl_2$ and 20 mM NaCl and that was buffered to pH 7.0 with 50 mM Na Cacodylate. Prior to being used, the DNA sample was purified by anion-exchange HPLC and desalted as described in the Materials and Methods section above.

Figure 14-15 shows that buffering the solution pH to 7.0 effectively inhibits the ability of spermine to precipitate the DNA. The effective diameter of the Dickerson DNA increased slightly from about 2 nm to about 3 nm as the concentration of spermine-4HCl increased from 0 to 6 mM. This final spermine concentration is four times higher than those typically used in the crystallization and solubility screens and the other DLS experiments. A slight increase in effective diameter indicates the DNA may be going from a duplex to a dimer of duplexes (or

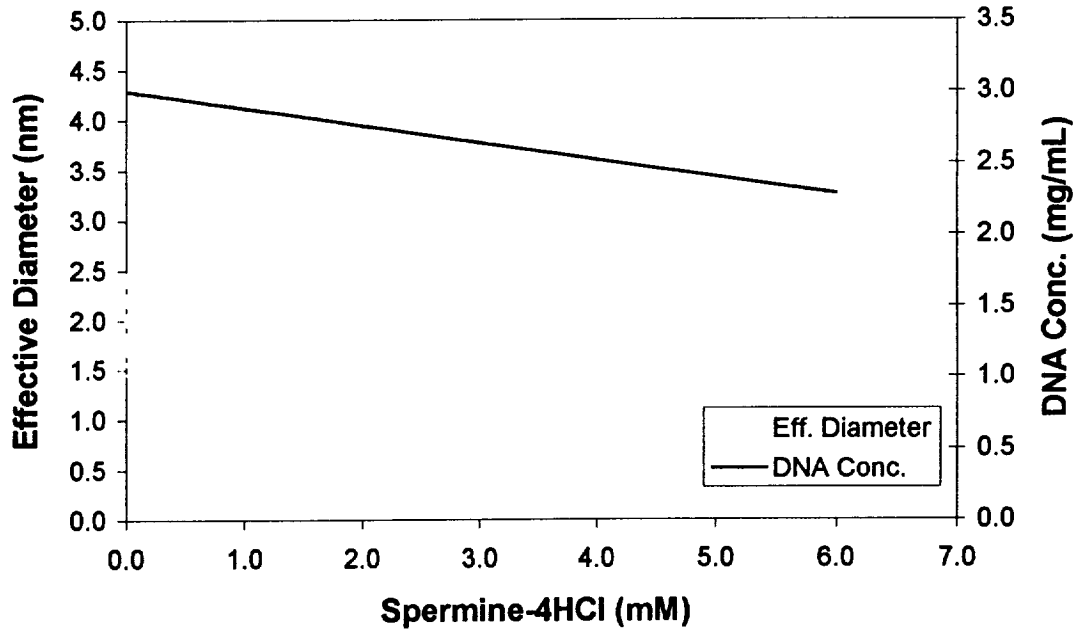

some combination of the two), but a high level of aggregation was not seen under

Figure 14-15: Effective diameter of a 3.0 mg/mL Dickerson DNA sample in 5 mM $MgCl_2$, 20 mM NaCl, and 50 mM Na Cacodylate, pH 7.0 as a function of spermine-4HCl concentration. Diameters were measured by DLS. The secondary axis shows the dilution of DNA due to the addition of concentrated (25 mM) spermine-4HCl solution, which also contained 5 mM $MgCl_2$, 20 mM NaCl, and 50 mM Na Cacodylate, pH 7.0.

these solution conditions at room temperature. However, it was observed in passing that slightly lowering the temperature of this DNA solution induced precipitation. In fact, the DNA sample used in this final DLS experiment produced showers of crystals

(some reasonably large, i.e. up to 50 to 70 μm in the smallest dimension) and crystalline precipitate when placed in a refrigerator (~4°C). Taking all the experiments described above in combination, it is clear that pH is key factor in the effectiveness of spermine to precipitate DNA, with acidic conditions favoring precipitation. Temperature also clearly appears to be a key factor, a line of investigation that was not pursued to any significant depth in this research.

14.4.2.3 Static light scattering experiments

With the solubility and crystallization screens and the DLS experiments described above as guidelines, several SLS experiments were designed and carried out with the Dickerson DNA. These experiments focused on the quantitative thermodynamic effect of spermine, since previous experience indicated it is the critical solution component in all the conditions tested in this study with the Dickerson DNA. The DLS experiment shown in Figure 14-15 was especially useful in the design of the SLS solution conditions.

Figure 14-16 shows the Debye plots for the Dickerson DNA in different concentrations of spermine tetrahydrochloride. At 0 and 0.5 mM spermine-4HCl, the positive slopes of the Debye lines give positive values for the osmotic second virial coefficients, showing that repulsive interactions dominate between the oligonucleotide molecules in solution. However, at 4.0 mM spermine-4HCl, attractive interactions dominate as indicated by the significantly negative slope. Non-linearity

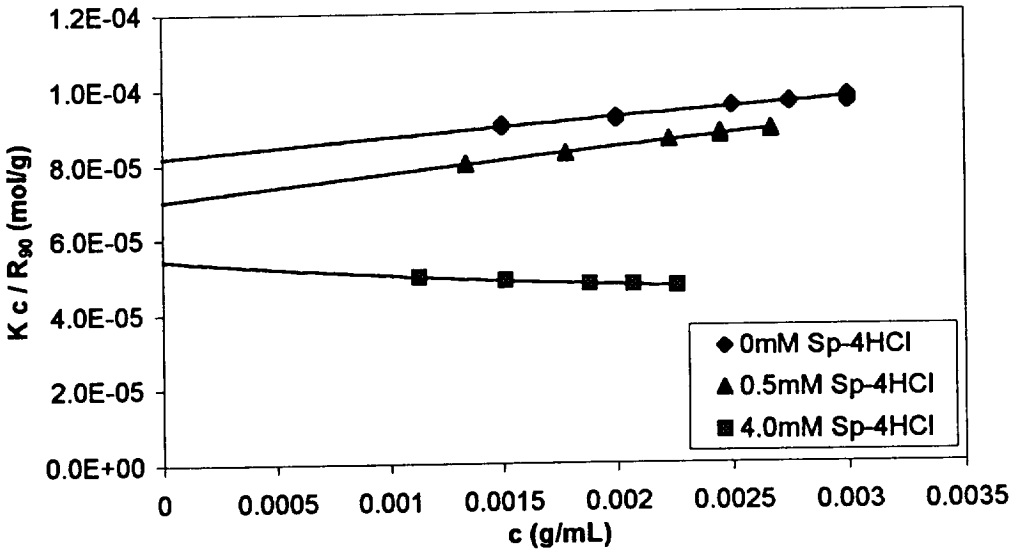

Figure 14-16: Debye plots for the Dickerson DNA at different spermine-4HCl concentration. In all cases, the solutions also contained 5 mM $MgCl_2$, 20 mM NaCl, and 50 mM Na Cacodylate, pH 7.0. A value of dn/dc = 0.19 mL/g was used to interpret the SLS data.

in the data at 4.0 mM also suggests that a significant and meaningful third virial coefficient can be determined. As the concentrations of spermine-4HCl increase, the intercepts of the Debye lines decrease, indicating increasing molecular weights.

Molecular weight as measured by SLS and effective diameter as measured by DLS are both shown in Figure 4.dls-dna as functions of spermine-4HCl concentration. The two independent measurements correlate well with each other. Somewhat surprisingly, the molecular weights seem quite high. This may be an indication that the *dn/dc* used is not as accurate as it should be, even though it is reasonable relative to values published in the literature (Jolly & Eisenberg, 1976; Kam *et al.*, 1981; Nieuwenhuysen *et al.*, 1981). Alternatively, it may indicate that under the solution conditions tested, the Dickerson DNA exists as a dimer of duplexes at 0 mM spermine-4HCl and as a trimer of duplexes at 4.0 mM spermine-4HCl.

Figure 14-17: Primary axis: M_W as a function of spermine-4HCl concentration for the Dickerson DNA. Determined from the Debye plots in Figure 4.sls-dna. The dashed lines indicate the molecular weight of a duplex (lower limit) or a dimer of duplexes (upper limit). Secondary axis: DLS measured effective diameters of the Dickerson DNA in the highest and lowest DNA concentration samples used in the SLS experiments. Error bars represent the standard deviation of the mean of multiple effective diameter measurements.

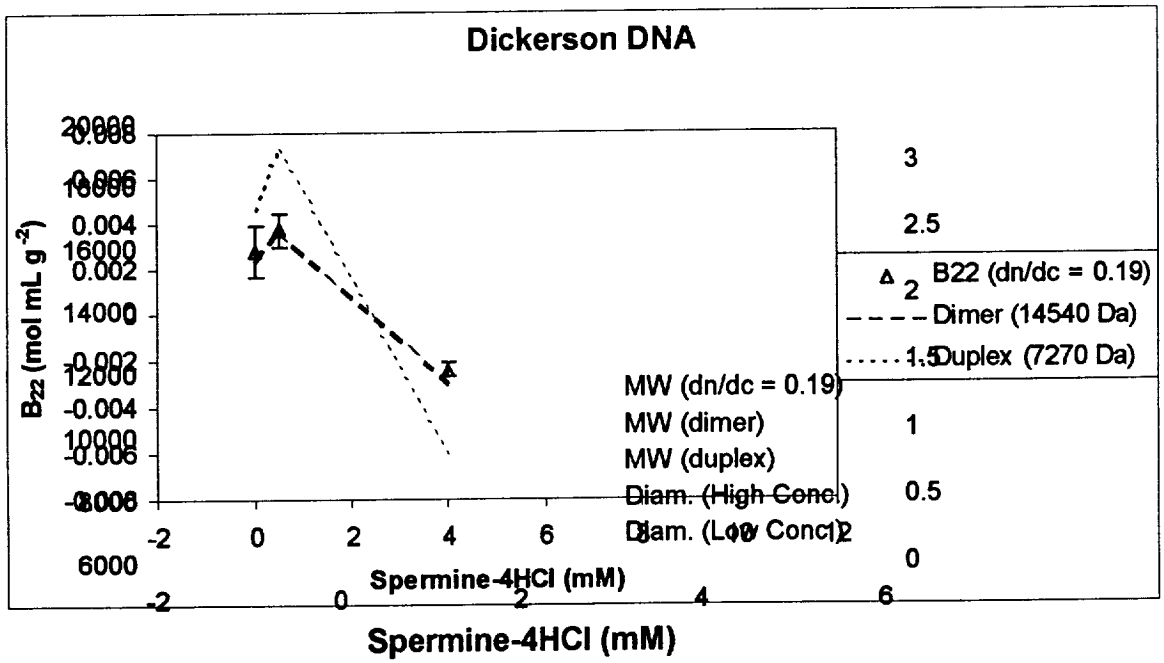

Spermine-4HCl (mM)

Dickerson DNA

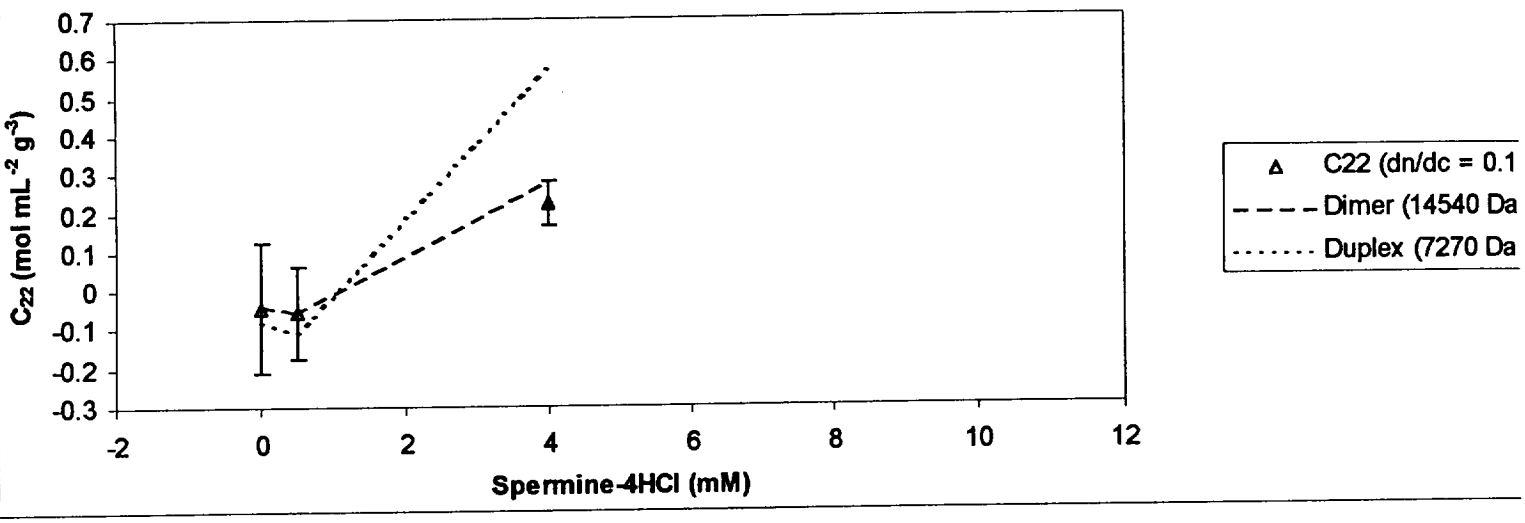

Spermine tetrahydrochloride (mM)	Dickerson DNA (*dn/dc* =0.19 mL/g)				
	M_W (g/mol)	B_{22} (x10^3) (mol mL g^{-2})	S.E. (x10^3)	C_{22} (mol mL^{-2} g^{-3})	S.E.
0	12223	2.77	1.13	-0.04	0.17
0.5	14219	3.70	0.72	-0.06	0.12
4	18400	-2.39	0.29	0.22	0.06

presentation of sls results

14.4.3 Holbrook RNA Dodecamer

14.4.3.1 Crystallization attempt

A crystallization screen was performed with the 5'-OH Holbrook RNA dodecamer at room temperature. Equilibrium solution involved varying $MgCl_2$ concentration between 2.5, 10 and 25 mM, Na Citrate concentration between 100 and 200 mM, and RNA concentration between 3 and 6 mg/mL. In addition, the dewatering factor was either two-fold or four-fold. At equilibrium, all solutions contained 30% PEG-400 and were buffered to pH 8.5 with 50 mM Tris. This screen incorporated published crystallization and attempted to reproduce the reported crystal growth success (Baeyens *et al.*, 1994). Unfortunately success was very limited. Gel-like precipitate and, in a couple of cases, showers of tiny crystals were observed at 200 mM Na Citrate for all $MgCl_2$ concentrations, RNA concentrations and dewatering factors, except the very lowest $MgCl_2$ and RNA concentration at two-fold dewatering. The limited success may possibly be explained by the fact that the RNA sequence whose structure was actually crystallized and solved to 2.0 Å resolution included a 5'-phosphate (Holbrook *et al.*, 1991). Restrictions on resources (time and material) did not permit for similar crystallization attempts with the 5'-P Holbrook RNA dodecamer.

A second screen attempted to check the effect of $MgCl_2$ concentration under conditions similar to those used in light scattering experiments with the UU-dodecamer and the Dickerson DNA. Equilibrium $MgCl_2$ concentrations varied between 5 and 50 mM. The hanging drops were set up to dewater two-fold, reaching equilibrium conditions that consisted of 3 mg/mL RNA, 20 mM NaCl and 50 mM Na Cacodylate, pH 7.0, all at room temperature. Problems apparently occurred with this screen and the drops seemed to have dewatered beyond expectation. All the drops produced showers of tiny crystals. Although this screen doesn't provide much information because of the problems just mentioned, it does indicate that $MgCl_2$ has a precipitating or crystallizing effect at least somewhat similar to that observed with the UU-dodecamer. Again, restrictions on available time and material resources did not permit further investigations along these lines. Instead, the focus was turned to static light scattering experiments with solution conditions similar to those previously used for the other oligonucleotides.

14.4.3.2 Static light scattering experiments with 5'-hydroxylated RNA

Figure 4.sls-5oh-hrna shows the Debye lines for the 5'-OH Holbrook RNA dodecamer in the presence of 5 and 25 mM $MgCl_2$, with the other solution conditions as indicated in the figure caption. The more negative slope at 25 mM and the decrease in the intercept indicate a more negative second virial coefficient and an increase in molecular weight. In fact, Figure 4.B22vMg-5oh-hrna shows that B_{22} is essentially zero at 5 mM $MgCl_2$ and decreases to a large negative value at 25 mM. Non-linearity

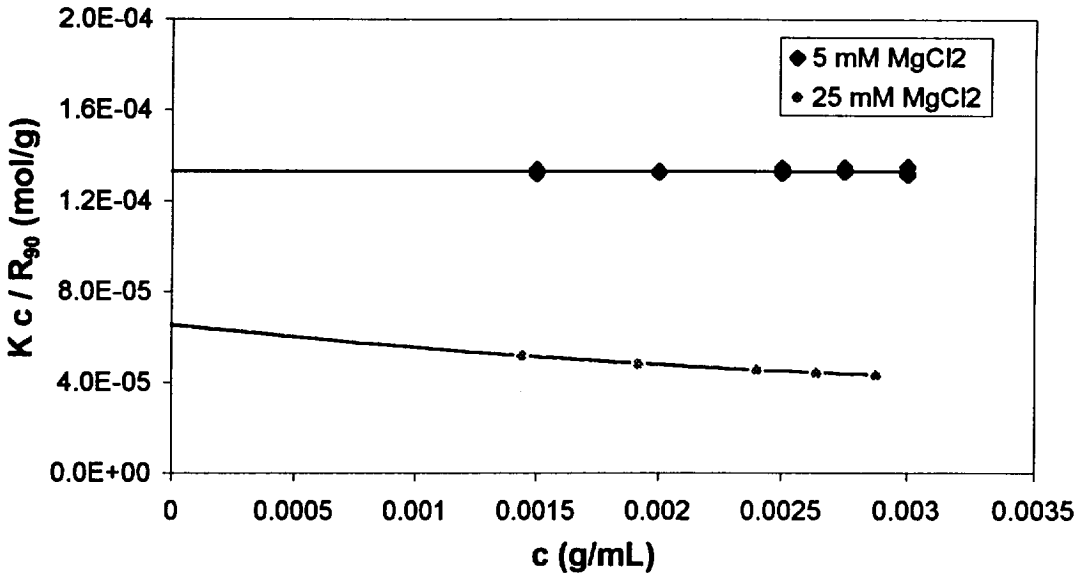

Figure 14-18: Debye plots for the 5'-OH Holbrook RNA at 5 and 25 mM $MgCl_2$. Solutions also contained 20 mM NaCl, and 50 mM Na Cacodylate, pH 7.0. A value of *dn/dc* = 0.175 mL/g was used to interpret the SLS data.

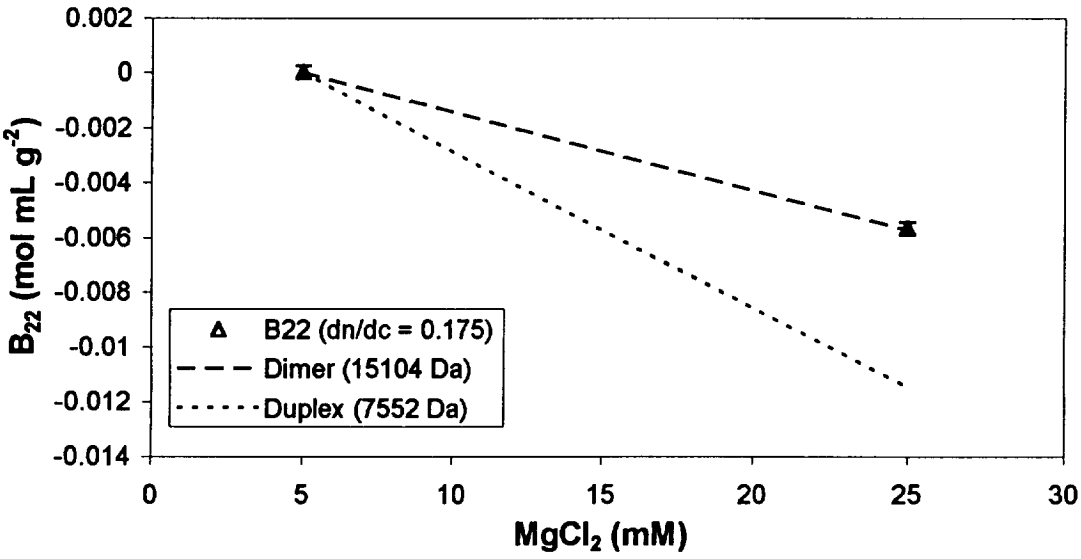

Figure 14-19: B_{22} as a function of $MgCl_2$ concentration for the 5'-OH Holbrook RNA. Determined from the Debye plots in Figure 14-18. The dashed lines indicate the values of B_{22} that would result if *dn/dc* were freely adjusted in each case to give the molecular weight of a duplex (lower limit) or a dimer of duplexes (upper limit). Error bars represent the standard error.

in the Debye line at 25 mM $MgCl_2$ indicates that a meaningful C_{22} can be measured. The molecular weight measured by SLS at 25 mM is double that measured at 5 mM, as seen in Figure 4.dls-5oh-hrna. At 5 mM $MgCl_2$, the RNA exists as a duplex and 25

mM $MgCl_2$, as a dimer of duplexes. These SLS measured molecular weights correlate well with the DLS measured effective diameters of the RNA in solution.

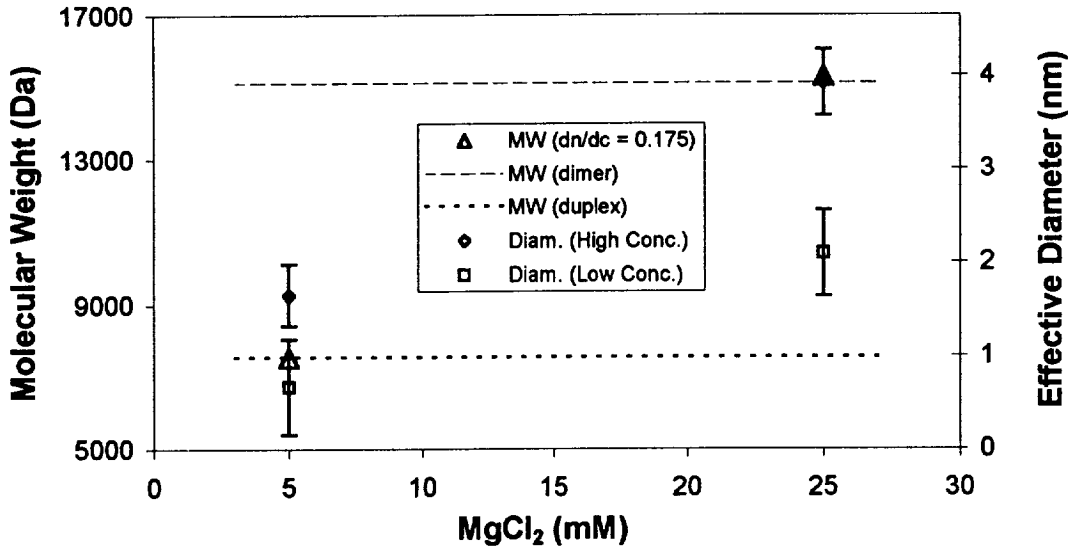

Figure 14-20: Primary axis: M_W as a function of $MgCl_2$ concentration for the 5'-OH Holbrook RNA. Determined from the Debye plots in Figure 4.sls-5oh-hrna. The dashed lines indicate the molecular weight of a duplex (lower limit) or a dimer of duplexes (upper limit). Secondary axis: DLS measured effective diameters of the 5'-OH Holbrook RNA in the highest and lowest RNA concentration samples used in the SLS experiments. Error bars represent the standard deviation of the mean of multiple effective diameter measurements.

14.4.3.3 Static light scattering experiments with 5'-phosphorylated RNA

Since the published crystallization conditions and the crystallization screens described above suggest that the 5' end group of the Holbrook RNA may be an important factor in the crystallizability of the molecule, SLS experiments identical to the ones just described were conducted with the 5'-phosphorylated Holbrook RNA. A quick comparison of Figure 14-21 to Figure 14-18 above reveals that qualitatively, the two RNA molecules which differ only at the 5' end have very different solution thermodynamics under the same conditions. $MgCl_2$ has a very small

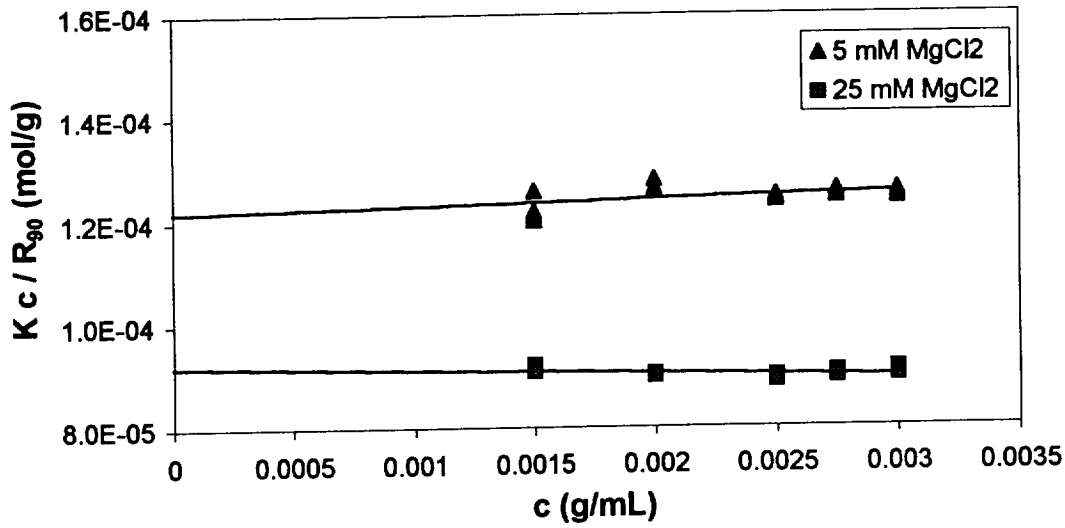

Figure 14-21: Debye plots for the 5'-P Holbrook RNA at 5 and 25 mM $MgCl_2$. Solutions also contained 20 mM NaCl, and 50 mM Na Cacodylate, pH 7.0. A value of *dn/dc* = 0.175 mL/g was used to interpret the SLS data.

effect on the osmotic second virial coefficient. Figure 14-22 shows that B_{22} decreases from a slightly positive value to a slightly negative one as $MgCl_2$ concentration increases from 5 to 25 mM. The molecular weight is likewise not strongly affected by $MgCl_2$. In Figure 4.dls-5p-hrna, molecular weight increases slightly from that of roughly a duplex when $MgCl_2$ concentration increases from 5 mM to 25 mM. The SLS measured molecular weights again correlate well with the DLS measured effective diameters using the same correlation proportionality as in the 5'-OH case.

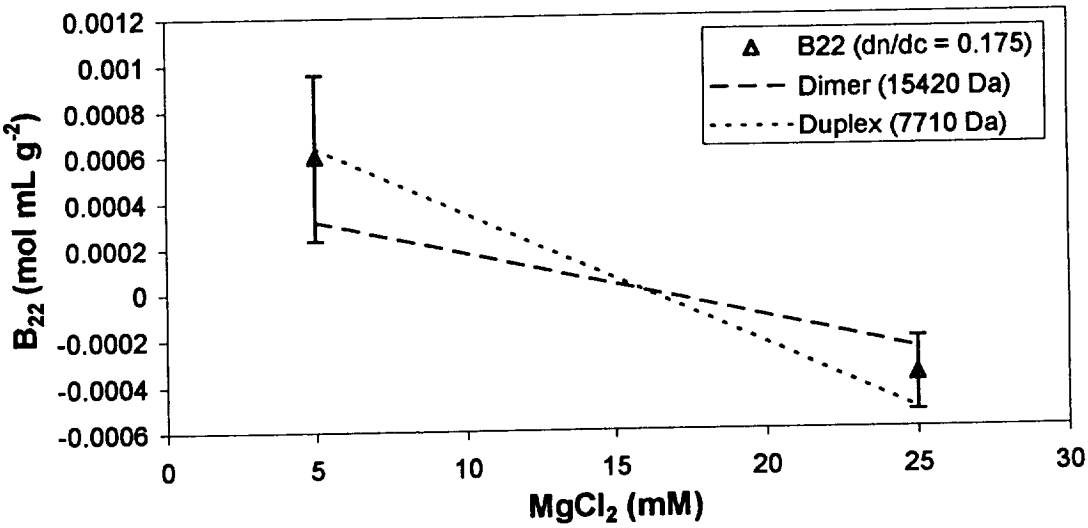

Figure 14-22: B_{22} as a function of $MgCl_2$ concentration for the 5'-P Holbrook RNA. Determined from the Debye plots in Figure 4.sls_5p-hrna. The dashed lines indicate the values of B_{22} that would result if *dn/dc* were freely adjusted in each case to give the molecular weight of a duplex (lower limit) or a dimer of duplexes (upper limit). Error bars represent the standard error.

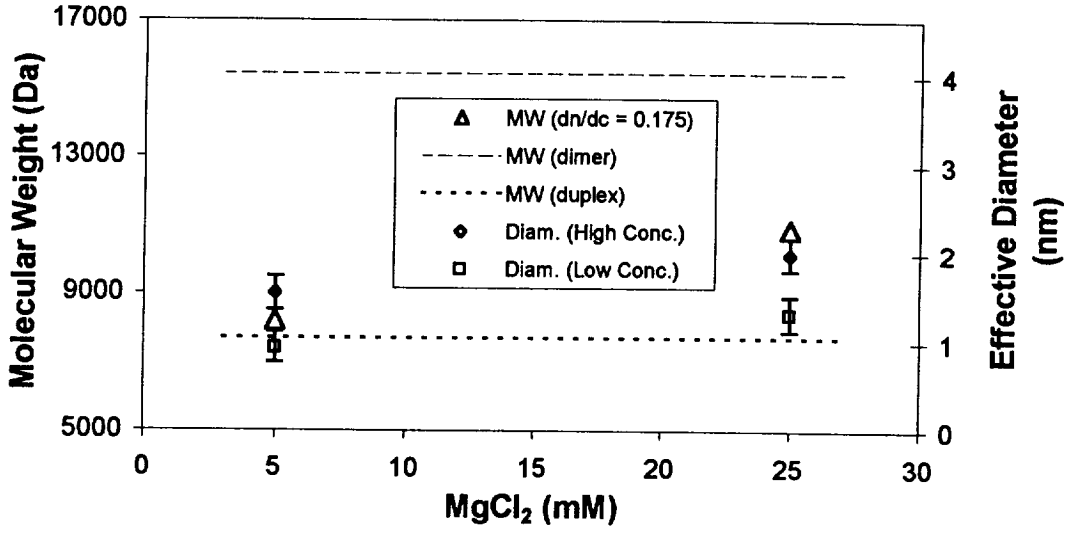

Figure 14-23: Primary axis: M_W as a function of $MgCl_2$ concentration for the 5'-P Holbrook RNA. Determined from the Debye plots in Figure 4.sls-5p-hrna. The dashed lines indicate the molecular weight of a duplex (lower limit) or a dimer of duplexes (upper limit). Secondary axis: DLS measured effective diameters of the 5'-P Holbrook RNA in the highest and lowest RNA concentration samples used in the SLS experiments. Error bars represent the standard deviation of the mean of multiple effective diameter measurements.

14.4.3.4 Summary of SLS results

Table 4.hrna numerically summarizes the SLS results for the Holbrook RNA presented graphically above. In this case it is clear that the 5' end of the Holbrook RNA molecule very significantly affects the solution thermodynamics.

Table 14-5: Summary of light scattering results for the Holbrook RNA in varied $MgCl_2$ concentrations and with differing 5' end groups, determined from the Debye plots shown in Figure 4.sls-5oh-hrna and Figure 4.sls-5p-hrna. Other solution conditions: 20 mM NaCl, and 50 mM Na Cacodylate, pH 7.0.

Molecule	$MgCl_2$ (mM)	*dn/dc*=0.175 mL/g					
		M_W (g/mol)	B_{22} (x10^3) (mol mL g^{-2})	S.E. (x10^3)	C_{22} (mol mL^{-2} g^{-3})	S.E.	Fit Order
5'-OH RNA	5	7519	0.02	0.21	---	---	linear
5'-OH RNA	25	15277	-5.66	0.22	0.42	0.03	quadratic
5'-P RNA	5	8210	0.59	0.36	---	---	linear
5'-P RNA	25	10874	-0.37	0.16	---	---	linear

14.5 DISCUSSION

14.5.1 Roles of Cations and Polyols

Multivalent cations, including divalent metal ions and polyamines such as spermidine and spermine are ubiquitous in oligonucleotide crystallization. Cations, especially divalent metal cations, with Mg^{++} being the most prominent player, are known to perform critical and indispensable roles in the function of catalytic RNAs such as ribozymes and in the structure (particularly tertiary structure) of RNAs and DNAs (Kasakov, 1996; Feig & Uhlenbeck, 1999; Sriram & Wang, 1996). While metal ions are accurately described as "stabilizers" of native oligonucleotide structure (Hermann & Patel, 1999) and as "ionic scaffolds" on which tertiary structure can form (Strobel & Doudna, 1997) the results in this study show that they can also provide the driving force for bringing the oligonucleotide molecules together. That is, they perform the role of "precipitant", a label rarely, if ever, applied to these components, especially at very low concentrations. In the case of the UU-dodecamer, millimolar amounts of $MgCl_2$ were sufficient to produce showers of small crystals and crystalline precipitate (see solubility and screen results in Chapter 3). With the proper kinetic control it should be possible to grow a smaller number of larger crystals which would be suitable for X-ray diffraction experiments.

Polyamines are often designated merely as "additives" in crystallization solutions, but as shown with the Dickerson DNA, spermine also plays the role of "precipitant" under appropriate conditions. Reasonably large crystals were grown by controlling the relative ratios of Mg^{++} and spermine concentration, pH, and temperature. The effect of pH will be discussed below. The ability of spermidine (a trivalent cation) and spermine (a tetravalent cation) to condense and precipitate large DNAs has been known for many years, as has been the ability of monovalent and divalent cations (such as Na^{+} and Mg^{++}) to reverse DNA condensation (Widom & Baldwin, 1980; Wilson & Bloomfield, 1979). Therefore, the antagonism between spermine and Mg^{++} observed in the screens and DLS-titration experiments in this study are consistent with the literature. Controlling this antagonism to produce crystals is also consistent since the difference between obtaining crystals and precipitate is often a matter of kinetics.

From the solubility and crystallization screen results, the pH measurements in Table 14-4 and the DLS titration experiments, it is clear that the effectiveness of spermine in aggregating or precipitating the Dickerson DNA is dependent upon the pH of the solution and the magnesium cation concentration. Acidic conditions favor the precipitating effect of spermine, while magnesium cations oppose this effect. This indicates that spermine most effectively interacts with and between DNA molecules (leading to aggregation) when it is positively charged (a state favored under acidic conditions) and can form electrostatic interactions with the highly negatively charged DNA. Magnesium cations compete with spermine (also a multivalent cation under acidic conditions) for the same binding sites on the DNA, thus explaining the solubilizing effect of magnesium salts (this claim will be more fully demonstrated below). Magnesium acetate more effectively solubilizes the spermine-precipitated

DNA because, in addition to the competition effect of Mg^{++}, the acetate anion neutralizes the spermine by decreasing and neutralizing the acidity of the solution.

Polyols such as MPD and PEG are also very common "precipitants" in oligonucleotide crystallization. MPD has been the overwhelming favorite in DNA crystallization. Most DNA crystallization solutions are variations on the following theme: 1 - 2 mM DNA, 0 - 1 mM spermine, 0 - 20 mM magnesium salt, and about 30% MPD with the pH maintained around 7 using sodium cacodylate (Berman, 1997). PEG-400 has been proposed as a generally useful substitute for MPD in the crystallization of RNA oligomers (Baeyens *et al.*, 1994). In this study, it has been shown that both MPD and PEG-400 can be eliminated from the crystallization solution. Showers of small crystals and crystalline precipitate can still be produced without these traditional "precipitants". With proper kinetic control of the crystallization process it should be possible to grow large, diffraction quality crystals.

The literature indicates that B-form DNA duplexes require MPD to crystallize, but that A-form and Z-form duplexes can be crystallized without using MPD. A-form duplexes were crystallized in some cases without any alcohol. In addition, it has been argued that the A-, B-, and Z-form duplexes can generally be differentiated by the relative ratios of spermine, magnesium, and base pairs (Timsit & Moras, 1992). Because of the uniformity of DNA oligonucleotide crystallization conditions relative to those for proteins, it has been suggested that these conditions may bias the comparisons that are made across the archive (Berman, 1997). A search of the Nucleic Acid Database demonstrates that the Dickerson DNA, in its unmodified sequence has been crystallized exclusively as the B-form duplex. Since the Dickerson DNA has been crystallized in this study using only spermine and $MgCl_2$, it would be useful to know what form it crystallized as. Unfortunately, this line of investigation was not pursued in this study because of time limitations.

Clearly, Mg^{++} and spermine must be very important in the crystal structure of the Dickerson DNA. The crystal structure of this molecule has been solved many different times by many different researchers: there are some 70 structure files deposited in the Nucleic Acid Database (NDB) for this particular DNA sequence. Shui *et al.* (1998a) solved the structure to 1.4 Å (NDB entry BDL084) and positively identified half of a spermine molecule (the other half was statistically disordered) and a fully hydrated magnesium ion in the structure. This hydrated magnesium ion has been shown to participate in cation-π interactions in the Dickerson DNA structure (McFail-Isom *et al.*, 1998).

Figure 14-24 shows a couple of views of symmetry-related duplexes of the Dickerson DNA. Frame a) shows two duplexes interacting via the hydrated magnesium ion. Through its hydration shell, the magnesium ion forms cation-π bonds with the pyrimidine rings of cytosine 1 and cytosine 21 in the major groove of one duplex (green duplex in frame a). The hydration shell of the magnesium also forms hydrogen bonds to the O6 and N7 positions of guanines 2 and 22 of the same duplex (green duplex in frame a). Hydrogen bonds are also formed between the hydration layer of this same magnesium and phosphate oxygen atoms of adenine 6 and thymine 7 of the second duplex (orange duplex in frame a). So in this case the hydrated magnesium cation is clearly mediating the interaction between these two duplexes. Frame b) of Figure 4.dna-structure shows three duplexes interacting via a spermine-water molecule bridge. The green duplexes in frames a) and b) are the same duplex.

Figure 14-24: Two views of symmetry-related Dickerson DNA duplexes (generated from the coordinate file of NDB entry BDL084): a) duplexes interacting through a fully hydrated magnesium ion, and b) duplexes interacting through a spermine molecule and a water molecule. Symmetry-related molecules were generated from the asymmetric unit using Swiss-PdbViewer (v3.1) and the molecular graphics were rendered using Rasmol (v2.7.1).

N5 of the spermine molecule hydrogen bonds to the N7 of guanine 10 in the major groove of the first duplex (green duplex in frame b). N1 of the same spermine molecule hydrogen bonds to a water molecule, which in turn hydrogen bonds to a phosphate oxygen of adenine 17 of a second duplex (cyan duplex in frame b) and to a phosphate oxygen of guanine 24 of a third duplex (yellow duplex in frame b).

Since the Dickerson DNA dodecamer is a self-complementary molecule, the two ends of the duplex formed from the single strands are identical in sequence. A quick review of the crystallographic structure reveals that both spermine and the magnesium cation interact with roughly the same bases in the major groove on opposite ends of the duplex. That is, the binding site for spermine and the binding site for hydrated Mg^{++} are essentially identical in the structure as displayed in Figure 4.dna-structure. Therefore, spermine and hydrated Mg^{++} compete with each other for the same binding sites, confirming the antagonism between these two species observed in the solubility and crystallization screens and the DLS-titration experiments (discussed above).

14.5.2 Virial Coefficients and Their Meaning

Multivalent cations affected the solution thermodynamics of the three different oligonucleotides in a similar way. The second virial coefficient decreased with increasing multivalent cation concentration. In the case of the UU-dodecamer, B_{22} started out already negative in the absence of Mg^{++} and became even more negative by about an order of magnitude as the concentration of $MgCl_2$ was increased to 10 mM. With the Dickerson DNA, B_{22} decreased from a significant positive value at 0 mM spermine-4HCl to a significant negative value at 4.0 mM. Finally, in the case of the 5'- hydroxylated Holbrook RNA, B_{22} went from essentially zero or slightly negative value at 5 mM $MgCl_2$ to a very significant negative value at 25 mM. With the 5'-phosphorylated Holbrook RNA, B_{22} decreased from a slightly positive value at 5 mM $MgCl_2$ to a slightly negative value at 25 mM.

$MgCl_2$ affects the solution thermodynamics of the UU-dodecamer much more strongly than it did the other two oligonucleotides. As discussed in the introduction,

the second virial coefficient is a measure of the two-body interactions in solution. A positive B_{22} means that repulsive interactions dominate, and a negative B_{22}, that attractive interactions dominate. Since B_{22} was significantly negative even in the absence of $MgCl_2$, the pair-wise interactions between UU-dodecamer duplexes are thermodynamically favored. Therefore, it is not surprising that the molecular weight of the UU-dodecamer increases sharply (from about that of a duplex to about that of a dimer of duplexes) as $MgCl_2$ is added to the solution. The strong thermodynamic affect of $MgCl_2$ on the UU-dodecamer measured by SLS agrees well with the observations that millimolar amounts (about 15 mM or greater) of $MgCl_2$ strongly precipitate or crystallize this RNA under the conditions tested.

At 5 mM $MgCl_2$ in the absence of spermine, repulsive pair-wise interactions dominate in the Dickerson DNA case. The large molecular weights (nearly that of a dimer of duplexes, or, 14,540 Da) measured under these conditions are upon first impressions quite surprising. In fact, if a somewhat smaller (although still in very good agreement with published values) *dn/dc* value of 0.174 mL/g instead of 0.19 mL/g were used to interpret the SLS data, the molecular weight would be precisely that of a dimer of duplexes. However, in light of the crystallographic data presented above, these results are reasonable. A hydrated magnesium ion mediates the interaction between Dickerson DNA duplexes. Under the appropriate magnesium ion concentrations, it is then very possible that the Dickerson DNA exists as a dimer of duplexes in solution. The pair-wise interactions measured by the second virial coefficient would then be between the dimers and not the individual duplexes. This appears to be the case at 5 mM $MgCl_2$. It is likely that at lower $MgCl_2$ concentrations (fractions of a mM to maybe a few mM), B_{22} would be negative and would reflect the attractive interactions between individual duplexes. At higher $MgCl_2$ concentrations, B_{22} should also go negative. This interpretation agrees with the DLS-titration experiments. Below some critical magnesium ion concentration, the scattering intensities and the effective diameters increased slightly, indicating a possible transition from duplexes to dimers of duplexes. Above the critical concentration, high levels of aggregation occurred. At some Mg^{++} concentration below the critical, one might expect that the duplexes are completely aggregated into dimers due to Mg^{++} mediation, but because of the even higher charge densities, the dimers repel each other. Even higher concentrations of cations would be required to screen these repulsive electrostatic interactions before higher levels of aggregation could occur. The inflection points seen in the DLS titration data most likely reflect the transitions from attractive to repulsive to again attractive interactions proposed here.

In the case of the Holbrook RNA, the 5'-end of the molecule has a large effect on the solution thermodynamics of the oligonucleotide. When the 5'-end is hydroxylated, increasing the amount of $MgCl_2$ from 5 mM to 25 mM greatly increased the attraction between the RNA molecules as indicated by the large negative second virial coefficient ($B_{22} \approx -7 \times 10^{-3}$ mol mL g^{-2}) at 25 mM $MgCl_2$. However, under the same conditions, when the 5'-end is phosphorylated, B_{22} only varies between a relatively slight repulsion (at 5 mM $MgCl_2$) to a relatively slight attraction. The additional negative charges from the 5'-phosphates inhibit the thermodynamic effect of $MgCl_2$ by a factor of about 15, as measured by the decrease in absolute value of second virial coefficient at 25 mM $MgCl_2$ relative to that at 5

mM. A smaller B_{22} is consistent with the higher repulsion that arises when each RNA strand has an extra negative charge, which occurs in the 5'-P case compared to the 5'-OH.

The molecular weights measured for the Holbrook RNA by SLS are somewhat lower than those measured for the UU-dodecamer RNA under similar solution conditions. As a reminder, this RNA molecule forms an exceptionally stable tetraloop not only in low salt conditions but even in higher salt conditions used to grow crystals (Kanyo *et al.*, 1996). Therefore, it is not surprising that with this RNA the SLS measured molecular weights are biased downward toward those of single-stranded hairpins, which should comprise under low $MgCl_2$ conditions a significant portion of the entire population of conformations. At the higher $MgCl_2$ concentration (25 mM) duplexes and dimers of duplexes are favored as reflected by molecular weights that are larger than those of duplexes (~7600 Da) but smaller than those of dimers of duplexes (~15,200 Da). In the 5'-phosphorylated case, molecular weights at 25 mM $MgCl_2$ are quite a bit lower than in the 5'-hydroxylated case, demonstrating that the higher intermoleculer repulsion due to the higher negative charge densities inhibit the formation of dimers. The effective diameters (D_{eff}) measured by DLS correlate well with the SLS measured molecular weights. Smaller values of D_{eff} were measured for the Holbrook RNA relative to the UU-dodecamer, providing more weight to the explanation just given for the smaller molecular weights observed.

Significant positive values for the third virial coefficent were measured for all the conditions tested with the UU-dodecamer, except at 0 mM $MgCl_2$ in the presence of PEG-400. C_{22} was quite large in the presence of $MgCl_2$. For the other two oligonucleotides, significant positive C_{22} values were measured at the highest multivalent cation concentrations. As discussed in the Introduction and in Chapter 2, the third virial coefficient is a measure of the three-body interactions. Positive C_{22} values mean that the three-body interactions are not favored, while negative values mean that they are. Third virial coefficients are typically not measured because there is usually not a sufficient level of three-body interactions occurring in the dilute solution conditions used in light scattering experiments. Here the DLS measurements show that in the cases where a measurable C_{22} occurred, there were quite significant differences in the effective diameters measured in the high and low concentration SLS samples. This indicates that at higher concentrations the oligonucleotides had a greater tendency to aggregate say from duplexes to dimers of duplexes. The various SLS samples then contained mixed populations of the monomeric and dimeric species. Measurable third virial coefficients reflect the interactions between three duplexes simultaneously, or a duplex with a dimer of duplexes. The formation of mixed populations of duplexes and dimers of duplexes is what contributes to a measurable C_{22}, even under what are considered dilute solution conditions. In all three oligonucleotides used in this study, the positive C_{22} values that occur alongside the large negative B_{22} values indicate that while the formation of dimers is strongly favored, the addition of monomers to form higher order aggregates is not favored. Note that in the case of the Dickerson DNA, where under the conditions tested, the molecules appeared to primarily occur as dimers of duplexes, the third virial coefficient measures the interaction between three dimers.

14.5.3 Oligonucleotides and the Protein Crystallization Slot

Solution conditions that produce high quality crystals of proteins are characterized by osmotic second virial coefficients that fall in a very narrow range of small negative values. Wilson and coworkers measured this range to be about -1×10^{-4} to -8×10^{-4} mol mL g^{-2} (George & Wilson, 1994; George *et al.*, 1997). Proteins in solutions with B_{22} values more positive than the upper limit of this range are

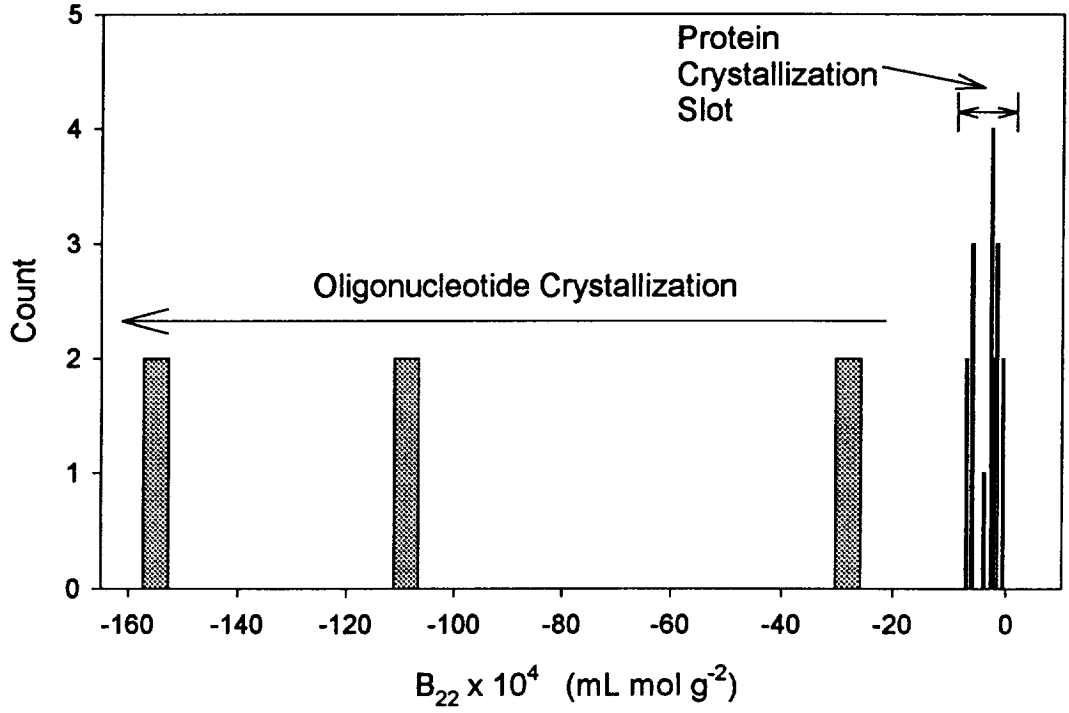

dissolved in good solvents and show no tendency to come out solution, unless protein concentration is taken to very high level. However, proteins in solutions with B_{22} values more negative than the lower limit of the crystallization slot lead to the formation of amorphous precipitates. In the case of proteins, small to moderate attractions are required for the formation of crystalline material.

Figure 14.25: Histrogram showing osmotic second virial coefficients measured for the UU-dodecamer RNA in comparison with the protein crystallization slot observed by Wilson and coworkers (George & Wilson, 1994; George *et al.*, 1997).

Figure 14-25 shows the protein crystallization slot and values of B_{22} for the UU-dodecamer in solutions that approach crystallization conditions. Clearly, the protein crystallization slot does not have much if any relevance to oligonucleotide

crystallization. Relative to proteins, second virial coefficients for UU-dodecamer crystallization solutions approach (and possibly equal or go beyond) values that are two orders of magnitude more negative than the lower limit of the protein crystallization slot. Although not as negative as in the UU-dodecamer case, values of B_{22} were measured for the Dickerson DNA and the Holbrook RNA in non-precipitating and non-crystallizing solutions that are also quite negative relative to those for proteins. The results in this study clearly show that if an oligonucleotide crystallization slot exists (something that cannot be determined from the present data), its characteristic range of second virial coefficients are very different from those for proteins. This conclusion is consistent with the fact that oligonucleotides have a much more negative charge density relative to proteins. It is reasonable, therefore, to expect that the interactions that govern oligonucleotide crystallization are significantly different from those in protein crystallization. Indeed, the large differences in solution thermodynamics between proteins and oligonucleotides strongly suggest that this is the case.

14.5.4 DLVO Theory and Oligonucleotide Solution Thermodynamics

Osmotic second virial coefficients that are very negative relative to those typically measured for proteins in crystallizing or precipitating solutions were consistently and reproducibly measured in this study for different oligonucleotides in non-crystallizing and non-precipitating solutions. Although the experimental results are very reliable, how do we explain the relatively large negative values of B_{22}? The model proposed here is that oligonucleotides can remain as soluble species under solution conditions where very strong attractive interactions dominate (as reflected by very negative B_{22} values) because they are electrokinetically stabilized colloids. A DLVO approach is employed to lend support to this model. An electrokinetically stabilized colloid will be characterized by a deep attractive well with a repulsive energy barrier.

It is known that B-form dodecamer DNA duplexes have helical diameters of about 2 nm and lengths of about 4 nm (~3.4 Å rise per base pair) (Long, 1996). The Dickerson DNA is a B-DNA and the crystallographic structures of the UU-dodecamer RNA (NDB entry URL050) and the Holbrook RNA (NDB entry ARL037) show that the duplexes of these molecules have geometric dimensions quite similar to B-DNA dodecamer duplexes. Spheres with radii of 1.44 nm have volumes equivalent to cylinders with diameters of 2 nm and lengths of 4 nm. Therefore, a radius of 1.44 nm was used in the DLVO model since the equations were developed for spherical geometry. Repulsive interaction potential energies (Φ_R) were modeled using the function given in Equation 14.1. Attractive potential energies (Φ_A) were modeled using the function given in Equation 14. attractive. The validity of these functions for the current model was discussed and justified in Chapter 2. The net interaction potential (Φ_{Net}) is given by the sum of the attractive and repulsive interactions (Equation 14.3).

$$\Phi_R(r) = 4\pi\psi_0^2 \varepsilon \varepsilon_0 a \frac{e^{-\kappa r}}{2 + r/a} \tag{14.1}$$

$$\Phi_A(r) = \begin{cases} -\dfrac{r}{r_{min}/\Phi_{min}} & 0 \le r \le r_{min} \\ -\Phi_{min}\left(\dfrac{r_{min}}{r}\right)^2 e^{-\kappa(r - r_{min})} & r > r_{min} \end{cases} \tag{14.2}$$

$$\Phi_{Net}(r) = \Phi_A(r) + \Phi_R(r) \tag{14.3}$$

where r is the surface to surface separation, a is the radius of the spherical particle, ψ_0 is the surface potential, Φ_{min} is the absolute value of the attractive energy well minimum, which occurs at a separation distance of r_{min}, κ is the Debye-Hückel

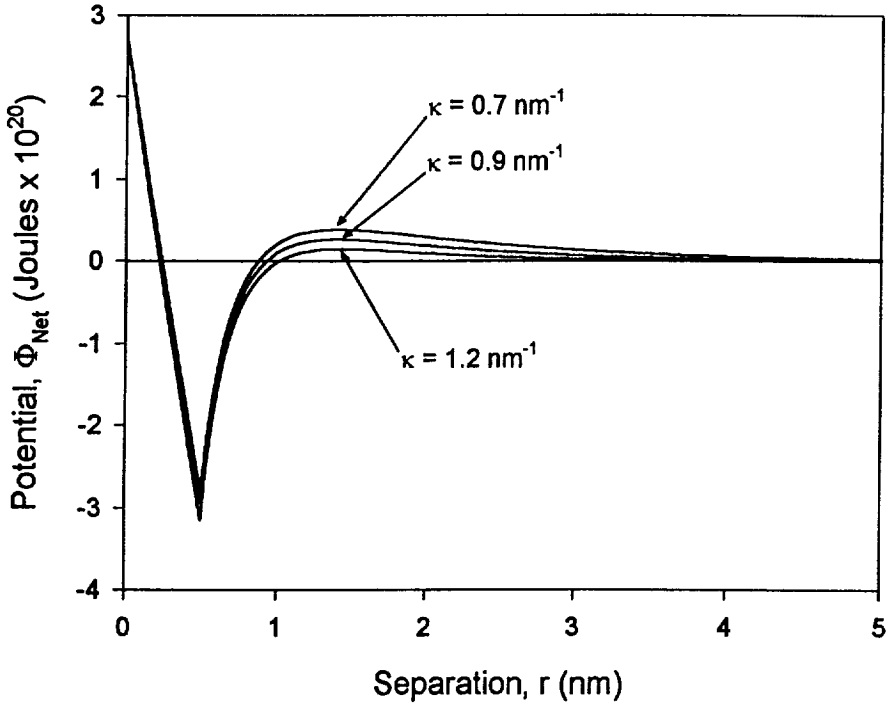

parameter, ε is the dielectric constant of the solvent, and ε_0 is the permittivity of free space.

Figure 14-26 shows the potential energy curves as a function of separation distance for charged spheres with a constant surface potential under different ionic strength conditions (as measured by κ). A zeta potential of 65 mV has been measured

Figure 14-26: DLVO diagram for dodecamer oligonucleotides under solution conditions with varied ionic strengths (i.e. varied Debye-Hückel parameters, κ). The net potential was determined using the attractive and repulsive potentials as described in Chapter 2. Parameter values used in the model: Ψ_0 = 65 mV, Φ_{min} = 4.4 × 10^{-20} J, r_{min} = 0.5 nm, a = 1.44 nm, ε = 80, ε_0 = 8.85 × 10^{-12} C^2 N^{-1} m^{-2}.

for oligonucleotides (Paul Todd and Don Voet). Although it almost certainly underestimates the actual surface potential, this empirically measured potential was used as an approximation of the surface potential in the DLVO model. The deep attractive well is assumed to be primarily due to electrostatic interactions between oligonucleotide duplexes mediated by multivalent cations such as Mg^{++} and spermine. These interactions consist of cation-π and direct lone-pair interactions (McFail-Isom *et al.*, 1998). As discussed in Chapter 2, the energy of these cation-mediated interactions was estimated to be up to about 200 kJ/mol (or about 3.3×10^{-19} J per interaction). The attractive energy minimum is assumed to occur at a separation distance of 0.5 nm, which is consistent with the interaction distances of Mg^{++} in cation-π bonds and direct interactions with phosphate oxygens (McFail-Isom *et al.*, 1998; Deerfield & Pedersen, 1995). In addition, analysis of the structural data for the Dickerson DNA (NDB entry BDL084) shows that the interhelical distance at the hydrated Mg^{++} ion mediated contact point is on the order of 5 Å. A dielectric constant of water ($\varepsilon = 80$) was assumed for the calculations. Values of the Debye-Hückel parameter, κ, were calculated as described in Chapter 2 for solutions of 20 mM NaCl and 50 mM Na Cacodylate, pH 7.0 with different concentrations of $MgCl_2$. For 0 mM $MgCl_2$, the calculations yielded $\kappa \approx 0.7$ nm^{-1}, for 10 mM $MgCl_2$, $\kappa \approx 0.9$ nm^{-1}, and for 25 mM $MgCl_2$, $\kappa \approx 1.2$ nm^{-1}.

The DLVO approach presented here confirms that solutions of oligonucleotide dodecamers can exist as electrokinetically stabilized colloids under solution conditions for which large negative osmotic second virial coefficients were measured. Figure 4.dlvo shows that with independently measured or estimated parameters characteristic of nucleic acid oligomers, the potential energy calculated for the system includes a deep attractive well and an energy barrier. These two features characterize electrokinetically stabilized colloids and were hypothesized for the oligonucleotide systems used in the LS experiments in this study. The attractive energy minimum used in the DLVO model ($\Phi_{min} = 4.4 \times 10^{-20}$ J) is almost an order of magnitude lower than the energies (3.3×10^{-19} J) estimated for cation-mediated interactions involving cation-π bonds and direct lone-pair interactions. However, this smaller well depth may occur because the surface potential of oligonucleotides is underestimated by the zeta potential used in the model. Another explanation is that the cation-mediated interactions are orientation dependent and the simple attractive potential function used here does not consider orientation. Therefore, the very large attractive energies that actually occur for a small number of orientation are averaged over all orientations in this model. Finally, the actual attractive well energy may indeed be smaller than estimated. The estimates were for Mg^{++} ions interacting directly with π systems, whereas the empirically observed cases involve Mg^{++} ions interacting with the π systems of nucleic acid bases through a hydration layer (McFail-Isom *et al.*, 1998).

The value of $\Phi_{min} = 4.4 \times 10^{-20}$ J was specifically chosen in the DLVO modeling effort because B_{22} values calculated using this value of Φ_{min} in the interparticle pair potential, $\Phi_{Net}(r)$, agree well with those measured experimentally in

this study. B_{22} values measured by SLS can be related to the interparticle pair potential by statistical mechanics. For spherical particles experiencing centrosymmetric interaction potentials, the relationship is given by

$$B_{22} = 2\pi\int_0^\infty r^2(1-e^{-\Phi(r)/kT})dr \tag{14.4}$$

where k is the Boltzmann's constant and T is the temperature. For separation distances less than r_{min}, the attractive potential function in the DLVO model above was defined as linearly decreasing from 0 to $-\Phi_{min}$ for $0 \le r < r_{min}$. This was done primarily for purposes of plotting the function. In reality, r_{min} should be considered the distance of closest approach in order to avoid particle overlap. Therefore, the particle radius, a, plus r_{min} represents an effective hard core radius. At separation distances less than r_{min}, the attractive potential function should be become repulsive very quickly due to the hard core repulsion. With the application of these considerations, Eq. 14.4 becomes

$$B_{22} = \left[\frac{2\pi}{3}(2a+r_{min})^3\right] + \left[2\pi\int_{r_{min}}^\infty r^2(1-e^{-\Phi(r)/kT})dr\right] \tag{14.5}$$

The first term in Eq. 4.3 is the repulsive contribution due to the effective hard core. The approach taken here in calculating B_{22} from the interaction potential is a slight modification of an approach given for globular proteins (Farnum & Zukoski, 1999). Note that second virial coefficients calculated using Eq. 4.B22hs have values in units of length cubed and that these values must be multiplied by a factor of N_A/M_W^2 in order to have B_{22} values with the same dimensions as those measured by static light scattering. N_A is Avogadro's number and M_W is the molecular weight of the particle with a hard core radius, a.

Values of B_{22} were calculated using Eq. 4.net and Eq. 4.B22hs for the Debye-Hückel parameters shown in Figure 4.dlvo. The values of the other parameters were as shown in the caption of Figure 4.dlvo. Assuming an oligonucleotide dodecamer duplex molecular weight of 7500 g/mol, for values of κ of 0.7, 0.9 and 1.2 nm^{-1}, the calculated osmotic second virial coefficients were -1.1×10^{-3}, -2.8×10^{-3} and -5.7×10^{-3} mol mL g^{-2}, respectively. These calculated second virial coefficients are quite consistent with the empirically measured ones.

4.5.5 A Rational Crystallization Strategy

The crystallization of biological macromolecules has a history that spans 150 years, although for most of that history the approaches taken have been described in terms like "black art" or "alchemy" rather than "science" (McPherson, 1999, pp. vii - 1). In the past several decades more scientific approaches have been taken. However, biomacromolecular crystals are overwhelmingly desired for X-ray crystallography studies, and therefore the emphasis is placed primarily on obtaining a diffraction quality crystal and not so much on understanding the how or why of the crystallization process. Arbitrary approaches that rely on and are guided by past successes in the general field of crystallization are currently the most popular approach for screening solution conditions. Although these approaches are frequently

successful (thus their popularity), they shed little light on the process of biological macromolecular crystallization. As pointed out by the guru of biological macromolecular crystallization, systematic and rational approaches are more intellectually and scientifically satisfying "because they utilize the investigator's knowledge and expertise, and they embody the traditional scientific philosophy" (McPherson, 1999, p. 273). Even when the scientific approach fails to produce the desired crystallization effect, valuable scientific information is still obtained. Unfortunately, systematic approaches often consume large amounts of valuable time and material, especially when there is a limited body of knowledge regarding the given macromolecule. The arbitrary screening approach can have a legitimate, scientifically useful purpose then for limiting the scope of the systematic investigations. Care must be taken, however, not to focus on what has worked in the past to the point where crystallization solution conditions are so similar that a bias is introduced in the results across the crystallization archive. Such a bias can inhibit valid investigations into the crystallization process and the effects of specific solution components on the crystal structure of the macromolecule. It has been argued that such a bias already exists in the DNA field, since crystallization conditions for all DNA are modest variations of a strong theme: 1 - 2 mM DNA, 0-1 mM spermine, 0 - 20 mM magnesium salt, about 30% MPD, with the pH buffered to around 7 using sodium cacodylate. There is a critical need then for structures determined from crystals grown under very different conditions (Berman, 1997).

In light of the results obtained in the current study, it is clear that the use of light scattering (both DLS and SLS) in combination with traditional systematic screening techniques provides a rational and quantitative approach for identifying the factors that most critically modulate the solution behavior and thermodynamics of biological macromolecules, specifically oligonucleotides in this case. Sound knowledge concerning these factors, allows the investigator to employ a rational experimental design in the pursuit of producing crystals, which incorporates a careful manipulation of these critical factors. For example, crystallization techniques such as osmotic dewatering or dialysis diffusion among others may be used to specifically control the kinetics of achieving supersaturation in terms of a critical solution component. Very different crystallization conditions for a particular oligonucleotide can then be discovered, allowing a broader understanding of the crystallization process and of the effects of specific components.

14.6 CONCLUSIONS

A number of conclusions can be made from the study presented in this chapter. For the oligonucleotides tested, multivalent cations strongly affected solution behavior, whereas traditional precipitants such as MPD and PEG-400 have a relatively small effect. Given the label "precipitant", these polyols would be expected to have a relatively strong effect. Statistically, PEG-400 had an insignificant effect on the solution thermodynamics of the UU-dodecamer RNA for the concentrations tested. The sum of the experiments presented here suggest that polyols may not be necessary for the crystal growth of any of the investigated oligonucleotides. Careful control of the concentrations of the oligonucleotides, multivalent cations and the kinetics of the crystallization process should produce diffraction quality crystals.

Light scattering is useful as a quantitative and predictive determinant of the factors that most strongly affect oligonucleotide crystallization and which must be most carefully controlled.

From the experimentally measured thermodynamics and the modeling effort, it was determined that oligonucleotides can exist as solutions of electrokinetically stabilized colloids. In such colloidal systems, pair-wise interactions are highly favored thermodynamically (as reflected in large negative B22 values) but higher order levels of interactions are not favored (as reflected by positive C22 values). In addition, the DLVO theory adequately describes the pair-wise interactions between oligonucleotides and provides reasonable quantitative agreement with measured second virial coefficients. Furthermore, a deep attractive well and a significant energy barrier were observed in the DLVO description of the oligonucleotide system, features that characterize electrokinetically stabilized colloids.

Chapter 15

Application of Osmotic Dewatering to the Crystallization of Oligonucleotides for Crystallography

C.-Y. Lee, Michael Sportiello, Stephen P. Cape, Sean Ferree, Paul Todd, Craig E. Kundrot and Cindy Barnes

Application of Osmotic Dewatering to the Crystallization of Oligonucleotides for Crystallography

Ching-Yuan Lee, Michael Sportiello, Stephen Cape, Sean Ferree, and Paul Todd,
Department of Chemical Engineering,

Craig E. Kundrot and Cindy Barnes,
Department of Chemistry and Biochemistry, University of Colorado, Boulder

Abstract

Rising interest in the application of oligonucleotides to medical problems has stimulated a need to determine the three-dimensional structures of oligonucleotides and their complexes with various ligands. Three-dimensional structure determination relies on high-quality crystals at least 0.5mm in length; however, only about a dozen RNA molecules have been crystallized, and a broad record of experience in oligonucleotide crystallization is lacking. Osmotic dewatering is a crystallization method in which oligonucleotide and its precipitant are concentrated at a controlled rate by the removal of water through a reverse-osmosis membrane using a specified concentration gradient. A multi-chamber osmotic dewatering crystallizer was built and its transport characteristics were successfully modeled under conditions used for the crystallization of an oligonucleotide "UU-dodecamer", synthesized by *in vitro* transcription using bacteriophage T7 RNA polymerase and an immobilized DNA template and purified by gel electrophoresis. Crystals were grown with and without the removal of the terminal 5' triphosphate. The osmotic dewatering method was also tested in various devices during low-gravity space flights. Experiments to date lead to the conclusion that both the nucleation and growth stages of crystallization can be controlled by regulating the concentration gradient across a reverse-osmosis membrane during crystallization.

1. Introduction

Since the discovery of their catalytic properties in the early 1980's (Cech et.al., 1981, 1987), ribonucleic acids (RNA) have opened an era in potential development of pharmaceutical drugs. For example, Tuerk et. al. (1992) showed that a pseudoknot RNA molecule could inhibit DNA synthesis by human immunodeficiency virus type 1 (HIV-1) reverse transcriptase. Wu et. al. (1989) demonstrated that RNA had the potential for the treatment of hepatitis. However, the strategy of designing RNA drugs depends on the knowledge of the three-dimensional structures of the RNA molecules. The determination of RNA three-dimensional structures by x-ray crystallography, in turn, depends on the availability of high quality crystals. The growth of diffraction-quality RNA crystals is therefore critical.

Although the history of biological macromolecule crystal growth can be traced back to more than 150 years ago (McPherson, 1991), extensive experience in crystallizing

RNA molecules is lacking. Only about a dozen RNA molecules have so far been successfully crystallized (Doudna et.al, 1993). Methods for crystallizing biological macromolecules include batch crystallization, temperature gradient crystallization, equilibrium dialysis crystallization, and vapor phase diffusion. These methods, however, allow very limited controlling parameters in crystal growth rate. In 1990, Todd et. al. introduced a novel method for obtaining high quality crystals of biological macromolecules, namely osmotic dewatering crystallization. This method was successfully applied to growing lysozyme crystals which diffracted to 2.3Å (Todd et.al., 1990). It has, over the traditional methods, the advantages of controlling the rate of water removal, which affects both the nucleation and growth rate of crystals, adjustable extent of water removal, which dictates the sizes of crystals, and reducing convective flow, which is generally considered to be detrimental to the crystal quality.

In this work, we present an application of the osmotic dewatering technique to the crystallization of an oligonucleotide (small RNA) "U-U dodecamer". We developed a transport model of osmotic dewatering and demonstrated some results in crystallizing the target RNA molecule, U-U dodecamer.

2. Transport Model of Osmotic Dewatering

In osmotic dewatering, a reverse osmosis membrane is used to separate two solutions having different solute concentrations. The lower-concentration solution contains the species to be crystallized. Due to the osmotic pressure, resulting from the difference in osmolarity across the membrane, water from the low concentration solution permeates through the membrane into the high concentration solution. This dehydration, at a controllable rate, gradually concentrates the low concentration solution and causes crystallization to occur in the presence of a suitable precipitant. Figure 1 illustrates the concept.

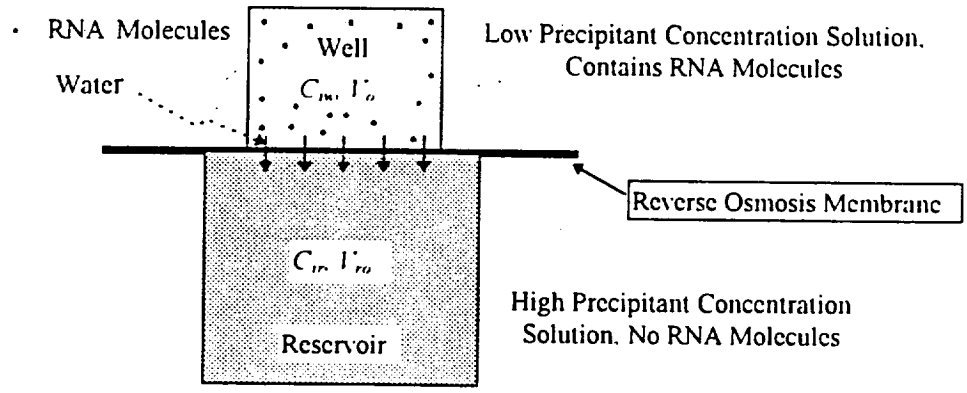

Figure 1. Concept of Osmotic Dewatering

The total pressure drop across the membrane can be represented by the sum of the gravity head and the Van't Hoff osmotic pressure for ideal solutions:

$$\Delta P = \rho g \Delta h + RT\Delta C$$

where ΔC is the total osmolarity difference across membrane, R is the ideal gas constant, and T is the temperature, °K. A typical initial osmotic pressure is around 2 Mpa, while that due to the difference in fluid head is around 20 Pa. Therefore, the gravity head contribution is generally neglected.

The flux of water across a membrane is governed by Darcy's Law:

$$\frac{1}{A}\frac{dV}{dt} = \frac{RT}{\mu R_m}\sum_{i=n}\Delta C_i \qquad (1)$$

where A is the cross-sectional area of reverse osmosis membrane, m^2, V is the volume of water that has permeated through the membrane, m^3, at time t, t is the time, hours, n is the number of solutes, μ is the viscosity of fluid, Pa-hr, and R_m is the membrane resistance, m^{-1}.

$$\text{Let} \quad \Delta C_i = C_{ir} - C_{iw} \quad \text{and} \quad R_i = \frac{C_{iwo}}{C_{iro}} \qquad (2)$$

where C_{ir} is the total osmolarity of species i in the reservoir, osmoles/m^3, C_{iw} is the total osmolarity of species i in well, osmoles/m^3, C_{iro}: initial total osmolarity of species i in the reservoir, osmoles/m^3, C_{iwo}: initial total osmolarity of species i in the well, osmoles/m^3, and R_i is the ratio of initial well concentration to initial reservoir concentration of species i.

At time t,

$$C_{ir}(V_{ro} + V) = C_{iro}V_{ro} \quad \text{and} \quad C_{iw}(V_o - V) = C_{iwo}V_o$$

where V_{ro} is the initial reservoir volume, µl, and V_o is the initial well volume, µl.
Therefore,

$$C_{ir} = \frac{V_{ro}}{V_{ro} + V}C_{iro} \qquad (3)$$

$$C_{iw} = \frac{V_o}{V_o - V}C_{iwo} = \frac{V_o}{V_o - V}R_iC_{iro} \qquad (4)$$

Combining equations (2), (3), and (4), we have

$$\Delta C_i = \frac{V_{ro}}{V_{ro} + V}C_{iro} - \frac{V_o}{V_o - V}R_iC_{iro}$$

and

$$\sum_{i=n}\Delta C_i = \frac{V_{ro}}{V_{ro} + V}\sum_{i=n}C_{iro} - \frac{V_o}{V_o - V}\sum_{i=n}R_iC_{iro} \qquad (5)$$

Let $\sum_{i=n} C_{iro} = C_{ro}$ and $\sum_{i=n} R_i C_{iro} = k$

where C_{ro} is the total osmolarity of all solutes in the reservoir, osmoles/m^3, constant, and k is a constant, osmoles/m^3.

Therefore

$$\sum_{i=n} \Delta C_i = \frac{V_{ro}}{V_{ro}+V} C_{ro} - \frac{V_o}{V_o - V} k \qquad (6)$$

The viscosity, μ, was measured over the range of different solution concentrations at constant temperature, 310°K, and was approximated by the following equation.

$$\mu = aM_w + b \qquad (7)$$

where M_w is the total molarity in well solution and a and b are constants. Substituting M_w with M_{wo}, we have

$$\mu = aM_{wo}\left(\frac{V_o}{V_o - V}\right) + b \qquad (8)$$

where M_{wo} is the total initial molarity in well solution.

Combining equations (1), (6), and (8), we obtain

$$\frac{dV}{dt} = \frac{ART}{R_m} \frac{\frac{V_{ro}}{V_{ro}+V} C_{ro} - \frac{V_o}{V_o - V} k}{aM_{wo}\frac{V_o}{V_o - V} + b}$$

Let $K_1 = \frac{ART}{R_m}$

Rearranging the above equation, we obtain

$$\frac{(aM_{wo}+b)V_o V_{ro} + (aM_{wo}V_o + bV_o - bV_{ro})V - bV^2}{(C_{ro}-k)V_o V_{ro} - (C_{ro}V_{ro} + kV_o)V} dV = K_1 dt$$

Let $\alpha = \frac{V_o}{V_{ro}}$

Dividing the above equation by $V_o V_{ro}$, and rearranging, we get

$$\frac{(aM_{wo}+b) + (aM_{wo}\alpha + b\alpha - b)\left(\frac{V}{V_o}\right) - b\left(\frac{V}{V_o}\right)^2}{(C_{ro}-k) - (C_{ro}+k\alpha)\left(\frac{V}{V_o}\right)} dV = K_1 dt$$

By separating the above equation into 3 parts and integrating them separately, with the initial condition that at $t=0$, $V=0$, we obtain:

$$\left[\frac{(C_{ro}-k)^2 b\alpha V_o}{(C_{ro}+k\alpha)^3}-\frac{(aM_{wo}\alpha+b\alpha-b)(C_{ro}-k)V_o}{(C_{ro}+k\alpha)^2}-\frac{(aM_{wo}+b)V_o}{C_{ro}+k\alpha}\right]\ln\left[1-\left(\frac{C_{ro}+k\alpha}{C_{ro}-k}\right)\left(\frac{V}{V_o}\right)\right]+$$

$$\left[\frac{(C_{ro}-k)b\alpha V_o}{(C_{ro}+k\alpha)^2}-\frac{(aM_{wo}+b\alpha-b)V_o}{C_{ro}+k\alpha}\right]\left(\frac{V}{V_o}\right)+\frac{b\alpha V_o}{2(C_{ro}+k\alpha)}\left(\frac{V}{V_o}\right)^2=\frac{ART}{R_m}t,$$

the Transport Equation for Osmotic Dewatering (TEFOD). Although TEFOD appears complicated, most of the terms are either constants or measurable values based on the actual experimental conditions.

3. Experimental

3.1 Materials

The structures of U-U dodecamer are shown in figure 2.

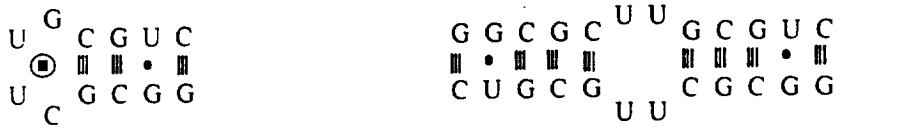

In Low Salt Concentration- Hairpin In High Salt Concentration- Double Stranded

Figure 2. Structures of U-U Dodecamer

U-U dodecamer was obtained by *in vitro* transcription using bacteriophage T7 RNA polymerase and immobilized DNA templates (Marble and Davis, 1995). Each 1-ml reaction contained 40mM Tris (pH=8.1), 20mM magnesium acetate, 5mM dithiothreitol (DTT), 1mM spermidine, 0.01% triton X-100, 6.4mM cytidine triphosphate (CTP), 4.8mM uridine triphosphate (UTP), 8.0mM guanodine triphosphate (GTP), 0.05mg/ml T7 RNA polymerase, and 1.0μM immobilized DNA template. The reactions were carried out at 37°C for about 5 hours. The reaction supernatant was ethanol precipitated and resuspended in water. A stir cell with a 1000 molecular weight cut off membrane (Amicon, YM1) was used to desalt the RNA broth. Calf intestinal alkaline phosphatase (CIAP) was then added to cleave the triphosphate group at the 5'-end of RNA molecules and replace with a hydroxyl group(Kundrot, 1995). This enzymatic reaction was carried out at 37°C for one hour and stopped by adding 1/10 volume of 500mM EDTA and raising the temperature to 65°C for 10 minutes. The desired U-U dodecamers were then purified from this reaction mixture by gel electrophoresis with 20% polyacrylamide gel. RNA product was extracted from the gel by crushing the gel with a mortar and pestle and eluting with an elution buffer containing 10mM Tris (pH=7.5), 1mM EDTA (pH=8.0), and 500mM NaCl. The elution process was usually repeated 3 times (5ml buffer each time) for maximum product recovery. The total eluent was then concentrated and

desalted by using the stir cell membrane. A typical final yield of dodecamer from a 1-ml reaction was between 350μg and 400μg. The final product in pure water was stored at -20°C until used in crystallization experiments.

3.2 Multi-Chamber Crystallizer

The schematic diagram of a multi-chamber crystallizer is shown in figure 3.

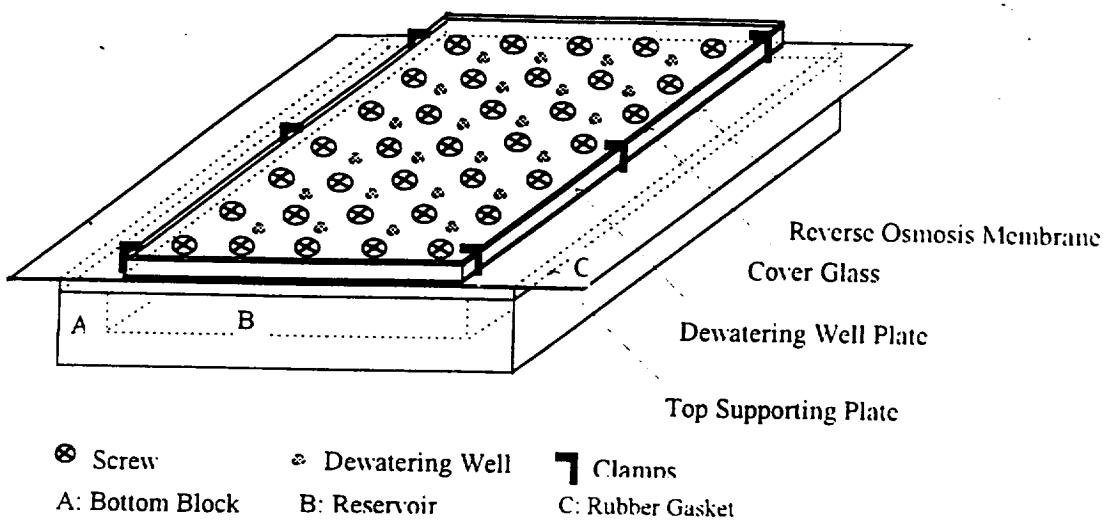

Figure 3. Schematics of a Multi-Chamber Crystallizer

There are a total of 24 osmotic dewatering wells. Each well holds up to 30μl of fluid. The volume of the reservoir is about 62ml. The reservoir and top supporting plate are polycarbonate plastic, the dewatering well plate is made of delrin, and the clamps are made of aluminum. They were all machined at the Chemical Engineering Departmental machine shop by Mr. Willy Grothe.

3.3 Dewatering Rate Measurements

Dewatering rate experiments were carried out at 37°C. The reservoir solution contained 10% (wt%) methyl 2,4 pentane diol (MPD, Sigma Chemicals, Inc. St. Louis, MO), 400mM ammonium acetate, 25mM magnesium chloride, and 50mM sodium cacodylate (pH 7.0). The concentrations of all the solutes in the solution for all the dewatering wells were exactly 50% of the those in the reservoir solution. After assembling the multi-chamber crystallizer, the reservoir solution was loaded first to saturate the RO membrane (MS-10,Osmonics, Inc. Minnetonka, MN) overnight. 30μl of well solution was loaded into each dewatering well. The volumes of the remaining well solutions were measured in each well at various time points to obtain the dewatering rate data.

3.4 Crystallization

The same compositions of both reservoir and well solutions as described in 3.3 were used for crystallization experiments, except that different concentrations of dodecamer were added to the well solution. After assembling the crystallizer, reservoir solution was added to saturate the membrane overnight. Well solutions were added the next day. A typical crystallization experiment had 4 different initial dodecamer concentrations, 0.6 mg/ml, 0.7mg/ml, 0.8 mg/ml, and 0.9 mg/ml. Each concentration of RNA-containing well solution was loaded into 6 wells, 15µl per well. The duration of the experiment was at least 7 days. At the end of the experiment, the remaining solution from each well was harvested into a depression slide by using a microdispenser (Drummond) and glass pipettes. Each solution was then examined by microscope.

4. Results

4.1 Dewatering Rate Measurement

Under the experimental conditions, the total well solution volume is 720µl. Compared with the reservoir solution volume 62ml, we have $V_{ro} >> V_o$, and, therefore, $\alpha \cong 0$. Since the initial total osmolarity in the well solution is exactly half of that in the reservoir solution, we have $k = 0.5C_{ro}$. Applying these two values to TEFOD, the equation can be simplified to

$$-[\frac{(2aM_{wo} + b)V_o R_m}{2ARTC_{ro}}]\ln(1 - 2\frac{V}{V_o}) + (\frac{bR_m V_o}{ARTC_{ro}})\frac{V}{V_o} = t \qquad (9)$$

The viscosity of a fluid is a function of temperature and composition of the fluid. In a dewatering experiment, the concentrations of solutes in the well solution increase as the volume of the well solution decreases. Therefore, the viscosity of the well solution is not a constant. Viscosity data of the well solution at different concentrations were measured and shown in Figure 4. The two constants in equation (7) were determined to be $a = 2 \times 10^{-10}$, $b = 5 \times 10^{-8}$.

The manufacturer's membrane resistance, R_m, depends not only on the properties of the membrane materials but also on the characteristics of the contacting fluids. Therefore, this value was determined empirically. From experimental data, at $t = 10$ hour, V was measured as 8.125µl or $8.125 \times 10^{-9} m^3$. Substituting these two numbers and the above constants, R_m was determined to be $4.858 \times 10^{16} m^{-1}$. Other constants were $A = 7.92 \times 10^{-6}$ m^2, $R = 8.314$ J/°K-sec, $T = 310$°K, $M_{wo} = 1321$ moles/m^3, and $C_{ro} = 1800$ moles/m^3.

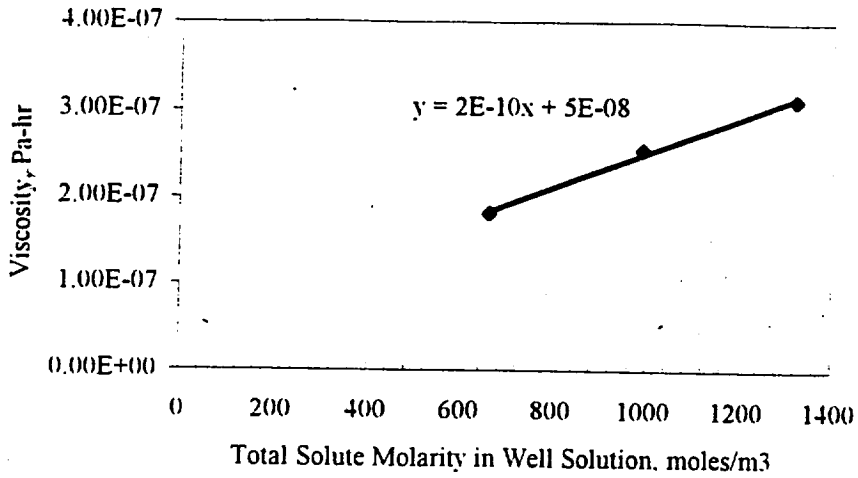

Figure 4. Viscosity as a Function of Total Solute Concentration

Therefore equation (9) becomes

$$-11.58\ln(1-2\frac{V}{V_0})+3.69\frac{V}{V_0}=t \qquad (10)$$

Equation (10) was then plotted and compared with two sets of experimental data. The result is shown in Figure 5.

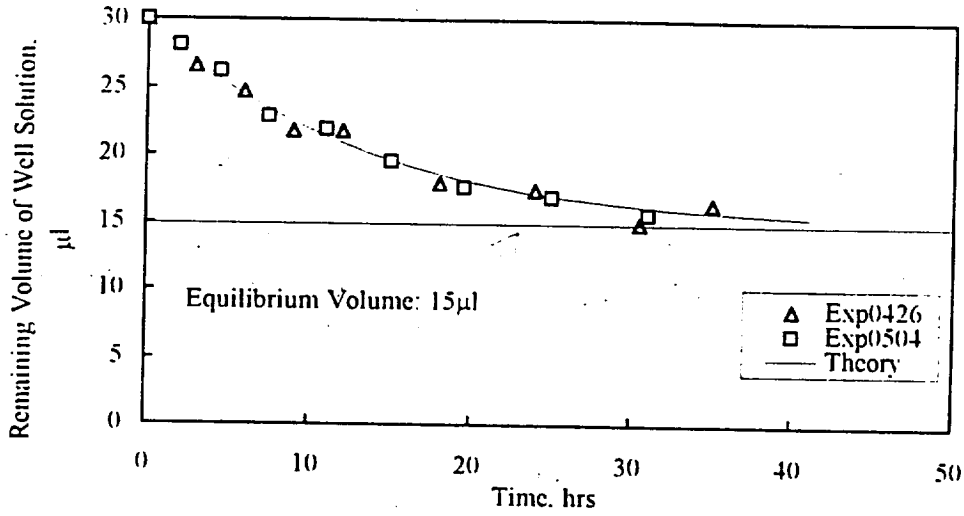

Figure 5. Comparison of Theoretical and Experimental Osmotic Dewatering Rate

4.2 Crystallization Experiments

Several crystallization experiments were performed, and dodecamer crystals were successfully obtained. Dodecamer molecules used in earlier experiments had triphosphate group on their 5'end. (In other words, CIAP reactions were not applied.) Therefore two

types of crystal morphologies were observed, as shown in Figures 6 and 7. The triphosphate dodecamer crystals display a so-called "coffin" shape as shown in figure 6. The hydroxyl dodecamer crystals tend to form twin crystals and display a "V" shape, as shown in figure 7.

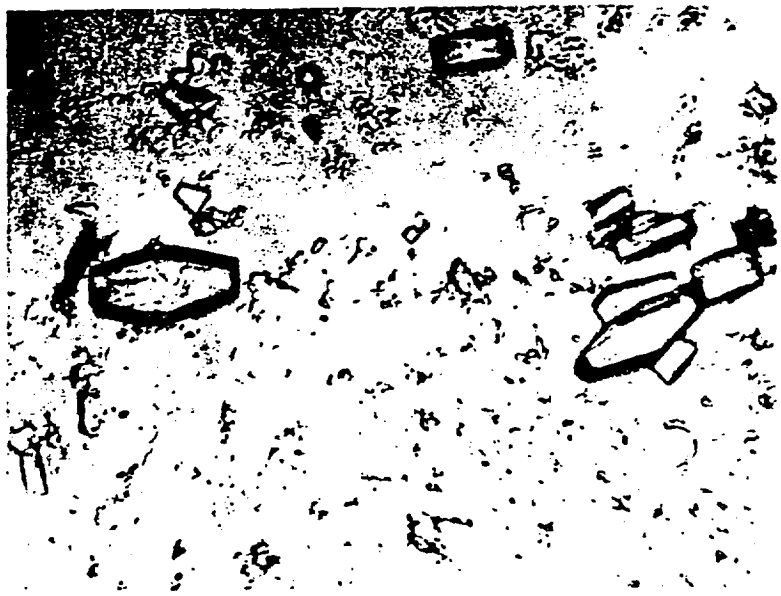

Figure 6. Triphosphate Dodecamer Crystal. (——— 100μm)

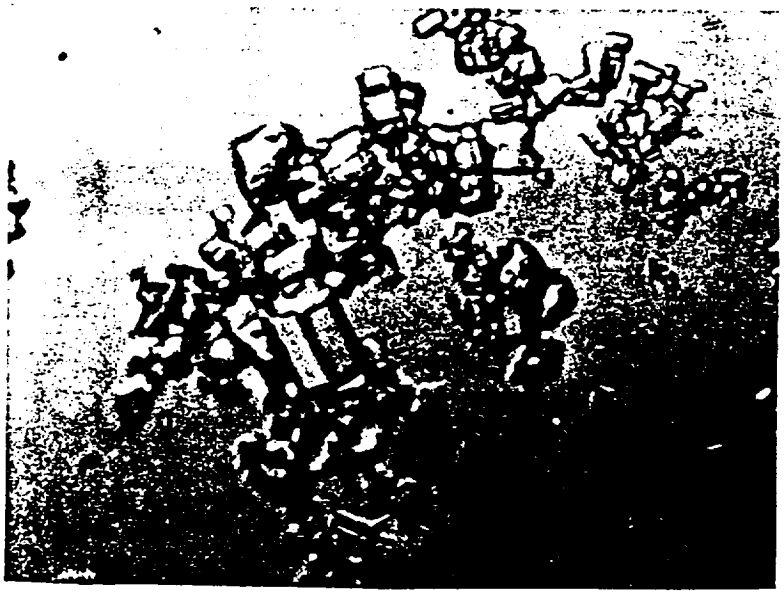

Figure 7. Hydroxyl Dodecamer Crystals. (———100μm)

5. Conclusions

A transport model was developed to describe the osmotic dewatering process. As shown in figure 5, with R_m the only fitted parameter, this model successfully predicted the dewatering rate in the crystallizer. This model will be very helpful in controlling the dewatering rate by controlling the total osmolarity difference across the membrane. This, in turn, enables the control of both the nucleation and crystal growth rates, which play important roles in crystal size and quality.

U-U dodecamer molecules were successfully crystallized in the multi-chamber crystallizer. However, the sizes of the crystals obtained so far were not adequate mounting for x-ray diffraction analysis. In order to get x-ray diffraction data to determine the quality of crystals, further improvement in the experimental strategies are needed to improve the sizes of crystals.

6. Acknowledgments

This work has been sponsored by NeXstar, the Colorado RNA Center, the Whitaker Foundation, Instrumentation Technology Associates, and the National Aeronautics and Space Administration (Grant NAGB-1167).

7. References

Cech, T.R.; Zaug, A.J.; Grabowski, P.J., "*In vitro* splicing of the ribosomal RNA precursor of tetrahymena: Involvement of a guanosine nucleotide in the excision of the intervening sequence", Cell, Vol. 27, p487 (1981)

Cech, T.R., "The chemistry of self-splicing RNA and RNA enzymes", Science, Vol. 236, p1532, 1987

Doudna, J.A.; Grosshans, C.; Gooding, A.; Kundrot, C.E., "Crystallization of RNA enzymes and small motifs using a novel sparse matrix approach", Proc. Natl. Acad. Sci. USA, 1993

Kundrot, C.E., "The preparation and crystallization of RNA: a sparse matrix approach", Methods in Enzymology, in press, 1995

Marble, H.A.; Davis, R.H, "RNA transcription from Immobilized DNA templates", Biotechnology Progress, Vol 11, p393, 1995

Todd, P.; Sikdar, S.K.; Walker C.; Korszun Z.R., "Application of osmotic dewatering to the controlled crystallization of biological macromolecules and organic compounds", Journal of Crystal Growth, Vol 110, p283, 1991

Tuerk, C.; MacDougal S.; Gold, L.; "RNA pseudoknots that inhibit human immunodeficiency virus type 1 reverse transcriptase", Proc. Natl. Acad. Sci. USA, Vol 89, p6988, 1992

Wu, H.N.; Lin, Y.J.; Lin, F.P.; Makina, S.; Chang, M.F.; Lai, M.M.C., "Human hepatitis δ virus RNA subfragments contain an autocleavage activity", Proc. Natl. Acad. Sci. USA, Vol. 86, p1831, 1989

Chapter 16

Characterization and Application of Osmotic Dewatering to the Crystallization of Oligonucleotides

C.-Y. Lee, Michael G. Sportiello, Stephen P. Cape, Sean Ferree and Paul Todd

Characterization and Application of Osmotic Dewatering to the Crystallization of Oligonucleotides

Ching-Yuan Lee, Michael G. Sportiello, Stephen P. Cape, Sean Ferree, and Paul Todd*

Department of Chemical Engineering, University of Colorado, Campus Box 424, Boulder, Colorado 80309-0424

Craig E. Kundrot, Susan Lietzke, and Cindy Barnes

Department of Chemistry and Biochemistry, University of Colorado, Campus Box 215, Boulder, Colorado 80309-0215

The recent increase in research and applications of oligonucleotides in new drug design has stimulated a need to determine the three-dimensional structures of oligonucleotides and their complexes with various ligands. Three-dimensional structure determination relies on X-ray diffraction data from high-quality crystals. However, only a very limited number of RNA molecules have been crystallized, and a broad record of experience in oligonucleotide crystallization is lacking. Osmotic dewatering is a crystallization method in which the oligonucleotide and its precipitant are concentrated at a controlled rate by the removal of water through a reverse-osmosis membrane using a specified concentration gradient. Therefore, rates of nucleation and crystal growth can be controlled. In this study, a transport model was developed to predict the water removal rates at various concentration gradients. Experimental dewatering rate data agreed very well with theoretical calculations. Model predictions were applied to different osmotic dewatering crystallization devices to crystalize a model RNA, "U-U dodecamer". High-quality dodecamer crystals were successfully grown and yielded a maximum X-ray diffraction resolution of 2.46 Å and usable resolution of 3.0 Å. The results of this research will facilitate the applications of osmotic dewatering to crystallographic studies and industrial purification of biopharmaceuticals.

1. Introduction

Since the discovery of their enzymatic properties (Altman et al., 1980; Cech et al., 1981, 1987) and their function as combinatorial (Gold et al., 1995) or antisense (Uhlmann and Peyman, 1990) ligands, ribonucleic acids (RNA) have opened an era of potential development of pharmaceutical agents. For example, Tuerk et al. (1992) showed that a combinatorially generated pseudoknot RNA molecule could inhibit DNA synthesis by human immunodeficiency virus type 1 (HIV-1) reverse transcriptase. Wu et al. (1989) demonstrated that RNA had the potential for the treatment of hepatitis. The enzymatic and/or ligand properties of RNA are related to their three-dimensional (3-D) structures; therefore, structural study holds the key to the success of designing RNA-based drugs. The determination of RNA 3-D structures by X-ray crystallography, in turn, depends on the availability of high-quality crystals. The growth of diffraction-quality RNA crystals is therefore critical.

Although the history of biological macromolecule crystal growth can be traced back to more than 150 years ago (McPherson, 1991), extensive experience in crystallizing RNA molecules is lacking. Only until recent years, successful RNA crystallizations (Kundrot, 1996; Berger et al., 1996; Wahl et al., 1996c; Baeyens et al., 1994; Doudna et al., 1993; Usman et al., 1992) and structural determinations (Cate et al., 1996; Lietzke et al., 1996a,b; Wahl et al., 1996a,b; Baeyens et al., 1995; Scott et al., 1995; Portmann et al., 1995; Betzel et al., 1994; Holbrook et al., 1991) have been reported. Methods for crystallizing biological macromolecules include batch crystallization, temperature gradient crystallization, equilibrium dialysis crystallization, and vapor phase diffusion. These methods, however, allow very limited control of the parameters involved in the nucleation and growth of macromolecule crystals. In 1990, Todd et al. introduced a novel method for obtaining high-quality crystals of biological macromolecules, namely osmotic dewatering crystallization. This method was successfully applied to growing lysozyme crystals which diffracted to 1.73 Å (Todd et al., 1991). It has, over the traditional methods, the advantages of controlling the rate of water removal, which affects both the nucleation and growth rate of crystals which dictates the sizes of crystals, and reducing convective flow, which is generally considered to be detrimental to the crystal quality.

In this work, we present the characterization and application of the osmotic dewatering technique to the crystallization of an oligonucleotide, the "U-U dodecamer". A transport model of osmotic dewatering was developed and tested, and crystals of the target RNA molecule, U-U dodecamer, were produced by this method.

2. Transport Model of Osmotic Dewatering

In osmotic dewatering, a reverse-osmosis (RO) membrane is used to separate two solutions having different solute concentrations. The lower-concentration solution contains the species to be crystallized. Due to the osmotic pressure, resulting from the difference in osmolarity across the membrane, water from the low-concentration

* Corresponding author. Phone: (303) 492-5936. E-mail: todd@spot.colorado.edu.

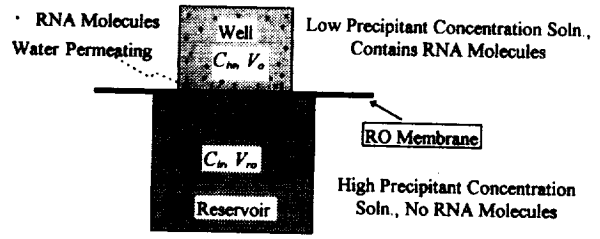

Figure 1. Concept of osmotic dewatering and definition of concentrations and volumes used in the model.

solution permeates through the membrane into the high-concentration solution. This dehydration, at a controllable rate, gradually concentrates the low-concentration solution and causes crystallization to occur in the presence of a suitable precipitant. Figure 1 illustrates the concept.

In the absence of an externally applied force, water flows down its osmotic gradient from the "well" (top) to the "reservoir" (bottom). The total pressure drop across the membrane can be represented by the sum of the gravity head and the Van't Hoff osmotic pressure for ideal solutions:

$$\Delta P = \rho g \Delta h + RT\Delta C$$

where ΔC is the total osmolarity difference across the membrane, R is the ideal gas constant, and T is the temperature (K). A typical initial osmotic pressure is around 2 MPa, while that due to the difference in fluid head is around 20 Pa. Therefore, the gravity head contribution is generally neglected.

The flux of water driven across a membrane by osmotic pressure is governed by Darcy's Law:

$$\frac{1}{A}\frac{dV}{dt} = \frac{RT}{\mu R_m}\sum_{i=1}^{n}(\Delta C)_i \qquad (1)$$

where A is the cross-sectional area of the reverse-osmosis membrane (m^2), V is the volume of water that has permeated through the membrane (m^3), at time t (h), n is the number of solutes, μ is the viscosity of pure water (Pa·h), and R_m is the overall membrane resistance (m^{-1}).

Let

$$(\Delta C)_i = C_{ir} - C_{iw} \qquad (2)$$

where C_{ir} is the total osmolarity of species i in the reservoir (osmoles/m^3) and C_{iw} is the total osmolarity of species i in the well (osmoles/m^3) as shown in Figure 1. Let C_{iro} be the initial total osmolarity of species i in the reservoir (osmoles/m^3), and C_{iwo} be the initial total osmolarity of species i in the well (osmoles/m^3).

At time t,

$$C_{ir}(V_{ro} + V) = C_{iro}V_{ro} \text{ and } C_{iw}(V_o - V) = C_{iwo}V_o$$

where V_{ro} is the initial reservoir volume (μL), and V_o is the initial well volume (μL).

Therefore,

$$C_{ir} = \frac{V_{ro}}{V_{ro} + V}C_{iro} \quad \text{and} \qquad (3)$$

$$C_{iw} = \frac{V_o}{V_o - V}C_{iwo} \qquad (4)$$

Combining eqs 2–4, we have

$$(\Delta C)_i = \frac{V_{ro}}{V_{ro} + V}C_{iro} - \frac{V_o}{V_o - V}C_{iwo}$$

and

$$\sum_{i=1}^{n}(\Delta C)_i = \frac{V_{ro}}{V_{ro} + V}\sum_{i=1}^{n}C_{iro} - \frac{V_o}{V_o - V}\sum_{i=1}^{n}C_{iwo} \qquad (5)$$

Let

$$\sum_{i=1}^{n}C_{iro} = C_{ro} \quad \text{and} \quad \sum_{i=1}^{n}C_{iwo} = C_{wo}$$

where C_{ro} is the total osmolarity of all solutes in the reservoir (osmoles/m^3) and C_{wo} is the total osmolarity of all solutes in the well (osmoles/m^3). Therefore

$$\sum_{i=1}^{n}(\Delta C)_i = \frac{V_{ro}}{V_{ro} + V}C_{ro} - \frac{V_o}{V_o - V}C_{wo} \qquad (6)$$

Combining eqs 1 and 6, we obtain

$$\frac{dV}{dt} = \frac{ART}{\mu R_m}\left(\frac{V_{ro}}{V_{ro} + V}C_{ro} - \frac{V_o}{V_o - V}C_{wo}\right)$$

Rearranging the above equation we obtain

$$\frac{V_oV_{ro} - V_{ro}V + V_oV - V^2}{(C_{ro} - C_{wo})V_oV_{ro} - (C_{ro}V_{ro} + C_{wo}V_o)V}dV = \frac{ART}{\mu R_m}dt$$

Let α be the ratio of original dewatering well solution volume to original reservoir solution volume, $\alpha = V_o/V_{ro}$, and divide the above equation by V_o/V_{ro}, and by rearranging we obtain

$$\frac{1 - (1 - \alpha)(V/V_o) - \alpha(V/V_o)^2}{(C_{ro} - C_{wo}) - (C_{ro} + C_{wo}\alpha)(V/V_o)}dV = \frac{ART}{\mu R_m}dt$$

By separating the above equation into three parts and integrating them separately, with the initial condition that at $t = 0$ and $V = 0$, we obtain

$$\left[\frac{(C_{ro} - C_{wo})^2\,\alpha V_o}{(C_{ro} + C_{wo}\alpha)^3} + \frac{(1 - \alpha)(C_{ro} - C_{wo})V_o}{(C_{ro} + C_{wo}\alpha)^2} - \frac{V_o}{C_{ro} + C_{wo}\alpha}\right]\ln\left[1 - \left(\frac{C_{ro} + C_{wo}\alpha}{C_{ro} - C_{wo}}\right)\left(\frac{V}{V_o}\right)\right] + \left[\frac{(C_{ro} - C_{wo})\alpha V_o}{(C_{ro} + C_{wo}\alpha)^2} + \frac{(1 - \alpha)V_o}{C_{ro} + C_{wo}\alpha}\right]\left(\frac{V}{V_o}\right) + \frac{\alpha V_o}{2(C_{ro} + C_{wo}\alpha)}\left(\frac{V}{V_o}\right)^2 = \frac{ART}{\mu R_m}t \qquad (7)$$

the transport equation for osmotic dewatering (TEFOD).

Although TEFOD appears complicated, all of the factors are constants or measurable values based on experimental conditions. In most of the cases, the reservoir solution volume is much larger than the well solution volume, $V_{ro} \gg V_o$, and $\alpha \to 0$, so the above equation simplifies to

$$\frac{\mu R_m V_o}{ARTC_{ro}}\left\{\left(\frac{V}{V_o}\right) - \frac{C_{wo}}{C_{ro}}\ln\left[1 - \left(\frac{C_{ro}}{C_{ro} - C_{wo}}\right)\left(\frac{V}{V_o}\right)\right]\right\} = t \qquad (8)$$

3. Experimental Section

3.1. Materials. The RNA U-U dodecamer GGCGCU-UGCGUC was obtained by *in vitro* transcription using

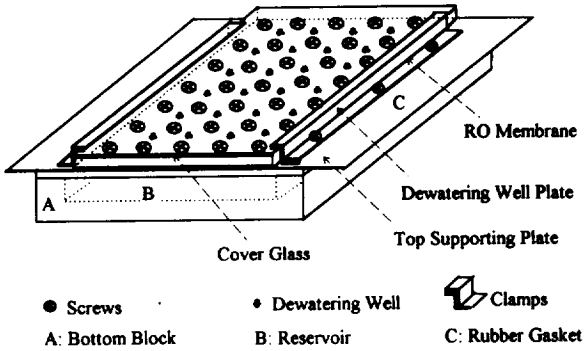

Figure 2. Schematic drawing of a MODC.

bacteriophage T7 RNA polymerase and immobilized DNA templates (Marble and Davis, 1995). Each 1-mL reaction solution consisted of 40 mM Tris (pH 8.1), 20 mM magnesium acetate, 5 mM dithiothreitol, 1 mM spermidine, 0.01% triton X-100, 6.4 mM cytidine triphosphate, 4.8 mM uridine triphosphate, 8.0 mM guanidine triphosphate, 0.05 mg/mL T7 RNA polymerase, and 1.0 μM immobilized DNA template. The reactions were carried out at 37 °C for about 5 h. The reaction products were precipitated with ethanol (3.5 volume ratio) and redissolved in 1 mL of water. A stir cell with a 1000 molecular weight cutoff membrane (YM1, Amicon, Beverly, MA) was used to concentrate and desalt the RNA solution. Calf intestinal alkaline phosphatase (CIAP) was then added to replace the triphosphate group at the 5′-end of RNA molecules with a hydroxyl group (Kundrot, 1996). CIAP, manufactured by Boehringer Mannheim, was obtained from the Chemistry Department stock room at University of Colorado. This enzymatic reaction was carried out at 37 °C for 1.5 h and stopped by adding 1/10 vol of 500 mM EDTA and raising the temperature to 65 °C for 10 min. The desired 5′OH U-U dodecamer was then purified from this reaction mixture by gel electrophoresis using a 20% polyacrylamide gel. RNA product was extracted from the gel segment by crushing the gel with a mortar and pestle and eluting with an elution buffer containing 10 mM Tris, 1 mM EDTA, and 500 mM NaCl (pH 7.5). The elution process was usually repeated twice (5 mL of buffer each time) for maximum product recovery. The total eluent was once again concentrated and desalted by using the stir cell unit. A typical final yield of dodecamer from a 1-mL reaction was 250−300 μg. The purified product was stored in pure water at −20 °C until used in crystallization experiments. Finally, before crystallization experiments, the dodecamer solution was heated to 65 °C in the presence of 10 mM magnesium chloride for 10 min and slowly cooled down to room temperature so that all dodecamer molecules were double-stranded duplexes (Lietzke et al., 1996a).

3.2. Crystallization Devices. A schematic diagram of a multichamber osmotic dewatering crystallizer (MODC) is shown in Figure 2. The dewatering well plate, made of delrin, measures 8.9 cm in length, 6.4 cm in width, and 0.6 cm deep. A total of 24 osmotic dewatering wells are machined into the plate. Each well is 0.3 cm in diameter and holds up to 30 μL of fluid. The reservoir is machined from a single Lexan polycarbonate block. It measures 8.9 cm in length, 7.0 cm in width, and 1.0 cm in depth and holds 62.4 mL of fluid. The reservoir top supporting plate is also made of polycarbonate plastic, and the clamps are made of aluminum. All were machined at the Chemical Engineering Departmental machine shop, University of Colorado. The screws are made of nylon and are available at hardware stores.

An additional dewatering device was adapted from the "fluid processing apparatus" (FPA), a chemical transfer system designed for automated experiments in space

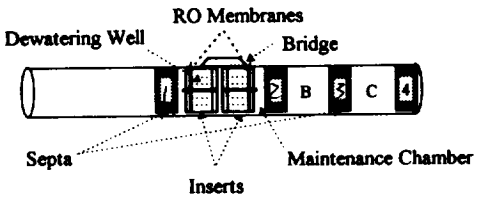

Figure 3. Schematic drawing of FPA (fluid processing apparatus), with two inserts, prior to activation. Each insert contains four sample wells.

Table 1. List of Solution Compositions in Dewatering Rate Experiments

	reservoir solution	well solutions		
		low	medium	high
MPD (%)	10	2.50	5.00	7.50
ammonium acetate (mM)	400	100	200	300
sodium cacodylate (mM)	50	12.5	25	37.5
magnesium chloride	25	6.25	12.5	18.75
$C_{ro} - C_{wo}$, mol/m^3	n/a	1350	900	450

(Luttges, 1992). A drawing of the FPA is shown in Figure 3 at its preactivation position. Four dewatering wells in each of the two inserts contain RNA solutions. The inserts stay in a chamber formed between septa 1 and 2, and this chamber contains fluid with exactly the same composition as the well solution (except RNA) to prevent any dewatering before activation. Chambers B and C (chamber C is optional) contain fluids with higher solute concentrations. Upon activation, septum 4 is pushed from right to left by a plunger. As soon as septum 2 passes by the bridge, chamber B solution mixes with maintenance solution and thus starts the dewatering process. The optional chamber C is used to further raise the concentration of the mixed fluid to promote maximum dewatering and crystal growth.

3.3. Dewatering Rate Measurements. Dewatering rate experiments were carried out at 37 °C, the temperature at which this RNA crystallizes. The reservoir solution contained 10% (w/w) 2-methyl-2,4-pentanediol (MPD, Sigma Chemicals, Inc., St. Louis, MO), 400 mM ammonium acetate, 25 mM magnesium chloride, and 50 mM sodium cacodylate (pH 7.0). Different starting concentrations of well solutions (without RNA) were used to test the dewatering rates at different concentration gradients. See Table 1 for details.

After the multichamber crystallizer was assembled, the reservoir solution was loaded first to saturate the RO membrane (MS-10,Osmonics, Inc., Minnetonka, MN) overnight. Before loading the well solution on the next day, filtered compressed air was used to blow dry the tiny amount of water that passed through the RO membrane during the membrane saturation period. Well solution (30 μL) was then loaded into each well. On subsequent days the remaining volumes of the well solutions were measured in each well at various time points to obtain the dewatering rate data. The remaining well solution volume was determined by measuring the length of the fluid when it was drawn into a 50-μL glass microdispenser (made by Drummond, purchased from Fisher Scientific, Pittsburgh, PA).

3.4. Crystallization. Reservoir and well solutions similar to those described in Table 2 were used for crystallization experiments, and different concentrations of dodecamer were added to the well solutions. Both the MODC and FPA (see section 3.2) were used as the crystallization devices. Table 2 lists two typical experimental conditions which successfully produced dodecamer crystals. The duration of each experiment was at least 7 days. The temperature was maintained at 37 °C. At the end of the experiment, the remaining solution from

Table 2. Compositions of Two Crystallization Solutions in Which U-U Dodecamer Crystals Were Successfully Grown

		RNA (well) solutions	
	reservoir solution	30 μL per well	15 μL per well
dodecamer (mg/mL)	n/a	0.35	0.7
MPD (%)	10	2.50	5.00
ammonium acetate (mM)	400	100	200
sodium cacodylate (mM)	50	12.5	25
magnesium chloride (mM)	25	6.25	12.5

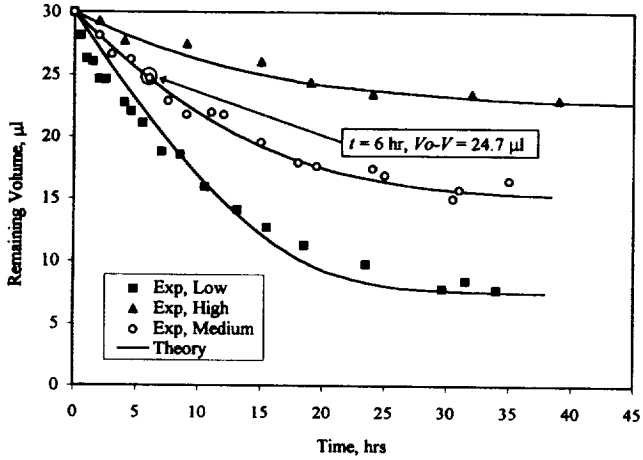

Figure 4. Comparison of theoretical (solid lines) and experimental dewatering curves (residual volume in well vs time) using the multichamber osmotic dewatering crystallizer with three initial concentrations in wells (given in Table 1).

each well was harvested into a glass dish by using a microdispenser and a glass pipet and was examined under the microscope for evidence of crystals or crystalline precipitates.

4. Results

4.1. Dewatering Rate Measurement. The total solution volume in the 24 MODC wells is 720 μL, and the reservoir volume is 62.5 mL. Since the reservoir solution volume is much greater than the total well solution volume ($V_{ro} \gg V_o$), the volume ratio, α, can be regarded as 0, and TEFOD can then be used in its simplified form (eq 8).

The experimentally measurable volume, $V_o - V$, is the remaining fluid volume in a well at time t. The fixed constants determined by the experimental conditions were $A = 7.92 \times 10^{-6}$ m^2, $R = 8.314$ J/K, $T = 310$ K, $\mu = 2.08 \times 10^{-7}$ Pa·h, and $C_{ro} = 1800$ mol/m^3. C_{wo}'s were 450, 900, and 1350 mol/m^3 for low-, medium-, and high-concentration solutions, respectively (Table 1). The manufacturer's value for the membrane resistance, R_m, depends not only on the properties of the membrane lot but also on the characteristics of the contacting fluids. Therefore, R_m was obtained empirically. Refering to Figure 4, the marked experimental data point (medium, $t = 6$ h, $V_o - V = 24.7$ μL) was used to calculate R_m from eq 8. And it was determined to be 8.91×10^{16} m^{-1}. The data from dewatering experiments at three different inital concentration gradients were compared with the theoretical predictions of eq 8. The results are shown in Figure 4. The theoretical predictions are consistent with the experimental data.

4.2. Crystallization Experiments. Dodecamer crystals were successfully grown using both MODC and FPA. Figure 5 shows dodecamer crystals obtained from MODC, and Figure 6 shows one of the crystals grown in FPA during the NASA space shuttle mission STS-69 in September 1995.

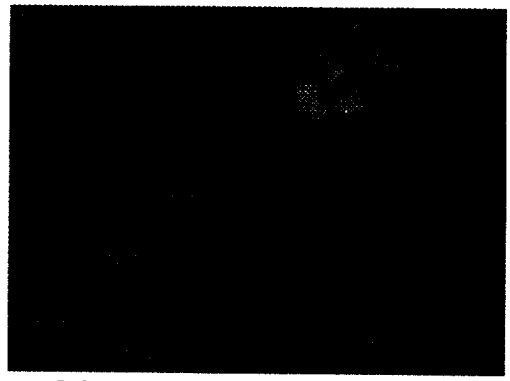

Figure 5. Polarized micrograph of dodecamer crystals grown in a MODC experiment. The major crystal is 187 × 100 × 90 μm.[3] The initial conditions were 0.35 mg/mL dodecamer, 2.5% MPD, 6.25 mM $MgCl_2$, 100 mM NH_4Ac, and 12.5 mM sodium cacodylate (pH 7). 75% of the initial volume (30 μL) was removed by osmotic dewatering.

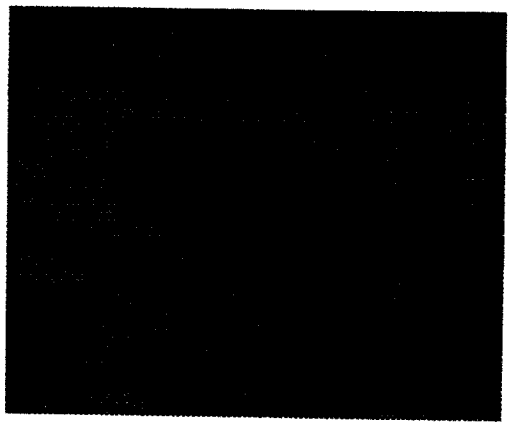

Figure 6. Polarized micrograph of dodecamer crystals grown in FPA in low gravity. Dimensions are 100 × 50 × 50 μm^3. The initial conditions were 0.7 mg/mL dodecamer, 5% MPD, 12.5 mM $MgCl_2$, 200 mM NH_4Ac, and 25 mM sodium cacodylate (pH 7). 50% of the initial volume (30 μL) was removed by osmotic dewatering.

The detector used for diffraction analyses was a Siemens X100 area detector and a Rigaku RU-200BH rotating-anode X-ray generator with a Huber graphite monochromator operated at 40 kV and 60 mA. All of the data frames were visualized with a software—XELOP—to determine the extent of diffraction by analyzing the intensity of the farthest diffraction spot. Spots on the diffraction pattern corresponding to greater than 500 intensity units were taken as the criterion for the average resolution. To date, the best X-ray diffraction data showed a maximum resolution of 2.46 Å and average resolution of 3.0 Å. This crystal was grown in an FPA as ground control for the STS-69 mission. Diffraction analyses were not performed on crystals grown in low gravity due to their smaller sizes.

5. Conclusions and Discussion

A transport model (TEFOD) was developed to describe the osmotic dewatering process. As shown in Figure 4, with R_m the only fitted parameter, this model successfully predicted the dewatering rates in the crystallizer at different osmotic pressure gradients. This model will aid in controlling the dewatering rate by controlling the total osmolarity difference across the membrane. This control, in turn, controls the rate of solute concentration, which enables the control of both the nucleation and crystal growth rates, both of which play important roles in crystal final size and quality. Like the vapor phase diffusion methods, osmotic dewatering transports only

water out of the crystallization solution. Unlike other membrane-based methods, such as equilibrium dialysis, osmotic dewatering does not permit the transport of any solutes.

An oligonucleotide was successfully crystallized in both MODC and FPA versions of osmotic dewatering crystallizers. X-ray diffraction analysis showed a maximum resolution of 2.46 Å for one crystal, comparable to that of crystals grown by conventional methods (Lietzke et al., 1996a). Dewatering conditions are being sought to obtain larger crystals with improved resolution.

Crystallization is receiving renewed interest as a separation/purification step in downstream bioprocessing to enhance final purity and to reduce total operating costs. The osmotic dewatering crystallization method offers scale-up capability and flexible controlling parameters for industrial crystallization applications. Future research in osmotic dewatering crystallization should include dynamic crystal growth modeling and design of industrial crystallizers.

Acknowledgment

This work was sponsored by the Colorado RNA Center (an agency of the Colorado Advanced Technology Institute), the Whitaker Foundation, NeXstar, Inc., Instrumentation Technology Associates, and the National Aeronautics and Space Administration (Grants NAG8-1165 and NAGW-1197).

Notation

A	cross-sectional area of reverse-osmosis membrane, m^2
C_{ir}	total osmolarity of species i in the reservoir, osmoles/m^3
$(\Delta C)_i$	defined by eq 2
C_{iro}	initial total osmolarity of species i in the reservoir, osmoles/m^3
C_{iw}	total osmolarity of species i in the well, osmoles/m^3
C_{ro}	total osmolarity of all solutes in the reservoir, osmoles/m^3
R	ideal gas constant
R_m	membrane resistance, m^{-1}
T	temperature, K
t	time
V	volume of water permeated through membrane, m^3
V_o	initial well solution volume, μL
V_{ro}	reservoir volume, μL
α	ratio of well volume to reservoir volume
μ	viscosity of fluid, Pa·h

Literature Cited

Baeyens, K. J.; Jancarik, J.; Holbrook, S. R. Use of low-molecular-weight polyethylene glycol in the crystallization of RNA oligomers. *Acta Crystallogr., Sect. D* **1994**, *50*, 764–767.

Baeyens, K. J.; De Bondt, H. L.; Holbrook, S. R. Structure of an RNA double helix including uracil-uracil base pairs in an internal loop. *Nat. Struct. Biol.* **1995**, *2*, 56–62.

Betzel, C.; Lorenz, S.; Fürste, J. P.; Bald, R.; Zhang, M.; Schneider, T. R.; Wilson, K. S.; Erdmann, V. A. Crystal structure of domain A of Thermus flavus 5S rRNA and the contribution of water molecules to its structure. *FEBS Lett.* *351*, 159–164.

Burger, I.; Kang, C.; Sinha, N.; Wolters, M.; Rich, A. A highly efficient 24-condition matrix for the crystallization of nucleic acid fragments. *Acta Crystallogr., Sect. D* **1996**, *52*, 465–468.

Cate, J. H.; Gooding, A. R.; Podell, E.; Zhou, K.; Golden, B. L.; Kundrot, C. E.; Cech, T. R.; Doudna, J. A. Crystal structure of a group I ribozyme domain: principles of RNA packing. *Science* **1996**, *273*, 1678–1685.

Cech, T. R. The chemistry of self-splicing RNA and RNA enzymes. *Science* **1987**, *236*, 1532–1539.

Cech, T. R.; Zaug, A. J.; Grabowski, P. J. In vitro splicing of the ribosomal RNA precursor of tetrahymena: Involvement of a guanosine nucleotide in the excision of the intervening sequence. *Cell* **1981**, *27*, 487–496.

Doudna, J. A.; Grosshans, C.; Gooding, A.; Kundrot, C. E. Crystallization of RNA enzymes and small motifs using a novel sparse matrix approach. *Proc. Natl. Acad. Sci. U.S.A.* **1993**, *90*, 7829–7833.

Gold, L.; Polisky, B.; Yarus, M. Diversity of oligonucleotide functions. *Ann. Rev. Biochem.* **1995**, *64*, 763–797.

Holbrook, S. R.; Cheong, C.; Tinoco, I., Jr.; Kim, S. H. Crystal structure of an RNA double helix incorporating a track of non-Watson-Crick base pairs. *Nature (London)* **1991**, *353*, 579–581.

Kole, R.; Baer, M. F.; Stark, B. C.; Altman, S. *E. Coli* RNAase P has a required RNA component *in vivo*. *Cell* **1980**, *19*, 881–887.

Kundrot, C. E. The preparation and crystallization of RNA: a sparse matrix approach. *Methods Enzymol.* **1996**, *276*, 143–157.

Lietzke, S. E.; Barnes, C. L.; Berglund, J. A.; Kundrot, C. E. The structure of an RNA dodecamer shows how tandem U-U base pairs increase the range of stable RNA structures and the diversity of recognition sites. *Structure* **1996a**, *4*, 917–930.

Lietzke, S. E.; Carperos, V. E.; Kundrot, C. E. Data reduction from twinned RNA crystals. *Acta Crystallogr., Sect. D* **1996b**, *52*, 687–692.

Luttges, M. W. Recognizing and optimizing flight opportunities with hardware and life sciences limitations. *Trans. Kansas Acad. Sci.* **1992**, *95*, No. 1/2, 76–84.

Marble, H. A.; Davis, R. H. RNA transcription from immobilized DNA templates. *Biotechnol. Prog.* **1995**, *11*, 393–396.

McPherson, A. J. A brief history of protein crystal growth. *J. Cryst. Growth* **1991**, *100*, 1–10.

Portmann, S.; Usman, N.; Egli, M. The crystal structure of r(CCCCGGGG) in two distinct lattices. *Biochemistry* **1995**, *34*, 7569–7575.

Scott, W. G.; Finch, J. T.; Klug, A. The crystal structure of an all-RNA hammerhead ribozyme: a proposed mechanism for RNA catalytic cleavage. *Cell 81*, 991–1002.

Todd, P.; Sikdar, S. K.; Walker, C.; Korszun Z. R. Application of osmotic dewatering to the controlled crystallization of biological macromolecules and organic compounds. *J. Cryst. Growth* **1991**, *110*, 283–292.

Tuerk, C.; MacDougal S.; Gold, L. RNA pseudoknots that inhibit human immunodeficiency virus type 1 reverse transcriptase. *Proc. Natl. Acad. Sci. U.S.A.* **1992**, *89*, 6988–6992.

Uhlmann, E.; Peyman, A. Antisense oligonucleotides: a new therapeutic principle. *Chem. Rev.* **1990**, *90*, 543–584.

Usman, N.; Egli, M.; Rich, A. Large scale chemical synthesis, purification and crystallization of RNA-DNA chimeras. *Nucleic Acids Res.* **1992**, *20*, 6695–6699.

Wahl, M. C.; Ban, C.; Sekharudu, C.; Ramakrishnan, B.; Sundaralingam, M. Structure of the purine-pyrimidine alternating RNA double helix, r(GUAUAUA)d(C), with a 3′-terminal deoxy residue. *Acta Crystallogr., Sect. D* **1996a**, *52*, 655–667.

Wahl, M. C.; Rao, S. T.; Sundaralingam, M. The structure of r(UUCGCG) has a 5′-UU-overhang exhibiting Hoogsteen-like trans U-U base pairs. *Nat. Struct. Biol.* **1996b**, *3*, 24–31.

Wahl, M. C.; Ramakrishnan, B.; Ban, C.; Chen, X.; Sundaralingam, M. RNA-synthesis, purification and crystallization. *Acta Crystallogr., Sect. D* **1996c**, *52*, 668–675.

Wu, H. N.; Lin, Y. J.; Lin, F. P.; Makina, S.; Chang, M. F.; Lai, M. M. C. Human hepatitis δ virus RNA subfragments contain an autocleavage activity. *Proc. Natl. Acad. Sci. U.S.A.* **1989**, *86*, 1831–1835.

Accepted November 22, 1996.[⊗]

BP960087L

[⊗] Abstract published in *Advance ACS Abstracts,* January 1, 1997.

Reprinted from BIOTECHNOLOGY PROGRESS, JANUARY/FEBRUARY 1997

Chapter 17

Control of Nucleation in Oligonucleotide Crystallization by the Osmotic Dewatering Method with Kinetic Water Removal Rate Control

C.-Y. Lee, Scott R. McEntyre, Paul Todd, Kurt Schaefer and Craig E. Kundrot

17

Reprinted from

JOURNAL OF CRYSTAL GROWTH

Journal of Crystal Growth 187 (1998) 490-498

Control of nucleation in oligonucleotide crystallization by the osmotic dewatering method with kinetic water removal rate control

Ching-Yuan Lee[a,1], Scott R. McEntyre[a], Paul Todd[a,*], Kurt Schaefer[b], Craig E. Kundrot[b]

[a] *Department of Chemical Engineering, University of Colorado, Campus Box 424, Boulder, CO 80309-0424, USA*
[b] *Department of Chemistry and Biochemistry, University of Colorado, Campus Box 215, Boulder, CO 80309-0215, USA*

Received 20 May 1997; accepted 19 December 1997

ELSEVIER

Journal of Crystal Growth

Scope of the Journal
Experimental and theoretical contributions are invited in the following fields: Theory of nucleation and growth, molecular kinetics and transport phenomena, crystallization in viscous media such as polymers and glasses. Crystal growth of metals, minerals, semiconductors, magnetics, inorganic, organic and biological substances in bulk or as thin films. Apparatus instrumentation and techniques for crystal growth, and purification methods. Characterization of single crystals by physical and chemical methods.

Abstracted/Indexed in:
Aluminium Industry Abstracts; Chemical Abstracts; Current Contents; Physical, Chemical and Earth Sciences; EI Compendex Plus; Engineered Materials Abstracts; Engineering Index; INSPEC; Metals Abstracts.

Subscription Information 1998
Volumes 182-194 of Journal of Crystal Growth (ISSN 0022-0248) are scheduled for publication. (Frequency: semimonthly.) Prices are available from the publishers upon request. Subscriptions are accepted on a prepaid basis only. Issues are sent by SAL (Surface Air Lifted) mail wherever this service is available. Airmail rates are available upon request. Please address all enquiries regarding orders and subscriptions to:

Elsevier Science, B.V., Order Fulfilment Department
P.O. Box 211, 1000 AE Amsterdam, The Netherlands
Tel: +31 20 485 3642; Fax: +31 20 485 3598

Claims for issues not received should be made within six months of our publication (mailing) date.

US mailing notice–*Journal of Crystal Growth* (ISSN 0022-0248) is published semimonthly by Elsevier Science B.V., Molenwerf 1, P.O. Box 211, 1000 AE Amsterdam, The Netherlands. Annual subscription price in the USA is US $7607 (valid in North, Central and South America only), including air speed delivery. Periodicals postage paid at Jamaica NY 11431.
US postmasters: Send address changes to Journal of Crystal Growth, Publications Expediting, Inc., 200 Meacham Avenue, Elmont NY 11003. Airfreight and mailing in the USA by Publications Expediting.

The paper used in this publication meets the requirements of ANSI/NISO Z39.48-1992 (Permanence of Paper)

PRINTED IN THE NETHERLANDS

North-Holland, an imprint of Elsevier Science

ELSEVIER

Journal of Crystal Growth 187 (1998) 490–498

JOURNAL OF CRYSTAL GROWTH

Control of nucleation in oligonucleotide crystallization by the osmotic dewatering method with kinetic water removal rate control

Ching-Yuan Lee[a,1], Scott R. McEntyre[a], Paul Todd[a,*], Kurt Schaefer[b], Craig E. Kundrot[b]

[a] *Department of Chemical Engineering, University of Colorado, Campus Box 424, Boulder, CO 80309-0424, USA*

[b] *Department of Chemistry and Biochemistry, University of Colorado, Campus Box 215, Boulder, CO 80309-0215, USA*

Received 20 May 1997; accepted 19 December 1997

Abstract

Crystallization of an RNA oligonucleotide-"U U dodecamer" (dodecamer) using a kinetically controlled osmotic dewatering method is presented. A concentration gradient across a reverse osmosis membrane is used to control the water-removal rate from the crystallization solution. By kinetically adjusting the dewatering rate, the number of crystals obtained was reduced, and crystal sizes were increased. Experimental results suggest that early rapid dewatering is needed to create a RNA-rich zone to promote nucleation. After the nucleation step, a slower dewatering rate is applied to suppress further nucleation and to provide an environment more suitable for crystal growth. The diffraction quality of dodecamer crystals grown by kinetically controlled osmotic dewatering is comparable with that of crystals grown by the hanging drop and sitting drop methods.

PACS: 81.10. – h

Keywords: Nucleation control; Oligonucleotide; RNA; Osmotic dewatering; Rate of water removal

1. Introduction

Due to the success of the SELEX technique, which selects ribonucleic acids (RNAs) that bind target molecules [1] and the discovery of their enzymatic properties [2–4], RNAs have become a new focus in the development of pharmaceutical agents. RNAs' enzymatic and binding properties depend heavily on their 3-D structures. Structural determination depends on X-ray crystallography, which, in turn, depends on obtaining high-quality single crystals. This surge in RNA science has been manifested clearly by the rapid progress of both the crystallization of different RNA molecules and their structural studies in the last few years [5–20].

It has been reported that the supersaturation ratio required for nucleation is normally much

* Corresponding author.

[1] Present address: Caleb Pharmaceuticals, Inc., 2F No. 18, Industry East Road 4, Science-Based Industrial Park, Hsinchu 300, Taiwan, ROC.

0022-0248/98/$19.00

PII S0022-0248(98)00027-X

higher than that needed for the best crystal growth environment [21,22]. This difference makes the control of crystallization processes difficult. Popular biomacromolecule crystallization methods, such as vapor-phase diffusion and membrane dialysis, offer some control over the time course of supersaturation but limited flexibility to change it once started.

The kinetics of dehydration, which controls the rate of approach to supersaturation, is expected to have a significant impact on the outcome of crystallization experiments. Fowlis et al. [23] developed a mathematical model to describe the water transport rates in vapor-diffusion system, and Luft et al. [24] measured the solvent evaporation rate in the hanging drop method as a function of the distance between the drop and the surface of the reservoir solution. Wilson et al. [25] used nitrogen gas to control the solvent evaporation rate in a hanging drop system. Larger lysozyme crystals were obtained from experiments with evaporation rate control. Temperature was also used as the parameter to kinetically control lysozyme crystallization [26,27]. High initial concentration gradients were used successfully to enhance nucleation in low-gravity liquid–liquid diffusion experiments [28], and late increases in dewatering rate using reverse-osmosis (RO) membranes [29] or vapor diffusion [30] were shown to increase the size of lysozyme crystals. Otherwise, the effect of equilibration rate has long been overlooked, and, traditionally, crystallization is achieved by obtaining the best equilibrium conditions experimentally.

In this work, we present a kinetic approach to the growth of diffraction-quality RNA crystals, using the osmotic dewatering method [29,31]. Based on the known equilibrium conditions which successfully produced crystals of the target RNA molecule, the dehydration rates were kinetically controlled during the nucleation stage. At the beginning of the crystallization process, a fast dewatering rate is applied creating a RNA-rich zone above the RO membrane and a favorable condition for nucleation. After the nuclei form, the dewatering rate is reduced by lowering the solute concentration gradient across the RO membrane. This change produces a suitable environment for crystal growth, but not nucleation, resulting in fewer and larger single crystals. Thus, the kinetic dewatering control strategy enables the choice of equilibration rates to achieve the goal of large, diffractable crystals. In this research, it was found that the diffraction quality of the crystals grown by the osmotic dewatering method with kinetic dewatering control was comparable to that of crystals grown by traditional vapor-phase diffusion methods under similar equilibrium conditions. It was further found that the naturally rapid initial dewatering that occurs in hanging drops favors the production of small numbers of large crystals.

2. Materials and methods

2.1. Target RNA molecule

The target molecule is a 12-nucleotide RNA-"U–U dodecamer". It was obtained by in vitro transcription using bacteriophage T7 RNA polymerase and immobilized DNA templates [31,32]. The self-complementary dodecamer was annealed in the presence of 10 mM $MgCl_2$ at 65°C for 10 min and allowed to cool down slowly to room temperature by holding the sample in still air at room temperature [12].

2.2. Dodecamer solubility

The solubility of the dodecamer was determined under the same solution conditions known to be appropriate for its crystallization [12]. The precipitant was 2-methyl 2,4 pentane diol (MPD), and other solutes were ammonium acetate (NH_4Ac), magnesium chloride ($MgCl_2$), and sodium (Na) cacodylate (pH 7.0). The concentrations of both dodecamer and MPD were varied systematically, and those of other solutes were fixed at 400 mM for NH_4Ac, 25 mM for $MgCl_2$, and 50 mM for Na cacodylate (pH 7.0). The solution conditions under which the dodecamer solubility at 37°C was determined are shown in Table 1. Solutions were placed in the glass sampling vial and insert (Cat. #: 95175 and 94470, All Tech, Deerfield, IL) for HPLC autosamplers. Additional sealing was achieved by applying parafilm outside the screw cap to prevent evaporation.

Table 1
Dodecamer and MPD concentrations in solutions used for solubility experiments in 400 mM NH_4Ac, 25 mM $MgCl_2$, and 50 mM Na cacodylate (pH 7)

Solution name	RNA (mg/ml)	MPD (wt%)
0.6_2	0.6	2
0.6_1	0.6	1
0.6_0.5	0.6	0.5
0.5_9	0.5	9
0.5_7	0.5	7
0.5_5	0.5	5
0.5_3	0.5	3

30 μl of each solution was loaded into the insert-and-vial assembly and incubated at 37°C. After a week, the assembly was observed under a microscope for evidence of any crystals and/or precipitates. If the samples yielded dodecamer crystals or precipitates, a new set of experiments was set up with decreased concentration of either MPD or dodecamer, or both. This trial-and-error procedure was repeated several times until a satisfactory equilibrium line was obtained. Re-dissolution experiments were not performed, so the equilibrium line represents the boundary between the solution phase and crystalline phase and not an actual solubility curve.

2.3. Osmotic dewatering

The osmotic dewatering crystallization device used was the multi-chamber osmotic dewatering crystallizer (MODC) consisting of twenty-four 30 μl wells separated from a reservoir solution by a RO membrane (MS-10, Osmonics, Inc., Minnetonka, MN) [31]. In order to perform kinetic dewatering control, modifications were made to the MODCs to facilitate a step-concentration-change scheme, as shown in Fig. 1, which reveals two fluid inlets installed near the opposite corners of a MODC. When the concentration-change operation starts, two syringes (with needles) are inserted into the reservoir through the two inlets. One syringe (I) contains a certain amount of solution with the same solutes but at different concentrations, the other syringe (R) is empty. The solution in the

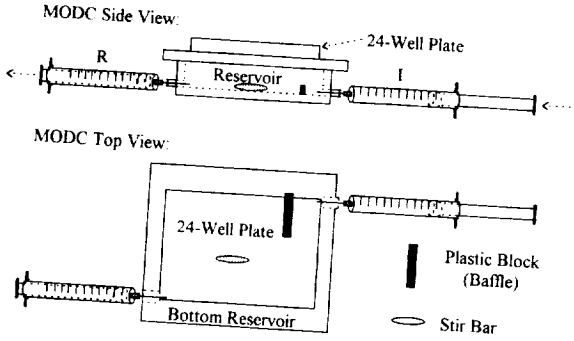

Fig. 1. Arrangement for effecting step-concentration changes in the reservoir solution of the MODC. The RO membrane is located immediately below the 24-well plate [31].

I syringe is then pushed gently into the reservoir. Due to the incompressibility of liquids, the same volume of the original reservoir solution is displaced out into the R syringe. In order to assure that the outgoing solution is at the same concentration as the original reservoir solution, a baffle was installed close to the inlet of the I syringe to prevent excess mixing during the injection process. After fluid displacement was complete, the MODC was carefully placed on a magnetic stir plate. The stir bar inside the MODC reservoir mixed the solution quickly.

The crystallization solution in each well initially contained 0.35–0.5 mg/ml of dodecamer, 2.5% MPD, 100 mM NH_4Ac, 12.5 mM Na Cacodylate (pH 7), and 6.25 mM $MgCl_2$. Reservoir solutions were either solution "10" (Table 2) or solution "12", which contained 12% MPD, 480 mM NH_4Ac, 60 mM Na cacodylate (pH 7), and 30 mM $MgCl_2$, or a combination of both as in those experiments with kinetic dewatering control.

Table 2
Solution compositions for hanging drop dewatering rate measurement experiments

Solution name / Components	Reservoir soln. "10"	Drop solutions "2.5"	Drop solutions "5.0"
MPD	10%	2.50%	5.00%
NH_4Ac	400 mM	100 mM	200 mM
Na cacodylate	50 mM	12.5 mM	25 mM
$MgCl_2$	25 mM	6.25 mM	12.5 mM
Initial osmolarity difference ($M_i m^3$)	*n/a*	1350	900

Table 3
Example of a concentration-change strategy in osmotic dewatering

	Starting reservoir soln.	First change	Second change
MPD	12%	10%	12%
NH_4Ac	480 mM	400 mM	480 mM
$MgCl_2$	30mM	25 mM	30 mM
Na cacodylate	60 mM	50 mM	60 mM
Duration	2 h	1 Day	6 Days
Purpose	Promote nucleation	Crystal growth	Promote growth

The kinetic control of dewatering was achieved by a timed strategy of changes in the concentration of the reservoir solutions. This strategy was based on the observed dewatering kinetics from vapor-phase diffusion experiments described below. At the beginning of an experiment, solution "12" was used as the reservoir solution for rapid dewatering in order to create a RNA-rich zone above the RO membrane. After 2 h, this reservoir solution was changed to solution "10" in order to slow down the water removal rate in order to create a better environment for crystal growth. This strategy is outlined in Table 3.

2.4. Vapor-phase diffusion

Vapor-phase diffusion crystallization and the water transport rate experiments were performed in Costar 24-well plates and Micro-bridges (Cat. #: HR3-114 and HR3-310, Hampton Research, Laguna Hills, CA). Micro-bridges were used in sitting-drop experiments. The glass coverslips for the wells were 18 mm in diameter and were silanized before use with a solution containing 3% (v/v) dichlorodimethylsilane and 97% (v/v) dichloromethane and kept in 70% ethanol solution for storage.

The equilibrium crystallization conditions for dodecamer were originally obtained from the vapor-phase diffusion method [12]. In order to guide the kinetic control strategy in the osmotic dewatering system, it is important to understand the dewatering kinetics in the vapor-phase diffusion system. Therefore, the appropriate values for the dewatering rates were first determined using hanging-drop evaporations with the reservoir and drop solutions listed in Table 2.

12 μl of each drop solution was loaded on a coverslip, which was then carefully inverted and sealed on top of each reservoir. After loading drops on 24 coverslips, the plate was put into a 37 C incubator. At different time points, the remaining drop volume was pipetted out and injected into a 50 μl glass microdispenser (made by Drummond, purchased from Fisher Scientific, Pittsburgh, PA). The length which the solution occupied was measured to determine the remaining drop volume.

2.5. Crystal quality comparison

For crystal quality comparison, parallel vapor-phase diffusion crystallization experiments were also performed. Both the hanging drop and sitting drop methods were used, and normally there were four drops for each condition. The drop solutions were the same as the starting well solution described above, and the reservoir solution used was as listed in Table 2. The procedures for setting up these experiments were described in the previous section.

At the end of each crystallization experiment, all the crystals were harvested and stored at room temperature in artificial mother liquors, consisting of 15% MPD, 20 mM NH_4Ac, 37.5 mM $MgCl_2$, and 75 mM sodium cacodylate, pH 7.

Crystals were mounted at room temperature with a minimal volume of artificial mother liquor, typically in a 0.7 mm capillary tube. X-ray diffraction data were collected at room temperature. The detector used was a Siemens X100 area detector and a Rigaku RU-200BH rotating-anode X-ray generator with a Huber graphite monochromator operated at 40 kV and 60 mA. Preliminary data

were collected for 180–300 s, with crystal still, at 2–3 different crystal angles separated by at least 45° to determine where the crystal diffracted the farthest and the strongest diffraction. 30 frames of diffraction data were then taken at 180 or 300 s per frame and a 0.2° rotation between successive pairs of frames. The swing angle of the detector face was 15°. All the data frames were visualized using XELOP software [33] to determine the extent of diffraction by analyzing the intensity of the farthest diffraction spot.

3. Results

3.1. Dodecamer solubility

Fig. 2 shows the equilibrium phase diagram derived from a summary of different sets of equilibrium experiments. The dodecamer has a low solubility in the presence of MPD. In most of the experiments, dodecamer came out of solution in crystals. Amorphous precipitates were observed in only one condition, with dodecamer at 1.0 μg/μl and MPD at 0.25%, which is represented by the left-most solid dot. Solubility data were used in selecting concentration gradients in osmotic dewatering crystallization experiments. Nucleation and crystal growth phases could then occur in a controlled manner relative to supersaturation.

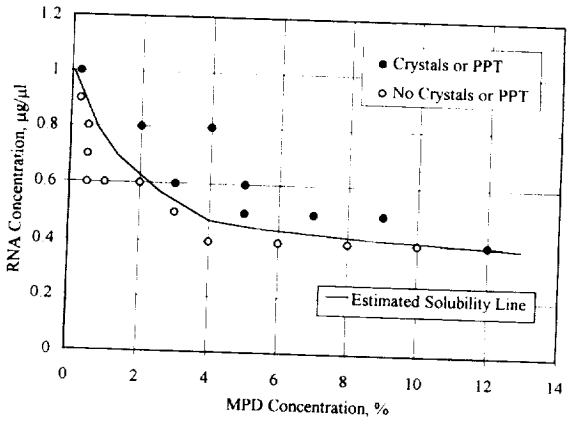

Fig. 2. Dodecamer solubility curve in the presence of MPD at 37°C determined on the basis of crystal or precipitate formation.

3.2. Hanging-drop dewatering rate measurement

Two experiments were performed using each of the concentration combinations described in Table 2. The experimental dewatering data are shown in Figs. 3 and 4. The theoretical calculations were based on the vapor-phase diffusion model developed by Fowlis et al. [23] evaluated under the conditions of the vapor diffusion experiments, as detailed above under "Materials and Methods" [34].

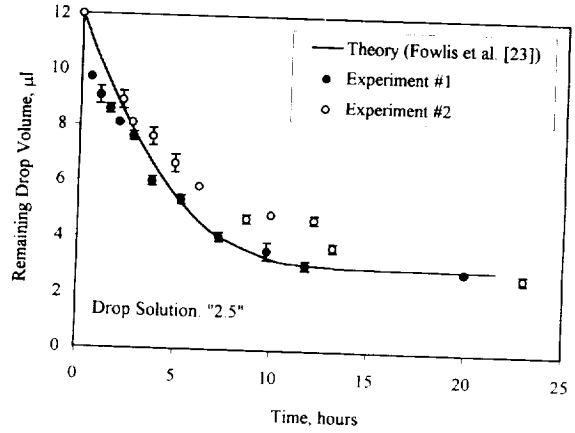

Fig. 3. Comparison of experimentally measured water removal rates with theoretical predictions using drop solution "2.5" (Table 2) in hanging drop method.

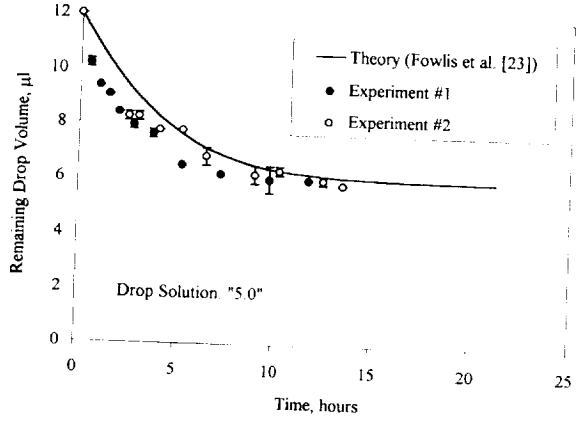

Fig. 4. Comparison of experimentally measured water removal rates with theoretical predictions using drop solution "5.0" (Table 2) in hanging drop method.

In the experiments with solution "2.5" as the drop solution, the theoretical prediction agreed with the experimental data reasonably well. However, in the second set of experiments with solution "5.0" as the drop solution, the theory underpredicted the dewatering rates in the initial stages. From the experimental data, it is clear that the initial rates of water removal from drops were high compared to predictions for both conditions.

The hanging drop dewatering data offered important kinetic information concerning how such systems approach equilibrium. This information provides guidance for controlling an osmotic dewatering system, with similar starting and equilibrium conditions, for the best nucleation and crystal growth environments.

3.3. Crystallization experiments using both methods

When only solution "10" or "12" was used in the reservoir, crystallization by osmotic dewatering yielded mostly small to medium crystals, and each dewatering well usually had 10–15 crystals. This problem of excess nucleation and smaller final crystal size was greatly ameliorated by the application of the kinetic control approach. By using concentration-change strategies, both nucleation and crystal growth were more favorably controlled, resulting in an average of four crystals per dewatering well and larger crystal sizes. Fig. 5 shows dodecamer crystals of typical size grown using the concentration-change scheme listed in Table 3. Parallel vapor-phase diffusion crystallization experiments produced dodecamer crystals with similar sizes and morphology.

Table 4
Comparison of diffraction resolution

Parallel crystallization experiments	Resolution of crystals grown from		
	Osmotic dewatering	Hanging drop	Sitting drop
EXP070296	3.12 Å	3.20 Å	n.a.
EXP082096	3.26 Å	3.05 Å	n.a.
EXP090996	3.10 Å	n.a.	3.08 Å

3.4. X-ray diffraction analysis

Since solving the crystal structure is not within the scope of this research, the resolution of dodecamer crystals was determined using a quantitative measurement from the XELOP program [33]. By the chosen intensity criterion most of the dodecamer crystals grown by either osmotic dewatering or vapor-phase diffusion diffracted to about 3.1 Å. Table 4 provides a comparison of the diffraction quality of crystals grown by these methods.

4. Discussion

4.1. Control of nucleation

When comparing the dewatering rate data of the hanging drop method with the theoretical

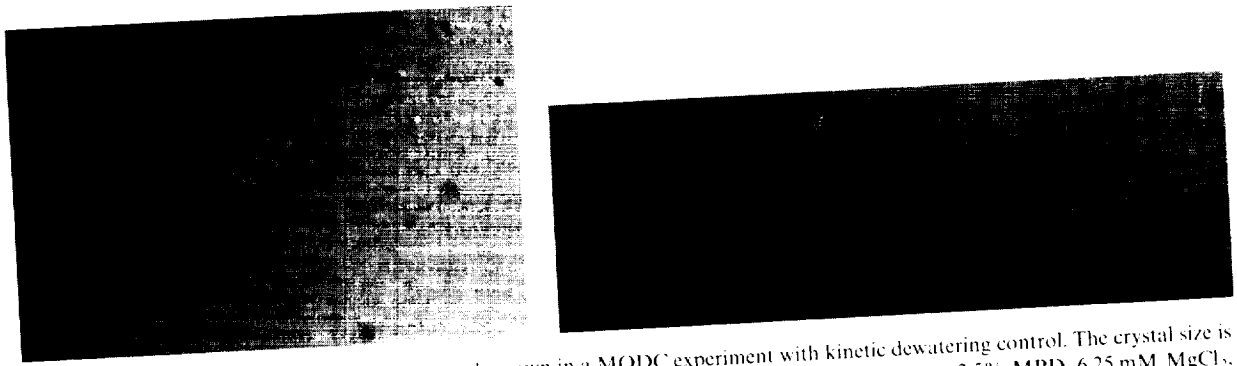

Fig. 5. Polarized micrograph of dodecamer crystals grown in a MODC experiment with kinetic dewatering control. The crystal size is 250 μm × 125 μm × 125 μm (not including the tips). The initial conditions were 0.5 mg ml dodecamer, 2.5% MPD, 6.25 mM $MgCl_2$, 100 mM NH_4Ac, and 12.5 mM sodium cacodylate pH 7. About 80% of the initial volume (30 μl) was removed by osmotic dewatering.

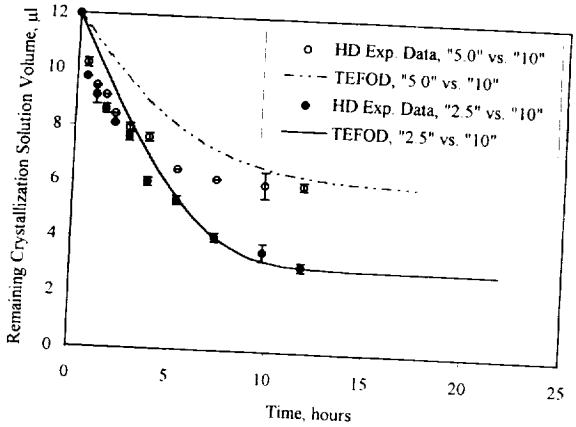

Fig. 6. Comparison between the hanging drop experimental dewatering data (Figs. 3 and 4) and theoretical osmotic dewatering predictions by TEFOD at the same concentration gradients.

dewatering rate predictions by the transport equation for osmotic dewatering (TEFOD) [31], as shown in Fig. 6, it is clear that at the early stage (during the first two hours), hanging drop systems have much higher dewatering rates than osmotic dewatering systems at the same concentration gradients.

In the actual crystallization experiments, when using the same concentration gradients as shown in Fig. 6, hanging drop systems were able to produce medium to large crystals, but osmotic dewatering systems consistently produced small to medium crystals with an average of more than 15 crystals per dewatering well. Despite having the same thermodynamic equilibrium, these two systems do not produce the same results.

In order for an osmotic dewatering system to have a similarly rapid initial dewatering rate, the initial concentration gradient has to be increased. With the same starting well solution, when a more concentrated reservoir solution, 12% MPD, 480 mM NH_4Ac, 30 mM $MgCl_2$, and 60 mM Na cacodylate, pH 7, is used, the initial dewatering rates in the osmotic dewatering system match closely those in both of the "2.5" versus "10" and "5.0" versus "10" hanging drop systems. However, most of these experiments yielded about the same number of crystals in each dewatering well. Although the average size of the crystals in each well was somewhat larger, due to higher extent of dewatering at the end, the problem of excess nucleation was still not solved.

The results from the higher initial concentration gradient experiments suggested that nucleation needs to be promoted rapidly in the early stage and be suppressed once nuclei are formed in order to favor the growth of crystals. This rationale was tested by implementing a kinetic control approach. The kinetic approach offers several advantages. During the early stage of a crystallization process, a macromolecule-rich zone will encourage nucleation. This can be created by using a higher concentration gradient to achieve rapid dewatering and, hence, a macromolecule-rich zone. After the nuclei form, further nucleation should be arrested, and crystal growth needs to be promoted in order to obtain fewer, but larger crystals. This can be achieved by using a lower concentration gradient to reduce the dewatering rate. Lastly, after equilibrium has been reached for the first time the reservoir concentration can be further increased so as to restart crystal growth.

In order to choose the proper gradients to optimize the kinetically controlled crystallization, theoretical dewatering rates predicted by TEFOD were calculated with changing reservoir concentrations to simulate the dewatering rates in a hanging drop system. The solid curve in Fig. 7 illustrates this kinetic simulation. The osmotic dewatering system starts with "2.5" versus "12" for the first 2 h and changes reservoir solution concentration to solution "10" for the rest of the dewatering process. The composite dewatering curve (solid line) closely matches the experimental dewatering curve of the hanging-drop system. The reservoir solution concentration can later be raised again to solution "12", shown by the discontinuity in the solid curve of Fig. 7 at 26 h, in order to promote more dewatering and, hence, more crystal growth.

Based on the above analysis, a kinetic approach scheme was set up, as shown in Table 3. As already summarized above, less nucleation and larger single crystals were achieved with fair reproducibility. These results demonstrated one of the major advantages offered by osmotic dewatering crystallization, namely, the precise control of water removal rates by dynamically controlling the concentration gradients across the RO membrane.

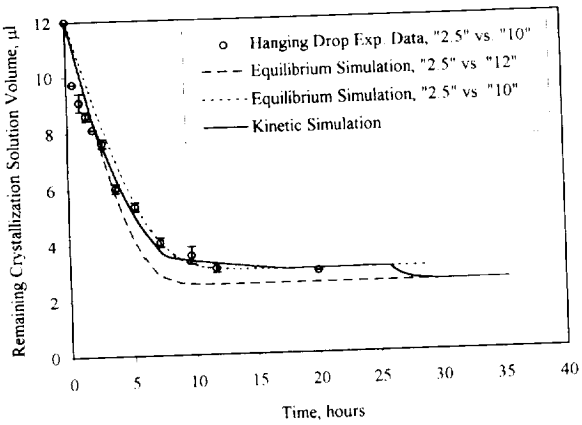

Fig. 7. Dewatering rate simulation: by varying the reservoir solution concentration at properly chosen stages, an osmotic dewatering system can simulate the dewatering rates in a hanging drop system, as indicated by the "Kinetic simulation" (solid) line. "Equilibrium simulation" curves represent osmotic dewatering conditions without changes in reservoir concentration.

This control can then be used for controlling both the nucleation and crystal growth stages in the crystallization processes.

4.2. Crystal quality comparison

The diffraction data showed that the quality of the crystals grown by the osmotic dewatering method is very similar to that of those crystals grown by vapor-phase diffusion methods. The best average resolution for the osmotic dewatering crystals in these parallel experiments was 3.10 Å, and that for the vapor phase diffusion crystals was 3.05 Å. Table 4 lists a few direct comparisons.

As a general observation, vapor-phase diffusion systems used in this study had a higher probability of producing crystals large enough for diffraction than the osmotic dewatering system did. In those parallel crystallization experiments between osmotic dewatering and vapor phase diffusion, on the average 25% (15 of 60) of the drops would produce crystals with sizes close to those shown in Fig. 5, and 10% (6 of 60) of the osmotic dewatering wells would produce crystals of similar size (significantly different at the 0.005 level). In addition to the inevitable stochastic factor in crystallization experiments, one possible explanation of the lower consistency of osmotic dewatering crystallization is the manner in which the kinetic control was performed. As described, the change of reservoir solution concentrations was done manually inside the 37 C incubator to avoid a temperature decrease that is known to enhance nucleation. During the operation, while the door of the incubator was open, the incubator chamber temperature would drop at least 0.5 C. Since the volume of the crystallization solutions was less than 30 µl, and the solutions were located on the top portion of the MODC, it is very easy for the crystallization solutions to be affected by this temperature change, resulting in enhanced nucleation, as was observed.

5. Summary

Results from kinetically controlled experiments demonstrated one important advantage of the osmotic dewatering crystallization method. With precise control of water removal rates by adjusting the concentration gradients across the RO membrane, the nucleation stage can be regulated so that less nuclei are formed and larger crystals can be obtained. This also suggests the importance of the kinetic water removal pattern in any crystallization process. Evidently, initial rapid water removal favors the formation of small numbers of nuclei. More research and optimization need to be done on the nucleation stage in order to guarantee better success in obtaining high-quality, diffractable macromolecular crystals.

References

[1] C. Teurk, L. Gold, Science 249 (1990) 505.
[2] R. Kole, M.F. Baer, B.C. Stark, S. Altman, Cell 19 (1980) 881.
[3] T.R. Cech, A.J. Zaug, P.J. Grabowski, Cell 27 (1981) 487.
[4] T.R. Cech, Science 236 (1987) 1532.
[5] K.J. Baeyens, H.L. De Bondt, S.R. Holbrook, Nature Struct. Biol. 2 (1995) 56.
[6] K.J. Baeyens, J. Jancarik, S.R. Holbrook, Acta Crystallogr. D 50 (1994) 764.
[7] C. Betzel, S. Lorenz, J.P. Fürste, R. Bald, M. Zhang, T.R. Schneider, K.S. Wilson, V.A. Erdmann, FEBS Lett. 351 (1994) 159.

[8] I. Burger, C. Kang, N. Sinha, M. Wolters, A. Rich, Acta Crystallogr. D 52 (1996) 465.
[9] J.H. Cate, A.R. Gooding, E. Podell, K. Zhou, B.L. Golden, C.E. Kundrot, T.R. Cech, J.A. Doudna, Science 273 (1996) 1678.
[10] J.A. Doudna, C. Grosshans, A. Gooding, C.E. Kundrot, Proc. Natl. Acad. Sci. USA 90 (1993) 7829.
[11] S.R. Holbrook, C. Cheong, I. Tinoco Jr., S.H. Kim, Nature 353 (1991, London) 579.
[12] C.E. Kundrot, Meth. Enzymol. 276 (1996) 143.
[13] S.E. Lietzke, C.L. Barnes, J.A. Berglund, C.E. Kundrot, Structure 4 (1996) 917.
[14] S.E. Lietzke, V.E. Carperos, C.E. Kundrot, Acta Crystallogr. D 52 (1996) 687.
[15] S. Portmann, N. Usman, M. Egli, Biochem. 34 (1995) 7569.
[16] W.G. Scott, J.T. Finch, A. Klug, Cell 81 (1995) 991.
[17] N. Usman, M. Egli, A. Rich, Nucleic Acids Res. 20 (1992) 6695.
[18] M.C. Wahl, C. Ban, C. Sekharudu, B. Ramakrishnan, M. Sundaralingam, Acta Crystallogr. D 52 (1996) 655.
[19] M.C. Wahl, S.T. Rao, M. Sundaralingam, Nature Struct. Biol. 3 (1996) 24.
[20] M.C. Wahl, B. Ramakrishnan, C. Ban, X. Chen, M. Sundaralingam, Acta Crystallogr. D 52 (1996) 668.
[21] F. Rosenberger, J. Crystal Growth 76 (1986) 618.
[22] R.C. DeMattei, R.S. Feigelson, J. Crystal Growth 122 (1992) 21.
[23] W.W. Fowlis, L.J. DeLucas, P.J. Twigg, S.B. Howard, E.J. Meehan Jr., J.K. Baird, J. Crystal Growth 90 (1988) 117.
[24] J.R. Luft, D.T. Albright, J.K. Baird, G.T. Detitta, Acta Crystallogr. D 52 (1996) 1098.
[25] L.J. Wilson, T.L. Bray, F.L. Suddath, J. Crystal Growth 110 (1991) 142.
[26] K.B. Ward, W.M. Zuk, M.A. Perozzo, M.A. Walker, G.I. Birnbaum, W. Kung, A. Cavaliere, D.R. Uffen, H. Scholaert, J. Crystal Growth 122 (1992) 235.
[27] C.A. Schall, J.S. Bonita, E. Li, E. Arnold, J.M. Wiencek, J. Crystal Growth 165 (1996) 299.
[28] J. Sygusch, R. Coulombe, J.M. Cassanto, M.G. Sportiello, P. Todd, J. Crystal Growth 162 (1996) 167.
[29] P. Todd, S.K. Sikdar, C. Walker, Z.R. Korszun, J. Crystal Growth 110 (1991) 283.
[30] K.M. Gernert, R. Smith, D.C. Carter, Anal. Biochem. 168 (1988) 141.
[31] C.-Y. Lee, M.G. Sportiello, S.P. Cape, S. Ferree, P. Todd, C.E. Kundrot, S. Lietzke, C. Barnes, Biotechnol. Progr. 13 (1997) 77.
[32] H.A. Marble, R.H. Davis, Biotechnol. Progr. 11 (1995) 393.
[33] W. Minor, XELOP Program, Purdue University, 1989.
[34] C.-Y. Lee, Crystallization of oligonucleotide by osmotic dewatering and cell separation by inclined sedimentation, Ph.D. Thesis, University of Colorado, Boulder, 1996.

Journal of Crystal Growth

Instructions to Authors (short version)

Submission of papers
Manuscripts (one original + two copies), should be sent to a member of the Editorial Board or preferably to an appropriate subject Associate Editor. News or announcements should be submitted through the Principal Editor; a duplicate should be sent directly to Elsevier Science B.V., address given below.
Original material. Submission of a manuscript implies it is not being simultaneously considered for publication elsewhere and that the authors have obtained the necessary authority for publication.

Types of contributions
Original research papers, Letters to the Editors and Priority communications are welcome. They should contain an Abstract (of up to 200 words) and a Conclusion section, which particularly in the case of theoretical papers translates the results into terms readily accessible to most readers.
As a guideline: *experimental papers* should not be longer than 16 double-spaced typed pages, and 8 figures + tables; for *theoretical papers* a maximum of 20 pages and 10 figures + tables is suggested.
Letters and Priority communications should not be longer than 5 double-spaced typed pages, and 3 figures + tables. They will be given priority in both the refereeing and production processes. The faster production schedule may preclude sending proofs of Letters and Priority communications to authors.

Manuscript preparation
Contributions may be written in English, French or German. They should have an abstract in English. The paper copies of the text should be prepared with double line spacing and wide margins, on numbered sheets.
Structure. Please adhere to the following order of presentation: Article title, Author(s), Affiliation(s), Abstract, PACS codes and keywords, Main text, Acknowledgements, Appendices, References, Figure captions, Tables.
Corresponding author. The name, complete postal address, telephone and fax numbers and the e-mail address of the corresponding author should be given on the first page of the manuscript.
Classification codes/keywords. Please supply one to four classification codes (PACS and/or MSC) and up to six keywords of your own choice that describe the content of your article in more detail.
References. References to other work should be consecutively numbered in the text using square brackets and listed by number in the Reference list. Please refer to the more detailed instructions for examples.

Illustrations
Illustrations should also be submitted in triplicate: one master set and two sets of copies. The *line drawings* in the master set should be original laser printer or plotter output or drawn in black india ink, with careful lettering, large enough (3–5 mm) to remain legible after reduction for printing. The *photographs* should be originals, with somewhat more contrast than is required in the printed version. They should be unmounted unless part of a composite figure. Any scale markers should be inserted on the photograph itself, not drawn below it.
Colour plates. Figures may be published in colour, if this is judged essential by the Editor. The Publisher and the author will each bear part of the extra costs involved. Further information is available from the Publisher.

After acceptance
Important. When page proofs of the accepted manuscripts are made and sent out to authors, this is in order to check that no undetected errors have arisen in the typesetting (or file conversion) process. At the proof stage only printer's errors may be corrected. No changes in, or additions to, the edited manuscript will be accepted.
Notification. The authors will receive the final answer of acceptance or rejection from the Office of the Principal Editor and will be invited to supply an electronic version of the accepted text, if this is not already available.
Copyright transfer. In the course of the production process you will be asked to transfer the copyright of the article to the Publisher. This transfer will ensure the widest possible dissemination of information.

Electronic manuscripts
The Publisher welcomes the receipt of an electronic version of your accepted manuscript. If there is not already a copy of this (on diskette) with the journal editor at the time the manuscript is being refereed, you will be asked to send a file with the text of the accepted manuscript directly to the Publisher by e-mail or on diskette (allowed formats 3.5" or 5.25" MS-DOS, or 3.5" Macintosh) to the address given below. (When e-mailing a non-ASCII word-processor file, you should encode it, e.g. with UUENCODE or BinHex, so as to retain all formatting codes.) The name and version of the word-processing program and the type of operating system should always be indicated. Please note that no deviations from the version accepted by the Editor of the journal are permissible without the prior and explicit approval by the Editor. Such changes should be clearly indicated on an accompanying printout of the file.

Author benefits
No page charges. Publishing in Journal of Crystal Growth is free.
Free offprints. The corresponding author will receive 50 offprints free of charge. An offprint order form will be supplied by the Publisher for ordering any additional paid offprints.
Discount. Contributors to Elsevier Science journals are entitled to a 30% discount on all Elsevier Science books.

Further information (after acceptance)

Elsevier Science B.V., J. Crystal Growth
Issue Management
Physics and Materials Science
P.O. Box 2759, 1000 CT Amsterdam
The Netherlands
Fax: +31 20 485 2319/ +31 20 485 2704
E-mail: a.koch@elsevier.nl

North-Holland, an imprint of Elsevier Science

Chapter 18

Direct Observation and Modeling of Vapor Transport in Protein Crystal Growth

Yanqiu Wang

Chapter 18

Direct Observation and Modeling of Vapor Transport in Protein Crystal Growth

By Yanqiu Wang

3.1 Detailed background

Experiments have been done in different ways by other researchers in order to understand the transport processes in the hanging drop crystallyzation method. Fowlis *et al.* (1988) did experiments on the earth. Evaporation experiments at 4 and 25 °C were carried out. The salt employed in the drops and reservoir was ammonium sulfate. No protein was used in their experiments. Drop volume was 25 μL and reservoir volume was 1.0 mL. The reservoir had twice the concentration of the ammonium sulfate as that in the drop. The distance from the drop to the surface of the solution in the reservoir was 1.2 cm and was not varied. Each droplet had a radius of 1.814×10^{-2} cm. The ratio of droplet radius to drop-reservoir distance was 0.015. The surface area and volume of the drop were calculated through the parameters ρ and α (please refer to Figure 2.1), which were measured using a microscope. To establish the progress of the evaporation at a given time, one or more drops were removed from the box. The refractive index of each drop was measured with a temperature-controlled refractometer. The ammonium sulfate concentration within the drop was determined using a previous calibration of refractive index versus concentration. Their results obtained with 25 μL drops at three differ-

ent concentrations were compared with their theory (equation A.30). It was stated that the theory is in qualitative agreement with experiment.

In Fowlis' experiments, there may have been enough vibration to cause the droplet to be well mixed, and step 4 (water vapor across the air space) was rate limiting. The procedure used to calculate surface area and volume of the drop was not very accurate as mentioned in the paper.

Mikol *et al.* (1990) did an experimental determination of water equilibration rates in the hanging drop method of protein crystallization. The three reference solutions were (1) 1.6 M ammonium sulfate buffered with 20 mM Bistris/HCl, pH 7.0 (AS); (2) 20% (W/V) polyethylene glycol 6000 and 20 mM Bistris/HCl, pH 7.0 (PEG); and (3) 20% (V/V) 2-methyl-2,4-pentanediol and 20 mM Bistris/HCl, pH 7.0 (MPD). Hen egg white lysozyme was used as crystallization protein. The crystallization containers were 24-well tissue culture trays. Each well had a cylindrical shape with a 1.6 cm inner diameter and a 1.7 cm height, approximately. The reservoir contained 1 mL (unless specified) of one of the three reference solutions (AS, PEG, and MPD) and the drop was made by diluting an aliquot of the reservoir with distilled water. The dilution factor, δ, defined as the ratio of the initial concentration of precipitant in the droplet over that of the reservoir, was either 1/2 or 2/3. The drop was placed on a silanized coverslip which was then sealed over the well with a silicone grease. For each condition tested, a series of drops with the same composition was prepared. To determine the water evaporation rate, drops were removed from boxes at various times and the concentration of precipitant in the drops was measured by refractometry. Experiments were performed at 3 and 20 °C and were continued until equilibrium was attained. The drop volumes ranged from 8 μL to 32 μL. The distance from drop to reservoir was changed from 2

mm to 10 mm by changing the volume of reservoir solution. The stated results of Mikol's experiments were: (1) the presence of protein has little influence on the water equilibration rate in the hanging drop protein crystallization; (2) the initial volume of the drop plays a major part in determining the evaporation rate. The rate of relative reduction of drop volume was clearly less when the initial volume was larger; this conclusion is consistent with our result of rate limiting step analysis (refer to Chapter 2 for details). When solute transfer in the droplet is the rate limiting step, systems with larger droplets would have lower mass transfer rates. (3) when analyzing the effect of initial dilution, δ (either 1/2 or 2/3), on the kinetics, the rate of concentration change was lower with $\delta = 2/3$ than with $\delta = 1/2$ (consistent with lower driving force); (4) the effect of temperature on the equilibration kinetics is conspicuous; the time increased to reach a certain concentration when the temperature was decreased from 20 to 3 °C. (5) The influence of the surface-to-volume ratio of the drops on the kinetics is demonstrated first by experiments with different drop sizes (here surface means the liquid/air interface from which water molecules can escape). As the ratio is lowered with large drops the kinetics of evaporation of water are indeed slowed down. Second, when the surface of the drop is increased by varying shape while holding a constant volume (nonsilanization versus silanization of glass coverslip), it can be noticed that the rate of equilibration is slightly increased. (6) Some experiments were performed in AS with larger reservoir volumes to decrease the air gap between drop and reservoir. The drop-to-reservoir distance can be estimated as about 10, 5, and 2 mm, respectively, with 1, 2, and 2.75 mL reservoir volumes. From the experiments, it appears that the kinetics were identical when the distance was reduced from 10 to 5 mm, but slightly shortened when the distance was reduced to 2 mm.

This conclusion is consistent with our theoretical analysis in Chapter 2 (see equations 2.4 and 2.6).

Sibille *et al.* (1991) analyzed the solvent evaporation rates in the vapor diffusion protein crystal growth experiments from the STS–61C Space Shuttle Mission. The apparatus specially designed for space flight is shown in Figure 3.1. A vapor diffusion crystal cell, which is typical of the many flown, is illustrated in Figure 3.1. In Figure 3.1a, they showed the cell in the pre-launch configuration, designed to secure it against launch acceleration. During the pre-launch phase, an aqueous solution of protein, buffer, and precipitating agent was placed in the syringe and a piston containing an o-ring was advanced from below to seal the tip of the syringe as shown. The sealing piston passed through a mass of cellulose wool, called the reservoir, which was soaked with an aqueous solution of the precipitating agent. The space between the syringe and the reservoir was filled with air. The entire cell was contained in a cavity machined in an aluminum block, that had plexiglas windows which separated its contents from the Shuttle cabin environment. The windows permitted visual observation and photography.

On orbit, as shown in Figure 3.1b, the sealing piston was retracted, and the injecting piston was advanced to create a droplet of protein-containing solution suspended on the tip of the syringe. As the concentration of the precipitating agent in the reservoir was twice that in the droplet, water evaporated from the syringe, diffused through the air space, and condensed onto the surface of the reservoir. The reduction in volume in the droplet caused the protein to supersaturate and to crystallize.

At the end of the mission, the injecting piston was retracted, withdrawing the contents of the droplet into the interior of the syringe. The sealing

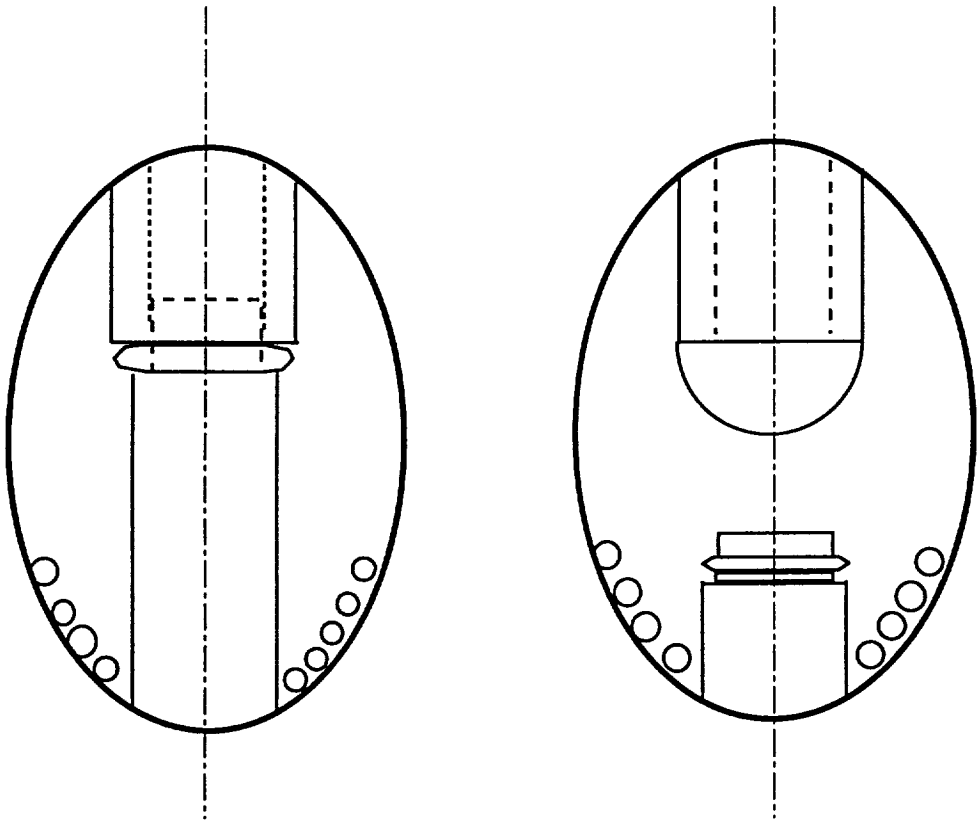

Figure 3.1: The experiment arrangement used by Sibille *et al.* (1991). (a) Protein crystal growth vapor diffusion apparatus in the pre-launch and post-launch configuration. (b) The apparatus in the flight configuration.

piston was advanced to close the tip of the syringe and to secure its contents for re-entry.

Their purpose was to analyze the in-flight photographs of evaporating droplets obtained on the STS-61C mission and to compare them with Fowlis' model, which assumes the rate limiting step is water transfer accross the air space from the drop surface to the reservoir. The conclusion was that the droplets on STS-61C seem to have evaporated more slowly than what Fowlis' theory predicted. This may indicate that the rate-limiting step is not diffusion of water vapor accross the air space.

In each of the experiments by Luft *et al.* (1996), a 24 μL hanging drop of 1.00 M NaCl was allowed to partially equilibrate with a reservoir containing 2.00 M NaCl. After a specified time the drop was retrieved and analyzed by refractometry to determine its sodium chloride concentration. Each experiment was conducted for a specific length of time and at a fixed value of the droplet to reservoir surface distance. The duration and/or the distance were varied from experiment to experiment. Two large sets of experiments were undertaken. In the first set droplet-reservoir separations ranging from 7.6 to 78.3 mm and equilibration durations from 20 to 121 hours were examined. In the second set separations ranging from 88.9 to 119.4 mm and durations of 120 to 168 hours were examined.

The experimental apparatus is shown in Figure 3.2. A standard laboratory test tube [Pyrex, 13.6 mm inside diameter(ID), 15.9 mm outside diameter(OD), 127 mm length, 17.5 ml volume] acted as the reservoir vessel. Using a steel rule and a simple alignment jig, a scribe mark of liquid level was placed on the outer wall of the test tube. The mark was placed a specified distance down from the top lip of the test tube. Reservoir solution, 2.00 M NaCl, was

introduced into the tube and adjusted dropwise until the meniscus just touched the scribe mark. Care was taken to prevent droplets of reservoir solution from adhering to the wall of the test tube above the scribe mark.

A droplet of 1.00 M was deposited, using a Gilson Pipetman micropipette set to deliver 24 μl on the adhesive side of the clear plastic label tape (Morris, Kim and McPherson 1988, Luft and DeTitta 1992, and Cody and DeTitta 1992) manufactured by Manco Co. that had been affixed to common flat washers (45 mm OD, 17 mm ID, 3 mm thickness, and 34 g). The washers offer firm support for the tape, keeping it taut and allowing for easy manipulation of the drop. The droplet was inverted and immediately sealed over the reservoir, with the tape adhesive making the seal and the weight of the washer helping to maintain it. The establishment of the seal marked the beginning of the partial equilibration. The droplet and reservoir, forming a closed system, were allowed to equilibrate for a specified time, undisturbed and at room temperature (*vide infra*).

Droplets were retrieved by gently prying the tape seal loose, using the washer as a lever. Once the seal was breached the tape could be smoothly peeled away from the rim of the test tube without fear of losing the droplet. The droplet was pipetted using a Gilson Pipetman and transferred immediately to the prism of a Bausch and Lomb Abbé 3L refractometer where its refractive index was recorded. Using a two-point interpolation scheme the refractive index of a partially equilibrated droplet was converted into a sodium chloride concentration.

Their results were that over the range of droplet-reservoir distances examined, 7.6 to 119.4 mm, the larger the distance that separated the droplet and reservoir, the slower the droplet equilibrated with the reservoir. The varia-

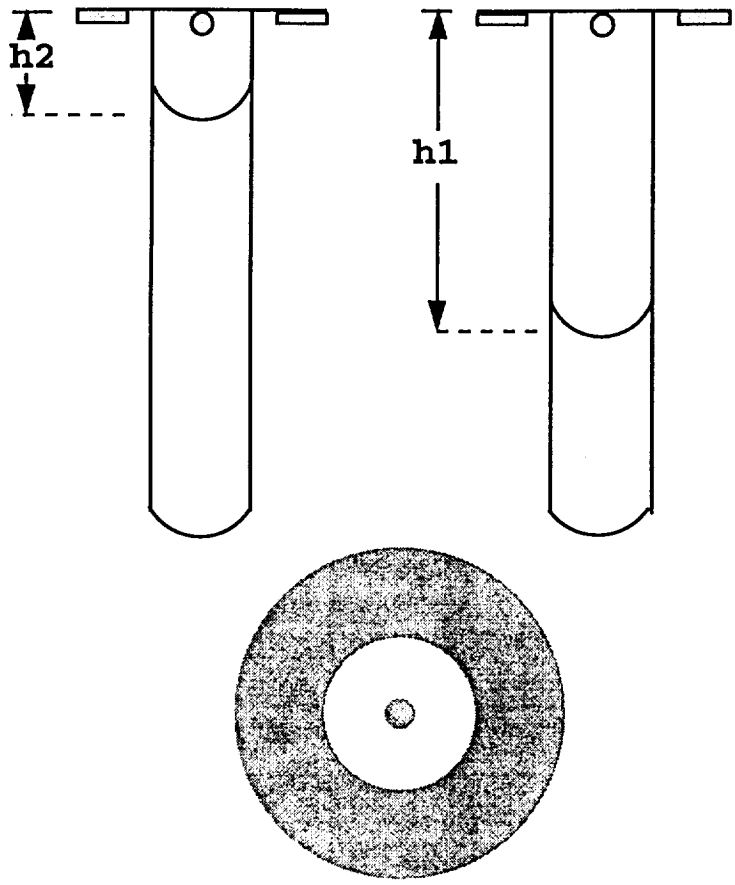

Figure 3.2: The experimental arrangement used by Luft *et al.* (1996).

tion of the rate of equilibration with droplet-reservoir distance was non-linear, and the rate was most senstive to variations in the droplet-reservoir separation at short separations. They claimed that their results are supportive of the contention that the rate limiting step in vapor diffusion is transit of water across the vapor space (which appear to be consistent with eq. 2.5).

There are two obvious drawbacks in the previous experimental investigations. One is that the crystallization process was interrupted when samples were collected. The other is that the data quality could not be guaranteed because of the inability to check the leakage of individual samples. The image recording method employed in the present study is noninvasive and *in situ*, and the system leakage can be inferred from the data. The data quality is guaranteed.

3.2 Materials and methods

3.2.1 Experimental set-up and procedure

The experimental set-up for crystallization experiments is schematically shown in Figure 3.3. A picture of this set-up is also given in Figure 3.4. The crystallization unit consisted of a plastic cuvette of 1 cm × 1 cm cross section and 4 cm in height, a plastic cover, and a glass capillary with a rubber plunger. The capillary had an outer diameter of 2.8 mm, and was calibrated so that a desired amount of liquid can be drawn into the capillary. The plastic cover is used to close up the cuvette. A CCD camera connected to an Apple Macintosh computer recorded the droplet dimension during the course of experiments. The images captured by the CCD camera were stored in the computer and shown on the computer monitor. The back light provided

the light source for the CCD camera.

The experimental procedures were as follows. First, vaccum grease was used to seal the gap between the capillary inner wall and the plunger. Next, the cuvette was filled with the desired amount of reservoir solution, and the capillary was filled with the desired amount of droplet solution. By varying the above two values, we should be able to examine the effects of droplet to reservoir distance on mass transfer rates. Next, the cuvette, the capillary, and the plastic cover were assembled as shown in Figure 3.5.a. Vacuum grease was used to seal the connections between the cuvette and the plastic cover and those between the plastic cover and the capillary. Then, the liquid was pushed out of the capillary to form a droplet, as shown in Figure 3.5.b. A picture of a droplet in one experiment is also shown in Figure 3.6. As soon as the droplet was formed, the experiment started. The images were captured by the CCD camera and were stored in the computer for later analysis.The entire set-up (light source, cuvette, and detector) was rigidly attached to a vibration isolation table.

3.2.2 Solutions

Lysozyme was used as crystallization protein, sodium acetate as buffer (pH=4.0), and sodium chloride as precipitating agent. The compositions of the droplets (about 20 μl) were: 3% lysozyme (3 g/100 ml), 1% NaCl, 0.1 M sodium acetate, pH 4.0. The compositions of the droplets in the experiments without the protein were the same as those with the protein except for the added protein. The reservoir solutions (0.5 ml to 2.5 ml) contain 4% NaCl, 0.1 M sodium acetate, and pH=4.0, regardless of whether experiments were with or without the protein in the droplets.

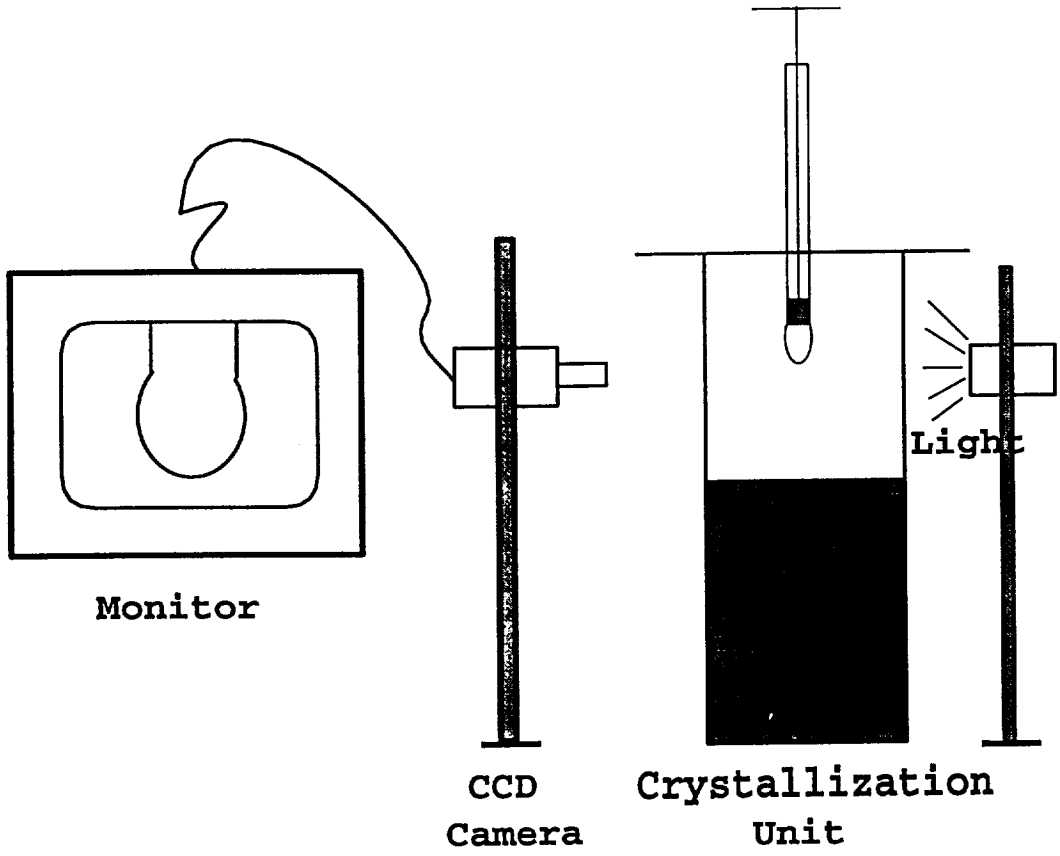

Figure 3.3: Schematic of experimental set-up.

Figure 3.4: Photograph of the experimental set-up.

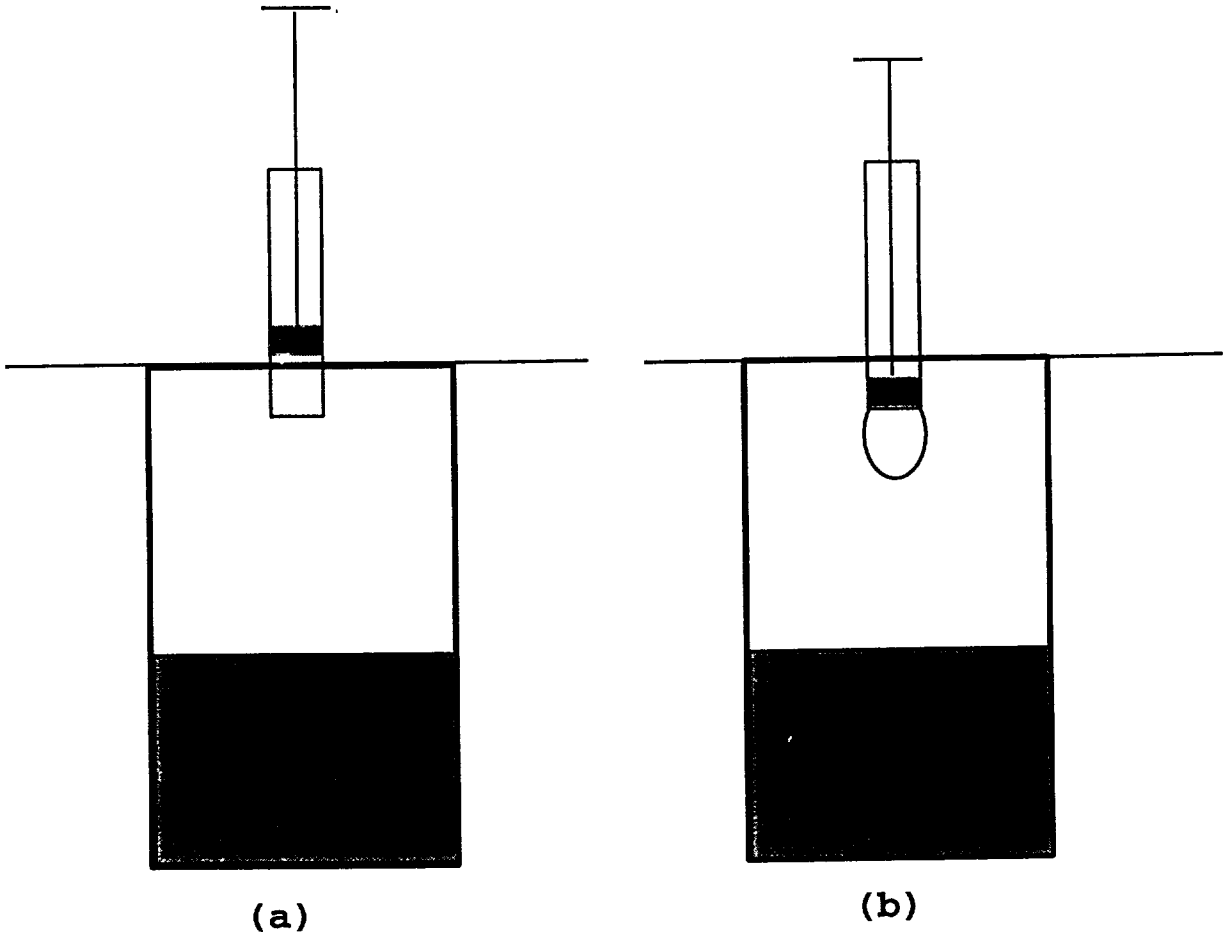

Figure 3.5: Procedure for forming the droplet in the crystallization unit. (a) before the experiment started, the liquid was in the capillary; (b) droplet was formed by squeezing out the liquid in the capillary, and an experiment started as soon as the droplet was formed.

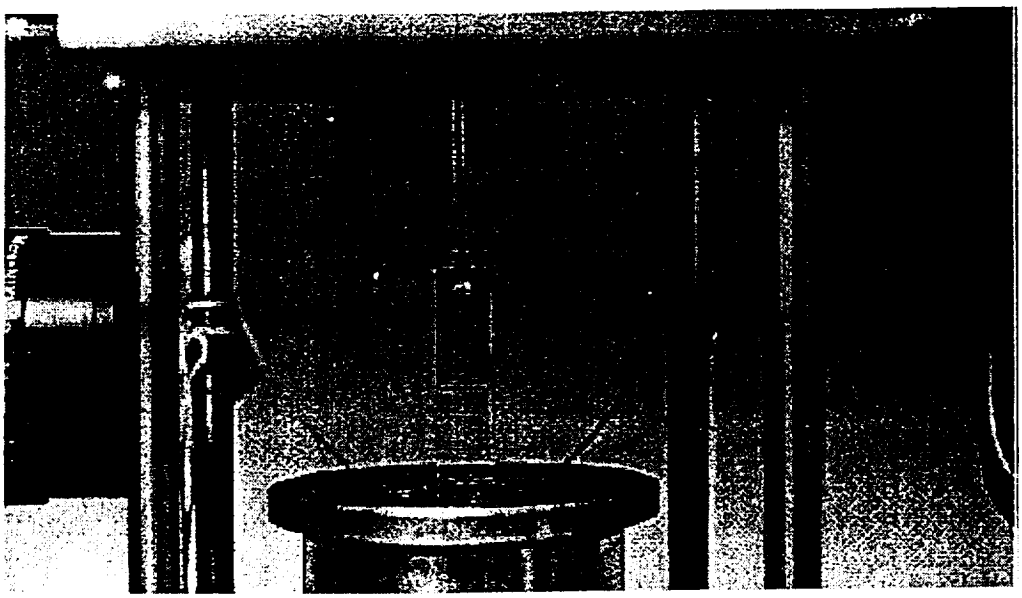

Figure 3.6: Photograph of the experimental set-up, showing drop and cuvette.

0.1 M sodium acetate stock buffer solution was made from 3 M sodium acetate solution, filtered DI water. 3 M HCl was used to adjust the pH of the stock solution to 4.0. 25% stock solution of NaCl was made from the above stock buffer solution and solid NaCl. The pH of this stock solution was also adjusted by adding 3 M HCl. 6% lysozyme stock solution was made from the above buffer stock solution and solid lysozyme, and this solution was filtered using a syringe filter. The reservoir solutions were made from the 25% NaCl stock solution and the 0.1 M sodium acetate stock buffer solution. The droplet solutions were made from the above three stock solutions.

3.2.3 Image data analysis

Figure 3.7 shows droplet image data obtained in one set of experiments. At the beginning of the experiment, the droplet was formed by squeezing the fluid out of the capillary. As soon as the droplet was formed, water in the droplet started to transport to the reservoir because of the difference of NaCl concentrations in the droplet and the reservoir, and the droplet became smaller and smaller with respect to time. This trend is clearly shown by the images at t_1 and t_2 in Fgiure 3.7. When the system reached equilibrium, no more water was transported from the droplet to the reservoir, so that the droplet size stoped decreasing. Experiments were stoped at this time, as shown in the last image of Figure 3.7.

Because the initial concentrations of the droplets and the reservoirs are known, the final volume of the droplets may be estimated, and the leakage information may be infered from the calculated and measured final volumes of the droplets. For example, the initial NaCl concentrations of the droplets and the reservoirs are 1% and 4%, respectively. The final NaCl concentration

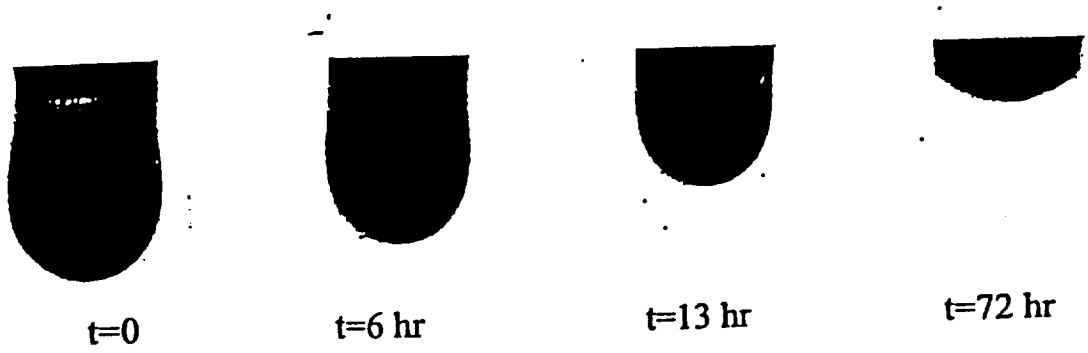

Figure 3.7: Droplet images captured by the CCD camera and stored in the computer during the course of experiments.

in the droplet cannot exceed 4% when the the system reaches equilibrium. As a result, the final volume of the droplet should never be less than 1/4 of its initial one. If it is, the system leaks.

A software package (using C language, listed in Appendix B) was developed to calculate the droplet volumes and surface areas of the images obtained in the experiments. The images were calibrated using the known outer diameter of the glass capillary (2.8 mm) before calculation of their volumes and surface areas. The volume and the surface area of a droplet were obtained by adding up the volumes and surface areas of small frustums of right cones. For a right cone with base radius of r_1, top radius of r_2, and altitude h, its volume and surface area are given by

$$V = \pi h(r_1^2 + r_1 r_2 + r_2^2)/3 \ , \tag{3.1}$$

and

$$A = \pi(r_1 + r_2)\sqrt{h^2 + (r_1 - r_2)^2} \ . \tag{3.2}$$

3.3 Results and diseussions

Four sets of experiments were performed to understand the effects of drop-reservoir distance and protein on the water transfer process in the hanging drop crystallization method. These four experiments are different in the drop-reservoir distance and the inclusion of lysozyme in the droplets as listed in Table 3.1, and the detailed experimental conditions of the experiments are listed in Tables 3.2 to 3.5. Droplet surface areas and volumes in each set of experiments were calculated using equations (3.1) and (3.2) and dimensions from the recorded images, as shown in Figure 3.7. The primary data appear

in Appendix C for reference. Figures 3.8 and 3.9 show the volumes and the surface areas of the drops in the four sets of experiments.

Table 3.1: Differences bewteen the four experiments in experimental conditions.

	Drop init vol $V_{di}(\mu L)$	Reserv vol $V_R(mL)$	Drop-reserv dist $b(cm)$	Lysozyme
1	20.23	0.5	3	3%
2	19.16	2.0	1.5	3%
3	21.63	2.5	1.0	3%
4	19.95	2.5	1.0	0

The droplets shrank as soon as the experiments started, indicating that water evaporated out of the droplets. In the first 40 hours of experiments, both the volumes and the surface areas were reduced almost linearly, and the volume reduction rates slowed down after 50 to 70 hours. The systems reached equilibrium after 80 hours, and the drop volumes did not change much after that.

The initial NaCl concentrations in the droplets and the reservoirs were 1% and 4%, respectively, in all four sets of experiments. Because the initial volumes of the reservoirs were at least 100 times larger (the smallest is set 2, 100) than their respective droplets, the final NaCl concentrations of the droplets and the reservoirs should be very close to 4%, when the systems reached equilibrium. As a result, the final volume of the droplets should be about 1/4 of their initial volumes. Any ratio less than 1/4 may indicate leakage of the system. Table 3.6 lists the initial and final volumes and their ratios for experiment sets 1 to 4. The ratios for sets 1 and 2 are much less than 1/4, indicating that leakage occured in these sets of experiments.

Polynomials (model-independent) were used to best fit the volumes

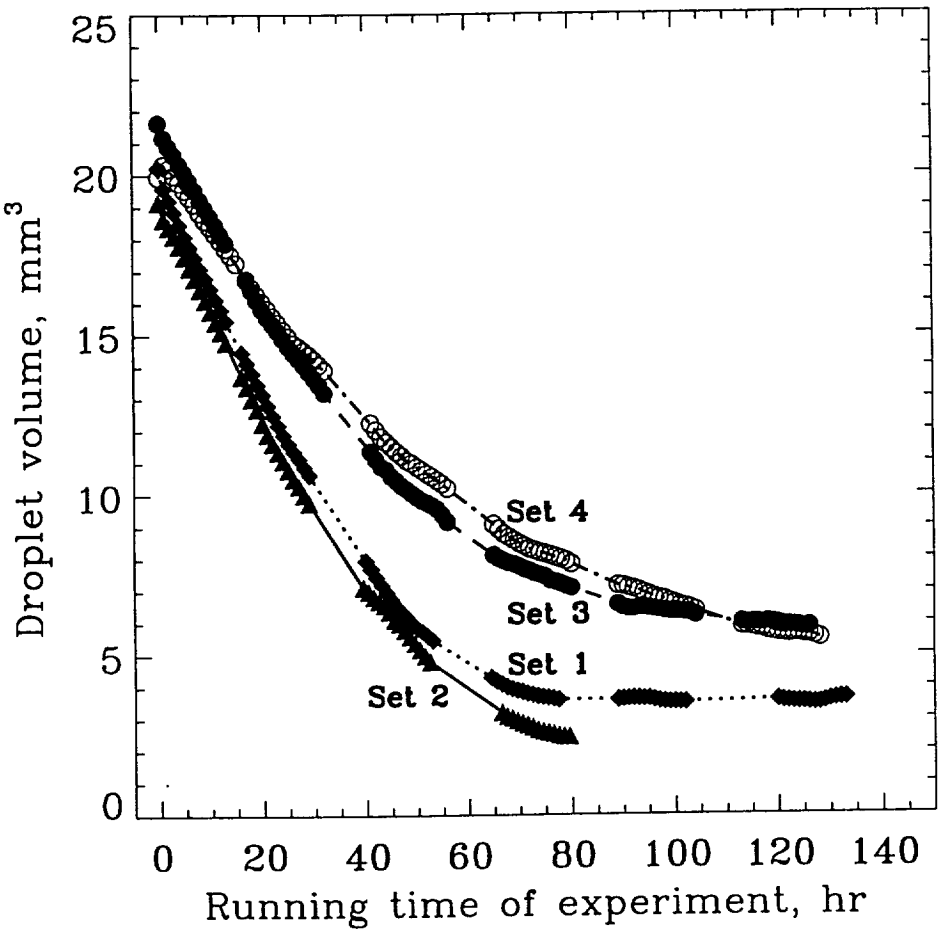

Figure 3.8: Droplet volume profiles in the four sets of experiments. Drop to reservoir distances (b) are 3, 1.5, 1, and 1 cm, and lysozyme concentrations are 3%, 3%, 3%, and 0% in experiment sets 1, 2, 3, and 4, respectively.

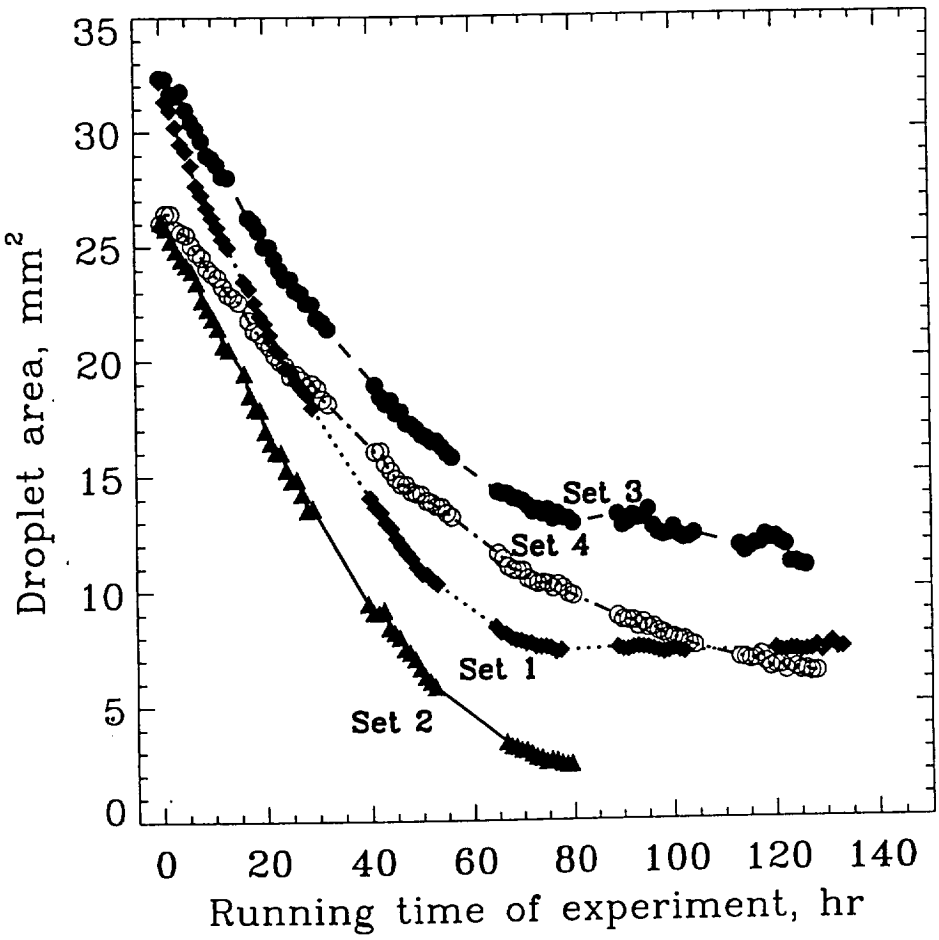

Figure 3.9: Droplet surface area profiles in the four sets of experiments. Drop to reservoir distances (b) are 3, 1.5, 1, and 1 cm, and lysozyme concentrations are 3%, 3%, 3%, and 0% in experiment sets 1, 2, 3, and 4, respectively.

Table 3.2: Experimental conditions for set 1

Variable	Droplet	Reservoir
NaCl	1% (1g/100 ml)	4%
Lysozyme	3%	0
Sodium Acetate	0.1 M	0.1 M
pH	4.0	4.0
Volume	0.02 ml	0.5 ml
drop-reservoir distance	3 cm	

and surface areas of the drops in experiment sets 3 and 4. The measured volumes and surface areas and their best-fit curves are depicted in Figures 3.10 and 3.11, respectively. The mass transfer rate, $N_v = -dv/dt.A$ in mm/hr was obtained from the best-fit curves. Figure 3.12 compares the effects of lysozyme on mass transfer rates. The initial mass transfer rate was higher for the drop with lysozyme than for the drop without lysozyme. When lysozyme was in the drop, the initial mass transfer rate was high for a very short time and was then decreased monotonically with time. However, the mass transfer rate for the drop without lysozyme remained constant for about 60 hours, and then was reduced quickly.

Lysozyme is a surfactant, which likes to stay on surfaces and reduce surface tension. The initial drop with lysozyme was elongated because the reduced surface tension by lysozyme could not keep the drop spherical, whereas the initial drop without lysozyme was more spherical because of its stronger surface tension, as shown schematically in Figure 3.13 at $t = 0$. The elongated drop with lysozyme had a shorter internal mass transfer distance in the droplet for water and a higher surface-to-volume ratio (Figure 3.11). As a result, the initial mass transfer rate in the drop with lysozyme was higher than that in the drop without lysozyme. However, lysozyme may have formed a layer on

Table 3.3: Experimental conditions for set 2

Variable	Droplet	Reservoir
NaCl	1% (1g/100 ml)	4%
Lysozyme	3%	0
Sodium Acetate	0.1 M	0.1 M
pH	4.0	4.0
Volume	0.02 ml	2.0 ml
drop-reservoir distance	1.5 cm	

the droplet surface, thereby reducing the concentration of water on the surface as well as the later water evaporation rate from the surface.

As more and more water was removed from the drop without lysozyme, salt concentration in the drop increased continuously. The depletion of water caused the reduction in mass transfer rate due to reduced driving force. Increased concentration of salt also caused an increment in the density of the drop, and the drop without lysozyme became enlongated after its surface tension was no longer able to hold it spherical, as shown in Figure 3.13 at $t = t1$.

3.4 Conclusions

The following are the conclusions from our experimental study.

- It is possible to detect leaks on the basis of final drop volume.
- There is no evidence for vapor-phase transport being the rate-limiting step (step 4).
- Lysozyme affects drop shape and increases the early mass transfer rate of water.

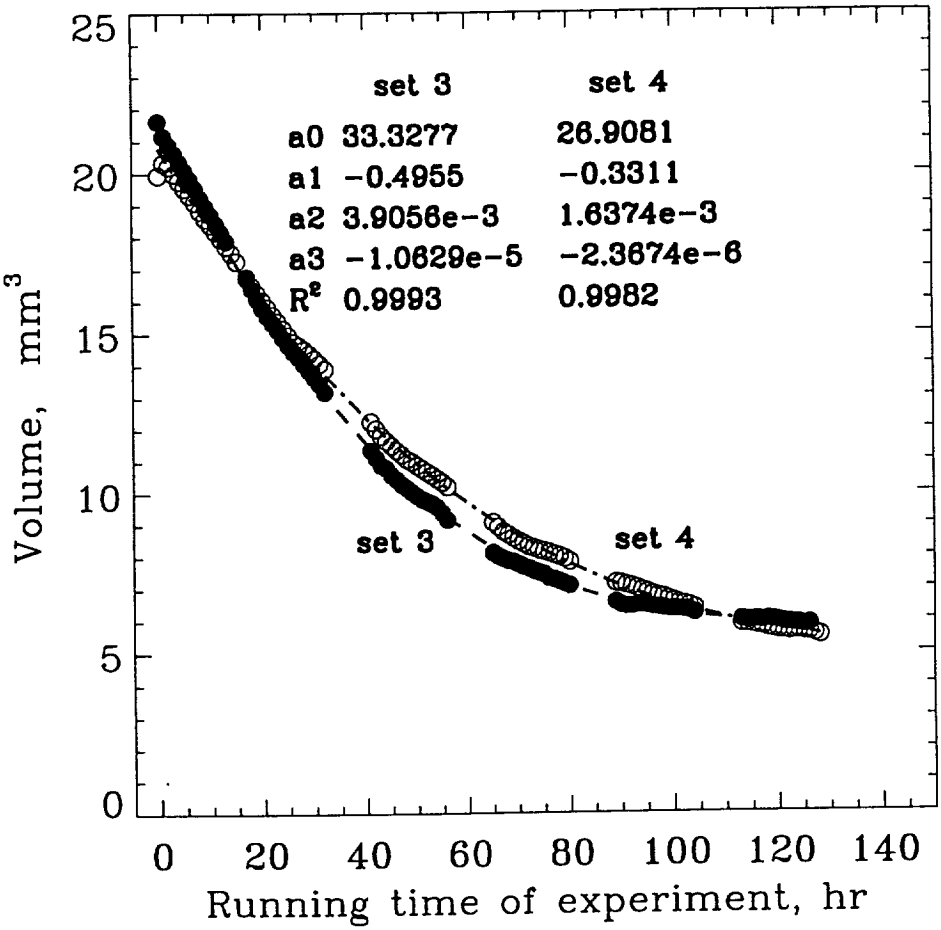

Figure 3.10: Measured and calculated volumes of the drops in experiment sets 3 and 4. Set 3: 3% lysozyme in the droplet; Set 4: no lysozyme.

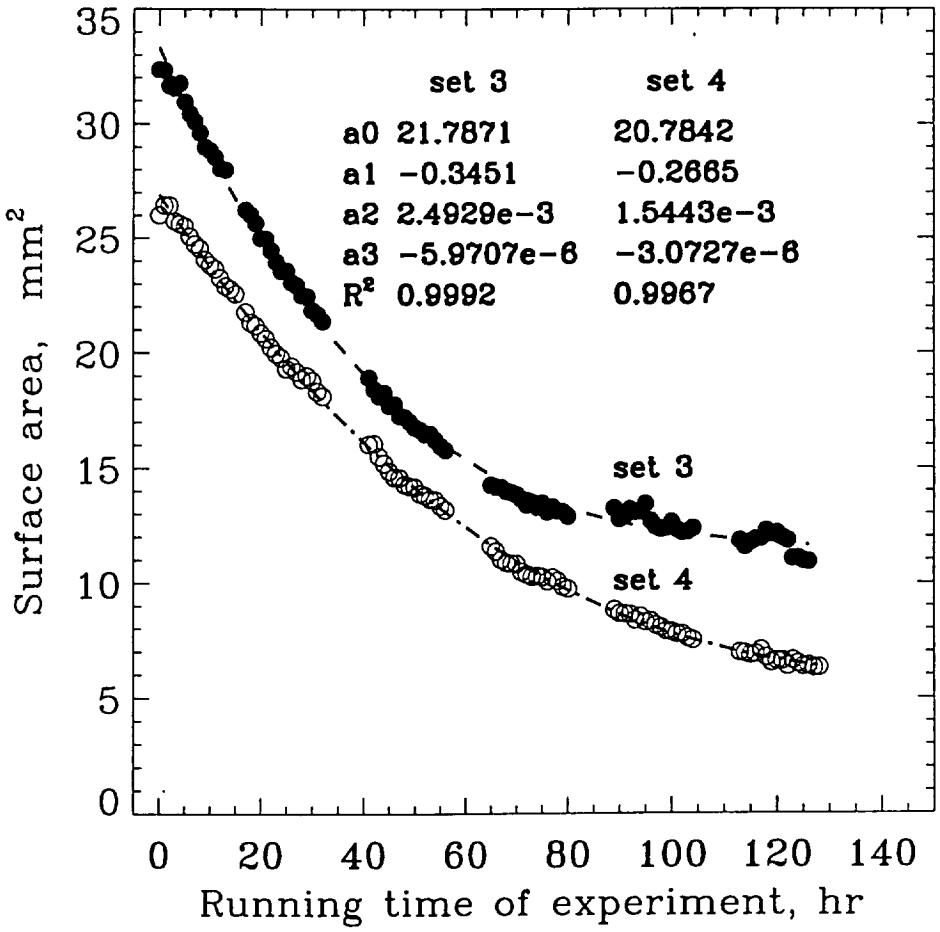

Figure 3.11: Measured and calculated areas of the drops in experiment sets 3 and 4. Set 3: 3% lysozyme in the droplet; Set 4: no lysozyme.

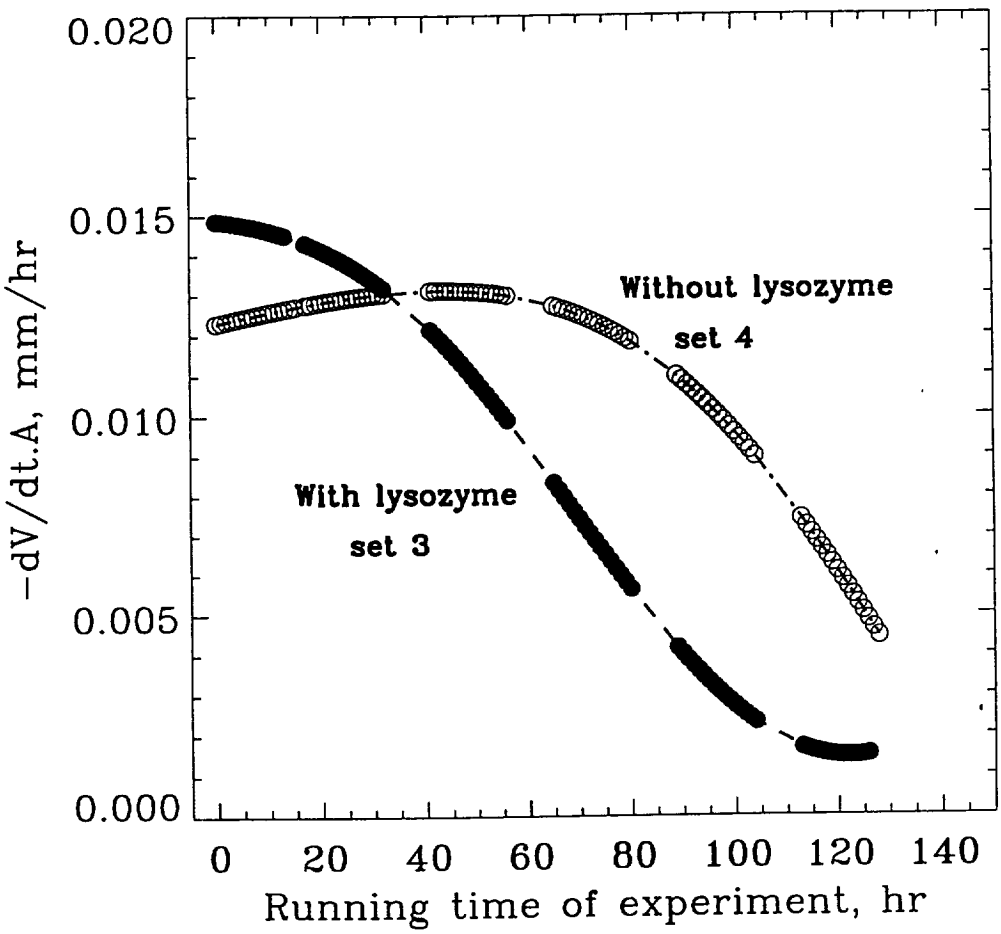

Figure 3.12: Comparison of mass transfer rates during experiments with and without lysozyme in the droplets.

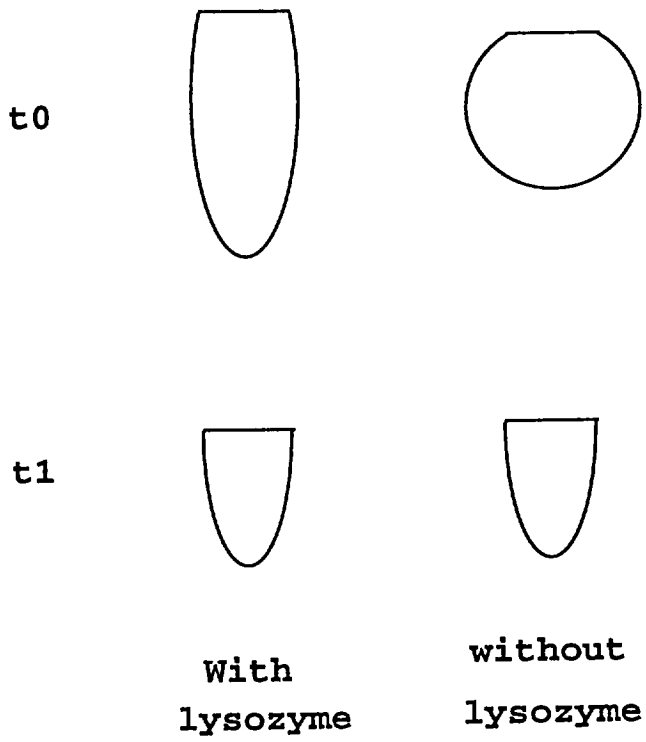

Figure 3.13: Schematic of initial and final shapes of droplets with and without lysozyme

Table 3.4: Experimental conditions for set 3

Variable	Droplet	Reservoir
NaCl	1% (1g/100 ml)	4%
Lysozyme	3%	0
Sodium Acetate	0.1 M	0.1 M
pH	4.0	4.0
Volume	0.02 ml	2.5 ml
drop-reservoir distance	1 cm	

- Lysozyme concentrating in the drop reduces later mass transfer rate of water.
- The last two conclusions clearly implicate events within the drop as being rate-limiting.

Table 3.5: Experimental conditions for set 4

Variable	Droplet	Reservoir
NaCl	1% (1g/100 ml)	4%
Lysozyme	0	0
Sodium Acetate	0.1 M	0.1 M
pH	4.0	4.0
Volume	0.02 ml	2.5 ml
drop-reservoir distance	1 cm	

Table 3.6: Initial and final volumes of the droplets and their ratios.

	Initial (μl)	Final (μl)	Ratio
set 1	20.23	3.63	0.18
set 2	19.16	2.45	0.13
set 3	21.63	5.86	0.27
set 4	19.95	5.49	0.28

REFERENCES

- Alberty, R. A. (1987), *Physical Chemistry* 7th ed, Wiley New York, 826.
- Blundell, T. L., and Johnson, L. N. (1976), *Protein Crystallography*, Academic Press, New York.
- Boistelle, R. and Astier, J. P. (1988), "Crystallization mechanism in solution" *Journal of Crystal Growth* **90**, 14.
- Cech, T. R. (1987), "The chemistry of self-splicing RNA and RNA enzymes", *Science* **236**, 1532.
- Crank, J. (1984), "Free and moving boundary problems", Oxford, Clarendon Press.
- Crank, J. (1975), "The mathematics of diffusion", Oxford, Clarendon Press.
- Feher, G. and Kam, Z. (1985), "Nucleation and growth of protein crystals: General principles and assays", *Methods in Enzymology* **114**, 77.

- Feigelson, R. S. (1988), "The relevance of small molecule crystal growth theories and techniques to the growth of biological macromolecules", *Journal of Crystal Growth* **90**, 1.

- Fowlis, W. W., DeLucas, L. J., Twigg, P. J., Howard, S. B., Meehan, E. J., and Baird, J. K. (1988), "Experimental and theoretical analysis of the rate of solvent equilibration in the hanging drop method of protein crystal growth", *Journal of Crystal Growth* **90**, 117.

- Gold, L., Poliski, B., and Yarus, M. (1995), "Diversity of oligonucleotide functions", *Annual Review of Biochemistry* **64**, 763.

- Guggeheim, E. A. and Stokes, R. H. (1969), *Equilibrium Properties of Aqueous Electrolyte Solutions*, Pergamon, Oxford, 14.

- Kam, Z., Shore, H. B., and Feher, G. (1978), "On the crystallization of proteins", *J. Molecular Biology* **123**, 539.

- Luft, J. R., Albright, D. T., Baird, J. K., and Detitta, G. T. (1996), "The rate of water equilibration in vapor-diffusion crystallization: Dependence on the distance from the droplet to the reservoir", *Acta. Cryst.* D**52**, 1098.

- McPherson, A. (1982), *Preparation and Analysis of Protein Crystals*, Wiley, New York.

- Mikol, V., Rodeau, J. L., and Giegé, R. (1990), "Experimental determination of water equilibration rates in the hanging drop method of protein crystallization" *Analyt. Biochem.* **186**, 332.

- Plaas-Link, A. and Cornier, J. (1988), "Concepts for Crystallization of Organic Materials under Microgravity", *Appl. Microgravity Tech.* **3**, 123.

- Pusey, M. and Naumann, R. (1986), "Growth kinetics of tetragonal lysozyme crystals", *Journal of Crystal Growth* **76**, 593.

- Sibille, L and Baird, J. K. (1991), "Analysis of solvent evaporation rates in the vapor diffusion protein crystal growth experiments from the STS-61C space shuttle mission", *Journal of Crystal Growth* **110**, 72.

- Todd, P., Sikdar, S. K., Walker, C., and Korszun, Z. R. (1991), "Application of osmotic dewatering to the controlled crystallization of biological macromolecules and organic compounds", *Journal of Crystal Growth* **110**, 238.

- Todd, P., Sportiello, M. G., Gregory, D., Cassanto, J. M., Alvarado, U., and Ostroff, R. (1993), "Transport phenomena in the crystallization of lysozyme by osmotic dewatering and liquid-liquid diffusion in low gravity", *31st Aerospace Sciences Meeting & Exhibit*, January 11–14, Reno, NV.

- Wakayama, N. I., Ataka, M., and Abe, H. (1997), "Effect of a magnetic field gradient on the crystallization of hen lysozyme", *Journal of Crystal Growth* **178**, 653.

- Wakayama, N. I. (1998), "Quantitative study of crystallization kinetics of hen egg-white lysozyme using magnetic orientation", *Journal of Crystal Growth* **191**, 199.

Chapter 19

Transport phenomena and hardware issues in the hanging drop crystallization method

Melissa Sampson
With Paul Scovazzo and Paul Todd

CHAPTER 19
TRANSPORT PHENOMENA AND HARDWARE ISSUES IN THE HANGING DROP CRYSTALLIZATION METHOD

Melissa Sampson
With Paul Scovazzo and Paul Todd

The purpose of this project was to continue the work done by Wang (1999, Chapter 18) and to create a full data set for determination of the rate limiting step in the hanging drop crystallization method. Due to hardware issues, the collection of data was significantly inhibited. The hardware issues and conclusions are discussed in detail here. Examination of the transport theory behind this crystallization method was also completed. Approximate numbers were placed into equations to determine if the hypothesized theory matched observation. The rate limiting step may be internal transport of water in the drop or vapor-phase diffusion from the drop to the reservoir, depending on the drop-to-reservoir distance.

INTRODUCTION

Proteins and other macromolecules are important because of their medicinal properties. Since many of these molecules are only available in limited quantities naturally, there are strong reasons for synthetic production of the molecules. In order to synthetically create a protein, its three dimensional structure must be known. The three dimensional molecular structure of a protein largely determines its biological activity. Structural determination is usually done through X-ray diffraction.

Crystal growth is dependent on supersaturation of a target molecule solution. Once the solution is supersaturated, controlled removal of the solvent induces nucleation and then crystallization. The quality of the crystals is directly related to the solvent removal rate. Study emphasis has been placed on the optimization of the solvent removal process.

The hanging drop crystallization method has proven especially effective in space flight and is the method discussed in this paper. Spaceflight has been found to increase the crystal quality since there is no crystal sedimentation and solutal convection in zero gravity. In hanging drop crystallization, a solution containing protein, buffer and a precipitating agent is suspended from a capillary above a reservoir containing a solution of buffer and the precipitating agent at a concentration higher than the drop's concentration. The concentration gradient causes water to evaporate from the drop and condense into the reservoir. The buffer continues to evaporate until equilibrium is reached between the concentration of the precipitating agent in the drop and reservoir.

This method has been proven in the lab, but the transport phenomena involved are poorly understood. In particular, the rate limiting step has not been identified. The rate limiting step is the slowest step in a process and therefore determines the overall rate of the process. The work presented here builds on the previous theoretical and experimental work done by Fowlis et al. (1988), Wang (1999), Luft (1996) and Mikol (1990). The experiments were performed to determine the rate-limiting step and resolve hardware issues with this method.

MATERIALS AND METHODS

The typical hanging drop set-up consists of a 1 cm x 1 cm x 4 cm cuvette and a coverslip on which to suspend the drop on. Since the chosen method of experimental observation is time lapse photography, some modifications were needed to this initial set-up.

First, the drop can not be photographed from the side when it is on a coverslip. This is because the drop is small and is too close to the top of the cuvette to provide accurate pictures. A capillary tube with a rubber plunger was designed to overcome this problem, as done by Wang (1999). The tube has a diameter of 0.25 cm, and the silicone rubber-tipped plunger fits inside the capillary. The capillary is inserted past the top of the cuvette and this allows for clear pictures of the drop to be taken. The precautions necessary in setting up the capillary, plunger and coverslip will be discussed in the Results section.

A Canon VC1 8mm video camera, Panasonic AG-1830 ProLine, digital, VCR and Sony Trinitron TV were connected to record images of the drop. The cuvette was placed in a vise, which was then mounted onto a variable camera mount for the needed height. The video camera was mounted with a double-ended screw into an adjustable camera table. The VCR was then programmed to record for a few minutes every three hours. Figure 1 illustrates the design of the experiment.

The buffer solution used was 0.1 M sodium acetate. This was made from a 3 M sodium acetate stock solution and filtered, deionized water. After the 0.1 M solution was created, it was buffered to 4.0 pH with 3 M HCl. A 25% stock solution of NaCl was created from the 0.1 M buffer solution and solid NaCl. These solutions were filtered individually using a 0.2 μm Nylon filter and syringe. The protein used for crystallization was hen-egg lysozyme. A 6% solution of lysozyme was mixed fresh for each experiment using the 0.1 M stock buffer solution and solid lysozyme from Sigma, L-2879 (St. Louis, MO). It is necessary to mix a fresh solution of lysozyme each time since the protein starts to denature as soon as it is mixed with buffer solution.

The drop volume was 20 μL for all runs discussed here. Its concentrations are as follows: 1.5% NaCl, 3% lysozyme and 0.1 M sodium acetate buffer. The reservoir volume was 2 mL and the concentrations were 4.5% NaCl in 0.1 M sodium acetate buffer, pH 4.0.

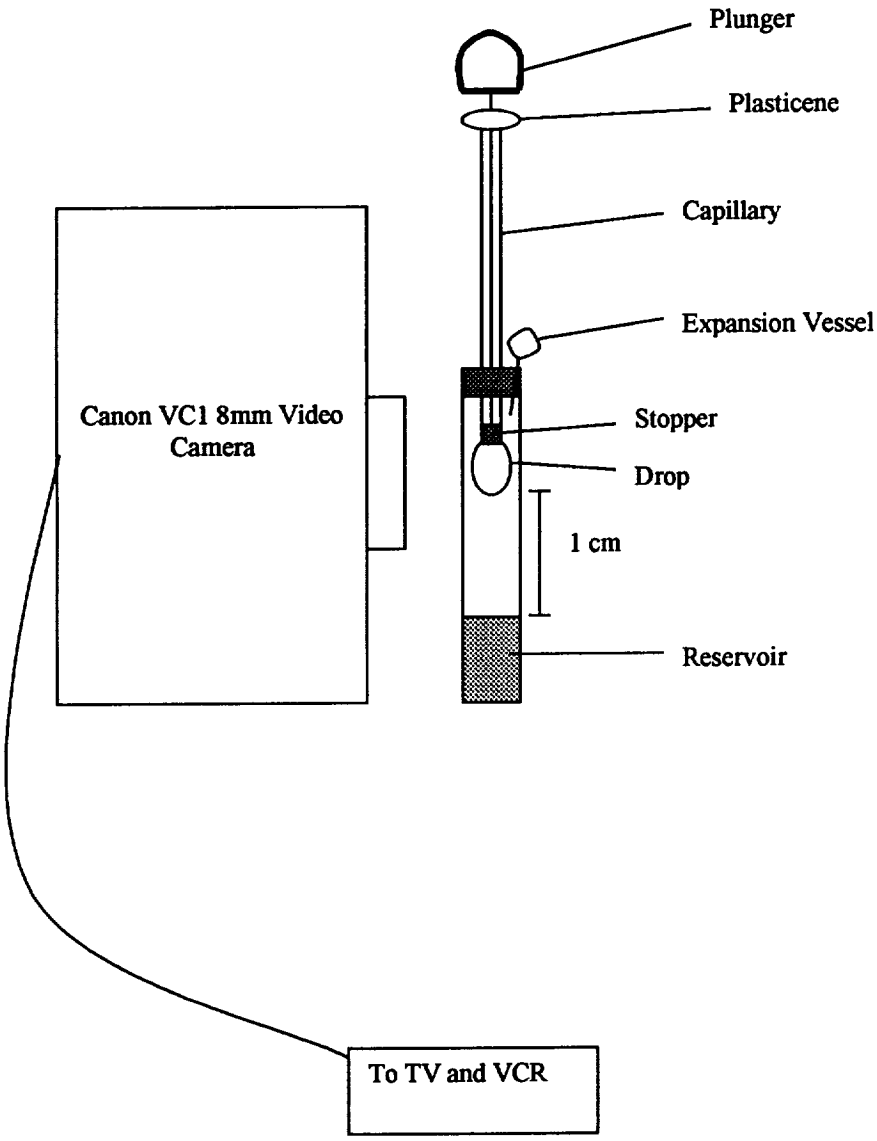

Figure 1. Arrangement for positioning and observing the hanging drop by video image recording. All components are seated on an optical table.

The distance between the drop and reservoir was held constant at 1 cm between the bottom of the drop and reservoir.

After all solutions were made, the experiment was initiated. The reservoir solution was placed in the cuvette through use of an auto-pipette to prevent any liquid contact on the cuvette walls. Drops on the walls would act as sinks for the vapor transport and give inaccurate results. The drop was placed into the capillary with an auto-pipette also for accurate volume measurement. After the cuvette and capillary/plunger were in place in front of the camera, the drop was extruded from the capillary and the experiment started.

In order to minimize internal convection in the drop, all experiments were performed on a vibration-free optical isolation table. This is done to prevent vibrationally driven mixing of the drop solution, a phenomenon that may not have been absent in previous work (Fowlis et al., 1988; Luft et al., 1996; Mikol et al., 1990). Also, vacuum grease is the sealant of choice for sealing the capillary to the stopper and the stopper to the cuvette.

RESULTS

While operating the set-up of this experiment and seeking to control artefactitious processes, several precautions were found necessary. Emphasis was placed on eliminating artifacts, and no water-loss or crystal-growth data were obtained during this study. The remainder of this section will cover the hardware issues. Subsequently the results of a transport modeling study are presented.

It was necessary to simplifiy the time-lapse photography method from that used by Wang, which was a CCD camera and an Apple Macintosh computer used to analyze the changing drop volume. An 8mm video camera, VCR and TV were used for this purpose. By placing the cuvette and capillary/plunger directly in front of the camera lens, macro, focused pictures could be taken. The VCR recorded for five minutes every three hours.

The coverslip seals to the cuvette well with vacuum grease, creating the necessary concentration gradient. This was demonstrated through dry runs. If a seal is not created and maintained throughout the experiment, the water in the drop just evaporates into the atmosphere, and equilibrium at the predicted final drop volume is not reached. Wang (1999) noted this criterion as means of selecting valid experimental data. Thus, the seal becomes the critical point of the experiment.

As mentioned in the Materials and Methods section, a simple coverslip and cuvette configuration could no longer be used due to the camera angle. Wang (1999, Chapter 18) drilled holes in coverslips to allow the capillary/plunger set-up into the cuvette. It was found, however, that the coverslip was difficult to seal, and large amounts

of vacuum grease were necessary. It was observed that drilling the hole in the coverslip and insertion of the plunger created stresses that caused the coverslip to not lie flat. While large amounts of vacuum grease usually solved this problem, the grease also blocked the view of the camera. It was decided that if the coverslip was weighted down, then it would not curl. Thus a stack of 18 washers was placed on top of the coverslip. This did allow a good seal to be created between the coverslip and the cuvette with reasonable amounts of vacuum grease.

It was found that sometimes there was an air space between the tip of the plunger and the drop. It was discovered that this air space causes the drop to be sucked back into the plunger in less than one minute after it is extruded. Once care was taken to eliminate the air space, the drop remained at the tip of the capillary. All further runs were set-up with no space between the drop and the tip of the plunger.

When the cuvette was illuminated from the side with a diffusive light it was determined that the light created too much heat, which could cause pressure changes in the closed volume of the cuvette; therefore, use of an illuminator was stopped, and care was taken to use uniform ambient room light around the clock.

After several runs with the coverslip weighted with washers, it was discovered that there was still leakage between the coverslip and cuvette top. It appears that the seal would initially hold, but as the experiment progressed, the seal was broken. This was evident through almost complete evaporation of the drop in less than 24 hours. If there was no leakage, the drop would only shrink to 1/3 of its size over approximately 120 hours as expected from the experiment design. The drop would be 1/3 of its original size since the ratio in NaCl concentrations between the drop and reservoir is 1:3.

To reduce the leakage around the coverslip a silicone rubber stopper was machined to replace the coverslip. The stopper, of approximately 1cm depth, was cut from a large rubber sheet to fit in the top of the cuvette. A small hole was then punched through the center of the stopper for the capillary. The stopper hole was smaller than the outer diameter of the capillary, so the seal between the capillary and the stopper was reliable. There was no leakage from between the stopper and cuvette.

The stopper was coated with vacuum grease before being placed into the cuvette. However, now when using the stopper, a thin syringe needle must be pierced through the stopper to allow for pressure equalization when the stopper is being instered into the top of the cuvette. If this is not done, the drop is immediately forced up the capillary. The plunger, above the tip, was also coated with vacuum grease to prevent leakage between the capillary and the plunger. In all future runs, the plunger was coated with vacuum grease unless otherwise stated. After 24 hours, the run appeared to be working. However, after 48 hours the drop had entirely disappeared. After examination of the capillary and plunger, it was observed that the drop had been sucked up the capillary and above the plunger tip. It is hypothesized this is due to temperature changes in the lab that cause pressure gradients. It seems that the stopper sealed the cuvette so well, that the only way the system had to equalize pressure was through the capillary.

We devised an expansion vessel to attempt to alleviate this problem. Part of a latex glove was cut out in the shape of a rectangle. This was placed over the open end of a syringe needle (the end that usually attaches to a syringe) and was kept in place with an O-ring. The underside of the glove/O-ring was also sealed with vacuum grease. This needle of the expansion vessel was pierced through the stopper and into the cuvette and left in place throughout the run.

For comparison, another method was tested to prevent the drop from being sucked back into the plunger. The capillary was filled with mineral oil in order to counterbalance the internal pressure. A single experiment then utilized the stopper, expansion vessel, capillary/plunger and mineral oil. After 24 hours, the drop appeared to be the same size as it was initially. Observations after 48 hours, during a two hours time period, showed significant shrinkage of the drop. After 72 hours, there was a distinct layer and interface in the reservoir. The experiment was stopped after 72 hours.

It was determined that the mineral oil leaked from the capillary, past the plunger and augmented the volume of the drop. The layer observed in the reservoir was oil and this was confirmed by disturbing the layer and observing the resulting separation between the buffer and the oil. It was also determined by review of the time lapse photo data that the oil was transferred between the drop and the reservoir by gravity and in bulk. The drop would grow until the weight overcame the surface tension and the drop would then fall into the reservoir. This explains the large changes in shape over the 2 hour observed period.

Instead of mineral oil Plasticene was used to seal the top of the capillary. The stopper and expansion vessel were still used. After 24 hours, the drop had again been sucked up the capillary, so the run was stopped.

A final test utilized the stopper, expansion vessel and Plasticene. The plunger was not coated with vacuum grease. The drop equilibrated to a consistent size over the last 48 hours of the experiment. This would seem to indicate that the vacuum grease on the plunger may be detrimental to the experiment. These data may be used to guide future experiments in hanging-drop equilibration kinetics.

DISCUSSION OF EXPERIMENTAL RESULTS

The greatest problem to overcome in this type of experiment is leakage. Leakage between the capillary and the coverslip and between the capillary and plunger caused considerable problems. Using a stopper to eliminate the coverslip did prevent leakage, but also created such a solid seal that the system was too volume-limited to equalize pressure. This created other problems, such as the drop being forced around the plunger and up the capillary.

While a successful solution has not yet assuredly been discovered to prevent the drop going up the capillary, it is hypothesized that a proper expansion vessel and precise plunger could resolve these issues..

The video camera, VCR and TV arrangement was highly successful and, of course, very inexpensive. The pictures are clear and the VCR can be set to record for any period desired. Since a computer is not being used, it does require manual measurement of the drop or digitization of the image using a frame grabber. These measurements could then be extrapolated to determine the volume of the drop over time. The run is considered successful if the drop shrinks to 1/3 of its original size (the equilibrium volume in the current design) and remains at this size for a period of time. The tests discussed above were not successful transport experiments *per se* because of leakage and pressure issues.

TRANSPORT MODELING

The basis of the above experiment design is the work done by Fowlis et al. to determine the rate limiting step (1988). Fowlis et al. hypothesized that the rate of evaporation was affected by the temperature, the vapor pressure of water, the ionization constant of the salt, the volume of the droplet, the contact angles between the drop and the coverslip, the number of moles of salt in the droplet, the number of moles of water and salt in the well, the molar volumes of water and salt, the distance from the drop to the reservoir and the coefficient of diffusion of water vapor through air (1988). Work done by Scovazzo and Todd extended this theory and came up with 4 possible rate-limiting steps (1999).

The water vapor transport is broken into 6 distinct steps. The first step is the movement of water from the center of the drop to the polymer film on the surface of the drop. The second step is the diffusion of the water across the polymer film to the surface of the drop. The third step is evaporation of water from the surface into the air gap between the drop and reservoir. The fourth step is transport of the water across the gap. The fifth steps is condensation of the water on the reservoir surface. The sixth step is movement of the water from the surface of the reservoir to the center of the reservoir. It has been assumed previously that steps 3 and 5 are instantaneous and therefore not rate-limiting, so analysis was done on steps 1, 2, 4, and 6 (Todd, 1999).

The derivation of the rate limiting step equations done by Dr. Scovazzo follows. The derivation is an extension of the work done by Fowlis et al. and Wang (1988; 1999). The first step is to set all mole currents equal.

$$I = \frac{\rho D_{AB} h}{MW_{H2O}(1 - h/a)} * \ln\frac{(1-w_{Aa})}{(1-w_{Ah})} \quad \text{Drop}$$

$$= \frac{\rho D_{AB} a}{MW_{H2O}(\Delta)} * \ln\frac{(1-w_{a,\Delta})}{(1-w_{A,a})]} \quad \text{Film}$$

$$= \frac{c\, D_{AB}\, a}{(1 - a/b)} * \ln \frac{(1-X_{A,b})}{(1-X_{A,a})} \quad \text{Air Gap}$$

$$= \frac{\rho\, D_{AB}\, b}{MW_{H2O}\,(1 - b/b+\delta)} * \ln \frac{(1-w_{a,\delta})}{(1-w_{A,b})} \quad \text{Reservoir}$$

I is molar current of water in the various locations of the experiment. A = water and B = other binary species and varies by step. In the drop, B = NaCl, in the film, B = polymer, in the air gap, B = air and in the reservoir, B = NaCl. ρ is the density, D_{AB} is the diffusivity, MW_{H2O} is the molecular weight of water, w_m is the mass fraction of m (mass of m/total mass), Δ is the thickness of the protein or polymer film in the drop, X_m is the mole fraction of m, δ is the thickness of the transport zone in the reservoir, b is the distance between the bottom of the drop and reservoir, a is the distance from the center of the drop to the edge (radius when the drop is approximated as sphere) and h is $a/2$. The definitions of h and a differ slightly from the definitions of Fowlis' et al. This is due to the shape of the drops. In the method of Fowlis et al., the drop shape approximates a hemisphere, whereas in this set of experiments, the drop is approximated as a sphere.

The driving force is the change in the mass fraction, Δw. From this, the total mass transfer coefficient for each step can be found.

$$[RS]_m = I / (\Delta w)_m = \text{liquid} = \rho\, D_{AB}\, r_1 / MW_{H2O}\,(1 - r_1/2)\,(w_B)_{ln}$$
$$\text{gas} = K\,(c\, D_{AB} / (1-a/b) * a * \ln X_B / X_A) / (X_B - X_A)$$

K is the relationship between X, mole fraction, and w, mass fraction; $X = Kw$. The gas equation can be approximated as: $\sim c\, D_{AB}\, a / (1 - a/b)\, X_{B,avg}$ since $X_A << X_B$ in a water vapor system. $X_{B,avg}$ is the average mole fraction of species B.

So finally the total mass transfer coefficients for each proposed rate limiting step are:

Step 1 – drop:

$$[RS\ 1] = [\rho\, D_{H2O,l}]\, h / MW_{H2O}\,(1 - h/a)\,(w_{NaCl})_{ln}$$

Step 2 – film:

$$[RS\ 2] = [\rho\, D_{H2O,polymer}]\, a^2 / MW_{H2O}\,(\Delta)\,(w_{polymer})_{ln}$$

Step 4 – air gap:

$$[RS\ 4] = [c_{gap}\, D_{H2O,v}]\, a\, K / (1 - a/b)\, X_{air,avg}$$

Step 6 – reservoir:

$$[RS\ 6] = [\rho\, D_{H2O,l}]\, b / (MW_{H2O}\,(1 - (b-\delta)/b)\,(w_{NaCl})_{ln}$$

Here, $K = p_{H2O,\,v} / p_{total}$. δ was calculated by dividing the volume transported by the surface area of the reservoir.

Now that the equations are derived, a sensitivity analysis can be done. For steps 1 and 2, there is no sensitivity. For step 4, if a/b <<1, then

$$[RS\ 4] = [c_{gap}\ D_{H2O,\,v}]\ a\ K / X_{air,\,avg}$$

The equation is now independent of b. For step 6, if δ << b, then the equation becomes

$$[RS\ 6] = [\rho_{res}\ D_{NaCl}]\ b^2 / [\delta\ MW_{H2O}\ (w_{NaCl})_{ln}]$$

The next step is to put in numbers and see if the units and magnitude for each step are reasonable.

$$[RS\ 1] = \frac{(1.106\ g/cm^3)(1.483 \times 10^{-5}\ cm^2/s)(.07\ cm)}{18.0\ g/mol\ [1-.(07\ cm/.14\ cm)](.015)}$$

$$= 8.5 \times 10^{-6}\ mol/s$$

The calculation of $(w_{NaCl})_{ln}$ assumes that all of the solute is evenly distributed within the drop. It assumes that there is no concentration gradient within the drop itself. This step also approximated the drop as a sphere, so for further calculations this step would need to be carefully examined.

$$[RS\ 2] = \frac{(.752\ g/cm^3)(1.731 \times 10^{-5}\ cm^2/s)(.14\ cm)^2}{\{(18.0\ g/mol)(.005\ cm)(1)}$$

$$= 7.0 \times 10^{-6}\ mol/s$$

This equation was derived using rectangular coordinates. These coordinates are assumed to be valid because $\Delta/a << 1$.

$$[RS\ 4] = \frac{(4.09 \times 10^{-5}\ mol/cm^3)(.239\ cm^2/s)\ (.14cm)(.0304)}{(1-.14cm/1cm)\ .96}$$

$$= 5.0 \times 10^{-8}\ mol/s$$

$$[RS\ 6] = \frac{(1.018\ g/cm^3)(1.484 \times 10^{-5}\ cm^2/s)(1cm)}{(18.0\ g/mol)[1-(1\ cm - .011\ cm)/1\ cm](.045)}$$

$$= 1.7 \times 10^{-3}\ mol/s$$

It can be seen from these order-of-magnitude calculations that step 4 is the smallest and therefore is the likely rate limiting step. This agrees with the proposed theory and hypothesis. An issue relative to this finding has arisen in the literature, and that is whether *[RS4]* is independent of *b* , the distance between the drop and the surface of the reservoir. Using the relationship initially derived for Step 4, above, where *[RS4]* depends on *1/(1-a/b)*, a plot as shown in Figure 2 is obtained. This result shows the vapor transport rate independent of *b* except when b is less than about 3 mm.

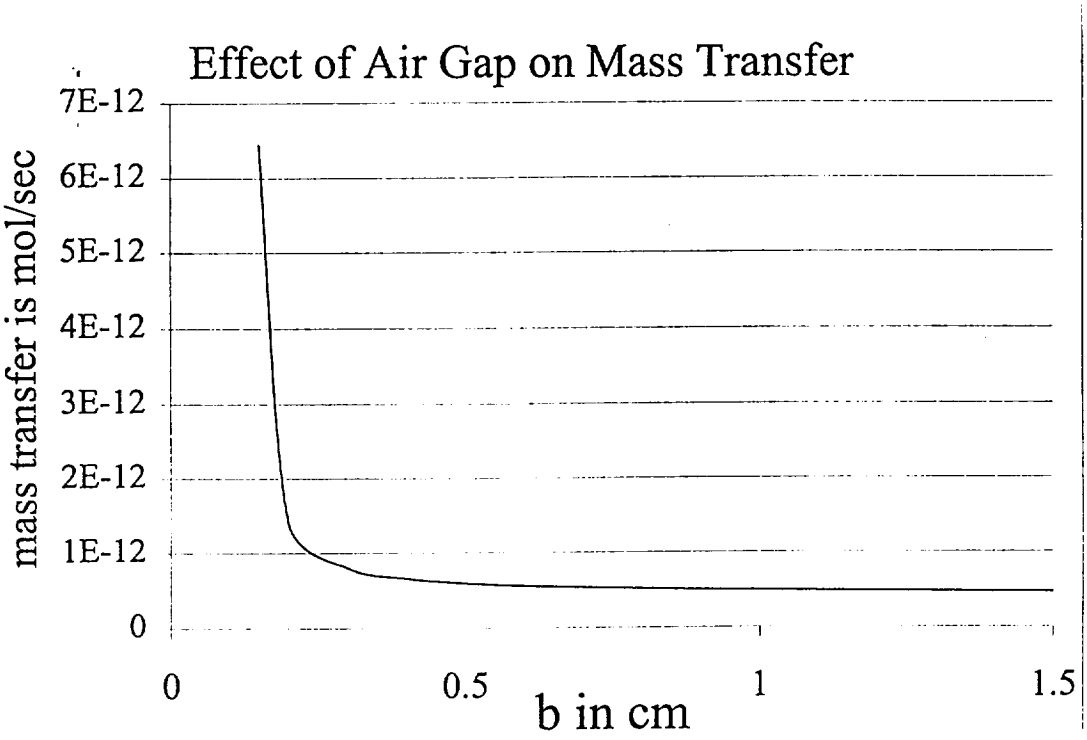

Figure 2. Plot of vapor-phase transport rate vs. distance between drop and reservoir surfaces using above relationship of [RS 4].

CONCLUSIONS

The hanging drop method of crystallization is reliable and to date, the preferred method for crystallization. Crystals grown in space are often of better quality than those grown on the Earth and proteins that are difficult to crystallize can often be crystallized in space. A crystal of a protein is necessary to determine its three dimensional structure. Once its structure is determined, the protein can then be produced synthetically. This is important because the structure determines its biological properties. So for proteins that are of medicinal value, the structure must be known.

The work presented here is an extension of Wang's work done in 1999. The goal was to complete more hanging drop experiments in order to complete the data set and

either confirm or refute the hypothesis of Fowlis et al. However, the hardware issues encountered were insurmountable in the time allotted. Much progress on the set-up and data collection methods was made, but not in time to collect viable data for analysis in this paper. The biggest problem was leakage from the cuvette and capillary. This was overcome by using a stopper in the top of the cuvette, but this then caused pressure equalization issues. The changes in pressure forced the drop around the plunger and up the capillary. A suitable solution to this problems is still being researched at the time of writing.

By completing order-of-magnitude calculations, it does appear that the theory is correct. Step 4, transport of the water vapor across the gap, is the slowest step. This is consistent with theoretical and observed data.

The work done here has found that new methods of observing and setting up the hanging drop experiment may be necessary to overcome the technical issues. The method itself is sound and effective. The problem is creating a hanging drop that can be observed by a video camera while retaining a closed system. Further study will need to be done to perfect the hardware. Initial calculations indicate that the hypothesis this work is based on is correct; that either the transport of water across the film or transport of water across the gap is the rate limiting step. Significant progress was demonstrated in terms of hardware and as further work is done, the rate limiting step can be positively identified.

REFERENCES

- Fowlis, W.W., DeLucas, L. J., Twigg, P. J., Howard, S. B., Meehan, E. J. and Baird, J. K. (1988), "Experimental and Theoretical Analysis of the rate of Solvent Equilibration in the Hanging Drop Method of Protein Crystal Growth," *Journal of Crystal Growth,* **Vol. 90,** p. 117.

- Luft, J. R., Albright, D. T., Baird, J. K., and Detitta, G. T. (1996), " The rate of water equilibrium in vapor-diffusion crystallization: Dependence on the distance from the droplet to the reservoir," *Acta. Cryst.* **D52**, p. 1098.

- Mikol, V., Rodeau, J. L., and Giege', R. (1990), "Experimental determination of water equilibrium rates in the hanging drop method of protein crystallization," *Analyt. Biochem.*, **Vol. 186**, p. 332.

- Scovazzo, P. (1999), "Derivation of rate-limiting steps," Personal Communication.

- Todd, P. (1999), "The Six Steps of Water Vapor Transport in the Hanging Drop Crystallization Method," Personal Communication.

- Wang, Y. (1999), "Transport Phenomena in the Hanging Drop Crystallization Method," *M.S. Thesis*, University of Colorado.

Chapter 20

Reverse Osmosis Membrane Characterization

C.-Y. Lee, Paul Todd and John Lock

CHAPTER 20

Reverse Osmosis Membrane Characterization

By C.-Y. Lee, John Lock and Paul Todd

Introduction

Among those osmotic dewatering crystallization experiments performed in the past, irregular dewatering patterns were constantly observed under the same experimental conditions. All the evidence seems to suggest that the consistency of the intrinsic resistance of the reverse osmosis (RO) membrane needs to be investigated.

In this work, characterization of a RO membrane, MS-10 (Osmonics, Inc.), was performed. Two approaches were used. The first one is to measure the trans-membrane flux under a fixed mechanical pressure and the second one is to measure the trans-membrane flux under a fixed osmotic pressure. Preliminary results are summarized and some recommendations are made for both future use of the membrane and further research tasks.

Experimental

Membrane:

The membrane used was MS-10. MS-10 membranes were obtained from two sources. The first source is the direct purchase from Osmonics, Inc. (OI). The second source is from Osmonics' subsidiary, Desalinization (Desal). Those from Desal were samples Desal used for quality control purpose. They were cell tested on tap water for one hour at 100 psi, then soaked in a glycerol solution and air dried before being sent to us. (The glycerol soaking step was for re-use purpose.) All the membranes are soaked in pure water or salt water overnight before use to get rid of glycerol.

Equipment:

Figure 1 shows the schematic of the mechanical pressurizing system (MPS). Pure water is pumped out from the reservoir to circulate the system. The system pressure can be raised by adjusting the pressure-adjusting valve and stabilized by the pressure-stabilizing tank. The amount of water permeate is measured at give time period. Permeation data are collected and stored by a personal computer. Excess water flows past over the RO membrane is recycled back to the reservoir.

Experimental data from this design should reveal two important pieces of information. The first one is the intrinsic resistance of the RO membrane, since pure water is used as the solution and a fixed mechanical pressure is the only driving force. Ultrafiltration membranes are known to show flux decline under mechanical pressure due to compaction of their internal structure. Experimental data will show the flux decline profile of MS-10 under a fixed mechanical pressure.

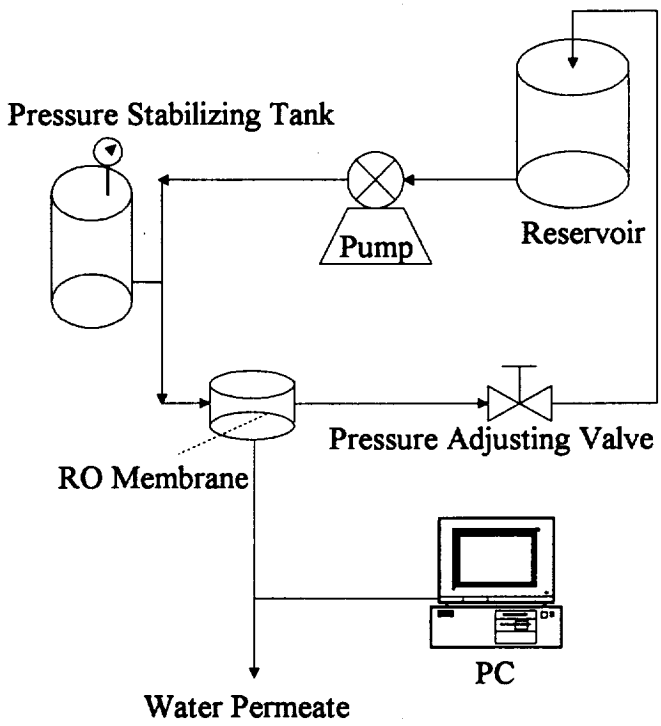

Figure 1. Schematic drawing of the water-pressurizing system.

Figure 2 shows the schematic of an osmotic pressure system (OPS). The stir cell contains a salt (NaCl) solution with a known concentration. A RO membrane is placed at the bottom of the stir cell unit. This membrane separates the salt solution from pure water underneath the RO membrane. Due to the osmotic pressure created by the trans-membrane salt concentration gradient, pure water permeates through the RO membrane into the stir cell. The weight loss of the reservoir unit is measured by a balance and data are collected and stored by a personal computer.

Experimental data from this design can illustrate if the membrane resistance is constant under osmotic pressure, and, from repeated experiments, how uniform the resistance is between different pieces of membranes (i.e. how consistent water removal rate can be expected).

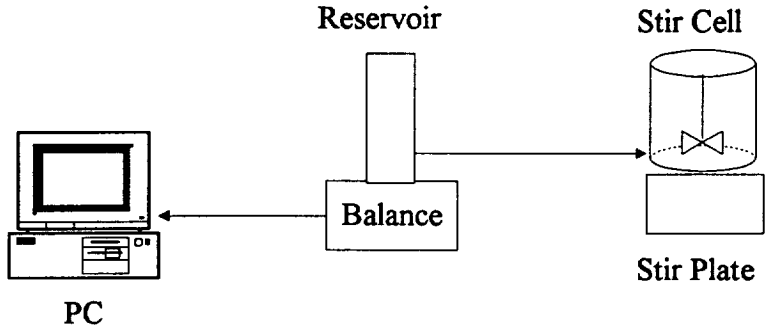

Figure 2. Schematic drawing of the OPS.

Procedures:

A. Mechanical Pressure System

a. Cut RO membrane into 6.25 inch diameter pieces and soak them in pure water overnight. (For consistency, cut those small pieces from the same piece of membrane.)

b. Carefully place one membrane on the support in the center of the bottom disk of the membrane unit. Put the top disk on and assemble two disks by tightening the four pairs of nuts and bolts.

c. Connect the membrane unit with the stainless tubing.

d. Fill the reservoir with clean DI water. Turn on the reservoir valve.

e. Turn on the tap water line for the pump. A minimal flowrate is sufficient.

f. Turn on the pump. Flush the system with DI water for a few minutes. (Let the DI water go down the drain in this step. Do not recycle it.)

g. Turn the pressure adjusting valve to raise the system pressure to about 20 psi and let the flushing process continue. This is to test to see if there's any pin-hole leakage on the membrane or mis-assembly of the membrane unit.

h. Run the permeation program.

1. in Windows 3.1, run Labview;
2. open the file: "C:\BOULDER\RORIK\LABVIEW\LIQ-COMP.LIB";
3. run "SEEWAVE";
4. give a name for the new data folder, such as
   C:\BOULDER\LEE\TEST-RUN;
5. click the "PERMEATION" bottom on the screen to turn it green;
6. click the "⇨" icon on the top left corner on the screen;
7. change the data collection time interval to 20 seconds;
8. click "WINDOW" on the menu bar, double click the "THIS VI'S CALLER" option, and choose "PERMEATION" icon to go to the flux monitoring screen;
9. change the data collection time interval to 20 seconds as well;
10. detach the permeation outlet at the bottom of the membrane unit from the permeate collecting vertical tube, watch for the flux values shown on the computer screen when data are taken every 20 seconds, adjust the "VOLTAGE OFFSET" values to zero the flux reading;
11. change the data interval to 60 seconds (or any other desired number);
12. . click "WINDOW" on the menu bar, double click the "VI'S CALLER" option, and choose "SEEWAVE" icon to go back to the main screen;
13. change the data interval to 60 seconds (or any other desired number);

i. reattach the permeation outlet to the permeate collecting vertical tube, and manually inject some DI water into the vertical tube through the "Y" connector to make sure water flows down the tube smoothly;

j. (if everything works) turn the pressure-adjusting valve to raise the system pressure to the desired value (600 psi in all the experiments, which is also the pressure in the pressure-stabilizing tank);

k. turn the two valves on the pressure-stabilizing tank on;

l. permeate data will be saved in a file named "PERM.DAT" in the folder specified in h-4;

m. to shut down the system:

1. close the pressure tank valves;
2. dial down the pressure-adjusting valve to release the system pressure;
3. unplug the pump, and turn off both the tap water and DI water;
4. close the valves on both sides of the membrane unit.

B. The Osmotic Pressure System:

a. cut RO membrane into 2.5 cm diameter pieces and soak them in pure water (or 3M NaCl solution) overnight (For consistency, cut those small pieces from the same piece of membrane.);

b. fill the reservoir (a 50 ml centrifuge tube) and the tubing with clean DI water;

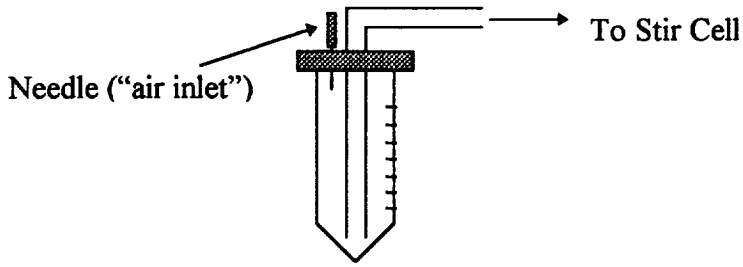

c. seal the connection between the tubing and the cap with grease to prevent water evaporation;

d. connect the tubing with the bottom support of the stir cell;

e. raise the reservoir so that water flows out from the reservoir into the stir cell bottom support till the bottom support is covered with water;

f. place a RO membrane on the support (RO side face up), put the rubber gasket around the membrane and tighten the stir cell assembly;

g. when performing the above step, make sure no bubbles are trapped underneath the RO membrane to ensure a 100% water-membrane direct contact;

h. put the reservoir on the balance and stir cell unit on a stir plate;

i. run the data collecting program:

1. run qbasic under DOS prompt;
2. open old file "LEE.BAS";
3. press "ALT-R" and "RETURN" to execute the program;
4. give a file name for the data file in 1st line, brief description of the experiment in the second line, and data frequency in the 3rd line;

j. rinse out the excess water in the stir cell with 3M NaCl; pour about 30 ml of fresh 3M NaCl into the stir cell;

k. press "R" on the PC keyboard to tare the balance;

l. press "B" for beginning taking data after the balance is tared.

Results

A. Mechanical Pressure System

All experiments were done with 600 psi pressure at room temperature. Each experiment lasted about 24 hours. Four experiments were performed. The experimental data are shown in Figure 3.

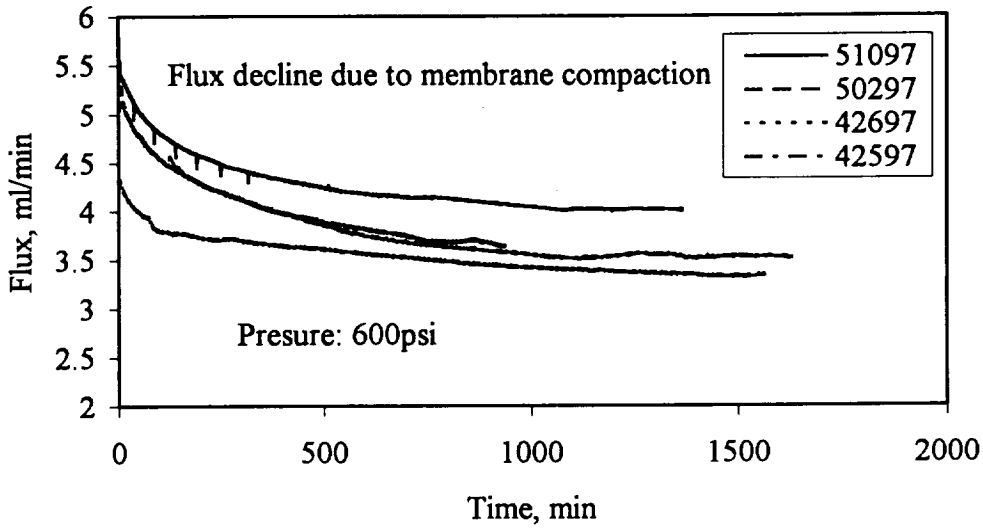

Figure 3. Flux vs. Time data from 4 permeation experiments with pure water in the MPS. The first line from top is 051097, the second line is 050297, the 3rd line is 042697, and the 4th line is 042597.

The membranes used in 051097, 050297 and 042697 were cut from the same big piece, and the one used in 052597 was cut from a different big piece. Both pieces were purchased at the same time from OI. Flux decline was observed in all four experiments. This indicates that RO membranes experience compaction when placed under mechanical pressure. From the experimental data, fluxed in all 4 experiments reached steady-state values at about 17th hour (1000th min). However, except experiments 042697 and 050297, the steady-state values are quite different between different pieces of membranes. This difference, about 20% maximum, indicates that RO membrane layer is not very uniform between one area to another. Therefore, different pieces of membrane have different overall resistance.

B. Osmotic Pressure System

In the OPS, the driving force is created by the concentration gradient between 3M NaCl and pure water. This driving force gradually decreases as experiment proceeds. Refer to Figure 2, as pure water permeates through the RO membrane into the stir cell, the concentration of salt solution gradually decreases. However, for experiments which ran longer times, the salt water in the stir cell was refreshed periodically to maintain the driving force near constant.

5 sets of experiments were performed with MS-10 from OI. The results are shown in Figure 4. These membrane pieces were call cut from the same big piece, and soaked in pure water over night before use. There must be some unknown bug in the data collecting program. For some reason, the program would stop collecting data randomly. Those "gaps" in the same data set were caused by the stops.

Several conclusions can be drawn from the experimental data. As observed in the MPS, the fluxes in different pieces of membrane are quite different. The membrane resistance is not uniform from spot to spot on the same big piece of membrane. This

resistance also doesn't seem to be constant through out the same experiment. All data sets display a faster water transport rate at the beginning and slower rates in later stages. This decrease can not be explained by the gradual decrease of the concentration gradient as mentioned above. Take the first data set from top as an example, each section of the line represents a re-start of the program due to the random stop mentioned above. Before restarting the program, the salt water in the stir cell was always poured out and replenished with fresh 3M salt solution. Had the membrane resistance been constant, each section of the line should display the same weight loss over the same period of time. As clearly indicated by the experimental data, the slope of the curve (flux) decreases as the experiment proceeds. The same trend is also found in other data sets, although the fluxes differ very much from one set of data to another. The difference in fluxes is much more significant among these 5 data sets. The bottom weight loss line has a slope which is about twice as much as the top line. The experimental data show a significant difference in membrane resistance from spot to spot on the same RO membrane sheet.

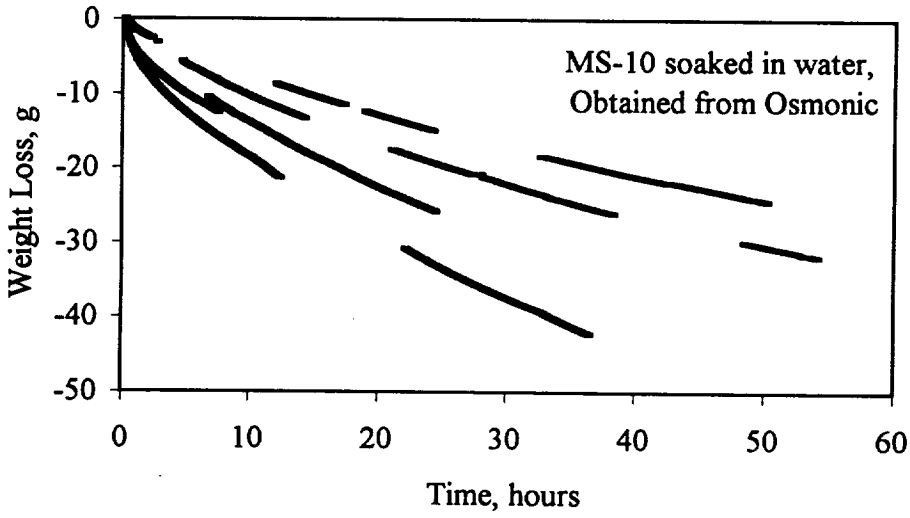

Figure 4. Weight loss vs. time data in 5 osmotic pressure runs. All membranes were cut from the same big piece.

More experiments were performed using the Desal MS-10 membranes. Figure 5 shows the weight loss vs. time plot from 3 different runs using Desal MS-10 membranes. The 3 smaller pieces were cut from the same big piece.

The most striking difference between these 3 data sets and the previous 5 data sets is the reproducibility. At the 6th hour mark, the difference between the 3 data sets is only about 7%. What's consistent between Figure 4 and Figure 5 is the pattern of flux decline. Figure 6 shows the flux vs. time information for the 3 Desal membrane runs. All the membranes pre-soaked in water show a very fast flux in the first 30 minutes after the start of the experiments. Fluxes then declined to a "steady-decline" pattern for the rest of the experiments. The following two quick calculations illustrate the above comment. From Figure 5, at the second hour mark, the weight loss is about 4 grams. That means about 4 ml of pure water goes into the stir cell. The salt solution is then diluted to 2.65M. From Figure 6, the flux at this point is about 1.25 ml/hr. At the 4th hour mark, the salt

concentration and flux are 2.52M and 0.95 ml/hr, and at the 8th hour mark, 2.31M and 0.6 ml/hr. Comparing the data at both second hour and 4th hour marks, the driving force decreases by a factor 0.95 (2.52M/2.65M), but the flux declines by a factor of 0.76 (0.95/1.25). Comparing the data at both 4th hour and 8th hour marks, the driving force decreases by a factor of 0.92 (2.31M/2.52M), but the flux declines by a factor of 0.63 (0.6/0.95).

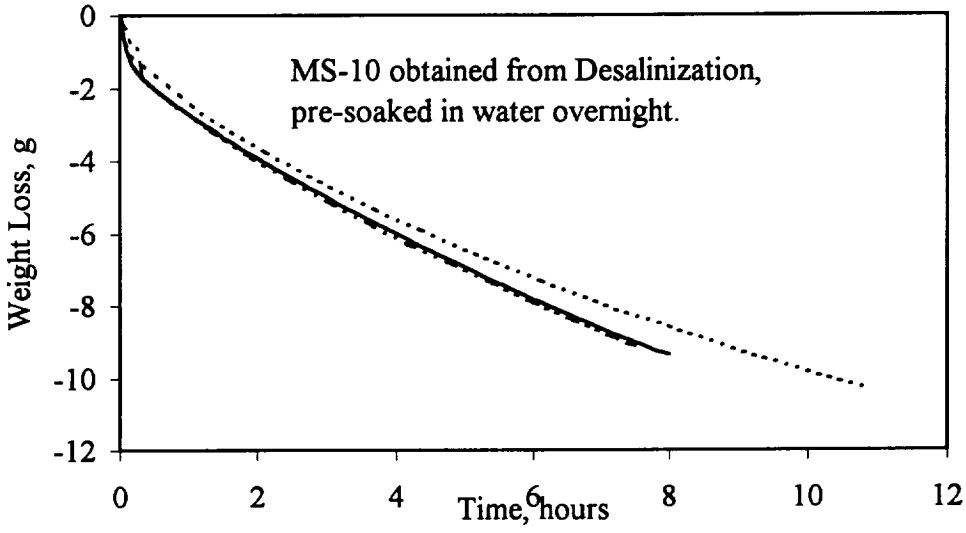

Figure 5.

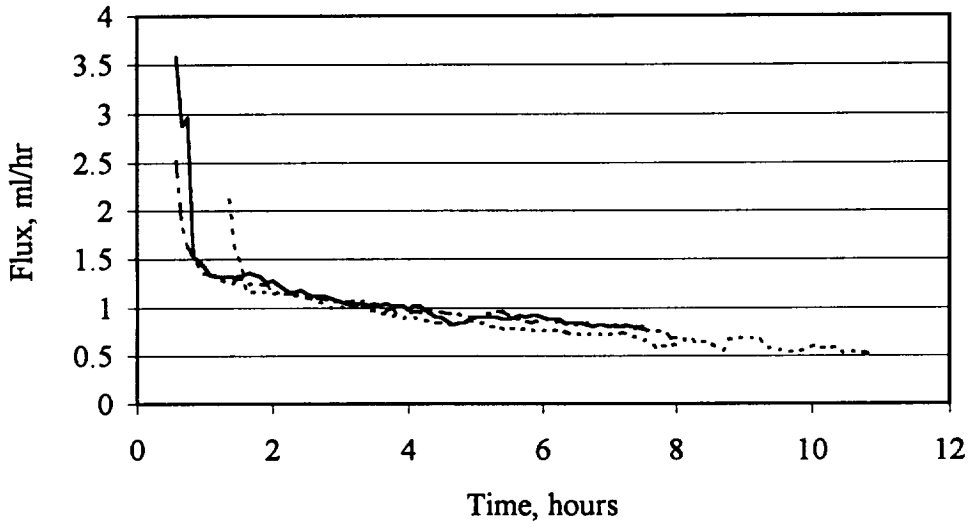

Figure 6.

This analysis indicates that the membrane resistance is not a constant (increasing) for these MS-10 membrane, pre-soaked in water, under osmotic pressure. The cause for change of resistance is not clear at this moment. It probably has something to do with a few factors, such as the swelling of RO membrane polymers after being soaked water and

the actual microscopic mechanism of how water molecules pass through the internal structure of the RO membrane. The following Figure shows the comparison between Desal and OI MS-10 membranes. The weight loss profile of Desal membrane falls within the range of those profiles of OI membranes.

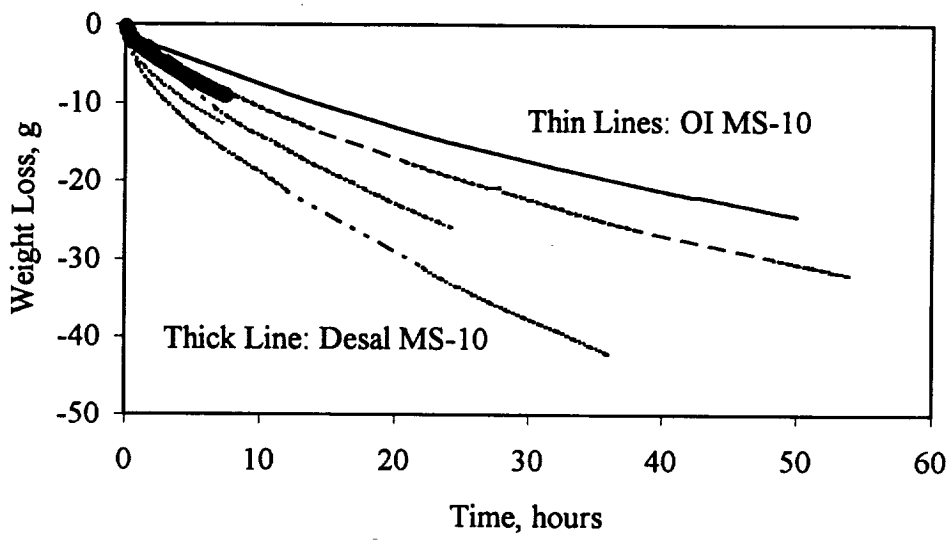

Figure 7.

Since the Desal membranes were cell tested under 100 psi beforehand, they have experienced the membrane compaction to some extent. Compaction reduces the internal porosity of the RO membrane. This might have helped to make the membrane more uniform from one area to another. Some future experiments will be recommended in later section to find out if compaction really helps.

The next question asked is the effect of pre-soaking. The original purpose of soaking membranes in water is to get rid of any glycerol on the RO membrane. Since the membranes are used to separate 3M NaCl solution from water, would it be better to pre-soak the membrane in 3M NaCl before use.

Figure 8 shows 2 experiment runs. Two Desal membranes, cut from the same large piece, were used. The two pieces were pre-soaked in 3M NaCl overnight. All the other experimental conditions were the same as previous ones. In Figure 8, the two lines show almost the same slope after the first half hour. It's not clear what makes the water transport rate different at the early stage. Except the early stage difference, the two data sets show very good reproducibility, and almost constant membrane resistance. From Figure 8, take the first line as example, the weight loss is 1.55g at 4th hour, 2.3g at 6th hour, and 3g at 8th hour. Therefore the salt solution concentration in the stir cell is 2.852M at 4th hour, 2.786M at 6th hour, and 2.727M at 8th hour. The flux value between 4th and 6th hours is (2.3-1.55)/2=3.75 ml/hr, and that between 6th and 8th hours is (3-2.3)/2= 3.5 ml/hr. There is a 93% decline (3.5/3.75=0.93). But the driving force also declines during this period. The decline of driving force is about 89% ((2.786-2.727)/(2.852-2.786)=0.89) Therefore, the decline of the flux between 4th and 8th hours

is mainly due to the decrease of the driving force, instead of the change of the membrane resistance.

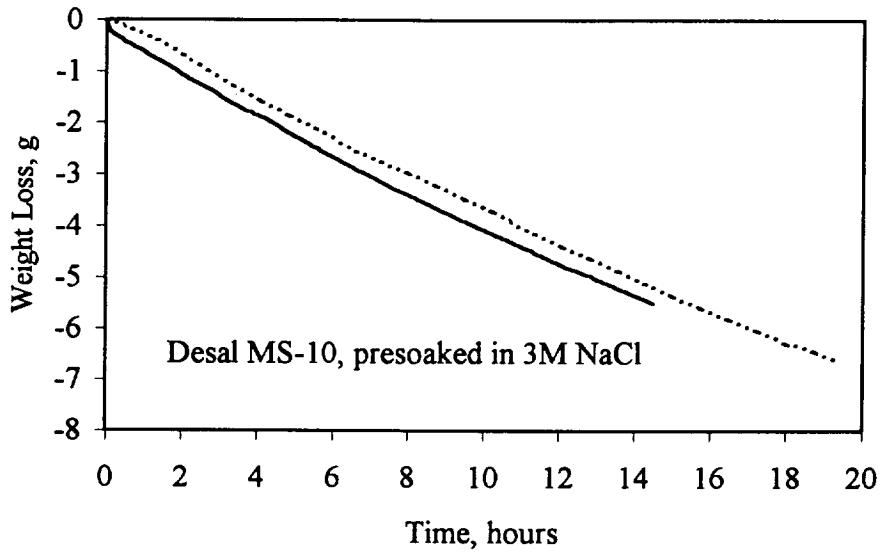

Figure 8.

Comparing Figures 5 and 8, the Desal membranes show very good consistency under the same pre-soak condition. However, there's a big difference in the water transport rates. Water transport rates in the water-soaked membranes are more than twice as fast as those in salt-soaked ones. Note that at the 4th hour, the water-soaked systems have lower driving force (2.52M) due to more dilution than salt-soaked system do (2.852M). Yet at this time point, the water-soaked membranes allow water to transport at about 0.95 ml/hr, but the salt-soaked membranes show a much slower rate at 0.375 ml/hr.

Since the membranes used in Figures 5 and 8 are from different Desal large pieces, the next question to be asked is whether the difference is from the different pieces of membranes from some unknown factor introduced by different soaking methods. In Figure 9, 3 more experimental data sets are shown. The 3 pieces of membrane are cut from the same large piece Desal membrane. One of them (water) is pre-soaked in water overnight, the second one (salt) in 3M NaCl overnight, and the 3rd one (dry) is not pre-soaked at all. The experimental data show a clear water transport rate difference between salt-soaked membrane and water-soaked membrane. The rates between dry membrane and salt-soaked membrane are about the same, as indicated by the data. Figure 10 shows the flux calculations of the three runs. The water-soaked membrane clearly allows much higher flux, especially in the first hour. The membrane resistance shows the same trend. Water-soaked membrane displays an increasing resistance, while salt-soaked and dry membranes show a constant resistance throughout the duration of the experiments. The cause for this difference is not clear at this moment.

Another observation is that in both water-soaked and salt-soaked membrane runs, the initial fluxes are always higher. But the dry-membrane run shows a graduate increase in the beginning. This is expected as it takes time for the dry membrane to be saturated wit water. The significant difference between the water-soaked and salt-soaked

membranes for initial fluxes is that the water-soaked membranes have a much higher initial fluxes and decline rapidly, while the salt-soaked membranes have a mildly higher rates and don't decline as much.

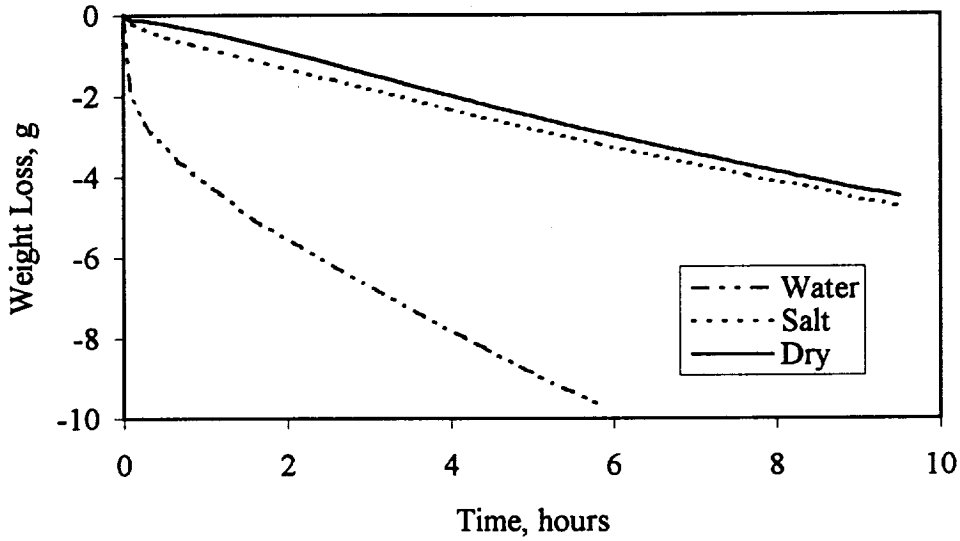

Figure 9.

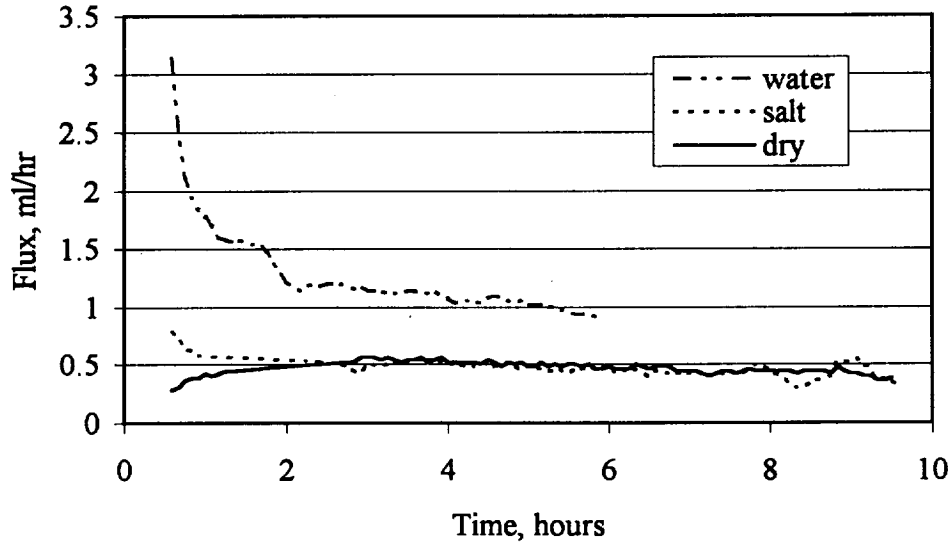

Figure 10.

An interesting question is if MS-10 membrane allows the same flux under different kinds of pressure driving forces. Compare one of the data sets, 042697, from the MPS with the water-salt-dry osmotic pressure data. All fluxes are normalized by pressure and effective surface area. In the MPS, the pressure is 600 psi, or 40 atm, and the effective surface area is 28.27 cm^2. In the OPS, the osmotic pressure is calculated according to Van't Hoff's Law, $\Delta P = RT\Delta C$. R equals 0.08205, T is 298°K, and ΔC equals 6 osmoles/liter. Therefore, ΔP is 146.7 atm and the effective surface area is 4.1 cm^2 in the

OPS. Figure 11 shows the normalized flux comparison. It's clear that there's a very significant difference in flux behaviors between the data set. However, it's not clear why.

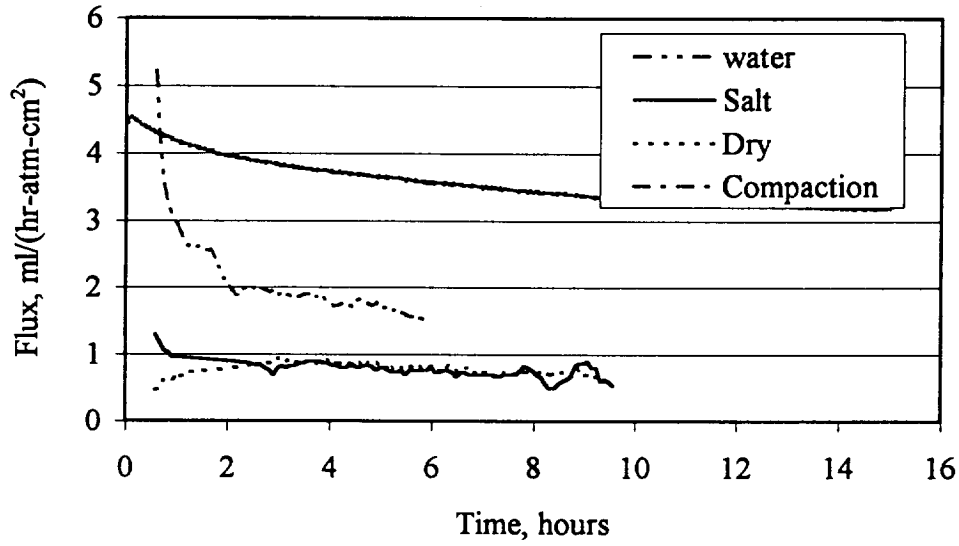

Figure 11. Normalized flux profiles for MS-10 under different driving forces and different membrane pre-treatment.

Conclusions

The results obtained to date are very preliminary. There are more questions to be answered than conclusions can be made.

1. The mechanical pressurizing experiments show that RO membranes experience compaction under mechanical pressure.

2. Under the same operating conditions, the MS-10 membranes purchased from Osmonics show a wide range of water transport rates in the OPS with membranes being pre-soaked in pure water.

3. Under the same operating conditions, the MS-10 membranes obtained from Desalinization show very consistent water permeation rates. One possible reason for Desal membranes to have consistent results is that those membranes have experienced compaction to some degree. The compaction might have helped make the internal structure of RO membrane more uniform.

4. Different methods of pre-soaking MS-10 make a huge difference in affecting the water transport rate and membrane resistance. Water-soaked membranes have higher water transport rates, and the membrane resistance seems increases as the experiments proceed. Salt-soaked membranes show lower water transport rate (less than half of the water-soaked membrane), and the membrane resistance maintains near constant throughout the duration of the experiments. Dry membrane has similar behavior as the salt-soaked membranes.

5. Water-soaked membranes show much higher initial fluxes. The high fluxes decline rapidly within the first hour. The reason is unknown.

6. Salt-soaked membranes show slightly higher initial fluxes, and the high fluxes also decline to a pretty steady value with the first hour.

Recommendations for Future Work

1. In MPS, MS-10 permeation experiment can be carried out first with pure water. When the flux reaches its steady-state, different solutions, such as NaCl and polyethylene glycol (PEG) which are often used in osmotic dewatering crystallization, can be used as the feed. This will reveal how much concentration polarization affects the water removal rate through the RO membrane. To do this experiment, the equipment Anurag Mairal established can be used since it is capable of switch solutions.

2. In order to find out if membrane compaction helps stabilize the membrane resistance, pure water permeation experiments can be carried out first in MPS using the MS-10 purchased from Osmonics, Inc. After fluxes reach steady-state, a smaller piece membrane can be cut from the compacted membrane and used for weight loss measurement in OPS. Since data from OPS experiments with uncompacted OI membranes show a wide range of resistance (Figure 4), if the compacted OI membranes show more consistent resistance, it might be suggested that all membranes purchased from OI need to be pre-treated with high pressure.

3. Pre-soak (overnight) a piece of Desal membrane in 3M NaCl and run the weight loss measurement for, say, 10 hours first. Rinse the membrane and soaked it again in pure water overnight. Run the same experiment again to obtain the weight loss data. Reverse the soaking order and repeat the experiment. The results could further confirm the role of soaking in affecting the fluxes. If the flux difference is still significant, attention need to be paid to the microscopic mechanism of water transport inside the RO membrane in order to understand this phenomenon.

4. Is the Van't Hoff's Law really valid in converting concentration gradient into osmotic pressure gradient? If it is, why the normalized flux profiles look so different between water-soaked membranes, one under mechanical pressure and the other under osmotic pressure, as shown in Figure 11?

Scanning Electronic Microscopy (SEM)

Some SEM pictures were taken from a few MS-10 membrane samples. The pictures labeled with "1" are from virgin OI membrane, those labeled with "2" and "3" are from OI membranes used in MPS experiments, and those labeled with "4" and "5" are from OI membranes used in OPS experiments. Except the virgin membrane, all other membranes were pre-soaked in DI water at least overnight before use. After use, they were stored in pure water for a few days. Before they were analyzed by SEM, they were air dried. The SEM samples and actual scanning were prepared and performed by Mr. John Lock, who is a ChE undergraduate student.

Chapter 21

Dynamics of reverse osmosis membranes and membrane pretreatment methods for applications in crystal growth by osmotic dewatering

Paul Scovazzo, Ching-Yuan Lee
and Paul Todd

CHAPTER 21
DYNAMICS OF REVERSE OSMOSIS MEMBRANES AND MEMBRANE PRETREATMENT METHODS FOR APPLICATIONS IN CRYSTAL GROWTH BY OSMOTIC DEWATERING

Paul Scovazzo[1], Ching-Yuan Lee[2], and Paul Todd[1&3]

[1] Department of Chemical Engineering; University of Colorado, Boulder
Campus Box 424; Boulder, CO 80309-0424

[2] Caleb Pharmaceuticals, Inc.; 2F No. 18 Industry East Road 4
Science-Based Industrial Park; Hsinchu, Taiwan 300, ROC

[3] Corresponding Author
Voice (303) 492-5936; FAX (303) 492-4341; EMAIL: todd@spot.colorado.edu

Short Running Title

"DYNAMICS OF RO MEMBRANES IN OSMOTIC DEWATERING CRYSTALLIZATION"

SUMMARY

Osmotic Dewatering Crystallization is a method for obtaining high-quality crystals of biological macromolecules through controlling the rate of water removal. In Osmotic Dewatering Crystallization a composite reverse-osmosis (RO) membrane separates the aqueous solution containing the macromolecules from a high-concentration solution. Operator adjustments to the concentration of the solute on the high-concentration solution controls the dewatering rate. Central to the active control of Osmotic Dewatering Crystallization is precise determination of the reverse-osmosis membrane performance. This investigation was designed to evaluate the membrane performance in terms of permeability dynamics, flux decline, saturation procedure, and role of the microporous membrane backing during the dewatering process. This investigation adopted literature models to predict membrane permeability under osmotic dewatering conditions, and then compared these models with laboratory data. Significant effects of membrane pretreatment methods on the repeatability of membrane permeability were found. The adopted literature models predicted the order of magnitude of the membrane permeabilities. The models, however, incorrectly predicted the optimum membrane orientation in an osmotic dewatering operation and the membrane permeability dynamics with dewatering rate. The composite membrane's porous media backing governs transport through a RO membrane during osmotic dewatering. Finally, due to internal polarization in the membrane backing, small mechanical pressures of 0.1% to 1.0% of the applied osmotic pressure difference can have an impact on the dewatering rate.

Keywords: Nucleation Control; Osmotic Dewatering; Reverse Osmosis Membranes; Crystal Growth; Crystallization

INTRODUCTION

The properties and activities of biological macromolecules depend on their three-dimensional structure. The determination of three-dimensional structures by X-ray crystallography, in turn, depends on the availability of high-quality crystals. Methods for crystallizing biological macromolecules include batch crystallization, temperature gradient crystallization, equilibrium dialysis crystallization, and vapor phase diffusion (McPherson, 1999; Blundell and Johnson, 1976). These methods, however, allow very limited control of the parameters involved in the nucleation and growth of macromolecule crystals. Todd, et al. (1991) introduced a novel method for obtaining high-quality crystals of biological macromolecules, namely Osmotic Dewatering Crystallization (OD). OD has, over the traditional methods, the advantages of actively controlling the rate of water removal, which affects both the nucleation and the growth rate of crystals, thereby dictating the sizes of crystals. OD also reduces convective flow, which is generally considered detrimental to the crystal quality.

In osmotic dewatering, a reverse-osmosis (RO) membrane separates two solutions having different solute concentrations. The lower-concentration solution contains the species to be crystallized and its precipitant. Due to the osmotic pressure resulting from the difference in osmolarity across the membrane, water from the low-concentration solution permeates through the membrane into the high-concentration solution. This dewatering, at a controllable rate, gradually concentrates the low-concentration solution and causes crystallization to occur in the presence of a suitable precipitant. C.Y. Lee, et al. (1997) developed a Transport Equation For Osmotic Dewatering (TEFOD). The form of TEFOD applicable to most cases of OD is:

$$\frac{V_o}{L_P S(RTC_{ro})}\left\{\frac{V}{V_o}-\frac{C_{wo}}{C_{ro}}\ln\left[1-\left(\frac{C_{ro}}{C_{ro}-C_{wo}}\right)\left(\frac{V}{V_o}\right)\right]\right\}=t\ . \qquad (1)$$

Where: L_P = Membrane permeability Coefficient (m/sec MPa), S = Surface area of membrane in (m^2), t = Elapsed time (sec), V = Volume of the water that has permeated through the membrane at time t (m^3), V_o = Initial volume of the low-concentration solution (m^3), C_{wo} = Initial osmolarity (total ion and non-ionic solute molarity) of the low-concentration solution (osmole/m^3), C_{ro} = Initial osmolarity of the high-concentration solution (osmole/m^3), R = Ideal gas constant (m^3MPa/mol K), and T = Absolute temperature (Kelvin).

Equation 1 assumes that the high-concentration solution volume is much larger than the low-concentration solution volume. The general form of TEFOD appears in C.Y. Lee, et al. (1997). The reader should note that equation (1) contains $1/L_p$ instead of μR_m (μ = fluid viscosity, R_m = membrane resistance) which appeared in C.Y. Lee, et al. (1997); this change reflects the intention, in the current work, to study membrane permeability per se. Furthermore, the RO skin of the membrane is not governed by Darcy's Law as assumed for the purpose of developing the TEFOD in C.Y. Lee, et al. (1997).

The studies to date using the TEFOD have assumed that the membrane permeability, L_p, is constant. L_p is the membrane property that controls the dewatering rate; therefore, its characterization is crucial to accurate application of the TEFOD. This work focuses on the membrane permeability, L_p, term in the TEFOD equation through the following three questions:

1. Is L_p a constant? Is it constant spatially across the membrane surface, and is it constant with time during an osmotic dewatering operation?
2. If L_p is not a constant, why not? What causes variations in L_p?
3. What are the effects of membrane pretreatment on membrane performance? How may the effects of pretreatment be explained?

The impetus for this work resulted from a number of observations made during the course of our osmotic dewatering operations. First was the consistent observation of irregular dewatering rate patterns resulting from the same experimental conditions. The irregular dewatering patterns were particularly evident among different membrane pretreatment methods. Second, the dewatering rates did not relate to the hydrodynamic permeabilities specified by the membrane vendor nor those determined in the laboratory. Finally, the use of a constant L_p underpredicted early fluxes and overpredicted late fluxes during the course of a dewatering operation.

BACKGROUND AND DEFINITION OF TERMS

Three mass transfer processes use membranes designed to regulate the flux of a solute (i.e. NaCl) relative to water flux; namely, Reverse Osmosis (RO), Osmosis (such as Osmotic Dewatering, OD), and Pressure-Retarded Osmosis (PRO). Physically RO uses mechanical pressures to drive water up the osmotic gradient to generate a solute free water permeate. OD allows water to flux down the osmotic gradient resulting in the dewatering of the lower solute concentration solution. PRO allows water to flux down the osmotic gradient to generate a pressure on the permeate side for exploitation in power generation. Mathematically, the following three equations define the water fluxes, J_w, in each of the three processes:

RO: $J_w = A(\Delta P - \sigma\Delta\pi)$ (2)

OD: $J_w = A(\sigma\Delta\pi)$ (3)

PRO: $J_w = A(\sigma\Delta\pi - \Delta P)$ (4)

Where: J_w = Water Flux (m/sec), A = Hydrodynamic Permeability (m/sec MPa), ΔP = Mechanical pressure difference across the membrane (MPa), σ = Solute reflection coefficient (dimensionless), and $\Delta\pi$ = Osmotic pressure difference across the membrane (MPa).

In addition to the three processes, we must define two membrane orientations relative to the higher solute concentration solution. Figure 1 summarizes membrane orientation and fluxes for the three osmotic processes. Conceptually all osmotic membranes contain a skin side and a backing-material side. The skin is the "working" component of the membrane capable of selecting water flux over salt flux; generally, it is a dense polymer film on the order of 0.1 μm thick. The backing is a porous material attached to the skin for overall mechanical strength. The combined thickness of the membrane is on the order of 150 μm, Mulder (1996). In "Normal" Orientation (standard RO operation orientation) the membrane skin faces the solution with the higher solute concentration (the solution with the highest osmotic pressure). In "Inverse" Orientation the membrane backing faces the solution with the higher solute concentration.

MATERIALS AND METHODS

All studies were performed using the MS-10 RO membrane manufactured by Osmonics DESAL™. The MS-10 membrane (Ionics-Desal, Vista, CA) is a multilayer composite consisting of a standard polyester paper backing 114 μm thick supporting an asymmetric polysulfone ultrafiltration (UF) layer 76 μm thick and having nominal pore size of 30 nm. This polysulfone layer is coated with a proprietary polymeric UF intermediate support that is only 5-10 nm thick but serves as a protective layer on which the RO polyamide skin is cast by interfacial polymerization to a thickness of 4-10 nm. The thinness of this skin is designed to provide high water flux at low RO pressures and is considered

suitable for brackish water desalination. The RO layer is not considered porous, but it is extremely hydrophilic and transports water by the solution-diffusion mechanism.

MS-10 membranes are generally available as dry sheets that have been dried after saturation with glycerol. Dry sheets need to be saturated with water prior to use. Wet sheets from the manufacturing plant are available, and these will not have been glycerol treated, but they must be kept wet with pure water.

This study tested the following five separate methods of pretreating the dry sheet membranes prior to use in an osmotic process:

- No pretreatment
- Soaking in pure water
- 50-psi (0.345 MPa) pressure pretreatment: With the membrane in the orientation shown in figure 1 for RO (distilled water instead of salt solution on the skin side and air on the backing side), cause a water flux to occur through the membrane by pressurizing the distilled water to 50 psi (0.345 MPa) for at least 1 hour.
- 100-psi (0.689 MPa) pressure pretreatment: The same as the 50-psi (0.345 MPa) pretreatment above except with a 100 psi (0.689 MPa) mechanical pressure.
- 50 psi/salt water soak: This pretreatment started with a membrane undergoing a 50 psi (0.345 MPa) pressure pretreatment followed by a soaking in a 3 molar NaCl solution for 28 to 47 hours.

Pretreatment of the membranes is not an issue in RO; however, the manufacturer advised against soaking in pure water as a pretreatment method. The manufacturer believed that soaking could cause residual chemicals from the manufacturing process to travel from the porous backing through the skin and, thereby, damage the skin.

Pressure Cell

It was important to determine whether the pressure pretreatments caused a compaction of the porous media membrane backing. We employed two methods to measure membrane compaction during a pressure pretreatment. The first method was flux decline resulting from reductions in backing permeability. The second method was Acoustic Time Domain Reflectometry (ATDR), which can measure compaction in real time with a resolution of 5 μm. In ATDR, high frequency sound signals or waves directed at a membrane surface "echo" from each discrete material interface. With the velocity in the medium known, the time delays between the launching of the emitted signal and the received echo gives a measure of propagation path or thickness. The delays between a series of arrivals can be used to measure layer thickness, Kools, et al (1998). An acoustic transducer (Panametrics Type VIII, 1/2 inch (1.27 cm) diameter, 10 MHz contact transducer) was mounted on the outside of the pressure cell so as to measure the acoustic signal from both sides of the membrane as described by Kools, et al (1998).

Figure 2 is a schematic of the mechanical pressurizing system (MPS) used for the pressure pretreatments. A pump circulates distilled water from a reservoir through the system. The pressure-adjusting valve regulates system pressure while the surge tank stabilizes the system pressure. Acoustic membrane thickness measurements (see above) require the use of the surge tank; otherwise the surge tank is optional. A personal computer measures and stores permeate flux data while excess water flows over the membrane and back to the reservoir. In addition to pretreating the membranes and measuring membrane compaction, the measurements of water fluxes during pressure pretreatments also allow calculation of the membrane's hydrodynamic permeability, A.

Stir Cell

Figure 3 is a schematic of the Osmotic Stir Cell System, in which the stir cell was an Amicon Model 8050 (Amicon, Inc., Beverly, MA). The initial solution in the stir cell was 30 ml of 3 molar NaCl or 30 ml of a 12% 2-methyl-2,4-pentanediol solution (see Osmotic Dewatering With MPD As Solute section below). The membrane placed in the bottom of the stir cell separated the solution from pure distilled water underneath the membrane. Due to the osmotic pressure created by the transmembrane solute concentration gradient, pure water from the reservoir permeated through the membrane into the stir cell. A balance measured the weight loss of the reservoir. A personal computer recorded the weight lost verses time.

Because the reservoir weight loss resulted in a change in solute concentration within the stir cell, the osmotic driving force was time dependent. With proper manipulation of the data a measure of the membrane permeability dependence on time results. Experimental data from the Osmotic Stir Cell System can reveal if the membrane permeability is a constant with time and, from repeated experiments under similar flux conditions, how uniform the permeability is among different membrane samples. For this reason, all osmotic flux conditions tested were repeated three or more times.

MODELS

Equation 3 applies to the osmotic dewatering stir cell experiments. In addition, we can define water flux based on membrane permeability:

$$J_w = L_p \Delta\pi \qquad (5)$$

By combining equations 3 and 5, we find

$$L_P = A\sigma \ . \qquad (6)$$

Note that the model for flux in the stir cell assumes that the mass transfer boundary layer resistance on the high solute concentration side of the membrane is negligible due to the actions of the stirrer and that there is no mass transfer boundary layer on the unstirred side since $C_l = 0$.

By conceptually dividing the membrane into two parts, the skin and the backing, we can write governing equations for both parts. Therefore the following equations apply to the skin, if the resistance to water flux in the backing is assumed to be negligible:

$$J_w = A\sigma_s(\pi_{sk} - \pi_f) \qquad (7)$$

$$J_s = B(C_{sk} - C_f) \qquad (8)$$

Where: σ_s = The skin solute reflection coefficient, J_s = Solute flux (moles/m^2 sec), B = Solute Permeability (m/sec), π_{sk} = Osmotic pressure on the skin side of the membrane (MPa), π_f = Osmotic pressure at the interface between the skin and the porous media backing (MPa), C_{sk} = Solute concentration on the skin side of the membrane (moles/m^3), and C_f = Solute concentration at the interface between the skin and the porous media backing, see figure 1 (moles/m^3).

In the porous media backing a solute balance at steady state gives

$$J_s = J_w C_s - D_e dC_s/dx \qquad (9)$$

Where: C_s = Solute concentration in the porous media backing at position x (moles/m^3) and D_e = The effective diffusivity of the solute in the porous media backing (m^2/sec).

Researchers of Pressure-Retarded Osmosis (PRO) have combined equations 7, 8, and 9 with appropriate boundary conditions to obtain the solutions given below using the following terms

(Jonsson, 1980; K.L. Lee, et al; 1981; Mehta and Loeb, 1978; Reali, et al, 1990): C_l = Solute concentration in the low concentration solution (moles/m^3), C_h = Solute concentration in the high concentration solution (moles/m^3), R_{ps} = Resistance to solute transport in the porous media membrane backing = $\Delta x / D_e$ (sec/m), Δx = The membrane thickness (due to the minimal thickness of the membrane skin $\Delta x \cong \Delta x$[porous backing]) (m), and π_h = Osmotic Pressure of the high-solute-concentration solution (MPa).

For RO processes in Normal Orientation, Jonsson (1980)

$$C_f = C_l \tag{10}$$

For OD processes in Normal Orientation, K.L. Lee, et al (1981), the solute concentration at the skin-backing interface is

$$C_f = J_s/J_w + (C_l - J_s/J_w)\exp(J_w R_{ps}) \tag{11}$$

And the water flux is

$$J_w = A\pi_h\sigma_s\left\{\frac{1-(C_l/C_h)\exp(J_w R_{ps})}{1+B/J_w\left[\exp(J_w R_{ps})-1\right]}\right\} \tag{12}$$

Finally, for OD processes in Inverse Orientation (See Appendix A for development), the solute concentration at the skin-backing interface is

$$C_f = J_s/J_w + (C_h - J_s/J_w)\exp(-J_w R_{ps}) \tag{13}$$

Equation 13 is consistent with the alternative derivation of Reali, et al (1990). While the solution for water flux in the Inverse Orientation is

$$J_w = A\pi_h\sigma_s\left\{\frac{\exp(-J_w R_{ps})-C_l/C_h}{1+B/J_w\left[1-\exp(-J_w R_{ps})\right]}\right\} \tag{14}$$

Note, in equations 12 and 14 that π_h appears and not $\Delta\pi$ explicitly. If C_l is equal to zero, as in this study's stir cell experiments, then $\pi_h = \Delta\pi$ and the following result from equations 6, 12, and 14:

In Normal Orientation OD

$$L_p = \frac{A\sigma_s}{1+B/J_w\left[\exp(J_w R_{ps})-1\right]} \tag{15}$$

and in Inverse Orientation OD

$$L_p = \frac{A\sigma_s\exp(-J_w R_{ps})}{1+B/J_w\left[1-\exp(-J_w R_{ps})\right]} \tag{16}$$

Figure 4 shows graphical representations of equations 12 and 14 while figure 5 shows graphical representations of equations 15 and 16. The conclusions from using these current literature models are the following:

- Membrane performance (flux or hydrodynamic permeability) in OD is significantly less than in RO
- "Internal concentration polarization" within the porous media backing (a reduction in osmotic driving force across the membrane skin due to a build up of rejected solute at the skin surface, normal orientation, or a sweeping away of solute from the skin surface, inverse orientation) significantly decreases the membrane performance
- Normal Orientation results in better performance than does Inverse Orientation; our results (below), however, do not favor this preferred orientation.
- L_p is a highly non-linear function of J_w for both Normal and Inverse Orientations

RESULTS AND DISCUSSION

Compaction Under Applied Mechanical Pressures During Membrane Pretreatment

Figure 6 shows the results of a flux decline test and an Acoustic TDR test performed over a 24-hour period in the pressure cell, using distilled water only. Both of these compaction tests indicate that no compaction occurred during a 100-psi (0.689 MPa) pretreatment. Since compaction is a direct function of applied pressure, we also concluded that compaction does not occur during a 50-psi (0.345 MPa) pretreatment. Flux decline tests done at an applied pressure of 600 psi (4.140 MPa) do indicate compaction, and scanning electron micrographs (data not shown) of the membrane subjected to 600 psi (4.140 MPa) also indicated compaction. Therefore, for the membranes used in this study, the onset of compaction occurs at some critical pressure between 100 psi (0.689 MPa) and 600 psi (4.140 MPa).

The finding of no compaction during pretreatment allows us to assume that the resistance to solute transport in the porous media membrane backing, R_{ps}, is a constant among the different pretreatment methods, including saturation at 50 psi.

Pseudo Steady State Permeability With NaCl As Solute

Figure 7 reports average permeabilities following the four different pretreatment methods obtained from stir cell tests in the normal orientation along with the relative standard deviations for each data set. Figure 8 reports the same information as figure 7 for stir cell test performed in the inverse orientation. The information reported in both figures 7 and 8 is for the 18th hour of operation, chosen to represent operation during steady state after the decay of any start-up transients.

Since in inverse orientation the porous backing is in contact with the salt solution, the 50-psi pretreatment plus salt-water soak has relevance. The 50-psi/salt-water soak does not have relevance for normal-orientation operation since the porous backing would be in contact with distilled water, and the effect of solute diffusion into the distilled water bulk from the salt soaked porous backing could not be adequately factored into the data evaluation. Measurements in the inverse orientation on membranes pretreated by soaking in pure water were not included for two reasons. First, this pretreatment was rejected on the basis of its normal orientation relative standard deviation, 43%, which placed the reported average permeability in serious doubt. The second reason was the manufacturer's recommendation against using water soaking as a pretreatment method.

Two things are immediately obvious from a comparison of figures 7 and 8. First, the average permeabilities in the inverse orientation were always higher than the average permeabilities in the normal orientation. This first observation is in conflict with the existing models in the literature (see figure 5). The second observation is that the pretreatment method governs the size of the relative standard deviations. The relative standard deviations are equivalent for the same pretreatment method irrespective of the operational orientation.

Since repeatability in crystallization is crucial, further exploration of the relative standard deviations was appropriate. The rank order from lowest to highest relative standard deviation is 50-psi (0.345 MPa) pressure pretreatment [8.1%], 50-psi/salt water soak [20.7%], 100-psi (0.689 MPa) pressure pretreatment [22.7%], no pretreatment [23.2%], and finally soaking in pure water [43.2%]. These variations result from variations in the "internal concentration polarization" which is a function of R_{ps}, B, and σ_s (equations 15 and 16). Since the resistance to solute transport in the porous media backing, R_{ps}, is constant among these pretreatment methods (compaction data above) then this increase in relative standard deviation apparently indicates increasing damage to the membrane skin. In transport modeling, this would result in increasing values of B, the solute permeability of the skin, and a decrease in σ_s, the solute reflection coefficient.

Dynamic Data: Permeability vs. Time With NaCl As Solute

Figure 9 presents the dynamic changes in the permeability of membranes following both the 50-psi (0.345 MPa) pressure pretreatment and 100-psi (0.689 MPa) pressure pretreatment operations under normal and inverse orientations with the osmotic driving force of NaCl solutions. Since these data result from stir cell experiments, the time axis also reflects a decrease in osmotic driving force, $\Delta\pi$, and a decrease in water flux, J_w. The dynamics of the normal orientation may reflect a growing concentration of solute in the porous media backing with time due to solute flux across the membrane skin.

The permeabilities of the membranes in the inverse orientation show approximately a 15% decrease in membrane permeability from the 1st to the 18th operational hours. This decrease is in contrast to the 46% permeability decrease observed in normal orientation. This last statement is in conflict with the existing models in the literature in two respects (see figure 5). First is the reduced sensitivity of the inverse orientation compared to normal orientation to changes in water flux and, second, the direct relation between J_w and L_p instead of its predicted inverse relationship.

Figure 10 presents the dynamic changes in permeability of membranes with no pretreatment. In comparison to the pressure treatments, the inverse orientation shows a greater change in permeability with time (32% decrease in permeability between the 1st and 18th operational hours vs. the 15% decrease in figure 9). This may indicate an increase in skin damage with time as the untreated membrane undergoes a soaking treatment during the course of the experiment.

The most probable explanation for the inverse orientation permeability decline is, in part, the counter-diffusion of the solute through the membrane. Such a counter-diffusion would change, with time, the solute concentration on the pure-water feed side of the membrane. Such a change in solute concentration, C_l, was not accounted for in calculating the time dependence of L_p (equation 16). The inverse orientation permeability decline, therefore, is a dynamic of the stir cell test equipment and not a dynamic of the membrane itself. This logic does not totally extend to the RO membranes in the normal orientation since their L_p time dependence is more dramatic in the initial hours of flux and becomes nearly time independent after 18 hours. In addition, after 18 hours, the L_p's in normal orientation decreased by 41% to 63% (Figure 9) while the L_p's in inverse orientation decreased by only 6% to 23%.

Osmotic Dewatering With MPD As Solute

In addition to sodium chloride solutions, MPD mother liquor, a common crystallization solution for nucleic acids, was studied. This solution consisted of 12% 2-methyl-2,4-pentanediol (pKa > 14.0), 0.4 molar ammonium acetate, and 0.025 molar magnesium chloride. In common use, the solution also contains sodium cacodylate as a preservative and buffer (buffering for a pH = 7.0). The

above solution maintained a pH of 6.95 to 7.0 throughout the experiments. No significant ion speciation change occurs in the above solution between pH of 7.0 and 6.95, and microorganism growth was not an issue. For purposes of safety and environmental waste minimization, we omitted the sodium cacodylate normally used with this solution, Kundrot (1997).

All of the osmotic flux experiments for MPD osmotic dewatering used membranes with a 50 psi (0.345 MPa) pressure pretreatment, the best of the tested pretreatment methods. Figure 11 presents the dynamic changes in membrane permeability for osmotic dewatering with MPD under both normal and inverse orientations. The 18th hour average permeability coefficients were 8.36×10^{-9} m/sec MPa in normal and 36.9×10^{-9} m/sec MPa in inverse orientation with a relative standard deviation of 23.8%. These results are consistent with the sodium chloride tests in that the permeability is higher in the inverse orientation than in the normal orientation. The dynamic results for the inverse orientation (figure 11) are similar to the no pretreatment dynamic (figure 10) with a 25% decrease in permeability between the 1st and 18th operational hours; this similarity may indicate an action of the solvent on the membrane.

Solvent interaction with membrane components could occur if there is a similarity in polymer and solvent solubility parameters, δ. A condition for solubility of a polymer in a solvent is for the $\delta(\text{solute}) \cong \delta(\text{polymer}) \pm 1.1$ $\text{MPa}^{1/2}$, Kildebrand and Scott (1964). The solubility parameter for 2-methyl-2,4-pentanediol is $\delta = 19.8$ $\text{MPa}^{1/2}$, Brandrup and Immergut (1975), while the materials in the composite RO MS-10 membrane sandwich have the following solubility parameters: fully aromatic polyamides, $\delta \cong 23$ $\text{MPa}^{1/2}$; polysulfones, $\delta \cong 21.5$ to 22.1 $\text{MPa}^{1/2}$; and polyesters, $\delta \cong 19.3$ to 21.6 $\text{MPa}^{1/2}$, Barton (1990). These similarities in solubility parameters, particularly for polyesters, indicate the possibility of membrane/solute interaction via polymer swelling and/or solubilization.

Equivalent Hydraulic Pressures, ΔP_e

Equivalent hydraulic pressure is defined as the mechanical pressure required to achieve the fluxes measured in the osmotic flux test

$$\Delta P_e = J_w/A \tag{17}$$

And can be estimated from

$$\Delta P_e \cong \sigma\Delta\pi = L_p\Delta\pi/A \tag{18}$$

Table 1, for the 18th hour in each experimental condition, presents the average osmotic driving force applied, the equivalent hydraulic pressure, and their ratio ($\Delta\pi/\Delta P_e \cong 1/\sigma = A/L_p$). By comparing the information in table 1 with the PRO flux equation (equation 4) it is seen that it is incorrect to assume that a large osmotic driving force allows the neglecting of small mechanical pressures during osmotic dewatering crystallization (equation 3).

CONCLUSIONS

The adopted literature models for membrane permeability in aqueous osmosis operations predict the order-of-magnitudes for the membrane permeability, L_p. The literature models, however, incorrectly predict the optimum membrane orientation in an osmotic dewatering operation and the membrane permeability relationship with dewatering rate (see figure 4). Internal concentration polarization within the reverse-osmosis membrane backing has a significant impact on the membrane permeability in that it reduces the effective hydraulic permeability by orders of magnitude. We also

conclude that the method of pretreatment of the reverse-osmosis membrane prior to its use has a significant effect on the repeatability of the osmotic dewatering crystallization process.

The overall water permeability of a membrane depends on the level of water saturation in the porous media components of the membrane. The level of water saturation in rigid porous membranes is a direct function of the pressure used in the pretreatment, Scovazzo, et al (1997). Since the permeabilities of the membranes in this test did not increase between the 50-psi (0.345 MPa) and 100-psi (0.689 MPa) pressure pretreatments, we conclude that complete saturation with water of the porous media backing occurs at low pretreatment pressures (less than or equal to 50 psi, 0.345 MPa or 3.4 atm).

The increase in relative standard deviation of the membrane permeability with pretreatment pressures indicates that, even without compaction of the membrane backing, damage to the membrane skin is a direct function of applied pressure.

K.L. Lee, et al (1981) validated the applicability of the normal orientation models (equations 12 and 15). Their observations, combined with the apparent lack of dependence of the permeability upon water flux, J_w, in inverse orientation invalidates the literature models (equations 14 and 16) for MS-10 composite membrane as used in osmotic dewatering. The normal models would predict the results of this study by using an effective NaCl diffusivity of 10^{-12} m^2/sec. This effective diffusivity is 3 orders of magnitude less than the diffusivity of NaCl in bulk water, apparently owing to the combined effects of the membrane composite interfaces, porosity, tortuosity, and adsorptivity/desorptivity of the porous media backing.

From a practical perspective in designing osmotic dewatering crystallization systems the following are the recommendations resulting from this work:

1. *Never soak the membrane in water as a pretreatment.* Based on the manufacturer's advice and the results of this work, pre-soaking without applied pressure leads to significant damage to the membrane skin and, therefore, poor repeatability of water flux among crystallization runs.
2. *Use a 50-psi (0.345 MPa) pressure pretreatment.* This results in the best repeatability (<10% normalized standard deviation) and the highest permeabilities in the inverse orientation.
3. *Use inverse orientation for the membrane.* This results in minimal dynamics in the membrane permeability and, therefore, gives a pseudo linear response between the applied osmotic driving force and the dewatering rate. *Warning: This result comes from the testing of MS-10 membranes only. One should confirm this recommendation for other membranes.*
4. *Be aware of potential solvent/membrane interactions.* When the crystallization mother liquor contains an organic compound, the potential may exist for this compound to have a detrimental interaction with the polymers in the membrane.
5. *Do not neglect small mechanical pressure differences across the membrane.* The equivalent hydraulic pressure calculations in the "Experimental Results and Discussion" section (table 1) indicate that mechanical pressures of only one hundredth (0.01x) to one thousandth (0.001x) of the applied osmotic driving force will have effects on the osmotic dewatering rates.

ACKNOWLEDGEMENTS

We thank D. Dela Cruz of Desalinization Systems, Inc., San Diego, and Osmonics Inc., Minnetonka, MN, for supplying expertise and membrane materials for this study. We also thank Dr.

Veronica Reinsch for operating the Acoustic TDR system used in this study and Mr. Michael G. Sportiello for supplying expertise in laboratory methods in osmotic dewatering. NASA Grant NAG8-1165 supported this research.

APPENDIX A: Development of the Osmotic Flux Equation and Solute Concentration in the Membrane Porous Backing Equation for Inverse Orientation Osmotic Dewatering

Assumptions 1. No fluid boundary layers, 2. Δx[porous backing] $\cong \Delta x$, 3. $x_h \cong \Delta x$, and 4. Ideal Solutions (van't Hoff equation applies)

Governing Equations for Membrane Skin (referencing figure A1)

Rewriting equation 7 in the main text gives for the water flux:

$$J_w = A\sigma_s\Delta\pi_{eff} \quad (A1)$$

Where: $\Delta\pi_{eff} = \pi_f - \pi_l$, π_f = Osmotic pressure at the interface between the skin and the porous media backing, and π_l = Osmotic pressure of the low-concentration solution.

Rewriting equation 8 in the main text gives the solute flux as:

$$- J_s = B(C_f - C_l) \quad (A2)$$

Governing Equations for the Membrane Porous Backing

Balance on solute in backing (equation 9):

$$J_s = J_w C_s - D_e dC_s/dx \quad (A3)$$

Where: C_s = Solute concentration in the porous media backing at position x and D_e = The effective diffusivity of the solute in the porous media backing.

Divide equation A3 by $-D_e$

$$-J_s/D_e = (-J_w/D_e)C_s + dC_s/dx \quad (A4)$$

The general solution of equation A4 for C_s via an "integral factor" application is:

$$C_s = Z\exp[(J_w/D_e)\, x] + J_s/J_w \quad (A5)$$

Apply the boundary condition at $x = x_h \cong \Delta x$; $C_s = C_h$ gives the following:

$$Z = (C_h - J_s/J_w)\exp[(-J_w/D_e)\,\Delta x] \quad (A6)$$

and

$$C_s = (C_h - J_s/J_w)\exp[(J_w/D_e)\,(x - \Delta x)] + J_s/J_w \quad (A7)$$

Apply the boundary condition at $x = 0$; $C_s = C_f$ and defining $R_{ps} = \Delta x / D_e$ gives the following:

$$C_f = (C_h - J_s/J_w)\exp[(-J_w R_{ps}] + J_s/J_w \quad \text{(A8)}$$

Note Equation A8 is also equation 13 in the main text.
Now, substitute equation A2 into equation A8, expand, and simplify:

$$C_f = \frac{\left[C_h - \left(\frac{B}{J_w}C_l\right)\right]\exp(-J_w R_{ps}) + \left(\frac{B}{J_w}\right)C_l}{1 + \frac{B}{J_w}\left[1 - \exp(-J_w R_{ps})\right]} \quad \text{(A9)}$$

Now,

$$\frac{\Delta\pi_{eff}}{\Delta\pi} = \frac{\pi_f - \pi_l}{\pi_h - \pi_l} \cong \frac{C_f - C_l}{C_h - C_l} \quad \text{(A10)}$$

Substitute A9 into A10, expand, and simplify:

$$\frac{\Delta\pi_{eff}}{\Delta\pi} = \frac{1}{1 - \left(\frac{C_l}{C_h}\right)}\left\{\frac{\exp(-J_w R_{ps}) - \left(\frac{C_l}{C_h}\right)}{1 + \frac{B}{J_w}\left[1 - \exp(-J_w R_{ps})\right]}\right\} \quad \text{(A11)}$$

Or,

$$\Delta\pi_{eff} = \frac{\Delta\pi}{1 - \left(\frac{C_l}{C_h}\right)}\left\{\frac{\exp(-J_w R_{ps}) - \left(\frac{C_l}{C_h}\right)}{1 + \frac{B}{J_w}\left[1 - \exp(J_w R_{ps})\right]}\right\} \quad \text{(A12)}$$

Note,

$$\frac{\Delta\pi}{1 - \frac{C_l}{C_h}} \cong \frac{\pi_h - \pi_l}{1 - \frac{\pi_l}{\pi_h}} = \pi_h \quad \text{(A13)}$$

Combine equations A1, A12, and A13 to get:

$$J_w = A\pi_h\sigma_s\left\{\frac{\exp(-J_w R_{ps}) - \left(\frac{C_l}{C_h}\right)}{1 + \frac{B}{J_w}\left[1 - \exp(-J_w R_{ps})\right]}\right\} \quad \text{(A14)}$$

Equation A14 is also equation 14 in the main text.

LIST OF SYMBOLS

A = Hydrodynamic Permeability (m/sec MPa)
B = Solute Permeability (m/sec)
C_f = Solute concentration at the interface between the skin and the porous media backing, see figure 1 (moles/m^3)
C_h = Solute concentration in the high concentration solution (moles/m^3)
C_l = Solute concentration in the low concentration solution (moles/m^3)
C_{ro} = Initial osmolarity of the high-concentration solution (osmoles/m^3)
C_s = Solute concentration in the porous media backing at position x (moles/m^3)
C_{sk} = Solute concentration on the skin side of the membrane (moles/m^3)
C_{wo} = Initial osmolarity of the low-concentration solution (osmoles/m^3)

D_e = The effective diffusivity of the solute in the porous media backing (m^2/sec).
J_s = Solute flux (moles/m^2 sec)
J_w = Water Flux (m/sec)
L_p = Membrane permeability coefficient (m/sec MPa)
Osmolarity = Total ion and non-ionic solute molarity (osmole/m^3)
R = Ideal gas constant (m^3MPa/mol K)
R_{ps} = Resistance to solute transport in the porous media membrane backing = $\Delta x / D_e$ (sec/m)
S = Surface area of membrane (m^2)
T = Absolute temperature (Kelvin)
t = Elapsed time (sec)
V = Volume of the water that has permeated through the membrane at time t (m^3)
V_o = Initial volume of the low-concentration solution(m^3)
$\Delta\pi$ = Osmotic pressure difference across the membrane (MPa)
π_f = Osmotic pressure at the interface between the skin and the porous media backing (MPa)
π_h = Osmotic Pressure of the high-solute-concentration solution (MPa)
π_{sk} = Osmotic pressure on the skin side of the membrane (MPa)
σ = Solute reflection coefficient (dimensionless)
σ_s = The skin solute reflection coefficient (dimensionless)
ΔP = Mechanical pressure difference across the membrane (MPa)
ΔP_e = Equivalent Hydraulic Pressures (MPa)
Δx = Membrane thickness (m)

References

Barton AFM; 1990; Handbook of Polymer-Liquid Interaction Parameters and Solubility Parameters; CRC Press; Boca Raton, Florida

Blundell TL, Johnson LN; 1976; in: Protien Crystallography, Eds. B. Horecker, J. Marmur and H.A. Scheraga; Academic Press, New York; p.68

Brandrup J, Immergut EH; 1975; Polymer Handbook, 2nd Edition; Wiley-Interscience Publication; New York

Hildebrand JH, Scott RL; 1964; The Solubility of Nonelectrolytes, 3rd Edition; Dover Publications; New York

Jonsson G; 1980; The Influence Of The Porous Sublayer On The Salt Rejection And Reflection Coefficient Of Asymmetric CA Membranes; *Desalination*, 34, 141-157

Kools WFC; Konagurthu S; Greenberg AR; Bond LJ; Krantz WB; van den Boomgaard T; Strathmann H; 1998; "Use of Ultrasonic Time-Domain Reflectometry for Real-Time Measurement of Thickness Changes During Evaporative Casting of Polymeric Films;" Journal of Applied Polymer Science; Vol. 69, No. 10; p. 2013

Kundrot CE; 1997; Preparation and Crystallization of RNA: A Sparse Matrix Approach; *Methods in Enzymology*; Vol. 276, p. 143

Lee CY, Sportiello MG, Cape SP, Ferree S, Todd, P; 1997; Characterization and Application of Osmotic Dewatering to the Crystallization of Oligonucleotides; *Biotechnol. Prog.* 13, 77-81

Lee KL, Baker RW, Lonsdale HK; 1981; Membranes For Power Generation By Pressure-Retarded Osmosis; *Journal of Membrane Science*, 8, 141-171

McPherson A; 1999; Crystallization Of Biological Macromolecules; Cold Spring Harbor Laboratory Press; Cold Spring Harbor, NY

Mehta GD, Loeb S; 1978; Internal Polarization In The Porous Substructure Of A Semipermeable Membrane Under Pressure-Retarded Osmosis; *Journal of Membrane Science*, 4, 261-265

Mulder M; 1996; Basic Principles of Membrane Technology; Kluwer Academic Publisher; Dordrecht, Netherlands

Reali M, Dassie G, and Jonsson, G; 1990; Computation Of Salt Concentration Profiles In The Porous Substrate Of Anisotropic Membranes Under Steady Pressure-Retarded-Osmosis Conditions; *Journal of Membrane Science*, 48, 181-201

Scovazzo, P, Todd P, Burgos J, Lattarulo N, Hoehn A; 1997; Membrane-Based Humidity Control in Microgravity - A Comparison of Membrane Material Performance and Design Equations; 27th International Conference on Environmental Systems; Lake Tahoe, Nevada; July 14-17, 1997; SAE Technical Paper Series #972275; Warrendale, PA.

Todd, P, Sikdar SK, Walker C, Korszun ZR; 1991; Application of Osmotic Dewatering to the Controlled Crystallization of Biological Macromolecules and Organic Compounds; *Journal of Crystal Growth*; 110, 283-292

FIGURES AND CAPTIONS

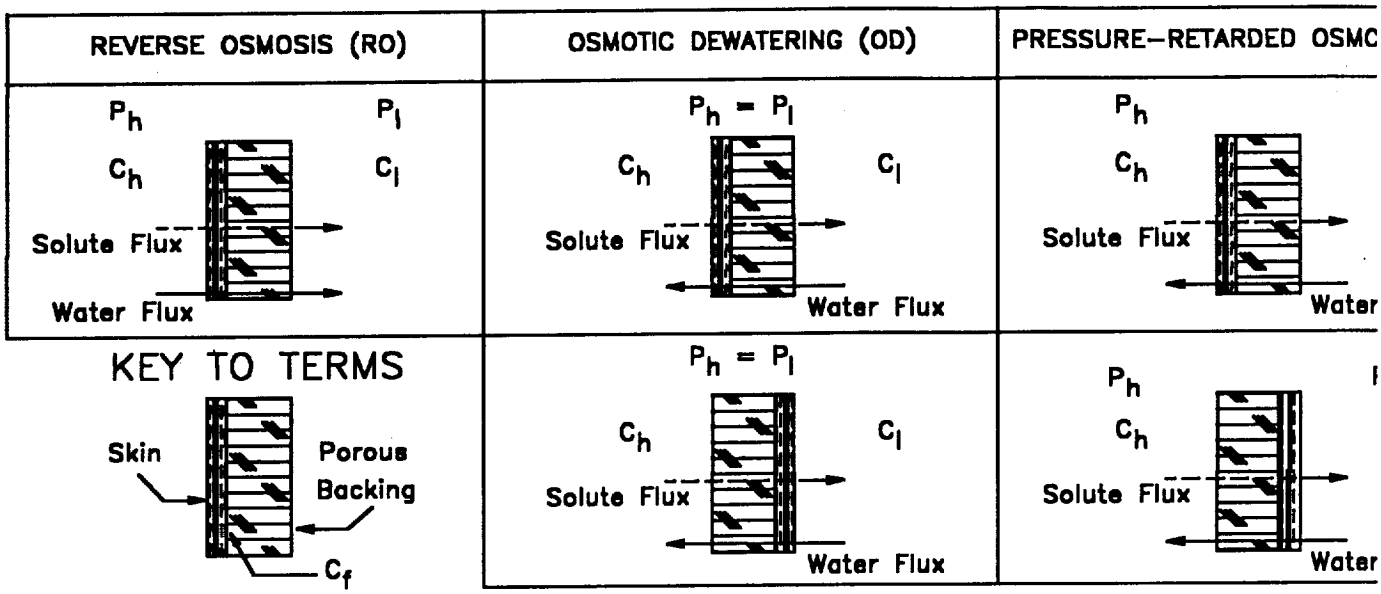

Figure 1: Membrane Processes and Orientations; Definitions of experimental conditions applied to RO membranes with microporous backing showing both orientations, "Normal" and "Inverse,' and the three applications. P_h = High Mechanical Pressure, P_l = Low Mechanical Pressure, C_h = High Solute Concentration, C_l = Low Solute Concentration, and C_f = Solute Concentration at the Skin/Backing Interface.

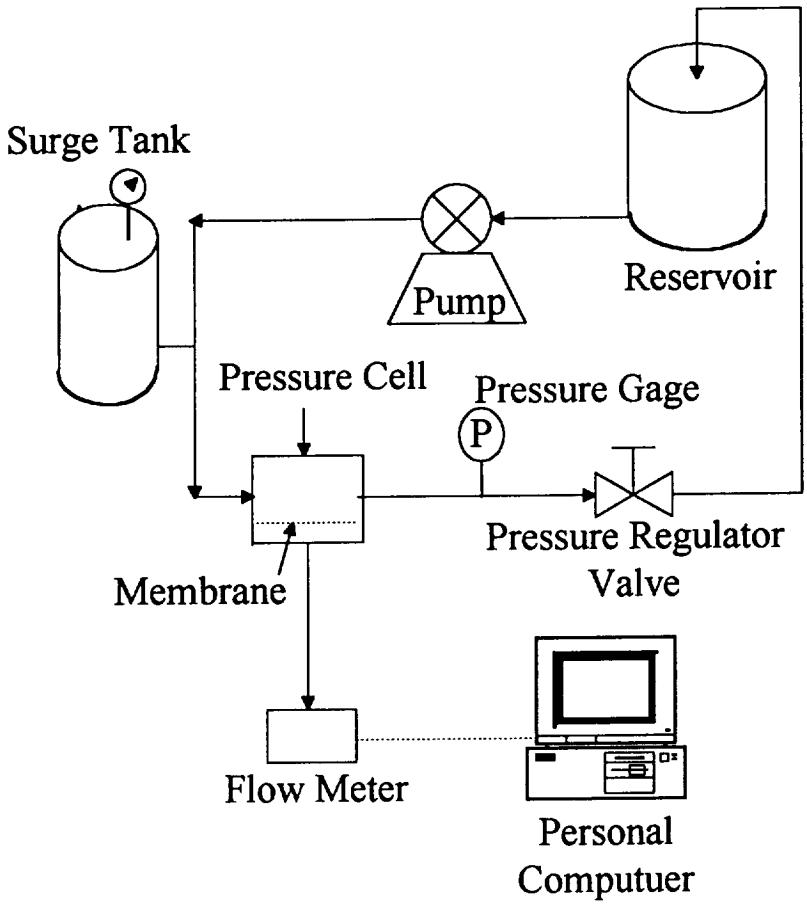

Figure 2: Mechanical pressurizing system used for pressurized pretreatments, flux measurements in mechanical pressure driven flow, and compaction measurements by ATDR.

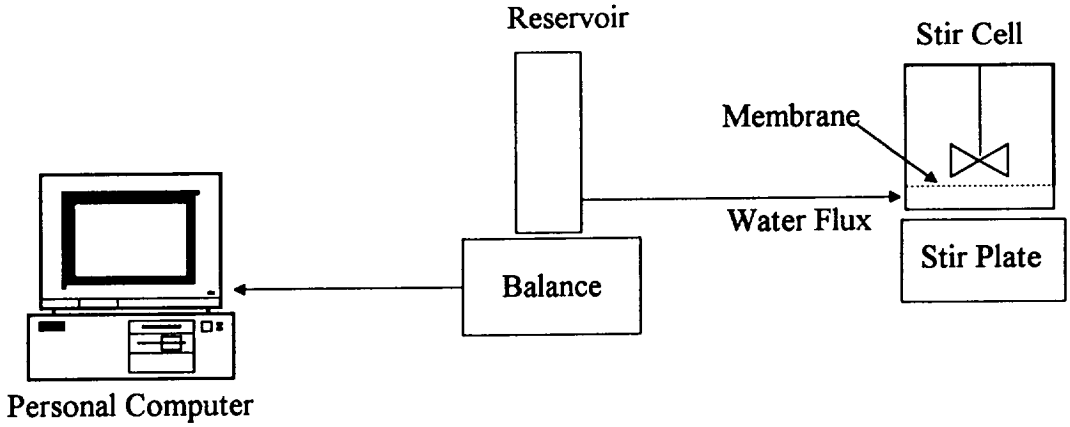

Figure 3: Osmotic stir cell system for determining the osmotic permeability coefficient

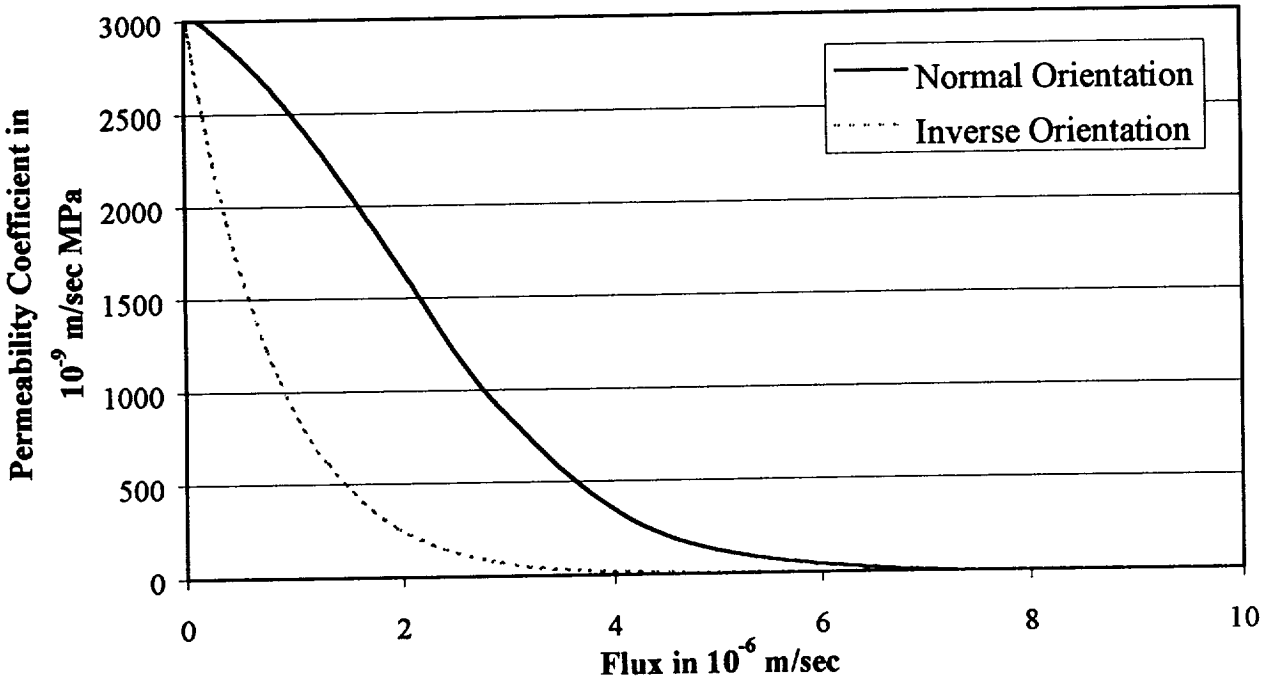

Figure 4: Model Prediction of J_w vs. $\Delta\pi$ in OD using equation (12) for Normal (solid line) and equation (14) for Inverse (dotted line) Orientations with the following parameters: Water Permeability, $A = 4 \times 10^{-5}$ m/sec MPa; Salt Permeability, $B = 2 \times 10^{-7}$ m/sec; Backing Resistance, $R_{ps} = 1.33 \times 10^{6}$ sec/m; Skin Reflection, $\sigma_s = 0.98$; and $C_l/C_h = 0$.

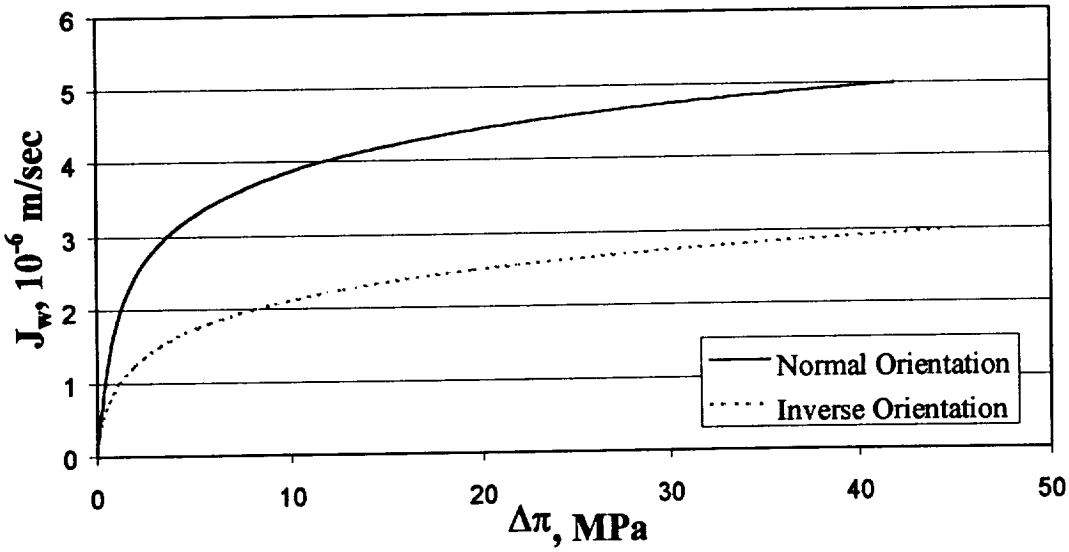

Figure 5: Model Prediction of L_p vs. J_w using equation (15) for Normal (solid line) and equation (16) for Inverse (dotted line) Orientations with the following parameters: Water Permeability, $A = 4 \times 10^{-5}$ m/sec MPa; Salt Permeability, $B = 2 \times 10^{-7}$ m/sec; Backing Resistance, $R_{ps} = 1.33 \times 10^{6}$ sec/m; Skin Reflection, $\sigma_s = 0.98$; and $C_l/C_h = 0$.

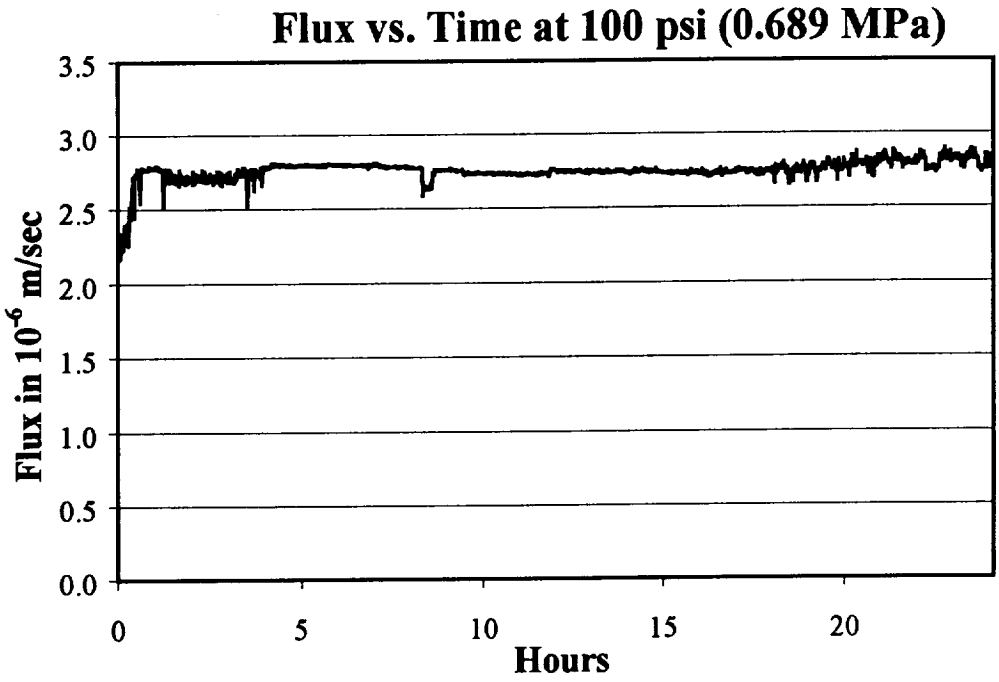

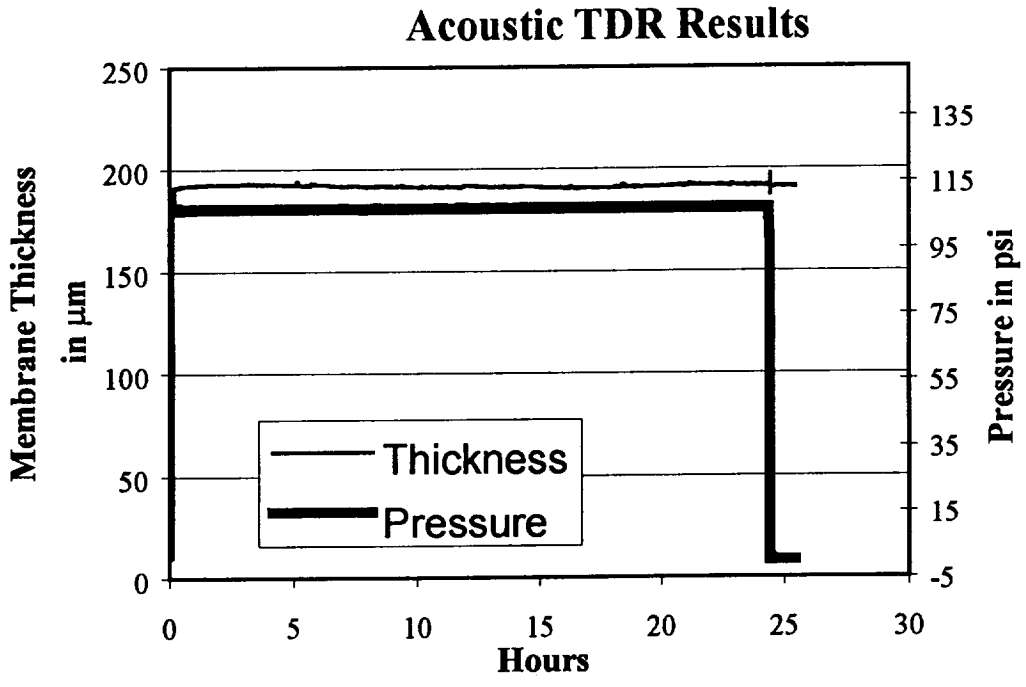

Figure 6: Compaction test results. Shows that at the RO membranes of this study do not undergo compaction at pressures of 0.689 MPa (100 psi) or less.

Figure 7: Pseudo steady-state permeabilities measured at the 18th hour of flux in normal orientation following four pretreatments. The relative standard deviation (standard deviation divided by mean permeability) points, connected by lines, show a consistent pattern between figures 7 and 8, which is the pattern in standard deviation vs. pretreatment method (for No Pretreatment, 50 psi Pretreatment, and 100 psi Pretreatment).

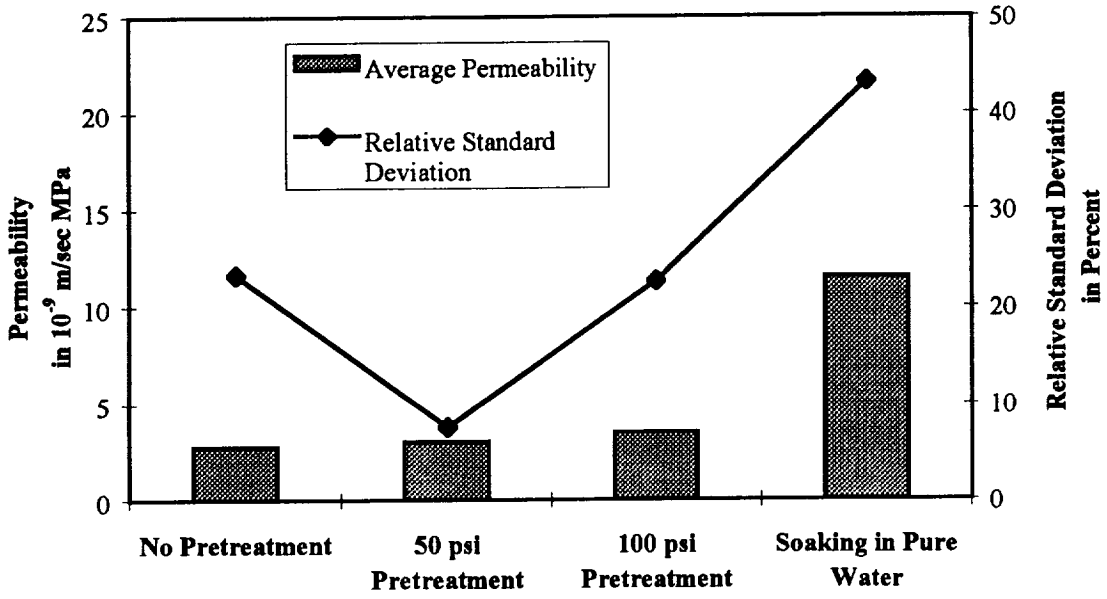

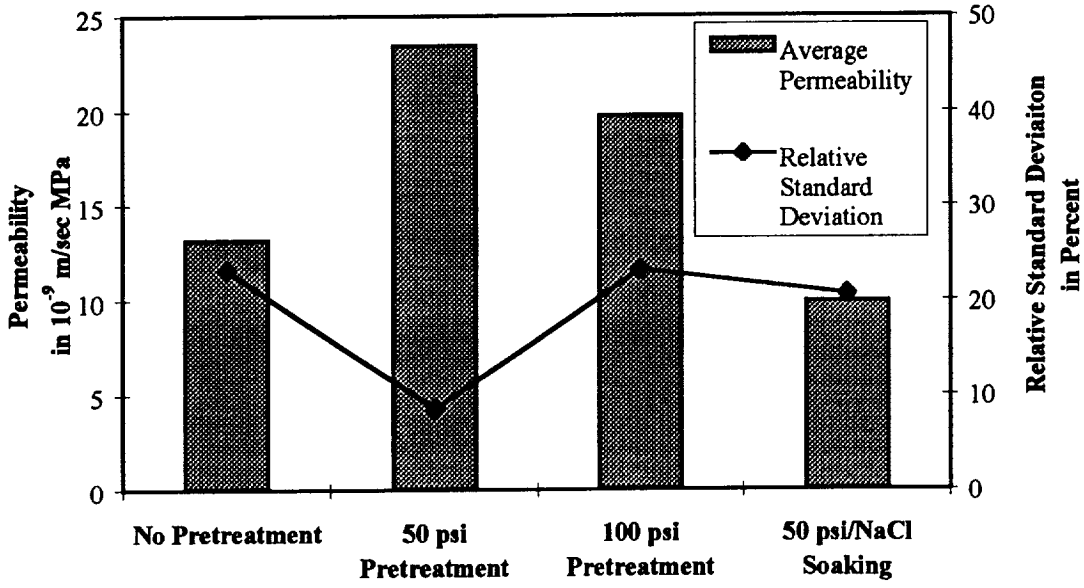

Figure 8: Pseudo steady-state permeabilities measured in the 18th hour of flux in inverse orientation following four pretreatments. The relative standard deviation (standard deviation divided by mean permeability) points, connected by lines, show a consistent pattern between

figures 7 and 8, which is the pattern in standard deviation vs. pretreatment method (for No Pretreatment, 50 psi Pretreatment, and 100 psi Pretreatment).

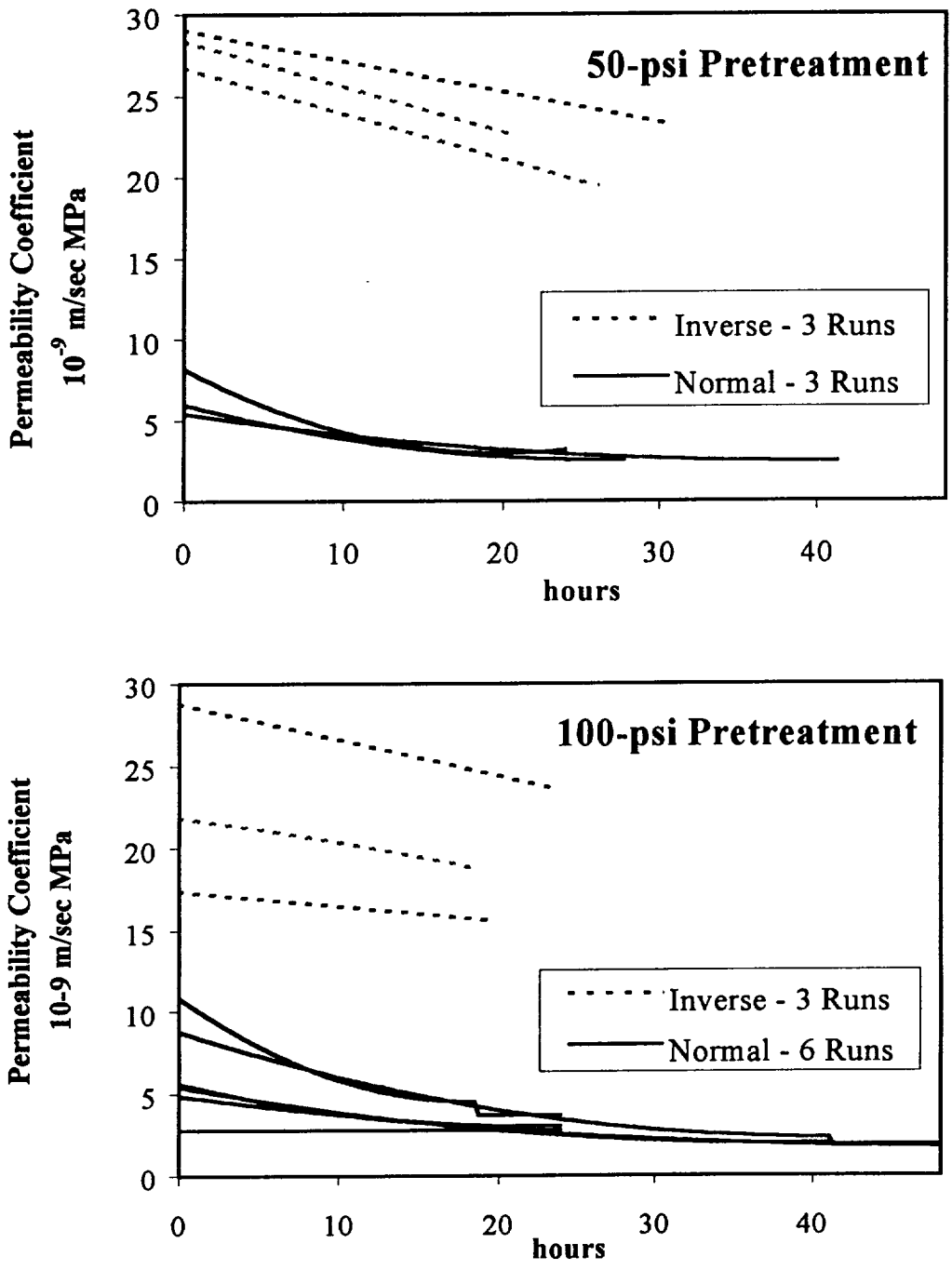

Figure 9: Permeability vs. time in two orientations for membranes subjected to 50-psi and 100-psi pretreatments. Table 1 gives the osmotic driving forces during the 18th of flux.

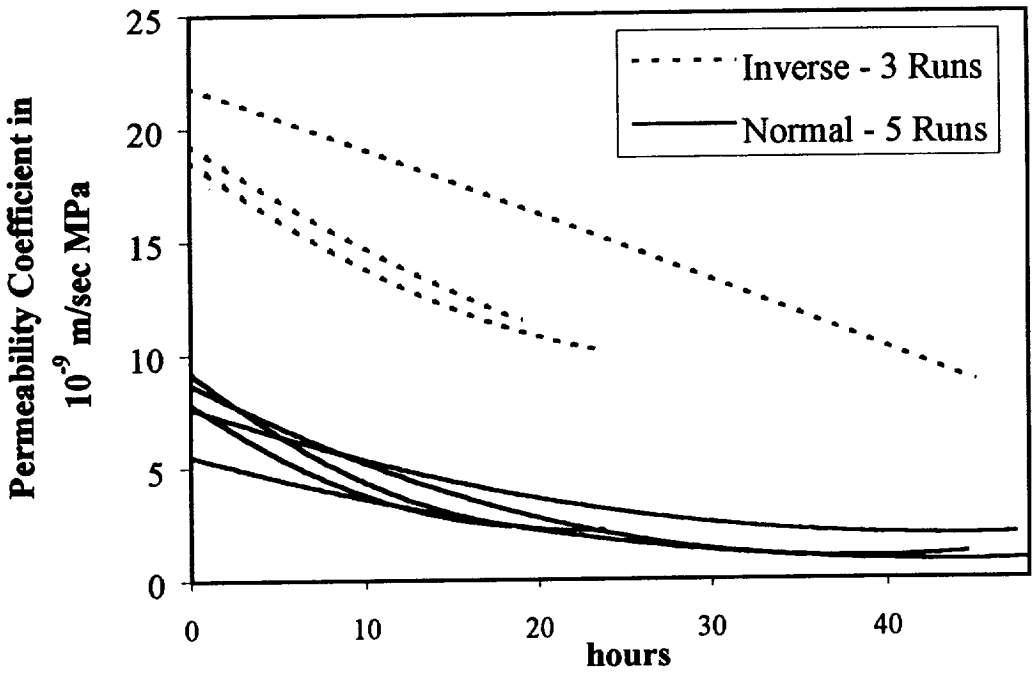

Figure 10: Permeabilities vs. time in two orientations for membranes subjected to no pretreatment. . Table 1 gives the osmotic driving forces during the 18th of flux.

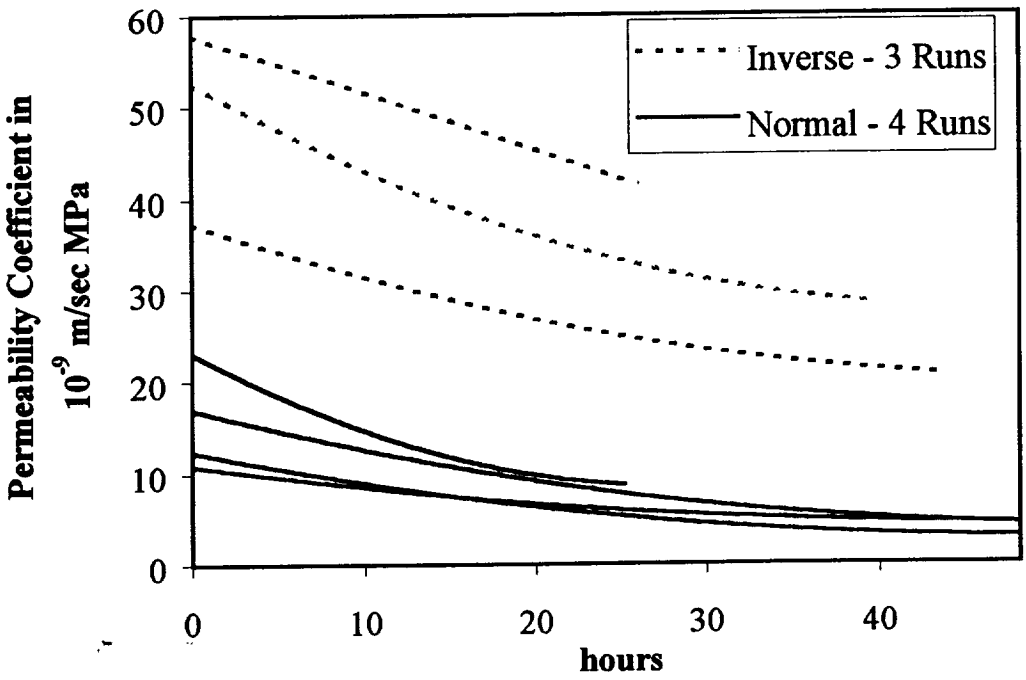

Figure 11: Permeabilities vs. time for MPD Osmotic Dewatering. Table 1 gives the osmotic driving forces during the 18th of flux.

Table 1: Equivalent Hydraulic Pressures for The 18th Hour of Osmotic Flux (Using A = 4×10^{-6} m/sec MPa)

	Applied Osmotic Pressure (MPa)	Equivalent Hydraulic Pressure (MPa)	Ratio (Osmotic/ Hydraulic)
No Pretreatment - Normal	12	0.0078	1560
No Pretreatment - Inverse	10	0.033	313
50-psi Pretreatment - Normal	12	0.0089	1370
50-psi Pretreatment - Inverse	8.8	0.051	174
100-psi Pretreatment - Normal	12	0.010	1217
100-psi Pretreatment- Inverse	9.4	0.045	2061
Soak in Pure Water - Normal	14	0.033	410
50/NaCl Soak - Inverse	11	0.029	379
MPD - Normal	4.0	0.0086	463
MPD - Inverse	3.4	0.031	108

APPENDIX B: Mathematical Processing of Stir Cell Data

In Figure 3 the computer logged datum is total grams lost from the reservoir with time. The objective is to calculate the time dependency of L_p. Starting with total grams lost, g_{lost}, from the reservoir from start of experiment until time T_y and

$$J_w = L_p \Delta\pi \qquad \text{(B1)}$$

Where: $\Delta\pi = RTM_iV_i/[V_i + \rho(g_{lost})]$

R = Ideal gas law constant

T = Absolute Temperature

M_i = Initial osmolarity of stir cell solution

V_i = Initial volume of stir cell solution

ρ = Density of water = 1.0 g/ml (1000 Kg/m^3)

then:

$$g_{lost} = \int_0^{Ty} SJ_w dt \tag{B2}$$

Where: S = Surface area of membrane. So:

$$g_{lost} = \int_0^{Ty} SJ_w dt = \int_0^{Ty} S(L_p \Delta\pi) dt \tag{B3}$$

Now S is a constant, so:

$$g_{lost}/S = \int_0^{Ty} L_p \Delta\pi dt \tag{B4}$$

Define $L_p(T_y)$ = Average L_m from 0 to T_y, now:

$$g_{lost}/S \cong L_p(T_y) \sum_0^{Ty} \Delta\pi\Delta t \tag{B5}$$

Rearranging,

$$L_p(T_y) = \frac{g_{lost}/S}{\sum_0^{Ty} \Delta\pi\Delta t} \tag{B6}$$

Now define the quantity ***permeability*hr*** = $L_p(T_y)$*T_y

This gives the time dependency of Lp as:

$$L_p = \frac{d[L_p(T_y) * T_y]}{dt} \tag{B7}$$

Due to numerical integration, the error in L_p is on the order of Δt^2.

Chapter 22

Osmotic dewatering fluxes in low-gravity crystallization hardware

Ariel Frometa, Paul Scovazzo and Paul Todd

CHAPTER 22
OSMOTIC DEWATERING FLUXES IN LOW GRAVITY CRYSTALLIZATION HARDWARE

Ariel Frometa, Paul Scovazzo, and Paul Todd
Department of Chemical Engineering
University of Colorado at Boulder, Boulder, CO 80309-0424

Abstract:

This NASA. funded research focuses on the dynamics of crystal growth in space flight equipment. Osmotic Dewatering Crystallization (OD) is a method that obtains high-quality organic molecule crystals via active control of the dewatering rate. In OD a concentration gradient is established across a reverse osmosis (RO) membrane as the driving force for the flux of water out of the lower concentration solution. The RO membrane's performance and the apparatus used in this research require a model which includes the concepts of gas diffusion, membrane internal polarization and mechanical pressures generation. The developed model predicts the water flux through a reverse osmosis membrane due to an osmotic pressure gradient. Experimental data was then compared to the predicted water fluxes.

Introduction:

Introduced in 1990 by Todd et. al., OD is a method that allows for control of a crystal's growth rate. Turbulence is a factor that determines the growth rate and size of crystals at the nucleation sites. However, this detrimental effect on the crystal quality is not found in microgravity situations. Therefore, highly ordered crystals grown in low-gravity situations can aid in determining the crystals' structure and properties which could lead to breakthroughs in pharmaceutical and biological fields.

In OD the lower-concentration solution contains the species to be crystallized due to the difference in osmolarity across the RO membrane. The osmotic pressure gradient acts as a driving force for the water to permeate through the membrane into the high-concentration solution. However, Paul Scovazzo et al. found a phenomenon known as internal polarization is indeed a factor in establishing the driving force. By using similar stir cell experiments, Scovazzo et al. developed a model to predict the concentration at the skin-backing interface which varied along the thickness of the membrane due to the polarization phenomenon.

This work adjusted that model to include any mechanical pressure generation and also included an additional resistance term due to gas diffusion. The FPA apparatus used in this research adopted OD to space flight and combined elements of Hanging Drop Crystallization with osmotic dewatering.

Materials and Methods:

Figure 1 shows the schematic of the insert used in the FPA. Each insert contains four dewatering wells. At the end of the insert a 50 psi pretreated RO membrane was placed between two protective teflon gaskets and then followed by a metal base. These parts contain holes with diameters the same as those of the dewatering wells. They are all aligned using a pin that extends from the polycarbonate insert through the metal base. The four dewatering wells were loaded with solutions of equal concentrations and then sealed on one end. (Refer to Appendix A for FPA Insert Assembly Procedure).

Figure 2 shows the schematic of the FPA glass barrel before activation (Refer to Appendix B for Loading and Lubricating Procedure For FPA Containing One Insert). In this experiment eight different cases were studied. Each two inserts were loaded with 0, 1, 2 and 3 molar (M) sodium chloride solutions. For each loaded insert with the four dewatering wells of the same solution, two experimental conditions were established. One loaded insert was run in a vertical orientation and the other in a horizontal orientation. To prevent any osmotic pressure gradient before activation, chamber A was filled with 1.5 ml of sodium chloride solution with the same molarity as that of the solution of the dewatering wells. Chamber B was then filled with 3 ml of the appropriate sodium chloride concentration such that when mixed with the chamber A solution a, 3 M sodium chloride final concentration would be obtained. The loaded FPA glass barrels were then put in sheaths and each capped with a plunger. The sheaths were then placed and covered in a GAP device.. A hand crank was then turned to push down on all of the plungers at once at a rate of 1 revolution every 4 seconds until all of the FPA glass barrels were activated (Refer to Figure 3).

Figure 4 shows a schematic of a dewatering well. After activation, the width (W) of the liquid in each dewatering well was measured using a calibrated ocular microscope over a period of several days. This experimental data was then graphed from which the flux rates could be determined.

Models:

The water flux is defined as the effective osmotic pressure difference across the membrane divided by the total sum of the resistances. In Scovazzo's et al. stir cell experiments internal polarization is taken into account by the following equation (See Figure 5):

$$J_w = A\Delta\Pi_e = ART(C_f - C_l)$$

$$J_w \neq A\Delta\Pi_a$$
$$\neq ART\,(C_h - C_l)$$

Where:

J_w	=	Water flux (cm/sec)
$\Delta\Pi_a$	=	Applied osmotic pressure difference (atm)
$\Delta\Pi_e$	=	Effective osmotic pressure difference (atm)
A	=	Hydrodynamic Permeability (cm/sec/atm)
R	=	Ideal gas constant
T	=	Absolute Temperature

In the porous media backing a solute balance at steady state gives

$$J_s = D_e dC_s/dx - J_w C_s$$

When this equation is solved with the appropriate boundary conditions the following equation is derived:

$$C_f = J_s/J_w + (C_h - J_s/J_w)\exp(-J_w R_{ps})$$

Where: J_s = Salt flux (osmol/cm^2/sec)

C_s= Solute concentration in the porous media backing at position x (mol/L)
D_e= Effective diffusivity of the solute in the porous media backing
R_{ps}= Resistance to solute transport in the porous media backing
Δx= Membrane thickness

However, the model must also take into account additional resistances. The first resistance is due to gas diffusion in the air gap in the well between the fluid and the membrane. The second is the resistance in the membrane and finally there is resistance in the boundary layer in the reservoir. The latter resistance was neglected in the initial development of the model.

Additionally, the osmotic pressure driving force was reduced by any mechanical pressures generated in the dewatering processes. First of all, the pressure generated by J_w leads to the compressibility of liquid water. For example, lets consider a 1M well solution at 50% dewatering. If septum 1 remained rigid, pressures of about 270 atm would be reached in the glass barrel. Consequently, this pressure is relieved by movement of the septum 1 at a pressure equal to the following:

Pressure = Static Friction/Area of septum 1

Experimental measurements of this pressure led to the following determination:

Pressure (gauge) $\cong$ 0.2 atm

Furthermore, as water continues to flux into the reservoir a pressure drop is established inside the dewatering well. 50% dewatering in a well with an initial concentration of 1M sodium chloride leads to a pressure drop of about 0.15 atm Therefore, a total mechanical pressure generation exits of about 0.35 atm. The total osmotic pressure difference is about 98 atm which leads to about a 0.4% impact on the osmotic driving force, and thereby significant. Since the pressure drop in the well is a function of J_w the following equation was derived:

$$P_{well} = P_i[1- (L_g/(L_g + \Sigma J_w \Delta t))]$$

Where:
P_{well} = Pressure drop in the well (atm)
P_i = Initial pressure of gas in the well (atm)
L_g = Initial length of gas (cm)
Δt = Elapsed time

Therefore, the model is developed under the following assumptions:

1. $J_s = 0 \Rightarrow \sigma_a = 1$
2. Mole fraction of water in air is negligible
3. Resistance due to boundary layer is negligible

The driving force was derived to be the following:

Driving force = $\Delta\Pi_e - \Delta P$

The resistance in the well due to the air gap was derived to be the following:

Air resistance = RTW/DV_m

Where: σ_a = Skin solute reflection coefficient (unitless)
ΔP = Mechanical pressure difference (atm)
D = Diffusivity of water vapor in air (cm^2/sec)
V_m = Molar volume of liquid (cm^3/mol)

The resistance in the RO membrane is defined as the following:

Membrane resistance = $1/A$

Therefore, the model equation for the water flux is equal to the following:

$$J_w = \frac{RT\left[\sigma C_{w,m} - C_{w,p}\right] - \left[P_{atm}\left(1 - \frac{L_w}{L_w + \int J_w dt}\right) + 0.2 \text{ atm}\right]}{\frac{RTW}{D V_w} + \frac{1}{A}}$$

Where: $\sigma = \text{Exp}(-JwRps)$

Experimental Results and Discussions:

The experimental results obtained were graphed in order to obtain profile of the reduction of liquid versus time (See Graphs 1-8). From this data the slopes of their linear fits (See Table 1-2) determined the water fluxes. The data indicates that over a period of about 80 hours the water fluxes increased with increasing osmotic pressure. A relatively accurate fit to the data is obtained by fitting the data to a line.

Moreover, due to the sensitivity of the exponential term in the final water flux the following assumption was made to fit the model:

$\sigma \cong \text{constant} = L_m/A\Delta x$

Where: L_m= Membrane permeability in barrers

This constant value was calculated from Scovazzo's stir cell experimental data.

The model was then compared to the experimental data for the case of the 0M well concentration for the horizontal case. It was also found that a 30% variation in the value of σ caused a substantial variation in the volume reduction profile. Then, keeping the value of σ fixed, an additional resistance term, Rbl was added to the flux model as a fitting parameter. This adjusted model contains Rbl as an additive term included to take into account and any additional resistances due to the boundary layer in FPA experiments. This number was then fitted until the model agreed with the experimental data for the case where $C_l = 0$ (See Graph 9). The following adusted model was derived:

$$J_v = \frac{RT\left[C_s - C_l\right] - \left[P_l\left(1 - \frac{L_o}{L_o + \int J_v\,dt}\right) + 0.2\ \text{atm}\right]}{\frac{RTW}{DV_m} + \frac{1}{A} + Rbl}$$

Conclusions:

The originally developed flux model does not accurately predict the flux rate observed from experimental data. For the 0M well concentrations the flux rate predicted by the model is of an order of magnitude greater that than observed. Upon addition of an additional resistance term as a fitting parameter, the model does agree with the data. This additive resistance is perhaps due to resistance in the boundary layer which may be in itself a function of the water flux and not a constant.

On the other hand the poor agreement of the originally developed model may be due to an error in the driving force predictions. Perhaps other mechanical pressure generations are involved that need to be determined.

Recommendations For Future Work:

The assumption that σ is a constant is due to the sensitivity of the exponential term, "exp($-J_wR_{ps}$)", while trying to solve for J_w. Consequently, complex numerical integration methods must be used to accurately solve for the water flux. Also, the R_{ps} value was calculated from stir cell experimental data performed by Scovazzo et. al. Any inaccuracy in this value may be magnified due to the sensitivity of the model. Therefore, an assumption was made that σ is approximately equal to $L_m/A\Delta x$. It was also found that the slightest change in σ caused the J_w as predicted by the model to dramatically change. Similarly, changing the total sum of the resistances in the model by an order of magnitude had a significant impact in the water flux profile as predicted by the model. This may be do to the fact that the assumption that the boundary layer resistance is negligible does not hold. An additive resistance due to the boundary layer may have to be included.

Moreover, in the final model for the water flux the "C_l" term is not a constant for the cases other than the 0M sodium chloride concentrations. Even though the concentration inside the well increase over time, this term can be modeled as a function of J_w. Furthermore, the initial length, "L", needs to be fixed for every case and for each dewatering well. This modification must be done in the loading procedure for the dewatering wells so that "L" is fixed and it must also allow for air to escape as the liquid enters the well.

Also, the inserts were machined from polycarbonate material which has limited transparency. Attempts to solvent polish the inserts with ethylene chloride in order to increase the transparency had limited success as deformations often occurred. Trying to smooth out the interior of the wells was another reason for solvent polishing the inserts. When the holes were drilled for the dewatering wells, the drill bit would catch the polycarbonate and create grooves in the wells. This rough interior would affect the any nucleation sites in crystal growth by osmotic dewatering. In the future perhaps the a more volatile organic solvent that methylene chloride may be used so that evaporation is faster and the contact time on the polycarbonate is decreased and results in less deformation of the plastic. On the other hand, perhaps the inserts can be manufactured from another type of material. For example, acrylic is more transparent than

polycarbonate and concern about having it crack is not an issue as the stress effects involved in the entire apparatus are minimal.

On a different note, a MODC apparatus is also used for osmotic dewatering crystal growth. Although this research focused on the dynamics involved with the FPA, the MODC deals with similar dynamics except for the fact that the gas diffusion step does not exist as it does in the FPA experiments. Attempts to use the MODC for OD were met with limited success due to the design of the apparatus. One suggestion for modifying the MODC is that the compression screw holes should not be drilled as through holes down to the reservoir. With the current design, the screws must be vacuum greased so that the reservoir solution does not leak up into the top supporting plate and then the dewatering plate. However, if the screw holes were drilled through the dewatering plate and top supporting plate but not to the reservoir this problem would be solved. Additionally, the screws are made out of nylon so that no damage is done to the grooves in the polycarbonate plates in the MODC. The current nylon material of the screws sometimes leads to their heads breaking off upon tight compression. If the screws were made out of metal and metal inserts were used in the polycarbornate blocks this problem may be solved. Another problem encountered in handling the MODC deals with the poor seal that the rubber gasket makes between the membrane and the dewatering well plate. This rubber gasket may be replaced with small O-rings to provide an adequate seal between each dewatering well.

Acknowledgements:

Michael Sportiello for supplying expertise for this study.

Willy Grothe for machining the FPA and MODC apparati and modifications.

References:

Bird, Byron R; Stewart, Warren E.; Lightfoot, Edwin N.; "Transport Phenomena;" pp,495-518; John Wiley and Sons, Inc.; New York; 1960.

DeLucas, Lawrence J.; Fowlis, William W.; Twigg, Pamela J.; "Experimental and Theoretical Analysis of the Rate of Solvent Equilibration in the Hanging Drop Method of Protein Crystal Growth;" Journal of Crystal Growth 90 (1988); pp. 117-129; North-Holland, Amsterdam.

Lee, Ching-Yuan; Sportiello, M.G.; Cape, S.P.; Feree, S.; and Todd, P.; "Characterization and Application of Osmotic Dewatering to the Crystallization of Oligonucleotides;" Biotechnol. Prog. 13, 77-81; 1997.

Scovazzo, Paul; Lee, Ching-Yuan; and Todd. P.; "Dynamics of Reverse Osmosis Membranes and Membrane Pretreatment Methods for Applications in Crystal Growth by Osmotic Dewatering;" Department of Chemical Engineering; University of Colorado at Boulder 1998.

APPENDIX A: FPA Insert Assembly Procedure

- Insert pin in the pin hole located on the insert (make sure pin is sufficiently long to extend through gaskets, membrane and metal base).
- Lightly grease the side of the insert opposite of that of the pinhole (make sure to grease in between the wells and not in the wells.

- Bring the plastic top and the insert together so that a good seal is formed and so that the wells are aligned with the fill ports in the plastic top
- In all the steps that follow, take care not to scratch or score the reverse osmosis (RO) membrane film (the glossy side of the membrane).
- Cut, carefully, with a pair of dissecting scissors an RO membrane disc with a diameter just larger than that of the insert.
- Punch a hole in the middle of the membrane using an 18 gauge needle. Start on the glossy side of the membrane and use the metal base of the insert as a backing for the membrane while punching out the hole. Make the hole only as big as it needs to be.
- Starting on the glossy side and using an 18 gauge needle, punch a hole in the membrane in the same location as the pin hole in the insert. Use the metal base as a reference for the pin hole and as for backing while punching the hole out.
- Assemble the various parts as shown below, taking care that the pin extends through the pin holes in the two gaskets, the membrane, and the metal base. The glossy side of the RO

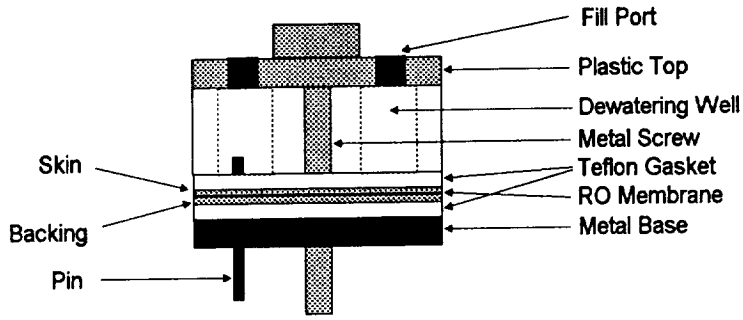

membrane must face into the well of the insert.

- Tighten the screw enough for the well to form a seal against the RO membrane. Once the screw has been tightened, do not untighten it such that the parts can rotate and misalign.
- Use a razor blade to gently shave off the excess membrane that hangs over after the parts have been assembled.
- Load each insert well with the appropriate solution using a pipettor equipped with a "gel-loading" (very fine) tip. Be careful not to touch the membrane surface with the pipettor tip. Make sure to allow for air to escape from the well when loading well fluid by pulling back the pipet slightly upon start of loading, leaving a small gap between the pipet and the fillport.
- Slowly rotate plastic top such that the fill ports and the main chamber wells are misaligned (the screw may have to be loosened slightly).
- The insert is ready to be loaded into the appropriate FPA.

APPENDIX B: Loading and Lubricating Procedure for FPA Containing One Insert

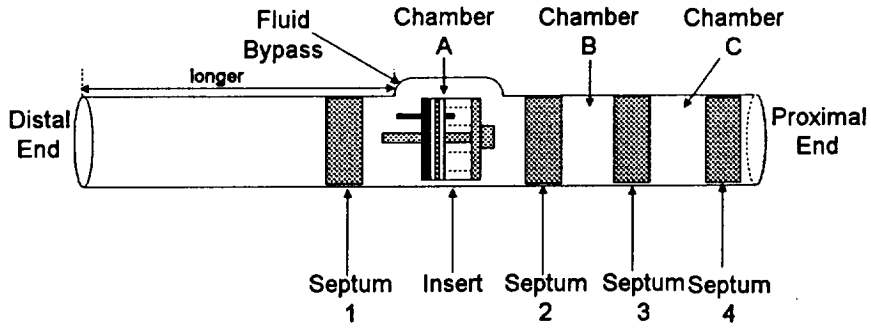

SIGMACOAT LUBRICATION PROCEDURE

NOTE: This procedure must be performed under a fume hood wearing protective clothing and goggles.

- Briefly dip the rubber septa in a bath of Sigmacoat siliconizing fluid (Sigma Chemical Corp.) and allow septa to air dry. 3 rubber septa for every FPA glass barrel to be loaded.
- Insert septum 1 into the distal end of the glass barrel (farthest from bypass) just far enough in to obtain a seal.
- Hold barrel vertically and partially fill with Sigmacoat siliconizing fluid. Using a gloved finger, seal the open end and invert the barrel 3 times being sure to wet the entire internal surface of the FPA. Pour off the excess Sigmacoat, remove stopper and allow barrel to air dry.
- Use the plastic rod loading device to push septum 1 in the now dry FPA barrel all the way to the proximal end.
- Hold barrel vertically and partially fill (2 cm deep) with Sigmacoat siliconizing fluid. Using a gloved finger, seal the open end and invert the barrel 3 times. Pour off the excess Sigmacoat, remove septum 1 and allow barrel to air dry.
- Repeat above steps for every FPA glass barrel to be loaded.

LOADING PROCEDURE FOR FPA

- Using the plastic rod loading device, move septum 1 in the glass barrel and place it at the appropriate preactivation position (just beyond the bypass on the distal side).
- Do the above steps for all FPA glass barrels to be loaded.
- Load the assembled inserts (refer to FPA insert assembly procedure on the last page).
- Add 1.5 ml of the appropriate Chamber A solution through the proximal end of the glass barrel.
- Place the insert in Chamber A with the metal base facing the distal end. Adding drops of solution from Chamber A to the holes in the metal base of an the insert before placing it in Chamber A helps prevent bubbles from being trapped in these holes.
- Place Sigmacoated rubber septum septum 2 at the proximal end of the glass barrel.

- Pierce the septum near the edge with a 25 gauge needle and push the septum using the plastic rod loading device to the surface of Chamber A solution, allowing air to escape through the needle (make sure that the glass rod loading device is lifted repeatedly to allow air to escape).
- Remove any air bubbles from Chamber A as thoroughly as possible and then carefully remove the needle.
- Add 3 ml of the appropriate Chamber B solution through the proximal end of the glass barrel.
- Seal Chamber B with Sigmacoated rubber septum 3 as described previously for Chamber A.
- The FPA glass barrel is now ready for activation.
- (Optional): Repeat for Solution C and rubber septum 4 if used.

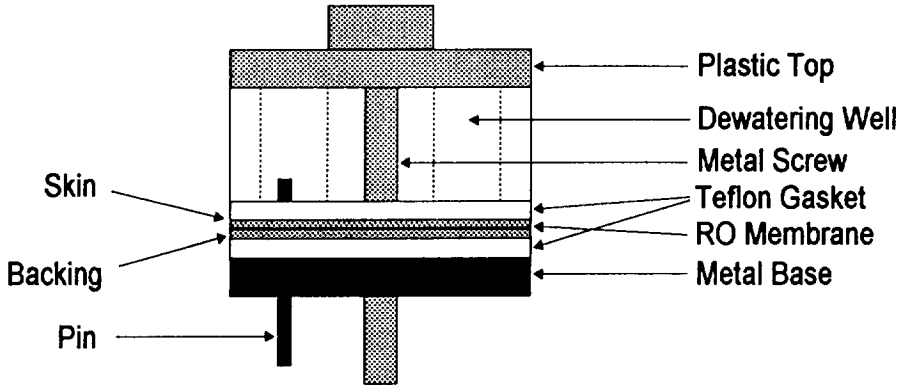

Figure 1. Schematic of an FPA Insert

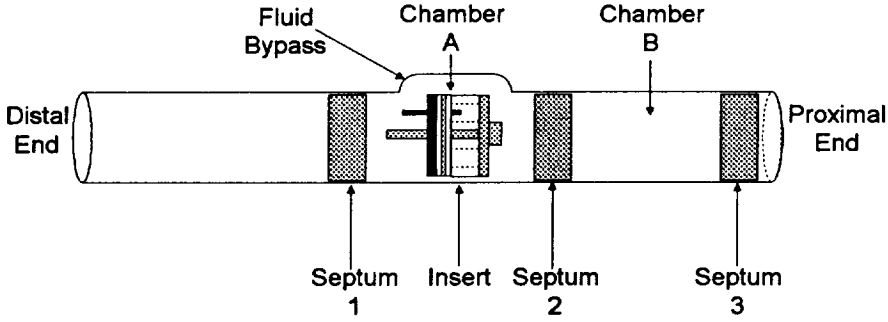

Figure 2. Schematic of an FPA glass barrel before activation

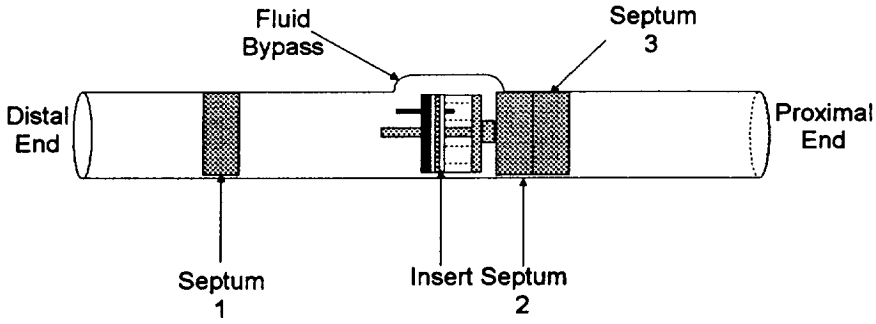

Figure 3. Schematic of an FPA glass barrel after activation

Dewatering Well:

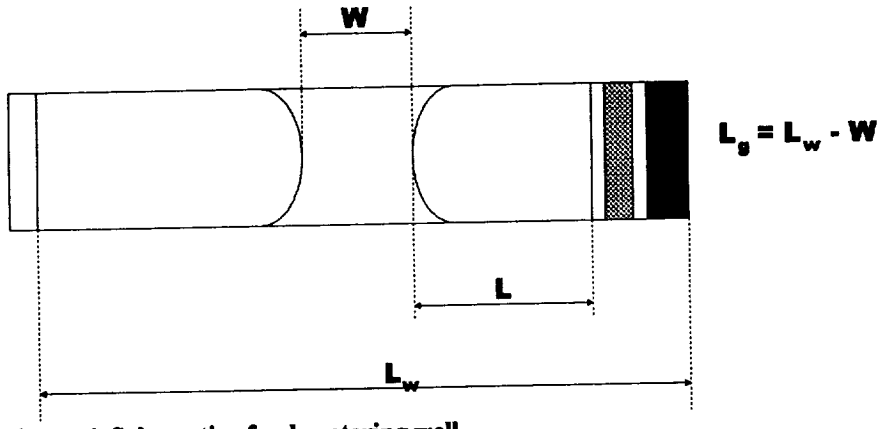

Figure 4. Schematic of a dewatering well

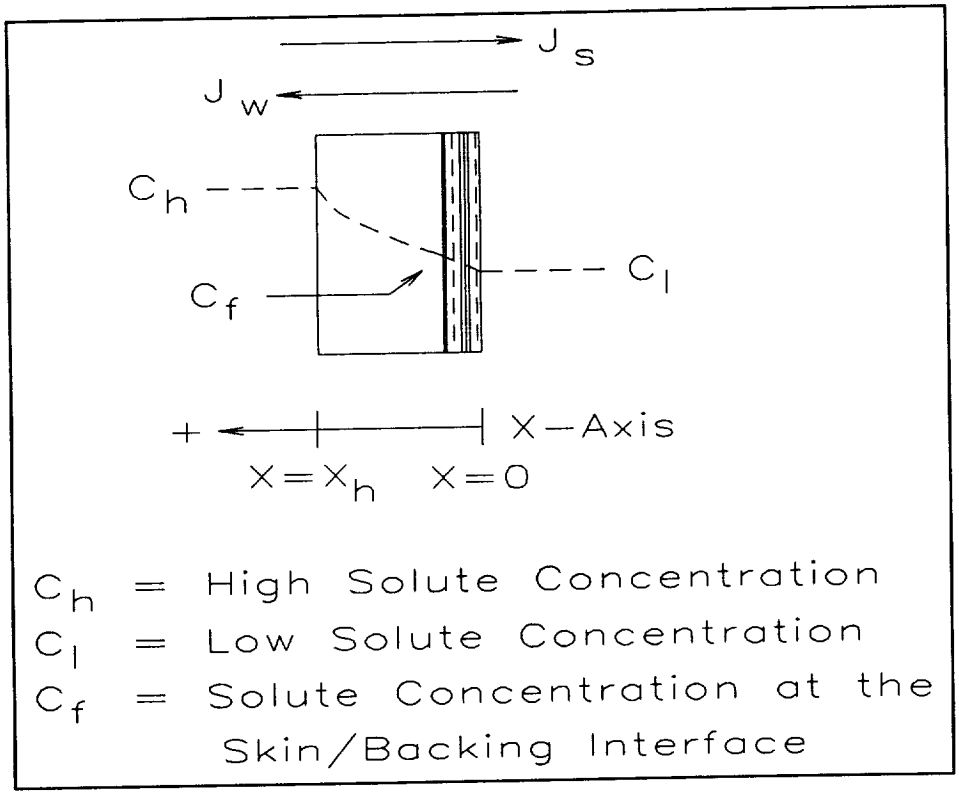

Figure 5. Concentration profile due to internal polarization.

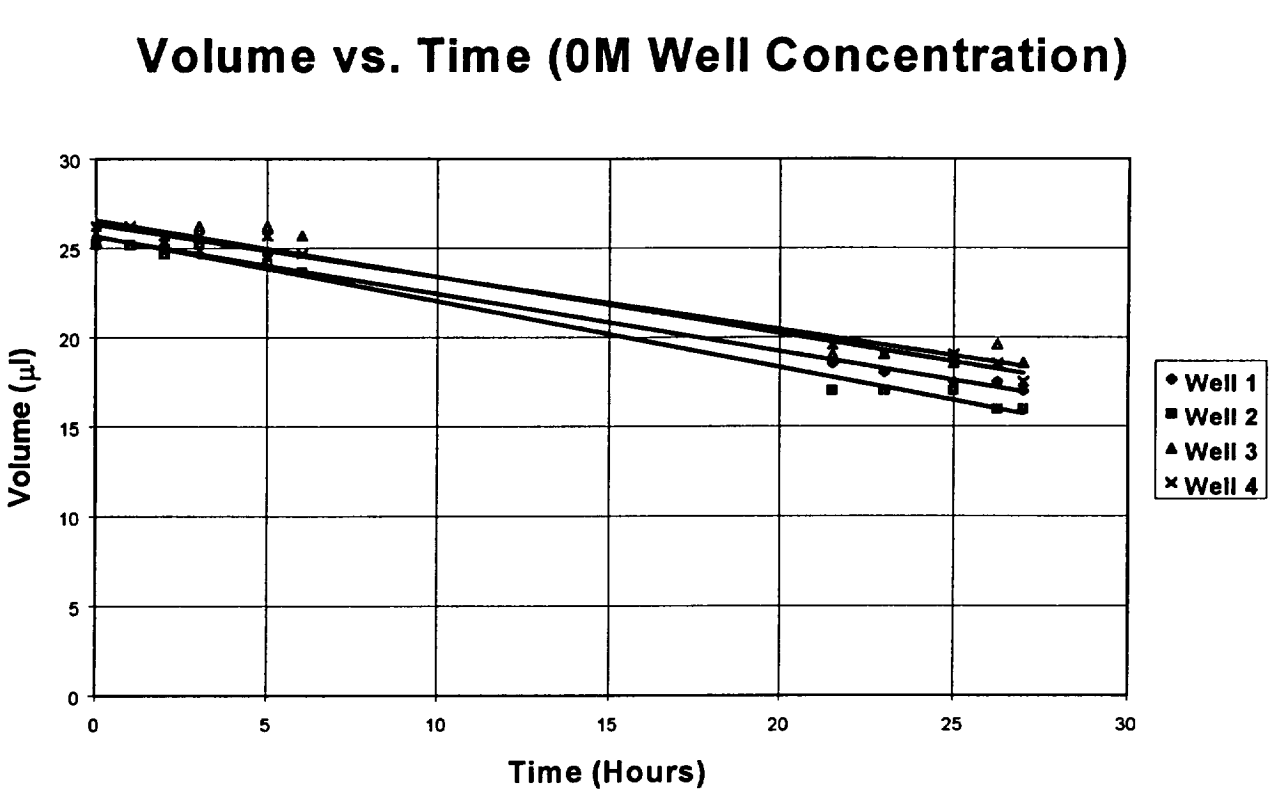

Graph 1. Reduction volume for vertical orientation, 0M gradient.

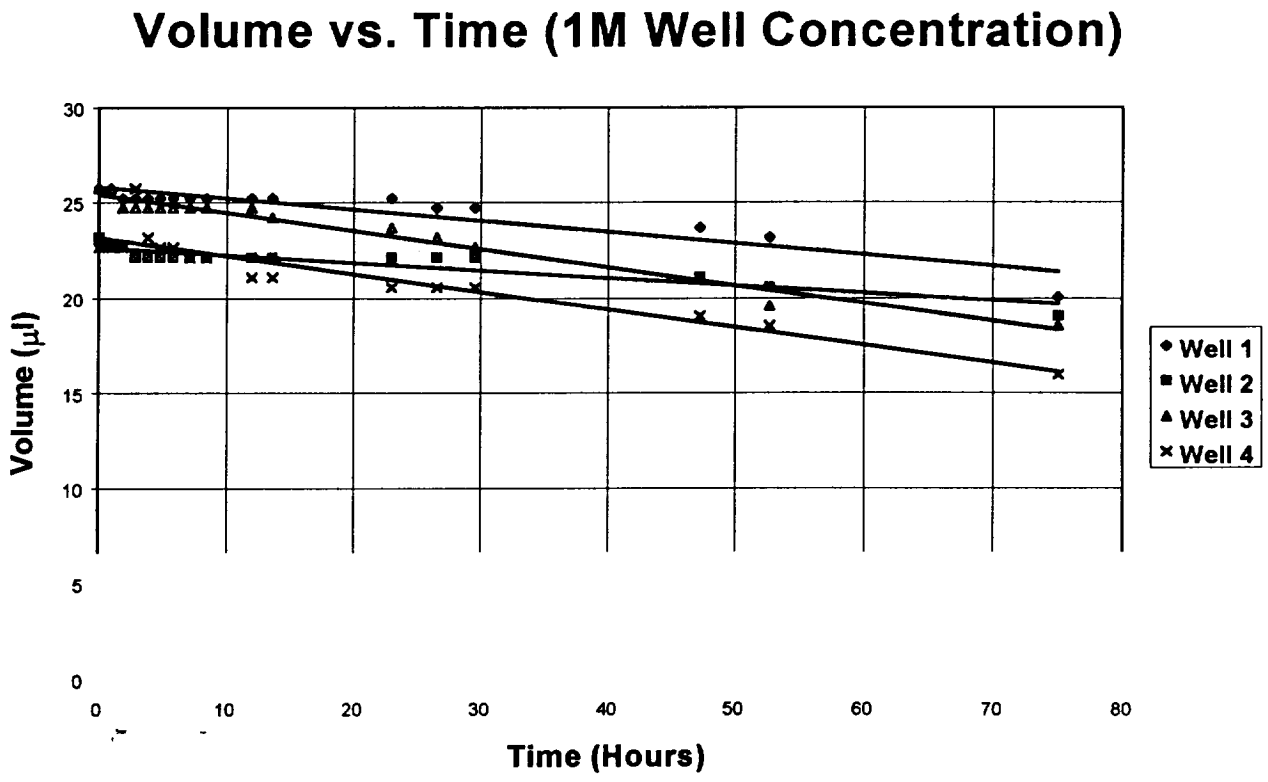

Graph 2 Reduction of volume for vertical orientation, 1 M gradient.

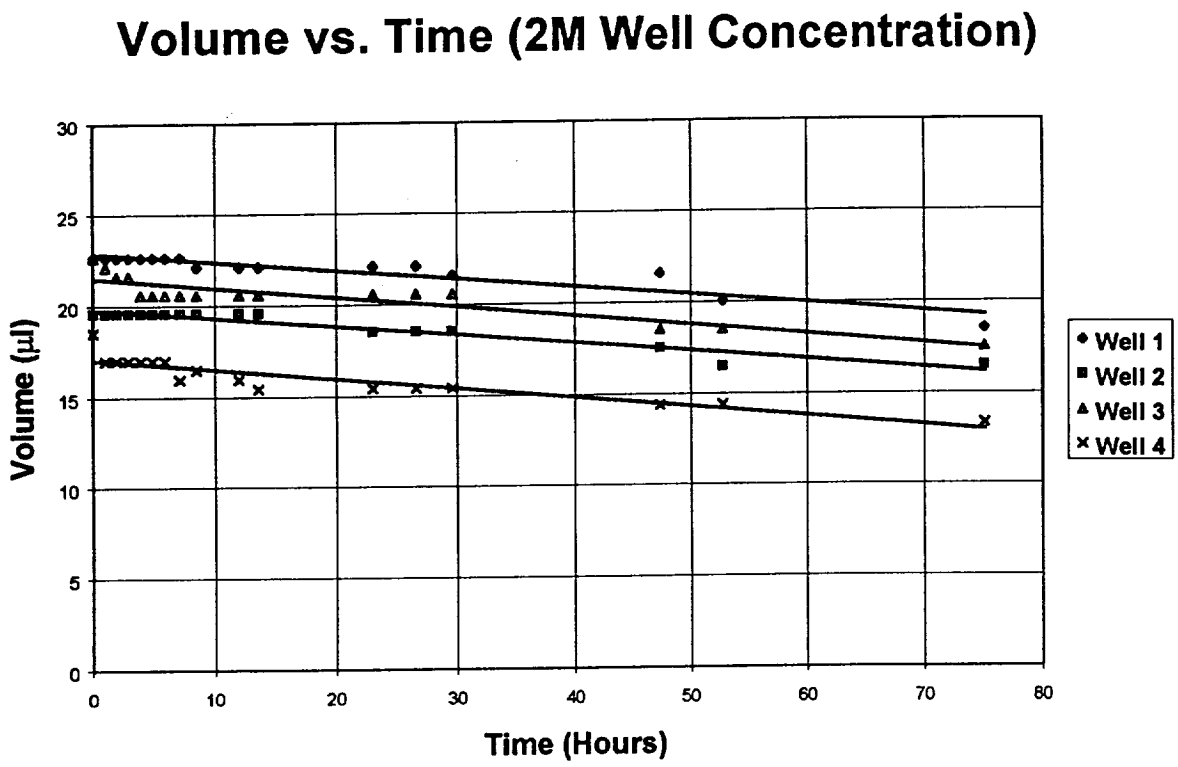

Graph 3. Reduction of volume for vertical orientation, 2M gradient.

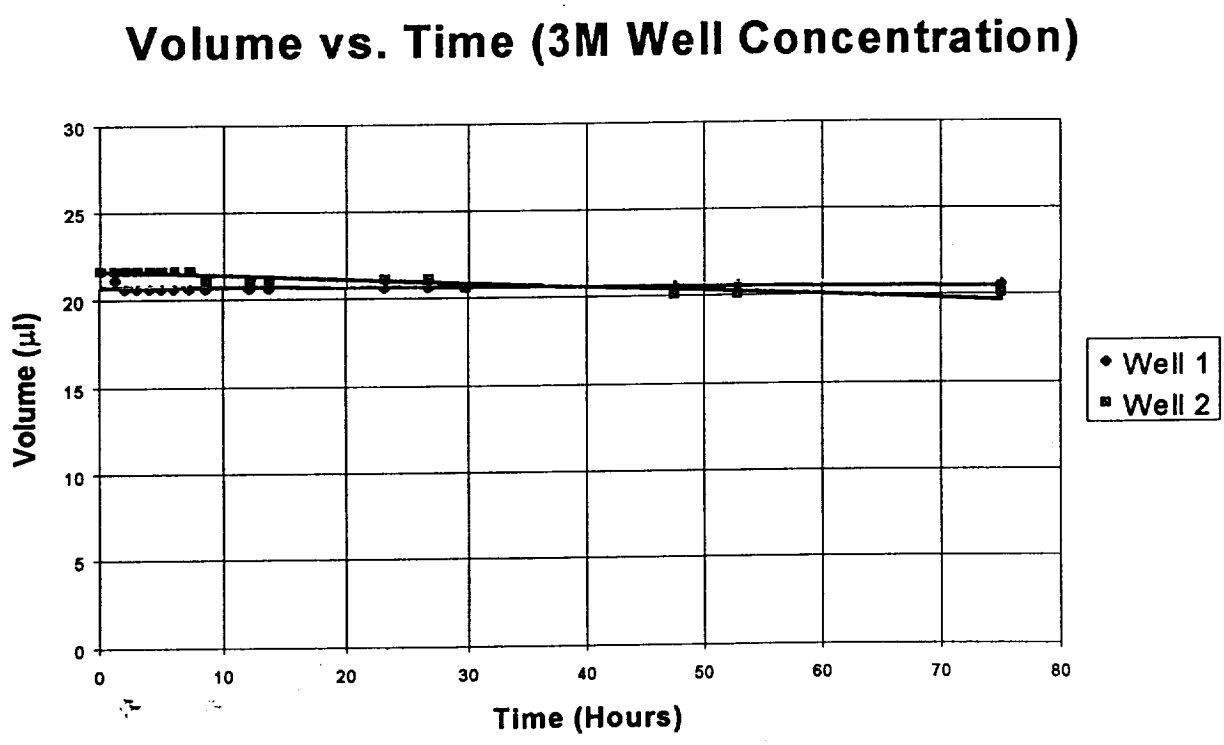

Graph 4. Reduction of volume for vertical orientation, 3 M gradient.

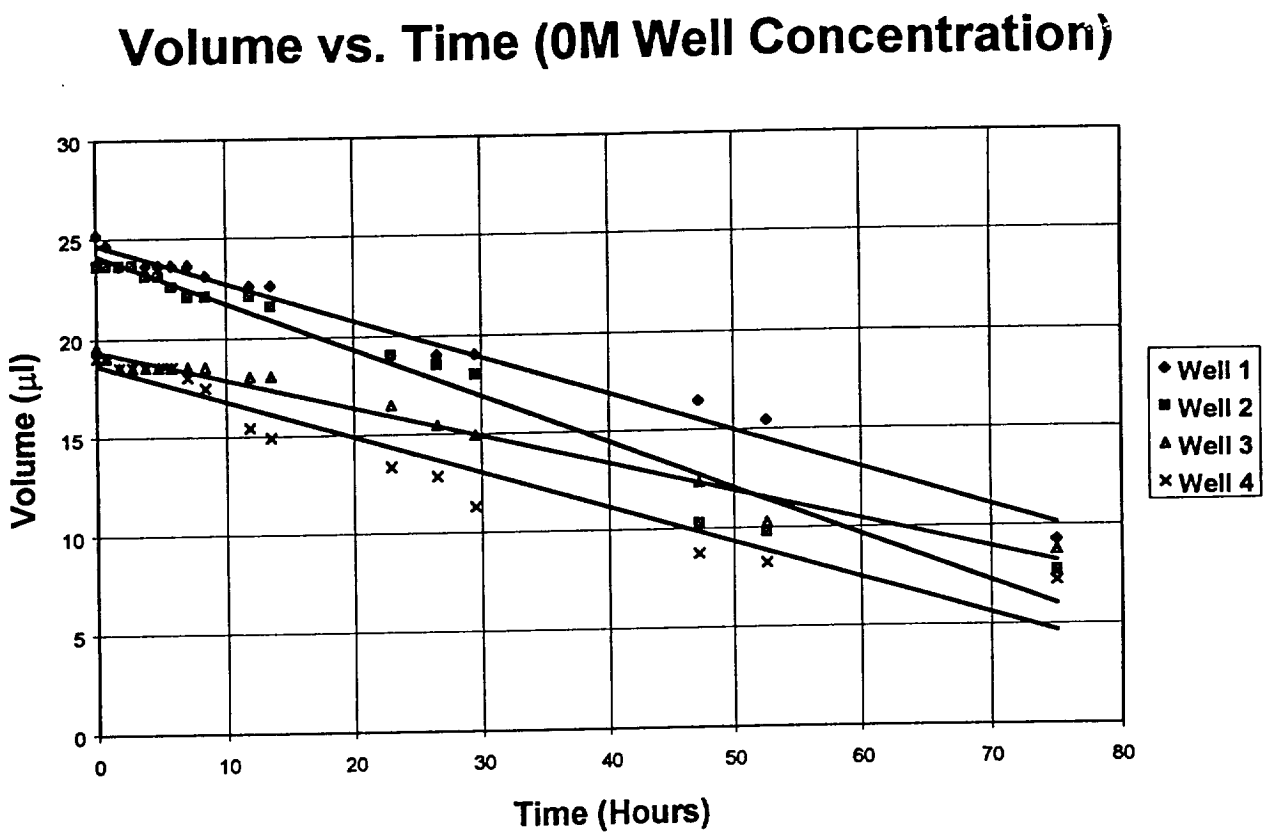

Graph 5. Reduction of volume for horizontal orientation, 0 M gradient.

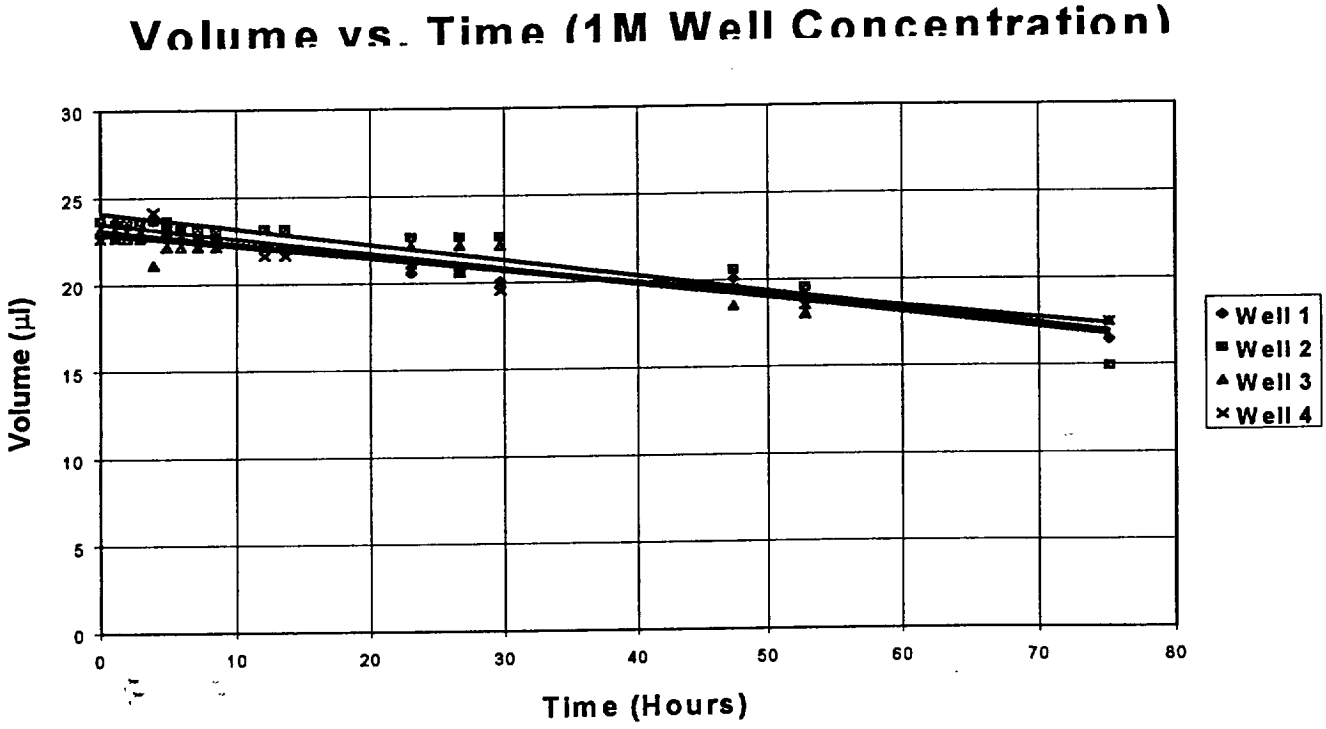

Graph 6. Reduction in volume for horizontal orientation, 1 M gradient.

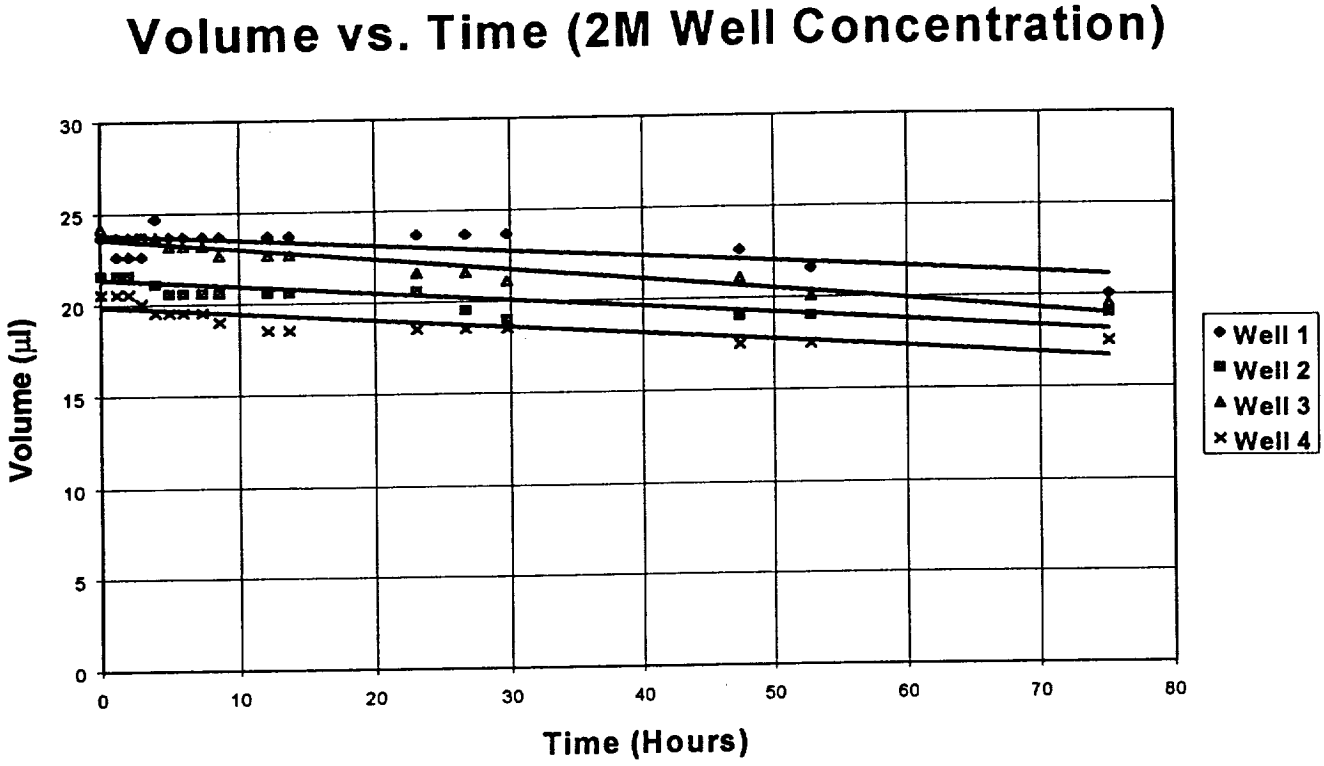

Graph 7. Reduction in volume for horizontal orientation, 2 M gradient.

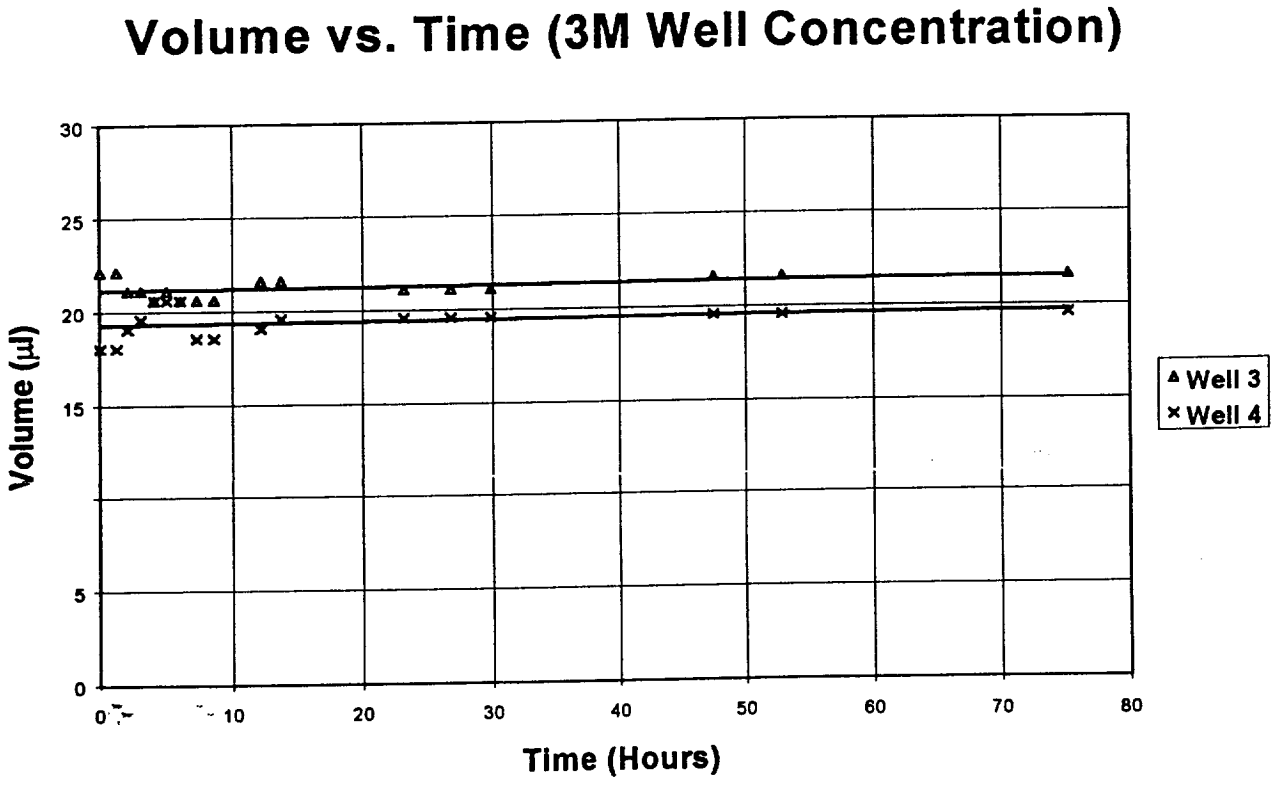

Graph 8. Reduction of volume for horizontal orientation, 3 M gradient.

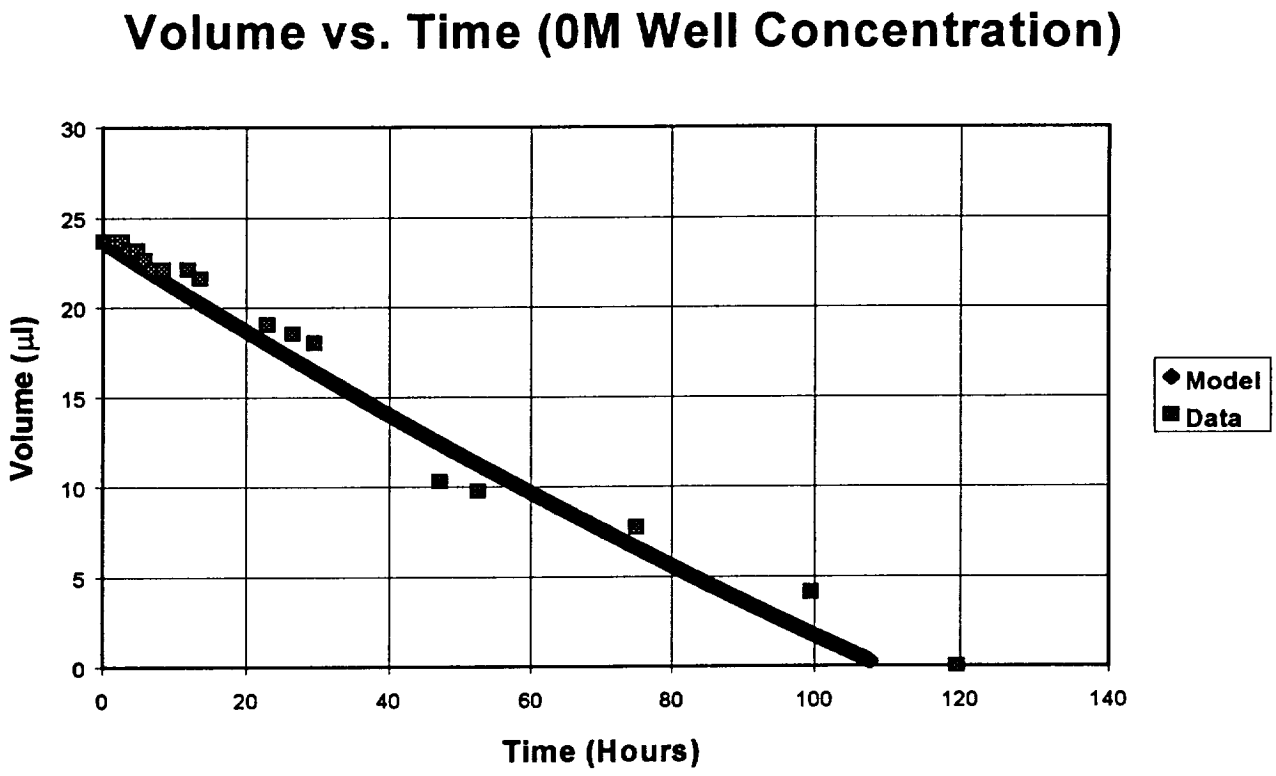

Graph 9. Model compared to experimental data for 0M well concentration.

Molarity of Well (mol/L)	Applied Osmotic Pressure (atm)	Water flux (cm/sec)	Standard Deviation (cm/sec)
0	146.8	1.15E-06	1.08E-07
1	97.8	2.51E-07	9.55E-08
2	49	1.76E-07	1.18E-08
3	0	5.18E-08	5.43E-08

Table 1. Resulting water fluxes from experimental data for vertical orientation

Molarity of Well (mol/L)	Applied Osmotic Pressure (atm)	Water flux (cm/sec)	Standard Deviation (cm/sec)
0	146.8	6.76E-07	1.35E-07
1	97.8	2.99E-07	3.32E-08
2	49	1.60E-07	3.73E-08
3	0	2.14E-08	1.49E-09

Table 2. Resulting water fluxes from experimental data for horizontal orientation

Chapter 23

The engineering, design and optimizationof membranes for osmotic dewatering crystallization: dense-film osmotic dewatering

Paul Scovazzo

CHAPTER 23
THE ENGINEERING, DESIGN, AND OPTIMIZATION OF MEMBRANES FOR OSMOTIC DEWATERING CRYSTALLIZATION - DENSE-FILM OSMOTIC DEWATERING

By Paul Scovazzo

1. Motivation

The equivalent hydraulic pressures developed within the reverse osmosis (RO) membranes used in osmotic dewatering were on the order of 0.008 to 0.05 MPa (1 to 7 psi) or 0.01x to 0.001x of the applied osmotic pressures. Equivalent hydraulic pressures of this magnitude mean that even low mechanical pressures developed within an osmotic dewatering device could have significant impact on the performance of the device. Low gravity crystallization in the Microgravity Osmotic Dewatering Crystallization Fluid Processing Apparatus (MODC-FPA) is a case in point. The operation of the MODC-FPA generates internal pressures that result in trans-membrane mechanical pressures of 0.02 MPa (5.2 psi). A RO membrane without internal polarization would have equivalent hydraulic pressures on the same order as the applied osmotic pressures. Osmotic dewatering devices, such as the MODC-FPA, using such a membrane would not have mechanical pressure performance effects.

The gaining of insight into the RO membrane-backing dynamics and its impact on the stir cell experiments, reported in Chapter 6, is a further motivation for looking at dense-film osmotic dewatering. Dense-film osmotic dewatering separates the dynamics of the skin and stir cell experimental equipment from the RO membrane-backing. Comparison of the dense-film osmotic dewatering results with the results of the RO membrane osmotic dewatering results will allow further extraction of information on the membrane-backing dynamics.

2. Why Dense-Film Membranes Should Transport Water and Be Better Than RO Membranes for Osmotic Dewatering

2.1 Why Dense-Film Membranes Should Work

The best permeability coefficient, L_p, for the RO membranes used in osmotic dewatering was 23×10^{-9} m/sec MPa. 50-psi pressure pretreated membranes operated in the inverse orientation achieved this permeability coefficient, see Chapter 6. This permeability is 0.006 times the permeability coefficient of the RO membrane's skin. Therefore, a dense-film membrane that has a thickness of 160 times the thickness of the RO membrane's skin should have the same performance or L_p in osmotic dewatering, assuming no concentration polarization. Using the manufacture's specifications for the MS-10 RO membrane (Ionics-Desal, Vista, CA), this would be a dense-film membrane of 0.6 μm to 6 μm. As noted below, we obtained dense-film membranes of 20 μm thickness that had L_p's of one-fourth of the RO membrane L_p's used in osmotic dewatering.

2.2 Why Dense-Film Membranes Should Be Better

RO membranes require a pretreatment in order to obtain high repeatability in L_p. Repeatability is a critical factor in biological macromolecule crystallization. Dense-film membranes should minimize the efforts required in pretreatment. More importantly, even properly pretreated RO membranes that are soaked after pretreatment and prior to use have low repeatability in L_p (high standard deviations). 50 psi pressure pretreated membranes soaked overnight in 3 molar sodium chloride (NaCl) solution had a relative standard deviation of 20% (Chapter 6 and table 7.1). The time line imposed on low gravity crystallization due to pre-launch loading times for space flight vehicles could result in the effective soaking of membranes prior to the start of osmotic crystallization, such as in the MODC-FPA. Assuming the soaking results in uneven solute impregnation of the membrane-backing, the elimination of the membrane backing, leaving a dense-film membrane, could increase the repeatability of low-gravity osmotic dewatering crystallization.

3 Materials and Methods

The following are the procedures and goals of the dense-film membrane research by task.

Task 1 - Manufacture four (4) dense-film membranes. This task also identified the most appropriate membrane casting solution for the thinnest membranes (low polymer concentration) with uniform surfaces and workable strength. The casting solution was a binary of cellulose acetate (CA) and acetone. The University of Colorado, Department of Chemical Engineering's institutional knowledge, from extensive work with CA membranes, caused the choice of this binary casting solution. The manufacturing of the membranes followed these steps:

- Step 1 - Mix overnight the appropriate weight percent ratio of CA and Acetone in a 20 ml sealed glass vial with a magnetic stir bar that was longer than the jar diameter.
- Step 2 - Stop mixing and let entrained air bubbles float out of the solution for five (5) to eight (8) hours.
- Step 3 - Cast solution on glass plate to an initial thickness of 254 μm using a "roller pin" caster (Dry Casting).
- Step 4 - Cure (air dry) the casted film (membrane) overnight.
- Step 5 - Mark the imperfections and usable areas in the air-dried membrane film with a permanent marker (Sharpie®).
- Step 6 - Soak the air-dried membrane in distilled water to release the film (membrane) from the glass surface.
- Step 7 - Cut out usable areas of membrane for use in the Hydraulic Permeability or the Osmotic Permeability Tasks.

Task 2 - Hydraulic Permeability Task. Obtain the hydraulic permeability coefficient, A, of one of the four manufactured CA dense-film membranes using the cross-flow membrane pressure cell unit described in section 6.4. This task followed

the steps and procedures described for determining the hydraulic permeability of the RO membranes (section 6.4) with the following changes.

Step 1 - Operate the pressure cell at 50 MPa gage (500 psig).

Step 2 - Run the hydraulic permeability test for 38 hours to minimize errors resulting from the low volume of permeate collected.

Step 3 - Obtain thickness of membrane after termination of hydraulic permeability task (see Task 4).

Task 3 - Osmotic Permeability Task. Obtained the osmotic dewatering permeability coefficient (L_p) for three of the manufactured CA dense-film membranes using the stir cell experimental equipment and procedures described in section 6.4. The initial charge of solute solution was 3 molar sodium chloride (NaCl).

Task 4 - Obtain the thickness of one of the dense-film membranes after termination of the osmotic permeability task and one dense-film membrane after termination of the hydraulic permeability task. Used a micrometer accurate to 1 μm for this task. Obtained 7 readings per membrane at various locations throughout the membrane surface.

4 Results and Discussion

Casting Solution

Two casting solutions were tried. The first, being 10 wt% CA mixed with 90 wt% acetone (10% CA/90% Acetone), produced pitted membrane surfaces. The pitting probably resulted from uneven evaporation of the acetone. The second, being 15 wt% CA mixed with 85 wt% acetone (15% CA/85% Acetone), produced smooth membrane surfaces. The 15% CA/85% Acetone casting solution produced membranes that would not separate from the casting glass plate during curing. Soaking the membrane and glass plate in distilled water broke the adhesion of the membranes to the glass plate.

Membrane Thickness

The thickness of the membrane after the termination of the osmotic permeability task was 20 μm ± 2.2. The thickness of the membrane after the termination of the hydraulic permeability task was 57 μm ± 4.1. In the case of the hydraulic permeability membrane, the membrane visibly had embossed onto it the pattern of the pressure cell's membrane support indicating that the membrane under the high mechanical pressure flowed into the open space of the support. The much higher thickness measurement of the hydraulic permeability membrane compared to the osmotic permeability membrane confirmed this flowing, since the micrometer's measurement footprint was large enough to measure the thickness of the embossed pattern. In other words, the thickness measurement for the hydraulic permeability membrane is a measurement of the ridge-to-valley "vertical" distance and not necessarily a measurement of the membrane thickness.

Hydraulic Permeability Coefficient

The hydraulic permeability coefficient of the dense-film membrane was 6.75×10^{-9} m/sec MPa or 0.2% of the RO membrane's hydraulic permeability. The RO membrane

would have this magnitude of hydraulic permeability if its skin was 560 times its manufactured thickness. The hydraulic permeability coefficient reported here assumed that the total surface area of the membrane was available for pressure-driven water flux. The thickness measurement of the skin membrane removed from the pressure cell along with visible observations of the membrane indicated that the mechanical pressure caused the membrane to flow into the holes of the pressure cell membrane support. If we assume that the open space of the membrane support limited the area available for pressure-driven water flux then the hydraulic permeability of the dense-film membrane would have been 30 x 10^{-9} m/sec MPa or 0.8% of the RO membrane's hydraulic permeability.

Osmotic Permeability Coefficient

Dynamics of the Permeability

Figure 7.1 shows the dynamic results of the three dense-film membranes tested for osmotic permeability. The calculation of the time dependence of L_p follows the procedure previously described for the RO membrane osmotic permeability test (section 6.4 and Appendix H). Over the 48 hour period the L_p values decreased by 30% to 50%. The most probable explanation for this decline is a counter diffusion of the solute into and through the membrane. Such a counter diffusion would change, with time, the solute concentration on the pure water feed side of the membrane. Such a change in solute concentration is not accounted for in calculating the time dependence of L_p.

The RO membranes also had a decrease with time of L_p and the time dependence pattern for the dense-film membranes matches the pattern for the RO membranes operated in inverse orientation and not normal orientation. Since the dense-film membranes have no membrane-backing dynamics, then the time dependence of the RO membranes in inverse orientation may also be due, in part, to the counter diffusion of solute through the membrane and into the pure water feed side of the membrane. What is occurring, therefore, is a dynamic of the stir cell test equipment and not a dynamic of the membranes. This logic does not totally extend to the RO membranes in the normal orientation since their L_p time dependence is more dramatic in the initial hours of flux and drops to near time independence after 18 hours following a decrease in the L_p's of 41% to 63%. After 18 hours the L_p's of the dense-film membranes have decreased 17% to 26%, while the L_p's of the RO membranes in inverse orientation have decreased 6% to 23%.

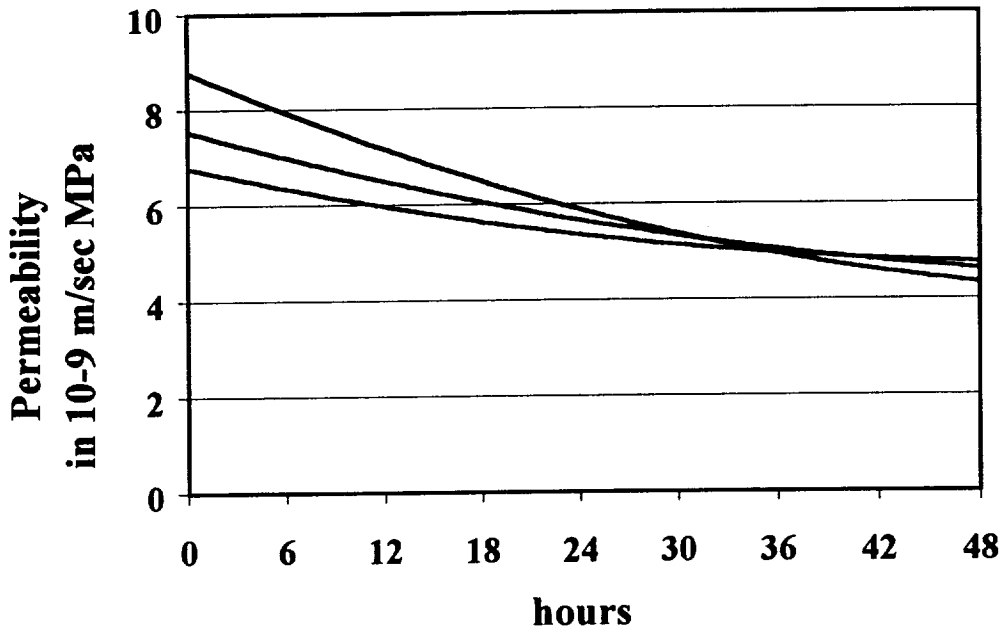

Figure 1: Dense-film membrane permeability dynamics, permeability vs. time. Driving force at the 18th hour was 12 MPa osmotic pressure.

Pseudo Steady State Osmotic Permeability

As with the RO membranes, it is illustrative to discuss the permeabilities of the dense-film membranes during the 18th hour of osmotic driven flux. The average osmotic permeability coefficient, L_p, of the dense-film membranes during the 18th hour is 6.02×10^{-9} m/sec MPa with a relative standard deviation of 5.59%. This is only 89% of the hydraulic permeability coefficient, A.

In comparing the dense-film membrane with the RO membranes, table 1 and figure 2 also report the L_p's for the 18th hour of RO membranes in the inverse orientation. The inverse orientation produced the highest L_p's and the least variability of the L_p's with time for the RO membranes. In addition, it is appropriate to use the inverse orientation since the L_p time dynamic for the dense-film membrane is similar to the RO inverse orientation time dynamic as discussed above.

Table 1: Comparison of dense-film membrane performance against inverse-orientation RO membranes during the 18th hour of osmotic dewatering.

	Average Osmotic Permeability (10^{-9} m/sec MPa)	Percent Relative Standard Deviation	Hydraulic Permeability (10^{-9} m/sec MPa)	Equivalent Hydraulic Pressure (MPa)	Applied Osmotic Pressure (MPa)
No Pretreatment	13.14	23.2	3750	0.033	10
50 psi Pretreatment	23.43	8.59	3750	0.051	8.8
100 psi Pretreatment	19.76	23.2	3750	0.045	9.4
50 psi/NaCl Soaking	9.94	20.7	3750	0.029	11
Dense-Film	6.02	5.59	6.8	10 (est.)	12

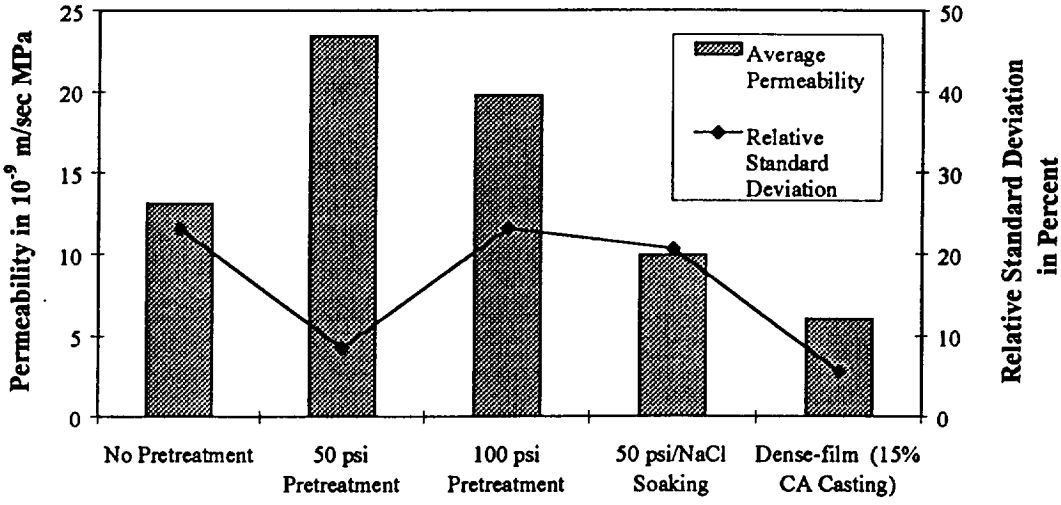

Figure 2: Comparison of dense-film membrane performance against inverse-orientation RO membranes. Pseudo steady-state permeabilities, measured at the 18th hour. The relative standard deviation points (standard deviation divided by mean permeability) point connected by lines show a pattern in standard deviation vs. pretreatment method.

Table 1 and figure 2 report the pseudo steady state osmotic permeabilities, L_p's, for RO membranes (different pretreatment methods) and the dense-film membranes. The dense-film membrane's average L_p is of the same order of magnitude as the RO membranes being 26% of the highest RO membrane L_p (50 psi pressure pretreatment). The repeatability of the dense-film membrane is slightly better than that of the 50 psi pressure pretreated RO membranes with relative standard deviations of 5.59% vs. 8.59%.

As stated in section 7.2.2, it is also important to compare the dense-film membrane performance against the performance of properly pretreated RO membranes that are soaked after pretreatment and prior to use. This is because of the time-line imposed on low gravity crystallization due to pre-launch loading times for space flight vehicles results in the effective soaking of membranes prior to the start of osmotic crystallization. Therefore, in reference to low gravity osmotic dewatering devices, such as MODC-FPA, note that the dense-film membrane L_p is only 60% of the L_p for the membrane pretreated by 50 psi pressure followed by soaking in 3 molar NaCl prior to use (50 psi/NaCl Soaking RO membranes). In addition the repeatability of the dense-film membrane is much better that the 50 psi/NaCl Soaking RO membranes, 5.59% vs. 20.7%. Of course this is not a direct comparison of repeatability, since there is no data for dense-film membranes pretreated by soaking in 3 molar NaCl solution. However, assuming the high relative standard deviation of the 50 psi/NaCl Soaking RO membranes resulted from uneven solute impregnation of the membrane-backing; then the dense-film membranes, having no membrane backing for solute impregnation, would still have a high repeatability after 3 molar NaCl soaking.

The more important observation from table 7.1 is that the equivalent hydraulic pressure of the dense-film membranes is 10 MPa (100 atm). This equivalent hydraulic permeability is only 89% of the applied osmotic pressure (compared to the less than 0.63% of the applied osmotic pressure for the RO membranes). This means that the performance of osmotic dewatering equipment operated with dense-film membranes would not be subjected to mechanical pressure effects.

5 Relevance of Dense-film Osmotic Dewatering to Power Generation by Pressure-Retarded Osmosis (PRO)

As stated in Chapter 6, Osmotic Dewatering and power generation by Pressure-Retarded Osmosis (PRO) share the same complications resulting from internal concentration polarization in the reverse osmosis membrane backing. In PRO the concentration polarization significantly reduces the power generated per membrane surface area and the overall theoretical efficiency of the power generation. This section evaluates the data in table 7.1 for application to PRO.

The theoretical maximum power generation per membrane surface area in PRO is [1]:

$$\text{Power} = A(\Delta P_e)^2/4 \qquad (1)$$

Where: A = Hydraulic membrane permeability (m/sec MPa)
ΔP_e = Equivalent Hydraulic Pressure (MPa)

Using equation (1) and the data in table 7.1, the following are maximum power generations:

RO membrane = 0.0024 W/m^2

Dense-film membrane = 0.17 W/m^2

This shows a significant advantage in PRO for the dense-film membranes; however, the composite RO membranes use in this thesis are not the best membranes for PRO [1]. Lee et al. [1] in a study of composite and asymmetric membranes found that the best membranes for PRO were asymmetric (Loeb-Type) membranes. Lee et al. also calculated power generations from various membranes and reported powers for composite membranes ranging from 0.003 to 0.17 W/m^2. The power generation calculations of Lee et al. for asymmetric membranes were inaccurate due to membrane compaction during their measurements of the hydraulic permeabilites of the asymmetric membranes; however, 0.31 W/m^2 is an estimate from their data. Therefore, the dense-film membrane of this study can have a power generation per membrane surface area equivalent to the current technology for PRO.

Now consider the efficiency of the PRO process. The power comes from the energy of mixing of the water flux with the high solute solution as defined below:

$$\text{Energy of Mixing} = J_w \Delta\pi \qquad (2)$$

Where: J_w = Water flux under the conditions of equation 1 assuming the water donating fluid is pure water (m/sec)

$\Delta\pi$ = Applied Osmotic Pressure (MPa)

The theoretical efficiency is the power generated divided by the change in energy of mixing resulting in the power generation (i.e. equation 1 divided by equation 2). The following are the percent efficiencies for each membrane calculated from the data in table 1 and the Lee et al. article:

(Composite) RO membrane in table 7.1	= 0.27%
Asymmetric membrane [1]	= 35%
Dense-film membrane	= 44%

Therefore, dense-film membranes may have an advantage in power generation by Pressure-Retarded Osmosis (PRO).

6 Conclusions

The following are the major conclusions from this dense-film osmotic dewatering study:

- Dense-film membranes offer the best alternative for osmotic dewatering systems
- Dense-film membranes have osmotic (water) permeabilities of the same order as RO membranes
- Dense-film membranes have higher repeatability in performance than RO membranes
- Dense-film membranes are not susceptible to mechanical pressure performance effects

- Dense-film membranes performance repeatability may be unaffected by soaking in a solute solution as would occur during the start-up of low gravity osmotic dewatering crystallization equipment, i.e. MODC-FPA.
- The stir cell data for the time dependence of osmotic permeability of membranes operated in the inverse orientation is, in part, due to the dynamics of the test equipment and not due to the membrane.

7 Future Work

Two important issues arise from this work. First, what is the performance (magnitude of L_p, standard deviation, and time dependence) of dense-film membranes pretreated by soaking overnight in 3 molar NaCl solution? Second, elimination of the time dynamics of the stir cell test equipment. Both of these issues would require testing the performance of the following in an osmotic unit with cross flow on both sides of the membrane:

- Normal orientation of 50psi pretreated RO membranes
- Inverse orientation of 50 psi pretreated RO membranes
- Inverse orientation of 50 psi pretreated RO membranes followed by soaking in a 3 molar NaCl solution prior to use in the osmotic unit
- Dense-film membranes
- Dense-film membranes soaked overnight in a 3 molar NaCl solution prior to use in the osmotic unit

List of Symbols

A = Hydraulic membrane permeability (m/sec MPa)
J_w = Water flux under the conditions of equation 1 (m/sec)
L_p = Osmotic permeability coefficient (m/sec MPa)
$\Delta\pi$ = Applied Osmotic Pressure (MPa)
ΔP_e = Equivalent Hydraulic Pressure (MPa)

References

[1] Lee, K.L.; Baker, R.W.; and Lonsdale, H.K.; "Membranes For Power Generation By Pressure-Retarded Osmosis;" *Journal of Membrane Science*, 8, 141-171; 1981

Chapter 24

Osmotic dewatering of biological macromolecule solutions with a phase Change

Keith Neeves

Chapter 24
Osmotic Dewatering of Biological Macromolecule Solutions with a Phase Change: A Novel Crystal Growth Technique

Keith Neeves

I. ABSTRACT

Osmotic dewatering is a membrane process used for controlling crystal nucleation and growth. Previous osmotic dewatering work using reverse osmosis (RO) membranes yielded erratic behavior due to a phenomenon known as internal concentration polarization. Internal concentration polarization is caused by solute fluxing from a high solute reservoir to a low solute reservoir in the backing of a reverse osmosis membrane. The result of internal concentration polarization is that permeability, and thus flux decrease with time. Ideally, to characterize membrane kinetics one would like to be able to design experiments with constant dewatering rates after. The novel technique of this study is to eliminate internal concentration polarization via a phase change. The distinct processes investigated: 1) Use a hydrophobic membrane that creates a gas membrane in its pores. 2) Use a hydrophilic membrane with a 2-3 mm air gap. In both cases the introduction of a vapor phase insures that solute molecules can not flux through the membrane. Employing a hydrophobic membrane resulted in the elimination of internal concentration polarization. We report within a 95% confidence interval the independence of permeability with time. Similarly, a RO membrane with an air gap yielded the same result. The hydrophobic membrane's permeability was approximately an order of magnitude higher than that of the hydrophilic membrane. As a result of crystallization and kinetic studies we recommend the hydrophobic membranes for liquid-liquid applications where the end result is purification. But, for structural analysis of biological macromolecules, a RO membrane with an air gap is the best option for high quality crystal growth.

II. INTRODUCTION AND BACKGROUND

Problem Statement

Previous work in osmotic dewatering using reverse osmosis (RO) membranes presented erratic behavior in crystallization of biological macromolecules[1]. Large standard deviations in permeability and measured permeabilities orders-of-magnitude below theoretical prediction led to this conclusion. Furthermore, Scovazzo et. al determined an internal concentration polarization in the porous backing of the reverse osmosis membrane to be causing this behavior[2]. The hypothesis is that eliminating the concentration polarization would eliminate these complications. Previous work suggested using a hydrophilic dense film with no porous backing to eliminate concentration polarization. Alternatively, we hypothesize the elimination of concentration polarization via a phase change. In this case there will be no back flux of salt into the low salt reservoir that provides the driving force. Elimination of salt back flux eliminates internal concentration polarization. This can be accomplished in two ways: i) Use a

hydrophobic porous membrane, by which water must vaporized to transport through the membrane pores. 2) Introduce an air gap between the low salt reservoir and the reverse osmosis membrane.

Objective and Motivation

Crystallization of biological macromolecules allows scientists to determine the structure and functionality of the molecules that hold the secrets of life. The most well known example is Watson and Crick's discovery of the structure of DNA via x-ray diffraction of crystals[3]. The properties and activities of biological macromolecules depend on their three-dimensional structure. The determination of this structure is dependent on high quality crystals. Unfortunately, in the years since the determination of the structure of DNA, there has yet to be a systematic methodology developed to successfully grow biological macromolecule crystals. The current practice is a trial-and-error of different conditions and methods. These methods include batch crystallization, temperature gradient crystallization, equilibrium dialysis crystallization, and vapor phase diffusion. Osmotic dewatering is a superior technique because it can control the water removal rate, which dictates crystal growth.

The objective of this study is to examine the kinetics of osmotic dewatering techniques using different membranes and configurations to provide a stable environment for crystal growth. More specifically we want to eliminate the phenomenon known as internal concentration polarization in membranes. Internal concentration polarization lowers the driving force, and thus the flux from predicted quantities, causing a variable environment for crystal growth. By eliminating internal concentration polarization one more variable is removed from the crystallization puzzle, making experiments more repeatable and reliable. Ultimately, these novel techniques will be used to grow crystals of molecules that are difficult or impossible to achieve using current practices.

Background

Osmotic dewatering is a membrane process for controlling crystal nucleation and growth. It is used for structural studies of highly ordered crystals and as a purification technique. This study is part of ongoing research in the area of osmotic dewatering in the Paul Todd Research Group. Osmotic dewatering involves a membrane partition between two solutions with different solute concentration. On one side of the partition a low solute concentration solution contains the molecule to be crystallized. The other solution is a high solute solution. The difference in osmotic pressure, due to differences in osmolarity, causes the water to flux across the partition from the low solute reservoir to the high solute reservoir. As the low solute reservoir dewaters, the biological macromolecule begins to crystallize. Osmolarity is defined as the concentration of ions in a solution. For example, a 3 M NaCl solution has an osmolarity of 6 M because each dissociated ion has a concentration of 3 M. In order for two reservoirs with different salt concentration to be in equilibrium, the high salt reservoir must be at a higher pressure than the low salt reservoir. This excess pressure is known as osmotic pressure. Osmotic pressure is analogous to absolute pressure, but instead of a density difference, a concentration difference is the driving force. Solute will diffuse across the membrane until an equilibrium hydrostatic pressure head has developed in the high salt reservoir.

My work is based on the research of two previous studies involving the characterization of membrane dynamics. C.Y. Lee et al. developed a Transport Equation For Osmotic Dewatering (TEFOD). The TEFOD equation for most applications is:

$$\frac{V_O}{L_p S(RTC_{RO})}\left\{\frac{V}{V_O}-\frac{C_{WO}}{C_{RO}}\ln\left[1-\left(\frac{C_{RO}}{C_{RO}-C_{WO}}\right)\left(\frac{V}{V_O}\right)\right]\right\}=t$$

The variables that we are interested for this study are the permeability (L_p) and the surface area (S). Lee also found that osmotic dewatering using a reverse osmosis (RO) membrane presented erratic behavior in crystallization due to large variations in permeability. Scovazzo et al. investigated the origin of this erratic behavior[4]. The decrease in permeability is a result of internal concentration polarization in the porous backing of the RO membrane. Internal concentration polarization in this application refers to the salt back fluxing through the porous backing (see *Theory and Modeling* section for more a more extensive explanation). As the salt diffuses into the membrane, the driving force decreases and thus water flux decreases.

The purpose of this study is to eliminate the internal concentration polarization problem via a phase change. Our ideas to try a hydrophobic membrane and/or an air gap come from two sources. The idea of using a hydrophobic membrane comes from a technique known as osmotic distillation. Osmotic distillation is a membrane transport process in which two solutions, one containing a volatile component in solution, contact a nonwetting membrane. The membrane's pores functions as a vapor gap between the two liquid phases. This approach has been used to concentrate fruit juices and for the concentration of aqueous solutions of thermally labile pharmaceutical products. The concept of an air gap outside of the membrane was first introduced by Sarti et al. for application to low temperature distillation through hydrophobic membranes[5]. Gas membrane separation processes have a partial pressure driving force. That is the driving force for mass transfer is a partial pressure gradient across the gas membrane. This process has been used as alternatives for ultrapure water production, desalination of brackish or sea water or for the concentration of dilute aqueous solutions. Our goal in this study is to investigate the potential use of these techniques in a crystal growth application.

III. LITERATURE REVIEW

Articles from a number of fields form the background for this study. The literature served two purposes; a background for what has been done in the field of osmotic dewatering and provide ideas for novel techniques. Brief reviews of the major references used are below.

My study is a result of a suggestion for future work from Paul Scovazzo's Ph.D. thesis. The idea of internal concentration polarization as a cause for the decrease in permeability and salt flux through the membrane as the cause of low repeatability is introduced Scovazzo's thesis[2]. Consequently, this study investigates new technique for eliminating internal concentration polarization and salt flux. In addition, Scovazzo supplied the governing equations for flux and permeability through an RO membrane used in this study. While this was our primary source, a number of other papers from the Paul Todd research group contributed to understanding the history of biological macromolecule crystal growth[6-8]. These articles provide a timeline of events and ideas that have shaped the field of osmotic dewatering as it is today.

The above sources furnished the problem, but the search for solutions led to fields outside of biotechnology. Hogan et. al. gave a good general background on recent developments and theories in osmotic distillation[9]. It provided clear advantages of osmotic distillation over conventional methods. The paper covered process fundamentals, process thermodynamics, membrane transport kinetics, thermal polarization moduli, and process design. Kunz et. al. wrote the best article on osmotic evaporation (also referred to as osmotic distillation) due to its excellent derivation and exploration of many different angles on mathematical models[10]. The authors summarized current research and theories on osmotic evaporation, and evaluated them to yield an optimal approach. It was especially effective in describing different diffusion models

through a membrane. But, the most ground breaking work was done be Sarti, et. al. in a series of articles describing various application of osmotic distillation[5]. Sarti introduced the techniques of using a hydrophobic membrane to maintain liquid-vapor interfaces and using an air gap with a membrane. Applications of this work include ultra pure water production, desalination, and concentration of aqueous solutions. In addition, these articles presented the most in depth modeling and empirical data in the field. We used sections of Hiemenz and Rajagopalan's **Principles of Colloid and Surface Chemistry** for developing the thermodynamics to support our hypothesis[11]. In particular, relating chemical potentials and compositions to osmotic pressure provided a fundamental basis for osmotic pressure as a driving force. Finally, Shofield et. al. modeled mass transfer through a hydrophobic membrane and determined whether it was dictated by Knudsen or molecular diffusion, which was an important part of our understanding of the mass transfer mechanism and how to manipulate it[12].

IV. MATERIALS AND METHODS

Materials

All hydrophobic membrane studies were performed using a polypropylene membrane manufactured by Minnesota Mining and Manufacturing. The membrane had a 2 micron pore diameter, 70% void volume, and a thickness of 42 microns. All hydrophilic membrane studies used a MS-10 RO membrane made by Osmonics DESAL^{tm}. The MS-10 is a multilayer composite consisting of a standard polyester paper backing 114 μm thick supporting an asymmetric polysulfone ultrafiltration layer 76 μm thick with a pore size of 30 nm. The polysulfone layer is coated with a proprietary polymeric UF intermediate support that is 5-10 nm thick and serves as a protective layer on which the RO polyamide skin is cast by interfacial polymerization to a thickness of 4-10 nm. The RO layer is not considered porous, but it is extremely hydrophilic and transports water by the solution-diffusion mechanism. The apparatus used to carry out membrane characterization experiments was a Spectra/Por® MacroDialyzer (Figure 1). The MacroDialyzer is designed for dialysis purposes, but has been modified for use as an osmotic dewatering apparatus. A 30% stainless steel screen was introduced to support the membrane, which is otherwise only supported by an O-ring seal and is susceptible to deformation from pressure effects. The screen was necessary for the polypropylene membrane only, because the RO membrane is rigid enough to with stand the internal pressures without significant deformation. A Cole-Parmer Masterflex peristaltic pump was used to create a total recycle stream in the top chamber of the MacroDialyzer. See Appendix A for a diagram of the experimental apparatus. The only chemicals used for our initial membrane characterization studies were deionized filtered water and 3 M sodium chloride (Aldrich, 99 + %) solution. Crystallization studies using lysozyme (Sigma, Grade VI from chicken egg white) in a sodium acetate (Malinckrodt, 99.34%) solution assessed the feasibility of crystal growth using our new techniques.

Pressure Cell

Previous work found that RO membranes work best if first pretreated with deionized water flux under pressure[4]. All RO membranes for this study were pressurized at 50 psi in a stir cell (Amicon Model 8050) with the deionized water pressurized with nitrogen gas. The procedure for pretreatment of RO membranes is:

1. Cut RO membrane to fit exactly inside circular base of the stir cell.

2. Place the O-ring on top of the membrane and snugly against the edge of the base.
3. Twist base and stir cell body together tightly.
4. Fill stir cell with 50 ml of deionized water.
5. Place top on stir cell, place inside metal support frame, and make sure pressure release valve is closed (pointing down)
6. Attach 1 ft of tubing to outlet of stir cell to measure volume fluxed during pressurization.
7. Apply 50 psi of nitrogen gas for 1 hour.
8. After 1 hour, close the regulator from the nitrogen tank.
9. Record the amount of water fluxed.
10. Allow the system to depressurize slowly through the intrinsic pressure leaks in the stir cell, that is, do not open any valves. The internal pressure returns to atmospheric in approximately ½ hour.

Membrane Characterization-Hydrophobic

The orientation used for our studies (Figure 1) draws water from the bottom reservoir of pure water into a 3 M sodium chloride upper reservoir. The hydrophobic polypropylene membrane is the partition between the two reservoirs and is supported by a steel screen. Both sides of the membrane are in direct contact with a liquid reservoir. No air gap exits in any of the hydrophobic membrane characterization studies. In order to insure a constant driving force the fluid in the upper chamber, the sodium chloride solution is recycled through a 500 milliliter reservoir. Since at most 20 milliliters of water flux through the membrane over the experiment time, having a large salt reservoir maintains essentially a constant driving force (5%-10% decrease over 24 hours). There is a water source that replaces the water that fluxes through membrane so as to keep the volume in the bottom reservoir constant. The weight loss of this source as a function of time was the data recorded. We collected data using a LabVIEW data acquisition program that took data every minute. Typical runs would last 20 to 24 hours.
The procedure for this is characterization is:

1. Cut a section of polypropylene membrane that is slightly larger than the diameter (3.38 cm) of the MacroDialyzer.
2. Fill the bottom reservoir with deionized water and attach the pure water source.
3. Place stainless steel screen in the groove on the lower chamber so it sits flush in the walls of the groove.
4. Make sure O-rings are well lubricated.
5. Insert stir bar in upper chamber and use another stir bar on the outside of the upper chamber to hold stir bar at the top of well.
6. Clamp the upper and lower reservoirs together with the membrane sandwiched between them.
7. Replace outside stir bar with stirrer and begin stirring.
8. Attach pump tubing so that sodium chloride solution is pumped into the chamber and is recycled to the sodium chloride solution reservoir. Arrange tubing so that the peristaltic pump draws from the sodium chloride solution reservoir.
9. Fill upper chamber and make sure all air bubbles are pumped out.
10. Eliminate air bubbles in the lower chamber by removing one of the three plugs and displacing the air with water from the pure water source.
11. Give the LabVIEW data acquisition program a file name in the space provided.
12. Hit START icon on LabVIEW program.

13. Allow experiment to run for 24 hours and then hit the stop sign icon in LabVIEW program.

Membrane Characterization-Hydrophilic

The procedure for the hydrophilic studies is very similar to the procedure for hydrophobic studies, except this time an air gap is present. So, instead of having liquid-to-membrane contact in the bottom reservoir there is a 2-3 mm air gap. This is achieved by allowing the bottom chamber to be filled to approximately the right height and then carefully placing the other half of the dialyzer unit on top. Use the hydrostatic head of the pure water reservoir to get the air gap just right, and then close the dialyzer with the clamps. Next turn on the peristaltic pump and fill the top reservoir with 3 M NaCl solution. Note that the top chamber need not be completely full of solution. The rest of the procedure is identical to that of the hydrophobic studies.

FPA Insert Assembly and Loading Procedure

Crystallization experiments took place in Bioserve's FPA crystal growth device. The FPA consists of a glass tube that is loaded with inserts that contain biological macromolecule solution. The inserts are surrounded by an appropriate salt solution that causes the desired dewering rate. The procedure for the insert assembly and loading is:

1. Bring the plastic top and the insert together so that a good seal is formed and so that the wells are aligned with the fill ports in the plastic top.
2. Cut with a pair of dissecting scissors an RO membrane disc with a diameter just larger than that of the insert.
3. Punch a hole in the middle of the membrane using an 18 gauge needle through the screw thread in the insert.
4. Assemble the various parts as shown in Figure 5.
5. Tighten the screw well enough for the well to form a seal against the RO membrane.
6. Use a razor blade to shave off the excess membrane that hangs over after the insert has been assembled.
7. Load each insert well with the appropriate solution using a pipettor equipped with a gel-loading tip.
8. Slowly rotate the plastic top such that the fill ports and the main chamber well are no longer aligned.
9. Using the plastic rod loading device, move septum 1 (see Figure 5) in the glass barrel and place it at the appropriate pre-activation position. Make sure all septums are liberally lubricated with Dow Corning vacuum grease.
10. Add 1.5 ml of the appropriate Chamber A solution through the proximal end of the glass barrel.
11. Place the insert in Chamber A with the metal base facing the distal end. Adding drops of solution from Chamber A to the holes in the metal base of the insert before placing it in Chamber A helps prevent bubbles from being trapped.
12. Place septum 2 at the proximal end of the glass barrel.
13. Pierce the septum near the edge with a 25 gauge needle and push the septum using the plastic rod loading device to the surface of Chamber A solution, allowing air to escape through the needle.
14. Remove any air bubble from Chamber A as thoroughly as possible and then carefully remove the needle.

15. Add 3 ml of the appropriate Chamber B solution through the proximal end of the glass barrel.
16. Seal Chamber B with septum 3.
17. Place FPA barrel in activation chamber and slowly push septums with plunger until septum 2 and 3 meet.

V. THEORY AND MODELING

Internal Concentration Polarization

In the case of an RO membrane, internal concentration polarization is caused by the tendency of solute molecules to diffuse across the porous backing against the direction of the water flux (Figure 3). The solute molecules, similar to the solvent, want to equalize the concentration gradient and thus diffuse from the high salt reservoir to the low salt reservoir. The result of this migration is a reduction in the dewatering driving force. Since the concentration of solute at the skin is lower than the bulk concentration the effective osmotic pressure is lower than the measured osmotic pressure. The diffusion of solute in the backing results in a decrease in measured driving force. This is undesirable from a crystal growth perspective because there is no control of the dewatering rate. Ideally, one wants to be able to set a dewatering rate by creating the necessary osmotic pressure difference, and hold it constant throughout an experiment. Note, this constant dewatering rate is not necessarily desired for crystal growth. Often, fast initial dewatering drives the system into the two-phase region to begin nucleation. But, for the characterization of membrane kinetics, we want constant dewatering. Therefore, the main objective of this study is to eliminate internal concentration polarization so as to have better control of dewatering rates.

Thermodynamic Argument

The novel approach taken in our study is the introduction of a phase change in an osmotic dewatering application. Starting with the basics of flux through a membrane:

$$J_w = L_p(\text{driving force})$$

where J_w is the water flux (m/sec), L_p is permeability (m/sec MPa) and the driving force is osmotic pressure. Osmotic pressure is defined as the pressure drop across the membrane that results from a difference in solute concentration. But, in our studies it is not really osmotic pressure that is the driving force, rather vapor pressure makes more sense in a vapor-liquid equilibrium application. The vapor pressure of the water on the low salt or pure water side of the membrane is higher than that of the water on the high salt side. Using a vapor pressure driving force makes comparing our results with previous work almost impossible. Thus, we can relate osmotic pressure to chemical potential, which is the thermodynamically correct state function that is trying to equilibrate. This was done by van't Hoff in 1901 and earned him the Nobel Prize. Setting the chemical potential of each side of the membrane yields:

$$\mu_1^o = \mu_1^o + RT \ln a_i + \int_{p_i^o}^{p_i^o+\pi} \bar{V}_1 \, dp$$

where μ is chemical potential, R is the gas constant, T is temperature, a is activity, $\underline{V_1}$ is molar volume, and p is pressure. Assuming molar volume is constant:

Now express chemical potential in terms of osmotic pressure:

$$\ln a_i = -\frac{\pi \cdot \bar{V}_i}{RT}$$

$$\mu_1 = \mu_1^o - \pi \cdot \overline{V}_1$$

Making the assumption that the solution is ideal, replacing activity by mole fraction gives:

$$\ln x_i = -\frac{\pi \cdot \overline{V}_1}{RT} = \ln(1 - x_2) \approx -x_2 - \frac{x_2^2}{2} - \ldots$$

where the approximation comes from the Taylor expansion of the natural logarithm function.

For an ideal, two-component solution:

$$x_2 = \frac{\pi \cdot \overline{V}_1}{RT}$$

Since real solutions tend to ideality as the solute concentration decreases[11]:

$$x_2 = \frac{n_2}{n_1 + n_2} \approx \frac{n_2}{n_1}$$

in which n is the number of moles of the indicated component. In the case of dilute solutions:

$$n_2 = \frac{n_1 \pi \overline{V}_1}{RT} = \frac{\pi V_1}{RT}$$

where V_1 is the volume of solvent in the solution. Even more important is relate vapor pressure to osmotic pressure to convince ourselves that osmotic pressure is an appropriate measure of the driving force across an air gap. The governing equation of water flux through an air gap is:

$$J_W = L_V \Delta P_W^{vap}$$

where J_W is water flux, L_V is permeability using vapor pressure as a driving force, and $\Delta P_W{}^{vap}$ is the difference in vapor pressure on either side of the gas interface. The vapor pressure can be expressed as[13]:

$$\Delta P_W^{vap} = P_W^{sat} \Delta x_W$$

where $P_W{}^{sat}$ is the saturation pressure of water, and Δx_W is the mass fraction of water in solution. Substituting in the salt mass fraction gives:

$$\Delta P_W^{vap} = P_W^{sat} \Delta(1 - x_S)$$

where x_S is the salt mass fraction. Conversion of mass fraction to concentration yields:

$$\Delta P_W^{vap} = P_W^{sat} MW_W \Delta c_S / \rho_W$$

where MW_W is the molecular weight of water, c_S is salt concentration and ρ_W is the density water. Substituting osmotic pressure for salt concentration ($\Delta\pi = RT\,\Delta c_S$):

$$\Delta P_W^{vap} = \frac{P_W^{sat} MW_W \Delta\pi}{\rho_W RT}$$

Finally, relating water flux through an air gap for a vapor pressure driving force to a osmotic driving force:

$$J_W = \left(\frac{L_V P_W^{sat} MW_W}{\rho_W RT} \right) \Delta\pi$$

This allows us to use osmotic pressure in water transport through a hydrophobic membrane and still obey the thermodynamics that govern the system.

Dewatering through RO Membranes

As stated previously, our main objective is to eliminate internal concentration polarization in a RO membrane. We have hypothesized that introducing an air gap on the low salt reservoir side of the membrane should stop the flux of solute across the membrane. By examining the permeability as a function of time we can determine whether or not internal concentration polarization occurs. Since RO membranes are composites of a thin polymer dense film supported by a thick porous backing, two orientation are possible. Normal orientation is defined as the skin facing the high salt reservoir. Conversely, inverse orientation is defined as the skin facing the low salt reservoir. The equations for the permeability (for a zero low salt concentration) of each respective orientation are[4]:

$$L_P^{inverse} = \frac{A\sigma \exp(-J_W R_{PS})}{1 + B/J_W [\exp(-J_W R_{PS}) - 1]}$$

$$L_P^{normal} = \frac{A\sigma}{1 + B/J_W [\exp(-J_W R_{PS}) - 1]}$$

where L_P is the membrane permeability coefficient (m/sec Mpa), A is hydrodynamic permeability (m/sec Mpa), σ is a solute reflection coefficient (dimensionless), J_W is water flux (m/sec), B is solute permeability (m/sec), and R_{PS} is the resistance to solute transport in the porous media membrane backing (sec/m). By introducing a vapor membrane between the low salt reservoir and the membrane, the solute permeability term is eliminated. So, as $B \rightarrow 0$ the permeability for each orientation becomes:

$$L_P^{inverse} = A\sigma \exp(-J_W R_{PS})$$

$$L_P^{normal} = A\sigma$$

For the inverse orientation, permeability is still a function of water flux and can vary with time. This makes sense because the porous backing is facing the high salt reservoir, so some diffusion of salt into the backing may still occur. The normal orientation results in a constant permeability

as the solute permeability is eliminated. This argument suggests that the magnitude of the permeability for normal orientation should be larger than the permeability for inverse orientation.

Another issue considered is that the introduction of an air gap dramatically increases the resistance of mass transfer. The effect of the air gap is consequently a decrease in water flux. Therefore, it is useful to evaluate the permeability equations as $J_W \rightarrow 0$, and compare to the results as $B \rightarrow 0$:

$$L_p^{inverse} = A\sigma$$

$$L_p^{normal} = A\sigma$$

In normal orientation the permeability is indistinguishable between low water flux and elimination of solute permeability. But, in inverse orientation there is a difference between the two conditions. The model predicts that the permeability is smaller in magnitude if solute permeability is zero than if the water flux is very small.

VI. RESULTS AND DISCUSSION

Hydrophobic Membranes: Liquid-Liquid Contact with Phase Change

The motivation for using a hydrophobic membrane is to eliminate the variation in flux over time found with hydrophilic membranes. For water to pass through a hydrophobic membrane it must vaporize at the low salt interface of the membrane and then condense on the high salt interface (Figure 4). The advantage of this membrane is that salts and other precipitants cannot permeate through the membrane. Theoretically, eliminating internal concentration polarization will result in constant permeability, and thus constant flux of water through the membrane.

To test the above theory, four experiments were done with liquid contact on both sides of a polypropylene membrane. The high salt reservoir contained a 3 M sodium chloride solution and the low salt reservoir was pure water. Each experiment ran for approximately 24 hours and fluxed 15-20 ml of water from the pure water reservoir. The first indication that concentration polarization was eliminated comes from examining the raw data. Figure 6 is grams of water lost from the water reservoir as a function of time for both the hydrophobic and hydrophilic membranes. The linear relationship of the data implies that flux is constant throughout the experiment. Notice the inflexion in the RO membrane data, suggesting a decrease in flux over time. Further statistical analysis of the permeability as function of time calculations (Table 1) shows that within a 95% confidence interval the slope of permeability for the polypropylene membrane is zero. The permeability is statistically independent time in three of the four experiments. A tear in the membrane or perhaps membrane fouling are possible explanations why the fourth experiment did not exhibit the same behavior. The result of these experiments is that concentration polarization can be eliminated via a phase change in a hydrophobic membrane.

Hydrophilic Membranes: Liquid-Liquid Contact for Baseline Data

The next set of experiments established a baseline with previous studies' results for RO membranes without an air gap. It should be noted that unless otherwise specified, all RO experiments have been done in an inverse orientation. Previous authors proved that the reduced permeability of RO membranes is due to internal concentration polarization (Theory and

Modeling)[2]. Internal concentration polarization is the result of salt fluxing against the water flux, that is from high salt to low salt, through the porous backing of the RO membrane. Consequently, the driving force decreases, which causes the flux to decrease. Examining the raw data (Figure 6) reveals that the water flux is not linear with time. The decaying nature of a second order polynomial fit suggests as time increases, the flux decreases.

Figure 7 compares liquid-liquid contact for both the polypropylene and RO membrane. The slope of the RO experiments is significantly greater than those of the polypropylene. Recall three of the four polypropylene slopes are statistically zero (Table 1) and that the appearance of a non-zero slope is simply the result of a linear fit to the raw data. There is also a difference in the repeatability of the two membranes. Note that the RO membrane has a starting permeability range of approximately 2.0×10^{-8} to 2.5×10^{-8} m/Pa s, whereas all polypropylene starts at about 1.4×10^{-8} m/Pa s. Therefore, the polypropylene membrane exhibits repeatable results. The variability in the RO results could be a result of the pretreatment. Since the rate at which the stir cell is depressurized may vary, this could cause a change in the permeability of the membrane. The above comparison illustrates the effectiveness of the phase change to eliminate variability in permeability.

Hydrophillic Membrane: Introduction of an Air Gap

The next novel approach is to use an air gap as a vapor boundary with a RO membrane. In this case there is a 2-3 mm gap between the pure water reservoir and the membrane surface. In a heat transfer analog the membrane is one resistance, and the introduction of an air is another resistance. Similar to the hydrophobic membrane, salt cannot transport across the air gap and, therefore, no concentration polarization should occur. Figure 8 is a comparison of the performance of the RO membrane with and without an air gap. The introduction of the air gap yields two important results. First, the time variance of permeability is eliminated. Five of six air gap experiments with a RO membrane in inverse orientation have a permeability slope of zero within a 95% confidence interval. Second, the magnitude of the permeability decreases approximately an order of magnitude. The drop in permeability is due to the added resistance term of the air gap, but is not necessarily an undesired result. In crystal growth, lower dewatering rates will generally yield higher quality crystals.

A second group of experiments used the RO membrane with an air gap in normal, rather than inverse, orientation. Recall that in normal orientation the skin interfaces with the high salt reservoir. Figure 9 compares RO air gap experiments between inverse and normal orientations. Three of four normal orientation experiments produce permeability that is statistically independent of time within a 95% confidence interval. The only difference between the two orientations is normal orientation has on average a lower permeability. This is the opposite the effect predicted by the model described in *Theory and Modeling*. But statistically speaking, for the 3 M NaCl/water system, permeability is virtually independent of orientation. This may not be the case for an actual crystal growth system, which would have salt and precipitates in the low salt reservoir rather than pure water.

Dewatering in FPA Crystal Growth Apparatus

Testing in the FPA crystal growth apparatus was the final method we used to evaluate the hydrophobic membrane. These experiments were primarily done to compare the performance of a hydrophobic membrane with previous studies of RO membranes[14]. The FPA contains cylindrical inserts that are immersed in a salt solution in glass tubes (see Figure 5). Each insert

has four cylindrical wells that hold the crystallization solution. FPA experiments are set up with an air gap in between the crystallization solution and the membrane. An air gap with a hydrophobic membrane was not studied in the previous section of experiments because the air membrane in the pores already takes care of a phase change. But, there are certain advantages to an air gap and a hydrophobic membrane. An air gap simply introduces another mass transfer resistance, thus a slower flux rate. For the growth of high quality crystals a slow dewatering rate is actually the desired condition. So, this combination may be the best alternative because of both a slow and constant dewatering rate. Another alternative is using hydrophobic membrane and decreasing the driving force to slow down dewatering.

For this comparison pure salt solutions were used for characterization purposes. The surrounding salt solution, or high salt reservoir, was held constant at 3 M NaCl. The solution in the insert, or low salt reservoir, varied in salt concentration so as to determine the effect of changing the driving force. Figures 10-13 are the results for 0 M, 1 M, 2 M, and 3 M solutions. The polypropylene membrane dewaters a larger volume over the experimental time for all cases. This is consistent with results from the membrane characterization experiments, where we found that permeability for the polypropylene membrane was about an order of magnitude higher than for the RO membrane. The difference in dewatering rate is not as drastic as what we observed in the characterization experiments. This seems to suggest that mass transfer through the air gap is the rate-determining step.

Lysozyme Crystallization

We spent the majority of this study characterizing membrane process kinetics and thermodynamics. But, the ultimate goal is to grow biological macromolecule crystals. Lysozyme is an excellent molecule to test our novel techniques because it is easy to crystallize and its crystal structure is well understood. Figures 14 and 15 show the results of our crystallization efforts for both RO and polypropylene membranes respectively. Lysozyme often precipitated out of solution with the polypropylene membrane because the dewatering rate was too fast. The crystals obtained from polypropylene membranes were mostly agglomerates of crystals that had grown into each other (Figure 15). Experiments with RO membranes yielded crystals like the kind desired for x-ray diffraction (Figure 14). The preferred crystals for analysis of a molecule's structure are single crystals with distinct dimensions. Therefore, the type of membrane chosen for crystallization is dependent on the application. If crystallization is a final purification step, then use the quick dewatering of a hydrophobic membrane. Of course decreasing the driving force could make hydrophobic just as effective as RO membranes for crystallization. But, RO membranes are more rigid and much easier to handle, so they may still be the desired membrane for crystal structure studies.

VII. SUMMARY

Conclusions

Our hypothesis was to eliminate internal concentration polarization by introducing a phase change. The idea of introducing a phase change originates from work done in osmotic distillation and has been modified for biological macromolecule crystal growth. Two different approaches were tested. The first, replacing the standard RO membrane with a hydrophobic membrane, creating a gas membrane in its pores. The second introduced a gas membrane via an air gap between the low salt reservoir and the RO membrane surface. In both cases, we were able to eliminate variability in membrane permeability over time within a 95% confidence

interval. A hydrophobic membrane (polypropylene) with liquid-liquid contact yields approximately the magnitude permeability, but without the decrease over time as exhibited in a RO membrane. Using a RO membrane with an air gap decreased the magnitude of the permeability an order of magnitude. Thus, applications that require higher flux rates or liquid-liquid contact should use a hydrophobic membrane rather than an RO membrane. In applications where a lower flux is desired, an RO membrane with an air gap is appropriate.

The end of these results is to apply them to understanding and controlling biological macromolecule crystal growth. The most significant result is that we can now control the dewatering rate of biological macromolecule solutions. In other words, once the kinetics of crystallization is determined for a particular molecule, experiments can be designed to dewater at a specified rate. For the purpose of growing difficult molecules the following is the optimal membrane conditions:

- Use a RO membrane, pretreated with deionized water flux under a head pressure of 50 psi nitrogen for one hour.
- Perform experiments using an air gap between the biological macromolecule solution and the membrane.
- Operate RO membrane in normal orientation, that is, with the porous backing contacting the air gap.

In general, the slower the dewatering rate, the higher the quality of crystals obtained. So, the air gap experiments yielded the lowest permeability and consequently the lower the water flux. Normal orientation is chosen because modeling predicts that permeability is independent of water flux (not true for inverse orientation). Further, in normal orientation the porous backing contacts the air gap, this makes it impossible for internal concentration polarization in the backing. In addition, dewatering with a phase change lends itself to fields beyond crystal growth including power generation, desalination, and the concentration of labile pharmaceutical products. For the sole purpose of purification, hydrophobic membranes are an attractive alternative because they dewater more quickly than RO membranes while eliminating internal concentration polarization.

Future Work

Now that the science for dewatering with a phase change has been investigated, the next step is to test this method with numerous biological macromolecules. The only molecule used for this study is the relatively easy lysozyme crystal. Indeed, the true test is to try to grow difficult molecules such as RNA (only 95 structures determined to date). Another path is to investigate alternative membranes. A hydrophobic membrane with a smaller pore size could decrease the water flux to conditions more conducive to crystal growth. Dense films are promising because of their transport properties would effectively reject salt back fluxing.

VIII. REFERENCES

1. Lee, C.Y. **Crystallization of Oligonucleotides by Osmotic Dewatering and Cell Separation by Inclined Sedimentation**. Ph.D. Thesis. University of Colorado at Boulder. 1996.

2. Scovazzo, Paul. **Multiple Phase Transport in Membranes and Porous Media in Low Gravity Experiments**. Ph.D. Thesis. University of Colorado at Boulder, 1998.

3. Watson, James. **Molecular Biology of the Gene**. New York: Addison-Wesley Pub Co, 1987.

4. Scovazzo, Paul, C.Y. Lee, and Paul Todd. "Dynamics of Reverse Osmosis Membranes and Membrane Pretreatment Methods for Applications in Crystal Growth By Osmotic Dewatering." Unpublished. University of Colorado at Boulder, 1999.

5. Sarti, G.C., C. Gostoli. "Low Temperature Distillation through Hydrophobic Membranes." **Separation Science and Technology**, 22 (1987), 855-872.

6. Todd, Paul, Subhas K. Sikdar, Cheryl Walker. "Application of osmotic dewatering to the controlled crystallization of biological macromolecules and organic compounds." **Journal of Crystal Growth**, 110 (1991), 283-292.

7. Lee, C.Y., Michael G. Sportiello, Stephen P. Cape, Sean Ferree, and Paul Todd. "Characterization and Application of Osmotic Dewatering to the Crystallization of Oligonucleotides." **Biotechnology Progress**, 13 (1997), 77-81.

8. Lee, C.Y., Scott R. McEntyre, Paul Todd, Kurt Schaefer, Craig E. Kundrot. "Control of nucleation in oligonucleotide crystallization by the osmotic dewatering method with kinetic water removal rate control." **Journal of Crystal Growth**, 187 (1998), 490-498.

9. Hogan, Paul A., R. Phillip Canning, Paul A. Peterson, Robert A. Johnson. "A New Option: Osmotic Distillation." **Chemical Engineering Progress,** July 1998, 49-57.

10. Kunz, Werner, Ali Benhabiles, Roger Ben-Aim. "Osmotic evaporation through macroporous hydrophobic membranes: a survey of current research and applications." **Journal of Membrane Science**, 121 (1996), 25-36.

11. Hiemenz, Paul C. **Principles of Colloid and Surface Chemistry**. New York: Marcel Dekker, 1997, 110-114.

12. Schofield, R.W., A.G. Fane, C.J.D. Fell. "Heat and Mass Transfer in Membrane Distillation." **Journal of Membrane Science**, 33 (1987), 299-313.

13. Cussler, E.L. **Diffusion: Mass Transfer in Fluid System**. New York: Cambridge University Press, 1997, 217-223.

14. Fromenta, Ariel, Paul Scovazzo, Paul Todd. "Osmotic Dewatering Fluxes in Low Gravity Crystallization Hardware." Unpublished. University of Colorado at Boulder, 1999.

FIGURES AND TABLES

Figure 1: Block diagram of dialyzer apparatus.

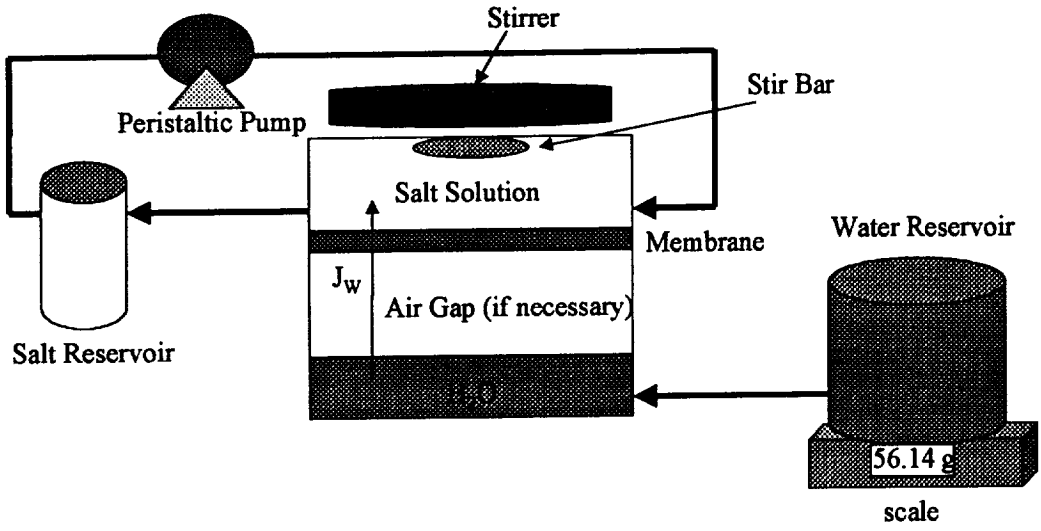

Figure 2: Osmotic dewatering diagram. Water fluxes from the low salt reservoir to the high salt reservoir, while the biological macromolecule crystallizes.

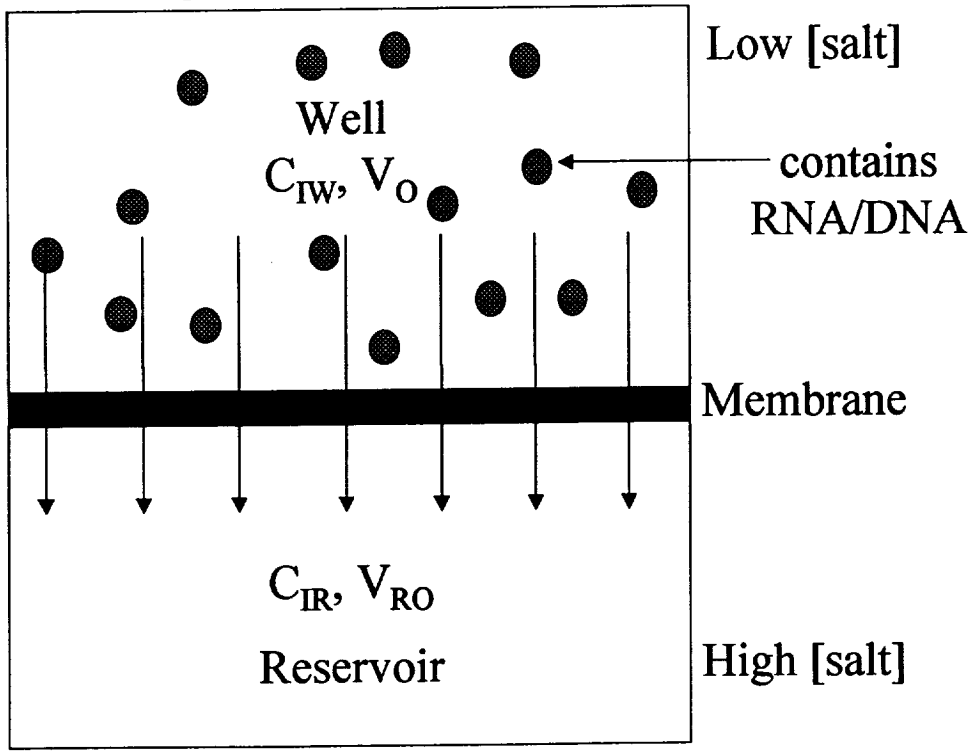

Figure 3: Internal concentration polarization. The effective osmotic pressure across the skin is dramatically less than the measure osmotic pressure due to the diffusion of salt through the porous backing of the RO membrane.

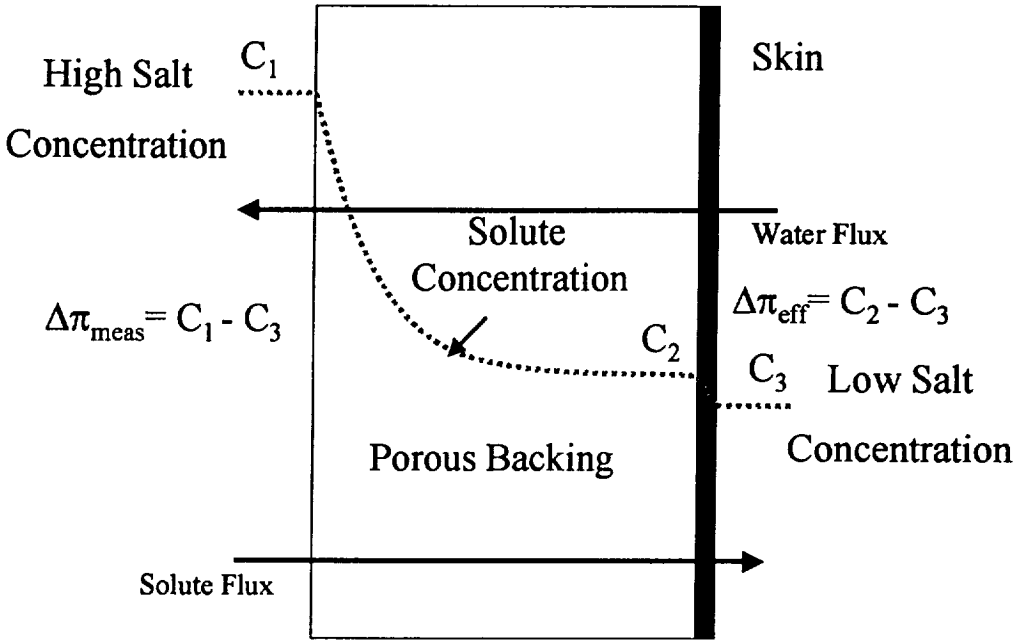

Figure 4: Physical explanation of osmotic dewatering with a hydrophobic membrane. Since the hydrophobic membrane does not wet, an air membrane is formed in the pores. Water fluxes by evaporating at the low salt reservoir interface and condensing at the high salt reservoir interface.

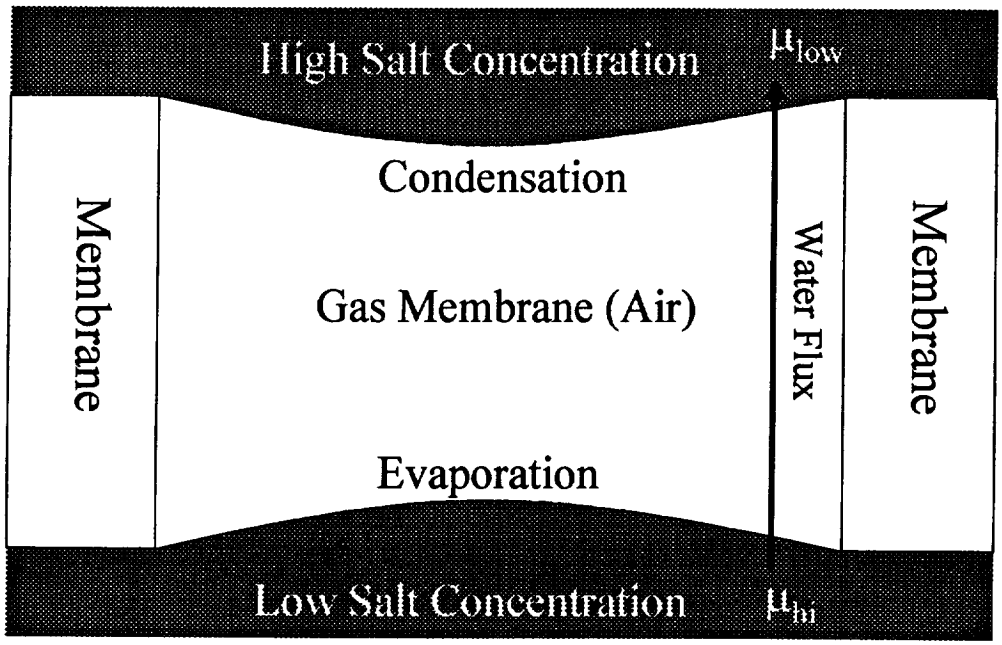

Figure 5: FPA Diagrams. Insert and tube before and after activation

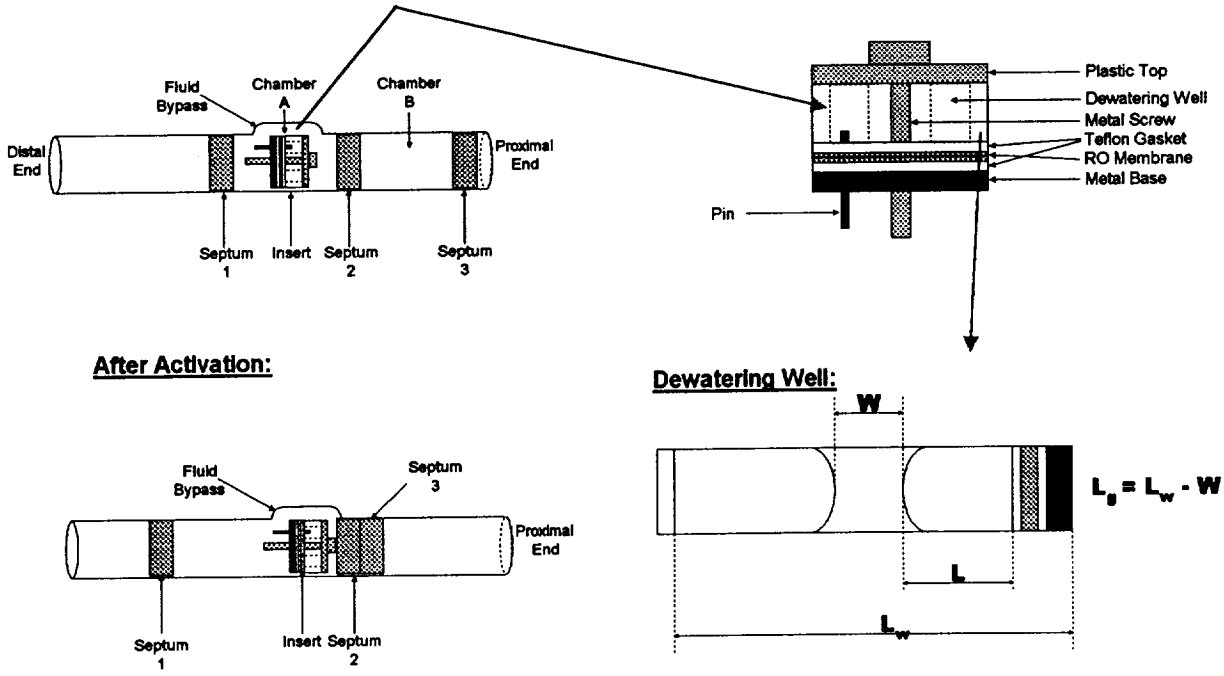

Table 1: Statistics on the slope of permeability as a function time. The slope is zero within a 95% confidence interval for all slopes except those highlighted.

Run	Slope	standard error	lower 95%	upper 95%
polypro 1	3.2E-11	3.5E-11	-3.6E-11	1.0E-10
polypro 2	6.0E-11	5.7E-11	-5.2E-11	1.7E-10
polypro 3	3.6E-11	3.4E-11	-3.1E-11	1.0E-10
polypro 4	-8.0E-11	7.5E-12	-9.5E-11	-6.5E-11
RO Airgap 1	2.3E-12	5.2E-12	-7.9E-12	1.2E-11
RO Airgap 2	-6.0E-12	2.9E-12	-1.2E-11	-3.3E-13
RO Airgap 3	-4.1E-12	4.3E-12	-1.3E-11	4.3E-12
RO Airgap 4	-7.7E-12	4.3E-12	-1.6E-11	8.7E-13
RO Airgap 5	3.9E-12	1.6E-11	-2.8E-11	3.6E-11
RO Airgap 6	-3.0E-12	5.1E-12	-1.3E-11	7.0E-12
RO Airgap N2	-6.1E-12	3.6E-12	-1.3E-11	1.0E-12
RO Airgap N3	-2.8E-11	9.7E-12	-4.7E-11	-8.6E-12
RO Airgap N4	4.1E-12	7.0E-12	-9.7E-12	1.8E-11
RO Airgap N5	6.6E-12	7.8E-12	-8.7E-12	2.2E-11
RO Baseline 1	-1.2E-09	9.6E-13	-1.2E-09	-1.2E-09
RO Baseline 2	-2.2E-10	6.6E-12	-2.3E-10	-2.1E-10
RO Baseline 3	-1.7E-10	1.4E-11	-2.0E-10	-1.4E-10

Figure 6: Raw data of liquid-liquid contact with polypropylene and RO membranes. Notice the linear relationship for the polypropylene membrane and the inflexion in the RO membrane.

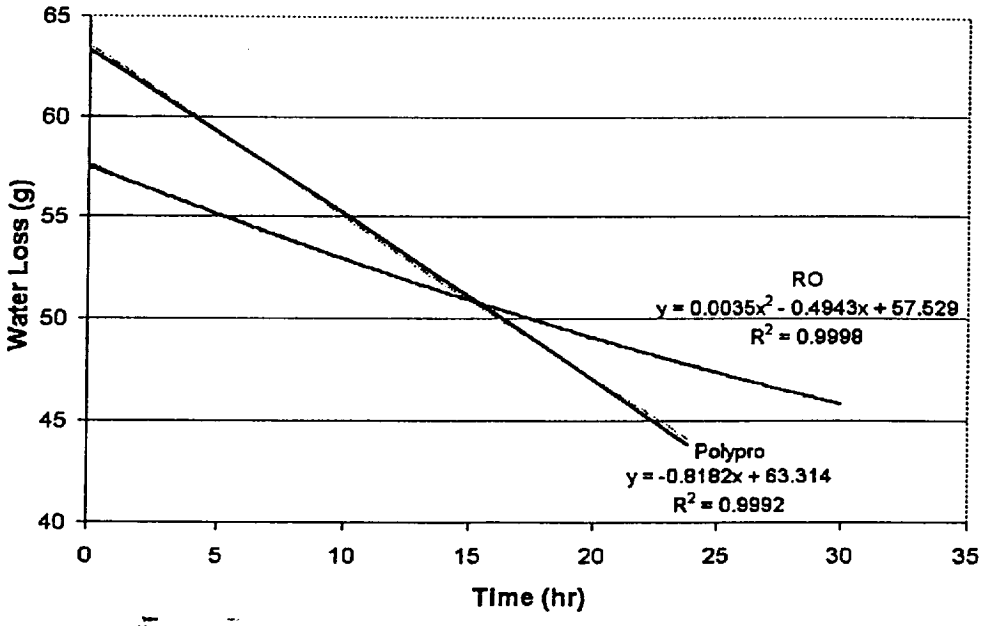

Figure 7: Liquid-liquid contact with membrane for a hydrophobic membrane (polypropylene) and hydrophilic membrane (RO).

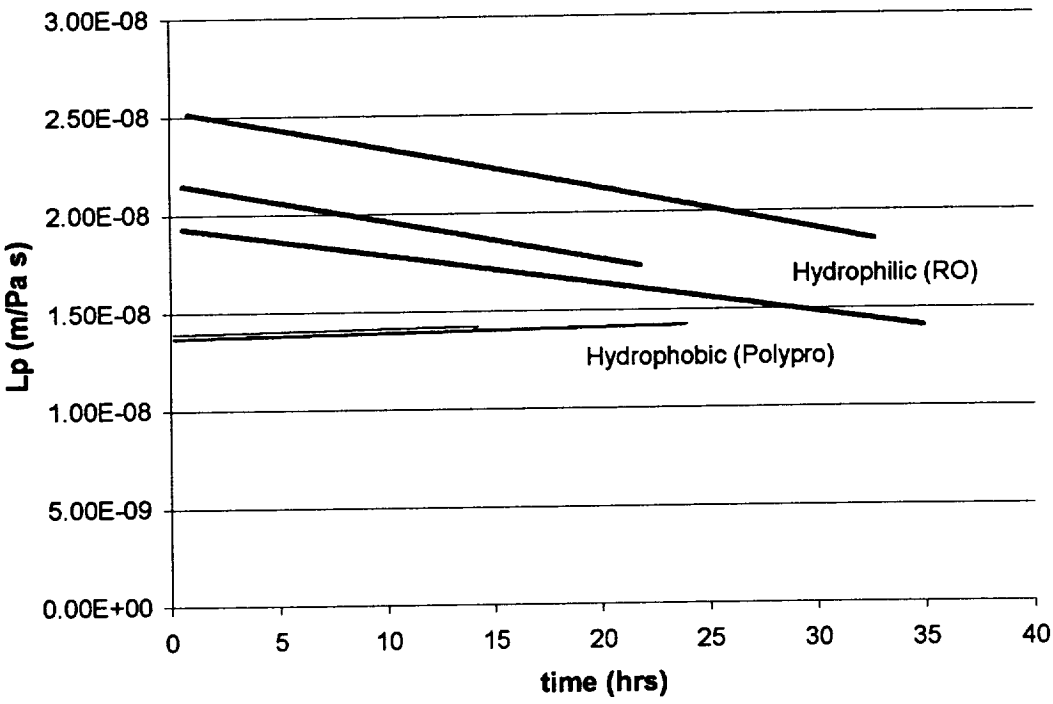

Figure 8: Comparison of liquid-liquid contact and an air gap for RO membrane in inverse orientation.

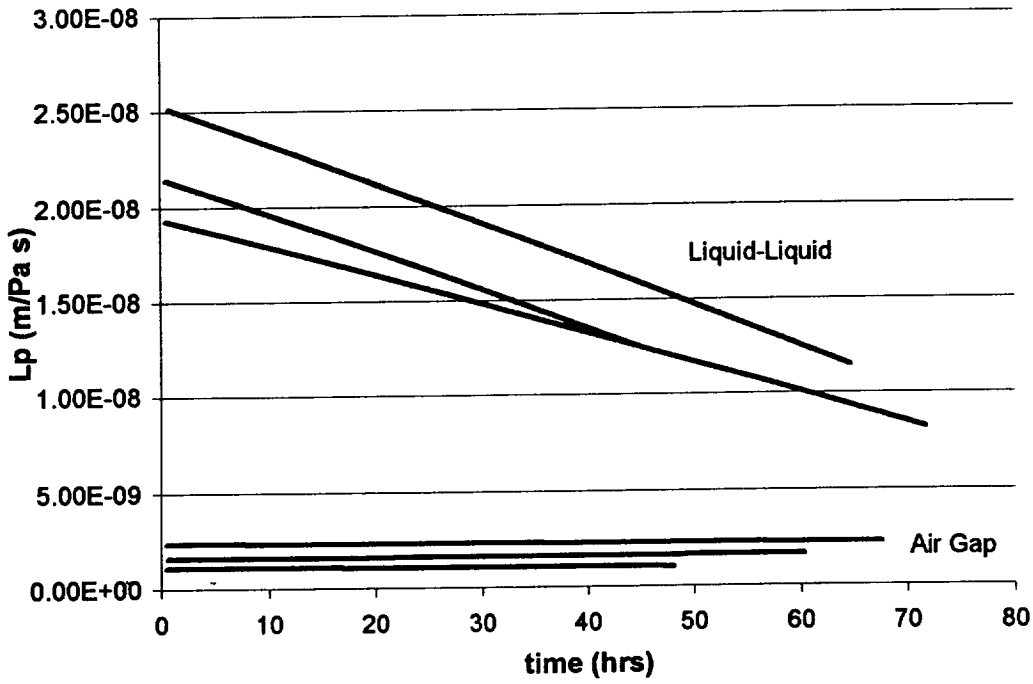

Figure 9: Comparison of inverse versus normal orientation for a RO membrane with an air gap.

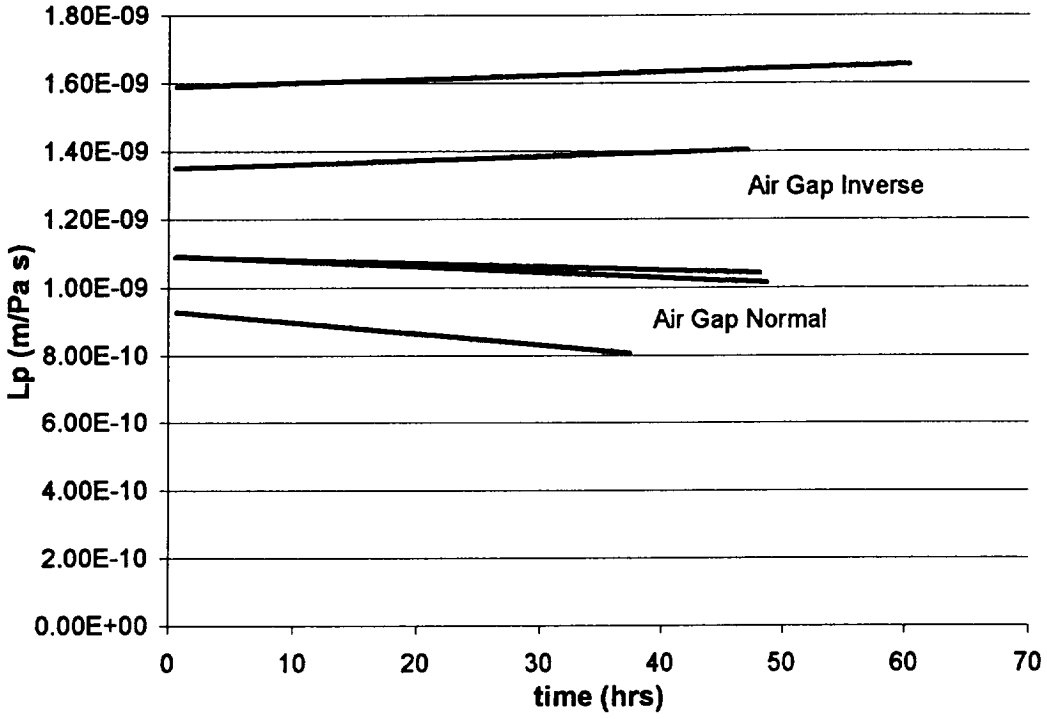

Figure 10: Polypropylene and RO FPA dewatering data for 0 M well concentration.

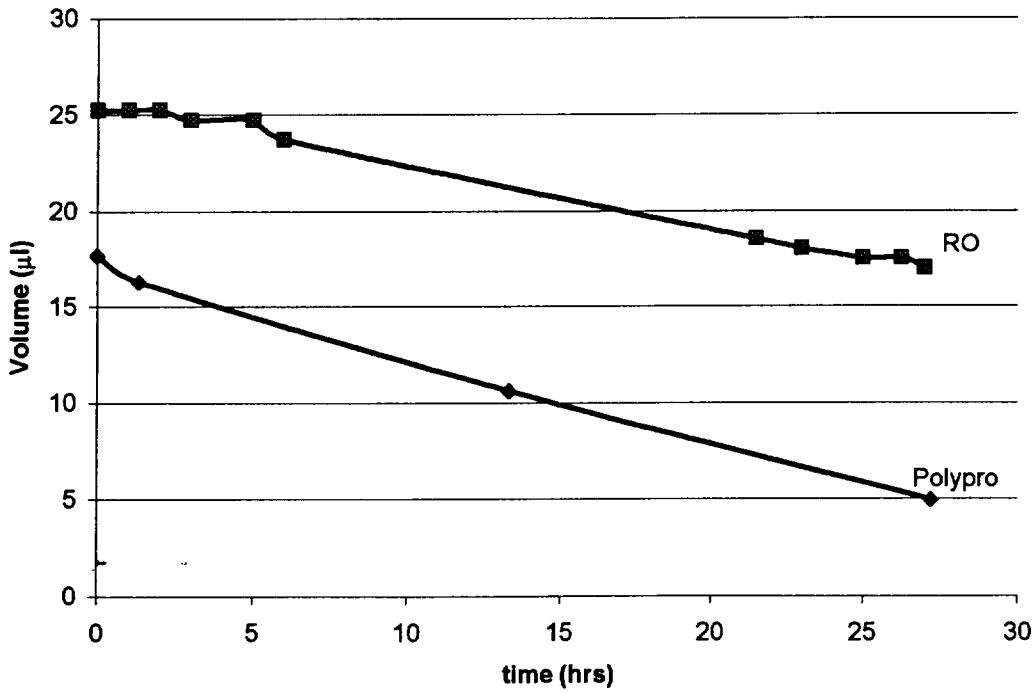

Figure 11: Polypropylene and RO FPA dewatering data for 1 M well concentration.

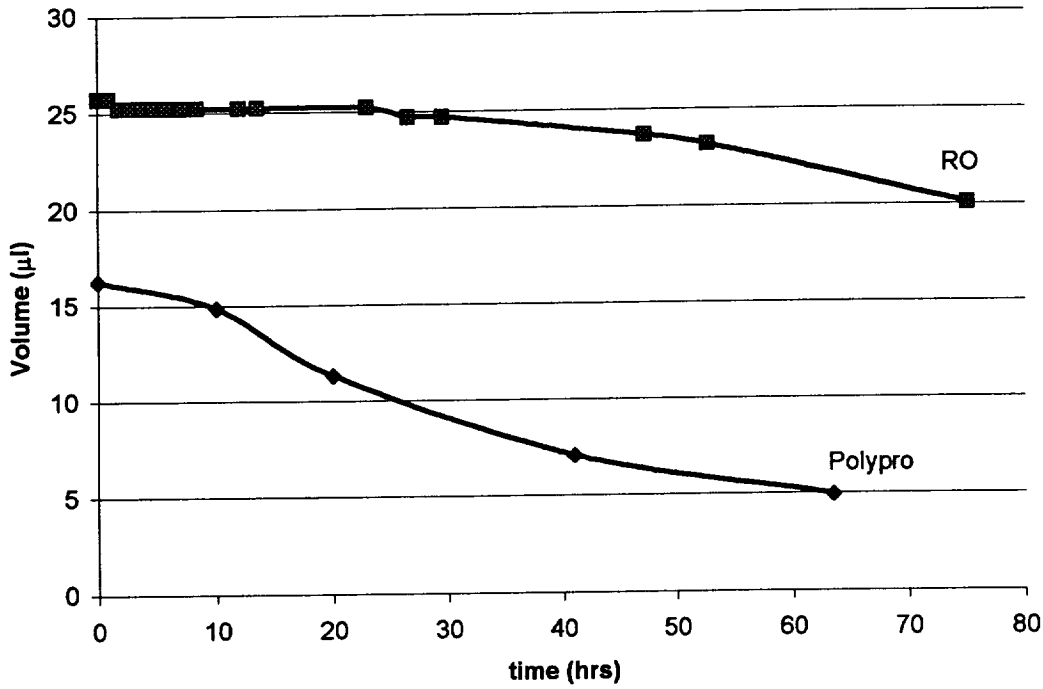

Figure 12: Polypropylene and RO FPA dewatering data for 2 M well concentration.

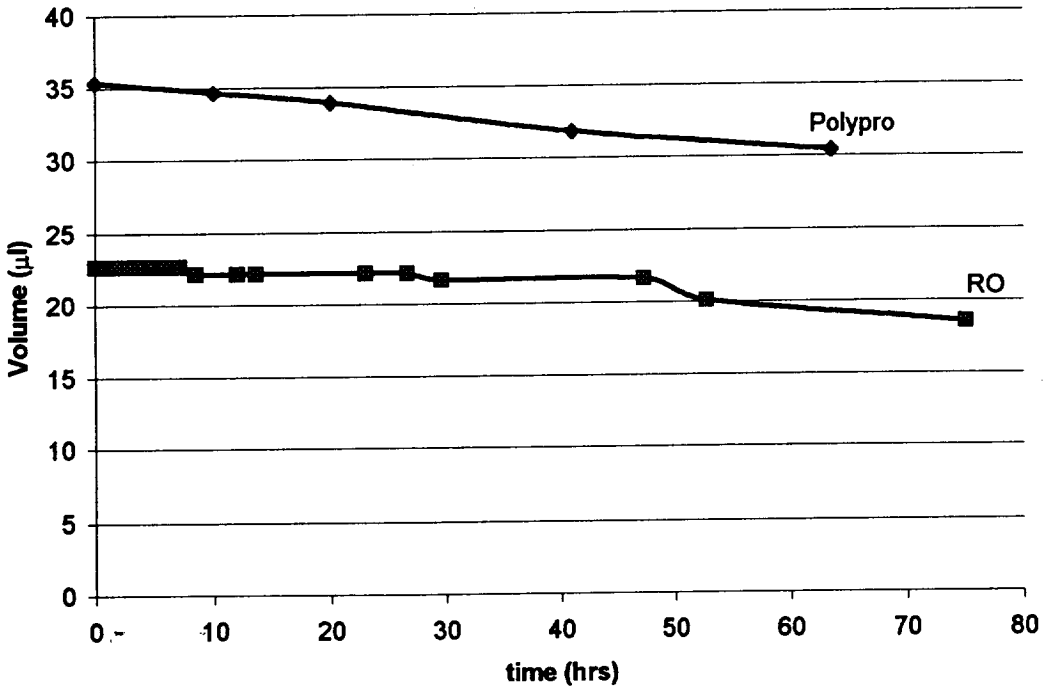

Figure 13: Polypropylene and RO FPA dewatering data for 3 M well concentration.

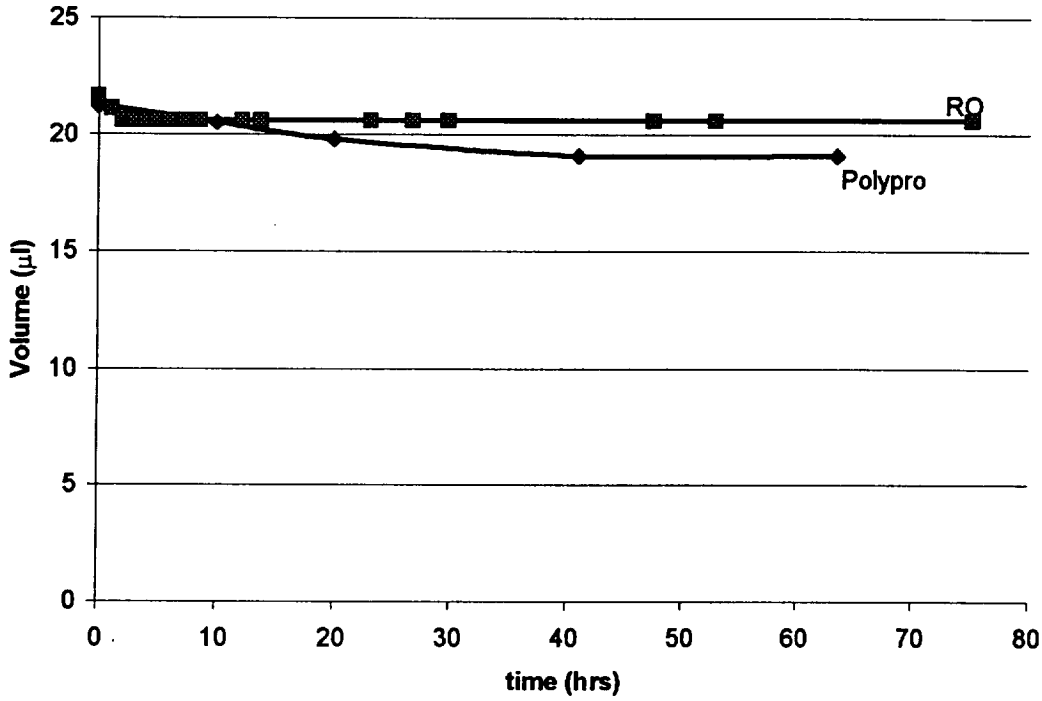

Figure 14: Lysozyme crystals from FPA using a RO membrane.

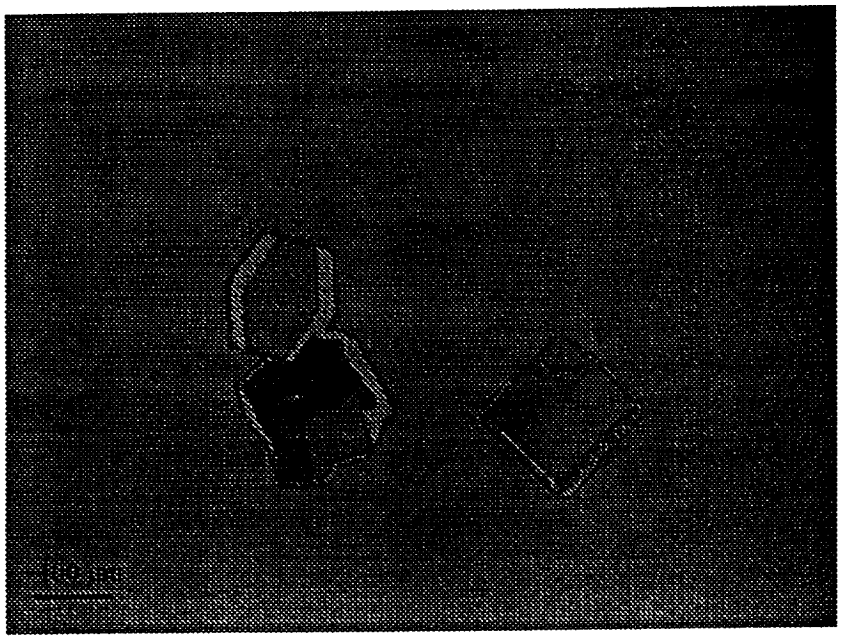

Figure 15: Lysozyme crystals from FPA using a polypropylene membrane.

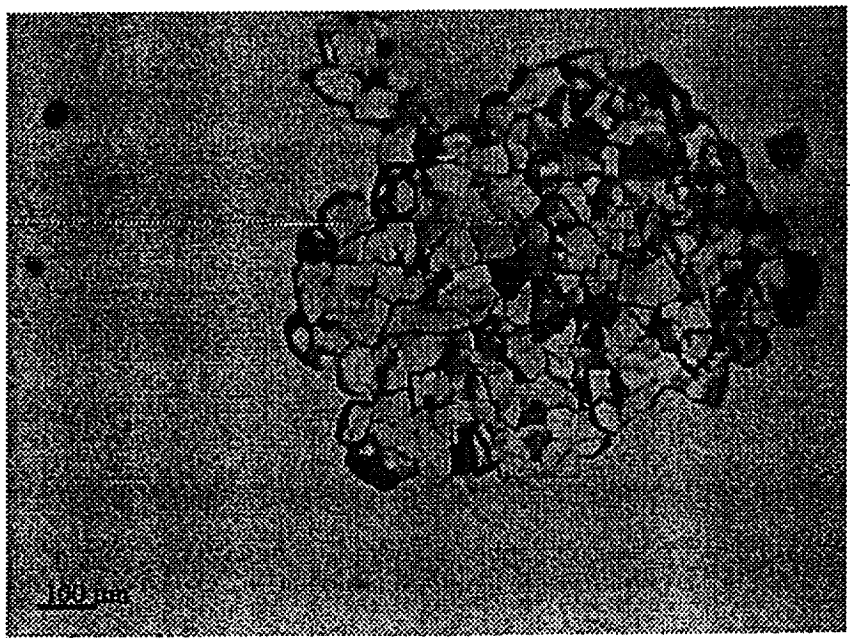

Chapter 25

Modeling Disjoining Pressure in Submicron Cylindrical Pores

Paul Scovazzo and Paul Todd

CHAPTER 25
MODELING DISJOINING PRESSURE IN SUBMICRON CYLINDRICAL PORES

By Paul Scovazzo

Abstract

Other researchers have previously considered the thermodynamics of transport in liquid/vapor-containing porous media, conceptually extending porous media transport laws and matrix potential to submicron pores and low saturation media. This previous work did not, however, give models for estimating the necessary thermodynamic terms in submicron pores. This present work proposed models for estimating the necessary thermodynamic terms in cylindrical pores. Specifically, it modeled disjoining pressures in cylindrical geometries. This work produced closed form cylindrical pore disjoining pressures for London/van der Waals and solute/pore wall interactions, which are the slit pore models with the characteristic pore size replaced by the radius and multiplied by 6, a 48-fold or more increase in magnitude. In addition this work contains a numerical solution for electrostatic interactions. The result of the numerical solution was a 9-fold increase in the modeled disjoining pressure compared to the slit pore model.

1. Background Thermodynamic Considerations

Nitao and Bear considered the thermodynamics of transport of aqueous solutions in porous media [1]. Their work conceptually extended Darcy's Law, porous media transport laws, and matrix potential to submicron pores and low saturation media. It did not, however, give models for estimating the necessary thermodynamic terms for this extension. This current work proposes models for this extension in cylindrical pores. The following paragraphs summarize the portions of their article that have relevance to this current work. The focus is on the thermodynamics of fluids in porous media.

The classical definition of fluid thermodynamics in porous media is via the definition of the porous media capillary pressure, P_c, determined from the following relationship:

$$P_c = P_g - P_l = \left\langle \frac{2\sigma\cos\alpha}{r} \right\rangle_{lg} \qquad (1)$$

Where: P_g = Pressure of the gas phase (Pa), P_l = Pressure of the liquid phase (Pa), σ = Liquid/gas surface tension (Pa m), α = Liquid/pore wall contact angle, r = Pore radius (m), and = Liquid/gas surface average of Term. Nitao and Bear noted that "at low saturations, when the liquid occurs only as $\langle \text{Term} \rangle_{lg}$ films on the walls of the pores in the porous media, most of the liquid/gas interfaces may be flat, so that the radii of curvature (r) becomes very large [1]." This means that as the saturation of the porous medium saturation approaches zero, r in equation (1) approaches ∞ and the capillary pressure becomes equal to zero. This is contrary to the observation of water potentials in porous media, defined as matrix suction, ψ, which approaches ∞ as matrix saturation approaches zero [2]. For this reason Nitao and Bear substitute matrix suction for capillary pressure and define it as follows [1]:

$$\psi = -\Sigma\omega\mu \qquad (2)$$

$$\psi = \left\langle \frac{2\sigma\cos\alpha}{r} \right\rangle_{lg} - \rho\langle\varphi\rangle_{lg} \qquad (3)$$

Where: ω = volume fraction of liquid component (m^3/m^3), μ = chemical potential of liquid component (J/m^3 or Pa), ρ = liquid density (Kg/m^3), and φ = potential energy per unit mass due to surface forces (J/Kg). The second term on the right-hand side of equation (3) accounts for the surface forces acting on fluid films within the porous media (*Disjoining Pressures* symbolized in this text by Π). For attractive surface forces, the magnitude of this Disjoining Pressure term grows as the saturation of the porous medium approaches zero and the adsorbed liquid film thins (as illustrated later in this text in equations 5 through 7 where h is the thickness of the adsorbed liquid film). So, at high saturations the first term on the right-hand side of equation (3) dominates, and at low saturations the Disjoining Pressure or second right-hand term dominates producing a matrix suction, ψ, that approaches ∞ as saturation approaches zero. Note also that at high saturations and small pore radii the Disjoining Pressure term may also dominate.

Nitao and Bear used this redefinition of matrix suction to refine Kelvin's Law, porous media diffusion transport, and Darcy's Law. In order to apply these equations redefined by Nitao and Bear, it is necessary to have some model of surface attractive forces, $\rho\varphi$. In flat films, the literature contains models for $\rho\varphi$ defined as disjoining pressures, $\Pi = -\rho\varphi$. The next section discusses these models. To adopt these flat models to unsaturated pores where the pore radius is significantly larger than the film thickness, h, Derjaguin and Churaev recommended the following [3]:

$$\Pi(\text{curved surface}) = \Pi(\text{flat surface}) + \sigma/r \qquad (4)$$

If $h << r$

This present work develops models for determining the disjoining pressures in saturated pores where the distance of surface force influence, h, is of the same order as the pore radius, a situation under which disjoining pressure might be significant for transport in porous media. This situation could arise in membrane processes as well as "...very dry soils, (or) soils with fine-grained material..."[1].

2. Disjoining Pressure

At a fluid interface pressure becomes anisotropic with normal and tangential components differing. The normal component is constant and balances the mechanical forces. The tangential component is not constant and leads to the concept of disjoining pressure. The definition of disjoining pressure is $\Pi = P - P_f$ where P = applied pressure and P_f is the fluid pressure in the interface film. Disjoining pressure is a function of fluid thickness, h, and is a unique thermodynamic characteristic of the fluid film that makes the film differ from the bulk phase. This thermodynamic characteristic affects the chemical potential, μ, of the solvent.

The equations below represent the flat plate film equation forms for some of the disjoining pressures relevant in porous media. Other non-DLVO (Double Layer and van der Waals) interaction disjoining pressures may be applicable for a specific porous medium problem; however, these three interactions illustrate the use of the proposed cylindrical pore models of this work.

Π_m = Flat Plate London/van der Waals Interactions [4] = $A/6\pi h^3$ (5)

Π_e = Flat Plate Electrostatic Interactions [5] = $D\exp(-\kappa h)$ (6)

Π_s = Flat Plate Solute/Pore Wall Interactions [4] = $2C_\infty A_o/V(h-\delta)^3$ (7)

Where: A = Hamaker constant (J), h = Film thickness (m), D = $(64nkT)\tanh^2[ze\Psi/4kT]$ (Pa), κ = Debye-Hückel reciprocal length = $(8\pi nz^2e^2/\varepsilon kT)^{-0.5}$ (m^{-1}), C_∞ = Bulk solute concentration (mol/mol), A_o = Solute/water interaction constant (J m^3), V = Molecular volume (m^3/mol), δ = Minimum solute approach distance (m), n = Ion number density (ions/m^3), k = Boltzmann constant (J/K), T = Absolute Temperature (K), z = Solute charge number (valence), e = Electron charge (Coulomb), Ψ = Electrostatic surface potential (volts), and ε = Dielectric constant ($Coulomb^2$/Jm).

3. Saturated Porous Media

In saturated porous media the disjoining pressures can influence transport if the characteristic length of the pores is small enough to allow the disjoining-pressure magnitudes to be on the same order as the other driving forces (mechanical pressures, osmotic pressure, etc.). Literature [6,7] reports that disjoining pressures start to affect mass transfer at pore characteristic lengths of less than 100 nm. This would indicate that disjoining pressure could affect mass transfer in ultrafiltration, nanofiltration, and reverse-osmosis membrane processes or any porous media where the predominant pore size is less than 100 nm.

In a completely saturated pore some generalities apply since all fluid/solid interfaces are identical:

- Π_m (London/van der Waals attraction) is always negative
- Π_s (solute/pore wall adsorption) is positive if the solute adsorbs to the pore walls and negative if the solute does not adsorb. Its magnitude is inversely related to h and directly related to the bulk concentration of the solute. When Π_s is positive h needs to be less than 5 nm, in a slit pore, for its magnitude to overcome the magnitude of Π_m [4]
- Π_e (electrostatic repulsion) is always positive and its magnitude is inversely related to both h and ions concentration

Considering these generalities, the sum of the three above disjoining pressures for non-adsorbing solutes becomes more negative with increasing solute concentration. If the solute adsorbs, the change in the disjoining pressure with solute concentration depends on the relative changes in Π_e and Π_s. The system used to illustrate the models in this work is an ultrafiltration polysulfone membrane in contact with aqueous sodium chloride (NaCl) solutions. The Na^+ ions in the bulk solutions are weak adsorbers.

3.1 Slit Pore Models

The literature contains closed-form (analytical) solutions for porous media disjoining pressures for slit pores only. As a starting point to illustrate the functional form of the different disjoining pressures, we will start with the slit pore models and then extend the concept to cylindrical pores.

Equation (5) through (7) are the literature solutions for the slit pore (and flat plate). Table 1 shows the calculations for 30 nm slit pore disjoining pressures in a polysulfone

membrane resulting from low and high concentration sodium chloride (NaCl) solutions (3×10^{-5} M and 3 M, respectively).

3.2 Cylindrical Pores

A slit pore is not a good disjoining pressure model for membrane pores, which more closely resemble cylindrical pores with cylinder radii of magnitudes similar to the surface interaction distances. The closest models found by the authors in the literature to fluids in cylindrical pores are models for surface interactions of particles with the cylinder wall [6]. These particle interaction solutions are not closed-formed (analytical).

This section describes three models for calculating fluid disjoining pressures in cylindrical pores. All three models have the following core logic:

1. Divide the geometry into differential area elements of flat plates, d(Area)
2. Define ΔG = appropriate interaction energy per surface area model for a differential area flat plate element (for example, one of the equations 5 through 7).
3. Calculate the total energy of interaction for the total geometry,
$$E = \int_{Area} \Delta G d(Area) \quad (8)$$
4. Calculate the total interaction energy per surface area, ΔG_T = E/geometric surface area
5. Disjoining pressure, $\Pi = d(\Delta G_T)/dr$, where r is the characteristic radius of the pore.

3.3 Geometry of the Cylindrical Pore Models

Figure 1 shows the geometry of the three cylindrical pore models. The following are the basic elements of each model using the common terms of Z = unit length of the cylinder, L = distance of the differential flat plate interaction, and r = radius of cylinder:

Two-Semicylinder Interaction - As in the classic Deryaguin approach, i.e. sphere interaction with a flat plate, this model only includes interactions between parallel differential flat plate elements. Since it is an interaction of a semicylinder with a semicylinder, the area of interaction is πrz.

The disadvantage of this model is that, unlike the sphere and flat plate model where non-parallel elements are at greater distances than are the parallel elements and therefore have weaker interactions, the non-parallel elements in a cylinder are closer to each other than the parallel elements. The next two models address this disadvantage by calculating both parallel and non-parallel interactions.

Internal Sweep Interaction - This model considers the interactions of a point on the pore wall with all of the other pore wall surfaces. For each differential element, da, there is a differential interaction energy, E(a), resulting from the element's interaction with all of the other elements, calculated by sweeping through one rotation of the angle, θ. The total energy of interaction, E, is the summation of the differential interactions,

$$\int_0^{2\pi} E(a)da. \quad (9)$$

The total surface area of interaction is $2\pi rZ$.

Pivot Interaction – This model also considers the interactions of a point on the pore wall with all of the other pore wall surfaces. However, this model weighs the strength of this

interaction, via d(Area), by how parallel the surfaces are. As with the internal sweep interaction, for each differential element, da, there is a differential interaction energy, E(a), resulting from the element's interaction with all of the other elements calculated by pivoting L through one half-rotation of angle, ϕ. The total energy of interaction, E, is the summation of the differential interactions,

$$\int_0^{2\pi} E(a)da\,. \qquad (9)$$

The total surface area of interaction is $2\pi rZ$.

Figure 2 compares the interaction energies predicted by the internal sweep and pivot models as a function of the interaction's circumferential distance from the reference point. The interaction energies in figure 2 are for electrostatic interactions in a 30 nm pore due to a weak solute solution (3×10^{-3} M) and the details for the calculation appear below in section 5, Computer Simulation of Electrostatic Cylindrical Pore Interactions. The effect of weighing the interaction by how parallel the surfaces are in the pivot model results in no energy of interaction for points next to each other on the cylinder wall, i.e. at 0 and 6.28 radians from the reference point, that is to say in the same local plane. No energy of interaction for points in the same local plane is consistent with the assumptions of the flat plate model. The predominant feature of the internal sweep model is the prediction of the largest interaction energies for points in the same local plane.

4. Illustration of Applying Cylindrical Pore Interaction Models

Consider London/van der Waals interactions as an illustration of modeling disjoining pressure in a cylinder. Table 2 gives the results of integration followed by differentiation with respect to radius for each model. All three models are undefined for the ideal limits of integration. The concept of *Horizon of Interaction* resolves this problem with the limits of integration.

Assume that a point only interacts with other points on the cylinder that rise above the "horizon." That is to say that a reference point can only interact with another point that is at least some radians distant from the reference point. At locations less than this number of radians distant, points appear to be on the same plane and therefore do not interact as assumed in a flat plate model. Defining the following form for the London/van der Waals interaction in a cylinder,

$$BA/\pi r^3, \qquad (10)$$

Where: B is a lumped factor designated as the Cylindrical Interaction Factor. The definition of the appropriate *Horizon of Interaction* results from plotting the Cylindrical Interaction Factor, B, vs. Horizon Angle, as in figure 3. By inspection of figure 3, the Horizon of Interaction Angle is the angle at which the sharp rise in "B" occurs. Table 3 gives the Horizon of Interaction for each of the models. Note that the definition of Horizon of Interaction is not the same as the integration angle definitions in each model as reflected in table 3's new limits of integration.

Inspection of figure 3 also suggests that the appropriate value of B is 1, particularly for the two-semicylinder and pivot models. Therefore, the cylindrical-pore London/van der Waals disjoining pressure is the slit pore model with the characteristic pore size replaced by the radius and multiplied by 6, a 48-fold increase in magnitude:

$$\Pi_m^{cyl} = A/\pi r^3 \qquad (11)$$

Application of this London/van der Waals interaction solution to Solute Interaction within cylindrical pores is straightforward due to the similarity in model form. The following is the solution:

$$\Pi_s^{cyl} = 12C_\infty A_o/V(r-\delta)^3. \qquad (12)$$

5. Computer Simulation of Electrostatic Cylindrical Pore Interactions

The exponential form of the electrostatic interaction does not allow a closed-form integral (defined or undefined) solution for any of the cylindrical pore models. Multiple numerical integrations at different radii does result in a solution for a given set of system parameters (surface charge, radius, solute charge, etc.).

Using the Pivot model as an illustration and the logic steps (section 3.2) for determining the disjoining pressure, the following are the steps in the computer simulation of the electrostatic cylindrical pore interaction.

1. $L = (r/\cos\phi)(1+\cos 2\phi)$

   $d(\text{Area}) = ZLd\phi$

2. $\Delta G = (D/\kappa)\exp(-\kappa L)$

3. $E(a) = \int_0^{2\pi} (D/\kappa)ZL\exp(-\kappa L)d\phi$

   (solved via simpson's rule or other appropriate method)

4. $E = \int_0^{2\pi} E(a)da$

5. $\Delta G_T = E/2\pi rZ$

6. Repeat steps 1 through 5 for $(r - \Delta r)$. Call the result ΔG_T^1

   (in the example below, $\Delta r = 0.1$nm)

7. Repeat steps 1 through 5 for $(r + \Delta r)$. Call the result ΔG_T^2

8. $\Pi_e = (\Delta G_T^2 - \Delta G_T^1)/2\Delta r$.

Table 4 gives the results for the disjoining pressures resulting from solvent, solute, and electrostatic interactions in a polysulfone membrane with pores of 30 nm diameter (radius of 15 nm). Comparison of the results in table 4 with the slit pore results in table 1 indicates that modeling the membrane pore as cylinders results in disjoining pressures of one order of magnitude or more greater than modeling the pores as slits. Specifically the Π_m increases by a factor of 48, Π_s increases by a factor of 62, and Π_e increases by a factor of 9 (pivot model). As expected for the electrostatic interactions, the Semicylinder model gives the lowest estimate of

disjoining pressure while the Internal Sweep model gives a 3 to 4-fold greater estimate than the other two models. Table 5 gives the variation of the disjoining pressure with various pore sizes. For low ion concentration solutions in charged surface pores, the Electrostatic Interactions dominate over the London/van der Waals and Solute/Pore Wall Interactions. However, high ion concentration solutions shield the electrostatic interactions of the pore walls resulting in the Solute/Pore Wall Interactions dominance in generating disjoining pressures.

List of Symbols

A = Hamaker constant (J)
A_o = Solute/water interaction constant ($J\ m^3$)
a = Interaction unit area angle (Radians)
B = Cylindrical Interaction Factor (Dimensionless)
C_∞ = Bulk solute concentration (mol/mol)
D = $(64nkT)\tanh^2(ze\Psi/4kT)$ (Pa)
E = Total energy of interaction (J)
e = Electron charge (Coulomb)
h = Film thickness (m)
k = Boltzmann constant (J/K)
L = Distance of the differential flat plate interaction (m)
n = Ion number density ($ions/m^3$)
P = Applied or bulk fluid pressure (Pa)
P_c = Porous media capillary pressure (Pa)
P_f = Fluid pressure near a surface such as, at the interface between the membrane skin and the porous media backing (Pa)
P_g = Pressure of the gas phase (Pa)
P_l = Pressure of the liquid phase (Pa)
r = Pore radius or radius of cylinder model of pore (m)
S = Surface of Interaction (m^2)
T = Absolute Temperature (K)
V = Molecular volume (m^3/mol)
Z = Unit length of cylinder (m)
z = Solute charge number (valence)
α = Liquid/pore wall contact angle (Radians)
δ = Minimum solute approach distance (m)
ε = Dielectric constant ($Coulomb^2/Jm$)
ϕ = Angle of rotation centered on a pivot point on the cylinder wall
φ = Potential energy per unit mass due to surface forces (J/Kg)
κ = Debye-Hückel reciprocal length = $(8\pi nz^2e^2/\varepsilon kT)^{-0.5}$ (m^{-1})
μ = Chemical potential (J/m^3 or Pa)
Π_i = Disjoining pressure from interaction i (Pa)
Π_m = London/van der Waals interaction disjoining pressure (Pa)
Π_e = Electrostatic interaction disjoining pressure (Pa)
Π_s = Solute/pore wall interaction disjoining pressure (Pa)
θ = Angle of rotation centered on cylinder axis (Radians)
ρ = Liquid density (Kg/m^3)
σ = Liquid/gas surface tension (Pa m)

ω = Volume fraction of liquid component (m^3/m^3)
Ψ = Electrostatic surface potential (volts)
ψ = Matrix suction (Pa or J/m^3)
ΔG = Total interaction energy per surface area (J/m^2)

$\langle Term \rangle_{lg}$ = Liquid/gas surface average of "Term"

References

[1] Nitao, J.J. and Bear, J.; "Potentials and Their Role in Transport in Porous Media;" Water Resources Research; Vol. 32, No.2, pg 225-250; February 1996.

[2] Corey, A.T.; Mechanics of Immiscible Fluids in Porous Media; Water Resources Publications; Highlands Ranch, CO; 1994.

[3] Derjaguin, B.V. and Churaev, N.V.; "On the Question of Determining the Concept of Disjoining Pressure and its Role in the Equilibrium and Flow of Thin Films;" Journal of Colloid and Interface Science; Vol. 66, No. 3, pg 389-398; October 1, 1978.

[4] Derjaguin, B.V. and Churaev, N.V.; "Disjoining Pressure of Thin Layers of Binary Solutions;" Journal of Colloid and Interface Science; Vol. 62, No. 3, pg 369-380; December, 1977.

[5] Slattery, J.C.; Interfacial Transport Phenomena; Springer-Verlag; New York; 1990

[6] Bhattacharjee, S.; Sharma, A.; and Bhattacharya, P.K.; "Estimation and Influence of Long Range Solute. Membrane Interactions in Ultrafiltration;" Ind. Eng. Chem. Res.; 35, 3108-3121; 1996.

[7] Churaev, N.V.; Novikova, A.V.; Petrov, A.K.; and Zorin, Z.M.; "Properties of Polymolecular Water Films on the Surface of Quartz Capillaries;" Journal of Colloid and Interface Science; Vol. 48, No. 3, pg 374-381; September, 1978

[8] Elimelech, M.; Gregory, J.; Jia, X.; and Williams, R.A.; Particle Deposition and Aggregation – Measurement, Modeling and Simulation; Butterworth Heinemann Ltd; Oxford, UK; 1995.

[9] Kim, K.J.; Fane, A.G.; Nystrom, M.; Pihlajamaki, A.; Bowen, W.R.; and Mukhtar, H.; "Evaluation of Electroosmosis and Streaming Potential for Measurement of Electric Charges of Polymeric Membranes;" Journal of Membrane Science; 116, 149-159; 1996.

Table 1: Slit Pore Disjoining Pressures

Bulk Solute (NaCl) Concentration	Π_m (Pa)	Π_s (Pa)	Π_e (Pa)
3×10^{-5} M	-20	1.6×10^{-5}	22
3 M	-20	1.6	0

h = 30 nm A = 1×10^{-20} J [8] $A_o = 1 \times 10^{-37}$ erg cm^3 [4]
δ = 2 nm Ψ = -18 mV [9] V = 18 cm^3/mol

Table 2: Closed-Form Functions and Results for Cylindrical Pore London/van der Waals Disjoining Pressure

MODEL	INTEGRATED FORM	LIMITS AND RESULTS
Semicylinder	$\frac{-A}{24\pi^2 r^3}(-\cot\theta)\Big\|_0^{\pi}$	Limits = 0 to π Result = $-\infty$ - ∞
Internal Sweep	$\frac{-A}{12\pi r^3}(-\cot\theta/2)\Big\|_0^{2\pi}$	Limits = 0 to 2π Result = $-\infty$ - ∞
Pivot	$\frac{-A}{12\pi r^3}\left[\ln\left(\tan(\frac{\pi}{4}+\frac{\phi}{2})\right)\right]\Big\|_{-\pi/2}^{\pi/2}$	Limits = $-\pi/2$ to $\pi/2$ Result = ln(tan[π/2]) – ln(0) Undefined

A = Hamaker Constant r = cylindrical pore radius

Table 3: Horizon of Interaction Angles and suggested limits of integration for each cylindrical model

MODEL	HORIZON OF INTERACTION ANGLE (In Degrees)	SUGGESTED LIMITS OF INTEGRATION (In Degrees)
Semicylinder	3	1.5 to 178.5
Internal Sweep	5	5 to 355
Pivot	0.5	-89.75 to 89.75

Table 4: Cylindrical Pore Disjoining Pressures for Pore Diameters of 30 nm

Bulk Solute (NaCl) Concentration/ MODEL	Π_m (Pa)	Π_s (Pa)	Π_e (Pa)
3 x 10^{-5} M	-940	1 x 10^{-3}	
Semicylinder			98
Internal Sweep			600
Pivot			192
3 M	-940	99	
Semicylinder			1.2 x 10^{-3}
Internal Sweep			3.5 x 10^{-7}
Pivot			2.4

r = 15 nm A = 1 x10^{-20} J [8] A_o = 1x 10^{-37} erg cm^3 [4]
δ = 2 nm Ψ = -18 mV [9] V = 18 cm^3/mol

Table 5: Disjoining Pressure Sensitivity to Cylindrical Pore Size

DISJOINING PRESSURE MODEL	Disjoining Pressures In Pa			
PORE SIZE	**100 nm**	**50 nm**	**20 nm**	**10 nm**
For 3 x 10^{-5} M of NaCl				
Π_m	-25	-200	-3200	-25 000
Π_s	2 x 10^{-5}	2 x 10^{-4}	4 x 10^{-3}	8 x 10^{-2}
Π_e (Semicylinder)	9.0	39	180	410
Π_e (Sweep)	54	240	1100	2600
Π_e (Pivot)	11	75	320	530
For 3 M of NaCl				
Π_m	-25	-200	-3200	-25 000
Π_s	2.0	18	423	8029
Π_e (Semicylinder)	0	3.3 x 10^{-8}	0.22	45
Π_e (Sweep)	0	0	2.1 x 10^{-3}	14
Π_e (Pivot)	5.4 x 10^{-3}	0.42	5.7	15

r = Pore Size/2 A = 1 x10^{-20} erg [8] A_o = 1x 10^{-37} erg cm^3 [4]
δ = 2 nm Ψ = -18 mV [9] V = 18 cm^3/mol

TWO SEMICYLINDER INTERACTION

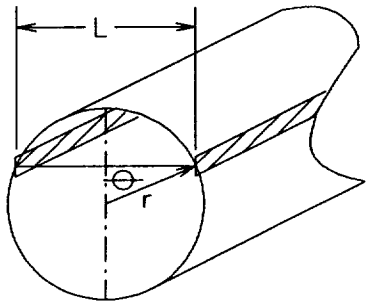

$L = 2r\sin\theta$

$d(Area) = Zrd\theta$

Ideal Limits of Integration
$0 \le \theta \le \pi$

$$E = Zr\int_{\theta} \Delta G d\theta$$

$$S = \int_0^{\pi} Zr\, da$$

INTERNAL SWEEP INTERACTION

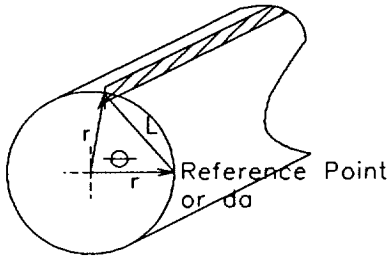

(Law of Cosines)
$L = [2r^2(1 - \cos\theta)]^{1/2}$

$d(Area) = Zrd\theta$

Ideal Limits of Integration
$0 \le \theta \le 2\pi$

a = Interaction unit area angle

$$E = \int_0^{2\pi} zr\int_{\theta} \Delta G d\theta\, da$$

$$S = \int_0^{2\pi} Zr\, da$$

PIVOT INTERACTION

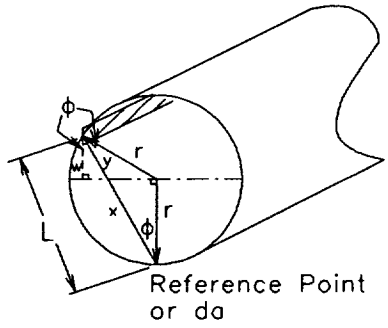

$L = x + y = r/\cos\phi + w/\cos\phi$
$w = r\cos 2\phi$

$L = (r/\cos\phi)(1 + \cos 2\phi)$

$d(Area) = ZLd\phi$

Ideal Limits of Integration
$-\pi/2 \le \phi \le \pi/2$

a = Interaction unit area angle

$$E = \int_0^{2\pi} Z\int_{\phi} L\Delta G d\phi\, da$$

$$S = \int_0^{2\pi} Zr\, da$$

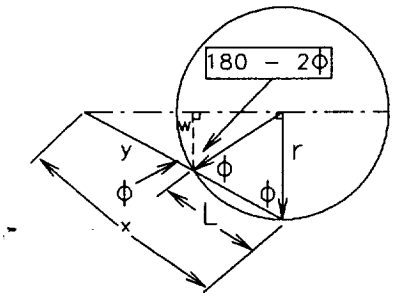

For $-\pi/2 \le \theta \le -\pi/4$
$L = x - y = r/\cos\phi - w/\cos\phi$
$w = r\cos(180 - 2\phi) = -r\cos(2\phi)$

$L = (r/\cos\phi)(1 + \cos 2\phi)$

Figure 1: Models For Disjoining Pressures in Cylindrical Pores
(Z = Unit length of cylinder and S = Surface of Interaction)

Figure 1

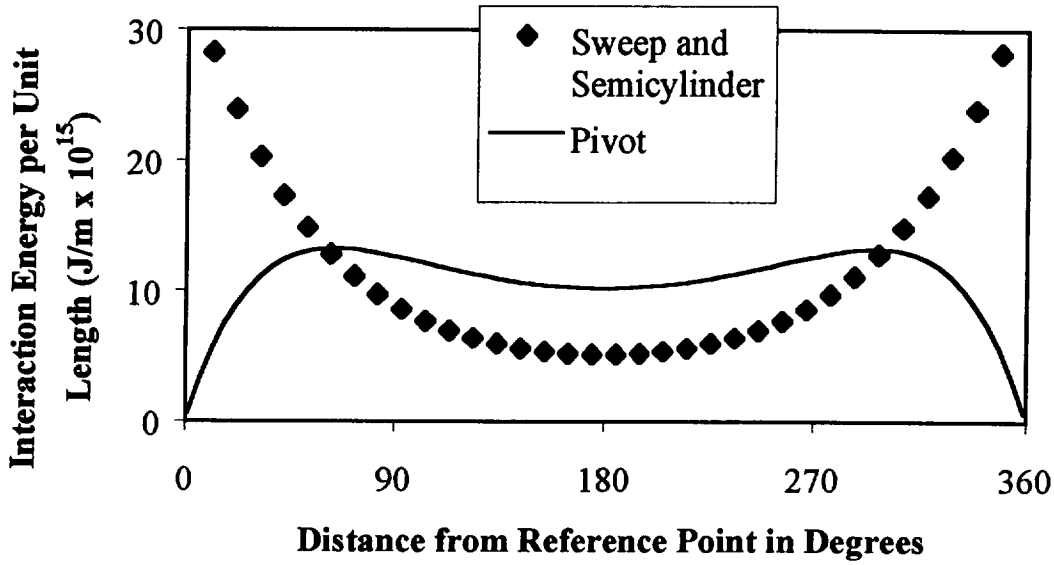

Figure 2: Interaction Energies vs. Circumferential Distance from the Reference Point. Energies calculated for unshielded electrostatic interactions (low ion concentration, 3 x 10^{-5} M NaCl) in a 30 nm polysulfone pore.

Figure 2

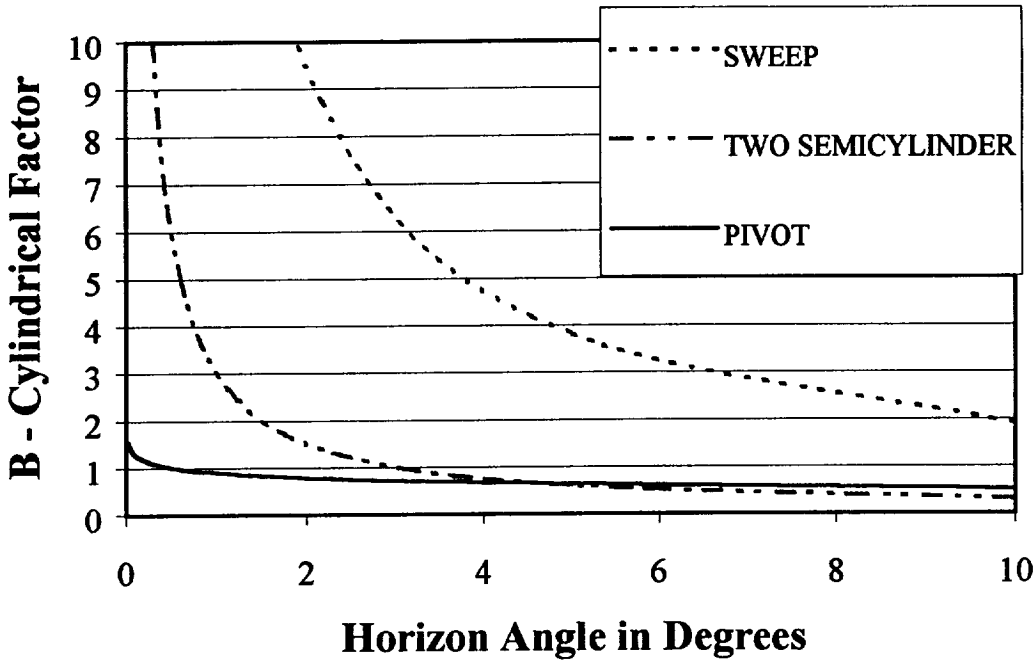

Figure 3: Cylindrical Interaction Factor, B, Vs Horizon Angle

Figure 3

Chapter 26

Oligonucleotide crystallization by controlling the rate of cation concentration

Stephen P. Cape, Michael G. Sportiello, Steve C. Schultz, Dan Harrington and Paul Todd

Chapter 26
Oligonucleotide Crystallization by Controlling the Rate of Cation Concentration

Stephen P. Cape, Michael G. Sportiello, Steve C. Schultz, Dan Harrington and Paul Todd

Introduction

The purpose of this brief chapter is to describe a small voluntary activity that began within two months of the end of the project and for which data are currently being analyzed, also as a voluntary activity. Its message embodies the ultimate goal of Task 2, to find a systematic pathway to the growth of oligonucleotide crystals. By integrating all of the findings under this task, namely thermodynamic conditions for nucleation, dynamic conditions for crystal growth, light-scattering based solutions models, and the detailed study of membrane processes used in crystallization, it is hypothesized that the diffusion of appropriate multivalent cations into an electrokinetically stabilized solution of oligonucleotide will produce diffraction-quality crystals. Data so far indicate that this is indeed the case.

Hypothesis

It was hypothesized that the diffusion of appropriate multivalent cations into an electrokinetically stabilized solution of oligonucleotide will produce diffraction-quality crystals.

(1) Light scattering experiments, both static and dynamic, had showed us that multivalent cations, and not polyols were precipitants for oligonucleotides. Furthermore, magnesium and spermine ions had been shown by others to occupy lattice positions in oligonucleotide crystals. We had access to the structural coordinates of the UU-dodecamer (Chapter 8 and NDB) and Dickerson DNA (Chapter 14 and NDB). To induce lattice-forming bonds, found to be very strong ones, the *appropriate* multivalent cations must be identified. In the case of the UU dodecamer, Mg++ was found to be adequate, while in the case of the Dickerson DNA spermine, presumably tetravalent, was required (Chapters 13 & 14).

(2) Light scattering experiments and electrophoresis data demonstrated that cations had a charge-screening effect on oligonucleotides, consistent with electrokinetically stabilized colloids. Indeed, independently estimated numerical values of DLVO parameters were found consistent with light-scattering observations (Chapter 14). Thus, Mg++ ions were playing at least two roles: Debye screening and participation in key lattice-forming bonds.

(3) We had access to nearly a dozen different physical methods of crystallization and a strong specialty in membrane-based methods. The hypothesis specified a method for transporting cations into the buffered, stabilized oligonucleotide solution. The

preferred method should allow one-way diffusion and avoid transport of the oligonucleotide so that both concentrations are controlled separately. Both interfacial diffusion and dialysis diffusion had been studied extensively in space (Chapters 28-30), and dialysis diffusion was the obvious choice, as described in Chapter 28, page 28-5.

(4) The solubility phase diagram for the Mg++ UU-dodceamer system had been determined (Chapter 13) in monovalent cation and PEG solutions. It was clear that neither PEG nor MPD should be necessary if the hypothesis were correct (Chapters 12 and 13), since UU-dodecamer crystals grew at room temperature (for the first time other than in space) without either polyol.

(5) Finally, the same diffraction methods and facilities as were used for the original structure determination of the UU-dodecamer (Chapters 7 and 8) were available for evaluation of any crystals that grew to adequate size. The first hypothesis-testing experiment might not be expected to yield the optimized crystals, but they would be produced with a minimal screen, some eight samples.

Approach

Using data of Chapter 13 electrokinetically stabilized solutions of UU-dodecamer in NaCl and cacodylate buffer were placed, at various concentrations near saturation, in the crystal-growth chambers of FPA inserts (Chapters 22 and 28). $MgCl_2$ at various concentrations around 10 mM (Chapter 13) was placed external to the inserts. The chambers of the inserts were separated from the external ("precipitant") solution using a 1000 molecular-weight cutoff dialysis membrane. This assembly was held at ambient temperature for 4 to 20 days, and crystals were harvested for microphotography and x-ray diffraction studies.

Results

Crystals 0.1 to 0.3 mm in length were harvested and photographed. The hexagonal double-wedge motif, best seen in Chapter 11, did not seem to prevail. The largest crystals were mounted for x-ray diffraction studies to determine space group, maximum resolution and possibly limited statistics. At the time of this writing (May 2000) the data are undergoing analysis.

Conclusions

It appears that the above hypothesis has not been falsified by this initial test. Unless contradictory findings arise, we may assume that an oligonucleotide solution behaves like an electrokinetically stabilized colloid, that selected multivalent cations lead to its crystallization, and that MPD or PEG may serve kinetic, rather than thermodynamic roles and in any case are unnecessary. Further a "screen" for crystallization conditions for an ologonucleotide needs to consist only of varying the identity of the multivalent cation and the rate at which it is fed to the stabilized oligonucleotide solution.

PART IV. TASK 3: MECHANISMS OF ACTION OF INERTIAL ACCELERATION

Chapter 27

Effects of Orbital Maneuvers on Biomolecule Crystal Growth from Solution: Modeling Studies

Paul Todd, C.-Y. Lee and Jurgen Sygusch

CHAPTER 27

MAY 11-15 MAI 1997 MONTREAL CANADA

SPACE OBJECTIVE

BOUND ESPACE 1997

Proceedings/Compte rendu

Radisson Hôtel des Gouverneurs
777 University Street
Montreal, Quebec, Canada H3C 3Z7

Hôtel Radisson des Gouverneurs
777, rue Université
Montréal, Québec, Canada H3C 3Z7

EFFECTS OF ORBITAL MANEUVERS ON BIOMOLECULE CRYSTAL GROWTH FROM SOLUTION: MODELING STUDIES

Paul Todd and Ching-Yuan Lee, University of Colorado, and Jurgen Sygusch, Université de Montreal

After a crystal has formed in low gravity it is suspended quiescently in mother liquor in a saturation zone where crystal growth is optimum. Inertial force on a growing crystal will remove it from this saturation zone thereby compromising crystal growth and final crystal quality. Calculations were performed and scenarios were studied in which orbital maneuvers of spacecraft would impose inertial acceleration on growing crystals of various sizes. Families of curves were generated giving velocity of crystal motion as a function of crystal size based on typical accelerations encountered in orbital maneuvers and other spacecraft activities. In an experimental approach a laboratory simulation experiment was performed, in which a crystallizer was operated in inverted position, and gravity deliberately forced nuclei to sediment out of the saturation zone. The resulting hundreds of oligonucleotide crystals were all approximately 5 μm in length, while in the absence of deliberate sedimentation only a few crystals formed, and they were 125 μm in length. It was concluded that, under a variety of plausible conditions on orbit, crystal growth experiments could be compromised by orbital maneuvers.

INTRODUCTION

There are three main categories of accelerations aboard orbiting spacecraft, and each possesses subcategories:

1. Steady natural accelerations. These are due to spacecraft inertial motions and consist of
   atmospheric drag
   gravity gradient accelerations.

2. Intermittent maneuvers. These are due to the operation of the spacecraft maneuvering and station-keeping engines and consist of
   vernier reaction control engines
   primary reaction control engines
   orbital maneuvering system engines.

3. Jitter motions. These are due to spacecraft and crew operations and result in variable-frequency and variable-amplitude vibrations consisting of
   crew movements at low frequency
   motorized equipment at high frequency.

A description of each follows with a typical "case study" as applied to the growth of biological macromolecule crystals from solution.

STEADY ACCELERATIONS

Case 1. Atmospheric drag. The magnitude of this acceleration can vary from 0.001 to 3.0 μg, it can remain nearly constant for hours or days, it has a strong dependence on orbit altitude, and it acts in a single direction which is the same as the direction of travel of the spacecraft [1]. In the gravity-gradient stabilized flight configuration, this usually means toward the belly of the spacecraft. As an example, a 0.5 mm protein crystal with specific gravity of 1.45 in a space shuttle orbiter flying belly forward experiences a steady acceleration toward the floor of the orbiter of 0.3 μg. In fluid with a viscosity of 0.014 P this corresponds to a unidirectional crystal migration velocity of about 30 μm/hour. This motion should be detectable in old photographs of hanging-drop protein crystallization experiments that have been performed over the past decade. Such photographs could be examined retrospectively for this motion. This concept was tested in video-recording experiments on space shuttle flight STS-80 [2].

Case 2. Tidal (gravity-gradient) accelerations. If an object is some distance from the center of gravity of the orbiting vehicle, then there is a steady acceleration away from the earth in the radial direction (orbit z-axis) and toward the center of gravity in the plane of the orbit (orbit y-axis). Along the z axis, using the appropriate universal constants it can be shown that

$$d^2z/dt^2 = 4.1 \times 10^{-7} z,$$

where z is the radial distance from the spacecraft's center of gravity [1]. For objects that are off-axis in the direction perpendicular to z and the direction of travel,

$$d^2y/dt^2 = -1.3 \times 10^{-7} y.$$

In other words, the radial acceleration is 3 times as effective in the radial direction as in the transverse direction. The same crystal as in Case 1, 1.6 m from the spacecraft c.g. on the orbit y axis, would be subjected to 0.22 μg resulting in a steady migration

toward the center of the spacecraft with a velocity of 27 μm/hour.

ORBITAL MANEUVERS

These result in steady but short acceleration loads of 1-15 s duration and 0.0002 to 0.02 g in magnitude. The Vernier Reaction Control System (VRCS) imparts accelerations up to 0.0002 g for up to 2 s. The Primary Reaction Control System (PRCS) imparts accelerations up to 0.01 g for 1-2 s periods, and these are followed by ringing vibrations in the spacecraft, and these vibrations are damped in a few seconds. The Orbital Maneuvering System (OMS) is used during rendezvous and major orbit-changing operations. An OMS "burn" could result in accelerations up to 0.02 g for 5 - 15 s. As the graphs below will show, some of these bursts could cause movement of crystals in solution.

Case 3. Orbital maneuvers. Many cases could be solved individually, but the assumption of Stokes flow at low Reynolds number provides a family of solutions, some of which are summarized in the two figures. Figure 1 shows a typical case of a 1.0 mm crystal (specific gravity 1.33) in an aqueous mother liquor. The distance migrated as a function of impulse duration is given for four different g-levels. It can be seen that, under certain extreme conditions, a large crystal could move the full length of its container. Figure 2 is intended to represent an opposite extreme, namely a small, 0.1 mm crystal in a viscous medium such as a solution of poly(ethylene glycol), which is often used as a precipitant. Under realistic conditions a 0.1-mm crystal will only travel a few μm. The impact of accelerations resulting from orbital maneuvers is obviously very dependent on the crystal size and the composition of the mother liquor.

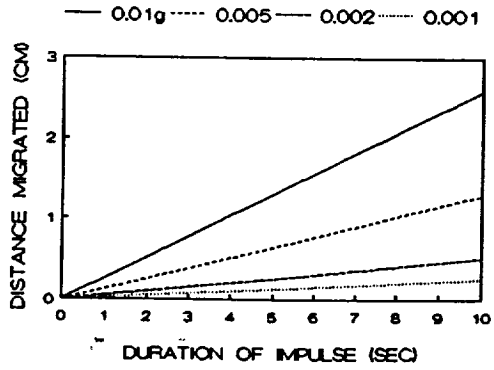

Figure 1. Distance migrated, calculated from simple Stokes flow at low Reynolds number, for a 1.0 mm crystal with specific gravity 1.33 suspended in water as a function of duration of inertial impulses of 0.001 to 0.01 g.

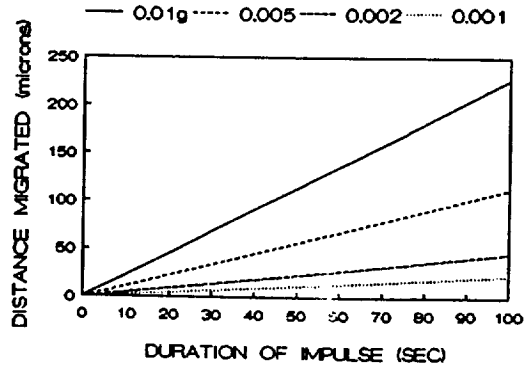

Figure 2. Distance migrated, calculated from simple Stokes flow at low Reynolds number, for a 0.1 mm crystal with specific gravity 1.33 suspended in a poly(ethylene glycol) solution as a function of duration of inertial impulses of 0.001 to 0.01 g.

JITTER MOTIONS

Of the two categories of jitter motions, the low-frequency motions are the most significant to crystal growth. Due to the shortness of the impulses in any one direction, the high-frequency (>5 Hz) vibrations, such as those due to motors, pumps, fans and environmental control machinery, can be neglected. The devices that cause these vibrations, on the other hand, may be of concern owing to torques that might be imposed by rotating machinery. The lower-frequency sources are most often associated with crew activities, such as treadmill, ergometer and just moving around.

Case 4. High-amplitude jitter. A case worthy of examination is the impact of treadmill operation at 2 Hz and 0.001 g (as on STS-32, for example) [3]. We wish to know whether or not a 0.1-mm crystal will be moved out of its 50μm-thick depletion layer in 0.5 sec, the duration of a unidirectional pulse at this frequency. This movement requires 0.06 g, but the source (treadmill) only produces 0.001 g. The same question may be asked another way: How large must a crystal be to be affected by this 0.001-g acceleration in 0.5 s? The answer is that it must be >5 mm.

It is therefore only in rare cases (very high acceleration and very low frequency) that jitter motions can be expected to cause significant crystal motion.

EFFECTS OF MOVEMENT ON CRYSTALLIZATION

Inertial and fluid forces can cause crystals to
- attach to a surface
- be removed from a surface
- migrate to a lower concentration zone
- migrate out of its depletion zone
  - (special case of previous condition)
- be surrounded by a convecting plume
  - in the depletion layer.

Briefly, the various crystallization methods employed to grow crystals in space will be affected by inertial forces differently. For example, crystals could be removed from the saturation zone in liquid-liquid diffusion systems; crystals could move within the drop in the hanging drop method; and crystals could migrate away from the membrane in dialysis diffusion and osmotic dewatering experiments. In this last case, the following experiment was performed: oligonucleotide crystals were grown in a multichamber osmotic dewatering device (MCOD)[4]. In this device water is removed from the mother liquor through a reverse-osmosis membrane beneath the saturation zone. Normally, nucleation occurs, as does subsequent crystal growth, near the membrane at the bottom of the chamber. The result is usually a small number (2-10) crystals 0.2 - 0.3 mm in length grown near the membrane. When, on the other hand, the MCOD was inverted, so that water was withdrawn through the membrane at the top of the chamber, nucleation occurred at the top of the chamber, and the resulting crystals quickly sedimented out of the saturation zone so that the product consisted of hundreds of crystals <5 μm long.

CONCLUSIONS

Drag and tidal accelerations produce slow, unidirectional crystal movements. Orbital maneuvers can produce significant crystal movements. Jitter motions affect only large crystals, and they are effective only at the lowest frequencies. Changes in crystal growth can be expected when any of these accelerations cause motion.

This research was supported by NASA Grants NAG8-1165 and NAGW-1197 and the Canadian Space Agency.

REFERENCES

[1] H. Hamacher, Simulation of weightlessness. in *Materials Sciences in Space*, Ed. B. Feuerbacher, H. Hamacher and R. J. Naumann, Springer-Verlag, Berlin (1986).

[2] M. G. Sportiello, Z. R. Korszun, J. Sygusch, P. Todd, A. Edmundson, and J. M. Cassanto. Video monitoring of protein crystal motion in low gravity. In Spacebound 97, Book of Abstracts, p. 25 (1997).

[3] B. J. Dunbar, D. A.Thomas and J. N. Schoess. The microgravity environment of the space shuttle Columbia middeck during STS-32. NASA Technical Paper 3140 (Nov 1991).

[4] C.-Y. Lee, M. G. Sportiello, S. P. Cape, S. Ferree, P. Todd, C. E. Kundrot, S. Lietzke, and C. Barnes. Characterization and application of osmotic dewatering to the crystallization of oligonucleotides. Biotechnology Progress 13, 77-81 (1997).

Chapter 28

Lysozyme Crystallization on Space Station Mir Using Five Techniques: Crystal Quality and g-Environment

Mike Sportiello, Alex Tran, Z. Richard Korszun, Eric Brucker, Milton E. Moskowitz and Paul Todd

CHAPTER 28

Lysozyme Crystallization on Space Station Mir Using Five Techniques: Crystal Quality and g-Environment

Michael G. Sportiello[1], Alex Tran[2], Z. Richard Korszun[2], Eric Brucker[3], Milton E. Moskowitz[4], and Paul Todd[1]

[1] University of Colorado-Boulder, Dept. of Chemical Engineering, Boulder, CO, 80309; [2] Brookhaven National Laboratory, Upton, NY, 11973; [3] Baxter Hemoglobin Therapeutics, Boulder, CO 80301; [4] Honeywell, Inc., Phoenix, AZ, 85027

1. Summary

Lysozyme crystallization experiments were performed on the four-month-long NASA 3 mission on the Space Station Mir from September 1996 to January 1997. Five different crystallization techniques were used for the experiments on Mir: batch, osmotic dewatering, step osmotic dewatering, dialysis diffusion, and step dialysis diffusion. All five techniques were performed using the Fluid Processing Apparatus, a flight-qualified apparatus developed and utilized by BioServe Space Technologies, a NASA-sponsored Commercial Space Center at the University of Colorado-Boulder. X-ray diffraction analysis was performed on the crystals grown on Mir using the X-12C beam line of the National Synchrotron Light Source at Brookhaven National Laboratory. This analysis showed that the lysozyme crystals grown using all five techniques were of comparably high quality, and all Mir-grown crystals showed less mosaicity than crystals grown on Earth using the osmotic dewatering technique. The high quality of the Mir-grown crystals corresponded with the relatively quiescent environment in the low frequency-g range on board Mir during the period of crystal growth as analyzed by the Space Acceleration Measurement System on Mir.

2. Introduction

Previous research has shown that growth of biomacromolecular crystals in low gravity can lead to increases in crystal size **(1-6)** and improvement of crystal quality as measured by reduction in crystal defects **(4)**, by diffraction (resolution) data **(2, 3, 4, 5, 7, 8)**, including I/σ **(6, 9, 10)**, and by mosaicity measurements **(11)**. For a brief review of this phenomenon, see McPherson LONG REVIEW **(12 eventually).** Reasons postulated for this enhancement of crystal quality in low gravity include the virtual absence of convection, which minimizes turbulence around the growing crystal and creates a stable diffusion layer around the crystal **(13, 14)**, the virtual absence of sedimentation, which allows a crystal to stay in the zone of supersaturation and also contributes to a stable diffusion layer around the crystal **(14)**, and reduced incorporation of large impurities into the crystal as a result of a lowered concentration of these impurities around the growing crystal (caused by the lack of convection and the dominance of diffusion-mediated transport) **(14, 15).** Conversely, some researchers theorize that movement of a crystal out of the region of the depletion zone (diffusion layer) is beneficial to enhanced crystal growth when the diffusion layer has been depleted to the point that the macromolecule concentration has fallen below supersaturation **(16)**. Movement of a crystal into a new environment, where supersaturation conditions again are present, can lead to further growth of

the crystal. Additionally, growth in a microgravity environment may decrease crystal quality in a crystallization system that features relatively slow surface kinetics and fast transport **(17)**, or in a system in which impurities are rejected by a growing crystal **(18)**. In the set of experiments presented here, hen egg white lysozyme was crystallized on Mir using five different techniques. Crystals produced by each technique were analyzed using x-ray diffraction. Additionally, the gravity environment on board Mir was analyzed in the lowest frequency ranges, which are the ranges to which crystals are most likely to be sensitive **(19-21)**.

3. Materials and Methods

Materials

Hen egg white lysozyme (cat. no. L 2879, Sigma Chemical Company, St. Louis, MO) was gently dissolved in 0.1 M sodium acetate (pH 4.0) and passed through a 0.2 μm filter. The precipitant used in the Mir experiments was sodium chloride, and this was also dissolved in 0.1 M sodium acetate (pH 4.0) and passed through a 0.2 μm filter.

Crystallization Hardware and Techniques

BioServe's crystal growth hardware utilizes a glass tube open at both ends; this tube is called the Fluid Processing Apparatus (FPA) **(22)**. The tube is divided into separate chambers using moveable butyl rubber septa. The glass barrel of the tube has an enlarged portion called a bypass; the bypass permits mixing of the contents of adjacent chambers upon attainment of orbital space flight. The volume of each chamber can vary from approximately 1 ml to 3ml, with the maximum total volume per FPA being approximately 6 ml. The glass barrel and septa are coated with Dow Corning Vacuum Grease (after steam sterilization) to lubricate these components to facilitate sliding of the septa during experiment activation. FPAs are activated on orbit using a microprocessor-controlled external DC motor drive **(23)**. The general FPA design is shown below in Fig. 1:

Fig.1

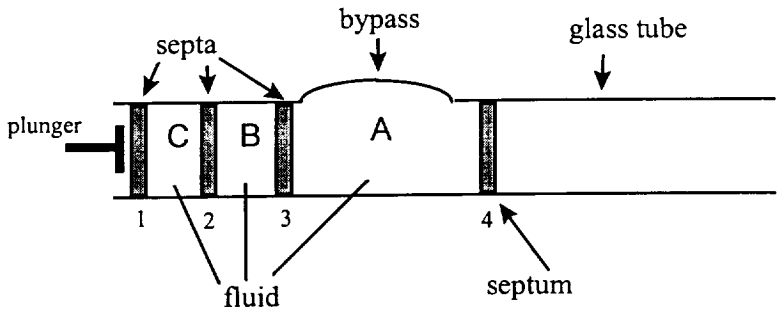

Fig. 1. Side view of the Fluid Processing Apparatus, showing the enlarged bypass portion and the individual chambers separated by rubber septa that can slide along the inner surface of the glass tube.

The experiment is activated by pushing the plunger against the proximal septum (septum 1 in Fig. 1), causing all the chambers to move distally until, in the diagram above, septum 3 moves far enough into the bypass to allow fluids from chambers B and A to mix. At a later time fluid from chamber C can also be added to the mixture of A and B fluids by the same mechanism.

The crystallization experiments were launched into space aboard the space shuttle orbiter Atlantis (STS-79) on September 16, 1996, and were transferred to Mir on September 20. The crystallization experiments were activated on Mir on the morning (EDT) of September 23, 1996. After approximately four months, the experiments were transferred to the orbiter Atlantis (STS-81) on the morning (EST) of January 18, 1997, and were returned to Earth aboard Atlantis on January 22, 1997. The Mir experiments (and concomitant control experiments on Earth) were conducted at ambient temperature (approximately 22°C) in FPAs using five different techniques: batch, osmotic dewatering, step osmotic dewatering, dialysis diffusion, and step dialysis diffusion. The latter four techniques utilize a small polycarbonate insert in chamber A (see Fig. 1). Each insert has four chambers. There are two sizes of insert; in the larger inserts each chamber holds a maximum volume of approximately 100 µl, and in the smaller inserts each chamber holds a maximum volume of approximately 30 µl. For the two types of osmotic dewatering techniques, as little as 5 µl can be used as the starting volume in the chambers of either of the inserts. The inserts, as shown in Fig. 2, contain a membrane at one end. This membrane is an ultrafiltration membrane for the two types of dialysis diffusion experiments and is a reverse osmosis membrane for the osmotic dewatering experiments.

Fig. 2

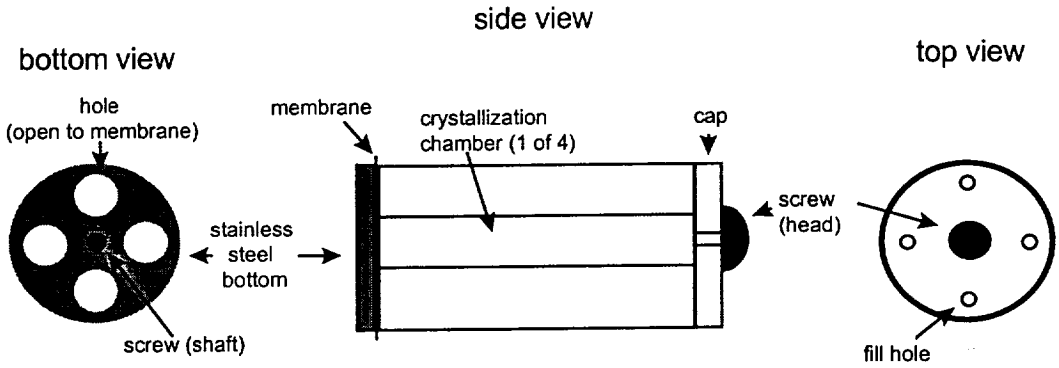

Fig. 2. Schematic diagram of the crystallization insert used in an FPA. The cap and main body of the insert are made of polycarbonate. The cap contains holes through which a needle can be inserted; the chambers can be filled with crystallization solution in this manner. After chambers are filled, the cap is rotated 45° to seal the tops of the chambers. A stainless steel disk is used as the bottom piece of the insert. This disk secures the membrane in place and has four chamber-sized holes in it to allow transport of water or molecules through the membrane and either into or out of the chamber.

Osmotic dewatering **(24)** involves use of a reverse osmosis membrane to separate the macromolecule solution (also containing precipitant) from a higher-concentration precipitant solution. Because of the osmolarity difference, water is removed from the macromolecule/low precipitant solution through the reverse osmosis membrane, thereby concentrating the macromolecule to the point of supersaturation (Fig. 3a).

Fig. 3a

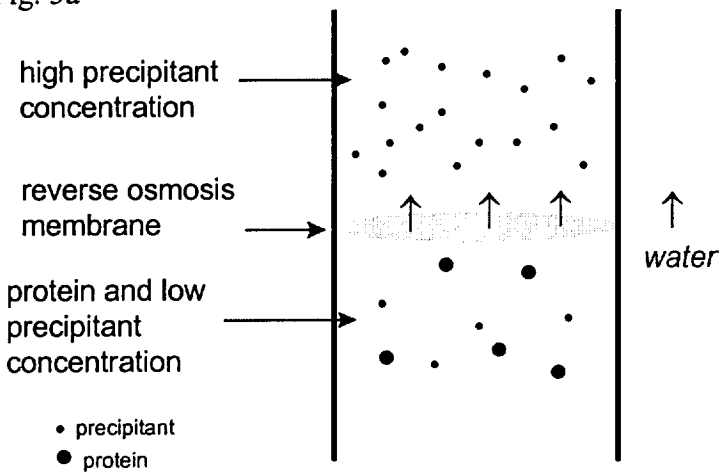

Fig. 3a. Osmotic dewatering: A reverse osmosis membrane separates a chamber containing a solution of macromolecule and a low concentration of precipitant from a solution with a higher precipitant concentration. The osmotic gradient drives the transport of water through the membrane toward the side of higher precipitant concentration, resulting in the macromolecule/low precipitant solution reaching supersaturation.

Fig. 3b

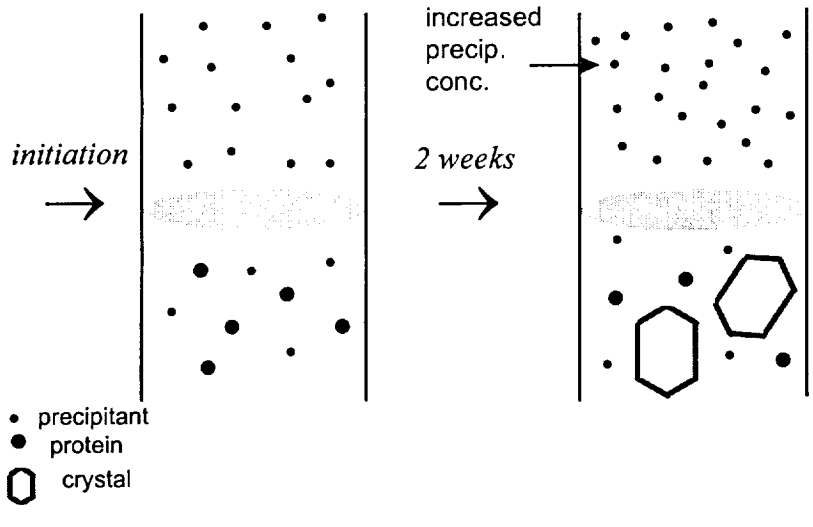

Fig. 3b. Step osmotic dewatering: Similar to osmotic dewatering, but performed with a series of different concentrations of precipitant on the side of the membrane opposite the macromolecule solution.

This technique can be used to finely control the rate of dewatering, allowing better control of nucleation and subsequent crystal growth. Step osmotic dewatering is a modification of the osmotic dewatering technique; it can be done in a variety of ways, but always uses a step change of the precipitant solution on the non-macromolecule side of the reverse osmosis membrane **(25)**. The first step can involve use of a very high precipitant concentration for a short period of time to promote rapid formation of a few stable nuclei. The next step would involve a lower precipitant concentration, one that will promote growth of the existing nuclei but will not allow more nuclei to form. Alternatively, the first step can utilize a concentration of precipitant high enough to promote dewatering, nucleation, and growth, and a second step of moderately higher precipitant concentration can promote continuation of growth when the first step has achieved virtual osmotic equilibrium between the two solutions on each side of the membrane. The lysozyme step osmotic dewatering experiment on Mir was performed using the latter technique: fourteen days after introducing a moderate concentration of precipitant outside the crystallization chamber, a slightly higher concentration of precipitant was used to promote further growth of a presumably already macroscopic crystal. For the osmotic dewatering and step osmotic dewatering experiments performed on Mir, the initial concentration of lysozyme used inside the crystallization chamber was 3% w/v and the concentration of NaCl was 1% w/v. The reservoir concentration of NaCl (i.e., the concentration of NaCl outside the crystallization chamber) was 10% w/v and 11% w/v in the two osmotic dewatering experiments. For the step osmotic dewatering experiments, the initial reservoir concentration was identical to that used in the osmotic dewatering experiments (i.e., 10% w/v NaCl in one experiment and 11% w/v NaCl in the other). The second step in these experiments consisted of reservoir concentrations of 14% w/v NaCl and 15% w/v NaCl, respectively.

For dialysis diffusion **(26)** (Fig. 4a) and step dialysis diffusion (Fig. 4b) experiments, the membrane used in the polycarbonate insert is an ultrafiltration or dialysis membrane with the appropriate molecular weight cut-off (MWCO), i.e., a MWCO that allows passage of precipitant but not of macromolecule.

Fig. 4a

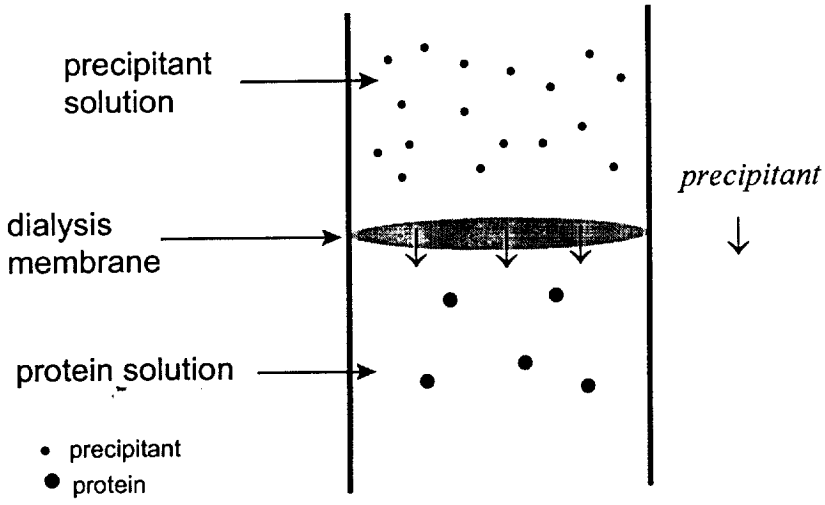

Fig. 4a. Dialysis diffusion: An ultrafiltration membrane separates a macromolecule solution from a precipitant solution. The MWCO of the membrane is chosen to allow passage of the precipitant but not the macromolecule. Passage of the precipitant into the macromolecule solution results in supersaturation conditions for the macromolecule.

Fig. 4b

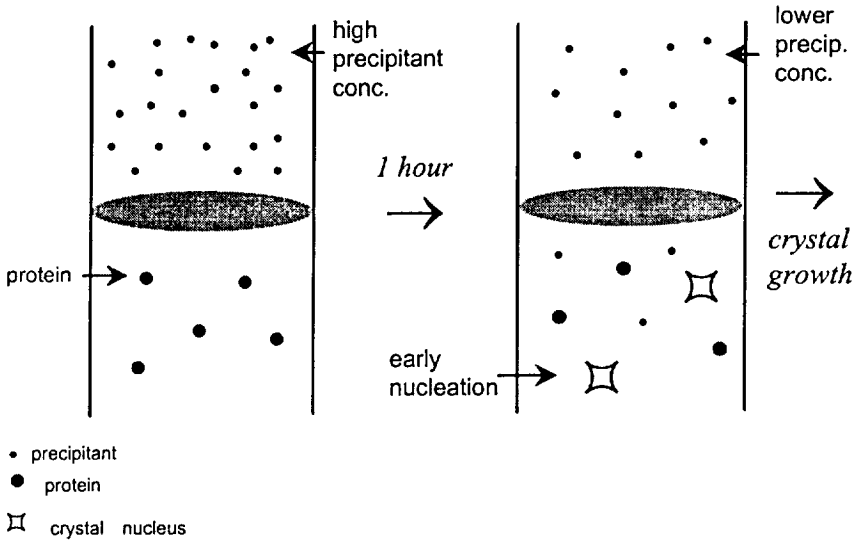

Fig. 4b. Step dialysis diffusion: Similar to dialysis diffusion, but utilizes an initial very high concentration of precipitant for a short period of time (~ 30-60 min.), followed by dilution of the precipitant on the non-macromolecule side of the membrane, allowing for further diffusion of precipitant across the membrane, but at a rate slow enough to preclude further formation of crystal nuclei.

Step dialysis diffusion, a membrane-based adaptation of step gradient diffusion **(27)** (Sygusch, J., Coulombe, R., Cassanto, J., Sportiello, M., and Todd, P.: Protein crystallization in low gravity by step gradient diffusion method. J Crystal Growth 162 (3/4):167-72, 1996), entails use of a very high precipitant concentration on the side of the ultrafiltration membrane opposite that of the macromolecule for a relatively short time (for these Mir experiments, 40 minutes), allowing enough precipitant to diffuse through the membrane to promote initiation of only a few crystal nuclei. After this short exposure to a high precipitant concentration, the high concentration is diluted so that no further nucleation occurs; however, this second precipitant concentration is still high enough to promote further growth of the (hopefully) few stable nuclei that have formed. In the Mir dialysis diffusion and step dialysis diffusion crystallization experiments, the lysozyme concentration inside the crystallization insert was either 7% w/v or 6% w/v (depending on the chamber). In the dialysis diffusion experiments, the reservoir concentration was either 6% w/v or 7% w/v NaCl, depending on the experiment. In the step dialysis diffusion experiments, the initial reservoir concentration was either 12% w/v or 10.5% w/v NaCl, depending on the experiment. After 40 minutes, this initial concentration was reduced to 6% w/v in all experiments.

Batch crystallization experiments are performed without an insert in chamber A in the FPA (Fig. 5). For the batch crystallization experiments performed on Mir, 2.0 ml of either 6% w/v or 7% w/v NaCl was mixed with 1.5 ml of 7% w/v lysozyme.

Fig. 5

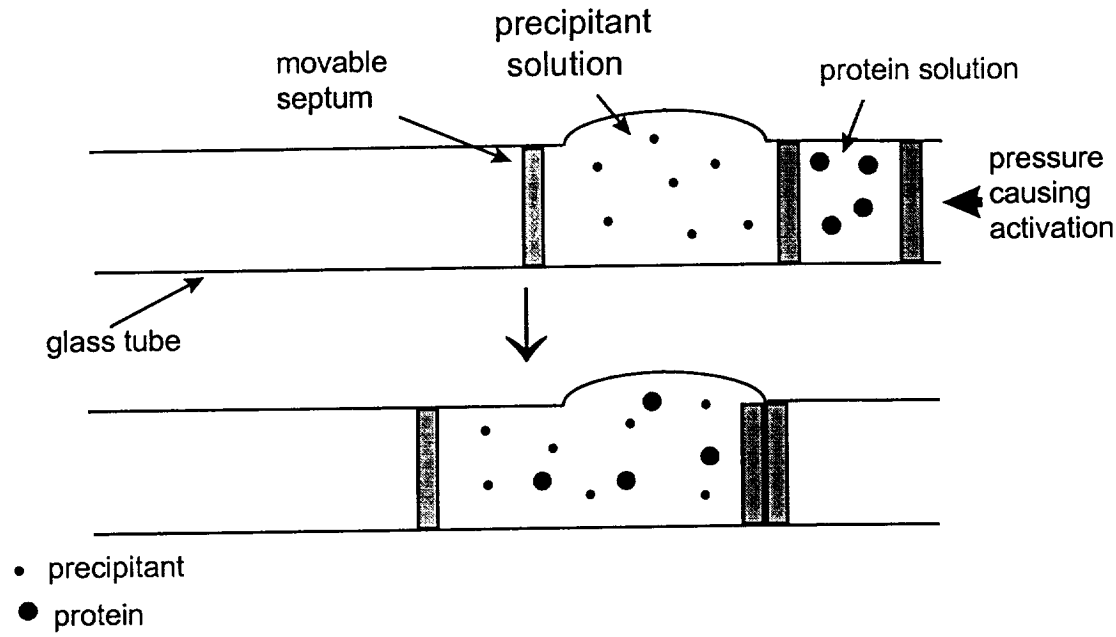

Fig. 5. Batch crystallization: No insert is used in the FPA. A chamber containing precipitant is separated from a chamber containing macromolecule. Upon activation of the experiment, the contents of the two chambers become mixed.

X-ray Diffraction Analysis

Crystals were diffracted at the X-12C beamline at Brookhaven National Laboratory using a wavelength of 1.0720 ⇒. Fine slices of 0.05° were taken over a range of 5° for each crystal diffracted. Mosaicity analysis was performed using Denzo, with input parameters for and set at and respectively.

g-Level Analysis

The Space Acceleration Measurement System (SAMS) aboard Mir was used for the g-measurements. The gRMS levels were determined by an integration of the Power Spectral Density (PSD) curve between the frequencies of interest. Gravity levels were analyzed for 20 minute time periods of exercise, sleep, "nominal" (neither exercise nor sleep), and pre- and post-sleep. Analysis was performed for each activity for Mission Days 15-18 (depending on the specific activity period), corresponding to days 7-10 of the crystallization experiments.

4. Results

Tetragonal lysozyme crystals were successfully grown on Mir with all five of the techniques that were used.

Batch:

The largest qualitative difference between Mir-grown and Earth-grown crystals was exhibited in this set of experiments. The FPAs from the Mir experiments contained many hundreds of tetragonal lysozyme crystals, apparently well-formed and with few visible defects, ranging in size from about 300 μm to 600 μm. These crystals were not attached to any surface and apparently nucleated in suspension. This contrasts with the Earth-grown batch crystals, which were attached either to the inside wall of the glass tube of the FPA or to one of the rubber septa. These crystals also were visibly of lower quality than their low g-grown counterparts, exhibiting many cracks and flaws. In addition, there were also significant numbers of needle-like crystals arranged in "starbursts," indicative of more rapid nucleation and growth and poorer crystal quality.

Osmotic Dewatering:

The Mir osmotic dewatering experiments produced tetragonal lysozyme crystals of various sizes, the largest being about 800 μm. Most crystals were attached to the inner wall of the crystallization chamber or the reverse osmosis membrane. The Earth-grown crystals were similar in size and appearance, though the maximum size of these crystals was significantly larger (about 1.2 mm).

Step Osmotic Dewatering:

The Mir osmotic dewatering experiments produced tetragonal lysozyme crystals of various sizes, the largest being about 1.2 mm. Again, virtually all crystals were attached to some surface of the crystallization chamber. The Earth-grown crystals were similar to the Mir crystals in size and appearance, with a maximum size of about 1 mm.

Dialysis Diffusion:

The Mir dialysis diffusion experiments produced tetragonal lysozyme crystals of various sizes, the largest being about 1 mm. The Earth-based experiments produced many fewer tetragonal crystals, the largest of which was about 900 μm, though most were significantly smaller (≤ 600 μm). Like the other experiments performed with a polycarbonate insert and membrane, virtually all crystals were attached to some surface.

Step Dialysis Diffusion:

The Mir step dialysis diffusion experiments produced the theorized result: there were fewer crystals per chamber than was observed with the dialysis diffusion experiments. The largest of these crystals was about 800 μm. The Earth-grown control experiments produced no

tetragonal crystals, only needle-like crystals arranged in "starbursts" as alluded to above. Again, virtually all crystals were attached to a chamber or membrane surface.

X-ray Diffraction Analysis

Crystals were diffracted at Brookhaven National Lab.

Show resolution data.

Table 1 shows (or will show) the rocking widths for representative crystals using each technique, and for a lysozyme crystal grown on Earth using the osmotic dewatering technique.

Table 1. Mir Results

Method	Mosaicity (°)
Batch	0.051
Osmotic Dewatering	0.061
Step Osmotic Dewatering	0.063
Dialysis Diffusion	0.055
Step Dialysis Diffusion	0.067
Ground (Osmotic Dewatering)	0.12

g-Environment on Mir

The relatively low mosaicity of the Mir-grown crystals (compared to the 1g-grown control crystal) corresponded with the relatively quiescent environment on board Mir during the period of crystal growth. Micro g-RMS levels were analyzed for the Mir mission for several frequency ranges (Table 2).

	0.05-0.5 Hz	0.5-1 Hz	1-2 Hz	2-2.5 Hz	2.5-4 Hz
Exercise 1	9.8	15.7	57.6	259.6	141.0
Exercise 2	9.0	17.8	63.6	5.4	39.9
Nominal 1	6.1	8.3	7.5	0.2	0.4
Nominal 2	8.5	8.2	17.2	0.3	0.6
Pre-Sleep	9.7	12.9	9.4	0.7	0.9
Sleep	2.2	2.2	2.6	0.2	0.4
Post-Sleep	14.7	10.7	9.1	0.2	0.3

Table 2. Acceleration levels on Mir. Values are in μgRMS; data are for 20 min. increments from Mission Day 15-18, corresponding to days 7-10 of crystal experiments.

5. Discussion

Crystallization results: habit and morphology

In terms of crystal morphology, the most significant difference between the lysozyme crystals grown on Mir and their counterparts grown on Earth was the high number of unattached crystals in the Mir-grown batch experiments. Littke and John **(1)** first described this sometimes-seen phenomenon of low-gravity crystallization and pointed out the perfect habit of crystals grown suspended in solution without contacting any solid surface. Interestingly, on this flight and in some of our previous low-gravity crystallization experiments, this phenomenon of free-floating, unattached crystal growth is seen much more often with batch experiments. This is likely due to the material of the crystallization chamber, as batch experiments are performed in Dow Corning vacuum grease-coated glass containers bounded on two ends with Dow Corning vacuum grease-coated rubber septa, whereas the membrane-based experiments are performed in uncoated polycarbonate chambers sealed on one end with a polymeric membrane. The contribution of the low-gravity environment, however, is apparent, as Earth-based batch experiments virtually never produce lysozyme crystals that are unattached to the grease-coated glass walls or septa.

The apparent improvement in crystal quality that the Mir experiments exhibited, in terms of optimal tetragonal habit and freedom from visible defects, was also more pronounced in the batch experiments than in the four membrane-based experiments. This may have been due in part to the nucleation in suspension, but also due to the intrinsically less-ordered conditions of the batch technique, which are more apt to produce convection in a 1g environment than the membrane-based techniques.

Advantages/disadvantages of low gravity, convection: Rosenberger, Microg Sci and tech 10:(1) 29-35 (1997), Chernov here?????

To a much higher extent in Mir-grown than in Earth-grown samples,
attachment, etc. (Littke and John – perfect habit of crystals growing free)
numbers of crystals
Discussion of Crystal Quality

While there was a significant difference between the mosaicity values for the Mir crystals and the mosaicity of the 1-g osmotic dewatering crystal, no significant difference in mosaicity was seen among the set of Mir crystals grown using five different techniques. Unlike some configurations of low-gravity vapor diffusion experiments, none of the five techniques used in the Mir experiments can be expected to exhibit significant Marangoni convection, which has been theorized to reduce crystal quality, even in low gravity **(8, 28)**. Marangoni convection in osmotic dewatering?

Chayen, Snell, Helliwell, Zagalsky JCG 171 (1997) 219-25: hanging drop low g : marangoni disruption; better ordering w/other techniques
Snell et al, Acta Cryst. D53 (1997), 231-239 APCF vapor diffusion crystals – also not optimal technique – Marangoni convection (no large difference in mosaicity between space and ground; anisotropy of mosaicity)

Table 2 shows μgRMS levels for a variety of activities and a range of frequencies on Mir during the period in which the lysozyme crystals were presumably growing. While the g-levels increased by more than an order of magnitude during exercise periods for the higher frequency ranges in the table, g-levels remained fairly low during all activity periods (~ 10^{-5} g or better, reaching a low of 2.2 x 10^{-6} g) for the lowest frequency range analyzed (0.05-0.5 Hz), and this is the range to which we expect the crystals to be most sensitive **(19)**. Higher frequencies will have minimal effects on movement of crystals of the size range produced in these experiments (≤ 1 mm). but will cause fluctuations in position (references).

The authors thank the staff of BioServe Space Technologies (NASA grant NAGW-1197) for their help with the Mir experiments and NASA for the funding for this research (NASA grant NAG 8-1165).

References

1 Littke, W., John, C.: Protein Single Crystal Growth Under Microgravity. Science, vol. 225. p. 203 (1984)

2 DeLucas, L.J., Suddath, F.L., Snyder, R., Naumann, R., Broom, M.B., Pusey, M., Yost, V., Herren, B., Carter, D., Nelson, B., Meehan, E. J., McPherson, A., Bugg, C.E.: Preliminary Investigations Of Protein Crystal Growth Using The Space Shuttle. Journal of Crystal Growth, vol. 76, no. 3, p. 681-693 (1986)

3 DeLucas, L.J., Smith, C.D., Smith, H.W., Vijay-Kumar, S., Senadhi, S.E., Ealick, S.E., Carter, D.C., Snyder, R.S., Weber, P.C., Salemme, F.R., Ohlendorf, D.H., Einspahr, H.M., Clancy, L.L., Navia, M.A., McKeever, B.M., Nagabhushan, T.L., Nelson, G., McPherson, A., Koszelak, S., Taylor, G., Stammers, D., Powell, K., Darby, G., Bugg, C.E.: Protein Crystal Growth In Microgravity. Science, vol. 246, no. 4930, p. 651-654 (Nov 3 1989)

4 Chayen, N.E., Gordon, E.J., Zagalsky, P.F. Crystallizaiton of Apocrustacyanin C_1 on the International Microgravity Laboratory (IML-2) Mission. Acta Crystallographica D, vol. 52. p. 156 (1996)

5 Carter, D.C., Wright, B., Miller, T., Chapman, J., Twigg, P., Keeling, K., Moody, K., White, M., Click, J., Ruble, J.R., Ho, J.X., Adcock-Downey, L., Bunick, G., Harp, J.: Diffusion-Controlled Crystallization Apparatus for Microgravity (DCAM): Flight and Ground-Based Applications. Journal of Crystal Growth, vol. 196. p. 602 (1999)

6 Carter, D.C., Wright, B., Miller, T., Chapman, J., Twigg, P., Keeling, K., Moody, K., White, M., Click, J., Ruble, J.R., Ho, J.X., Adcock-Downey, L., Dowling, T., Chang, C.-H., Ala, P., Rose, J., Wang, B.C., Declercq, J.-P., Evrard, C., Rosenberg, J., Wery, J.-P., Clawson, D., Wardell, M., Stallings, W., Stevens, A.: PCAM: A Multi-User Facility-Based Protein Crystallization Apparatus for Microgravity. Journal of Crystal Growth, vol. 196. p. 610 (1999)

7 DeLucas, L.J., Long, M.M., Moore, K.M., Rosenblum, W.M., Bray, T.L., Smith, C., Carson, M., Narayana, S.V.L., Harrington, M.D., Carter, D., Clark, Jr., A.D., Nanni, R.G., Ding, J., Jacobo-Molina, A., Kamer, G., Hughes, S.H., Arnold, E., Einspahr, H.M., Clancy, L.L., Rao,

G.S.J., Cook, P.F., Harris, B.G., Munson, S.H., Finzel, B.C., McPherson, A., Weber, P.C., Lewandowski, F.A., Nagabhusan, T.L., Trotta, P.P., Reichert, P., Navia, M.A., Wilson, K.P., Thomson, J.A., Richards, R.N., Bowersox, K.D., Meade, C.J., Baker, E.S., Bishop, S.P., Dunbar, B.j., Trinh, E., Prahl, J., Sacco, Jr., A., Bugg, C.E.: Recent Results and New Hardware Developments for Protein Crystal Growth in Microgravity. Joural of Crystal Growth, vol. 135. p. 183 (1994)

8 Chayen, N.E., Snell, E.H., Helliwell, J.R., Zagalsky, P.F.: CCD Video Observation of Microgravity Crystallization: Apocrustacyanin C_1. Journal of Crystal Growth, vol. 171. p. 219 (1997)

9 DeLucas, L.J., Smith, C.D., Carter, D.C., Snyder, R.S., McPherson, A., Koszelak, S., Bugg, C.E.: Microgravity Protein Crystal Growth; Results and Hardware Development. Journal of Crystal Growth, vol. 109. p. 12 (1991)

10 DeLucas, L.J., Smith, C.D., Smith, W., Vijay-Kumar, S., Senadhi, S.E., Ealick, S.E., Carter, D.C., Snyder, R.S., Weber, P.C., Salemme, F.R., Ohlendorf, D.H., Einspahr, H.M., Clancy, L.L., Navia, M.A., McKeever, B.M., Nagabhusan, T.L., Nelson, G., McPherson, A., Koszelak, S., Taylor, G., Stammers, D., Powell, K., Darby, G., Bugg, C.E.: Protein Crystal Growth Results for Shuttle Flights STS-26 and STS-29. Journal of Crystal Growth, vol. 110. p. 302 (1991)

11 Snell, E.H., Weisberger, S., Helliwell, J.R.: Improvements in Lysozyme Protein Crystal Perfection Through Microgravity Growth. Acta Crystallographica D, vol. 51. p. 1099 (1995)

12

13 McPherson, A.: Effects of a Microgravity Environment on the Crystallization of Biological Macromolecules. Microgravity Science and Technology, vol. 1/2. p. 101 (1993)

14 McPherson, A., Malkin, A. J., Kuznetsov, Y. G., Koszelak, S., Wells, M., Jenkins, G., Howard, J., Lawson, G.: The Effects of Microgravity on Protein Crystallization: Evidence for Concentration Gradients Around Growing Crystals. Journal of Crystal Growth, vol. 196. p. 572 (1999)

15 Carter, D.C., Lim, K., Ho, J. X., Wright, B.S., Twigg, P. D., Miller, T. Y., Chapman, J., Keeling, K., Ruble, J., Vekilov, P. G., Thomas, B. R., Rosenberger, F., Chernov, A. A.: Lower Dimer Impurity Incorporation May Result in Higher Perfection of HEWL Crystals Grown in Microgravity - A Case Study. Journal of Crystal Growth, vol. 196, nos. 2-4. p. 623 (1999)

16

17 Rosenberger, F., Vekilov, P. G., Lin, H., Alexander, J. I. D.: A Rationale System-dependent Advantages and Disadvantages of Solution Crystal Growth at Low Gravity. Microgravity Science and Technology, vol. X/1. p. 29 (1997)

18 Chernov, A. A.: Crystal Growth and Crystallography. Acta Crystallographica A, vol. 54. p. 859 (1998)

19 Todd, P., Lee, C.-Y., Sygusch, J.: Effects of Orbital Maneuvers on Biomolecule Crystal Growth from Solution: Modeling Studies. Proceedings, Spacebound 1997, held May 11-15, Montreal, Quebec, Canada.

20

21

22 Luttges, M. W.: Recognizing and Optimizing Flight Opportunities with Hardware and Life Sciences Limitations. Transactions of the Kansas Academy of Science, vol. 95, nos. 1-2. p. 76 (1992)
23 Lam, K. S., Mamber, S. W., Pack, E. J., Forenza, S., Fernandes, P.B., Klaus, D. M.: The Effects of Space Flight on the Production of Monorden by *Humicola fuscoatra* WC5157 in Solid-State Fermentation. Applied Microbiology and Biotechnology, vol. 49. p. 579 (1998)
24 Todd, P., Sikdar, S. K., Walker, C.: Application of Osmotic Dewatering to the Controlled Crystallization of Biological Macromolecules and Organic Compounds. Journal of Crystal Growth, vol. 110. p. 283 (1991)
25 Lee, C.-Y., McEntyre, S.R., Todd, P., Schaefer, K., Kundrot, C.E.: Control of Nucleation in Oligonucleotide Crystallization by the Osmotic Dewatering Method with Kinetic Water Removal Rate Control. Journal of Crystal Growth, vol. 187. p. 490 (1998)
26 Zeppezauer, M.: Formation of Large Crystals. Methods in Enzymology , vol. 22. p. 253 (1971)
27 Sygusch, J., Coulombe, R., Cassanto, J., Sportiello, M., and Todd, P.: Protein crystallization in low gravity by step gradient diffusion method. Journal of Crystal Growth, vol. 162 (3/4):167-72, 1996
28 Snell, E. H., Cassetta, A., Helliwell, J. R., Boggon, T. J., Chayen, N. E., Weckert, E., Holzer, K., Schroer, K., Gordon, E. J., Zagalsky, P. F.: Partial Improvement of Crystal Quality for Microgravity-Grown Apocrustacyanin C_1. Acta Crystallographica D, vol. 53. p. 231 (1997)

Chapter 29

STS-95 lysozyme crystallization experiments in SHOT ADSEP hardware

Michael G. Sportiello, John Vellinger, Mark S. Deuser and Paul Todd

Chapter 29
Experimental Summary:
STS-95 Lysozyme Crystallization Experiments in SHOT ADSEP Hardware

Mike Sportiello
University of Colorado-Boulder
December 28, 1998

1. Objectives

There were four objectives of the lysozyme crystallization experiments performed in SHOT's ADSEP hardware aboard STS-95:

1) perform batch lysozyme crystallization experiments using two grades of lysozyme to characterize any difference in crystallization performance between the two grades,
2) perform magnetically-mixed lysozyme crystallization experiments using two grades of lysozyme to characterize any difference in crystallization performance between the two grades,
3) compare batch-produced lysozyme crystals with magnetic mixing-produced lysozyme crystals, and
4) evaluate both batch and magnetic-mixing as feasible techniques for growing crystals in the ADSEP hardware in low gravity.

2. Experimental Plan

Lysozyme crystallization experiments were performed using two sets of ADSEP plates. In each of the 44 wells used for these experiments, the bottom half of the well (i.e., the well in the bottom plate) contained sodium chloride in 0.1 M sodium acetate, pH 4.0. The top half of the well contained lysozyme in the same 0.1 M sodium acetate buffer. The wells in which magnetic mixing was used contained a magnet in the bottom half of the well. The magnets were rotated at a low rate of rotation for 60 seconds soon after the top and bottom halves of the wells were aligned. The experimental plan for all wells is summarized in Table1.

3. Results

Crystals were produced in 43 of the 44 wells; the other well, number 15 in plate 1, may have also produced crystals, though it will be difficult to determine this until the contents of this well are removed (microscopic analysis of the well is inconclusive). The results of each of the 44 experiments are summarized in Table 2 below.

Table 1. Experimental plan for 44 experiments in ADSEP wells.

Plate	Wells	Lysozyme source	Lysozyme concentration (w/v %)	Sodium Chloride concentration (w/v %)	Expt. Type (batch or magnetic mixing)
1 (10051/ 10045)	1 + 2	Sigma	6	8	batch
	3 + 4	Seikagaku	6	8	batch
	5 + 6	Sigma	6	8	magnetic mixing
	7 + 8	Seikagaku	6	8	magnetic mixing
	9 + 10	Sigma	6	7	batch
	11 + 12	Seikagaku	6	7	batch
	13 + 14	Sigma	6	7	magnetic mixing
	15 + 16	Seikagaku	6	7	magnetic mixing
	17 + 18	Sigma	7	6	batch
	19 + 20	Seikagaku	7	6	batch
	21 + 22	Sigma	7	6	magnetic mixing
2 (10041/ 10046)	1 + 2	Seikagaku	7	6	magnetic mixing
	3 + 4	Sigma	7	7	batch
	5 + 6	Seikagaku	7	7	batch
	7 + 8	Sigma	7	7	magnetic mixing
	9 + 10	Seikagaku	7	7	magnetic mixing
	11 + 12	Sigma	7	8	batch
	13 + 14	Seikagaku	7	8	batch
	15 + 16	Sigma	7	8	magnetic mixing
	17 + 18	Seikagaku	7	8	magnetic mixing
	19 + 20	Sigma	6	6	batch
	21 + 22	Seikagaku	6	6	batch

The observations listed in the "Results" column of Table 2 were taken in the early morning hours of November 8, approximately 16 hours after the shuttle landed at Kennedy Space Center.

At some future date we hope to perform x-ray diffraction analysis on some of the crystals produced from these experiments in order to obtain further information about the quality of the crystals that were grown. This diffraction analysis would provide additional information that would help fulfill each of the four Objectives listed in Section 1 of this document. The preliminary analysis conducted thus far, however, results in the following preliminary conclusions, organized according to the four Objectives:

Objective 1: perform batch lysozyme crystallization experiments using two grades of lysozyme to characterize any difference in crystallization performance between the two grades

Preliminary conclusion: No significant difference was observed between the Sigma and Seikagaku crystals in the batch wells in terms of characteristics such as crystal habit, crystal

Table 2. Results of lysozyme crystallization experiments in each ADSEP well.

Plate	Well	Lysozyme Source	Lyso. conc. (w/v %)	NaCl conc. (w/v %)	Expt. Type	Results
1	1	Sigma	6	8	batch	many unattached crystals
	2	Sigma	6	8	batch	many unattached crystals
	3	Seikagaku	6	8	batch	many unattached crystals
	4	Seikagaku	6	8	batch	same as 1-3, but solution slightly cloudy
	5	Sigma	6	8	mag.	xtals attached to wall; fewer xtals than 1-4
	6	Sigma	6	8	mag.	unattached xtals; fewer xtals than 1-4
	7	Seikagaku	6	8	mag.	attached and unattached xtals
	8	Seikagaku	6	8	mag.	attached and unattached xtals
	9	Sigma	6	7	batch	like 1-3, except more xtals
	10	Sigma	6	7	batch	like 1-3, except more xtals
	11	Seikagaku	6	7	batch	like 1-3, except more xtals
	12	Seikagaku	6	7	batch	like 1-3, except more xtals
	13	Sigma	6	7	mag.	many unattached xtals; solution slightly cloudy
	14	Sigma	6	7	mag.	slightly fewer xtals than 13
	15	Seikagaku	6	7	mag.	cloudy pink solution; no visible xtals
	16	Seikagaku	6	7	mag.	relatively few xtals (attached and unattached)
	17	Sigma	7	6	batch	like 1-3
	18	Sigma	7	6	batch	like 1-3
	19	Seikagaku	7	6	batch	like 1-3
	20	Seikagaku	7	6	batch	like 1-3
	21	Sigma	7	6	mag.	like 13 – many xtals, solution slightly cloudy
	22	Sigma	7	6	mag.	like 13 – many xtals, solution slightly cloudy
2	2	Seikagaku	7	6	mag.	solution pinkish; xtals
	3	Sigma	7	7	batch	many unattached xtals
	4	Sigma	7	7	batch	many unattached xtals
	5	Seikagaku	7	7	batch	many unattached xtals
	6	Seikagaku	7	7	batch	many unattached xtals
	7	Sigma	7	7	mag.	attached xtals, but not very many
	8	Sigma	7	7	mag.	attached and unattached xtals
	9	Seikagaku	7	7	mag.	like 7 (wheel 2)
	10	Seikagaku	7	7	mag.	many unattached xtals
	11	Sigma	7	8	batch	many unattached xtals
	12	Sigma	7	8	batch	many unattached xtals
	13	Seikagaku	7	8	batch	many unattached xtals
	14	Seikagaku	7	8	batch	many unattached xtals
	15	Sigma	7	8	mag.	attached and unattached xtals
	16	Sigma	7	8	mag.	attached and unattached xtals
	17	Seikagaku	7	8	mag.	solution pink; a few large xtals
	18	Seikagaku	7	8	mag.	attached and unattached xtals - few
	19	Sigma	6	6	batch	attached and many unattached xtals
	20	Sigma	6	6	batch	attached and many unattached xtals
	21	Seikagaku	6	6	batch	attached and many unattached xtals
	22	Seikagaku	6	6	batch	attached and many unattached xtals

number per well, percent of crystals that grew in suspension (unattached crystals) as opposed to those that nucleated on the inner surface of the well (attached crystals), and crystal size.

Objective 2: perform magnetically-mixed lysozyme crystallization experiments using two grades of lysozyme to characterize any difference in crystallization performance between the two grades

Preliminary conclusions: There do appear to be differences in how the two grades of lysozyme crystallized; there appeared overall to be more crystals produced from the Sigma lysozyme than from the Seikagaku lysozyme, and the largest crystals produced from these magnetically-mixed experiments were produced from a well that contained Seikagaku lysozyme. There did not appear to be any recognizable difference in percent of crystals that were attached or unattached between the Sigma and Seikagaku groups.

Objective 3: compare batch-produced lysozyme crystals with magnetic mixing-produced lysozyme crystals

Preliminary conclusions: With the Sigma lysozyme, there appeared to be more consistent results with the batch grown crystals than with the crystals grown by magnetic mixing. With the Seikagaku lysozyme, there was a clear difference in the results from the two methods; consistently, more crystals were produced using the batch technique than using magnetic mixing.

Objective 4: evaluate both batch and magnetic-mixing as feasible techniques for growing crystals in the ADSEP hardware in low gravity

Preliminary conclusions: As was seen on a previous low-gravity mission (Conquest 1), the ADSEP plates do seem to produce adequate crystals from a batch lysozyme crystallization experiment, at least in terms of number of crystals and crystal habit. Many of the crystals produced were not attached to any surface, which does aid in harvesting the crystals without damage for further analysis. This result also has been seen in low gravity with some other (though not all) types of space flight crystallization hardware.

The results of the magnetic mixing experiment provided some good baseline information, as this was the first time this type of protein crystallization experiment has been attempted in low gravity with the ADSEP hardware. A variety of other mixing regimens would need to be attempted (varying duration of mixing, time of mixing during the mission, speed of magnet rotation, magnet geometry, magnet coating, etc.) to provide enough information to make a sound judgment on the utility of this method for low-gravity protein crystallization. X-ray diffraction analysis would need to be performed on the crystals to determine the effect of magnetic mixing on crystal quality, but, again, preliminary analysis suggests that the batch experiments were able to produce lysozyme crystals in a more consistent manner. I have noticed today, December 28, that there appears to be some type of corrosion on some of the magnets, and this will also need to be explored with some thoroughness.

Chapter 30

Biochemical and x-ray analysis of impurity doped microgravity and ground-grown lysozyme crystals

Russell A. Judge, Edward H. Snell, Michael Sportiello, H. Bellamy, G. E. Borgstahl, M. Pokros, M. L. Pusey, J. M. Cassanto and P. Todd

Chapter 30
Biochemical and X-ray mosaicity analysis of impurity doped microgravity and ground-grown lysozyme crystals

Russell A. Judge[a], Edward H. Snell[a]., Sportiello, M., Bellamy, H., Borgstahl, G.E., Pokros, M., Pusey, M.L., Cassanto, J. & Todd, P.

[a]Code SD48, NASA MSFC, Huntsville, AL 35812, USA, [b]University of Colorado at Boulder, Department of Chemical Engineering, Boulder, Colorado, 80309-0424, USA, [c]Stanford Synchrotron Radiation Laboratory, PO Box 4349, MS 99, Stanford, California 94309, [d]The University of Toledo, Department of Chemistry, 2801 West Bancroft Street, Toledo, OH, 43606, USA.

Correspondence e-mail: eddie.snell@msfc.nasa.gov

(Draft version September 6th, 1999)

Abstract

Chicken egg-white lysozyme was grown in microgravity using the liquid-liquid diffusion method. Various amounts of a naturally occurring dimer impurity were added and the samples examined both biochemically and using X-ray mosaicity analysis on the return to Earth. Ground control samples were also grown and examined using similar techniques. Microgravity reduces mosaicity, while impurities increase it. Microgravity samples were, on average, larger than ground samples grown with similar impurity levels. This volume increase corresponded to an increase in the signal to noise ratio of the structural X-ray data. Biochemical analysis displayed no differences between the microgravity and Earth-grown crystals.

Introduction

Microgravity is seen as an environmental variable that has the potential to produce high-quality crystals for structural studies. The experiments themselves are small, have low mass, can be remotely operated and potentially have a high payback. To date, growth of macromolecular crystals in microgravity has had mixed results with enhancement in some studies, (McPherson, 1993; DeLucas et al, 1994; Snell et al., 1995; Ng et al, 1997) and no positive or even detrimental effects in others (Hilgenfeld, 1992; Vaney et al 1996). Lysozyme has been a model protein used in a number of low-gravity studies with reports of decreased mosaicity (Snell et al., 1995; Helliwell et al., 1996), increased diffraction resolution (Carter et al., 1999) and no effects (Vaney et al., 199X).

Carter et al. (1999) and Chernov (1998) report impurity partitioning for lysozyme crystals grown in microgravity in comparison to those grown on the ground. We have carried out a similar experiment, under more controlled conditions, incorporating ground

controls, X-ray mosaicity analysis and biochemical measurements. In part this was to explore the interesting conundrum of how microgravity might act in this purification process.

Experimental

Protein preparation

Lysozyme was extracted directly from fresh chicken eggs using a two step cation exchange chromatography technique (Judge et al., 1998). The impurity of choice, a lysozyme dimer which is eluted at a later retention time was also collected during the lysozyme purification. This naturally occurring dimer of lysozyme was first discovered by (Back, 19xx) and later described by Thomas et al (199X). The material was pooled, concentrated, dialyzed against 0.05 M sodium phosphate pH 7.0, then rechromatographed on a semi-preparative cation exchange HPLC column (HEMA --) using a gradient of X to Y % NaCl in phosphate buffer. The purified dimer fraction was pooled, concentrated by ultrafiltration, and stored at 4°C until used.

Physiological lysozyme dimer impurity preparation and characterization: The dimer enriched lysozyme fraction could be conveniently further purified by rechromatography on a semi-preparative HPLC column using a NaCl gradient (Figure 1). The pooled dimer fractions were found to be ~XY% pure as judged by SDS PAGE electrophoresis. Addition of β-mercaptoethanol to the electrophoretic samples did not result in dimer dissociation into monomers. Measurement of the activity using *Lysococcus microdicticus*, after correcting for the monomer present, indicated that the dimer's specific enzymatic activity was ~ YZ% of the monomer's per unit mass. Preliminary peptide analysis using trypsin digestion of the carboxymethylated dimer did not reveal an obvious cross-linking peptide (data not shown). While this suggests that the cross-linkage is through a disulfide bond, the SDS PAGE results with β-mercaptoethanol suggest otherwise.

Crystallization

Crystallization took place in parallel on the ground and on the STS-95 mission launched on October 29th, 1998, landing on November 7th. Crystals were grown by the batch method on the ground and by liquid-liquid diffusion in a specially designed minilab, the Dual Materials Dispersion Apparatus (DMDA) built by Instrumentation Technology Associates (ITA, Exton, PA). The DMDA is a multiwell apparatus of a sliding block design. The top well of each experiment contained 122 µl of 7% w/v NaCl solution, with a similar volume and concentration of protein solution in the bottom well. These wells were initially separated, and the experiment was activated upon attainment of low Earth orbit by bringing both wells into alignment. Approximately 6 hours after landing the crystals were harvested from the DMDA using the existing mother liquor. The wells were then rinsed with an artificial mother liquor to recover any remaining crystals. Crystal samples were returned to the University of Colorado, then transported in large capillary tubes to NASA MSFC where they were stored at 22°C until the beamtime became available (X days after the return of the mission). Due to constraints on beamtime, flight sample 5 and the two freshly grown ground-controls had data that were collected some XX days after the first samples.

X-ray analysis

The techniques used in the X-ray mosaicity analysis are described in detail elsewhere

(Bellamy et al., 1999). In this case we made use of beamline 1.5 at the Stanford Synchrotron Radiation Source (SSRL) operating in an unfocused mode. The wavelength of the beam is tuned by a double crystal Si(111) monochromator giving a $\delta\lambda/\lambda$ of approximately $2x10^{-4}$. The wavelength is calibrated by measuring the x-ray absorption of metal foils to locate an edge. In our case we operated with a wavelength of 1⇒throughout. An ADSC Quantum 4 CCD detector was used to collect the data operating in binned mode for the fastest readout time. A Huber 4-circle goniometer is used but due to constraints with the detector we could only make use of the phi axis on this.

Crystals were mounted in quartz glass capillaries and data were collected at 22°C using a FTS air stream temperature controller. Table 1 summarises the crystals and data collection. Four microgravity and two ground-control crystals were studied. Flight crystals 1 to 3 were recorded during the first beamtime (XX months after the flight) with the remaining samples (one ground and three flight) recorded later (XXX months after the flight). During the data collection on ground 1, communication errors between the detector and data collection computer developed and the data collection had to be interrupted at several stages. This problem was rectified and a second, 0% impurity ground crystal, ground 2, was collected. It was possible to use data from both crystals. Initially a 5s exposure time was used for the fine slicing work but this was reduced to 2s for Flight 5 and Ground 1 and 2. Ground 3 (4% impurity) required a larger exposure time because it was not as strongly diffracting as the previous ground samples (0% impurity).

The data were processed using ? to evaluate the reflection profiles and deconvolute Lorentz, geometrical and spectral effects using the program, Beamish (Bellamy et al., 1999). As part of the processing method an orientation matrix is required. Although it has proved possible to evaluate this from the fine slicing data directly a more effective method has been collecting a coarse slice of data covering the same area of reciprocal space as the fine phi slicing. Consequently for each crystal studied several degrees of 1degree oscillation data were collected (table 1). This was processed using MOSFLM and CCP4 (19XX) software to integrate, merge and reduce the data.

Biochemical analysis

The constituent protein was analyzed before crystallization.

After crystallization the crystals were examined by dissolving and using SDS-PAGE Phastsystem, Phastgel 8-25% gels. Lysozyme and the lysozyme dimer were quantified using lysozyme standards on the same gel.

Results

Crystals

The resulting crystals were examined visually under the microscope. Volume information was recorded.

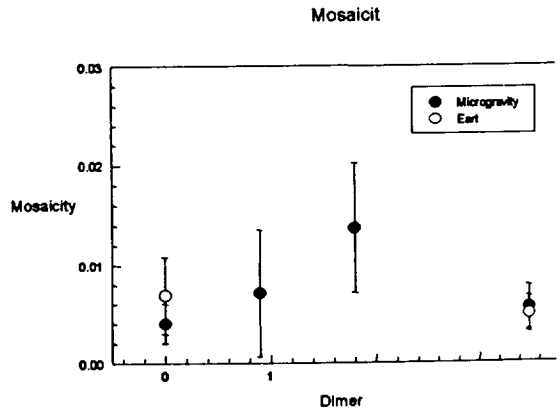

Figure 4. Plot of measured mosaicity against di concentration

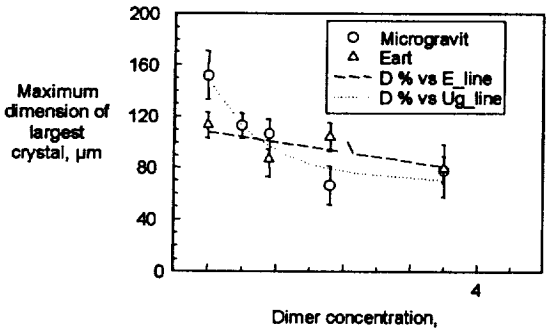

Figure 1. Plot of the maximum dimensions of crystals as a function of dimer concentration.

X-ray analysis

The 1 degree oscillation images were used for indexing the sample giving the cell parameters, table 1. Different exposure times were used such that a complete set of the fine slicing data could be recorded without being affected by a beam dump and corresponding fill. Figure 2 illustrates 4 images from quadrants of the 4 chip ADSC Quantum IV CCD detector used to collect the X-ray data. In 2(a) and 2(b) microgravity is compared

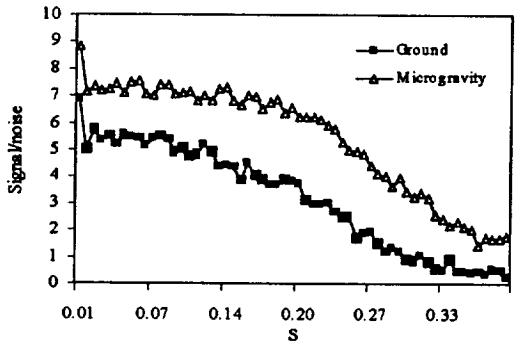

Figure 3 Signal to noise plot for 0% impurity microgravity and ground crystals.

with Earth with no impurity present. Identical exposure times were used and the intensity range used to display the figures are also identical. The increased diffracting volume is evident in the strength of the diffraction seen from the microgravity crystal in 2(a), beyond the 2⇒ outer ring. The images in 2(c) and (d) are from microgravity samples, with an exposure time of 60s, with 1% and 4% impurity incorporated respectively. The image seen here is rotated 90 degrees from how it is recorded.

Figure 3 shows the signal to noise plots of the 0% microgravity and earth samples. The microgravity sample is markedly improved throughout its diffracting range.

Biochemical analysis

Tabe 2 gives the effective partitioning coefficients K_{eff}, for crystals grown in microgravity and on the ground. K_{eff} is defined as $Keff = [<n_{iS}>/<n_{pS}>]/[<n_{iL}>/<n_{pL}>]$ (Carter et al. 1999) where n_{iS} and n_{iL} are the concentrations of impurity in solid and liquid phase and n_{pS} and n_{pL} are the concentrations of pure material in the solid and liquid phase

	Lysozyme dimer, %		
	0.9	1.8	3.5
K_{eff} - earth	0.7	1.0	1.0
K_{eff} - microgravity	1.2	0.6	0.7

Table 2. Partitioing coefficients for respectively. The error in the measured K_{eff} value is +/-0.3. These values are illustrated in figure X.

Discussion and Conclusions

Otalora, Capelle, Ducruix & Garcia-Ruiz (1999) report rocking widths of 0.003 degrees for microgravity grown tetragonal lysozyme crystals.

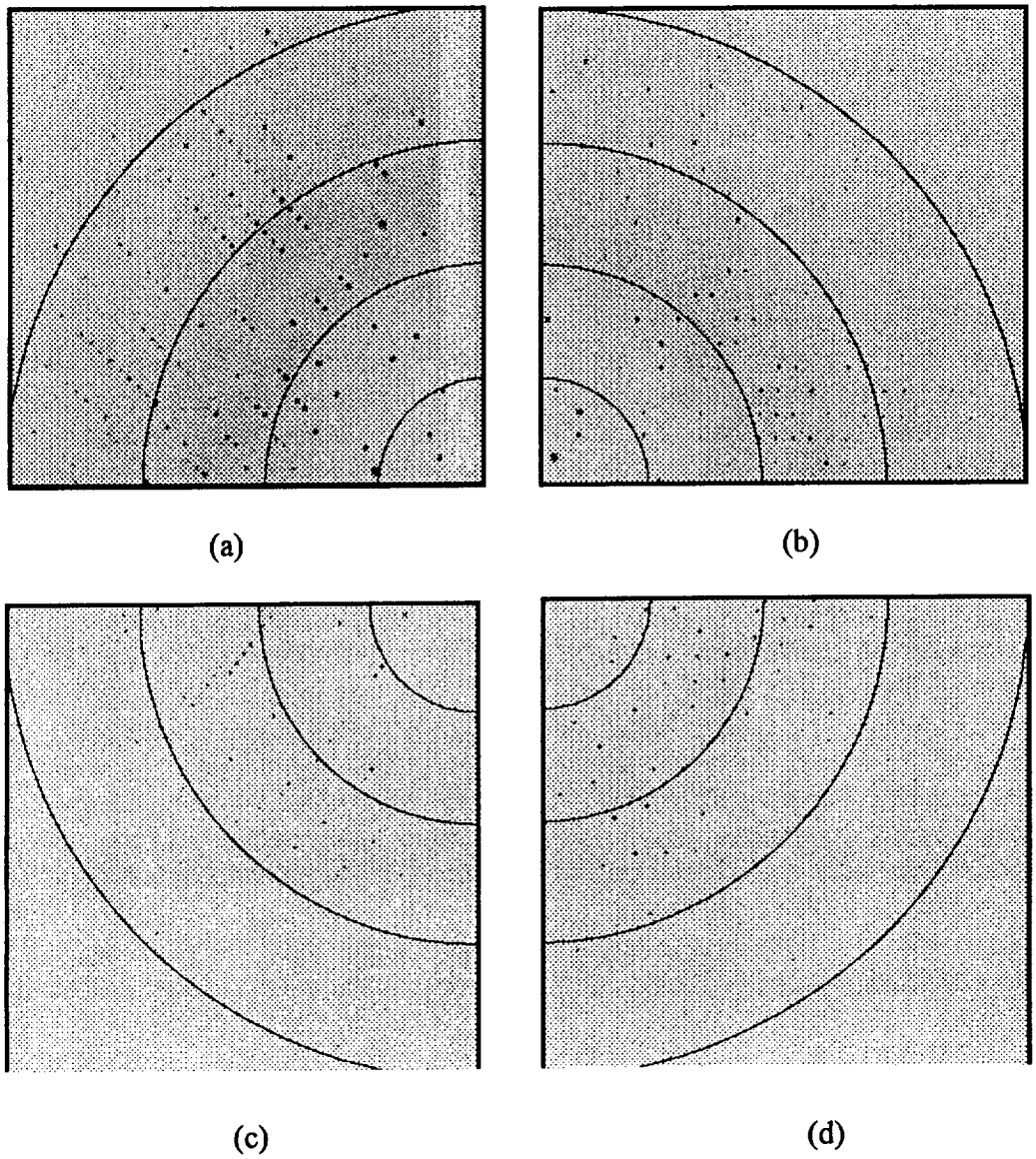

Figure 2. Four quadrants from CCD recorded images of lysozyme crystals, microgravity and ground grown, 0% impurity (a and b respectively) and microgravity crystals with 2% (c) and 4% (d) of the dimer impurity. In each case a 1 degree oscillation is used with exposure times of 20s (a,b) and 60s (c,d). A horizontal rotation axis is used with the beamstop, seen as white shadow, 2(a).

One recent theory has been that growth in a microgravity environment enables diffusive partitioning of impurities from the solute of choice due to the suppression of density gradient-driven convective flows, which would otherwise actively transport those impurities to the growing crystal surface. Carter et al. (1999 and references therein) tested this theory during several microgravity lysozyme crystal growth experiments. In the latter experiments the partitioning of the naturally occurring dimer was used as an example of the improvements to be obtained in the presence of microheterogeneous impurities. Previous experiments were carried out using a synthetic dimer prepared by peroxide crosslinking of a lysozyme solution. Neglecting other parameters, the crystal growth rate is a function of the

concentration of growth units at the growth interface, and this also holds true for the incorporation of impurities. More simply put, if they are not at the interface then they cannot add on, and the rate at which they add on is a function of their local concentration at that point. The microheterogeneous dimer, by virtue of is increased mass (MW 28 KDa) is postulated to diffuse more slowly to the surface. Having a lower concentration at the surface results in a lower rate of incorporation, and Carter et al. used the differences in impurity concentration in the crystal vs. the solution to define an effective partitioning coefficient.

The above theory rests on several questionable assumptions. First, dimerization cannot be considered as a microheterogeneity, but one of a rather more macroscopic nature. True microheterogeneity is defined in terms of conformational motility, "breathing" of the overall structure, point mutations in the amino acid sequence, etc.. Dimerization results in a diffusivity of ~70% relative to the monomer, and true microheterogeneity would result in diffusivities virtually identical to that of the "native" structure.

Second, it does not take solution interactions between solute molecules into account. A considerable body of evidence has recently shown that, in the case of tetragonal lysozyme, there are extensive intermolecular interactions occurring in crystallizing solutions (Minezaki *et al.*, 1996; Niimura et al., 1999; Michinomae et al., 1999; Bessho et al., 1994), Behlke – to be found, (Nadarajah et al., 1995; Wilson and Pusey, 1992; Wilson et al., 1993) – also, AFM papers, (Georgalis et al., 1993; Georgalis et al., 1997; Schaper et al., 1997; Georgalis et al., 1992). Regardless of the growth mechanism, reversible self-association in the bulk solution will produce a population of solute with a mixture of diffusivities. If current theory is correct for tetragonal CEWL then the basic growth unit is a tetramer or multiple thereof, and in this case the dimer would actually have a greater diffusivity than the growth units. Also, interactions between the dimer and other oligomers in the solution will also affect the dimer's transport to and incorporation onto the surface.

Third, the dimer is in fact composed of units which, save for their geometric orientation to each other, are essentially equivalent to the monomeric solute species. Thus the dimer would be expected to participate in any interactions which the monomer may have with other molecules in the solution or the crystal surface which involve the same surfaces of the dimer which are free, i.e., do not participate in or are sterically blocked by the dimerization process. Crystal growth is a reversible process, with the molecules adding on and departing. It is only as the added molecules become further "tied down" by addition of adjacent units or over-layering that the addition process becomes progressively more irreversible. If the impurity is assumed to have a lower affinity for the surface than the growth unit, then "entrapment" in this case would be enhanced by more rapid growth rates and reduced by slower rates. On Earth density gradient driven flow serves to keep the interfacial concentration high, approximately at bulk solution concentrations, and thus maintain a high growth rate. In a microgravity environment the establishment of a concentration gradient keeps the interfacial concentration of all solute and thus the growth rate low, and allows the impurity more time to desorb from the surface before becoming trapped by succeeding units. If the dimer has a higher affinity for the surface than the growth unit then the growth process will preferentially adsorb dimer from the solution, and upon return to an Earth

environment (with concomitant mixing of the solutions) the remaining dimer will also preferentially bind to the crystal relative to the monomer. i.e., one would not be able to measure any difference in partitioning coefficient.

Two types of dimers were used in the results reported by Carter et al. and references therein. The first were prepared by random peroxide cross-linking of the monomeric protein, with no control over the actual cross-linking site. These undefined dimers will have a variety of configurations which may be more or less able to participate in the crystal growth process, and thus affect the results obtained. The second dimer, used in the study reported herein, is the physiological dimer found in eggs (Back et al. ref). The occurrence of this dimer in lysozyme solutions is apparently a function of the age of the eggs from which the protein is purified. It is apparently formed by a membrane-associated process, and once removed from the membranes the protein is no longer dimerized. Preliminary tests on purified dimer in this laboratory (data not shown) have so far not revealed a clear cross-linking site, while SDS-PAGE results indicate that the dimerization is not through a disulfide linkage. Regardless, the regular behaviour of this material in purification, and its generation by an apparently physiological process, combine to suggest that the cross-linkage site is not random but specific, and that the physiological dimer has a defined structure.

We do not see the effect of a preferential impurity partitioning process in microgravity from our biochemical analysis. We note in the Carter et al (1999) study that the equations given for optical density (eqn. 3) do not match the tabulated data; in fact, when we use these equations with the tabulated optical density the resulting concentrations would seem to be in agreement with ours. It is difficult to explain the differences in the reported results; in our study all the samples were grown on the same mission by liquid-liquid diffusion at a constant temperature 22C+/-2C with some temperature fluctuations observedwhereas the Carter *et al.* (1999) results were from samples grown on Mir in DCAM (Carter *et al.* 1999) between the STS-81 and STS-84 missions. During this time a fire broke out onboard Mir and later during the mission a cooling loop broke down resulting in temperatures hovering in the 32°C range for many days. The DCAM's were flown at ambient temperature. Crystals grown in the DCAM were grown with a concentration of 25 mg/ml with a final NaCl concentration of 6.4%. The dimer impurity in the initial protein used was approximated to 1% w/v based on Thomas et al. (1999). Carter et al. report improved resolution and lower B-factors from the microgravity samples, in the X-ray analysis case. These were grown by vapor diffusion on the shuttle orbiter unlike the crystals used for biochemical analysis, which were grown on Mir. The microgravity X-ray data were collected from three crystals on a Siemens multiwire detector, which typically uses a small oscillation data collection method (fractions of a degree) in comparison to the ground data, from a single crystal, which was collected on an image plate. No details on the data collection were given. It certainly seems possible that, despite the different detectors, possibly different data collection parameters, and the use of three crystals versus a single sample, that improvements could be caused by a reduction in the mosaicity of the samples – seen in other studies (Snell et. al., Ng et al.) and the work presented here.

We have been careful to use samples grown on the same mission in the same experimental cells for both the X-ray and biochemical analysis. Temperatures were

controlled throughout ???. X-ray analysis was carried out using a quantitative technique, mosaicity (the instrument deconvoluted rocking width) analysis, which is directly comparable between samples despite exposure time or incident X-ray intensity. We see two results: the microgravity samples display reduced mosaicities over the ground grown crystals, and impurity incorporation increases the mosaicity, which is still lower in microgravity samples than 1-g samples.

The difference between our results and those of Carter et. al. demonstrate the importance of control experiments performed under the same conditions with the exception of the parameter being investigated, in this case different gravitational fields.

Acknowledgments

This work was funded by NASA grant NAG8-1165. EHS holds a national Research Council (MSFC) Research Associateship. This work is based upon research conducted at the Stanford Synchrotron Radiation Laboratory (SSRL), which is funded by the Department of Energy, Office of Basic Energy Sciences. The Biotechnology Program is supported by the National Institutes of Health, National Center for Research Resources, Biomedical Technology Program and the Department of Energy, Office of Biological and Environmental Research.

References

Bessho,Y., M.Ataka, A.Michihiko, and T.Katsura. 1994. Analysis of the Crystallization Kinetics of Lysozyme using a Model with Polynuclear Growth Mechanism. *J. Biophys.* 66:310-313.

Carter, D.C., Lim, K., Ho, J.X., Wright, B.S., Twigg, P.D., Miller, T.Y., Chapman, J., Keeling, K., Ruble, J., Vekilov, P.G., Thomas, B.R., Rosenberger, F. & Chernov, A.A. Lower dimer impurity incorporation may result in higher perfection HEWL crystals grown in microgravity A case study. (1999) J. Cryst. Growth 196, 623-627.

Chayen, N.E., Snell, E.H., Helliwell, J.R. & Zagalsky, P.F. CCD video observation of microgravity crystallization: apocrustacyanin C_1. *J. Cryst. Growth* **171**, 219-225 (1997).

Georgalis,Y., A.Zouni, W.Eberstein, and W.Saenger. 1993. Formation dynamics of protein precrystallization fractal clusters. *J. Cryst. Growth* 126:245-260.

Georgalis,Y., A.Zouni, and W.Saenger. 1992. Dynamics of protein precrystallization cluster formation. *J. Cryst. Growth* 118:360-364.

Georgalis,Y., P.Umbach, J.Raptis, and W.Saenger. 1997. Lysozyme Aggregation Studied by Light Scattering. II. Variations of Protein Concentration. *Acta. Cryst. D.* 53:703-712.

Hilgenfeld, R., Liesum, A. & Storm, R. Crystallization of two bacterial enzymes on an unmanned space mission. *J. Cryst. Growth* **122**, 330-336 (1992).

Helliwell, J.R., Snell, E.H., & Weisgerber, S. An Investigation of the perfection of lysozyme protein crystals grown in microgravity and on earth. *Proceedings of the 1995 Berlin Microgravity Conference* edited by Ratke, L., Walter, H. & Feuerbache, B. Springer Verlag, 155-170 (1996).

McPherson, A. Virus and protein crystal growth on earth and in microgravity. *J. Phys. D. Appl. Phys.* **26**, B104-B112 (1993).

Michinomae,M., M.Mochizuki, and M.Ataka. 1999. Electron Microscopic Studies on the Initial Process of Lysozyme Crystal Growth. *J. Crystal Growth* 197:257-262.

Minezaki,Y., N.Niimura, M.Ataka, and T.Katsura. 1996. Small Angle Neutron Scattering from Lysozyme solutions in unsaturated and supersaturated States (SANS from Lysozyme Solutions). *Biophysical Chemistry* 58:355-363.

Nadarajah,A., E.L.Forsythe, and M.L.Pusey. 1995. The Average Face Growth Rates of Lysozyme Crystals: the Effect of Temperature. *j. Cryst. Growth* 00:1-10.

Ng et al.

Niimura,N., Y.Minezaki, I.Tanaka, S.Fujiwara, and M.Ataka. 1999. Polar Structure of Lysozyme Aggregates in Unsaturates Solution Determined by Small-Angle Neutron Scattering - Contrast Variation Method. *J. Crystal Growth* 200:265-270.

Otalora, F., Capelle, B., Ducruix, A. & Garcia-Ruiz, J.M. (1999) Acta Cryst. D55, 644-649.

Ries-Kautt et al. 1997.

Savino, R. & Monti, R. Bouyancy and surface-tension-driven convection in hanging drop protein crystallizer. *J. Cryst. Growth* **165**, 308-318 (1996).

Schaper,A., Y.Georgalis, P.Umbach, J.Raptis, and W.Saenger. 1997. Precrystallization Stuctures in Supersaturated Lysozyme Solutions Studied by Dynamic Light Scattering and Scanning Force Microscopy. *J. Chem. Phys.* 106:8587-8594.

Snell, E.H., Weisgerber, S., Helliwell, J.R., Weckert, E., Hölzer, K. & Schroer, K. Improvements in lysozyme protein crystal perfection through microgravity growth. *Acta Cryst.* **D51**, 1099-1102 (1995).

Snell, E.H., Boggon, T.J., Helliwell, J.R., Moskowitz, M.E., & Nadarajah, A. CCD video observation of microgravity crystallization of lysozyme and correlation with accelerometer data. *Acta Cryst.* **D**. submitted

Vaney, M.C., Maignan, S., Riès-Kautt, M., & Ducruix, A high resololution structure (1.33 Å) of a HEW lysozyme tetragonal crystal grown in the APCF apparatus. Data and structural comparison with a crystal grown under microgravity from SpaceHab-01 mission. *Acta Cryst.* **D52**, 505-517 (1996).

Vekilov, P.G., Alexander, J.I.D., & Rosenberger, F. Nonlinear response of larger growth dynamics in the mixed kinetics-bulk-transport regime. *Physical Review E*, **54**, 6650-6660 (1996).

Wilson,L.J., L.D.Adcock, and M.L.Pusey. 1993. A Dialysis Technique for Determining Aggregate Concentrations in Crystallizing Protein Solutions. *J. Phys. D:Appl. Phys, b* 26:113-117.

Wilson,L.J. and M.L.Pusey. 1992. Determination of monomer concentrations in crystallizing lysozyme solutions. *J. Cryst. Growth* 122:8-13.

Crystal	Impurity	Size(mm)	Data Collection	Cell Parameters a=b, c (A) and volume	M
Flight 1	0%	1.12 x 0.96 x 0.72	2 x 10°, 90° apart, 1° oscillations (20 s) 2 x 1°, 90° apart, 0.001° oscillations (2 s)	78.933, 38.019 (236874)	0.0042 1495
Flight 3	1%	0.40 x 0.26 x 0.19	2 x 10°, 90° apart, 1° oscillations (1 min) 2 x 1°, 95° apart, 0.001° oscillations (5 s)	78.872,37.871 (235587)	0.0096 606
Flight 4	2%	0.32 x 0.28 x 0.13	2 x 10°, 90° apart, 1° oscillations (2 min) 2 x 1°, 95° apart, 0.001° oscillations (5 s)	79.095, 38.003 (237747)	0.0130 854
Flight 5	4%	0.54 x 0.37 x 0.26	2 x 10°, 90° apart, 1° oscillations (1 min) 2 x 1°, 95° apart, 0.001° oscillations (5 s)	78.887, 38.063 (236872)	0.0057 1146
Ground 1	0%	0.86 x 0.40 x 0.40	2 x 10°, 90° apart, 1° oscillations (20 s) 3 x 1°, 90° apart, 0.001° oscillations (2 s)	79.089, 38.089 (238249)	0.0074 556
Ground 2	0%	0.88 x 0.48 x 0.38	2 x 10°, 90° apart, 1° oscillations (20 s) 3 x 1°, 90° apart, 0.001° oscillations (2 s)		
Ground 3	4%	0.48 x 0.35 x 0.32	2 x 10°, 90° apart, 1° oscillations (15 s) 3 x 1°, 45° apart, 0.001° oscillations (4 s)		

Table 1. Experimental data collection parameters, crystal sizes and resulting mosaicity.

Chapter 31

The interplay between inertial acceleration and impurities in determining crystal quality and composition

Chapter 31
The Interplay Between Inertial Acceleration and Impurities in Determining Crystal Quality and Composition

Introduction

A few studies have been performed, including the one described in Chapter 30 and others cited in Chapter 30, in which proteins solutions having deliberately manipulated purities and/or well-defined contaminants were crystallized in low gravity and on the ground. While there is not full concurrence concerning the results of such experiments, certain trends seem to be emerging. The applicabilityof these trends to oligonucleotied crystallization remains to be tested. However, a certain amount of data is available from this project, and the limited data indicate that an impurity can co-crystallize with the target molecule without reducing crystal mass or modifying the amount of contaminant relative to that in the mother liquor.

Hypotheses

Two different, generic hypothese have been typically under test in low gravity crystallization research with contaminants. In one case the question being asked is a test of the hypothesis that high-quality crystals can be grown from less-pure samples if crystals are grown in low gravity. The second hypothesis is more fundamental and states that low-gravity experiments should reveal a role for convection in depletion zones in the incorporation of impurities into growing crystals. The test of these hypotheses is to add impurities at known concentrations and grow crystals in low gravity and on the ground. Subsequently two types of measurements must be make: the measurement of biochemical purity in the crystals and mother liquor and the measurement of crystal quality by diffraction studies.

Approach

Three approaches were used in the research described in this Report:

(1) The UU-dodecamer was studied extensively using the hanging-drop method in the laboratory (Chapter 11). The 5'phosphorylated and 5'hydroxyl versions of the molecule were mixed at various ratios for crystallization experiments. After conditions were established, an attempt was made to repeat these experiments in low gravity under sub-optimal conditions.

(2) Lysozyme samples having two different manufactured purities were crystallized on the ground and in spaceflight using ADSEP plates of SHOT, Inc. on shuttle mission STS-95 (Chapter 29) using two crystallization methods, batch mixing and interfacial diffusion.

(3) Lysozyme crystals were grown from mixtures of lysozyme protein monomer and dimer in various proportions (Chapter 30). These experiments were performed under the same approach as the Chapter 11 experiments with UU-dodecamer. Crystals returned to Earth were subjected to both biochemical and x-ray diffraction analysis.

Results

The results, summarized again, of each of the above experiments were as follows

(1) The UU-dodecamer crystals that grew were too small for either biochemical or x-ray diffraction analysis. However, the growth habit could be noted in photomicrographs, and it was clear that the crystal morphologies that occurred in crystals grown from varous ratios of phosphorylated to unphosphorylated UU-dodecamer were the same as their counterparts on the ground. The corollary to these morphologies, based on biochemical measurements by HPLC on crystals and mother liquor, was that crystals always contained the same ratio as the mother liquor from which they grew. There was no "purification" during crystallization on the ground, and this situation, based on morphological grounds, seemed to prevail in low gravity as well.

(2) Lysozyme from two sources had different purities. The lower purity resulted in lower-quality crystals based on two methods in space.

(3) Deliberately adding lysozyme dimer resulted in the addition of dimer molecules to the crystal structure. This resulted in lower quality crystals both on the ground and in low gravity, although low-gravity grown crystals were generally of higher quality. The effects of dimer contaminant on crystal size, crystal mosaic spread and per cent dimer in crystals did not seem to be modified by crystal growth in low gravity using the liquid-liquid diffusion method on Mir space station (Chapter 30).

Conclusions

This field of study is still controversial, as pointed out in Chapter 30. The emerging trend, however, is leading to a weak dependence upon gravity of the incorporation of impurities into growing crystals and an interpretation that impurity partitioning may not be greatly modified but may depend on the identity of the contaminant in low gravity experiments.

REPORT DOCUMENTATION PAGE

Form Approved
OMB No. 0704-0188

PLEASE DO NOT RETURN YOUR FORM TO THE ABOVE ADDRESS.

1. REPORT DATE (DD-MM-YYYY)	2. REPORT DATE	3. DATES COVERED (From - To)
29-05-2000	29-05-2000	1/7/1995 -- 29/02/2000

4. TITLE AND SUBTITLE
Preparation and Analysis of RNA Crystals

5a. CONTRACT NUMBER

5b. GRANT NUMBER
NAG8-1165

5c. PROGRAM ELEMENT NUMBER

6. AUTHOR(S)
Paul Todd

5d. PROJECT NUMBER

5e. TASK NUMBER

5f. WORK UNIT NUMBER

7. PERFORMING ORGANIZATION NAME(S) AND ADDRESS(ES)
University of Colorado
Boulder, Colorado 80309

8. PERFORMING ORGANIZATION REPORT NUMBER

9. SPONSORING/MONITORING AGENCY NAME(S) AND ADDRESS(ES)
National Aeronautics and Space Administration
George C. Marshall Space Flight Center
Marshall Space Flight Center, AL 35812

10. SPONSOR/MONITOR'S ACRONYM(S)
NASA MSFC

11. SPONSORING/MONITORING AGENCY REPORT NUMBER

12. DISTRIBUTION AVAILABILITY STATEMENT
Available for distribution , NASA Center for Aerospace Information and from the author

13. SUPPLEMENTARY NOTES

14. ABSTR The crystallization of RNA was studied from the standpoint of mechanisms of crystal growth in three tasks: (1) preparation of high-quality crystals of oligonucleotides for x-ray diffraction, (2) finding pathways to the growth of high-qualilty crystals for x-ray diffraction and (3) investigation of mechanisms of action of inertial acceleration on crystal growth. In these tasks (1) RNA crystals were prepared and studied by x-ray diffraction; (2) a pathway to high-quality crystals was discovered and characterized; a combination of kinetic and equilibrium factors could be optimized as described below; (3) an interplay between purity and gravity was found in a combination of space and ground experiments with nucleic acids and proteins. Most significantly, the rate of concentration of precipitant and RNA can be controlled by membrane-based methods of water removal or by diffusion of multivalent cations across an interface stabilized by a membrane. Oligonucleotide solutions are electrokinetically stabilized colloids, and crystals can form by the controlled addition of multivalent cations.

15. SUBJECT TERMS
RNA, oligonucleotides, crystallization, crystal growth, low gravity, space shuttle, Mir space station, colloids, membranes, osmotic dewatering

16. SECURITY CLASSIFICATION OF:			17. LIMITATION OF ABSTRACT	18. NUMBER OF PAGES	19a. NAME OF RESPONSIBLE PERSON
a. REPORT	b. ABSTRACT	c. THIS PAGE		347	Paul Todd
					19b. TELEPONE NUMBER (Include area code) 812-923-9591 x242